

ABSTRACT

Title of Dissertation: “MEASUREMENTS AND CHARACTERIZATION OF
OPTICAL PROPERTIES IN THE CHESAPEAKE BAY’S
ESTUARINE WATERS USING IN-SITU MEASUREMENTS,
MODIS SATELLITE OBSERVATIONS, AND RADIATIVE
TRANSFER MODELING”

Maria Tzortziou, Doctor of Philosophy, 2004

Dissertation directed by: Professor Robert Hudson,
Department of Meteorology.
Dr Jay Herman
NASA, Goddard Space Flight Center.

The core subject of this thesis is the development of coordinated atmospheric, in-water, and laboratory measurements leading to characterization of in-water optical properties in the estuarine environment of northern Chesapeake Bay, where natural and human-induced processes strongly interact. One of the main objectives is obtaining a sufficiently complete suite of measurements, combined with detailed radiative transfer calculations, so as to produce a closure experiment for the underwater inherent and apparent optical properties. The in-situ results are applied to the interpretation of satellite (MODIS) water leaving radiance data and their validation. The applicability of bio-optical models and

parameterizations currently used in satellite algorithms are examined for the case of the optically complex Chesapeake Bay waters. Relationships between remotely sensed water leaving radiances and properties of optically active components in these waters are investigated. The resulting techniques and analysis should be broadly applicable to other coastal areas of the world. The results from this thesis, and other future work, will contribute to our ability to obtain more accurate information from remotely measured optical characteristics of estuarine and coastal regions. The combined use of in-situ measurements and detailed radiative transfer modeling enables the improvement of both the theoretical models and satellite remote sensing algorithms needed to a better understanding of biotic responses to environmental forcing.

“MEASUREMENTS AND CHARACTERIZATION OF OPTICAL PROPERTIES
IN THE CHESAPEAKE BAY’S ESTUARINE WATERS
USING IN-SITU MEASUREMENTS, MODIS SATELLITE OBSERVATIONS,
AND RADIATIVE TRANSFER MODELING”

by

Maria Tzortziou

Dissertation submitted to the Faculty of the Graduate School of the
University of Maryland, College Park in partial fulfillment
of the requirements for the degree of
Doctor of Philosophy
2004

Advisory Committee:

Professor Robert Hudson, Chair
Professor Neil Blough
Professor Anthony Busalacchi
Professor James Carton
Dr. Chuck Gallegos
Dr. Jay Herman
Dr. Patrick Neale

To my parents,
who taught me, from early on,
that it's all about having fun following your dreams

ACKNOWLEDGEMENTS

This work was funded by NASA-Goddard Space Flight Center, the University of Maryland, and the Smithsonian Pre-doctoral Fellowship program. Field work in Chesapeake Bay was funded in part by the Coastal Intensive Site Network (CISNet) program of the United States Environmental Protection Agency through grant R826943-01-0. I gratefully acknowledge this support.

I would like to thank my professors, Dr Christos Zerefos, Dr James Carton, Dr Robert Ellingson, Dr Da-Lin Zhang, Dr Kenneth Pickering, Dr Rachel Pinker, for introducing me to atmospheric science and oceanography and making research in this field seem so exciting.

I am extremely thankful to Dr Patrick Neale and Dr Chuck Gallegos, my advisors at SERC, who taught me how to work in the field and at the lab, and offered their help and support continuously since the first day of this project. I would not have been able to enjoy the experience of taking measurements in the Bay, if it wasn't for them. I also want to thank the crew of the boat, Karen Yee, Derrick Sparks, Mike Mallonee and our captain Sam Benson, for their assistance in the field and at the lab, and for making each cruise so much fun.

I thank the members of my committee for all the meetings we had, for following closely my progress, for all their constructive comments and their support. I am extremely grateful to Dr Ajit Subramaniam, for all the hours we spent discussing remote

sensing issues, for all his comments, his endless support and for all his help towards gaining a better understanding of remote sensing in coastal regions.

I feel I do not have enough words to express how thankful I am to my advisors, Dr Jay Herman, from NASA-Goddard, and Dr Robert Hudson, from the University of Maryland. They offered me so generously a perfect working environment at Goddard, support, and help whenever I needed it. I feel so lucky for just having the opportunity to work with them and learn from them, during my studies.

Finally I would like to thank my parents Eleni and Stergios, as well as Victoria and Tasos, and all of my friends, for always being by my side, and for frequently reminding me, that it's all about enjoying this journey.

TABLE OF CONTENTS

	page
LIST OF TABLES.....	viii
LIST OF FIGURES.....	xi
 CHAPTER 1: “General Introduction”	
1.1 Outline of the Thesis	1
1.2 Why I am particularly interested on Coastal Environments.....	6
1.3 Chesapeake Bay.....	10
1.4 Classification of ocean waters.....	17
1.5 Optical properties of natural waters.....	21
1.5.1 Composition of natural waters.....	21
1.5.2 Optical characteristics of pure sea-water. Absorption and scattering.....	26
1.5.3 Absorption characteristics of phytoplankton.....	35
1.5.4 Absorption by non-pigmented particulate matter.....	41
1.5.5 Scattering by particles.....	44
1.5.6 Optical properties of chromophoric dissolved organic matter	49
 CHAPTER 2: “Field Observations of Optical Properties in the Chesapeake Bay estuarine waters ”	
2.1 Introduction.....	54
2.2 Methodology	
2.2.1 Location and duration of measurements.....	55
2.2.2 Theory on instrumentation used.....	57
2.2.2.1 Measurements of absorption and attenuation using the AC9 instrument.....	60
2.2.2.2 Spectrophotometric measurements of absorption characteristics by particulate and dissolved material.....	64
2.2.2.3 Amplification factor β , and particulate absorption at NIR wavelengths.....	67
2.2.2.4 Measurements of backscattering using the ECO-VSF instrument.....	76
2.2.2.5 Measurements of underwater radiation fields.....	78
2.2.2.6 Self Shading Correction.....	81
2.3 Results	
2.3.1. Temperature and Salinity.....	85
2.3.2 Total absorption and attenuation.....	91
2.3.3 Total backscattering.....	103
2.3.4 Absorption spectra by non-pigmented particulates, phytoplankton, CDOM	
2.3.4.1 Particulate non-pigmented absorption.....	108
2.3.4.2 Particulate pigmented (phytoplankton) absorption.....	113
2.3.4.3 Chromophoric Dissolved Organic Matter absorption spectra.....	117
2.3.4.4 Contribution to total a_{t-w} absorption.....	125

2.4 Discussion.....	131
2.5 Summary and Conclusions.....	147
CHAPTER 3: “Model estimations of underwater radiation fields and water-leaving radiances in the Chesapeake Bay – Closure Experiment”	
3.1 Introduction – Background.....	150
3.2 Hydrolight Model	
3.2.1 Description of the model – Input data needed and assumptions.....	152
3.2.2 Hydrolight Sensitivity Studies	
3.2.2.1 Changes in downwelling irradiance E_s	159
3.2.2.2 Absorption at 715 nm.....	162
3.2.2.3 Scattering phase function.....	168
3.2.2.4 Variations in measured backscattering coefficient, b_b	172
3.2.2.5 Variation in measured underwater absorption and attenuation.....	174
3.2.2.6 Inelastic Scattering processes.....	177
3.2.2.7 Changes in percent cloud cover.....	188
3.2.2.8 Changes in surface wind speed, u (m/s).....	191
3.3 “Closure” Experiment in the Chesapeake Bay waters - Methodology	
3.3.1 Radiative Transfer Model Calculations using Hydrolight.....	194
3.3.2 In-situ measurements of underwater and water-leaving radiances	196
3.4 “Closure” Experiment in the Chesapeake Bay waters – Results.....	202
3.5 Discussion.....	215
3.6 Summary - Conclusions.....	229
CHAPTER 4: “Observations of Remote Sensing Reflectance in the Chesapeake Bay, using the MODIS/Terra satellite instrument and in-situ measurements”	
4.1 Remote Sensing in Ocean studies.....	232
4.1.1 Brief description of the MODIS instrument.....	235
4.1.2 MODIS measurements of water-leaving radiance and atmospheric correction algorithm.....	241
4.2 In-situ measurements and Satellite (MODIS) estimates of Remote Sensing Reflectance – Methodology	
4.2.1 In-situ measurements and theoretical estimations of Remote Sensing Reflectance	247
4.2.2 Satellite pixels around the location of each station.....	249
4.2.3 Satellite Observations of Remote Sensing Reflectance.....	250
4.3 MODIS and in-situ measurements of Remote Sensing Reflectance – Results.....	256
4.4 MODIS and in-situ measurements of Remote Sensing Reflectance – Discussion and Conclusions.....	284
CHAPTER 5: “In-situ and satellite measurements of Remote Sensing Reflectance and their relation to chl-a concentration and in-water optical properties”	
5.1 Introduction.....	298
5.2 Methodology	
5.2.1 In-situ measurements of chl-a concentration.....	303

5.2.2. MODIS chl-a algorithms, bio-optical models and empirical relationships.....	304
5.2.2.1 Chlorophyll-a concentration, HPLC – Empirical MODIS algorithm.....	304
5.2.2.2 MODIS OC3M - SeaWiFS analog chl-a algorithm.....	306
5.2.2.3 MODIS Semianalytic chl-a algorithm , Case 2 waters.....	307
5.3 Results	
5.3.1 In situ measurements of chlorophyll concentration in the Chesapeake Bay waters.....	312
5.3.2 Comparisons between in-situ and MODIS chlorophyll concentration measurements.....	318
5.3.3 Relationships between chlorophyll concentration and Remote Sensing Reflectance in the Bay waters.....	323
5.3.4 Relationships between Remote Sensing Reflectance, total absorption and backscattering.....	326
5.3.5 Relationships between Remote Sensing Reflectance, total backscattering and absorption by non-pigmented particulate matter.....	329
5.4 Discussion and Conclusions	
5.4.1 In-situ Measurements of [Chl-a] in the Chesapeake Bay waters.....	334
5.4.2 MODIS measurements of [Chl-a] and quality of MODIS nLw, Rrs values.....	337
5.4.3 Relationships between [Chl-a] and Rrs in the Chesapeake Bay waters.....	340
5.4.4 Rrs and total absorption and backscattering in the Chesapeake Bay waters.....	349
5.4.5 Backscattering and Remote Sensing Reflectance in Chesapeake Bay.....	350
CHAPTER 6: “Summary and Conclusions”.....	355
APPENDIX.....	370
NOTATION.....	382
REFERENCES.....	384

LIST OF TABLES

	page
CHAPTER 1:	
Table 1.3-1: Chesapeake Bay physical characteristics.....	10
Table 1.5-1: Absorption maxima by chlorophyll, carotenoids and biliproteins phytoplankton pigments.....	38
CHAPTER 2:	
Table 2.2-1: Dates of cruises in Chesapeake Bay.....	56
Table 2.2-2: In- water and above-water measurements performed in the Chesapeake Bay-Instrumentation.....	59
Table 2.3-1: Range in absorption values at 412 nm, as measured during the spring, summer, early and late fall cruises.....	99
Table 2.3-2: Range in absorption values at 676 nm, as measured during the spring, summer, early and late fall cruises.....	100
Table 2.3-3: Range in attenuation values at 412 nm, as measured during the spring, summer, early and late fall cruises.....	101
Table 2.3-4: Range in attenuation values at 676 nm, as measured during the spring, summer, early and late fall cruises.....	102
Table 2.3-5: Minimum, maximum and average b_b/b values measured at 450, 530 and 650 nm during the 2001-2002 cruises in the northern Chesapeake Bay.....	106
Table 2.3-6: Average normalized spectra, $a_{npp}(\lambda)/a_{npp}(440)$, measured at HB, JT, PI and TI stations, (412-715 nm) along with the standard deviations (stdev).....	109
Table 2.3-7: Values of S_{npp} , A and R^2 corresponding to eq.(2.3-1) for absorption by non-pigmented particulate matter at HB, JT, PI and TI stations (exponential fits shown in fig. 2.3-9(A)).....	112
Table 2.3-8: Average normalized spectra, $a_{phyt}(\lambda)/a_{phyt}(676)$, measured at HB, JT, PI and TI stations, (412-715 nm) along with the standard deviations (stdev).....	113
Table 2.3-9: Minimum, maximum and average $a_{CDOM}(440)$ values measured at the four stations HB, JT, PI and TI during the 2001-2002 cruises in the northern Chesapeake Bay.....	120
Table 2.3-10(a): Minimum, maximum and average $a_{CDOM}(440)$ and S_{CDOM} values (estimated after applying an exponential fit to a_{CDOM} measurements in the wavelength region 400-700 nm), at the four stations HB, JT, PI and TI.....	123
Table 2.3-10(b): Minimum, maximum and average $a_{CDOM}(440)$ and S_{CDOM} values (estimated after applying an exponential fit to a_{CDOM} measurements in the wavelength region 290-700 nm), at the four stations HB, JT, PI and TI.....	123
Table 2.3-11(a): Average percent contribution of a_{phyt} , a_{npp} , a_{CDOM} to a_{t-w} , along with the (stdev) standard deviation values. Only water samples from 0-1m depths were examined.....	127
Table 2.3-11(b): Average percent contribution of a_{phyt} , a_{npp} , a_{CDOM} to a_{t-w} , along with the (stdev) standard deviation values. Only water samples from 5m depth were	

examined.....	127
Table 2.5-1: Chapter 2 - Significant points.....	148
 CHAPTER 3:	
Table 3.2-1: Hydrolight Model characteristics and assumptions.....	154
Table 3.3-1: Dates of cruises in the Bay, and instrumentation for measurements of radiation fields.....	196
Table 3.4-1: Percent differences in estimated upwelling radiances, L_u , at depth = 1 m, and various wavelengths (412-685 nm) using in-situ measurements and model simulations (negative values correspond to $L_{u(\text{InSitu})}$ estimates smaller than the Hydrolight estimated $L_{u(\text{model})}$).....	204
Table 3.4-2: Percent differences in estimated downwelling irradiances, E_d , at depth = 1 m, and various wavelengths (412-685 nm) using in-situ measurements and model simulations (negative values correspond to $E_{d(\text{InSitu})}$ estimates smaller than the Hydrolight estimated $E_{d(\text{model})}$).....	204
Table 3.4-3: Percent differences in estimated water leaving radiances, L_w , at various wavelengths (412-685 nm) using in-situ measurements and model simulations (negative values correspond to $L_{w(\text{InSitu})}$ estimates smaller than the Hydrolight estimated $L_{w(\text{model})}$).....	205
Table 3.5-1: Range of values (min-max) of IOPs for which Hydrolight simulations were performed in the Chesapeake Bay waters.....	227
Table 3.5-2: Range of atmospheric and air-water surface boundary conditions for which Hydrolight simulations were performed in the Chesapeake Bay waters.....	227
Table 3.6-1: Chapter 3 – Conclusion and Significant Points.....	230
 CHAPTER 4:	
Table 4.1-1: MODIS Data Levels.....	237
Table 4.1-2: MODIS 36 spectral bands and their primary use (information from MODIS website, MODIS Technical specifications).....	238
Table 4.1-3: MODIS Ocean product parameters (numbers 1-40) (MODIS Ocean User’s Guide).....	239
Table 4.1-4: MODIS Ocean Quality Control (QC) parameters (1 km) (parameter numbers 41-78) (information obtained from MODIS Ocean User’s Guide).....	240
Table 4.1-5: MODIS Level 4 Ocean Primary Productivity products (information obtained from MODIS Ocean User’s Guide).....	240
Table 4.2-1: Cruise Summary and Instrumentation.....	248
Table 4.2-2: MODIS overpasses during the dates of the cruises.....	251
Table 4.2-3: MODIS ‘common’ and ‘product specific’ flags (from ‘productflags.V4.html’, K. Kilpatrick, 2003, MODIS website).....	255
Table 4.2-4: Level 2 Quality-Level Flags (Terra Collection 4) for nLw	

parameters (from “L2QLflags.V4.html” K. Kilpatrick, 2003, MODIS website).....	255
Table 4.3-1: Quality of in-situ measurements and satellite pixels. Measurements performed in the Chesapeake Bay during June-November 2001 (yellow background for those days when MicroPro instrument was used).....	271
Table 4.3-1 (continued): Measurements performed in the Chesapeake Bay during May-November 2002.....	272
Table 4.3-2: Number of MODIS pixels with nLw = 0 at some of the wavelength bands (“total pixels” in the third column is the total number of pixels with positive nLw values at more than one wavelength bands. Only the pixels with positive nLw values at more than one wavelength have been examined).....	273
Table 4.3-3 (a): “closest” pixel	281
Table 4.3-3 (b): “best” pixel	281
Table 4.3-4 (a): clearest days.....	282
Table 4.3-4 (b): days with large AOT.....	282
Table 4.3-5(a): TI station.....	283
Table 4.3-5(b): PI station.....	283
Table 4.3-5(c): HB station.....	283
Table 4.3-5(d): JT station.....	283
Table 4.4-1:Chapter 4 – Significant points and Conclusions.....	296
 CHAPTER 5:	
Table 5.2-1: MODIS chlorophyll algorithms. Significant points.....	311
Table 5.2-2: Summary of MODIS empirical chl-a algorithms.....	311
Table 5.4-1:Chapter 5 – Conclusions and Significant points.....	353

LIST OF FIGURES

	page
CHAPTER 1:	
Figure 1.2-1: The high percentage of human population living along the world's coastlines is revealed in this composite satellite view of Earth at night (courtesy NASA).....	6
Figure 1.3-1: The Mid-Atlantic coast of the United States and the Chesapeake Bay (Ellison and Nichols, 1975).....	11
Figure 1.4-1: Downwelling Irradiance Diffuse Attenuation Coefficient, $K_d(\lambda)$, used to define the Jerlov water types (by Austin and Petzold, 1986).....	20
Figure 1.5-1: Absorption coefficients for pure seawater as determined by Smith and Baker (1981).....	28
Figure 1.5-2: Spectral absorption coefficients for sea water (380 nm- 620 nm) as determined by Pope and Fry (1997) and by Smith and Baker (1981).....	30
Figure 1.5-3. Absorption by pure water as measured by Pope and Fry (1997) in the wavelength region 380-700nm, and Quickenden and Irvin (1980) at 280-320 nm....	31
Figure 1.5-4: Volume Scattering function for pure water and pure sea water, for $\lambda=500$ nm	33
Figure 1.5-5 Smith and Baker scattering coefficients for pure sea-water.....	34
Figure 1.5-6: Basic structure of a chlorophyll molecule. For chl-a, R = -CH ₃ , while for chl-b, R = -CHO (Kirk, 1994).....	37
Figure 1.5-7: Absorption by chl-a and chl-b, in diethyl ether at a concentration of 10 μ g/ml and 1 cm pathlength. After Kirk (1994), using data by French (1960). (chl-a: solid line, chl-b: dashed line).....	38
Figure 1.5-8: Absorption by chl-c ₁ and chl-c ₂ , in acetone containing 2% pyridine with a pathlength of 1cm. After Kirk (1994), using data by Jeffrey S.W. (chl-c ₁ (2.68 μ g/ml): solid line, chl-c ₂ (2.74 μ g/ml): dashed line).....	38
Figure 1.5-9: Chl-specific absorption spectrum of eight phytoplankton species based on laboratory measurements (Sathyendranath et al., 1987).....	40
Figure 1.5-10: Absorption spectra of detrital material, a_d , measured by Bricaud and Stramski (1990) at various depths (5-250 m) in the Sargasso Sea (figure by Bricaud and Stramski, 1990).....	43
Figure 1.5-11: Absorption spectra of suspended particles, total particulate material, a_p , non-pigmented particulate matter, here shown as a_d , and the difference $a_p - a_d = a_{ph}$, which corresponds to absorption by pigmented, phytoplankton particles (figure obtained by Kishino et al., 1986).....	43
Figure 1.5-12: Particle volume scattering functions $\beta_p(\psi, \lambda)$ determined from in-situ measurements in a variety of waters, for various wavelengths (Kullenberg, 1974).....	46
Figure 1.5-13: Absorption spectra of chromophoric dissolved organic material, $a_g(\lambda)$, ("g" for gelbstoff) as measured by Roesler et al (1989) at San Juan Islands.....	51

CHAPTER 2:

Figure 2.2-1: Location of in-situ measurements (HB, PI , TI and JT stations)..... 55

Figure 2.2-2: The AC9 instrument (far right in the picture), the Hydrolab (white instrument in the middle) and the ECO-VSF instrument (far left) that were used during one of our cruises in the Chesapeake Bay..... 58

Figure 2.2-3: A diagram of the AC9. The absorption and attenuation beam paths and flow tubes are shown between the receiver and transmitter housings (from WETLabs AC9 User’s Guide, 2003)..... 60

Figure 2.2-4: Optical density of the particle-retaining filter (four replicates) and the estimated average OD_f 69

Figure 2.2-5: Optical density of CDOM (obtained by filtering the water sample through the 0.22 μm filters) placing the 1cm cuvette (a) at the entrance port of the integrating sphere and (b) inside the integrating sphere (measurements performed on 18 June 2003)..... 70

Figure 2.2-6: Relation between the optical densities of the non-scattering dissolved material measured outside and inside the integrating sphere (measurements performed on 18 June 2003)..... 71

Figure 2.2-7: Measurements of the particulate absorption, a_p , performed with the 1-cm cuvette inside and outside of the integrating sphere. A closer look at the 700-750 nm wavelength region (fig. 2.2-7(b)) shows positive absorption values measured below 730 nm both inside and outside of the sphere..... 72

Figure 2.2-8: Values of the β amplification factor, estimated (for the specific set of measurements performed on 18 June 2003) by comparing the optical density values in particle suspension and on filters..... 73

Figure 2.2-9: Values of the β amplification factor, estimated, for measurements performed on 15 July 2003, by comparing particulate absorption values measured in particle suspensions and on glass-fiber filters..... 74

Figure 2.2-10: Relation between particulate absorption measured on filters and in particle suspensions. The lines $\beta=1.5$ (solid thin line), $\beta=2$ (dashed thick line) and the linear least-squares fit (solid thick line) are also shown..... 75

Figure 2.2-11: Optical configuration of ECO-VSF 3 (from ECO-VSF 3 User’s Guide, 14 April 2003)..... 76

Figure 2.2-12: MicroPro instrument, free fall profiling deployment. The four optical sensors (two radiance and two irradiance OCR-507 sensors) are located at the top of the instrument’s body..... 79

Figure 2.2-13: The self-shading correction factor, $\frac{Lu_{true}}{Lu_{meas}} = \frac{1}{1 - e_{ss}}$, was estimated for the MicroPro instrument, as a function of wavelength: (a) for $\theta_o=40^\circ$, the mean ratio E_{diff}/E_{dir} (J.O. Reilly , 1999) and for the four total absorption spectra shown in fig. 2.2-13b, (c) for the total absorption measured at PI station on 28 September 2001 ($a_t(676)=0.64\text{m}^{-1}$), the mean ratio E_{diff}/E_{dir} (J.O. Reilly , 1999), and for $\theta_o = 30^\circ, 40^\circ, 50^\circ, 60^\circ$, (d) for the total absorption measured at PI station on 28 September 2001 ($a_t(676) = 0.64\text{m}^{-1}$), for $\theta_o = 40^\circ$ and for the three different measurements of the ratio E_{diff}/E_{dir} (provided by J.O. Reilly, 1999)..... 84

Figure 2.3-1: (A) Seasonal variation of temperature (in °C) as measured during the cruises performed in the northern part of the mainstream of Chesapeake Bay (blue pixels correspond to measurements performed in summer and fall 2001, red pixels correspond to measurements performed in 2002). (B) Profiles of temperature (in °C) measured at the four stations HB (blue), JT (red), PI (yellow), TI (green) during the fall 2001 cruises: a) 26 Sept. b) 28 Sept. c) 4 Oct. d) 30 Oct. e) 13 Nov., and during the spring and summer cruises in 2002: f) 6 May g) 15 May h) 22 May i) 6 June j) 18 June k) 28 June..... 88

Figure 2.3-2: (A) Seasonal variation of salinity (in ppt) as measured during the cruises performed in the northern part of the mainstream of Chesapeake Bay (blue pixels correspond to measurements performed in summer and fall 2001, red pixels correspond to measurements performed in 2002). (B) Profiles of salinity (in ppt) measured at the four stations HB (blue), JT (red), PI (yellow), TI (green) during the fall 2001 cruises: a) 26 Sept. b) 28 Sept. c) 4 Oct. d) 30 Oct. e) 13 Nov., and during the spring and summer cruises in 2002: f) 6 May g) 15 May h) 22 May i) 6 June j) 18 June k) 28 June..... 89

Figure 2.3-3: Daily total rainfall amount (in inches) recorded at the SERC site, during the years 2001 and 2002. The dates of the seventeen cruises performed in the northern part of the Chesapeake Bay, are also shown as red lines..... 90

Figure 2.3-4(a): Profiles of $a_{t-w}(412)$ (in m^{-1}) measured at the HB, JT, PI and TI stations, during the spring, summer, early and late fall cruises of 2001 and 2002..... 94

Figure 2.3-4(b): Profiles of $a_{t-w}(676)$ (in m^{-1}) measured at the HB, JT, PI and TI stations, during the spring, summer, early and late fall cruises of 2001 and 2002..... 95

Figure 2.3-4(c): Profiles of $c_{t-w}(412)$ (in m^{-1}) measured at the HB, JT, PI and TI stations, during the spring, summer, early and late fall cruises of 2001 and 2002..... 96

Figure 2.3-4(d): Profiles of $c_{t-w}(676)$ (in m^{-1}) measured at the HB, JT, PI and TI stations, during the spring, summer, early and late fall cruises of 2001 and 2002..... 97

Figure 2.3-5: Average values of $a_{t-w}(412)$, $a_{t-w}(676)$, $c_{t-w}(412)$ and $c_{t-w}(676)$, along with the standard deviations (x-axis error-bars), for each 'season'(spring, summer, early, late fall), at HB (blue pixels), JT (red pixels), PI (yellow pixels), TI (green pixels) stations..... 98

Figure 2.3-6: Profiles of $b_b(530)$ (in m^{-1}) measured at the HB, JT, PI and TI stations, during the spring, summer, early and late fall cruises of 2001 and 2002..... 104

Figure 2.3-7: Temporal variation in surface (0-1m) total backscattering values at 530 nm, $b_b(530)$, measured at HB, JT, PI and TI stations..... 105

Figure 2.3-8: Backscattering fraction, b_b/b , measured (a) at various depths in the water column (0-9m) and (b) only within the 3 meters below the water surface, at the stations HB, JT, PI and TI, during the 2001-2002 cruises in the Chesapeake Bay. (HB station: blue diamonds, JT station: red squares, PI station: yellow triangles, JT station: white circles). The two largest b_b/b values, $b_b/b = 0.026$ and $b_b/b = 0.036$ (shown in (a)) were measured at JT station on 9 July 2001, at depths 4.9 and 5.4 m respectively, close to the bottom of the water column at JT station during that cruise..... 107

Figure 2.3-9(A): Normalized spectra, $a_{npp}(\lambda)/a_{npp}(440)$, measured at (a) HB (b) JT (c) PI and (d) TI stations (400-715nm). The average normalized spectra along

with the standard deviations and the non-linear exponential fit, are shown in figures (e), (f) (g) (h).....	110
Figure 2.3-9(B): Normalized spectra, $a_{npp}(\lambda)/a_{npp}(440)$, measured at (a) HB (b) JT (c) PI and (d) TI stations (300-750nm). The average normalized spectra along with the standard deviations, are shown in figures (e), (f) (g) (h) for each station...	111
Figure 2.3-10: Temporal variation in $a_{npp}(440)$ measured at the four stations HB (blue circles), JT (red squares), PI (yellow triangles), TI (white circles), during the 2001 and 2002 cruises in the Bay.....	112
Figure 2.3-11(A): Normalized spectra, $a_{phyt}(\lambda)/a_{phyt}(676)$, measured at (a) HB (b) JT (c) PI and (d) TI stations (300-750 nm). The average normalized spectra along with the standard deviations are shown in figures (e), (f) (g) (h) for each station.....	114
Figure 2.3-11(B): Normalized spectra, $a_{phyt}(\lambda)/a_{phyt}(676)$, measured at HB, JT, PI and TI stations during the fall 2001 (a,b,c,d) and also during the spring and summer 2001-2002 (e,f,g,h) cruises when strong absorption by MAAs was evident in the UV wavelengths.....	115
Figure 2.3-12: Temporal variation in $a_{phyt}(676)$ measured at the four stations HB (blue circles), JT (red squares), PI (yellow triangles), TI (white circles), during the 2001 and 2002 cruises in the Bay.....	116
Figure 2.3-13(A): Normalized spectra, $a_{CDOM}(\lambda)/a_{CDOM}(440)$, measured at (a) HB (b) JT (c) PI and (d) TI stations (400-715 nm). The average normalized spectra along with the standard deviations are shown in figures (e), (f) (g) (h) for each station.....	118
Figure 2.3-13(B): Normalized spectra, $a_{CDOM}(\lambda)/a_{CDOM}(440)$, measured at (a) HB (b) JT (c) PI and (d) TI stations (300-750 nm). The average normalized spectra along with the standard deviations are shown in figures (e), (f) (g) (h) for each station.....	119
Figure 2.3-14: Measurements of $a_{CDOM}(440)$ performed at the four stations, HB (blue pixels), JT (red squares), PI (yellow triangles) and TI (white circles).....	120
Figure 2.3-15: Comparison between S_{CDOM} values obtained when applying a non-linear exponential fit to measured $a_{CDOM}(\lambda)$ values in the wavelength regions 290-700 and 400-700 nm.....	122
Figure 2.3-16: Comparison between the measured and fitted a_{CDOM} values at the visible wavelengths 443, 488 and 555 nm, for the two cases when the non-linear exponential fit was applied to a_{CDOM} measurements i) in the 290-700 nm wavelength region (blue pixels) and ii) in the visible wavelengths 400-700nm (white pixels).....	122
Figure 2.3-17: Average values of the residuals $a_{CDOM}(\lambda)_{measured} - a_{CDOM}(\lambda)_{fitted}$, at several visible wavelengths, along with the estimated standard deviations, for the two cases when the non-linear exponential fit was applied to measurements (a) in the 290-700 nm wavelength region and (b) in the visible wavelengths 400-700nm...	123
Figure 2.3-18: Relationship between (a) $a_{CDOM}(440)$ (m^{-1}) and $S_{CDOM(400-700nm)}$ (nm^{-1}), (b) $a_{CDOM}(440)$ (in m^{-1}) and $S_{CDOM(290-700nm)}$ (in nm^{-1}), for measurements performed at HB, JT, PI and TI stations.....	124

Figure 2.3-19: Relationship (a) between $a_{CDOM(440)}$ (m^{-1}) and salinity (in ppt) (blue circles) and $S_{CDOM(400-700nm)}$ (nm^{-1}) and salinity (white circles), (b) between $a_{CDOM(340)}$ (m^{-1}) and salinity (in ppt) (blue circles) and $S_{CDOM(290-700nm)}$ (nm^{-1}) and salinity (white circles), for measurements performed at HB, JT, PI and TI stations... 124

Figure 2.3-20: Average percent contribution of phytoplankton (graph at the top) non-pigmented particulate matter (at the middle) and CDOM (at the bottom) to total (minus pure water) absorption, a_{t-w} , along with the ± 1 standard deviation ($n=136$). Results are shown at the nine wavelengths 412, 443, 488, 510, 532, 555, 650, 676 and 715 nm..... 126

Figure 2.3-21: Average percent contribution of phytoplankton (graph at the top), non-pigmented particulate matter (graph at the middle) and CDOM (graph at the bottom) to total (minus pure water) absorption, a_{t-w} , at the four stations HB (blue pixels), JT (blue squares), PI (white triangles) and TI (white squares). Results are shown at the nine wavelengths 412, 443, 488, 510, 532, 555, 650, 676 and 715 nm. Standard deviations are not shown (in order to be easier to separate the various symbols), but are similar to those shown in figure 2.3-20..... 128

Figure 2.3-22: Relationship between $a_{npp(440)}$ and $a_{phyt(676)}$ measured at (a) HB (b) JT (c) PI and (d) TI station..... 129

Figure 2.3-23: Relationship between $a_{CDOM(440)}$ and $a_{phyt(676)}$ measured at (a) HB (b) JT (c) PI and (d) TI station..... 130

Figure 2.4-1: Decrease in salinity (in psu) measured at the SERC dock (black line) and at the mouth of the Rhode River sub-estuary (red line), probably associated with a spike in flow from the Susquehanna River about 2 weeks earlier (Gallegos, personal communication)..... 142

CHAPTER 3:

Figure 3.2.2.1: Average downwelling surface irradiance, $E_{s,avg}(\lambda)$, measured at PI station on 28 September 2001, bracketed by the lines of $\pm 3\%$, MicroPro irradiance sensors' accuracy..... 161

Figure 3.2.2.2: Percent change in (a) $Ed(z)$ and (b) $Lu(z)$, estimated at depths $z = 0, 1, 2, 3, 4, 5, 6m$, according to: $\frac{Ed_{(Es=Es_{avg} \pm 3\%)} - Ed_{(Es=Es_{avg})}}{Ed_{(Es=Es_{avg})}}$ (similarly for Lu).... 161

Figure 3.2.2.3: Percent change in (a) Lw and (b) Rrs estimated according to: $\frac{Lw_{(Es=Es_{avg} \pm 3\%)} - Lw_{(Es=Es_{avg})}}{Lw_{(Es=Es_{avg})}}$ (similarly for Rrs)..... 161

Figure 3.2.2.4: Percent differences of (a) the total minus the water absorption, a_{t-w} and (b) the total absorption, $a_t = a_w + a_{PA} + a_{CDOM}$, between case-1 (assumption that $a_{t-w}(715) = 0$) and case-2 ($a_{t-w}(715) = [(a_{PA}(715) / \beta) + a_{CDOM}(715)]$ for $\beta=2$), and between case-1 and case-3 ($a_{t-w}(715) = [(a_{PA}(715) / \beta) + a_{CDOM}(715)]$ for $\beta=1$)..... 164

Figure 3.2.2.5: Percent differences in $Ed(\lambda)$, between (a) case-1 and case-2 and

(b) case-1 and case-3, estimated as $\frac{Ed_{(case2_or_case3)} - Ed_{(case1)}}{Ed_{(case1)}}$, for various depths	
(0-6m)	166
Figure 3.2.2.6: Percent differences in $Lu(\lambda)$, between (a) case-1 and case-2 and	
(b) case-1 and case-3, estimated as $\frac{Lu_{(case2_or_case3)} - Lu_{(case1)}}{Lu_{(case1)}}$, for various depths	
(0-6m).....	166
Figure 3.2.2.7: Percent differences in (a) Lw and (b) Rrs estimated according	
to: $\frac{Lw_{(case2_or_case3)} - Lw_{(case1)}}{Lw_{(case1)}}$ (similarly for Rrs).....	167
Figure 3.2.2.8: (a) Lw and (b) Rrs spectra estimated for cases 1, 2, 3. Low Ed and Lu values in the blue and red wavelengths are due to the high absorption by CDOM and non-pigmented particulate matter (blue wavelength region) and by pure sea-water (red region). The maximum in Lu at ~ 685 nm is due to the chlorophyll fluorescence.....	167
Figure 3.2.2.9: Measurements of b_b/b , performed at depths 0-6 m, at PI station, on 28 September 2001, using an ECOVSF instrument (to measure backscattering, b_b , at 450, 530 and 650 nm) and an AC9 instrument (to measure scattering, b_{t-w} , at seven wavelengths in the region 412-715 nm).....	169
Figure 3.2.2.10: Estimated b_b/b using (a) the ‘average particle’ Petzold phase function ($b_b/b=1.83\%$) and (b) a Fournier-Forand phase function with $b_b/b=1.5\%$...	169
Figure 3.2.2.11: (a) $Ed(z=5m)$ and (b) $Lu(z=0^-)$ spectra estimated using the three different b_b/b ratios.....	170
Figure 3.2.2.12: Percent differences in $Ed(z)$ (depths 0-5m) estimated between (a) case 3 ($b_b/b=0.015$) and case 1 (b_b/b measured using ECOVSF) and (b) case 2 (b_b/b Petzold “average particle”) and case 1 (b_b/b measured using ECOVSF). The percent differences were estimated according to: $\frac{Ed_{(case3_or_case2)} - Ed_{(case1)}}{Ed_{(case1)}}$	170
Figure 3.2.2.13: Percent differences in $Lu(z)$ (depths 0-5m) estimated between (a) case 3 ($b_b/b=0.015$) and case 1 (b_b/b measured using ECOVSF) and (b) case 2 (b_b/b Petzold “average particle”) and case 1 (b_b/b measured using ECOVSF) . The percent differences were estimated according to: $\frac{Lu_{(case3_or_case2)} - Lu_{(case1)}}{Lu_{(case1)}}$	170
Figure 3.2.2.14: (a) Rrs spectra estimated using the three different b_b/b ratios and (b) percent differences in Rrs between cases 2 and case 1 (solid line) and case 3 and case 1 (dotted line).....	171
Figure 3.2.2-15: Percent differences in (a) $Ed(z)$ (depths 0-5m) and (b) $Lu(z)$ (depths 0-5m), estimated between running Hydrolight with $b_b = b_{b\ avg}$ and $b_b = b_{b\ avg} + \text{standard-error}$ (dotted lines) and between running Hydrolight with $b_b = b_{b\ avg}$ and $b_b = b_{b\ avg} - \text{standard-error}$ (solid lines). The percent differences were	

estimated for Ed (and similarly for Lu) according to: $\frac{Ed_{(bb_{avg} \pm sterror)} - Ed_{(bb_{avg})}}{Ed_{(bb_{avg})}}$ 173

Figure 3.2.2-16: (a) Rrs spectra and (b) percent differences in Rrs , estimated between running Hydrolight with $b_b = b_{b\ avg}$ and $b_b = b_{b\ avg} + \text{standard-error}$ (dotted lines) and between running Hydrolight with $b_b = b_{b\ avg}$ and $b_b = b_{b\ avg} - \text{standard-error}$ (solid lines). The percent differences were estimated

according to: $\frac{Rrs_{(bb_{avg} \pm sterror)} - Rrs_{(bb_{avg})}}{Rrs_{(bb_{avg})}}$ 173

Figure 3.2.2-17: Percent change in (a) $Ed(z)$ and (b) $Lu(z)$, estimated at depths $z = 0, 1, 2, 3, 4, 5m$, according to: $\frac{Ed_{(a=a_{mean} \pm st.error)} - Ed_{(a=a_{mean})}}{Ed_{(a=a_{mean})}}$ and similarly for Lu .

As was expected increased absorption by the water medium results in lower Ed and Lu values in the water column..... 175

Figure 3.2.2-18: Percent change in (a) $Ed(z)$ and (b) $Lu(z)$, estimated at depths $z = 0, 1, 2, 3, 4$ and $5m$, according to: $\frac{Ed_{(c=c_{mean} \pm sterror)} - Ed_{(c=c_{mean})}}{Ed_{(c=c_{mean})}}$ (similarly for Lu).... 176

Figure 3.2.2-19: Percent changes in water leaving radiance, Lw , estimated for (a) changes in mean measured absorption, a , by \pm standard error and (b) changes in mean measured attenuation, c , by \pm standard error..... 176

Figure 3.2.2-20: Percent differences in the estimated by the model (a) $Ed(z)$ and (b) $Lu(z)$ values, between case 1 (chl-fluorescence included, for the measured chl- a concentration, $[Chl-a] = 7.25mg\ m^{-3}$) and case 2 (chl-fluorescence not included), and between case 1 and case 3 (chl- fluorescence included, for $[Chl-a] = 14.5\ mg\ m^{-3}$). The % differences were estimated as:

$\frac{Ed_{(no-Chl-fluor)} - Ed_{([Chl]=7.25)}}{Ed_{([Chl]=7.25)}}$, $\frac{Ed_{([Chl]=14.5)} - Ed_{([Chl]=7.25)}}{Ed_{([Chl]=7.25)}}$ (similarly for Lu)..... 179

Figure 3.2.2-21: Model estimations of (a) Rrs and (b) Lw , for case 1 (chl-fluorescence included, $[Chl-a]=7.25mg\ m^{-3}$) (solid line), for case 2 (chlorophyll fluorescence not included) (squares, dotted line), and case 3 (chlorophyll fluorescence included, $[Chl-a]=14.5mg\ m^{-3}$) (squares, solid line)..... 179

Figure 3.2.2-22: Percent differences in the model estimated (a) Rrs and (b) Lw values, between case 1 (chl-fluorescence included, for the measured $[Chl-a]$, $[Chl-a]=7.25mg\ m^{-3}$) and case 2 (chl-fluorescence not included), and between case 1 and case 3 (chlorophyll fluorescence included, for $[Chl-a] = 14.5\ mg\ m^{-3}$). Percent

differences were estimated as: $\frac{Rrs_{(no-Chl-fluor)} - Rrs_{([Chl]=7.25)}}{Rrs_{([Chl]=7.25)}}$ and

$\frac{Rrs_{([Chl]=14.5)} - Rrs_{([Chl]=7.25)}}{Rrs_{([Chl]=7.25)}}$ (similarly for Lw)..... 180

Figure 3.2.2-23: Percent differences in the estimated by the model (a) $Ed(z)$ and (b) $Lu(z)$ values, between case 1 and case 3 (positive % changes) and between case 2 and case 3 (negative % changes). The percent differences were estimated

according to: $\frac{Ed_{(case1_or_case2)} - Ed_{(case3)}}{Ed_{(case3)}}$ (similarly for Lu)..... 183

Figure 3.2.2-24: Percent differences in the model estimated Rrs and Lw values, between case 1 and case 3 (solid line) and between case 2 and case 3 (dotted line).

The percent differences were estimated as: $\frac{Rrs_{(case1_or_case2)} - Rrs_{(case3)}}{Rrs_{(case3)}}$

(similarly for Lw)..... 183

Figure 3.2.2-25: Percent differences in the model estimated (a) Ed(z) and (b) Lu(z), between case 1 (CDOM fluorescence included, for the measured CDOM absorption spectrum, $a_{CDOM}(440)=0.3m^{-1}$ and $S_{CDOM} = 0.019nm^{-1}$) and case 2 (CDOM fluorescence not included), and between case 1 and case 3 (CDOM fluorescence included, for $a_{CDOM}(440)=0.6m^{-1}$). The percent differences were

estimated according to: $\frac{Ed_{(no-CDOM-fluor)} - Ed_{(aCDOM=0.3)}}{Ed_{(aCDOM=0.3)}}$ and

$\frac{Ed_{(aCDOM=0.6)} - Ed_{(aCDOM=0.3)}}{Ed_{(aCDOM=0.3)}}$ (similarly for Lu)..... 185

Figure 3.2.2-26: Percent differences in the estimated by the model Rrs and Lw values, between case 1 (CDOM fluorescence effect included, for the measured CDOM absorption spectrum, $a_{CDOM}(440)=0.3m^{-1}$ and $S_{CDOM} = 0.019nm^{-1}$) and case 2 (CDOM fluorescence not included), and between case 1 and case 3 (CDOM fluorescence included, for $a_{CDOM}(440)=0.6m^{-1}$). The percent differences were

estimated as: $\frac{Rrs_{(no-CDOM-fluor)} - Rrs_{(aCDOM=0.3)}}{Rrs_{(aCDOM=0.3)}}$ and $\frac{Rrs_{(aCDOM=0.6)} - Rrs_{(aCDOM=0.3)}}{Rrs_{(aCDOM=0.3)}}$

(similarly for Lw)..... 185

Figure 3.2.2-27: Percent differences in the estimated by the model (a) Ed(z) and (b) Lu(z) values, between case 1 (Raman scattering included) and case 2 (Raman scattering not included), estimated as:

$\frac{Ed_{(no_Raman)} - Ed_{(Raman)}}{Ed_{(Raman)}}$ (similarly for Lu)

at depths 0-5m..... 187

Figure 3.2.2-28: Percent differences in the model calculated (a) Rrs and (b) Lw

values, estimated according to: $\frac{Rrs_{(no_Raman)} - Rrs_{(Raman)}}{Rrs_{(Raman)}}$ (similarly for Lw)..... 187

Figure 3.2.2-29: Percent difference in estimated Ed values (a) just below the water surface and (b) at 5 meters below the water surface, for clear skies (0% cloudiness) and cloud cover of 10, 30, 50, 80 and 100%. The percent differences

were estimated according to: $\frac{Ed_{(clouds)} - Ed_{(clear)}}{Ed_{(clear)}}$ (sza=20°)..... 189

Figure 3.2.2-30: Percent difference in estimated Lu values (a) just below the water surface and (b) at 5 meters below the water surface, for clear skies (0% cloudiness) and cloud cover of 10, 30, 50, 80 and 100%. The percent differences

were estimated according to: $\frac{Lu_{(clouds)} - Lu_{(clear)}}{Lu_{(clear)}} (sza=20^\circ)$ 189

Figure 3.2.2-31: Percent differences in estimated (a) Rrs (sza=52°), (b) Lw (sza=52°), (c) Rrs (sza=20°), and (d) Lw (sza=20°) for clear skies (0% cloudiness) and cloud cover of 10, 30, 50, 80 and 100%. The percent differences

were estimated according to: $\frac{Rrs_{(clouds)} - Rrs_{(clear)}}{Rrs_{(clear)}} (similarly\ for\ Lw)$ 190

Figure 3.2.2-32: Percent difference in estimated Ed values (a) just below the water surface and (b) at 5 meters below the water surface, for wind speed, u_i , 1, 3, 5, 7, 10 m/s (compared to 0m/s). The % differences were estimated according to:

$\frac{Ed_{(u_i)} - Ed_{(u=0)}}{Ed_{(u=0)}}$ 192

Figure 3.2.2-33: Percent difference in estimated Lu (a) just below the water surface and (b) 5 meters below the water surface, for wind speed, u_i , 1, 3, 5, 7, 10 m/s (compared to $u=0$ m/s). The percent differences were estimated according to:

$\frac{Lu_{(u_i)} - Lu_{(u=0)}}{Lu_{(u=0)}}$ 192

Figure 3.2.2-34:(a) Estimated Rrs for various wind speeds (0, 1, 3, 5, 7, 10m/s) (b) percent differences in estimated Rrs values for 1, 3,5, 7, 10 m/s (compared to 0 m/s). Percent differences were estimated according to:

$\frac{Rrs_{(u_i)} - Rrs_{(u=0)}}{Rrs_{(u=0)}}$ 192

Figure 3.2.2-35: Percent difference in estimated (a) Lu values just below the water surface and (b) Rrs, for $sza=20^\circ$, and for wind speed of 1, 3, 5, 7, 10 m/s (compared to 0 m/s). The percent differences were estimated according to:

$\frac{Lu_{(u_i)} - Lu_{(u=0)}}{Lu_{(u=0)}}$ and $\frac{Rrs_{(u_i)} - Rrs_{(u=0)}}{Rrs_{(u=0)}}$ 193

Figure 3.3-1: Measurements of Lu(z) (in $\mu Wnm^{-1}cm^{-2}sr^{-1}$) and Ed(z) (in $\mu Wnm^{-1}cm^{-2}$) (logarithmic scale) at (a) 443, (b) 555 and (c) 670 nm, performed at PI station on 28 September 2001, using the MicroPro Satlantic multi-spectral profiler..... 197

Figure 3.3-2: Measurements of downwelling surface irradiance, Es, (in $\mu Wnm^{-1}cm^{-2}$) performed at PI station on 28 September 2001 198

Figure 3.3-3: Fresnel reflectance, r, as a function of incident angle θ' , for index of refraction of seawater $n_w=1.367$ and $n_w=1.329$. After Mobley (1994)..... 201

Figure 3.4-1: In-situ measurements (blue lines) and model estimations (red lines) of upwelling radiances (Lu) and downwelling irradiances (Ed), at 412, 555 and 670 nm, for 26 September 2001 206

Figure 3.4-2: Same as figure 3.4-1, for 28 September 2001..... 207

Figure 3.4-3: Same as figure 3.4-1, for 30 October 2001..... 208

Figure 3.4-4: Same as figure 3.4-1, for 6 May 2002..... 209

Figure 3.4-5: Same as figure 3.4-1, for 15 May 2002.....	210
Figure 3.4-6: Same as figure 3.4-1, for 22 May 2002.....	211
Figure 3.4-7: Water-leaving radiances, L_w , measured in-situ (red pixels) and estimated by the model (blue line), for measurements performed on 26 September 2001.....	212
Figure 3.4-8: Same as figure 3.4-7 for measurements performed on 28 September 2001.....	212
Figure 3.4-9: Same as figure 3.4-7 for measurements performed on 30 October 2001.....	213
Figure 3.4-10: Same as figure 3.4-7 for measurements performed on 6 May 2002.....	213
Figure 3.4-11: Same as figure 3.4-7 for measurements performed on 15 May 2002.....	213
Figure 3.4-12: Same as figure 3.4-7 for measurements performed on 22 May 2002.....	214
Figure 3.5-1: Comparison between measured (blue lines) and model-estimated (thick red lines) $Lu(z)$ and $Ed(z)$ profiles at 443, 555 and 670 nm, for measurements performed at TI station, on 26 September 2001, (a) assuming that $a_{t-w}(715)=0$ and (b) assuming that $a_{t-w}(715)=a_{CARY}(715)$. When the assumption $a_{t-w}(715)=0$ was used, the model overestimated both $Ed(z)$ and $Lu(z)$ at 555 nm (and similarly for other wavelengths close to 555nm, such as 510 and 532 nm, not shown here). Similar results were obtained when comparing Hydrolight simulations to in-situ measurements performed during the rest of the cruises at PI, HB, TI and JT stations.....	221

CHAPTER 4:

Figure 4.1-1: Water leaving radiances (blue and green lines) and radiances measured by a satellite at the top of the atmosphere (purple and yellow lines) in high ($[Chl-a]=10\text{mgm}^{-3}$) and low ($[Chl-a]=1\text{mgm}^{-3}$) chlorophyll waters. The MODIS wavelength bands are also shown (Esaias et al, 1997).....	242
Figure 4.3-1: Satellite and in-situ (or model estimated) nLw spectra, 4 June 2001. Satellite zenith angle over the Chesapeake Bay region was 35° . (a) MODIS view of Chesapeake Bay (b) MODIS $nLw(551)$ values (color bar in $\text{Wm}^{-2}\mu\text{m}^{-1}\text{sr}^{-1}$ units). The location of the four stations and the route of the boat are also shown. (c) In-situ and MODIS nLw spectra (in $\mu\text{Wcm}^{-2}\text{nm}^{-1}\text{sr}^{-1}$ units) at the stations where measurements were performed during this cruise. In-situ nLw spectra are shown as a thick yellow line. MODIS measurements (5x5 pixels around each station) are shown as red lines for pixels of quality level 0, and blue lines for pixels of quality level 2 or 3.....	258
Figure 4.3-2: Same a figure 4.3-1, for measurements on 11 June 2001. Satellite zenith angle over the Chesapeake Bay region was 42°	259
Figure 4.3-3: Same a figure 4.3-1, for measurements on 9 July 2001. Satellite zenith angle over the Chesapeake Bay region was -61°	260
Figure 4.3-4: Same a figure 4.3-1, for measurements on 21 September 2001.	

Satellite zenith angle over the Chesapeake Bay region was -18° . No satellite pixels of quality level 0 (concerning nLw products) were found at TI and JT stations during this day.....	261
Figure 4.3-5: Same a figure 4.3-1, for measurements on 26 September 2001.	
Satellite zenith angle over the Chesapeake Bay region was 15°	262
Figure 4.3-6: Same a figure 4.3-1, for measurements on 4 October 2001. Satellite zenith angle over the Chesapeake Bay region was -57°	263
Figure 4.3-7: Same a figure 4.3-1, for measurements on 30 October 2001.	
Satellite zenith angle over the Chesapeake Bay region was -8°	264
Figure 4.3-8: Same a figure 4.3-1, for measurements on 13 November 2001.	
Satellite zenith angle over the Chesapeake Bay region was 16°	265
Figure 4.3-9: Same a figure 4.3-1, for measurements on 15 May 2002. Satellite zenith angle over the Chesapeake Bay region was 26°	266
Figure 4.3-10: Same a figure 4.3-1, for measurements on 22 May 2002. Satellite zenith angle over the Chesapeake Bay region was 36°	267
Figure 4.3-11: Same a figure 4.3-1, for measurements on 6 June 2002. Satellite zenith angle over the Chesapeake Bay region was -38°	268
Figure 4.3-12: Same a figure 4.3-1, for measurements on 18 June 2002. Satellite zenith angle over the Chesapeake Bay region was 5°	269
Figure 4.3-13: Same a figure 4.3-1, for measurements on 8 November 2002.	
Satellite zenith angle over the Chesapeake Bay region was -57°	270
Figure 4.3-14: Location of the 5x5 MODIS pixels around each station (PI, HB, TI and JT) during the cruises in the Chesapeake Bay. i) MODIS pixels with negative (nLw=-1 or nLw = -5) or zero normalized water-leaving radiances at all of the MODIS wavelength bands are shown as black pixels. ii) MODIS pixels with negative (nLw=-1) or zero normalized water-leaving radiances at some of the MODIS wavelengths are shown as blue pixels. iii) MODIS pixels with nLw > 0 at all wavelengths are shown as red pixels. The MODIS pixel with water leaving radiances that showed the best agreement with the in-situ measurements, is shown as white pixel.....	275
Figure 4.3-15: In-situ measurements of normalized water-leaving radiances, nLw(λ) and MODIS nLw(λ) values measured at the 7 wavelengths 412, 443, 488, 531, 551, 667 and 678 nm. The in-situ nLw(λ) are compared to the MODIS nLw(λ) measured (a) at the geographically “closest” pixel (b) at the “best” MODIS pixel. The R^2 , slope and intercept between the in-situ and satellite data are shown in tables 4.3-3 (a) and 4.3-3 (b). Pixels of all quality levels have been included in the comparisons (pixels of quality 0 shown as empty symbols, while pixels of quality 1-3 are shown as full symbols). The 1:1 line is also shown for comparison.....	281
Figure 4.3-16: Comparison between in-situ nLw measurements and MODIS nLw values measured at the ‘best’ pixels (a) for those cases when almost clear atmospheric conditions (AOT values of less than 0.2) and not very large satellite zenith angles were observed (days: 4 June 2001, 26 September 2001, 30 October 2001, 13 November 2001, 22 May 2002) (b) for those cases when large aerosol optical thickness was measured in the atmosphere above the location of the four	

stations (days: 11 June 2001, 21 September 2001, 6 June 2001 and 18 June 2002). Pixels of all quality levels have been included in the comparisons. The R^2 , slope and intercept between the in-situ and satellite data are shown in tables 4.3-4(a),(b).. 282

Figure 4.3-17: Comparison between the satellite and in-situ measurements of nLw, for measurements performed at the four stations (a) TI, (b) PI, (c) HB and (d) JT, during all of our cruises in Chesapeake Bay. Pixels of all quality levels have been included in these comparisons. The R^2 , slope and intercept values are shown in tables 4.3-5(a)-(d)..... 283

CHAPTER 5:

Figure 5.3-1: Frequency histogram of the surface [Chl-a] log-transformed values measured at the four stations, in the northern part of the Chesapeake Bay..... 312

Figure 5.3-2: Temporal variation of [Chl-a] measured within the first meter below the water surface. Measurements are from cruises performed during 2001 and 2002 at HB, JT, PI and TI stations..... 313

Figure 5.3-3: (a) Phytoplankton absorption spectra (300-750nm), measured at HB, PI, TI and JT stations, during the phytoplankton bloom observed on 11 June 2001. High absorption in the UV range (~ 325 nm) was probably caused by the presence of MAAs. (b) Phytoplankton absorption spectra measured at HB, PI, TI and JT stations, during 28 September 2001, when waters in the Bay were relatively clear. (Particulate absorption values were calculated using $\beta=1.5$)..... 314

Figure 5.3-4: Vertical profiles of chl-a concentration measured at Chesapeake Bay during the cruises 28 September 2001(a) - 8 November 2002(j)..... 315

Figure 5.3-5: Comparison between surface [Chl-a] values estimated as the average i) within the first meter and ii) within the first three meters below the water surface. The comparison is close to 1:1 line for almost all of the cases..... 316

Figure 5.3-6: Relation between [Chl-a] and phytoplankton absorption at 676 nm, $a_{\text{phyt}}(676)$, measured using the CARY spectrophotometer (methodology in paragraph 2.2.2.2, Chapter 2). Measurements performed on 11 June 2001 (large phytoplankton bloom) are shown as white squares..... 317

Figure 5.3-7: Comparison between in-situ [Chl-a] measurements and the MODIS [Chl-a] products (a) “chlor_a_2” (c) “chlor_a_3” (e) “chlor_MODIS”. MODIS measurements were obtained for the “best” pixel around the location of each site. MODIS [Chl-a] were flagged (-1) for those cases when the chl-algorithms failed (e.g due to negative or flagged nLw(443), nLw(488) values) (red circles). The satellite [Chl-a] values were underestimated for pixels with overestimated nLw(443), nLw(488) (white squares) (days with high AOT). The rest of the pixels are shown as blue pixels (also in log-log scale at figures (b),(d),(f))... 320

Figure 5.3-8: Comparisons between in-situ $\log_{10}(\text{Chl-a})$ and chlorophyll concentrations estimated using the MODIS empirical algorithms and measurements of Rrs (or nLw) as input information (in logarithmic values). The MODIS chl-algorithms used were: (a) “chlor_a_2” (eq.5.2-5), (b)-(c) “chlor_a_3” (eq. 5.2-6) for the “unpackaged” and the “fully packaged” cases, (d)-(e) “chlor_MODIS” (eq. 5.2-3, 3rd order polynomial for the case of high Chl-a pigment and eq.5.2-4, 5th order polynomial)..... 322

Figure 5.3-9: Relationship between laboratory measurements of [Chl-a] and in-situ measured or Hydrolight estimated $Rrs(\lambda_i)/Rrs(554)$ for $\lambda_i = 412, 443, 488, 510, 532, 670$ and 677 nm.....	324
Figure 5.3-10: Cubic regression on the log transformed laboratory measurements of [Chl-a] and in-situ measurements of $Rrs(488)/Rrs(554)$. A 3-rd order polynomial between $\log_{10}[\text{Chl-a}]$ and $\log_{10}(Rrs(488)/Rrs(554))$ is used in the MODIS empirical algorithms “chlor_a_2” and “chlor_a_3” (table 5.2-2). The 3 rd order polynomial used in the “chlor_a_3” MODIS algorithm to estimate [Chl-a] from the MODIS $Rrs(488)/Rrs(554)$ values, is also shown (red line) for comparison.....	325
Figure 5.3-11: Relation between measured $Rrs(\lambda)$ values and measured $\frac{b_b(I)}{a(I)+b_b(I)}$ (yellow pixels) and between model-estimated $Rrs(\lambda)$ values and measured $\frac{b_b(I)}{a(I)+b_b(I)}$, (blue pixels) at (a) 440 nm, (b) 530 nm and (c) 670 nm. The linear least-squares regression fits are also shown, for each case.....	328
Figure 5.3-12: Relation between measured b_b and measured (yellow pixels), as well as model-estimated (blue pixels) Rrs at the wavelengths (a) 443 nm (b_b measured at 450 nm), (b) 532 nm (b_b measured at 530 nm) and (c) 670 nm (b_b measured at 650 nm).....	330
Figure 5.3-13: (a) Relation between in-situ and MODIS $Rrs(670)$. For almost all of the cases MODIS underestimated $Rrs(670)$ compared to the in-situ and modeled estimated $Rrs(670)$ values. (b) Relation between measured $b_b(650)$ and MODIS Rrs at 670 nm.....	330
Figure 5.3-14: Relation between surface [Chl-a] and surface $b_b(650)$ measurements in the Chesapeake Bay waters.....	331
Figure 5.3-15: Relation between measured surface b_b at 530 nm and surface measurements of absorption by non-pigmented material at (a) 412 nm and (b) 380 nm.....	332
Figure 5.3-16: Relation between measured surface b_b at 650 nm and surface measurements of absorption by non-pigmented material at (a) 412 nm and (b) 380 nm.(c), (d): same as (a), (b) but two cases where not included in the linear least-squares fits.....	332
Figure 5.3-17: Relation between measured or model-estimated (based on measured IOPs) Rrs values at 670 nm and surface measurements of absorption by non-pigmented material at (a) 412 nm and (b) 380 nm.....	333
Figure 5.4-1: Satellite and in-situ nLw spectra for 11 June 2001 (AOT(550) = 1.2 at the time of the MODIS overpass). The in-situ nLw spectrum is shown as a thick yellow line. MODIS nLw spectra (5x5 pixels around each station) are shown as red lines for pixels of quality level 0, and blue lines for pixels of quality level 2 or 3. The quality of the MODIS nLw values is reduced ($nLw < 0$ at $\lambda > 550$ nm) even at pixels of the best quality level (quality level=0) concerning the nLw values.....	339
Figure 5.4-2: Relationship between [Chl-a] and $a_{t-w}(676)$. Measurements were	

performed on water samples collected from PI, HB, TI and JT. Measurements performed on 11 June 2001 (large phytoplankton bloom) are shown as open circles.....	344
Figure 5.4-3: (a) Relationship between $b_b(530)$ and $b_b(650)$ from measurements performed in Chesapeake Bay, using the ECOVSF instrument (measurements performed at all depths and during all cruises are included here) (b) Relationship between $a_{t-w}(554)$ and $a_{t-w}(677)$ from measurements performed using the AC9 instrument.....	346
Figure 5.4-4: Approximate relationship between $Rrs(677)/Rrs(554)$ and [Chl-a], estimated based on eq (5.4-4) and in-situ measurements of backscattering and absorption, without accounting for the effect of chl-a fluorescence (blue solid line) and assuming an increase of $Rrs(677)$ by 30 and 50% (dotted lines) (the effect of chl-a fluorescence for measurements performed at PI station on 28 September 2001 was ~40% increase in $Rrs(677)$). The measured [Chl-a] and $Rrs(677)/Rrs(554)$ are also shown (blue pixels, with the logarithmic best fit shown as thick line).....	347
Figure 5.4-5: Comparison between MODIS and in-situ measurements of Rrs (a) at 554 nm and (b) 677 nm. (c) Comparison between the MODIS and in-situ Rrs ratios at 677 and 554 nm, $Rrs(677)/Rrs(554)$	348

CHAPTER 1

General Introduction

1.1 Outline of the thesis

Human activities have fundamentally affected marine ecosystems over the whole world, especially within the last decades, via over-fishing, aquaculture, addition of nutrients and chemical pollutants, industry, agricultural runoff, modification or destruction of critical habitats. According to the 1998 Report of the OEUVRE (Ocean Ecology: Understanding and Vision for Research) Workshop, little if any of the ocean remains, today, unaffected, either directly or indirectly, by humans. And, as the human population increases, according to current projections, the effects on coastal regions and open oceans will be more and more profound. As a result, there is an urgent need to develop new techniques that enable us to recognize ecological changes and perturbations, understand the effects of these perturbations on marine ecosystems, and try to facilitate restoration of damaged communities. The first step to protect marine ecosystems is to gain knowledge of how ocean systems function and obtain a better understanding of the responses of aquatic organisms to physical and chemical forces. To accomplish this goal we require a combination of in-situ and laboratory measurements to determine the in-water physical, biological, optical properties and marine composition (chlorophyll, dissolved organic matter, land runoff pollutants, etc.) within regional scales, as well as validated remote sensing observations to extend in-situ measurements over the vast areas encompassed by coastal and open-ocean areas. The research described in this thesis is an attempt to combine in-situ and laboratory measurements of optical properties with

detailed radiative transfer modeling of underwater radiation fields and satellite remote sensing observations of ocean color for a region within the Chesapeake Bay.

Three decades ago, detecting anthropogenic change on a global scale was not possible. Today, in-situ measurements and satellite sensors have the potential to provide the previously unavailable information. Remote sensing observations rely on measurements of the spectral composition of light that emerges from the ocean surface (ocean color), carrying information on the optical characteristics of the water and its constituents. By using appropriate bio-optical models and previous knowledge on how various substances influence the ocean color, remote sensing measurements can provide information on the water composition, the chlorophyll content and the primary production in the upper ocean. However, current uncertainties in our knowledge of marine optical characteristics and our ability to model the underwater radiation fields strongly indicate that much additional research is still needed, especially in the more complicated estuarine and coastal regions.

This project is focused on a study of the inherent optical properties of the estuarine Chesapeake Bay waters and how these properties affect the light penetration into the water column and especially the effective amount of light radiating from the ocean surface, since this is the quantity measured remotely by a satellite sensor or an airborne instrument. At the same time, I am interested in the inverse problem of how water leaving radiance measurements could be used to get information on the amount and composition of optically active components (such as phytoplankton, dissolved material and non-pigmented particulate matter) present in these waters. Measurements of the relative amounts of these components bear directly on quantifying changes in water quality.

In-situ measurements of in-water properties, together with theoretical models and laboratory experiments are essential to our efforts to understand and study light in the marine environment. Validation of remote sensing observations from satellite instruments with in-situ measurements and radiative transfer modeling permit these ‘ocean color data’ to be used to investigate biological activity, marine optical properties, and changes in the concentration and composition of material in surface waters, over larger temporal and spatial scales. Since both satellite and in-situ measurements are available for studies of light penetration in the Chesapeake Bay waters, it is important to study the degree of agreement between these two types of measurements and the main issues that affect the accuracy of satellite estimations. A specific question addressed in the framework of this thesis, is how well satellite estimations of water-leaving radiances and surface chlorophyll concentrations compare with in-situ measurements under varying conditions of water optical properties and atmospheric composition in the estuarine environment of Chesapeake Bay?

To address the above issues, I have performed in-situ measurements of in-water optical properties and radiation fields, analyzed laboratory measurements of marine optical properties, as well as made measurements of atmospheric transmission characteristics, within the northern Chesapeake Bay area, using measuring equipment from NASA, Goddard Space Flight Center (GSFC) and the Smithsonian Environmental Research Center (SERC) (chapter 2). The measured data have been combined and analyzed using detailed radiative transfer modeling of the underwater environment. The combination of detailed in-situ and laboratory measurements is essential in gaining a better knowledge of the optical characteristics of the less thoroughly studied, case 2, estuarine waters.

In-situ measurements of upwelling and downwelling radiation within the water and just above the water surface permit the validation of the components of the radiation field resulting from radiative transfer model estimations (chapter 3). The combination of measurements performed in the framework of our detailed measurements program in Chesapeake Bay, forms a “closure experiment”, since measured inherent optical properties can be used as input information to perform the model simulations, while measured radiance and irradiance profiles can be compared to the model’s output. Such a closure experiment may reveal errors related to the accuracy of instruments or the methodology of the in-situ measurements, as well as uncertainties in parameterizations used in satellite algorithms, or in assumptions of underwater optical properties used in the model estimations. The extensively validated Hydrolight underwater radiative transfer program (Mobley, 1989) has been used in the framework of this project to perform the model calculations. The results demonstrate the conditions under which theoretical calculations can produce close agreement with experimental results, and show the causes of any disagreement between measured and modeled quantities.

The in-situ results were also applied to the interpretation and validation of satellite (MODIS) observations, under various atmospheric conditions and in-water optical characteristics (chapter 4). Most of the satellite algorithms used in estimates of chlorophyll concentration and attenuation in the water are based on “standard” parameterizations and bio-optical models (chapter 5). One of the goals in my research project is to study how absorption by phytoplankton, non-pigmented particulate matter and dissolved material could be modeled for some specific sites in the Chesapeake Bay area. What is the contribution of these components to the total attenuation of light and

what are the relationships between remote sensing reflectances and water optical properties (such as chlorophyll concentration and backscattering) that could be used in this optically complex, estuarine environment? Are the bio-optical models used currently in satellite algorithms applicable for the Chesapeake Bay waters?

Coastal and estuarine areas, such as the Chesapeake Bay, are among the most biologically productive and vulnerable areas of the world oceans, and as such they are some of the most intensely studied areas for environmental scientific research. However, due to the complexity of the interactions between physical, chemical and biological phenomena along these regions, near shore waters are among the most challenging sites for systematic scientific study. The presence of quite shallow areas, high turbidity in the water, and suspended sediments, greatly complicates theoretical model calculations of light propagation in these waters. Satellite ocean color observations over coastal regions, are significantly affected by proximity to land, shallow and turbid waters, urban pollution, and large concentrations of highly absorbing aerosols carried over the oceans by the wind. A major obstacle to the remote estimation of concentrations of optically active components (such as chlorophyll) in case 2 waters, has been the lack of precise information concerning the optical characteristics of inland, estuarine or coastal waters. The core subject of this thesis is the characterization and modeling of in-water optical properties in the estuarine environment of northern Chesapeake Bay, where natural and human-induced processes strongly interact. Because of the complications mentioned above, and also because of the direct importance of estuarine and coastal regions to human interests, more research in the future should be directed toward these regions of the ocean.

1.2 Why I am particularly interested on Coastal Environments

Throughout history, human populations have shown a tendency to settle along the world's 440,000 km of coastline. Out of the 71% of Earth covered by ocean, it is this narrow coastal strip that has significantly influenced, and is influenced by, human activities. Today, over half the people in the world are estimated to live within 100 km off the coast for the region's real and intangible benefits (see, e.g. figure 1.2-1). Coastal regions support tourism, recreational activities, they are important for fishing, shipping and national security. Therefore, from a human perspective, coastal areas are among the most desirable areas of the world. Moreover, near-shore regions contain some of the most diverse and biologically productive habitats on our planet. As the population has increased, these regions have been under the greatest environmental stress during the last decades and, as coastal population continues to grow more rapidly than total world population, the effects of human activities will become increasingly and distressingly apparent.



Figure 1.2-1: The high percentage of human population living along the world's coastlines is revealed in this composite satellite view of Earth at night (courtesy NASA).

Coastal zones are complex and dynamic environments, where terrestrial, oceanic, atmospheric and human inputs of energy and matter converge. Residential and commercial development, water pollution and waste disposal are concentrated around bays and estuaries where the sea's richest fisheries are found. An increasing pollution load entering the oceans worldwide comes from human activities, especially the introduction of nutrients, sediments and pathogens from land-based sources. Agricultural and urban waste flows into the water from the land, smoggy clouds originating in industrial areas deposit their contaminants into the coastal waters, and shipping vessels flush their tanks discharging hazardous wastes and non-indigenous species. The pollutants coming from these activities contribute significantly to an increased incidence of toxic algal blooms (red tides), increased blocking of sunlight in coastal waters, anoxic conditions and suffocating of fish in coastal habitats (e.g., the "dead-zone" in the Gulf of Mexico). As a result, coastal habitats and fisheries are declining from pollution and excessive fishing, causing disruptions that affect the whole ocean ecosystem. At the same time, human health is also affected through changes in food supplies, water quality, and accumulation of wastewater.

Since coastal and estuarine waters are among the most important and vulnerable areas of the world oceans, there is a need to increase the coastal research and monitoring programs, so as to improve our understanding of how coastal ecosystems function, and how to better manage interactions between human-induced and natural processes within these regions. In these research efforts, measurements of light penetration into the water column and studies of the water optical properties play a critical role, since the water

optical characteristics are strongly related to biological, chemical and physical processes in the water. Continuous in-situ measurements of water optical properties are used to determine changes in the biological composition and concentration of optically active substances in coastal regions, monitor the water quality and identify the underlying causes (human activities or natural processes) of any changes in the water characteristics. At the same time, remote sensing observations of ocean parameters rely on detecting the electromagnetic radiation, which, after interacting with the water and its constituents, emerges from the ocean carrying with it information about the water's optical characteristics. By using appropriate bio-optical models remote sensing measurements of ocean color can provide information on the distribution and abundance of dissolved and particulate material in the upper ocean, over large temporal and spatial scales. This information can be used to investigate biological productivity in the oceans, and study the interaction between physical processes (e.g. currents) and ocean biology as well as the effects of human activities on the oceanic environment.

However, the large variety of physical, chemical and biological phenomena along the coastal regions poses great difficulties for systematic scientific studies. The presence of quite shallow areas, high turbidity and re-suspended sediments in the water, as well as the proximity to landmass, greatly complicate both measurements and model calculations. Satellite estimations of underwater properties are also significantly complicated by atmospheric urban pollution and large concentrations of highly absorbing aerosols carried over the oceans by the wind (e.g., dust and smoke plumes blown off the coasts, notably western Africa and eastern Asia). Relative to the total radiation intensity emerging at the

top of the atmosphere and measured by a sensor on a satellite, the underwater radiance emerging from the ocean represents only a few percent (10% or less) of the total signal. For a clear, clean atmosphere, removal of the atmospheric portion of the signal requires accurate modeling of the molecular atmosphere. When pollution is present, the perturbed atmospheric conditions complicate atmospheric correction algorithms in satellite retrievals, reducing the accuracy of satellite-estimated ocean optical characteristics. In addition to the atmospheric correction problem, a major obstacle to the remote observations of coastal chlorophyll concentrations or distribution of other optically active substances, has been the lack of precise information concerning the optical properties of inland, estuarine and coastal waters. While bio-optical models currently used in satellite algorithms adequately describe the optical properties of open-ocean waters, where phytoplankton is the major optical component, they are not necessarily applicable in the coastal zones, where bio-optical characteristics depend on the composition, distribution and concentration of various living and non-living, dissolved and particulate, autochthonous and allochthonous material. My interests in the research described in this thesis, as well as the desire to continue similar work in the future, are driven by a desire to understand the complexities of the interaction between optical properties and biological processes in coastal environments, and the direct economic and environmental importance of estuarine and coastal regions.

1.3 Chesapeake Bay

Chesapeake Bay is the largest estuary in the United States, and, historically, one of the most productive in the world. The Bay extends from the mouth of the Susquehanna River at Havre de Grace, Maryland, in the north, to the Cape Henry and Cape Charles in Virginia, in the south (fig. 1.3-1). As with most estuarine environments, Chesapeake Bay supports several plant communities, fresh, brackish and saltwater wetlands, phytoplankton, benthic algae, epiphytic algae, submerged aquatic vegetation, and a wide variety of fish and other marine creatures. As a result, the Bay is a “powerhouse” of photosynthetic activity. At the same time, the abundance of nutrients (such as nitrogen and phosphorus) and the presence of dissolved organic material, detritus, other suspended organic particles and inorganic compounds such as clay minerals and quartz sand, significantly complicate the chemical, biological and optical properties of these estuarine waters, making the research in this type of environment extremely interesting and challenging.

Table 1.3-1: Chesapeake Bay physical characteristics

Physical characteristics of Chesapeake Bay	
Area	2500 sq miles
Length	200 miles (320 km)
Minimum Width	4 miles (near Annapolis, MD)
Maximum Width	30 miles (mouth of Potomac River)
Average depth	21 ft (6.4 m)
Maximum depth	174 ft (53 m)
Drainage Area	64,000 sq miles
Shoreline	11,684 miles

Chesapeake Bay is a typical temperate coastal plain estuary, very long (320 km), narrow (20 km) and shallow (mean depth = 6.5 m) (table 1.3-1). With an opening to the

sea in the south, tidal flushing and circulation of oxygen and nutrients in the bay are vigorous. A dynamic interaction among freshwater input to the bay, the salinity input from the ocean, and the tidal flow, drives the estuarine circulation with strong north-south gradients in nutrient concentrations and phytoplankton biomass.



Figure 1.3-1: The Mid-Atlantic coast of the United States and the Chesapeake Bay (Ellison and Nichols, 1975).

One hundred and fifty rivers, creeks and small streams that drain six states, are sources of fresh water in the bay, as well as an input of detritus, dissolved gases, nutrients and minerals, each important to plant growth and the whole food chain in the estuary. Eight

out of the forty-six major tributaries, (the Susquehanna, Patuxent, Potomac, Rappahannock, York, James, and Choptank rivers and the West Chesapeake drainage area) contribute about 90% of the inflowing fresh water to the Bay. The largest single source of freshwater is the Susquehanna River, which accounts for 50% of freshwater inflow to the entire bay (80% to 90% to the region above the Potomac River mouth), 70% of the nitrogen load and 60% of the phosphorus load (C. White, 1989). Although this freshwater input is barely one ninth of the volume of seawater flowing into the bay at any moment, it has a significant influence on the estuary, since it can alter the salinity structure and the net outflow to the ocean. Fresh water from inland sources is less saline and dense than salt water inbound from the Atlantic. The difference in density causes the fresh and ocean waters to occupy different layers in the estuary, with the lighter, less saline water at the upper layers and the heavier, salty water at larger depths. Frictional forces between the two layers of fresh and salty water cause some mixing and exchange of water across the density barrier, creating a “moderately stratified environment” in the Chesapeake Bay estuary. In the zone of maximum turbidity, nutrients, sediments and other organic and inorganic particles are mixed, affecting the biological and optical properties in the water column. The basic surface (horizontal) salinity pattern in the Bay is an increase of salinity seaward, as the input of the high-density salty water occurs at the mouth of the estuary. At the same time, due to the rotation of the earth, the Northern Hemisphere Coriolis force deflects flowing water to the right. As a result, fresh water moving south down the Chesapeake Bay estuary is forced towards the western shore, while the saltier, ocean water moving north up the estuary is deflected toward the eastern shore.

The slow mixing of fresh and salt water creates distinct biological zones along the salinity gradient, affecting the distribution of plant and animal species within the Bay. The salinity gradient varies in amplitude, depending on the seasons and the amount of year-to-year rainfall. During the spring, rainfall and melting snow from inland send a freshwater flow into the estuary decreasing salinity, compared to salinity levels observed during the dry, winter months. Strong riverine discharges, during storm and rainfall events, carry large amounts of fresh water and nutrients into the Bay, significantly affecting the water quality and the bio-chemical processes in the Bay.

Tidal currents also play a very important role on the salinity structure and circulation patterns in the bay. These currents are moderate averaging less than 0.5 knots or 0.925 km/hr (White, 1989) except in narrows and bottlenecks where they can reach 3 knots. As the tide moves into the bay, it drives salt water from the ocean further up to the estuary, changing the salinity patterns. The vertical range of the tides averages 0.6 m at the area of the main Bay, and it can reach 0.7-0.8 m at the capes. The average time for a tide to travel up, from the mouth of the estuary to the northern part of the bay, is 12-13 hours, just about the same as the time between two adjacent tidal highs. Therefore, when a tidal high reaches the upper limit of the bay, the next tidal high begins at the mouth, and a semi-diurnal tidal pattern persists in the Bay.

Thousands of years of continuous change since the last ice age have resulted in the form and conditions of Chesapeake Bay as we know it today. Humans have been a part of this complex ecosystem, first for subsistence living, and then for the past 200 years

with activities that significantly affect the Bay's ecology (Boynton, 1995). Modern industrial and agricultural activities, as well as residential development, affect the ecosystem balance mostly in a negative way. Although nutrients are essential to plant life, an excess of nutrients can be harmful. During the last years, the amount of nutrients entering the Bay's water through run-off has increased considerably. This excess amount of nutrients can cause dense algal blooms that block sunlight from reaching critical depths. Without sufficient light, plants cannot photosynthesise and survive, with negative effects for the whole food chain. These dense phytoplankton blooms are critical to deleterious processes in the estuary, such as the seasonal development of subpycnocline anoxia, which has become a pervasive problem in the Chesapeake Bay waters, with severe biological and economic consequences. (Taft et al., 1980; Officer et al., 1984; Seliger et al, 1985; Tuttle et al, 1987; Cooper and Brush, 1991; Malone, 1992; Harding et al. 1994)

The magnitude, timing, position, and longevity of the phytoplankton blooms in the Chesapeake Bay are mainly dependent on photic conditions, the intensity of vertical density stratification, and the magnitude of freshwater flow, carrying nutrients and suspended particulate matter in the Bay waters (Harding and Itsweire, 1991; Harding et al, 1986; 1994; Fisher et al, 1988; Malone et al, 1986; 1988).

To study the Bay's water quality and assess progress in reversing the Bay eutrophication, in-situ measurements of optical properties as well as physical, chemical, and biological indicators of the Bay's health, have been performed in the framework of

several ship-based monitoring programs, during the last decades. These programs include, among others, the extensive multi-agency monitoring program of the EPA (Environmental Protection Agency) Chesapeake Bay Program (CBP), the Chesapeake Bay Remote Sensing Program (CBRSP), the Chesapeake Bay Observing System (CBOS), and the Land-Margin Ecosystem Research (LMER) Trophic Interactions in Estuarine Systems (TIES) programs (University of Maryland, Center for Environmental Sciences; Maryland Sea Grant; funded by NOAA, NASA, NSF), measurements performed by Naval Research Laboratory (NRL), monitoring of freshwater flow through USGS (U.S. Geological Survey), water quality monitoring through the NOAA/NERRS (National Estuarine Research Reserve System) program (e.g. Harding et al, 1992; Harding et al, 1994, Glibert et al, 1995; Hopkinson et al, 1998; Darrell et al, 1998; Langland, 1998; Johnson et al, 2001; Langland et al, 2002)

Although continuous in-situ measurements are very important in monitoring water-quality in the Chesapeake Bay estuarine waters, the spatial and temporal coverage of ship-board measurements is often insufficient in studies of ephemeral and localized phytoplankton bloom events. The application of remote sensing (satellite observations, or aircraft measurements for higher spatial resolution) can provide synoptic observations of surface water optical properties at temporal and spatial scales unattainable with ship-board measurements alone (Harding et al, 1994).

Within the last decades, several aircraft ocean color instruments (using both “passive” and “active” systems) have been used to remotely measure chlorophyll concentrations in

the Chesapeake Bay (e.g. Hoge and Swift, 1981; Grew, 1981; Campbell, 1981, Lobitz et al, 1998). Observations performed in the framework of the Chesapeake Bay Remote Sensing Program (CBRSP) (University of Maryland, Center for Environmental Sciences) comprise one of the largest datasets of remotely sensed observations in estuarine waters using aircraft ocean color sensors (e.g. Harding et al, 1992; Harding, 1994; Harding et al, 1994; Harding et al. 1995; Harding and Perry; 1997; Harding et al, 2002).

Although great progress has been made recently on ocean color observations using satellite sensors (SeaWiFS and MODIS), only a limited number of studies (e.g. Harding and Magnuson, 2001 using SeaWiFS data and algorithms) have been published on the interpretation and validation of satellite imagery for the Chesapeake Bay. The detailed in-situ measurements of water optical properties, performed in the northern Chesapeake Bay region, in the framework of this thesis, are applied to the interpretation of MODIS ocean color data and their validation. The applicability of bio-optical models and parameterizations currently used in MODIS algorithms are examined for these optically distinct, case 2, estuarine waters.

1.4 Classification of ocean waters

The degree of optical complexity of natural waters can vary greatly among different aquatic environments that are influenced by a variety of physical, biological and chemical processes. Since water bodies that are of similar optical character can often be described by similar bio-optical models, it was long ago realized that it would be useful to classify marine waters into different categories, depending on their optical characteristics and the way these affect the magnitude and spectral quality of light penetrating into the water column.

A number of schemes have been proposed in order to describe the optical complexity of natural waters. Pelevin and Rutkovskaya (1977) proposed that the waters be classified according to values of the irradiance diffuse attenuation coefficient at 500 nm, $K_d(500)$. According to Smith and Baker (1978), in regions not significantly influenced by terrigenous material or resuspended sediments, phytoplankton and covarying detrital material are mainly responsible for light attenuation. Therefore, in such regions, the total aquatic content of chlorophyll and chlorophyll-like pigments could provide a sufficient basis for optical classification of the waters. Kirk (1980) proposed an optical classification scheme applicable mainly to inland waters, which was based upon the spectral absorption properties of particulate and soluble fractions measured in Australian waters. The classification by Kirk separates the waters into type G (“gelbstoff” or chromophoric dissolved organic matter (CDOM) dominated), type T (“tripton” or non-pigmented particulate matter dominated) and type A (phytoplankton dominated) and various combinations of these types. A similar classification for open-ocean, as well as

for coastal and inland water masses, was proposed by Prieur and Sathyendranath (1981), based on the relative proportions of absorption due to algal pigments, dissolved organic matter and non-pigmented particles of biologic or terrestrial origin. Different waters are classified as C' (contribution by phytoplankton pigments is predominant), Y' (absorption by CDOM dominates) or P' type (light attenuation mainly due to the presence of non-chlorophyllous particles), or a combination of these basic types, C'Y', C'P', P'Y'.

Two of the most frequently used classification schemes are those proposed by Morel and Prieur (1977) and Jerlov (1976). These two schemes are described in more details in the following paragraphs.

Classification by Morel and Prieur

An optical classification scheme that has been applied widely, especially in studies relating to remote sensing observations, is the one proposed by Morel and Prieur (1977). According to Morel and Prieur, oceanic waters may be classified into two basic optical types: case 1 and case 2 waters. Case 1 are these waters where the concentration of phytoplankton is high compared to nonbiogenic particles and the phytoplankton pigments and covarying detrital material play an important role in actual absorption. Depending on the phytoplankton concentration, case 1 waters can range from very clear (oligotrophic) to very turbid waters (eutrophic). In case 2 waters other substances, which may not covary with chlorophyll, significantly affect water optical properties. Such substances include suspended inorganic sediments, CDOM, coccolithophores, detritus (non-living

organic particles) and bacteria. Absorption by pigments is relatively less important in determining the total absorption in case 2 waters. According to Morel and Prieur (1977) an ideal case 1 would be a pure culture of phytoplankton and an ideal case 2 a suspension of non-living material with a zero concentration of pigments. Natural waters can be characterized as case 1 or case 2 depending on whether the chlorophyll concentration is high or low relative to the scattering coefficient (Morel and Prieur, 1977).

According to Mobley (1994), roughly 98% of the world's open ocean and coastal waters fall into the case 1 category. Most bio-optical research has been directed toward these relatively 'less-complex', phytoplankton-dominated waters, and many bio-optical models and parameterizations have been developed (Prieur and Sathyendranath, 1981; Gordon and Morel, 1983; Gordon et al, 1988; Morel, 1991), that relate water's optical properties (such as absorption and backscattering) to remote sensing reflectances and chlorophyll concentration, in case 1 waters. Such bio-optical models, however, are not applicable to case 2 waters. Case 2 are typically near-shore, coastal and estuarine waters, characterized by higher degree of optical complexity. Within such environments, natural as well as human-induced processes are sources of significant optical variability.

Jerlov Classification scheme of ocean waters

Another frequently used classification scheme for oceanic waters was developed by Jerlov (1976). This classification scheme is based on the spectral shape of the downwelling irradiance diffuse attenuation coefficient, $K_d(z, \lambda)$, defined as:

$$K_d(z, \lambda) = -d [\ln E_d(z, \lambda)] / dz \quad (1.4-1)$$

where $E_d(z, \lambda)$ is the downwelling irradiance at depth z and wavelength λ . The bulk diffuse attenuation coefficient could be regarded as a quasi-inherent optical property of the water whose variability does not depend significantly on the changes in the external environment, but on the variability of the inherent optical properties of the water (e.g. total absorption and backscattering). Observations show that $K_d(z, \lambda)$ is rather insensitive to environmental effects (Baker and Smith, 1979) except for extreme conditions such as in the case of very large solar zenith angles and, according to Gordon (1989), in most cases corrections can be made for the environmental effects present in K_d . The Jerlov classification of ocean waters is based on water clarity as quantified by the spectral shape of diffuse attenuation coefficient, $K_d(w, \lambda)$ where w is the depth just below the water' surface (fig. 1.4-1). The types are numbered I (clearest), IA, IB, II and III (most turbid) for open ocean waters and 1 (clearest) through 9 (most turbid) for coastal waters. The Jerlov types I – III generally correspond to case 1 waters (according to Morel & Prieur) where phytoplankton is the predominant absorbing component and types 1-9 correspond to case 2 waters where CDOM and non-pigmented particles dominate the optical properties.

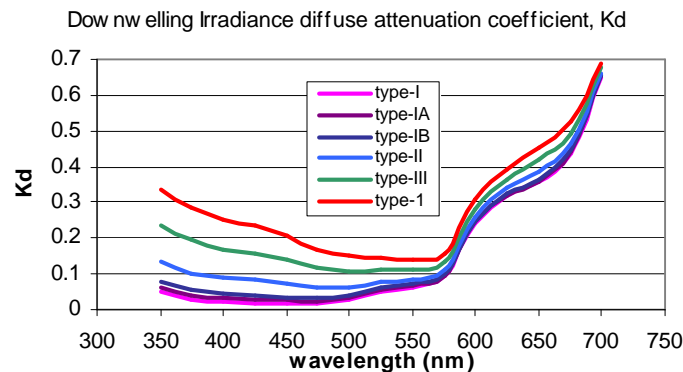


Figure 1.4-1: Downwelling Irradiance Diffuse Attenuation Coefficient, $K_d(\lambda)$, used to define the Jerlov water types (revised values by Austin and Petzold, 1986)

1.5 Optical Properties of natural waters

The amount of light that penetrates to a given depth depends mainly on the properties of the air-water interface and the optical properties of the water column, such as the bulk absorption, scattering, and scattering phase function. The transmission of solar radiation through the air-water interface varies with time, primarily depending on cloud cover, wind speed and solar zenith angle. Changes in the angular distribution of incident irradiance and the effect of surface waves, are factors that both modulate the intensity at a particular depth and the amount of light reflected back into the air.

According to Preisendorfer (1976), the optical properties of water can be divided into two groups: inherent and apparent properties. Apparent optical properties (AOPs) depend on both the water's composition and the geometrical distribution of the light field. AOPs include properties such as vector and scalar irradiances, reflectances, average angles of incident radiation and irradiance attenuation coefficients. Inherent optical properties (IOPs) depend solely on the water's composition and the optical characteristics of each individual constituent and include absorption, scattering and attenuation coefficients, index of refraction, scattering phase functions, all of which are spectrally dependent.

1.5.1 Composition of natural waters

Natural waters are complex media composed by living or non-living, organic or inorganic, "dissolved" or "particulate" mater. Although seawater contains a continuum of

discrete units varying in size from that of large mammals to that of a water molecule, the constituents of natural waters are traditionally divided into “dissolved” and “particulate” matter, based on the operational definition that “dissolved” material is everything that passes through a filter whose pore size is $\sim 0.2 - 0.4 \mu\text{m}$. Pure sea water, particulate matter and dissolved substances, all determine the optical characteristics of natural water bodies and affect the amount of light that can penetrate to a certain depth.

i) Pure seawater consists of pure water plus various dissolved salts that average about 35‰ (35 parts per thousand) by weight. These salts increase scattering by about 30%, relative to pure water. Their effect on absorption is considered to be negligible at visible wavelengths (Mobley, 1994). However, these dissolved salts can increase absorption slightly at ultraviolet wavelengths and significantly at very long wavelengths ($\lambda > 0.1 \mu\text{m}$) (paragraph 1.5.2).

ii) Both fresh and saline waters contain varying concentrations of dissolved organic material (DOM). Autochthonous primary production and river run-off of terrestrial organic matter (allochthonous production) are the major sources of DOM. The optically active fraction of dissolved organic matter is known as chromophoric dissolved organic material, CDOM, and plays a major role in determining underwater light availability in oceans. Due to its strong absorption in the short, ultraviolet wavelengths (see also paragraphs 1.5.6 and 2.3.4.3), CDOM is one of the major components controlling the amount of underwater UV, especially in lakes, rivers, estuaries and coastal environments where its concentration is usually higher than in open ocean waters.

iii) Particulate matter consists of a) living organic particles such as zooplankton, phytoplankton, viruses and bacteria, b) non-living organic particles such as colloids and organic detritus and c) inorganic particles.

Zooplankton are small (sizes range from tens of μm to 5 cm), living organisms of only limited mobility. They are generally considered to be ineffectual aquatic colorants and, consequently, are ignored in most water-color models. One reason for this is their small concentration compared to the many orders of magnitude higher concentrations of phytoplankton and bacterioplankton. However, there are locations where zooplankton populations can be substantial enough to affect water optical properties. Even at large concentrations, these large particles tend to be missed by optical instruments that randomly sample small volumes of water (Mobley, 1994).

Phytoplankton, the principal primary producers of the oceans, are free-floating microscopic plants with sizes from $2\mu\text{m}$ (nanoplankton) to more than 2cm (macroplankton). Phytoplankton are primarily responsible for determining the optical properties of most oceanic (case 1) waters. Their chlorophylls (a, b, c) and other photosynthetic pigments strongly absorb light in the red and blue wavelength range. Phytoplankton are also efficient scatterers of light, influencing the total scattering properties of sea water. Due to their relatively large size, the larger phytoplankton species contribute relatively little to backscattering in the visible. The principal phytoplankton taxonomic groups include diatoms (class Bacillariophyceae), dinoflagellates (class Pyrrophyceae), coccolithophores (class Prymnesiophyceae) and silicoflagellates (class

Chrysophyceae). In estuarine, lake and coastal environments other taxonomic groups may locally predominate, such as euglenoid flagellates (class Euglenophyceae), green algae (class Chlorophyceae), blue-green algae (class Cyanophyceae) and brown colored phytoflagellates (class Haptophyceae) (Kennish, 2001).

Living bacteria are microscopic unicellular organisms, in the size range 0.2-2 μ m in diameter. Recent studies (Spinrad et al 1989, Morel and Ahn 1990, Stramski and Kiefer 1991) suggest that free-living heterotrophic bacteria are significant scatterers and absorbers of light, especially at blue wavelengths and in oligotrophic waters with low chlorophyll concentrations. According to Stramski and Kiefer (1991) and Morel and Ahn (1990) heterotrophic bacteria are likely the most significant backscatterers among microorganisms.

The concentration of virus particles (size range: 20-250 nm) in natural marine waters can range from 10^6 to as high as 10^{15} particles per m^3 in eutrophic regions (Kepner et al, 1998, Bergh et al 1989). Viruses infect all members of the marine plankton and are thought to play an important role in the ecological control of planktonic microorganisms (Proctor and Fuhrman, 1990). In spite of their large numbers, it is unlikely that viruses contribute significantly to the absorption and total scattering properties of natural waters, since they are inefficient absorbers and scatterers on a per particle basis (Mobley, 1994). However, since they are very small particles, there have been speculations that viruses may contribute significantly to the backscatter coefficient, b_b , at least at blue and UV wavelengths in very clear waters. According to a recent study by Balch et al. (2000), this

is not very likely. Laboratory experiments in which the volume scattering functions of four bacterial viruses (bacteriophages) of varying sizes were measured with a laser – scattering photometer using a He-Ne and/or Argon ion laser (632.8 and 514 nm, respectively) suggest that viruses, while highly abundant in the sea, are not a major source of backscattering (Balch et al, 2000).

Inorganic particles generally consist of trace metals, clay minerals, sand, quartz, silt, in a wide range of sizes. Little is known on the optical properties of inorganic particles present in natural waters. However, it is recognized that these particles can significantly affect light penetration especially in turbid, coastal waters, where their concentration can be substantially high as a result of large river discharges, heavy sediment load and long and short range transport of atmospheric particulates followed by dry deposition. Detrital particles are non-living organic particles of various sizes, fragments of decayed plants and animals along with their excretions. Absorption by non-pigmented particulate matter, including contribution by detrital and inorganic, mineral substances, is more significant at the shorter wavelengths and generally decreases in an exponential fashion with increasing wavelength (Kishino et al, 1985, Roesler et al, 1989) (paragraph 2.3.4). According to Stramski and Kiefer (1991) sub-micron detrital and mineral particles of low-index-of-refraction are among the most significant backscatterers in the ocean.

1.5.2 Optical characteristics of pure sea water. Absorption and scattering

“Pure” water is most often taken to imply water that is free from the optical effects of any terrestrially, atmospherically, biologically derived organic and inorganic matter. According to Bukata et al (1995), pure water can be defined as a chemically pure substance comprised of a mixture of several water isotopes of various molecular masses. Pure sea-water consists of pure water plus various dissolved salts that average about 35‰ (35 parts per thousand) by weight (Mobley, 1994). Several studies (Pegau and Zaneveld, 1993, Hojerslev and Trabjerg, 1990, Buiteveld et al, 1994) have shown that absorption by water is weakly dependent on temperature, especially in the red and near-infrared ($\partial a/\partial T \approx 0.003 \text{ m}^{-1} \text{ }^\circ\text{C}^{-1}$ between 10°C and 30°C over the wavelength range 400-600 nm according to Hojerslev and Trabjerg (1990), $\partial a/\partial T \approx 0.01 \text{ m}^{-1} \text{ }^\circ\text{C}^{-1}$ at $\lambda=750 \text{ nm}$ according to Pegau and Zaneveld (1993), $\partial a/\partial T \approx 0.016 \text{ m}^{-1} \text{ }^\circ\text{C}^{-1}$ at $\lambda=750 \text{ nm}$ according to Buiteveld et al (1994)) and slightly dependent on salinity. Absorption by water molecules is dominant relative to scattering by water at wavelengths larger than 550 nm. However, water scattering becomes very important at wavelengths smaller than 500 nm.

Since pure water is the main component of natural waters, knowledge of its spectral optical characteristics is very important for biological, chemical, physical, meteorological studies. Therefore, a large number of researchers have studied the scattering and absorption properties of pure water, using a variety of techniques (Sawyer, 1931; Hodgman, 1933; Grundinkina, 1956; Sullivan, 1963; Hale and Querry, 1973; Palmer and Williams, 1974; Hass and Davisson 1977; Tam and Patel, 1979; Ravisankar et al, 1988;

Quickenden and Irvin, 1980; Smith and Baker, 1981; Sogandares and Fry, 1997; Pope and Fry, 1997).

Absorption properties of pure water

The numerical values derived for the water absorption spectra show some inconsistencies, particularly in the spectral region below 500 nm, that could be attributed to the use of different methods in the estimation of these values, to experimental errors, or even to the variability in sample purity used by different investigators. Fournier (2002) suggests that most of the problem of inconsistent values in the ultraviolet wavelength range can be accounted for by the presence of residual dissolved oxygen and trace organic materials in the water samples.

A set of absorption values for pure sea-water that has been widely used since its publication in 1981, is the Smith and Baker water absorption coefficients. Smith and Baker made an indirect determination of the upper boundary of the spectral absorption coefficient, $a_w(\lambda)$, of pure sea water in the wavelength range $200 \text{ nm} < \lambda < 800 \text{ nm}$. In their work they assumed that for the case of 'clearest waters': i) absorption by salts or other dissolved substances is negligible ii) the only scattering is by water molecules and salt ions and iii) there is no inelastic scattering. Based on these assumptions they derived (from radiative transfer theory) the relation:

$$a_w(\lambda) \leq K_d(\lambda) - \frac{1}{2} b_{sw}(\lambda) \quad (1.5-1)$$

where b_{sw} is the spectral scattering coefficient for pure sea water. Assuming that b_{sw} is known, and using measured values of the diffuse attenuation function $K_d(\lambda)$ from very clear waters, Smith and Baker estimated $a_w(\lambda)$ from eq. (1.5-1). These values of the absorption coefficients for pure seawater are shown in figure 1.5-1.

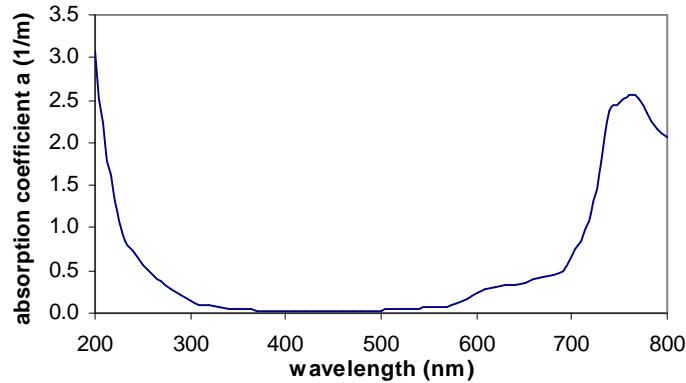


Figure 1.5-1: Absorption coefficients for pure seawater as determined by Smith and Baker (1981).

Since these values of the absorption coefficient $a_w(\lambda)$ are upper bounds, the true absorption of pure water is likely to be somewhat lower, at least at violet and blue wavelengths (Sogandares et al, 1991). According to Smith and Baker, uncertainties in these values can be due to the fact that K_d , an apparent optical property, is influenced by environmental conditions. Also, the values of $a_w(\lambda)$ at wavelengths below $\lambda = 300$ nm are ‘merely an educated guess’ (Mobley, 1994). Smith and Baker estimated that the accuracy of these values is between +25% and -5% for wavelengths between 300 and 480 nm, and +10% to -15% for wavelengths between 480 and 800 nm.

Sogandares and Fry (1997) estimated the absorption by pure water (340-640 nm) using photothermal deflection spectroscopy. Their spectrum showed an absorption minimum in

the blue wavelengths that is significantly lower than the Smith and Baker data. According to Sogandares and Fry this difference is most probably due to the high purity of the sample used and the fact that their technique is independent of scattering effects in the sample. However, according to Fry (2000) this technique is very difficult to implement.

Another set of values for the spectral absorption coefficient of pure water was obtained by Pope and Fry (1997) using an integrating cavity absorption meter (ICAM) that was developed by Fry, Kattawar and Pope (Fry et al, 1992). According to Pope and Fry (1997) the integrating cavity technique is essentially free of scattering effects in the sample, is relative simple to implement and is very sensitive to weak absorption. The Pope and Fry absorption coefficients cover the spectral region between 380 and 700 nm and are probably one of the most reliable sets in the visible wavelength range (Zhao et al, 2002). As in the case of the Sogandares and Fry (1997), the Pope and Fry absorption coefficients in the blue wavelengths are much lower compared to those estimated by Smith and Baker.

According to Pope and Fry (1997), absorption values for pure seawater measured by Tam and Patel (1979), Smith and Baker (1981), Buiteveld et al (1994), Sogandares and Fry (1997) and Pope and Fry (1997), are in very good agreement in the near-infrared region of the spectrum (wavelengths greater than 600nm). In this area of the spectrum scattering by water molecules is insignificant and the absorption coefficients are relatively large. However, as we move to the shorter wavelengths large inconsistencies become apparent (fig. 1.5-2). This could be because i) absorption coefficients get lower

and small inaccuracies in the measurements affect the result significantly, ii) contamination can easily dominate the water absorption and iii) scattering effects become large comparing to absorption. Measurements in the near- ultraviolet spectral region ($\lambda < 400$ nm) become even more difficult.

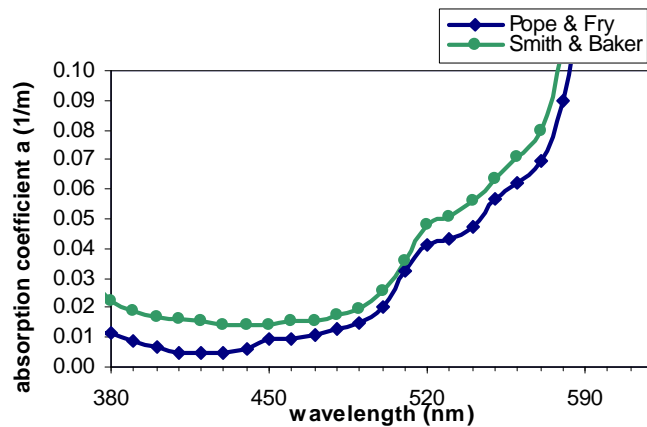


Figure 1.5-2: Spectral absorption coefficients for sea water (380 nm- 620 nm) as determined by Pope and Fry (1997) and by Smith and Baker (1981).

Studies by Grudinkina (1956) (from 210 nm to 350 nm), Quickenden and Irwin (1980) (from 190 nm to 220 nm) and Boivin et al (1986) (254, 313 and 366 nm), were among those focused on the pure water absorption characteristics in the UV region. In their study Quickenden and Irwin demonstrated the effect of subsequent purification steps on the water absorption spectrum. Traces of UV-absorbing contaminants can produce substantial enhancement of the pure-water absorption coefficient in the shorter wavelengths. According to Quickenden and Irwin (1980) and Fournier (2002) the presence of residual dissolved oxygen may also affect the measurements of pure water absorption coefficients in the blue wavelengths.

For the pure water absorption coefficients in the UV-visible-NIR wavelength region, a combination of absorption data sets can be used. According to Fry (2000) the most reliable data for the wavelength region 380 to 700 nm appear to be those of Pope and Fry (1997). For shorter wavelengths in the region 196 to 320 nm, the most reliable data are probably those of Quickenden and Irvin (1980). For the gap between these two data sets, Fry (2000) suggests that a best guess is a straight extrapolation between the 320 nm data of Quickenden and Irvin and the 380 nm data of Pope and Fry (fig. 1.5-3).

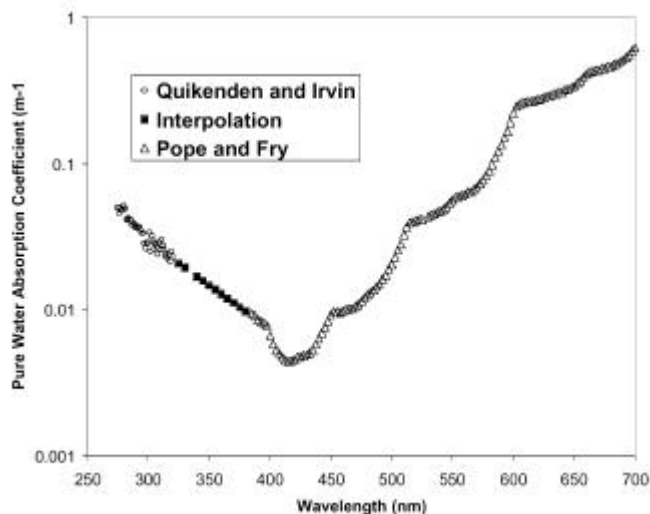


Figure 1.5-3. Absorption by pure water as measured by Pope and Fry (1997) in the wavelength region 380-700nm, and Quickenden and Irvin (1980) at 280-320 nm.

In the infrared region of the spectrum, the liquid-water absorption spectrum is driven by harmonics of the O-H vibrational modes whose fundamental frequencies are $\nu_1=3280 \text{ cm}^{-1}$ for the symmetric stretch, $\nu_2=1645 \text{ cm}^{-1}$ for the scissors mode, and $\nu_3=3490 \text{ cm}^{-1}$ for the anti-symmetric stretch. In the liquid phase, these features are significantly broadened and shifted by intermolecular interaction. As wavelength

decreases from the near infrared to the shorter wavelengths, the third-, fourth-, fifth-, and sixth-harmonic combinations of the O-H stretch modes appear as shoulders in the spectrum at approximately 960, 740, 600, and 520 nm, respectively. Data from Sogandares and Fry (1997) showed shoulders due to the seventh- and eighth- harmonics at 455 and 405 nm.

Scattering properties of pure water

The theory and observations pertaining to scattering by pure water and by pure seawater have been reviewed in detail by Morel (1974). Random molecular motions give rise to fluctuations in the number of molecules in a given volume ΔV . According to the Einstein – Smoluchowski “fluctuation theory” of scattering, these fluctuations in molecule number density are associated with fluctuations in the index of refraction, and the interaction of the radiation field with these inhomogeneities gives rise to scattering. What happens in sea water is that random fluctuations in the concentrations of the various ions (Cl^- , Na^+ , etc) give even larger index of refraction fluctuations and thus, greater scattering. The volume scattering function for pure water or pure sea-water (fig. 1.5-4) has the form:

$$\beta_w(\psi, \lambda) = \beta_w(90^\circ, \lambda_o) [\lambda_o / \lambda]^{4.32} (1 + 0.835 \cos^2 \psi) \quad (1.5-2)$$

where $\beta_w(\psi, \lambda)$ is the volume scattering function for pure water, ψ is the scattering angle and λ is the wavelength.

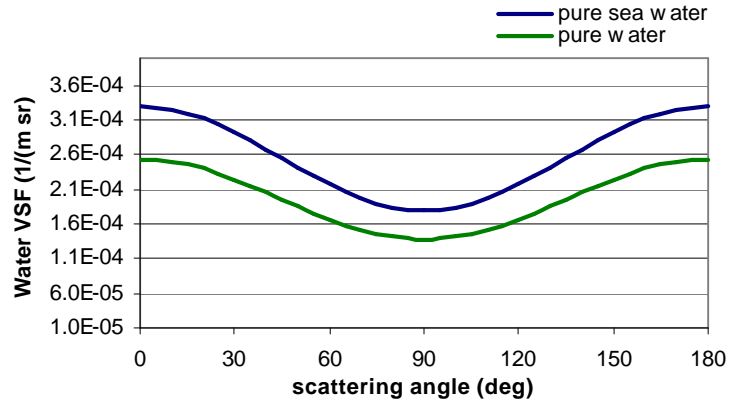


Figure 1.5-4: Volume scattering function for pure water and pure sea water, for $\lambda=500\text{nm}$

The function in eq 1.5-2 is similar to the function for atmospheric Rayleigh scattering:

$$\beta_{\text{Rayleigh}}(\psi, \lambda) = \beta_{\text{Rayleigh}}(90^\circ, \lambda_0) [\lambda_0 / \lambda]^4 (1 + \cos^2 \psi) \quad (1.5-3)$$

The wavelength dependence of $\lambda^{-4.32}$ (rather than λ^{-4}) in eq. 1.5-2 results from the wavelength dependence of the index of refraction in sea water, while the 0.835 factor (rather than 1) is attributable to the anisotropy of the water molecules. There is a similar, but smaller, anisotropy function for air. Because of the similarity between eq (1.5-2) and eq (1.5-3), scattering by pure water is also commonly known as Rayleigh scattering. The total scattering coefficient $b_w(\lambda)$ is given by:

$$b_w(\lambda) = 16.06 [\lambda_0 / \lambda]^{4.32} \beta_w(90^\circ, \lambda_0) \quad (1.5-4)$$

According to Morel (1974), the pure seawater (salinity, $S = 35-39 \text{‰}$) scattering coefficients are about 30% greater than the pure water values (measurements in the 350-600 nm shown in Morel (1974)) because of the presence of the dissolved salts. The Smith and Baker scattering coefficients for pure seawater are shown in figure 1.5-5.

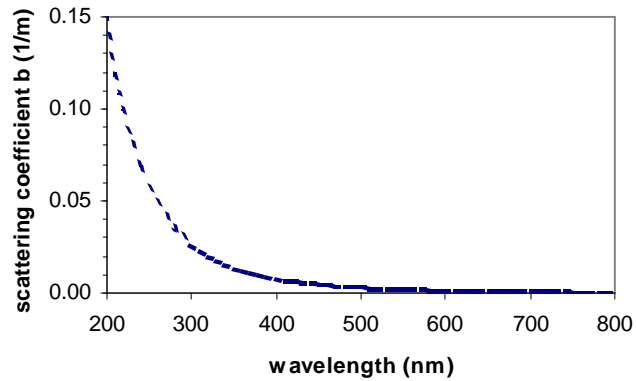


Figure 1.5-5 Smith and Baker scattering coefficients for pure sea-water.

The effect of inelastic Raman scattering by water molecules also affects light penetration into the water in the green to red ($\lambda > 550$ nm) wavelength region (Chang and Young, 1972; Sugihara et al, 1984; Marshall and Smith, 1990). Raman scattering is a process by which an incident photon excites a molecule into a higher rotational and vibrational quantum state. The excited molecule emits a photon of wavelength longer than that of the incident photon, while the energy difference is retained by the molecule as internal (vibrational or rotational) energy. If the molecule is already in an excited state, then the molecule may emit a photon of shorter wavelength than the incident photon, returning to the ground state. However, at the temperatures of liquid water, Raman scattering from longer to shorter wavelengths is insignificant (Mobley, 1994). An appropriate volume inelastic scattering function, that can be used in order to incorporate Raman scattering into radiance transfer equations, has been developed by Haltrin and Kattawar (1991, 1993).

1.5.3 Absorption characteristics of phytoplankton

Phytoplankton, microscopic, plantlike organisms that float or swim in waters (phytoplankton comes from the Greek words phyton = plant + planktos = wandering) are among the most significant live substances that determine the optical and biological characteristics of open ocean and coastal waters. Phytoplankton occur with incredible diversity of species, size, shape and concentration. Their cell size can range from less than 1 μm to more than 200 μm . On a global scale, phytoplankton are the most important biomass producers in aquatic ecosystems. They constitute the basis for the intricate food web in the oceans and are thus a prerequisite for the production of fish, crustaceans and mollusks. Phytoplankton account for nearly half of the total photosynthesis on the planet, reducing the amount of carbon dioxide in the atmosphere while releasing oxygen.

For growth and reproduction, phytoplankton require sunlight, water, and nutrients, such as nitrogen and iron. Because sunlight is most abundant at and near the sea surface, most phytoplankton must remain in the upper part of the water column (near-surface and mid water column). When surface waters are cold, deeper waters can upwell, bringing essential nutrients toward the surface where the phytoplankton may use them. However, when surface waters are warm and less dense (as during an El Niño), they do not allow the colder, deeper currents to upwell and effectively block the flow of life-sustaining nutrients. As phytoplankton starve and die, so too do the fish and mammals that depend upon them for food. Some smaller phytoplankton ($< 2 \mu\text{m}$) can be increasingly important, in terms of community and structure, deep in the water column. According to Johnson et al (1999) during the US JGOFS Arabian Sea cruises (1994-1996) a strong,

secondary chlorophyll maximum was observed at the base of the euphotic zone (120-140 m depth) at several locations. This chlorophyll maximum was coincident with the transition layer between oxic and anoxic conditions. At these depths, nutrients were found to be high (Johnson et al., 1999). However, light levels were extremely low, suggesting light limitation for phytoplankton production. If light is limited and there are adequate nutrients immediately above the deep population maximum, there must be an additional advantage for this population of small phytoplankton, such as predator avoidance due to anoxic conditions at that water column location (Johnson et al., 1999).

Light absorption by phytoplankton occurs in various photosynthetic pigments and depends on the particular species, as well as cell size and physiological state, which in turn depend on environmental factors (such as ambient light and nutrient availability, mentioned above). Phytoplankton pigments absorb light and transform the energy of sunlight into chemical energy through the process of photosynthesis. Since each pigment displays a characteristic absorption spectrum, the absorption properties of different species of phytoplankton cells depend upon their pigment composition. There are three basic types of photosynthetic pigments, the chlorophylls, the carotenoids and the biliproteins. While all photosynthetic plants contain chlorophyll and carotenoids, the biliprotein chloroplast pigments are most often found in certain blue-green and red algae (divisions of Rhodophyta, Cryptophyta and Cyanophyta).

Chlorophylls are the main photosynthetic pigments in plants. There are several chemically distinct types of chlorophyllous pigments, chlorophylls a, b, c and d. All photosynthetic plants contain chl-a, while most classes of plants contain in addition chl-b

or chl-c. It is still uncertain as to whether or not chl-d plays a role in photosynthesis (Bukata et al, 1995). The basic structure of a chlorophyll molecule is a porphyrin ring, co-ordinated to a central magnesium atom (fig. 1.5-6). The difference between the two pigments chl-a and chl-b is in the composition of a sidechain. In chl-a this sidechain is a $-CH_3$, while in chl-b it is a $-CHO$. This difference 'tunes' the absorption spectrum to slightly different wavelengths in the two chlorophylls. Chlorophylls -a and -b have one strong absorption band (band 'a') in the red region of the spectrum (~ 675 nm for chl-a and ~ 650 nm for chl-b), and a stronger absorption band ('Soret' band) in the blue wavelengths (~ 440 nm for chl-a and ~ 460 nm for chl-b) (fig. 1.5-7). Chl-c represents a mixture of slightly spectrally distinct components chl-c₁, chl-c₂ and chl-c₃, which absorb strongly in the blue region of the spectrum (intense Soret band), while they show some smaller absorption maxima at larger wavelengths (~ 580 and ~ 630 nm) (fig. 1.5-8) (table 1.5-1). The term "chlorophyll concentration" in practice refers to the sum of the main chlorophyllous pigment chl-a, and the related pheophytin-a (a pheophytin-a molecule is a chl-a without the magnesium atom). This sum is often called 'pigment concentration'. Chlorophyll concentrations range from 0.01 mg m^{-3} in the clearest waters, to more than 100 mg m^{-3} in eutrophic estuaries or lakes (Mobley, 1994).

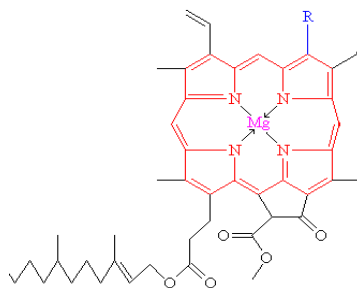


Figure 1.5-6: Basic structure of a chlorophyll molecule. For chl-a, R = $-CH_3$, while for chl-b, R = $-CHO$ (Kirk, 1994)

Table 1.5-1: Absorption maxima by chlorophyll, carotenoids and biliproteins phytoplankton pigments

Pigment groups			Main Absorption
chlorophylls	a		~ 440 nm, ~675 nm
	b		~ 460 nm, ~650 nm
	c	c1	~ 460 nm
		c2	~ 580 nm
c3		~ 630 nm	
carotenoids			450 - 550 nm
biliproteins			480 - 600 nm

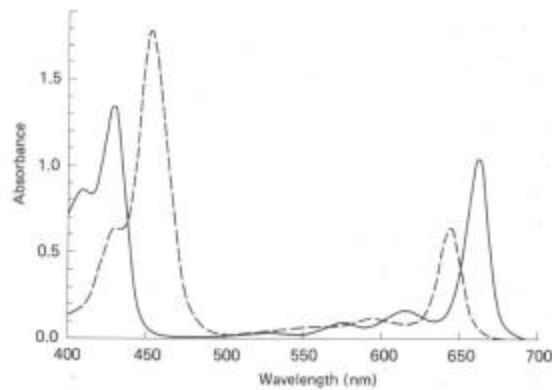


Figure 1.5-7: Absorption by chl-a and chl-b, in diethyl ether at a concentration of 10 μ g/ml and 1 cm pathlength. After Kirk (1994), using data by French (1960). (chl-a: solid line, chl-b: dashed line)

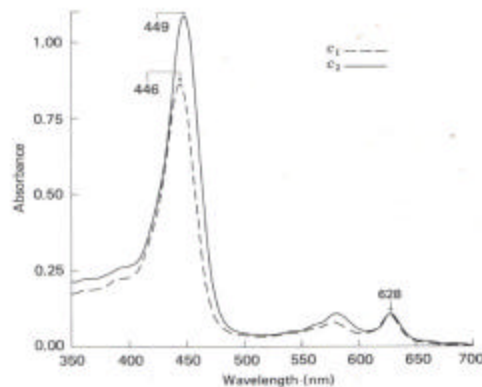


Figure 1.5-8: Absorption by chl- c_1 and chl- c_2 , in acetone containing 2% pyridine with a pathlength of 1cm. After Kirk (1994), using data by Jeffrey S.W. (chl- c_1 (2.68 μ g/ml): solid line, chl- c_2 (2.74 μ g/ml): dashed line)

Accessory pigments (such as biliproteins and carotenoids) assist plants in catching radiant energy by having absorption bands at different wavelengths than chlorophyll. In this way, changes in the spectral distribution of light can be compensated by phytoplankton making more accessory pigments. This ability of phytoplankton to change the amount and type of pigments in response to changes in the intensity and spectral distribution of light is called photoadaptation. The carotenoids represent more than 100 different pigments that absorb mainly between 450 nm to 550 nm. For example, chloroplast carotenoids include α -carotene, β -carotene, diadinoxanthin, fucoxanthin, diatoxanthin, peridinin and other pigments. β -carotene is present in all phytoplankton, except Cryptophyta. Since carotenoids absorb in the green-blue wavelengths, their characteristic colors are yellow to red. The biliproteins are found only in red and blue-green algae (divisions Rhodophyta, Cryptophyta and Cyanophyta). The biliprotein pigments are divided into three classes, the phycoerythrins - phycoerythrocyanins, the phycocyanins, and the allophycocyanins. Their main absorption is between 480 -600 nm.

Different species of phytoplankton contain photosynthetic pigments in different proportions. Diatoms (class Bacillariophyta, division Chrysophyta), at times the major components of phytoplankton in most marine and fresh water environments (Kirk, 1994), are usually yellow, yellow-brown due to xanthophyll (fucoxanthin and diatoxanthin) carotenoids. Dinoflagellates (division Pyrrophyta), second to diatoms in total marine abundance (Kennish, 2001), are characterized by a brownish to reddish color that becomes most prominent during dinoflagellates bloom events, known as 'red tides'. The reddish color is caused by the carotenoid pigment 'peridinin', present in some

dinoflagellates, which shows strong absorption bands in the 500-560 nanometer range. Coccolithophorids (division Chrysiophyta, class Haptophyceae), major constituents of the marine phytoplankton particularly in the warm open ocean waters, have also yellow, yellow-brown cells. Since the coccolithophorid-cells are covered externally by small calcareous plates that strongly reflect light, bloom events may appear as milky turquoise patches in the ocean. Green algae, found mainly in freshwater environments, form the phylum Chlorophyceae and are named for their green chloroplasts (dominant pigments chl-a, chl-b). Figure 1.5-9 shows the chlorophyll-specific phytoplankton absorption spectra, $a^*_{\text{phyt}}(\lambda)$, (absorption per unit concentration of chl-a + pheopigments) for eight species of phytoplankton based on laboratory measurements made by Sathyendranath, Lazzara and Prieur (1987). Considerable variability among the phytoplankton absorption curves is observed. The eight phytoplankton species belong in the groups of Chlorophyceae, Haptophyceae and Bacillariophyceae. According to Sathyendranath et al. (1987), specific absorption at the Soret band, $a^*_{\text{phyt}}(440)$, varied between 0.019 and 0.047 m^2mg^{-1} , while $a^*_{\text{phyt}}(676)$ varied between 0.011 and 0.023 m^2mg^{-1} . Studies by Prieur and Sathyendranath (1981) found $a^*_{\text{phyt}}(440)$ to vary within the range 0.013 to 0.077 m^2mg^{-1} .

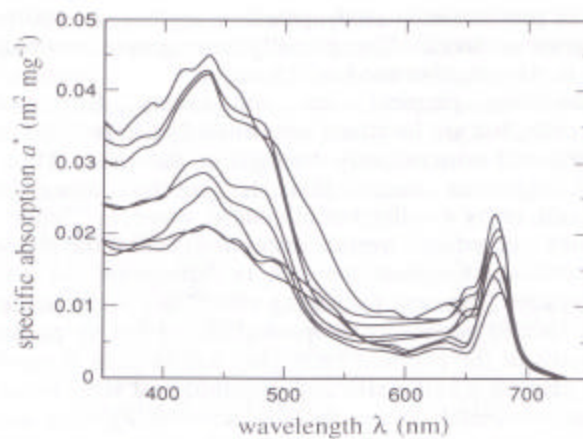


Figure 1.5-9: Chl-specific absorption spectrum of eight phytoplankton species based on laboratory measurements (Sathyendranath et al., 1987).

1.5.4 Absorption by non-pigmented particulate matter

Non-pigmented particulate matter includes suspended, non-living, organic and inorganic particles, or sediments re-suspended during mixing processes (e.g. wind-induced turbulence, tidal currents). Detrital particulates are non living organic particles, fragments of decayed plants and animals along with their excretions. Inorganic particles may include minerals, such as fine clay, silt particles, sand, or precipitates such as iron and manganese hydroxides and calcium carbonate (Bukata et al, 1995).

A number of different methods have been used to separate the total particulate absorption into absorption by living phytoplankton and non-living, non-pigmented particulate matter. Itturiaga and Siegel (1989) used a microphotometric technique, based upon the direct determination of the absorption efficiency factor, geometric cross sectional area and taxonomic information for many individual particles. Another approach is to use statistical methods based on typical absorption spectra of phytoplankton and detritus (Morrow et al , 1989) or modeling based on assumed functional form for detrital absorption (Bricaud and Stramski, 1990). A method that has been widely used is the method proposed by Kishino et al (1985), which is based on measurements of particulate absorption retained on glass fiber filters, before and after chemical extraction (e.g. using methanol) of the living phytoplankton pigments. A disadvantage of the chemical extraction method is that some detrital pigments such as pheophytin and pheophorbide are also extractable using methanol, while some of the phytoplankton pigments are not easily extracted. As a result absorption associated with these pigments may be included in the 'non-pigmented' absorption spectrum.

From early measurements of non-pigmented particulate absorption (Yentch, 1962) it became apparent that the non-pigmented particulate component intensifies particulate absorption at the short, ultraviolet wavelengths, and that the spectral shape of non-pigmented particulate absorption is similar to that of chromophoric dissolved organic material (more details on CDOM absorption are given in paragraph 1.5.6). More recent studies on the absorption characteristics of non-pigmented particles (Kishino et al, 1985; Roesler et al, 1989; Morrow et al, 1989) have shown that non-pigmented particulate absorption increases exponentially with decreasing wavelength. According to Roesler et al (1989) an exponential model can be used to fit the absorption spectra:

$$a_{\text{npp}}(\lambda) = a_{\text{npp}}(\lambda_o) \cdot \exp[-S_{\text{npp}} \cdot (\lambda - \lambda_o)] \quad (1.5-5)$$

where $a_{\text{npp}}(\lambda)$ and $a_{\text{npp}}(\lambda_o)$ are the non-pigmented particulate absorption coefficients at wavelength λ and a reference wavelength λ_o and S_{npp} is a constant that defines how rapidly the absorption decreases with increasing wavelength. Roesler et al (1989), using water samples from different sites near the San Juan Islands, Washington, found an average value of 0.011 nm^{-1} for the exponential coefficient, S_{npp} (measurements performed in the wavelength range 400-750nm). Measurements performed by Gallegos et al (1990) in the Rhode River, a turbid sub-estuary on the western shore of Chesapeake Bay, showed that S_{npp} had a mean value of 0.0104 nm^{-1} . Other studies on the absorption by non-pigmented particulate material present in water samples collected from various aquatic environments (e.g. Kishino et al, 1986 (studies in NW Pacific); Maske and Haardt, 1987(studies in Kiel Harbor); Morrow et al, 1989; Iturriaga and Siegel, 1988; Bricaud and Stramski (studies in the Sargasso Sea)) found values for the exponential coefficient S_{npp} in the range 0.006 to 0.014 nm^{-1} . Measurements of non-pigmented

particulate matter absorption spectra, $a_{\text{pp}}(\lambda)$, that show the exponential decrease of absorption with increasing wavelength, are shown in figures 1.5-10 and 1.5-11.

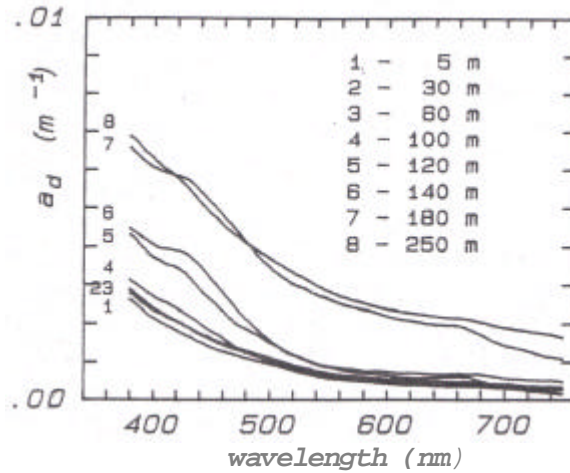


Figure 1.5-10: Absorption spectra of detrital material, a_d , measured by Bricaud and Stramski (1990) at various depths (5-250 m) in the Sargasso Sea (figure by Bricaud and Stramski, 1990).

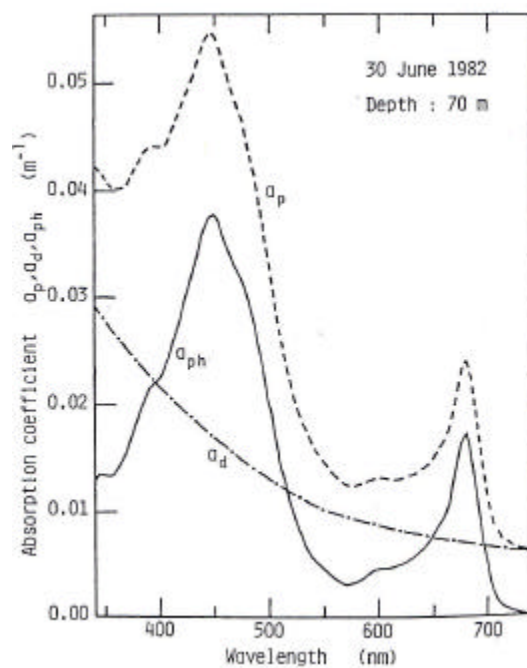


Figure 1.5-11: Absorption spectra of suspended particles, total particulate material, a_p , non-pigmented particulate matter, here shown as a_d , and the difference $a_p - a_d = a_{\text{ph}}$, which corresponds to absorption by pigmented, phytoplankton particles (figure obtained by Kishino et al., 1986)

1.5.5 Scattering by particles

Particulate matter, which is always present even in the “clearest” natural waters, affects the propagation of light within the aquatic medium not only through the process of absorption, but also through forward and backward scattering. Scattering intensifies attenuation mainly by increasing the pathlength a photon must traverse (and therefore the likelihood of this photon being absorbed), as well as by redirecting light into the backscattered direction and eventually out of the water. The total scattering coefficient by particles, b_p , and the backscattering coefficient, b_{bp} , (measured in m^{-1}) are defined as:

$$b_p(I) = 2p \int_0^p \beta_p(\mathbf{y}, I) \sin y dy \quad (1.5-6)$$

$$b_{bp}(I) = 2p \int_{p^2}^p \beta_p(\mathbf{y}, I) \sin y dy \quad (1.5-7)$$

where λ is the wavelength, ψ is the scattering angle and $\beta_p(\psi, \lambda)$ is the particles' volume scattering function that describes the angular distribution of scattered radiation (Preisendorfer, 1961). Particles that occur in natural waters have a continuous size distribution. The Rayleigh (for gasses) and Einstein-Smoluchowski (for liquids) theories of molecular scattering apply only when the scattering centers are small relative to the wavelength of light. A theoretical basis for predicting the light scattering behavior of spherical particles of any size was developed by Mie (1908). Mie scattering calculations can reproduce measured volume scattering functions and scattering coefficients, given the appropriate particle refractive indexes and size distributions (Stramski and Kiefer, 1991).

The scattering coefficients of most natural waters are much higher than pure sea-water. Scattering coefficients for various types of waters are given in Kirk (1983) (in his table 4.1), with $b(\lambda)$ values in the visible wavelengths ranging from as low as 0.016 m^{-1} (at 546 nm, in Tyrrhenian Sea, 1000 m depth) to more than 50 m^{-1} (400-700 nm) in certain inland and estuarine waters. Estuarine and coastal waters are typically characterized by much higher scattering (Kirk, 1983) than open oceanic, oligotrophic waters, mainly due to the much larger concentration of organic particulate matter, the presence of terrigenous particles and minerals in coastal regions and the re-suspension of sediments (caused from wave action, tidal currents and wind-induced turbulence in shallow waters).

The volume scattering functions measured in natural waters are significantly different from the symmetric (around $\psi=90^\circ$) volume scattering function of pure water, and they are highly peaked in the forward direction. Several particle volume scattering functions determined from in situ measurements in a variety of waters, ranging from very clear to very turbid, are shown in figure 1.5-12 (Kullenberg, 1974). As is shown in figure 1.5-12, the particles cause significant increase (at least a four-order magnitude increase) in the forward scattering, between $\psi = 90^\circ$ and $\psi = 1^\circ$ (Mobley, 1994). The contribution of water (density fluctuation scattering) to the total scattering is small, except at backscattered directions ($\psi \geq 90^\circ$) in clear natural waters (Morel and Prieur, 1977; Morel and Gentili, 1991). Among the most widely cited measurements of volume scattering function are those performed by Petzold (1972) in clear (Bahama Islands), coastal ocean (San Pedro Channel, California) and moderately turbid waters (San Diego Harbor). According to these measurements, the backscattering ($\psi > 90^\circ$) to total scattering ratio,

b_b/b , is 4.4% in the case of clear waters (50% for pure sea water) and only 1.3 % in the case of coastal ocean and 2% in the case of turbid-harbor waters (Mobley, 1994; his table 3.11). The “average particle” Petzold phase function (with $b_b/b = 0.018$), estimated by three sets of Petzold’s data from waters with high particulate load, has been widely used, as being typical for moderately turbid waters. However, b_b/b values can vary considerably, depending on the water type, and measurements of the backscattering fraction b_b/b are really important for accurate predictions of the underwater light field using radiative transfer calculations (Mobley, 2002) (see also discussion in chapter 3).

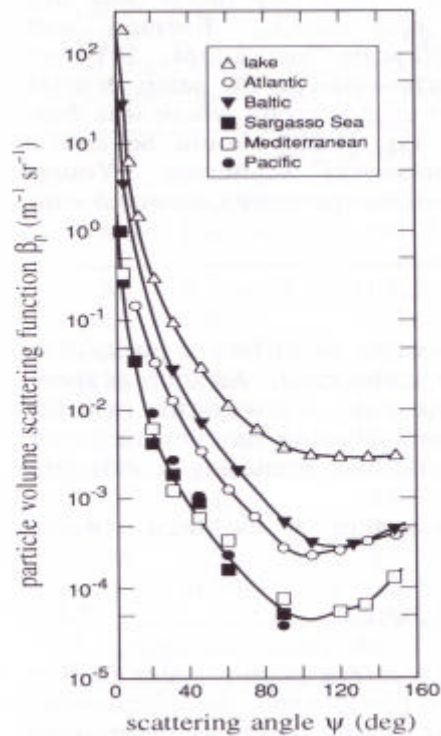


Figure 1.5-12: Particle volume scattering functions $\beta_p(\psi, \lambda)$ determined from in-situ measurements in a variety of waters, for various wavelengths (Kullenberg, 1974)

Scattering by phytoplankton cells varies from one species to another. According to Kirk (1983) algae such as diatoms, in which a substantial proportion of the total biomass

consists of mineralized cell walls, scatter more light (per unit chlorophyll) than 'naked' flagellates. Coccolithophores exhibit enhanced backward scattering, caused mainly by the presence of small calcareous plates that cover externally the living algal cells. This is why coccolithophoric bloom events may appear as milky turquoise patches in the ocean. The presence of gas vacuoles in blue-green algae also increases the intensity of scattering. According to Stramski and Kiefer (1991) small microbes in the size range 0.2-8 μm are responsible for the largest proportion of the light scattering by living organisms. Free-living heterotrophic bacteria (size fraction 0.2-2 μm) appear to account for 10 to 50% of the total particulate scattering. However, microorganisms larger than 2 μm appear to have negligible effect on backscattering, while backscattering is more important in the small, picoplankton cells, such as heterotrophic bacteria (Stramski and Kiefer, 1991).

According to studies by Bricaud et al (1983) and Stramski and Morel (1990), the backscattering fraction b_b/b is much lower for living cells (0.1% - 0.4%), than for mineral and detrital particles (~1.9 %). This could be due to the difference in the refractive indexes between living cells and inorganic particles (Bricaud et al, 1983). According to Morel and Bricaud (1981), Stramski and Kiefer (1991), Bukata et al (1991), Gallie and Murtha (1992), Whitlock et al (1981), the major source of particulate backscattering is associated with small (<0.6 μm), non-living, organic (detrital) or inorganic suspended material, whose concentrations are considerably larger in turbid, estuarine and coastal waters compared to open oceans.

Scattering by pure water shows significant wavelength dependence ($b \sim \lambda^{-4.3}$). Although particle scattering is not as strongly wavelength dependent as the ‘density fluctuation’ scattering, studies by Morel (1973), Kopelevich (1983), Kopelevich and Mezhencher (1983) suggest that particulate matter scatters the shorter wavelengths more intensely than longer wavelengths. According to measurements of particle volume scattering functions performed by Morel (1973), $\beta(\psi, \lambda)$ shows a wavelength dependence of the form $\beta(\psi, \lambda) \sim \lambda^{-n}$ (for measurements in the clear Tyrrhenian Sea waters and the turbid English Channel (Morel, 1973) n was in the range 0.8-1.9). A stronger wavelength dependence is expected for backward scattering, since the contribution by ‘density fluctuation’ scattering is more pronounced for $\psi > 90^\circ$ (backward directions). According to Kopelevich (1983) and Kopelevich and Mezhencher (1983), ‘small’ particles (mostly minerals less than 1 μm in size and with high index of refraction relative to water) contribute more to scattering at large angles, have a more symmetric (about $\psi=90^\circ$) scattering phase function and stronger wavelength dependence, $n=1.7$. For ‘larger’ particles (biological particles larger than 1 μm in size and with a low index of refraction), diffraction dominated scattering shows scattering phase function highly peaked at small angles (in agreement to studies by Bricaud et al, 1983 and Stramski and Morel, 1990, mentioned above), while the wavelength dependence is weak, $n=0.3$. More studies on the backscattering properties of particulate matter are definitely needed, especially since backscattering is extremely important in the estimation of water-leaving radiances and the interpretation of remote sensing observations.

1.5.6 Optical properties of chromophoric dissolved organic matter

Both fresh and saline waters contain varying concentrations of dissolved organic material. Dissolved organic matter (DOM) is recognized as one of the largest reactive pools of organic carbon in the biosphere and, as such, is a major component of the global carbon cycle. Processes that control DOM production, consumption, and distribution are biochemically significant with regard to carbon export and carbon storage within the ocean. Understanding these processes is critical to climate-change studies. The optically active fraction of dissolved organic matter, known as chromophoric dissolved organic material, plays a major role in determining the underwater light field in oceans.

CDOM, or else ‘yellow’ substance, ‘gilvin’, ‘aquatic humus’ or ‘gelbstoff’ (a term that means ‘yellow’ and was adopted by early German oceanographers, Jerlov (1976) and Leyendekkers (1967)), consists mainly of fulvic and humic acids. These compounds are yellow or brown in color and, therefore, when concentration of CDOM is large, water may have a yellowish brown color. Autochthonous primary production and river run-off of terrestrial organic matter (allochthonous production) are the major sources of CDOM in natural waters. According to Kopelevich and Burenkov (1977) oceanic CDOM consists mainly of two components, a component resulting from recent decomposition of phytoplankton (in agreement with reported observations of large CDOM concentrations during phytoplankton bloom events), as well as a more stable, much older component that results from biological activity in oceans, averaged over a long period (Bricaud et al, 1981). According to Blough and Del Vecchio (2002) the precise mechanisms and magnitude of the autochthonous CDOM production are still not well known. In the

complex and dynamic estuarine and coastal environments, where terrestrial, oceanic, atmospheric and human inputs of energy and matter converge, CDOM is subject to various transformations. Mixing, photochemical and microbial processes, as well as human activities (such as agriculture, changes in land use, logging and wetland drainage), can significantly impact delivery of dissolved material to the estuary and, most importantly, alter CDOM's composition, structure and optical properties.

Dissolved organic material is considered to be non-scattering. However, due to its strong absorption in the short, ultraviolet wavelengths CDOM is one of the major components controlling the amount of underwater UV, especially in lakes, estuaries and coastal environments where its concentration is usually found to be higher than in open ocean waters. Radiation in the short, ultraviolet wavelengths causes a broad spectrum of genetic and toxic effects on aquatic organisms and affects many photochemical processes (Smith and Cullen, 1995; Neale et al, 1998; Neale, 2000; Neale and Kieber, 2000). According to recent studies (Gibson et al 2000, Pienitz and Vincent 2000) climate-change related modifications of CDOM concentrations in aquatic environments, through changes in cloudiness, intensity and frequency of storm events, mixing processes and river runoff, affect biologically destructive UVB (290-315 nm) exposure to an extent comparable to ozone depletion, with significant consequences on the aquatic biota, the composition of the aquatic food webs and the overall structure and dynamics of the ecosystem. In addition, CDOM changes affect the underwater penetration of UVA (315-400 nm), which is almost unaffected by ozone changes. In coastal waters, CDOM absorption can extend well into the visible wavelengths, resulting in significant reductions in photosynthetically

active radiation available to phytoplankton. Moreover, because of its impact upon the underwater light field, CDOM can influence the accuracy of global satellite-based measurements of ocean chlorophyll and primary productivity. Although there has been a growing research effort, recently, towards obtaining a better understanding of the optical characteristics, transformation and cycling of CDOM in estuarine and coastal ecosystems, our current knowledge is still limited.

CDOM absorption spectra typically decrease with increasing wavelength, in an exponential fashion. Therefore, CDOM absorption can be described by the model (Bricaud et al, 1981):

$$a_{\text{CDOM}}(\lambda) = a_{\text{CDOM}}(\lambda_0) \cdot \exp[-S_{\text{CDOM}} \cdot (\lambda - \lambda_0)] \quad (1.5-8)$$

where $a_{\text{CDOM}}(\lambda)$ and $a_{\text{CDOM}}(\lambda_0)$ are the absorption coefficients at wavelength λ and at a reference wavelength λ_0 (often chosen to be $\lambda_0 = 440$ nm), and S_{CDOM} is the spectral slope coefficient that determines the rate of the exponential decline at longer wavelengths.

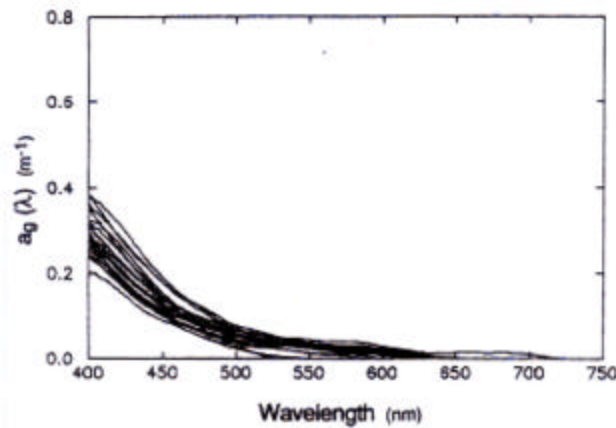


Figure 1.5-13: Absorption spectra of chromophoric dissolved organic material, $a_g(\lambda)$, (“g” for gelbstoff) as measured by Roesler et al (1989) at San Juan Islands.

The magnitude of CDOM absorption may vary substantially across fresh and marine waters. According to studies on CDOM optical characteristics (e.g. Green and Blough, 1994; Carder et al, 1989; Vodacek et al, 1997; Seritti et al, 1997) values of CDOM absorption coefficients at 355 nm, $a_{\text{CDOM}}(355)$, may range from less than 0.05 m^{-1} , in very clear, oligotrophic waters, to more than 15 m^{-1} in some rivers, lakes, and coastal regions (Table I, in Blough and DelVecchio, 2002). Variability in S_{CDOM} is associated with changes in the composition of the dissolved material present in the water. Values of S_{CDOM} have been observed to vary between 0.011 and 0.035 nm^{-1} .

Transect studies in coastal waters of eastern US (Vodacek et al, 1997) have shown that CDOM absorption coefficients decrease, while values of S_{CDOM} increase with distance off shore. This is probably because dissolved materials originating from the land usually show larger values of absorption and lower values of spectral slope. Variations of the absorption and slope, S_{CDOM} , may be related to differing proportions of fulvic and humic acids contained within CDOM. According to measurements in the Gulf of Mexico, performed by Carder et al (1989), fulvic acids are characterized by higher S_{CDOM} and lower mass-specific absorption coefficients at 440 nm, $a_{\text{CDOM}}^*(440)$, ($S_f = 0.0194 \pm 0.00044 \text{ nm}^{-1}$, $a_{\text{CDOM}}^*(440) = 0.007 \pm 0.001 \text{ m}^2 \text{ g}^{-1}$) compared to humic acids ($S_h = 0.011 \pm 0.00012 \text{ nm}^{-1}$, $a_{\text{CDOM}}^*(440) = 0.1302 \pm 0.00005 \text{ m}^2 \text{ g}^{-1}$). Therefore, the larger spectral slopes of marine CDOM may be related to the higher percentage of fulvic acids in marine CDOM (Malcolm, 1990). At the same time photochemical or biological processes, or a combination of the two, can result in changes of S_{CDOM} values. According to Pages and Gadel (1990) and Vodacek et al. (1997) photochemical degradation and bacterial activity

may alter the molecular weight of CDOM and cause subsequent increases in S_{CDOM} . Recent studies in the Chesapeake and San Francisco Bays (Boyd and Osburn, 2003) suggest that bacterial degradation of specific components of CDOM may impact CDOM's spectral characteristics. Coble and Brophy (1994) have suggested that biological production of certain compounds, such as proteins and amino acids, that absorb more strongly in UV than in the visible, may result in changes in the value of the CDOM exponential slope. According to Whitehead et al (2000) photobleaching of low molecular weight CDOM, can result in increase of the slope S_{CDOM} , since, as Gao and Zepp's (1998) studies indicate, photobleaching of low molecular weight (LMW) material under full-spectrum light is slower in the UVB wavelength range than in the UVA range.

The above studies, among many others, suggest that the CDOM optical properties are partially a function of the CDOM's origin and mixing history. More research on the mixing, photochemical and biological processes that affect CDOM's composition, structure and optical properties is definitely needed.

CHAPTER 2

Field Observations of Optical Properties in the Chesapeake Bay estuarine waters

2.1 Introduction

In the framework of this research project, I performed in-situ measurements of in-water optical properties and radiation fields, analyzed laboratory measurements of phytoplankton, non-pigmented particulate matter and CDOM absorption properties, and made measurements of atmospheric transmission characteristics within the northern part of the main stem of the Chesapeake Bay estuary. This has been a detailed measurements program that started in June 2001, in collaboration with the Smithsonian Environmental Research Center (SERC) and NASA, Goddard Space Flight Center (GSFC). Measurements were taken by using the SERC's and GSFC's facilities and instrumentation.

The combination of detailed in-situ and laboratory measurements is essential in gaining a better knowledge of the optical characteristics of the less thoroughly studied, case 2, estuarine waters. Among the main objectives of the project was obtaining a sufficiently complete suite of measurements so as to be able: i) to perform detailed radiative transfer calculations with minimum assumptions on the water's optical characteristics and produce a closure experiment for the underwater inherent and apparent optical properties in these optically complex waters, ii) to apply the detailed in-situ and laboratory measurements to the interpretation and validation of satellite ocean color observations.

2.2 Methodology

2.2.1 Location and duration of measurements

Seventeen cruises were performed between 4 June 2001 and 8 November 2002. The in-situ measurements were made at a location in the Chesapeake Bay that is sufficiently wide to have several satellite (MODIS) pixels sampling the water (highest satellite spatial resolution of 1 km x 1 km at nadir). This area extends from 76.34W to 76.54W longitude and from 38.71N to 38.89N latitude (fig. 2.2-1).

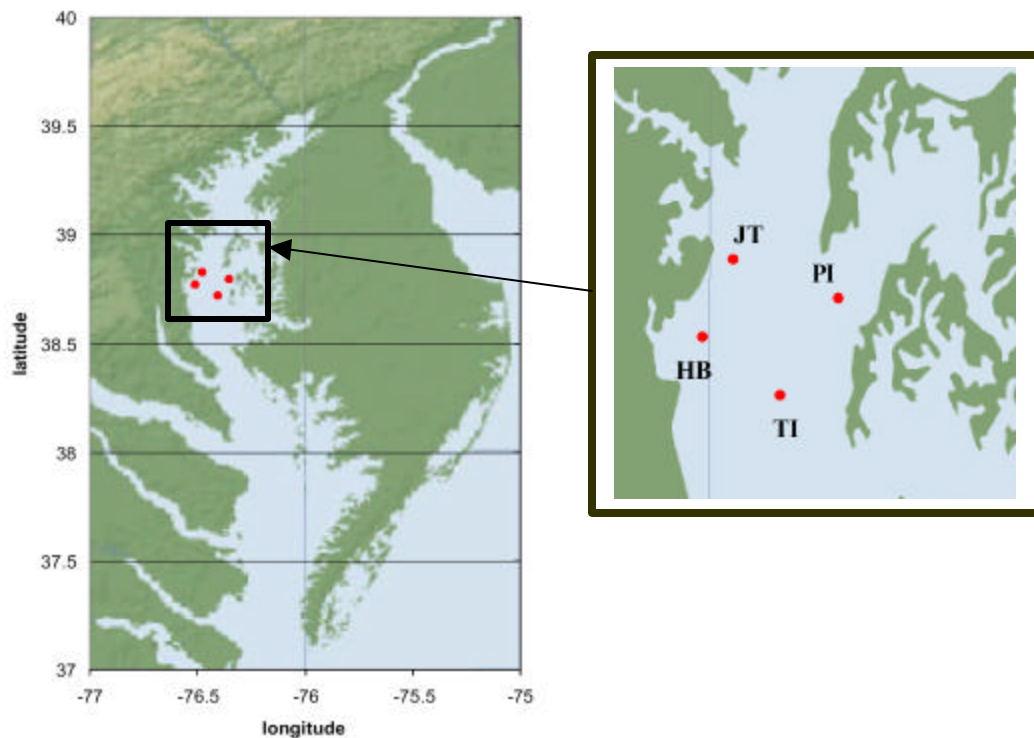


Figure 2.2-1: Location of in-situ measurements (HB, PI, TI and JT stations).

Upwelling and downwelling radiance and irradiance profiles, and profiles of absorption, attenuation, scattering, backscattering, temperature, salinity and chlorophyll-a concentration, [Chl-a], in the water have been measured at four sites, PI (Poplar Island),

HB (Herring Bay), TI (Tilghman Island) and JT (Jetta), to study the spatial variation of the water optical properties (fig. 2.2-1). The “starting point” of each cruise was the SERC dock, located at latitude 38.39°N and longitude 76.54°W, in the Rhode River sub-estuary, along the western shore of Chesapeake Bay.

Specific cases of phytoplankton blooms events, relatively clear waters, storm events and riverine discharges have been examined in order to study the penetration of light into the water column under various conditions (table 2.2-1). Simultaneous observations of atmospheric characteristics have been obtained during each cruise to complement the measurements of in-water radiation fields. These measurements were used to study how various atmospheric conditions affect the comparison between in-situ measurements of water-leaving radiances and those estimated from model calculations and satellite observations.

Table 2.2-1: Dates of cruises in Chesapeake Bay

no	Date of cruise	Comments
1	2001, June 4	
2	2001, June 11	Bloom event
3	2001, June 25	Bloom event
4	2001, July 9	
5	2001, September 21	
6	2001, September 26	Relatively clear waters
7	2001, September 28	Relatively clear waters
8	2001, October 4	Relatively clear waters
9	2001, October 30	Relatively clear waters
10	2001, November 13	Relatively clear waters
11	2002, May 6	
12	2002, May 15	
13	2002, May 22	
14	2002, June 6	Rain event previous day
15	2002, June 18	Bloom event
16	2002, June 28	Rain event
17	2002, November 8	Relatively clear waters

2.2.2 Theory on instrumentation used

In-water measurements were taken by using the SERC's facilities and instrumentation (table 2.2-2). A WETLabs Spectral AC-9 instrument was used to measure attenuation and absorption in the water, over nine wavelengths from 412 to 715 nm. The Satlantic OCI-200 7-channel irradiance sensors were used to simultaneously measure the underwater upwelling (E_u) and downwelling (E_d) spectral irradiance profiles, as well as the above water surface downwelling irradiance (E_s) in the visible and UV (downwelling only). During some of the cruises, the in-water upwelling radiance (L_u) and downwelling irradiance (E_d) and the surface incident irradiance (E_s) were measured using a Satlantic MicroPro free-falling radiometer. An ECO-VSF3 instrument was used to measure the total in-water backscattering coefficient. Temperature and salinity profiles were measured using a Hydrolab instrument (fig. 2.2-2). Water samples, collected from discrete depths at the four sites PI, HB, TI and JT, were filtered and analyzed, using a Cary spectrophotometer at the laboratory, to estimate chlorophyll concentrations and the contribution of phytoplankton, non-pigmented particulate matter and dissolved material to the total light absorption.

Measurements of atmospheric characteristics were performed using the GSFC's instrumentation. A CIMEL-sunphotometer (a multi-channel, automatic sun- and sky-scanning radiometer) was used to measure atmospheric aerosol optical thickness, water vapor and solar irradiance at the Earth's surface in eight visible and near-infrared wavelengths. A Micropulse-Lidar (MPL), a ground-based optical remote sensing system designed to profile cloud and aerosol structures of the atmosphere, was also used during

some of the cruises. Measurements of direct solar radiation, total ozone, aerosol optical thickness and total water vapor were performed onboard the vessel using a 5-channel, hand-held MICROTOPS sunphotometer. Shipboard measurements of total incident UV irradiance in 18 channels between 290 and 330 nm were made with the SERC SR-18 UV spectroradiometer.

Figure 2.2-2: The AC9 instrument (far right in the picture), the Hydrolab (white instrument in the middle) and the ECO-VSF instrument (far left) that were used during one of the cruises in the Chesapeake Bay.



Table 2.2-2: In- water and above-water measurements performed in the Chesapeake Bay. Instrumentation

In Situ measurements	Wavelength-range (in nm)	Instrument Used
Total absorption (minus absorption by pure water), a_{t-w}	412, 440, 488, 510, 532, 555, 650, 676, 715	AC-9
Total attenuation (minus attenuation by pure water), c_{t-w}	412, 440, 488, 510, 532, 555, 650, 676, 715	AC-9
Total backscattering, b_b	450, 530, 650	ECO-VSF
Temperature, T_w		Hydrolab
Salinity, S_w		Hydrolab
In-water Upwelling radiance profiles, L_u	400, 412, 443, 455, 490, 510, 532, 554, 564, 590, 625, 670, 684, 700	MicroPro, free-falling radiometer
In-water Downwelling irradiance profiles, E_d	400, 412, 443, 455, 490, 510, 532, 554, 564, 590, 625, 670, 684, 700	MicroPro, free-falling radiometer
In-water Upwelling irradiance profiles, E_u	412, 443, 490, 510, 554, 665, 684	Satlantic, OCI-200
In-water Downwelling irradiance profiles, E_d	325, 340, 380, 412, 443, 490, 510, 532, 554, 620, 665, 684, 706	Satlantic, OCI-200
Laboratory measurements	Wavelength-range (in nm)	Instrument Used
Chlorophyll-a concentration, [Chl-a]		Spectrophotometric measurements
Phytoplankton absorption, a_{phvt}	290 – 750	CARY spectrophotometer
Non-pigmented particulate absorption, a_{npp}	290 – 750	CARY spectrophotometer
CDOM absorption, a_{CDOM}	290 – 750	CARY spectrophotometer
Atmospheric observations	Wavelength-range (in nm)	Instrument Used
Downward Surface Irradiance, E_s	400, 412, 443, 455, 490, 510, 532, 554, 564, 590, 625, 670, 684, 700	Satlantic OCR-507 Irradiance Sensors
Aerosol Optical Thickness, AOT	340, 380, 440, 500, 870	Microtops
Aerosol Optical Thickness, AOT	340, 380, 440, 500, 670, 870, 1020	CIMEL
Water Vapor		CIMEL, Microtops
Total Incident UV Spectral irradiance	290-330 nm, 18 channels, 2 nm resolution	SERC SR-18 UV spectroradiometer

2.2.2.1 Measurements of absorption and attenuation using the AC9 instrument

The AC9, an instrument widely used today in measurements of the spectral transmittance of water, was used to measure the water's attenuation, $c(\lambda)$, and absorption, $a(\lambda)$, characteristics (referenced to absorption and attenuation by pure water) at nine visible wavelengths (412, 440, 488, 510, 532, 555, 650, 676 and 715 nm) (fig. 2.2-3). The scattering coefficient, $b(\lambda)$, is estimated as the difference between the attenuation and the absorption measured. The precision of the instrument according to the manufacturers is $\pm 0.003 \text{ m}^{-1}$ at 6Hz scan rate and $\pm 0.001 \text{ m}^{-1}$ at 1Hz scan rate, while the accuracy is reported to be $\pm 0.01 \text{ m}^{-1}$ (WETLabs, AC9 User's Guide, Revision L, January 2003).

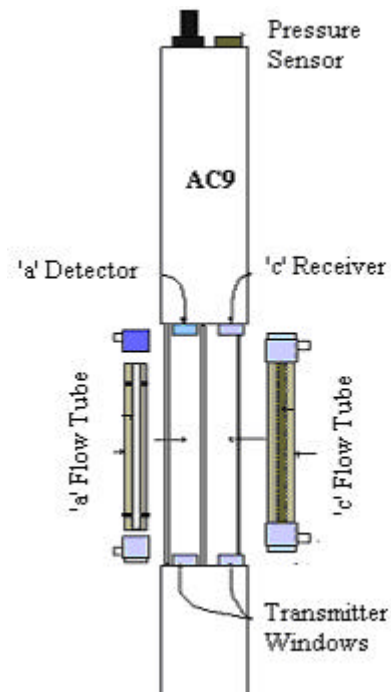


Figure 2.2-3: A diagram of the AC9. The absorption and attenuation beam paths and flow tubes are shown between the receiver and transmitter housings (from WETLabs AC9 User's Guide, 2003)

The AC9 performs simultaneous measurements of the water's absorption and attenuation characteristics, by incorporating a dual path optical configuration in a single instrument (AC9 User's Guide, WETLabs, 2003). Each path contains its own source of light, optics, and detectors appropriate to the given measurement (absorption or

attenuation), while the two paths share a common filter wheel and control and acquisition electronics. For measurements of absorption and attenuation at the nine AC9 wavelengths, light from a DC incandescent source passes through bandpass filters mounted upon a rotating filter wheel, creating a narrow band spectral output. The filter wheel holds nine, 10 nm full-width-half-maximum (FWHM) filters. For the measurement of the water's attenuation, $c(\lambda)$, the light is directed to a sample water volume enclosed by a non-reflective flow tube ("c" flow tube in fig. 2.2-3). Scattered light that hits the blackened surface of the flow tube is absorbed. Therefore, the scattered light is not included in the transmitted intensity measured by the detector, and the light radiated through the flow path is subject to both scattering and absorptive losses by the water mass. For the measurement of the absorption coefficient, $a(\lambda)$, light is directed to a sample water volume enclosed by a reflective flow tube ("a" flow tube in fig. 2.2-3). Light passing through the tube is absorbed by the water volume. However, in this case, forward scattered light is not lost but is reflected back into the water volume by the reflective tube. A clear quartz tube is employed for this purpose. The outer perimeter of the tube is enclosed by a thin annular volume of air. With an index of refraction of 1.33 in water and index of refraction of 1 in air, the total internal reflection is achieved to 41.7 degrees with respect to the optical axis. The light is then collected by a detector at the far end of the flow tube.

Temperature and salinity correction: According to Pegau and Zaneveld (1993), absorption by water is weakly dependant on temperature and also slightly dependent on salinity. While throughout the visible portion of the spectrum the temperature and salinity effects can be neglected (since $\partial a / \partial T = 0.0015 \text{m}^{-1} \text{K}^{-1}$ at $\lambda=600\text{nm}$), these effects must be

taken into account at infrared wavelengths, ($\partial a / \partial T = 0.01 \text{m}^{-1} \text{K}^{-1}$ at $\lambda=750\text{nm}$). The absorption, $a(\lambda)$, and attenuation, $c(\lambda)$, measured by the AC9 instrument at 715 nm were corrected for temperature and salinity effects according to :

$$a_{\text{mts}} = a_{\text{m}} - [\Psi_{\text{t}} * (T - T_{\text{r}}) + \Psi_{\text{sa}} * (S - S_{\text{r}})] \quad (2.2-1)$$

and

$$c_{\text{mts}} = c_{\text{m}} - [\Psi_{\text{t}} * (T - T_{\text{r}}) + \Psi_{\text{sc}} * (S - S_{\text{r}})] \quad (2.2-2)$$

where a_{mts} and c_{mts} are the water temperature and salinity corrected absorption and attenuation respectively, a_{m} and c_{m} are the measured absorption and attenuation, Ψ_{t} and Ψ_{s} are the water-specific absorption corrections due to temperature and salinity respectively, T , S are the water temperature and salinity at the time of measurement and T_{r} , S_{r} are the water temperature and salinity relative to which the correction is applied ($T_{\text{r}} = 24.4 \text{ C}$ and $S_{\text{r}} = 0$) (values of Ψ_{t} and Ψ_{s} are given in the WETLABs AC9 User's Guide, 2003)

Scattering Correction: Reflecting tube absorption meters (“a” flow tube in AC9 instrument) and spectrophotometers do not collect all of the light scattered from the beam. The uncollected scattered light causes the instrumentation to overestimate the absorption coefficient. There are several methods to correct absorption measurements for scattering errors. One method is to subtract the absorption measurement at a reference wavelength (for example at $\lambda= 715 \text{ nm}$). This method is based on the assumption that at the reference wavelength the absorption by particulate and dissolved materials is negligible, so it is assumed to be zero. That is, it is assumed that the measured absorption coefficient at this reference wavelength is caused strictly by scattering. Monte Carlo (Kirk, 1992) modeling of radiative transport within the reflective tube absorption meter

demonstrated that the scattering error is proportional to the total scattering coefficient, b ($= c_m(\lambda) - a_m(\lambda)$), and the coefficient of proportionality depends on the shape of the volume scattering function and optical characteristics of the instrument (e.g. acceptance angle of detector, path length, reflectivity of the tube). Therefore, another method to correct for scattering errors is to subtract a fixed fraction of the scattering coefficient, $b(\lambda)$, $a'(\lambda) = a_m(\lambda) - e [c_m(\lambda) - a_m(\lambda)]$, where e is the proportion of the scattering coefficient not detected by the sensor. Recent studies have shown that this parameter has a value of ~ 0.14 for waters where biological particles dominate scattering and increases to ~ 0.18 when sediments dominate the scattering. A third method, widely used, is the “Zaneveld correction”, which is a combination of the first two methods and is based on the assumption that there exists a reference wavelength at which the absorption coefficient of particulate and dissolved materials is zero ($\lambda = 715$ nm). This reference wavelength is used to determine the proportion of the scattering coefficient to be subtracted from the initial signal. The correction technique (which is applied after applying the temperature and salinity correction) is written as:

$$a' = a_{mts}(\lambda) - [a_{mts}(\lambda_{ref}) / b(\lambda_{ref})] * [b(\lambda)] \quad (2.2-3)$$

or:

$$a' = a_{mts}(\lambda) - \frac{a_{mts}(\lambda_{ref})}{[c_{mts}(\lambda_{ref}) - a_{mts}(\lambda_{ref})]} * [c_{mts}(\lambda) - a_{mts}(\lambda)] \quad (2.2-4)$$

This method allows for changes in the scattering correction magnitude with wavelength and changes in types of materials present. In the framework of this project, the widely used Zaneveld correction was used and evaluated for the Chesapeake Bay waters, where total (minus pure water) absorption at 715 nm was typically low, but not zero.

2.2.2.2 Spectrophotometric measurements of absorption characteristics by particulate and dissolved material

Water samples, collected from discrete depths at the four stations HB, JT, PI and TI, were filtered and analyzed, using a Cary-IV dual beam spectrophotometer at the laboratory, to estimate the contribution of phytoplankton, non-pigmented particles and dissolved material to the total light attenuation. The absorbance scans, with 1-nm bandwidth and interval, covered the wavelength range from 290 to 750 nm.

Particulate Material (Phytoplankton and non-pigmented particles): The absorption properties of the particulate matter, phytoplankton (pigmented material) and non-pigmented material, were measured using the quantitative filter technique (QFT) which consists of concentrating the marine particles on glass fiber filters and then measuring the optical density (OD) of the material with the dual-beam spectrophotometer (Yentsch 1962, Mitchell 1990). The optical density is estimated as the ratio of the transmittance through a reference, $T_r(\lambda)$, and a sample, $T_s(\lambda)$, filter according to:

$$OD(I) = -\log_{10} \frac{T_s(I)}{T_r(I)} \quad (2.2-5)$$

The attenuation of the incident beam can be described by the natural logarithm of the change in the emergent beam through the sample:

$$K = -I_g^{-1} \log_e [T_s(\lambda) / T_r(\lambda)] \quad (2.2-6)$$

where K is the diffuse attenuation coefficient and I_g is the geometric pathlength of the sample. Therefore, the diffuse attenuation coefficient is related to the optical density:

$$K = \log_{10}(e) OD(\lambda) / I_g \quad (2.2-7)$$

If scattering losses are minimized and the configuration of the detector is such that the collection of forward scattering is maximized, the absorption coefficient can be approximated by the measured attenuation, as:

$$a = \frac{2.303 \cdot OD(I)}{l_g} \quad (2.2-8)$$

where the factor 2.303 converts \log_{10} to \log_e . However, multiple scattering inside the glass-fiber filters results in amplification of the optical pathlength and, consequently, in amplified measured optical density (OD_f) values. Therefore, when using the filter technique, the correct particulate absorption should be estimated from optical density measurements according to:

$$a_p(I) = 2.303 \frac{OD_f(I)}{l_g \cdot \beta} \quad (2.2-9)$$

where $l_g \cdot \beta$ is the amplified optical pathlength (due to scattering) and β is the pathlength amplification factor defined, following Butler (1962), as $\beta = l_a / l_g$ (discussion also in paragraph 2.2.2.3).

During the cruises in the Chesapeake Bay, samples of particulate matter (pigmented and non-pigmented) were concentrated onto 25 mm glass fiber filters (Whatman GF/F) and frozen at -20° C. The diameter of the GF/F filters used, is 2.54 cm, but the inside diameter of the filtration tower, which governs the filtered area is 1.65 cm. Therefore the clearance area, A_c , of the filter is 2.138 cm^2 . For the measurements, filters were wetted with 200 μl of filtered distilled water and scanned against a wetted blank GF/F filter in a Cary-IV spectrophotometer, to estimate total particulate absorption coefficients in the spectral range 290 to 750 nm. A separate scan, $OD_{\text{blank}}(\lambda)$ with reference samples (distilled water) in both the reference and the sample filter-holders, was always subtracted from each scan ($OD_f = OD_f' - OD_{\text{blank}}$). Filters were then extracted into 100%

methanol (for a minimum period of 4 hours), to remove phytoplankton pigments. The filters were rinsed and rescanned to determine absorbance by non-pigmented particulate material from 290 to 750 nm. Absorbance by phytoplankton pigments was, thus, estimated as the difference between absorbance by total particulate matter and absorbance by non-pigmented particulate matter. Measured absorbances were converted into in-situ particulate absorption coefficients by multiplying by 2.303, dividing by the geometric pathlength and correcting for the pathlength amplification (the methodology used to estimate the pathlength amplification factor is described in paragraph 2.2.2.3). The geometric pathlength for the filters is given by the ratio V/A_c , where V is the volume filtered. Therefore, the particulate absorption was estimated as:

$$a_p(I) = 2.303 \frac{OD_f}{V/A_c \cdot b} = 2.303 \cdot 2.138 \frac{OD_f}{V \cdot b} (m^{-1}) \quad (2.2-10)$$

Dissolved Material: To determine the absorbance of dissolved material in the water, water samples were collected and filtered through 0.22 μm pore-diameter polycarbonate membrane filters. Each filtered seawater sample was then put into a 5-cm pathlength quartz cell and was scanned against a cell containing only filtered nanopure water (blank), in the Cary-IV dual beam spectrophotometer. A separate scan, $OD_{\text{blank}}(\lambda)$ with reference samples in both the reference and the sample cuvettes, was subtracted from each scan ($OD_c = OD_c' - OD_{\text{blank}}$). Measurements of CDOM absorbance covered the spectral range from 290 to 750 nm. Measured optical densities (OD_c) were converted into absorption coefficients by multiplying by 2.303 and dividing by the pathlength (0.05 m for a 5 cm cuvette). Therefore, CDOM absorption was estimated as:

$$a_{CDOM}(I) = 2.303 \frac{OD_c}{l_g} = 2.303 \cdot \frac{OD_c}{0.05} (m^{-1}) \quad (2.2-11)$$

2.2.2.3 Amplification factor β , and particulate absorption at NIR wavelengths

The absorption properties of aquatic particulate material (phytoplankton and non-pigmented particulate matter) are usually measured using the quantitative filter technique (QFT) which consists of concentrating the marine particles on glass fiber filters and then measuring the optical density (OD) of the material with a dual-beam spectrophotometer (Yentsch 1962, Mitchell 1990). This methodology and its application to measurements performed during our cruises in the Chesapeake Bay waters, was discussed in more details in the previous paragraph. As was mentioned in paragraph 2.2.2.2, when using the filter technique, the correct particulate absorption should be estimated from optical density measurements according to eq. 2.2.2-9:

$$a_p(\lambda) = 2.303 \frac{OD_f(\lambda)}{l_g \cdot \beta}$$

where $l_g \cdot \beta$ is the amplified (due to scattering) optical pathlength and β is the pathlength amplification factor defined, following Butler (1962), as $\beta = l_a / l_g$.

The pathlength amplification factor can be estimated empirically by comparing particulate optical density measured on filters and in particle suspension (Mitchell et al, 2000). In the measurements of the optical density of particle suspension, the sample is usually placed as close as possible to the detector or at the entrance port outside of an integrating sphere (Kirk, 1994), to partially collect photons scattered from the sample. However, in these configurations, although most of the light scattered by the material in forward directions is captured by the detector, backward scattered light (scattering angles larger than 90°) is not detected, which can result in overestimates of the absorption by the

particulate matter. To minimize the scattering error and detect most of the light scattered in forward and backward directions, the particle suspension sample can be placed inside an integrating sphere. The problem when placing the sample inside the integrating sphere is that scattered or transmitted photons may re-enter the sample after reflection at the sphere surface, which would result in amplified absorption (Nelson and Prezelin, 1993). Therefore, when using the integrating sphere with the sample mounted inside, the sphere should be empirically calibrated in order to account for this increase in the optical pathlength.

In this study we compare the optical density measurements of particles retained on glass-fiber filters to the optical density of particles suspension in a small cuvette of 1 cm pathlength placed outside and inside of an integrating sphere. The water sample was collected from the Rhode-River sub-estuary on 18 June 2003.

To estimate the absorption by particulate matter using the filter technique, the water sample was concentrated onto 25 mm glass-fiber Whatman GF/F filters under vacuum. Four replicate filters were made. The sample volume filtered for each case was 50ml. The same volume of distilled water was filtered to obtain reference filters. Samples of dissolved material were obtained by filtering the water sample through 0.22 μm pore-diameter polycarbonate membrane filters. The particle-retaining filters were then scanned against a reference filter, in a CARY-IV spectrophotometer and the optical density of the particle-retaining filter, $OD_f'(\lambda)$, was measured in the wavelength range 290-750nm (fig. 2.2-4), assuming zero absorption at the reference wavelength 750 nm. A separate scan,

$OD_{\text{blank}}(\lambda)$ with reference in both the reference and the sample filter-holders, was always subtracted from each scan ($OD_f = OD_f' - OD_{\text{blank}}$). The particulate absorption, before correcting for the pathlength amplification was estimated from:

$$a_p(I) = 2.303 \frac{OD_f}{V/A_c} = 2.303 \cdot 2.138 \frac{OD_f}{0.5} (m^{-1}) \quad (2.2-12)$$

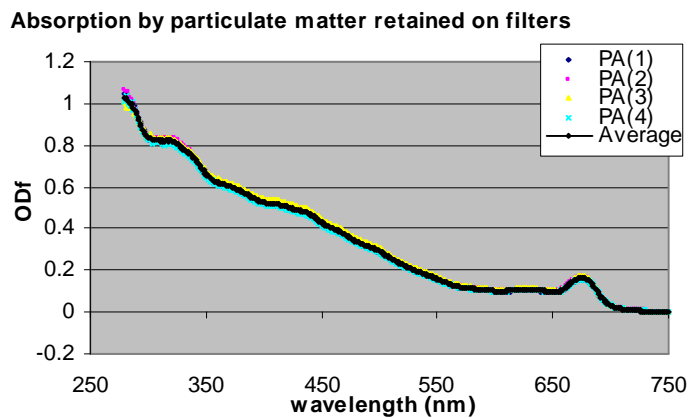


Figure 2.2-4: Optical density of the particle-retaining filters (four replicates) and the estimated average OD_f

Measurements of the optical density of the particle suspension were also made using the Cary Internal Diffuse Reflectance Accessory, which has a 110 mm integrating sphere coated with polytetrafluoroethylene. The optical density of the dissolved material that was obtained by filtering the water sample through the 0.22 μm pore-diameter polycarbonate membrane filters, was first measured. Measurements were performed by placing the 1-cm quartz cuvette filled with the dissolved material, first outside and then inside of the integrating sphere. Several scans were made of each filling, and several replicate fillings were made of the cuvette.

Dissolved material from the Rhode River is characterized by high absorption and no scattering. Therefore, differences in the optical density of the dissolved material measured with the cuvette placed outside and inside the sphere would be mainly due to amplified absorption when the sample is inside the sphere, caused by photons re-entering the cuvette after reflection inside the sphere. The measured optical densities are shown in figures 2.2-5 and 2.2-6, with OD values measured inside the integrating sphere being indeed a little higher than those measured with the cuvette placed at the sphere's entrance port. The relation between the optical densities of the dissolved non-scattering material, measured with the cuvette inside and outside the integrating sphere can be used to empirically calibrate the integrating sphere (Nelson and Prezelin, 1993). In order to account for the amplification of the signal by the integrating sphere, a quadratic function was fit to the data (fig. 2.2-6):

$$OD_d = 0.8967 OD_{sp}^2 + 0.7679 OD_{sp}, \quad R^2 = 0.9945 \quad (2.2-13)$$

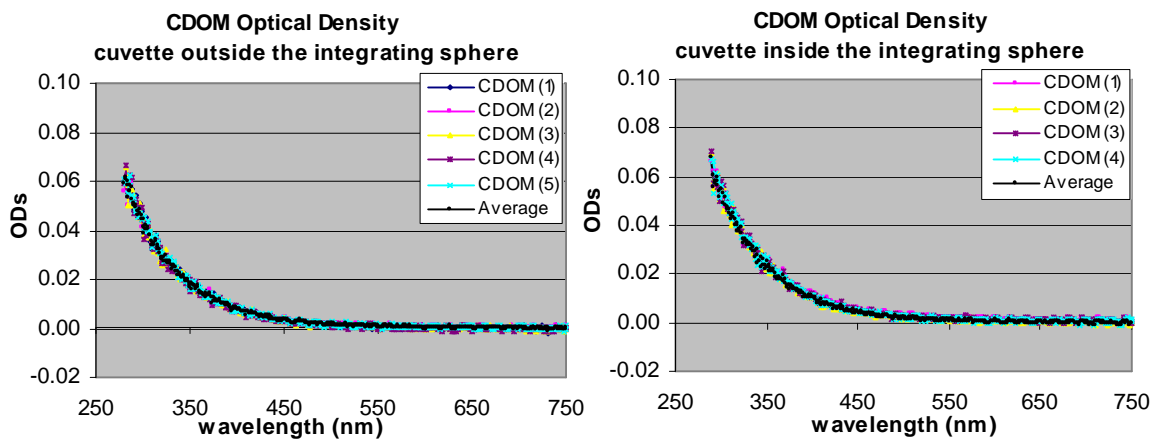


Figure 2.2-5: Optical density of CDOM (obtained by filtering the water sample through the 0.22 μm filters) placing the 1cm cuvette (a) at the entrance port of the integrating sphere and (b) inside the integrating sphere (measurements performed on 18 June 2003).

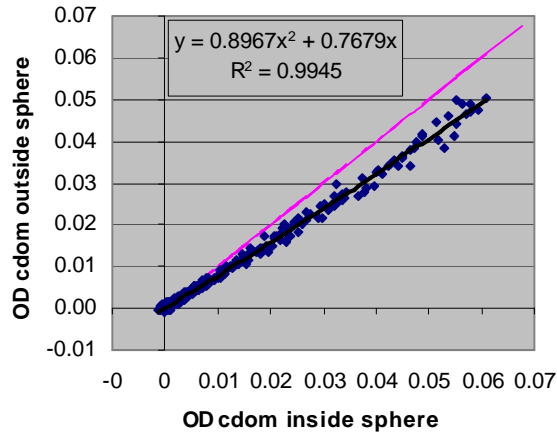


Figure 2.2-6: Relation between the optical densities of the non-scattering dissolved material measured outside and inside the integrating sphere (measurements performed on 18 June 2003).

The optical density of the whole water sample (consisting of both dissolved material and particle suspension) was measured by placing again the 1-cm cuvette outside and inside the integrating sphere. The optical density of the particle suspension was then estimated as the difference $OD_{PA} = OD_{\text{sample}} - OD_{\text{dissolved}}$ for both cases with the sample inside and outside of the sphere. To account for the amplification of the signal inside the sphere, the measurements of the particle suspension optical density with the sample inside the sphere were corrected according to eq. (2.2-13). The particulate absorption, $a_p(\lambda)$, was estimated from the optical density values, as:

$$a_p(I) = 2.303 \frac{OD_{PA}(I)}{l_g} = 2.303 \frac{OD_{PA}(I)}{0.01} \quad (2.2-14)$$

where $l_g = 0.01$ m for the 1cm cuvette. According to the measurements (fig. 2.2-7), and after applying a non-linear least-squares fit to the data in the wavelength region 700-750 nm, $a_p(715) = 0.09 \pm 0.042 \text{ m}^{-1}$ ($a_p(715)$ significantly different than zero within 2 standard deviations).

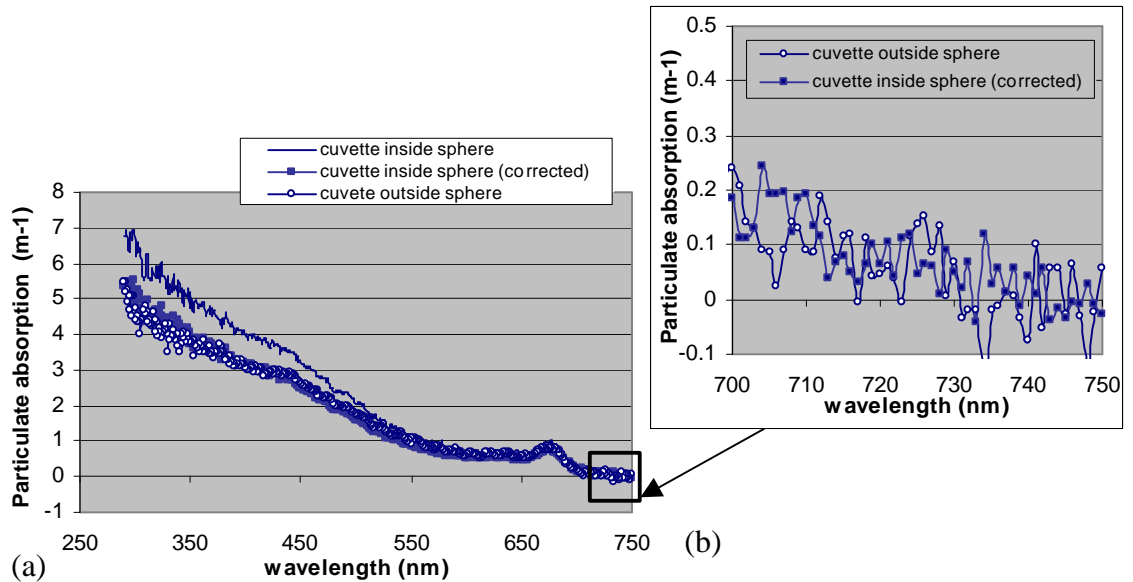


Figure 2.2-7: Measurements of the particulate absorption, a_p , performed with the 1cm cuvette inside and outside of the integrating sphere. A closer look at the 700-750 nm wavelength region (fig. 2.2-7(b)) shows positive absorption values measured at wavelengths shorter than 730 nm both inside and outside of the sphere.

Use of the integrating sphere in the estimation of absorption by particulate material showed that absorption in the wavelength region 700-730 nm is non-zero in these highly absorbing estuarine waters. Therefore scattering correction methods that are used in absorption measurements based on the assumption that absorption at a NIR reference wavelength (for example 715 nm) is zero, should be used with caution in these waters.

The pathlength amplification factor was estimated for this specific set of measurements, by comparing the optical density values in particle suspension and on filters (figure 2.2-8).

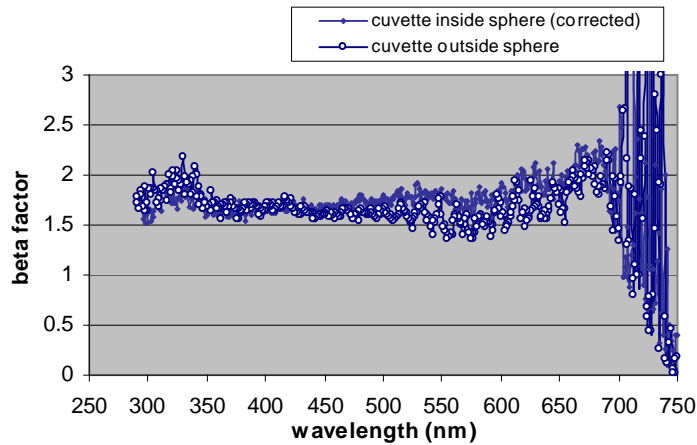


Figure 2.2-8: Values of the β amplification factor, estimated (for the specific set of measurements performed on 18 June 2003) by comparing the optical density values in particle suspension and on filters

Additional measurements of absorption by particle suspension (in 1 cm cuvette placed outside the integrating sphere) and by particles retained on glass-fiber filters were performed using water samples collected on 15 July 2003 from two sites in the Rhode River sub-estuary (1A station, at the mouth of the Rhode River sub-estuary, and 4B station, at the SERC dock). Water sample from the 4B station was also diluted by 50%, with filtered water from the same sample, to study the behavior of β at lower particle concentration in the cuvette. In this case, too, the optical density by particle suspension was measured as the difference between the optical density of the whole water sample (consisting of both dissolved material and particle suspension) and the optical density of the dissolved material that was previously obtained by filtering the water samples through 0.22 μm filters. The sample volume filtered to measure the particulate absorption on the filter pads was, in each case, 50 ml, so as to obtain optical densities in the range of optical densities measured during the 2001-2002 cruises in the Chesapeake Bay waters. The

pathlength amplification factor was then estimated by comparing the absorption values in particles suspension and on filters (fig. 2.2-9). The estimated β had an average value of $\beta_{\text{avg}} = 1.5$ ($\beta_{\text{avg}} = 1.46$, stdev=0.13 for 1A station, $\beta_{\text{avg}} = 1.56$, stdev=0.14 for 4B station), and a small wavelength dependence with slightly smaller values within the 550-600 nm wavelength region (where most of the attenuation is due to scattering) and larger values close to the 650-680 nm (near the chlorophyll absorption peak). Dilution of water samples collected from the 4B station by 50% increased slightly the overall beta (average $\beta = 1.64$) and, as expected, enhanced the noise in the estimated absorption values. Significant noise was also observed at wavelengths above 700 nm, since overall absorption in this region is low, although non-zero as mentioned in previous paragraphs. When interpreting these results, one should keep in mind that increase of the optical pathlength due to scattering on the particles inside the cuvette (more pronounced at larger particle concentrations) might result in slightly overestimated absorption by the particle solution.

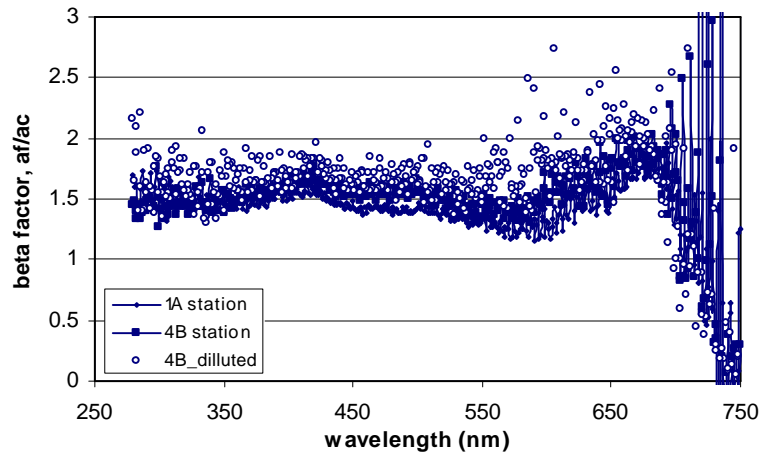


Figure 2.2-9: Values of the β amplification factor estimated (for measurements performed on 15 July 2003) by comparing particulate absorption values measured in particle suspensions and on glass-fiber filters.

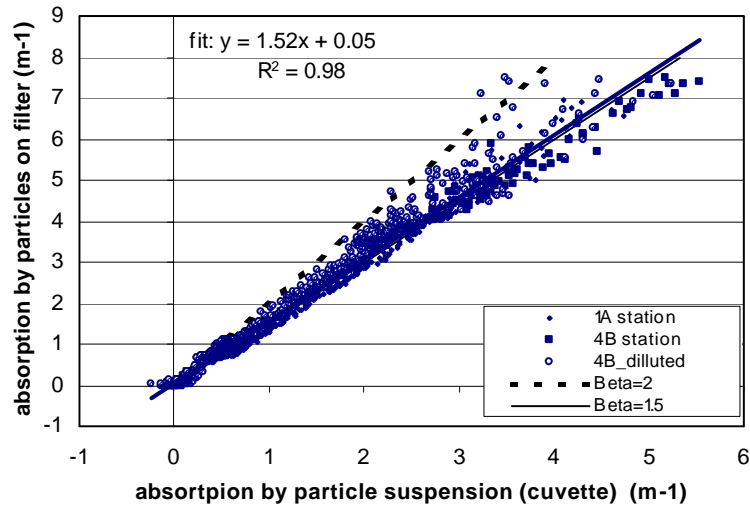


Figure 2.2-10: Relation between particulate absorption measured on filters and in particle suspensions. The lines $\beta=1.5$ (solid thin line), $\beta=2$ (dashed thick line) and the linear least-squares fit (solid thick line) are also shown.

Figure 2.2-10 shows the relation between particulate absorption measured on filters and in particle suspensions, along with the lines $\beta=1.5$ (solid line) and $\beta=2$ (dashed line). A beta factor $\beta=2$ was proposed by Roesler (1998), based on the assumption that the glass-fiber filter method estimates the diffuse absorption of a sample, which is two times the volume absorption coefficient. As shown in figure 2.2-10 (and also in fig. 2.2-9 and fig. 2.2-8), the estimated β -factor values are in almost all of the cases between the two lines $\beta=1.5$ and $\beta=2$. The results of a linear least-squares regression between absorption by particles retained on filters and particulate absorption in particle suspensions (measured on waters samples from both 1A and 4B stations, including the 50% diluted sample from station 4B), gave a slope of 1.52, a small intercept (0.05) and $R^2=0.98$. Therefore, a constant value of $\beta=1.5$ provides a good overall fit to the data.

2.2.2.4 Measurements of backscattering using the ECO-VSF instrument

The amount of light that is scattered in the backward direction, and the angular distribution of the backscattered radiation, are extremely important in the interpretation of remote sensing measurements, estimations of irradiance reflectance, investigations of particle shape and simulations of radiative transfer in seawater. The *ECO-VSF3* instrument was used in this project to measure the backscattering of light in the water (fig. 2.2-11).

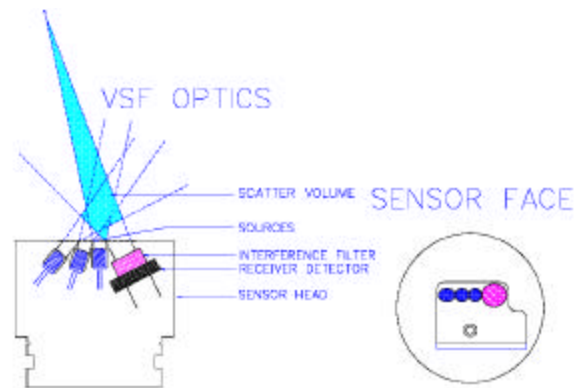


Figure 2.2-11: Optical configuration of the ECO-VSF 3 instrument (from ECO-VSF 3 User's Guide, 14 April 2003)

The optics of the ECO-VSF3 include three sets of three LED-based transmitters (three wavelengths) that couple to three receivers (three scattering angles). The transmitters and receiver are located in such a way as to establish centroid light scattering angles of approximately 100, 125, and 150 degrees respectively. Therefore, scattering measurements are performed at the three distinct angles, and at three wavelengths, 450, 530 and 650 nm. This way, information on the shape of the volume scattering function (VSF) throughout its angular domain can be obtained. The three-angle measurements allow determination of specific angles of backscattering through interpolation, as well as estimation of the total backscattering coefficient, b_b , by integration and extrapolation from 90 to 180 degrees. The sensitivity of the instrument is reported to be 0.005 m^{-1} .

Attenuation Correction in ECO-VSF:

High attenuation of the incident beam from the light source to the sample volume and the light that is scattered in the sample volume towards the detector, can result in significant underestimations of the scattering measurements. Therefore, many scattering sensors require a subsequent attenuation correction. This is typically a function of the propagation distances of the light as well as the magnitude of the water attenuation.

Because the *ECO-VSF 3* incorporates very short pathlengths and scattering volumes in its measurements, the attenuation correction is considered to be significant only for large values of attenuation (c larger than 5 m^{-1}). As discussed in Twardowski et al (2001) each elementary scattering volume of the total sample volume, has a specific pathlength from the light source to the detector. This pathlength and the beam attenuation coefficient determine the effect of attenuation on the light received from that elementary volume.

Integrating over all elementary volumes gives the total dependence on the beam attenuation coefficient. Since the calibration of the ECOVSF uses microspherical scatterers, the component of c that can be attributed to scattering is incorporated into the scaling factor, i.e., the calibration itself. Therefore, only absorption, a , of the incident beam needs to be included in the correction. The attenuation correction applied to the measurements taken using the ECO-VSF is given in equations 2.2-15(a)-(c), where the measured scattering function at a given value of a , $\beta_{\mu}(\theta, a)$, is corrected to the value for $a = 0 \text{ m}^{-1}$:

$$\beta_{\mu}(100^{\circ}, a) e^{0.0314a} = \beta_{\mu}(100^{\circ}, a = 0); \quad (2.2-15 \text{ a})$$

$$\beta_{\mu}(125^{\circ}, a) e^{0.0441a} = \beta_{\mu}(125^{\circ}, a = 0); \quad (2.2-15 \text{ b})$$

$$\beta_{\mu}(150^{\circ}, a) e^{0.0804a} = \beta_{\mu}(150^{\circ}, a = 0); \quad (2.2-15 \text{ c})$$

Estimation of the Total Backscattering Coefficient:

The backscattering coefficient, b_b , is estimated from the volume scattering function, $\beta(\theta_i)$ measured at the three angles, 100° , 120° , 150° , first by multiplying the $\beta(\theta_i)$ measurements at the three angles by $2\pi \sin(\theta_i)$ to convert to a polar steradian area, $A(\theta_i)$. Since, for $\theta = 180^\circ$ we have: $2\pi \sin(\pi) = 0$, four values of $A(\theta_i)$ are actually known in the backward hemisphere, for i : 100° , 125° , 150° , and 180° , where $A(180^\circ) = 0$. Then, a third order polynomial is fit to $A(\theta_i)$, and integration is performed from $\pi/2$ to π . According to Twardoski et al (2001), testing this approach with all of the Petzold (1972) volume scattering functions (excluding filtered freshwater and filtered seawater) results in a maximum error of about 1.1%.

2.2.2.5 Measurements of underwater radiation fields

Measurements of underwater profiles of downwelling irradiance, $E_d(\lambda)$, and upwelling radiance, $L_u(\lambda)$, or upwelling irradiance, $E_u(\lambda)$, were made, during the cruises in the Bay, using the Satlantic optical sensors with a free-fall or a frame-mounted deployment.

During seven of the cruises in the Bay the Satlantic MicroPro free-falling radiometer was used for measurements of $E_d(\lambda)$ and $L_u(\lambda)$ profiles (fig. 2.2-12). The MicroPro instrument, operated by L. Harding's research group (Horn Point laboratory, University of Maryland), has a smaller diameter (6.4 cm) compared to other radiometric instruments and as a result is less subject to instrument self-shading (Harding and Magnuson, 2001).

The MicroPro instrument uses the high resolution Satlantic OCR-507 irradiance and radiance optical sensors for measurements of underwater Ed and Lu at 14 bands (400, 412, 443, 455, 490, 510, 532, 554, 564, 590, 625, 670, 684 and 700 nm). The accuracy of the irradiance and radiance sensors is reported to be $\pm 3\%$ and $\pm 4\%$, respectively (personal communication Scott McLean, Satlantic). The instrument contains a pressure sensor that provides high accuracy depth data, and also a miniature biaxial clinometer (tilt sensor), for tilt measurements (accuracy of 0.2°) in two axes (X and Y, or pitch and roll). The instrument also contains a thermal probe that is used to determine the water temperature T_w (0.15% full-scale accuracy over an operating range of -2.5°C to 40°C) (Satlantic MicroPro operation manual, June 2002).

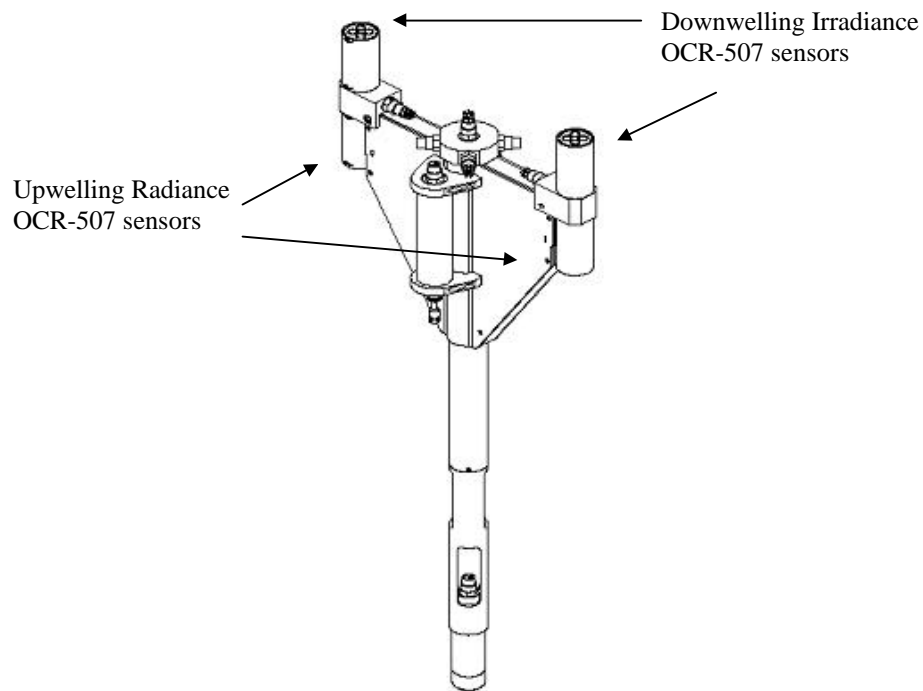


Figure 2.2-12: MicroPro instrument, free fall profiling deployment. The four optical sensors (two radiance and two irradiance OCR-507 sensors) are located at the top of the instrument's body.

Measurements of $L_u(z)$ and $E_d(z)$ were corrected for the depth offset between the radiance and irradiance sensors (fig. 2.2-12), as well as for self-shading effects (discussion and methodology in paragraph 2.2.2.6). A correction was also applied to the measurements, though the instrument's calibration, for the immersion effect (correction due to the difference in indices of refraction between air, where the instrument is built, and water, where the instrument is used).

The MicroPro surface reference system (OCR-507 irradiance sensors) was also used during the cruises (mounted on the boat) for simultaneous measurements of downwelling irradiance, E_s , just above the water's surface. Measurements of E_s were also performed at the 14 wavelength bands mentioned above.

For those cruises when the MicroPro instrument was not available, the Satlantic OCI-200 sensors (diameter 8.9 cm), mounted on a frame, were used for measurements of downwelling surface irradiance, E_s , and underwater downwelling irradiance, E_d , at 14 wavelengths (325, 340, 380, 412, 443, 490, 510, 532, 554, 555, 619, 665, 683 and 705 nm), as well as for measurements of underwater upwelling irradiance, E_u , at 7 wavelengths (412, 443, 490, 510, 554, 665 and 684 nm).

2.2.2.6 Self Shading Correction

Underwater measurements of upwelling radiance fields are subject to errors introduced by the instrument's own shadow. Recent studies (Gordon and Ding, 1992, Zibordi and Ferrari 1995) have shown that the magnitude of an instrument's self-shading error depends mainly on the size of the radiometer, the type of the incident sunlight (direct or diffuse irradiance) and the total absorption of the medium. In coastal and estuarine waters large concentrations of absorbing material can result in self-shading errors that significantly affect the upward radiance and irradiance measurements, both in the infrared region of the spectrum where there is strong absorption by the water, as well as in the blue region of the spectrum where absorption by CDOM and non-pigmented particulate matter can be significantly large.

The self-shading error, ϵ_{ss} , is defined as the percentage difference between the actual (Lu_{true}) and the measured (Lu_{meas}) upwelling radiance (and similarly for the upwelling irradiance, E_u):

$$\mathbf{e}_{ss}(\mathbf{I}) = \frac{Lu_{true}(\mathbf{I}) - Lu_{meas}(\mathbf{I})}{Lu_{true}(\mathbf{I})} \quad (2.2-16)$$

from which:

$$Lu_{true}(\mathbf{I}) = \frac{Lu_{meas}(\mathbf{I})}{1 - \mathbf{e}_{ss}(\mathbf{I})} \quad (2.2-17)$$

Gordon and Ding (1992) evaluated ϵ_{ss} through Monte-Carlo simulations and they showed that it can be modeled according to :

$$\mathbf{e}_{ss}(\mathbf{I}) = [\mathbf{e}_{ss\ sun}(\mathbf{I}) + \mathbf{e}_{ss\ sky}(\mathbf{I}) \cdot r] / (1 + r) \quad (2.2-18)$$

where r is the ratio of the diffuse to the direct sun irradiance, $r = E_{diff} / E_{dir}$ and $\epsilon_{ss\ sun}(\lambda)$,

$\epsilon_{ss\ sky}(\lambda)$ are the errors due to the direct and diffuse solar radiance contribution

respectively. Following Gordon and Ding (1992), $\epsilon_{ss\ sun}(\lambda)$ and $\epsilon_{ss\ sky}(\lambda)$ are expressed as:

$$\epsilon_{ss\ sun}(\lambda) = 1 - \exp(-k_{sun}a(\lambda)R) \quad (2.2-19)$$

$$\epsilon_{ss\ sky}(\lambda) = 1 - \exp(-k_{sky}a(\lambda)R) \quad (2.2-20)$$

where R is the radius of the radiometer, $a(\lambda)$ is the total absorption of the medium and k_{sun} , k_{sky} are functions of the solar zenith angle, θ_o , estimated from Gordon and Ding for $30 < \theta_o < 70$.

For the case of upwelling radiance, Lu , and for a point sensor:

$$k_{sun,o} \tan\theta_{ow} = 2.07 + 5.6 \cdot 10^{-3} \theta_o \quad (2.2-21)$$

while for a finite sensor with diameter equal to the diameter of the instrument

$$k_{sun,l} \tan\theta_{ow} = 1.59 + 6.3 \cdot 10^{-3} \theta_o \quad (2.2-22)$$

where θ_o and θ_{ow} are the solar zenith angles in air and water ($\theta_{ow} = \sin^{-1}(\sin\theta_o / n_w)$).

According to Zibordi and Ferrari (1995) use of the $k_{sun,o}$ coefficient estimated for a point sensor always results in overestimations of ϵ_{ss} , while use of the $k_{sun,l}$ coefficient estimated for a finite sensor occupying the full diameter of the instrument always underestimates ϵ_{ss} . Following the Ocean Optics Protocols for Satellite Ocean Color Sensor Validation, Rev 3 (Mueller, 2002) a better estimation of k_{sun} is given as:

$$k_{sun} = (1-f) k_{sun,o} + f k_{sun,l} \quad (2.2-23)$$

where f is the ratio sensor-to-instrument diameter.

For the self-shading error on Lu due to the diffuse solar radiance, the coefficient k_{sky} is expressed as:

$$k_{sky} = 4.61 - 0.87 f \quad (2.2-24)$$

Similarly, for the case of upwelling irradiance, Eu, and for a point sensor:

$$k_{sun,o} = 3.41 - 1.55 \cdot 10^{-2} \theta_o \quad (2.2-25)$$

while for a finite sensor with diameter equal to the diameter of the instrument

$$k_{sun,l} = 2.76 - 1.21 \cdot 10^{-2} \theta_o \quad (2.2-26)$$

$$k_{sun} = (1-f) k_{sun,o} + f k_{sun,l} \quad (2.2-27)$$

For the self-shading error on Eu due to the diffuse solar radiance, the coefficient k_{sky} is expressed as:

$$k_{sky} = 2.70 - 0.48 f \quad (2.2-28)$$

Estimates of the self-shading correction factors for upwelling radiance, $\frac{Lu_{true}}{Lu_{meas}} = \frac{1}{1 - e_{ss}}$, are shown in figures 2.2-13(a) –2.2-13(d), for absorption spectra characteristic of the Chesapeake Bay waters (the absorption spectra used in the specific cases for the estimation of self-shading correction factors, are shown in figure 2.2-13(b)). The self-shading correction factors have been estimated for the Satlantic MicroPro radiometer (instrument diameter = 6.4 cm, sensor diameter = 10 mm) for four solar zenith angles $\theta_o=30^\circ, 40^\circ, 50^\circ, 60^\circ$ and three different ratios of diffuse to direct sun irradiance. The ratios of the diffuse to direct sun irradiance are minimum, average and maximum values of the ratio, measured at the Venice tower site (provided by J.O. Reilly , 1999).

However, the Gordon and Ding model is based on the assumption that scattering is small relative to absorption. According to Zibordi and Ferrari (1995) the presence of highly scattering material (such as in the case of the highly turbid Chesapeake Bay waters) could reduce the instrument self-shading error below that theoretically predicted by the Gordon and Ding model.

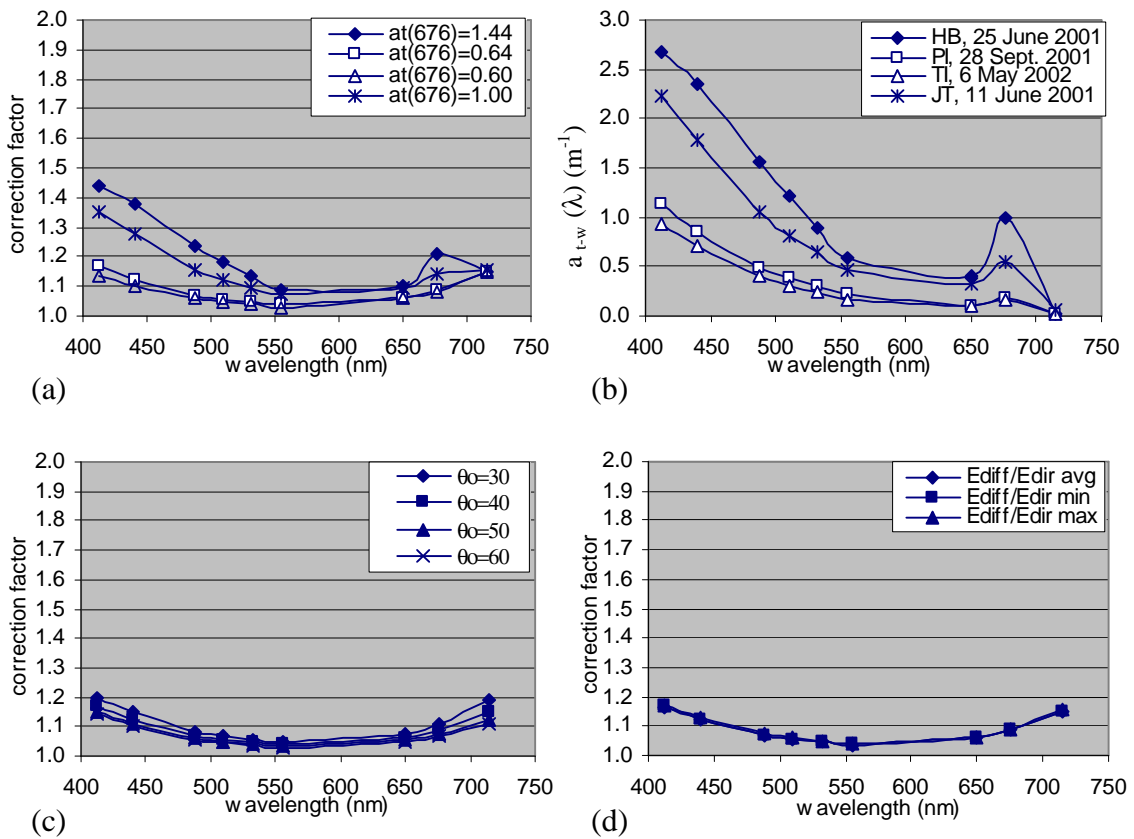


Figure 2.2-13: The self-shading correction factor, $\frac{Lu_{true}}{Lu_{meas}} = \frac{1}{1 - e_{ss}}$, was estimated for the

MicroPro instrument, as a function of wavelength: (a) for $\theta_0=40^\circ$, the mean ratio E_{diff}/E_{dir} (J.O. Reilly, 1999) and for the four total absorption spectra shown in fig. 2.2-13b, (c) for the total absorption measured at PI station on 28 September 2001 ($a_t(676)=0.64\text{m}^{-1}$), the mean ratio E_{diff}/E_{dir} (J.O. Reilly, 1999), and for $\theta_0 = 30^\circ, 40^\circ, 50^\circ, 60^\circ$, (d) for the total absorption measured at PI station on 28 September 2001 ($a_t(676) = 0.64\text{m}^{-1}$), for $\theta_0 = 40^\circ$ and for the three different measurements of the ratio E_{diff}/E_{dir} (provided by J.O. Reilly, 1999).

2.3 Results

2.3.1. Temperature and Salinity

Measurements of water temperature and salinity have been performed during the 2001-2002 cruises in the northern part of Chesapeake Bay, using a Hydrolab instrument. The water temperature varied seasonally from low values of 12-14 °C in late fall (cruise on 13 November 2001) to high values of 26-28 °C in summer (cruise on 9 July 2001). Salinity varied seasonally from 6 ppt in late spring (cruise on 22 May, 2002) to 16-17.5 ppt in late fall (cruise on 13 November 2001).

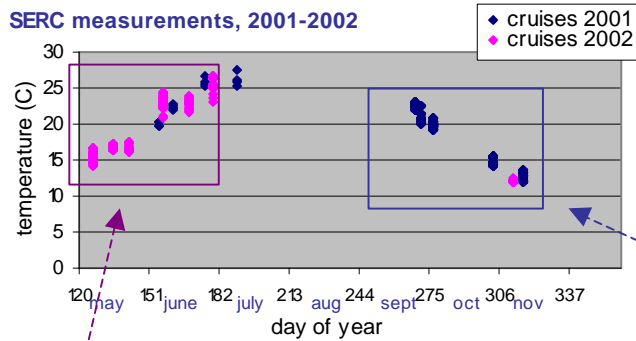
Figures 2.3-1(A) and 2.3-2(A) show the seasonal variation in temperature (in °C) and salinity (in ppt) observed during the measurements in 2001-2002. The temperature increased monotonically from early summer (4 June) to mid summer (9 July) in 2001 and then decreased monotonically to the lowest values measured during the last cruise (13 November) in fall of 2001. A monotonic increase in temperature was observed again from spring (5 May) to summer (28 June) during the 2002 cruises. Salinity showed minimum values during the late spring-early summer months, while it increased during the fall months, reaching the highest values in late fall. Figure 2.3-3 shows the seasonal variation observed in rainfall amounts in the northern part of the Chesapeake Bay. The rainfall measurements were performed at the SERC station during the years 2001 and 2002. According to these measurements, higher rainfall amounts, associated with larger quantities of freshwater input to the Bay, were measured during the spring-summer

months, while drier conditions were observed during the fall season, especially during 2001.

Figures 2.3-1(B) and 2.3-2(B) show vertical profiles of temperature and salinity measured at each one of the four stations, during the fall 2001 and summer 2002 cruises. Strong vertical mixing during the fall months (26 September to 13 November 2001) resulted in vertically homogeneous waters and measured temperature and salinity profiles that were almost constant with depth. Stronger vertical structure in temperature and salinity was observed during some of the spring and summer 2002 cruises, with higher temperature and lower salinity values measured within the upper water layers. No measurements of temperature and salinity profiles were performed during the summer cruises of 2001. Vertical structure in temperature and salinity was observed during the cruises on 6 and 15 May 2002, and 6 and 18 June 2002. Very low salinity values, of ~ 6 ppt, were measured at HB station, located close to the western Chesapeake Bay shore, during measurements performed on 22 May 2002. On June 5, 2002, there was a large storm event in the Chesapeake Bay region. Measurements of temperature and salinity performed at HB, PI, TI and JT during the next day (6 June 2002), showed some stratification in the water with higher temperature (~24 °C) and lower salinity (10-10.5 ppt) values close to the surface (0-2m depth) and a decrease in temperature (21-22 °C) and increase in salinity (11-12 ppt) with depth. However, during some of the spring and summer 2002 cruises, vertically homogeneous waters were observed. Windy conditions observed on 15 May 2002 resulted in rough water surface and well-mixed (due to wave action), homogeneous waters with almost constant temperature and salinity vertical

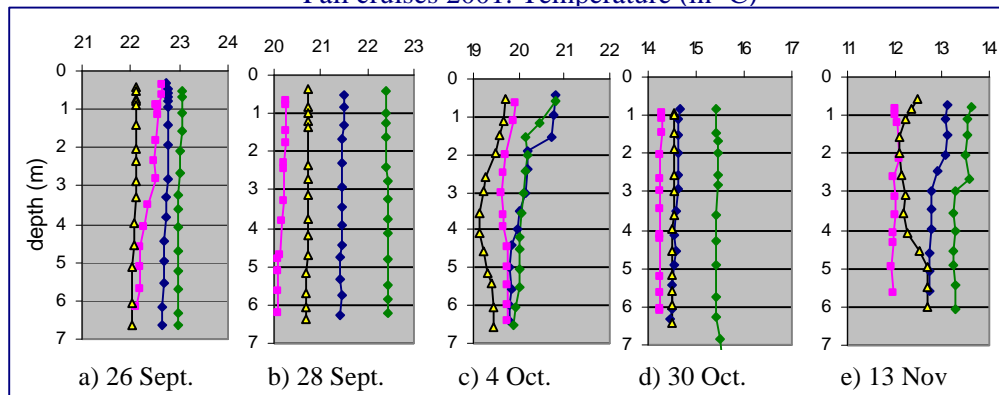
profiles. An increase in salinity was observed only close to the bottom at the HB station. On the 28 June windy conditions were, again, observed during the cruise. The water was well mixed and temperature and salinity were almost constant with depth at the PI and TI stations. Small variation in temperature with depth was observed at HB station, deeper than 5 meters in the water column.

During almost all of the cruises the highest salinity values were observed at the TI station (figure 2.3-2(B), green solid line), that is located towards the middle of the mainstream of the Chesapeake Bay (fig. 2.2-1). The lowest salinity values were observed, during almost all of the cruises, at the JT station (figure 2.3-2(B), red solid line), that is located close to the land and closest to the mouth of the Rhode River sub-estuary (fig. 2.2-1). However, the salinity gradient among the four stations was, during all of the cruises, very small and the differences in salinity values measured at the four stations were at the most 2-3 ppt.

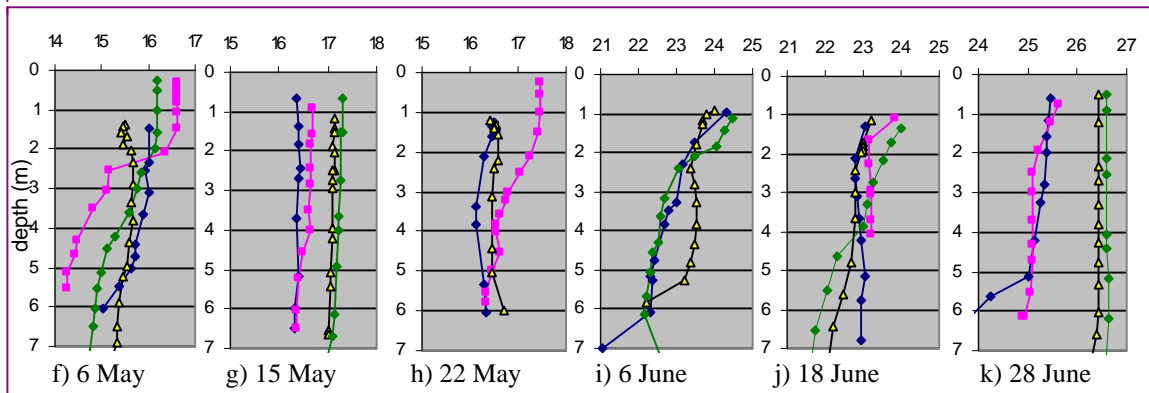


(A)

Fall cruises 2001: Temperature (in °C)



Summer cruises 2002: Temperature (in °C)



(B)

Figure 2.3-1: (A) Seasonal variation of temperature (in °C) as measured during the cruises performed in the northern part of the mainstream of Chesapeake Bay (blue pixels correspond to measurements performed in summer and fall 2001, red pixels correspond to measurements performed in 2002). (B) Profiles of temperature (in °C) measured at the four stations HB (blue), JT (red), PI (yellow), TI (green) during the fall 2001 cruises: a) 26 Sept. b) 28 Sept. c) 4 Oct. d) 30 Oct. e) 13 Nov., and during the spring and summer cruises in 2002: f) 6 May g) 15 May h) 22 May i) 6 June j) 18 June k) 28 June

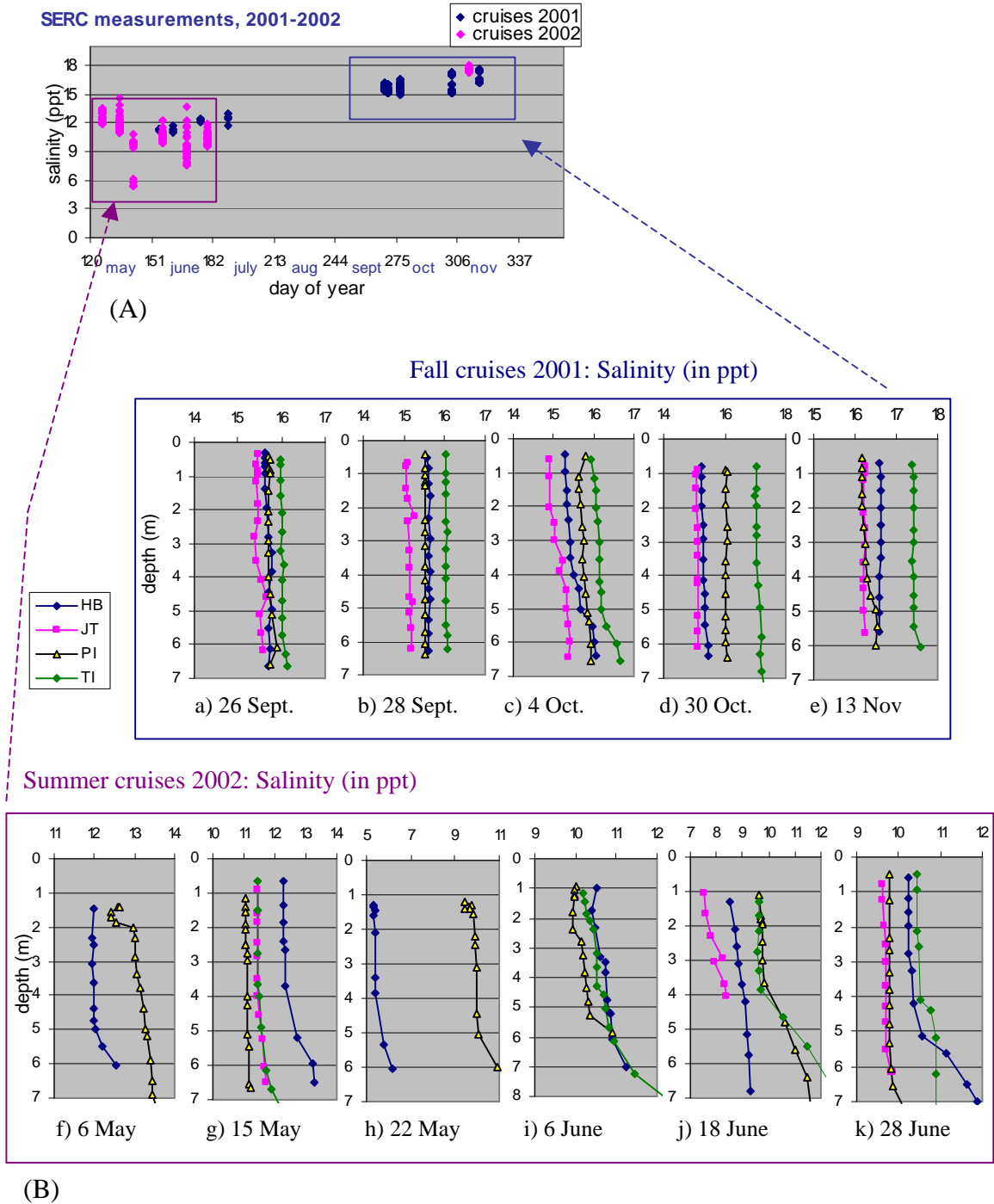


Figure 2.3-2: (A) Seasonal variation of salinity (in ppt) as measured during the cruises performed in the northern part of the mainstream of Chesapeake Bay (blue pixels correspond to measurements performed in summer and fall 2001, red pixels correspond to measurements performed in 2002). (B) Profiles of salinity (in ppt) measured at the four stations HB (blue), JT (red), PI (yellow), TI (green) during the fall 2001 cruises: a) 26 Sept. b) 28 Sept. c) 4 Oct. d) 30 Oct. e) 13 Nov., and during the spring and summer cruises in 2002: f) 6 May g) 15 May h) 22 May i) 6 June j) 18 June k) 28 June

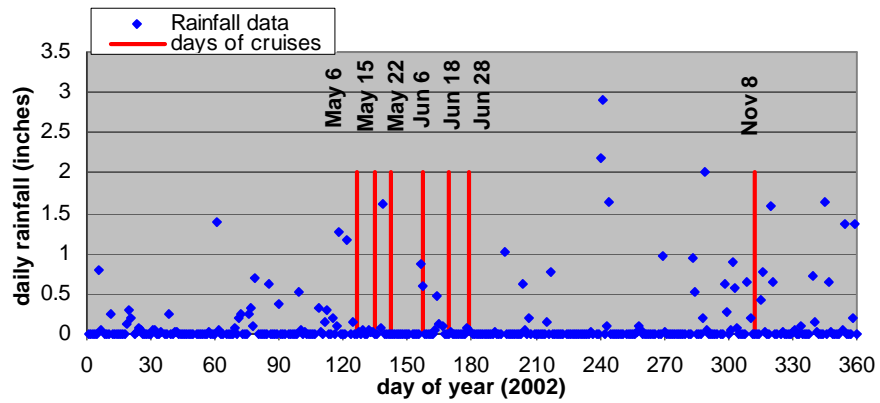
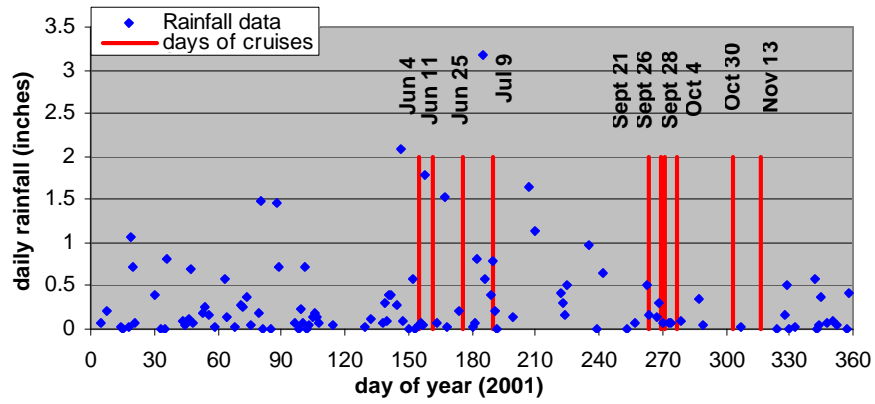


Figure 2.3-3: Daily total rainfall amount (in inches) recorded at the SERC site, during the years 2001 and 2002. The dates of the seventeen cruises performed in the northern part of the Chesapeake Bay, are also shown as red lines

2.3.2 Total absorption and attenuation

Measurements of total-minus-water absorption, a_{t-w} , and attenuation, c_{t-w} , at nine wavelengths (412, 443, 490, 510, 532, 555, 650, 676 and 715 nm) were performed using the AC9 instrument, a spectral absorption-attenuation meter. Figures 2.3-4(a)-(d) show the vertical profiles of absorption and attenuation at 412 and 676 nm, measured at each station during four ‘seasons’, one in spring-early summer (cruises: 4 June 2001, 6,15 and 22 May 2002, 6 June 2002), one in mid summer (cruises: 11 and 25 June 2001, 9 July 2001, 18 and 28 June 2002), one time-period in early fall (cruises: 21, 26 and 28 September and 4 October 2001) and one in late fall (cruises: 30 October and 13 November 2001). Measurements are shown at 412 and 676 nm. Absorption at 676 nm is mostly controlled by chl-a pigments, since 676 nm is a maximum in the chl-a absorption spectrum and absorption by dissolved material and non-pigmented particulate matter is usually much lower at this wavelength. At 412 nm, absorption by non-pigmented particles and CDOM is the largest compared to other AC9 wavelengths, due to the exponential increase of absorption by CDOM and non-pigmented particles with decreasing wavelength.

Average values of $a_{t-w}(412)$, $a_{t-w}(676)$, $c_{t-w}(412)$ and $c_{t-w}(676)$, along with the standard deviations have been estimated for each ‘season’ and each station (fig. 2.3-5). The average, minimum, and maximum $a_{t-w}(412)$, $a_{t-w}(676)$, $c_{t-w}(412)$ and $c_{t-w}(676)$ values observed at HB, PI, TI and JT stations are given in tables 2.3-1 – 2.3-4, for several depths in the water column, from 0.5 to 6 m.

Total water absorption at both 412 and 676 nm was lowest during the beginning of the spring 2002 (6 and 15 May 2002), and during the cruises performed in late fall 2001. The total attenuation in the water was lowest at both 676 nm and 412 nm during the late fall season, at all four stations. Maximum values of absorption at both 412 and 676 nm were observed during the early summer cruises (fig. 2.3-4). Specific phytoplankton bloom events were observed, associated with high light exposure, abundance of nutrients and the presence of more well-stratified waters during this time of the year. A phytoplankton bloom, observed at HB station on 11 June 2001, resulted in absorption values at 412 nm as high as 4 m^{-1} within the first meter below the water surface, while absorption at 676 nm reached 1.8 m^{-1} . These were among the largest $a_{t-w}(412)$ and $a_{t-w}(676)$ values measured in the Chesapeake Bay waters during our cruises. The water during this day was also characterized by high total attenuation, c_{t-w} . Attenuation at 412 and 676 nm reached values of $c_{t-w}(412) = 13 \text{ m}^{-1}$, $c_{t-w}(676) = 11 \text{ m}^{-1}$, which were among the largest attenuation values (c_{t-w}) measured in the Bay. Another phytoplankton bloom was observed at HB station during the following cruise, on 25 June 2001. Maximum absorption was observed within the first 1.5 meters with $a_{t-w}(412) = 4.1 \text{ m}^{-1}$ and $a_{t-w}(676) = 2 \text{ m}^{-1}$. Total attenuation was high within the first 1.5 meters, with $c_{t-w}(412) = 14 \text{ m}^{-1}$ and $c_{t-w}(676) = 12.5 \text{ m}^{-1}$, and high again close to the bottom, with $c_{t-w}(412) = 13 \text{ m}^{-1}$ and $c_{t-w}(676) = 9 \text{ m}^{-1}$. High absorption values were observed at the JT station on 18 June 2002, when $a_{t-w}(412)$ reached 4.4 m^{-1} and $a_{t-w}(676)$ reached 2 m^{-1} within the first meter below the water's surface. High surface attenuation values were again observed, with $c_{t-w}(412) = 14 \text{ m}^{-1}$, $c_{t-w}(676) = 12.7 \text{ m}^{-1}$.

The largest variation with depth was observed in absorption and attenuation values measured during the spring and summer seasons. This is in agreement with measurements of temperature and salinity that showed a general pattern of larger stratification in the water column during the spring and summer months. Absorption and attenuation at all wavelengths (figure 2.3-4 showing selectively 412 and 676 nm) showed only small change with depth during the early fall cruises, and they were almost constant with depth during the late fall cruises (30 October and 13 November 2001) when vertical profiles of temperature and salinity were also constant with depth.

Absorption values at 412 nm were, on average, higher (during almost all of the cruises and during all seasons) at HB and JT stations, the two stations located closer to the western shore of the Chesapeake Bay (fig. 2.3-5). Total attenuation in the water, at both 412 and 676 nm, was consistently higher at the JT station. Total attenuation was usually lower at the PI and TI stations. The PI and TI stations showed, also, the lowest variability in total absorption and attenuation characteristics during the spring, summer and early fall seasons (average values of absorption and attenuation estimated during these seasons at PI and TI showed the lowest standard deviations; figure 2.3-5, and tables 2.3-1 – 2.3-4).

absorption (in m^{-1}) at 412 nm

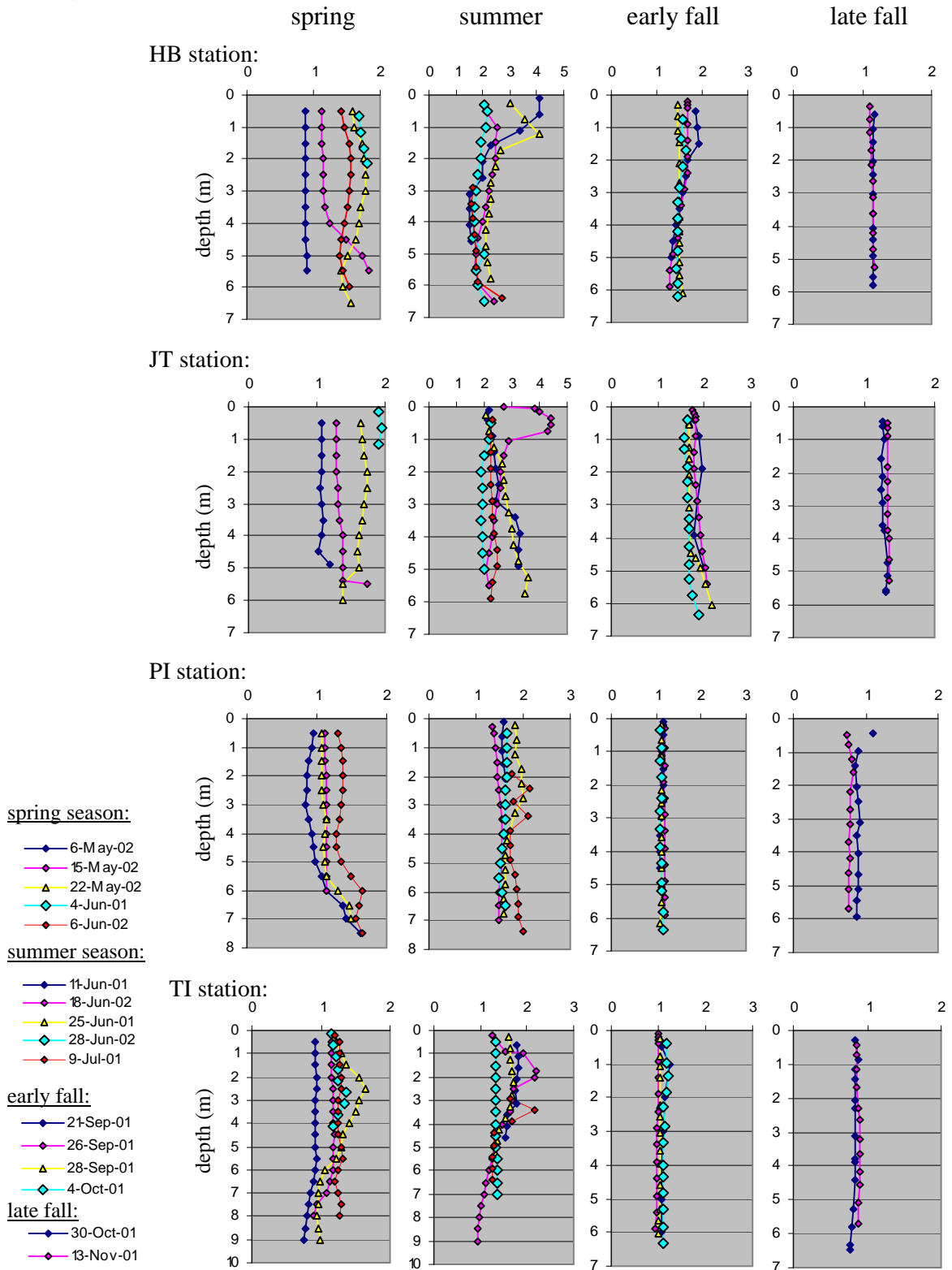


Figure 2.3-4(a): Profiles of $a_{t-w}(412)$ (in m^{-1}) measured at the HB, JT, PI and TI stations, during the spring, summer, early and late fall cruises of 2001 and 2002.

absorption (in m^{-1}) at 676 nm

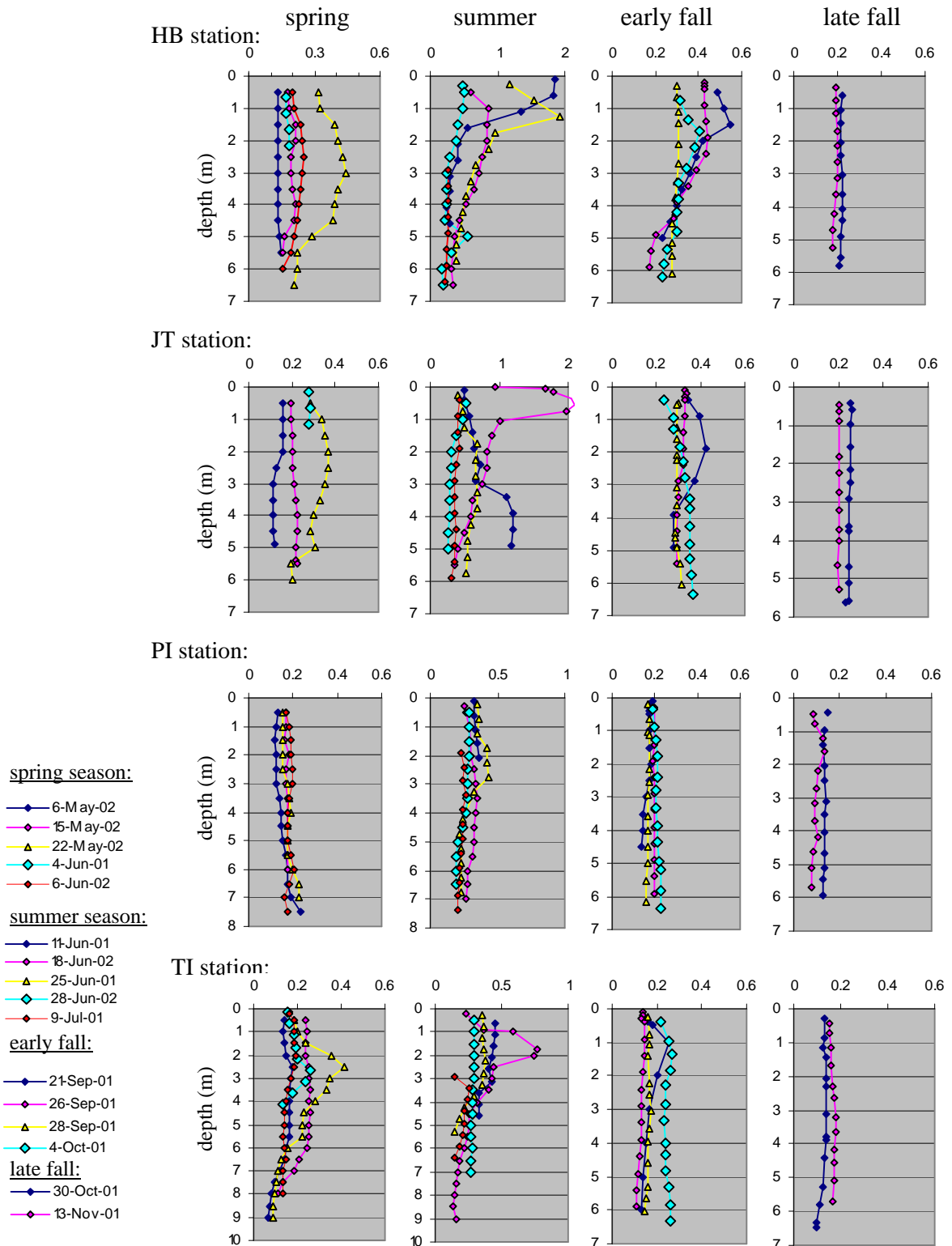


Figure 2.3-4(b): Profiles of $a_{t-w}(676)$ (in m^{-1}) measured at the HB, JT, PI and TI stations, during the spring, summer, early and late fall cruises of 2001 and 2002.

attenuation (in m^{-1}) at 412 nm

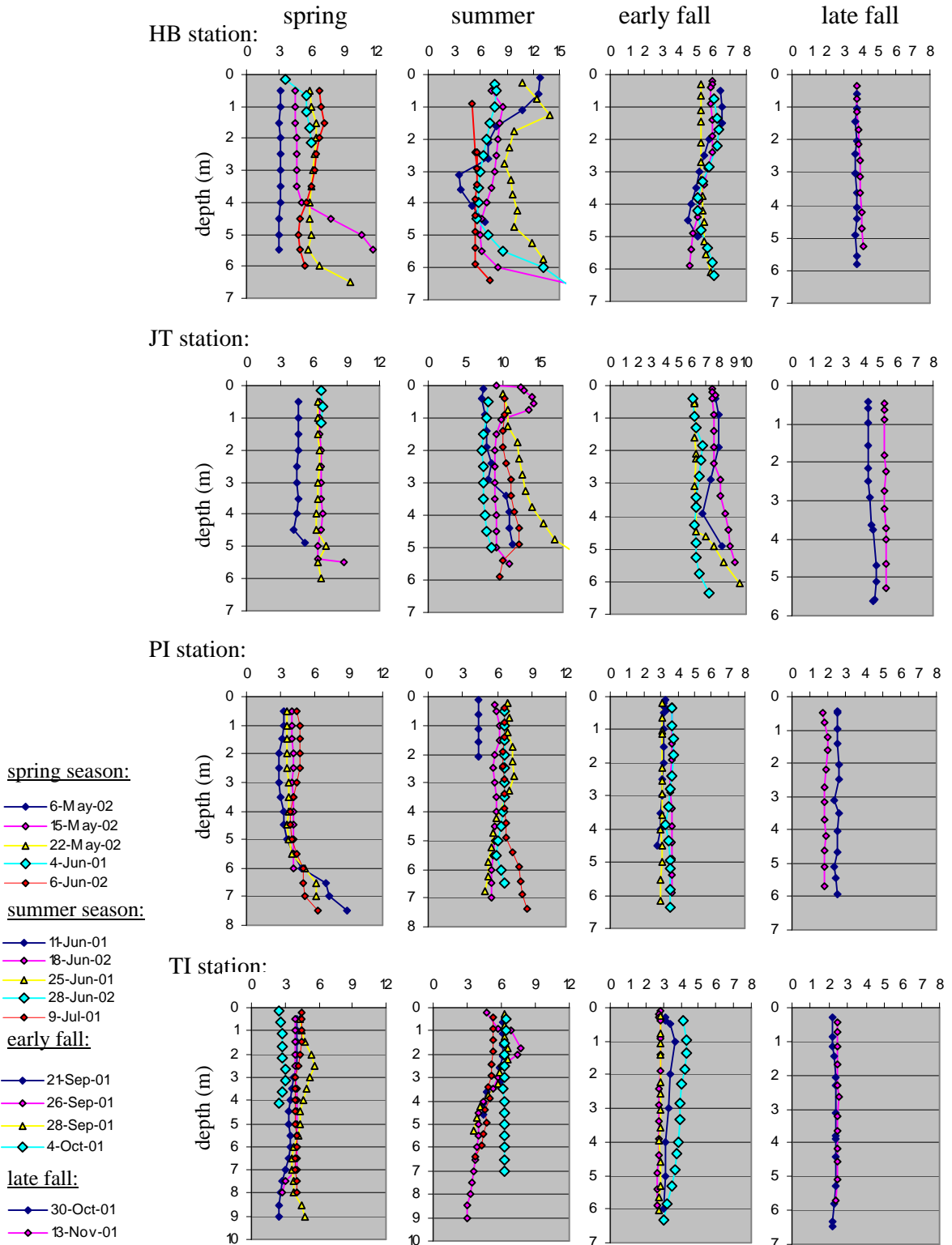


Figure 2.3-4(c): Profiles of $c_{t-w}(412)$ (in m^{-1}) measured at the HB, JT, PI and TI stations, during the spring, summer, early and late fall cruises of 2001 and 2002.

attenuation (in m^{-1}) at 676 nm

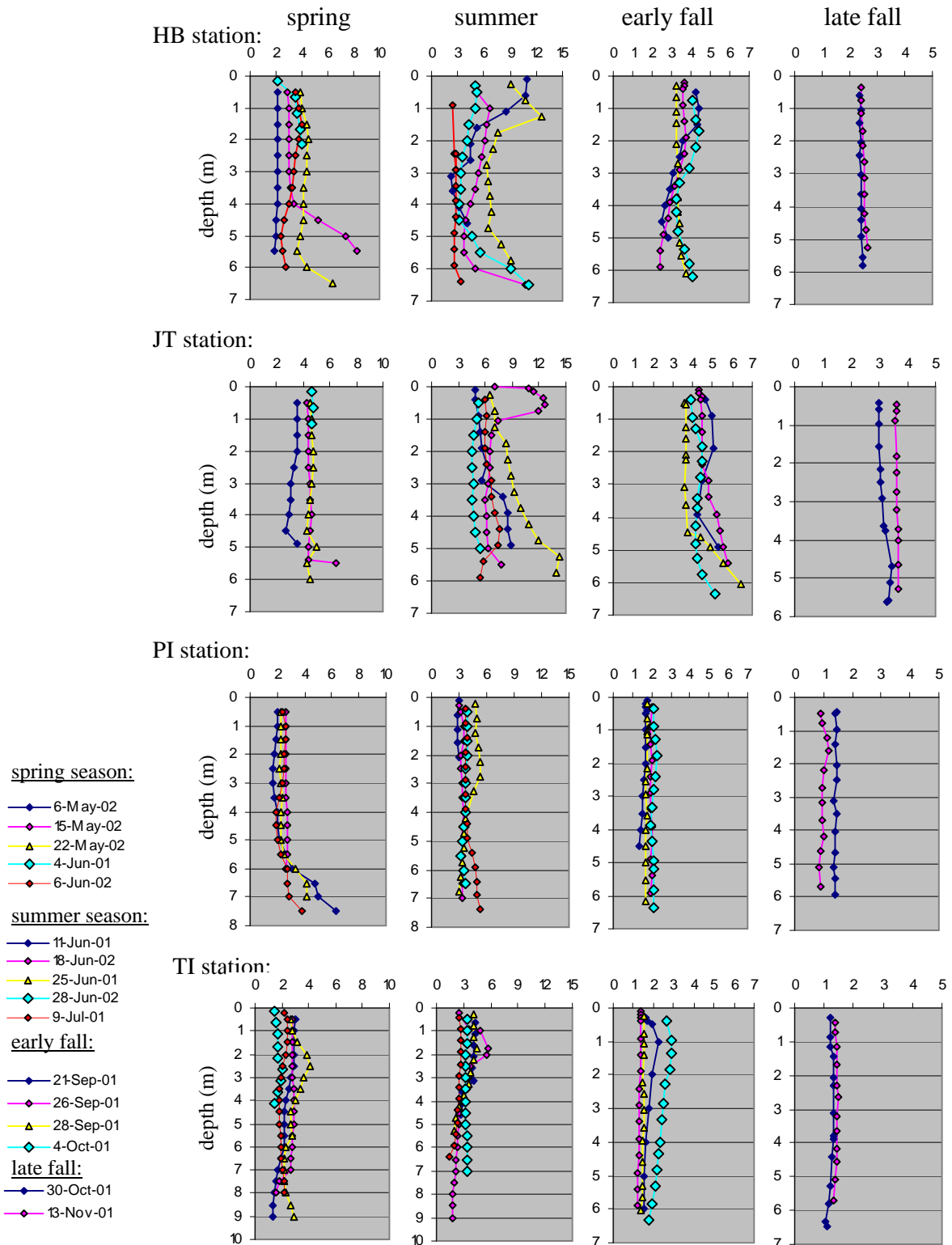


Figure 2.3-4(d): Profiles of $c_{t-w}(676)$ (in m^{-1}) measured at the HB, JT, PI and TI stations, during the spring, summer, early and late fall cruises of 2001 and 2002.

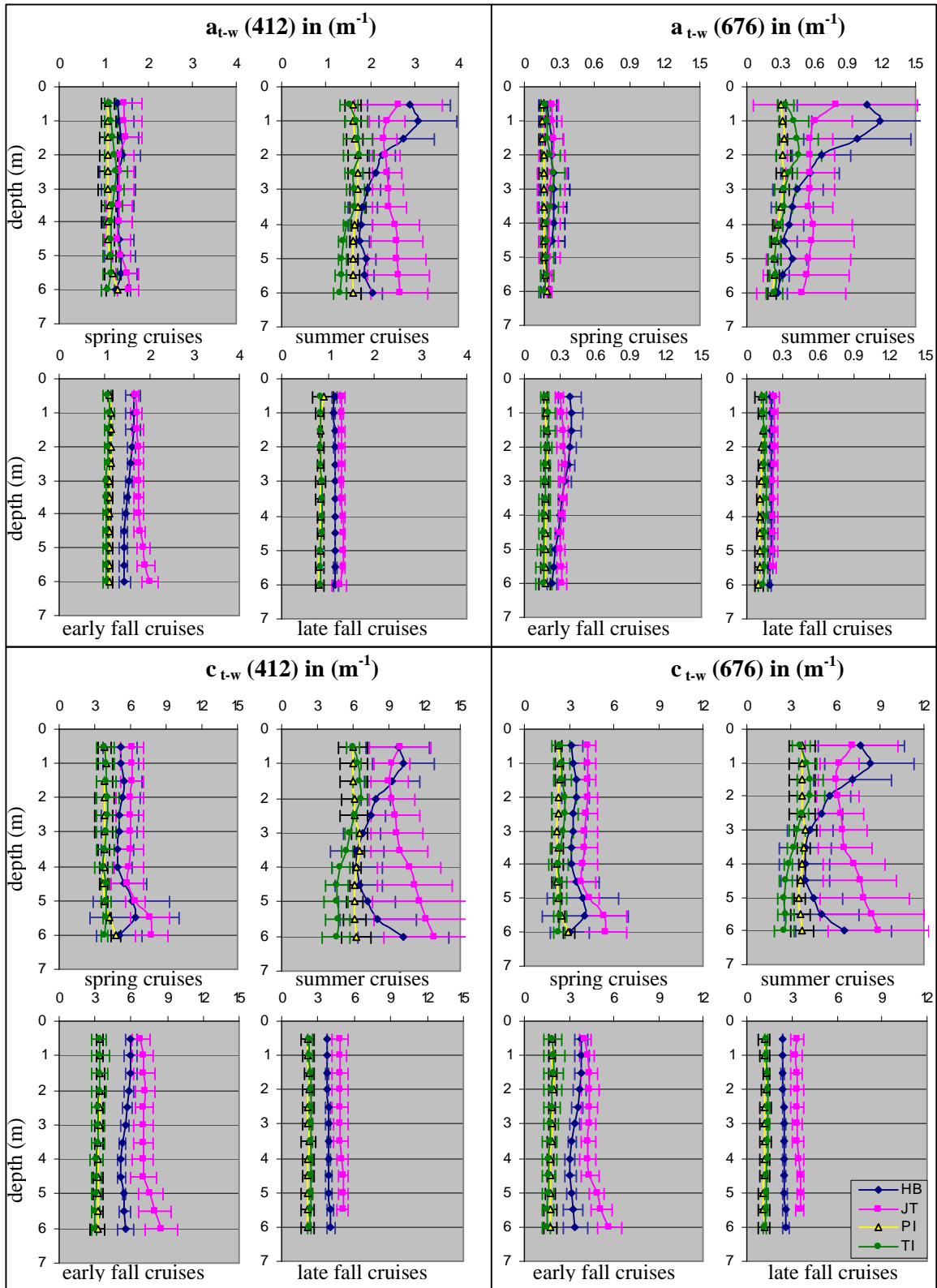


Figure 2.3-5: Average values of $a_{t-w}(412)$, $a_{t-w}(676)$, $c_{t-w}(412)$ and $c_{t-w}(676)$, along with the standard deviations (x-axis error-bars), for each ‘season’ (spring, summer, early, late fall), at HB (blue pixels), JT (red pixels), PI (yellow pixels), TI (green pixels) stations

Table 2.3-1: Range in absorption values at 412 nm, as measured during the spring, summer, early and late fall cruises

	depth	Spring					Summer					Early Fall					Late Fall				
		min	max	avg	stdev		min	max	avg	stdev		min	max	avg	stdev		min	max	avg	stdev	
HB	0.5	0.889	1.678	1.339	0.328	2.093	4.082	2.895	0.937	1.466	1.867	1.65	0.168	1.115	1.174	1.145	0.042				
	1	0.889	1.703	1.357	0.342	2.119	3.865	3.073	0.878	1.476	1.91	1.654	0.189	1.112	1.147	1.129	0.025				
	3	0.885	1.775	1.336	0.396	1.593	2.269	1.936	0.311	1.488	1.655	1.543	0.077	1.144	1.152	1.148	0.006				
JT	6	0.912	1.53	1.293	0.333	1.805	2.333	2.038	0.253	1.308	1.557	1.445	0.126	1.143	1.199	1.171	0.04				
	0.5	1.075	1.932	1.483	0.381	2.106	4.399	2.634	0.989	1.623	1.763	1.702	0.061	1.265	1.341	1.303	0.054				
	1	1.078	1.92	1.486	0.379	2.152	3.125	2.383	0.416	1.563	1.827	1.717	0.12	1.279	1.332	1.306	0.037				
PI	3	1.063	1.697	1.359	0.319	1.917	2.828	2.408	0.336	1.656	1.875	1.765	0.109	1.265	1.336	1.3	0.05				
	6	1.387	1.734	1.56	0.245	2.031	3.465	2.668	0.633	1.805	2.152	2.012	0.183	1.143	1.353	1.248	0.148				
	0.5	0.953	1.304	1.115	0.145	1.375	1.842	1.613	0.195	1.09	1.19	1.135	0.042	0.747	1.064	0.905	0.224				
TI	1	0.923	1.345	1.118	0.174	1.427	1.846	1.622	0.175	1.103	1.182	1.136	0.034	0.78	0.903	0.841	0.087				
	3	0.844	1.358	1.108	0.21	1.515	1.917	1.74	0.205	1.089	1.193	1.132	0.044	0.777	0.921	0.849	0.102				
	6	1.138	1.649	1.309	0.24	1.482	1.867	1.628	0.167	1.064	1.198	1.127	0.057	0.764	0.875	0.819	0.078				
	0.5	0.92	1.26	1.146	0.133	1.331	1.784	1.531	0.211	0.985	1.173	1.065	0.083	0.849	0.858	0.854	0.006				
	1	0.912	1.29	1.17	0.153	1.338	1.926	1.675	0.254	1	1.226	1.106	0.109	0.832	0.86	0.846	0.02				
	3	0.92	1.551	1.249	0.23	1.33	1.85	1.659	0.197	0.986	1.123	1.062	0.063	0.836	0.897	0.867	0.043				
6	0.922	1.258	1.104	0.145	1.186	1.508	1.322	0.141	0.951	1.101	1.029	0.064	0.787	0.876	0.831	0.063					

Table 2.3-2: Range in absorption values at 676 nm, as measured during the spring, summer, early and late fall cruises

	depth	Spring					Summer					Early Fall					Late Fall				
		min	max	avg	stdev		min	max	avg	stdev		min	max	avg	stdev		min	max	avg	stdev	
HB	0.5	0.131	0.319	0.2	0.071	0.518	1.839	1.072	0.629	0.302	0.302	0.5	0.384	0.098	0.193	0.219	0.206	0.018			
	1	0.131	0.329	0.205	0.075	0.485	1.702	1.183	0.609	0.305	0.305	0.527	0.399	0.101	0.191	0.216	0.204	0.018			
	3	0.133	0.441	0.254	0.133	0.249	0.723	0.449	0.222	0.302	0.302	0.413	0.347	0.047	0.2	0.219	0.209	0.013			
JT	6	0.152	0.223	0.178	0.039	0.166	0.372	0.271	0.091	0.188	0.188	0.278	0.234	0.045	0.178	0.204	0.191	0.018			
	0.5	0.159	0.285	0.232	0.064	0.413	2.089	0.787	0.729	0.24	0.331	0.296	0.04	0.201	0.257	0.229	0.04				
	1	0.155	0.336	0.243	0.082	0.408	1.19	0.612	0.325	0.276	0.365	0.315	0.039	0.201	0.254	0.228	0.037				
PI	3	0.113	0.35	0.224	0.119	0.285	0.758	0.557	0.219	0.293	0.391	0.332	0.043	0.2	0.248	0.224	0.034				
	6	0.201	0.228	0.215	0.019	0.23	1.168	0.488	0.399	0.292	0.361	0.322	0.036	0.119	0.199	0.159	0.057				
	0.5	0.132	0.171	0.156	0.017	0.27	0.359	0.31	0.04	0.17	0.196	0.184	0.013	0.086	0.147	0.117	0.043				
TI	1	0.126	0.18	0.157	0.023	0.285	0.36	0.317	0.035	0.17	0.197	0.184	0.014	0.103	0.135	0.119	0.023				
	3	0.128	0.199	0.167	0.029	0.255	0.388	0.312	0.06	0.165	0.205	0.184	0.02	0.095	0.138	0.116	0.03				
	6	0.174	0.204	0.189	0.016	0.188	0.28	0.228	0.038	0.117	0.227	0.176	0.048	0.077	0.125	0.101	0.034				
	0.5	0.137	0.235	0.18	0.037	0.285	0.443	0.345	0.074	0.133	0.223	0.174	0.038	0.131	0.154	0.142	0.016				
	1	0.137	0.242	0.189	0.038	0.293	0.592	0.423	0.129	0.142	0.256	0.204	0.058	0.127	0.154	0.141	0.019				
	3	0.169	0.352	0.237	0.075	0.193	0.428	0.336	0.097	0.133	0.235	0.176	0.043	0.138	0.176	0.157	0.027				
6	0.143	0.242	0.173	0.047	0.166	0.323	0.245	0.069	0.11	0.26	0.162	0.067	0.106	0.168	0.137	0.044					

Table 2.3-3: Range in attenuation values at 412 nm, as measured during the spring, summer, early and late fall cruises

	depth	Spring					Summer					Early Fall					Late Fall				
		min	max	avg	stdev		min	max	avg	stdev		min	max	avg	stdev		min	max	avg	stdev	
HB	0.5	3.08	6.72	5.13	1.40	7.27	12.65	9.76	2.65	5.33	6.51	5.96	0.49	3.71	3.80	3.75	0.06				
	1	3.08	6.96	5.22	1.49	7.57	12.98	10.25	2.62	5.30	6.57	6.00	0.54	3.74	3.79	3.76	0.04				
	3	3.09	6.24	5.05	1.50	5.49	9.05	6.75	1.51	5.14	5.85	5.51	0.32	3.72	3.96	3.84	0.17				
JT	6	3.06	6.78	5.06	1.88	6.02	13.78	10.19	3.82	4.78	6.06	5.56	0.69	3.80	4.29	4.04	0.34				
	0.5	4.67	6.90	6.13	1.00	7.29	14.04	9.96	2.64	6.13	7.51	6.82	0.77	4.30	5.27	4.79	0.69				
	1	4.67	6.82	6.13	0.99	7.34	10.62	9.27	1.55	6.22	7.80	6.97	0.85	4.29	5.23	4.76	0.66				
PI	3	4.60	6.77	5.95	1.17	7.47	12.83	9.73	2.19	6.24	7.92	7.06	0.82	4.44	5.27	4.85	0.59				
	6	6.78	8.78	7.78	1.41	9.21	19.41	12.77	4.15	6.94	9.40	8.52	1.37	3.91	5.39	4.65	1.04				
	0.5	3.24	4.48	3.84	0.53	4.34	6.98	5.98	1.18	3.08	3.67	3.39	0.31	1.72	2.52	2.12	0.56				
TI	1	3.24	4.70	3.90	0.63	4.32	7.00	6.05	1.20	3.12	3.66	3.40	0.28	1.84	2.54	2.19	0.49				
	3	2.82	4.47	3.75	0.71	5.72	7.30	6.56	0.65	3.07	3.63	3.33	0.29	1.82	2.38	2.10	0.40				
	6	4.12	5.15	4.78	0.46	5.24	7.95	6.26	1.22	2.47	3.69	3.18	0.57	1.80	2.50	2.15	0.50				
	0.5	2.56	4.54	3.87	0.77	5.22	6.37	6.01	0.53	2.80	4.18	3.31	0.64	2.19	2.43	2.31	0.17				
	1	2.66	4.54	3.91	0.75	6.18	6.85	6.42	0.30	2.85	4.36	3.44	0.72	2.22	2.44	2.33	0.15				
	3	3.01	5.19	3.98	0.78	5.02	6.29	5.76	0.47	2.78	3.98	3.23	0.55	2.35	2.51	2.43	0.11				
6	3.52	4.11	3.86	0.27	3.85	6.27	4.58	1.13	2.66	3.20	2.91	0.25	2.24	2.39	2.31	0.11					

Table 2.3-4: Range in attenuation values at 676 nm, as measured during the spring, summer, early and late fall cruises

	depth	Spring					Summer					Early Fall					Late Fall				
		min	max	avg	stdev	min	max	avg	stdev	min	max	avg	stdev	min	max	avg	stdev	min	max	avg	stdev
HB	0.5	2.08	3.91	3.19	0.71	5.20	10.81	7.74	2.95	3.26	4.30	3.80	0.45	2.38	2.41	2.40	0.03				
	1	2.08	4.02	3.27	0.77	5.00	11.54	8.32	3.00	3.24	4.40	3.86	0.53	2.39	2.41	2.40	0.01				
	3	2.09	4.33	3.22	0.93	2.73	6.39	4.32	1.53	3.03	3.73	3.40	0.30	2.39	2.52	2.45	0.09				
JT	6	1.83	4.41	3.01	1.30	2.85	9.44	6.56	3.20	2.45	4.00	3.39	0.83	2.46	2.78	2.62	0.22				
	0.5	3.50	4.70	4.26	0.54	4.90	12.62	7.11	3.16	3.59	4.46	4.08	0.40	3.01	3.63	3.32	0.44				
	1	3.50	4.64	4.27	0.53	4.97	8.19	6.28	1.36	3.64	4.80	4.22	0.51	3.00	3.59	3.29	0.41				
PI	3	3.02	4.64	4.04	0.89	4.63	9.02	6.51	1.60	3.62	4.70	4.33	0.50	3.12	3.61	3.37	0.35				
	6	4.46	6.42	5.44	1.38	5.18	13.82	8.92	3.43	4.78	6.40	5.68	0.82	2.42	3.71	3.06	0.92				
	0.5	2.05	2.62	2.31	0.24	2.90	4.87	3.71	0.86	1.69	2.13	1.89	0.21	0.89	1.44	1.16	0.39				
TI	1	2.07	2.62	2.38	0.27	2.87	4.90	3.76	0.85	1.69	2.15	1.89	0.21	1.01	1.44	1.22	0.31				
	3	1.69	2.66	2.23	0.40	3.28	5.01	3.95	0.74	1.59	2.05	1.83	0.22	0.95	1.36	1.16	0.29				
	6	2.67	3.39	2.99	0.34	3.26	4.85	3.71	0.76	1.09	2.12	1.72	0.46	0.88	1.41	1.15	0.37				
TI	0.5	1.54	2.98	2.45	0.55	2.97	4.25	3.67	0.62	1.35	2.70	1.87	0.60	1.21	1.39	1.30	0.13				
	1	1.63	2.92	2.51	0.53	3.32	4.80	4.12	0.61	1.40	2.92	2.02	0.71	1.23	1.40	1.31	0.12				
	3	1.89	3.62	2.58	0.71	2.53	3.96	3.42	0.55	1.32	2.49	1.77	0.51	1.32	1.44	1.38	0.09				
	6	1.95	2.83	2.31	0.38	1.76	3.33	2.51	0.65	1.21	1.86	1.50	0.27	1.11	1.29	1.20	0.13				

2.3.3 Total backscattering

Measurements of total backscattering, b_b , at 3 wavelengths (450, 530 and 650 nm) were performed using an ECOVSF instrument. The vertical profiles of backscattering at 530 nm, $b_b(530)$, measured at the four stations HB, PI, TI and JT during the 2001 and 2002 cruises (spring, summer, early and late fall seasons) are shown in figure 2.3-6. Similar vertical structure was also obtained for backscattering at 450 and 650 nm.

High backscattering measured close to the surface at HB station on 11 June 2001, was associated with high amounts of particulate matter and high absorption by both pigmented and non-pigmented particulate matter (high $a_{t-w}(676)$ and $a_{t-w}(412)$ values measured during the specific cruise, fig. 2.3-4). High backscattering was also measured close to the surface (along with high absorption and total attenuation values) at JT station on 18 June 2002. Relatively high backscattering was observed during some of the cruises close to the bottom of the water column (5-8 m depth), which was most probably due to the presence of re-suspended inorganic sediments that are characterized by high backscattering properties.

Backscattering was generally lower at each station, during the fall months (cruises 21 September - 13 November), when the water was also characterized by lower total absorption and attenuation. The measured backscattering profiles showed small vertical variation with depth during the cruises performed in late and early fall seasons, which is in agreement with the higher vertical homogeneity of the water (well mixed water, almost

backscattering (in m^{-1}) at 530 nm

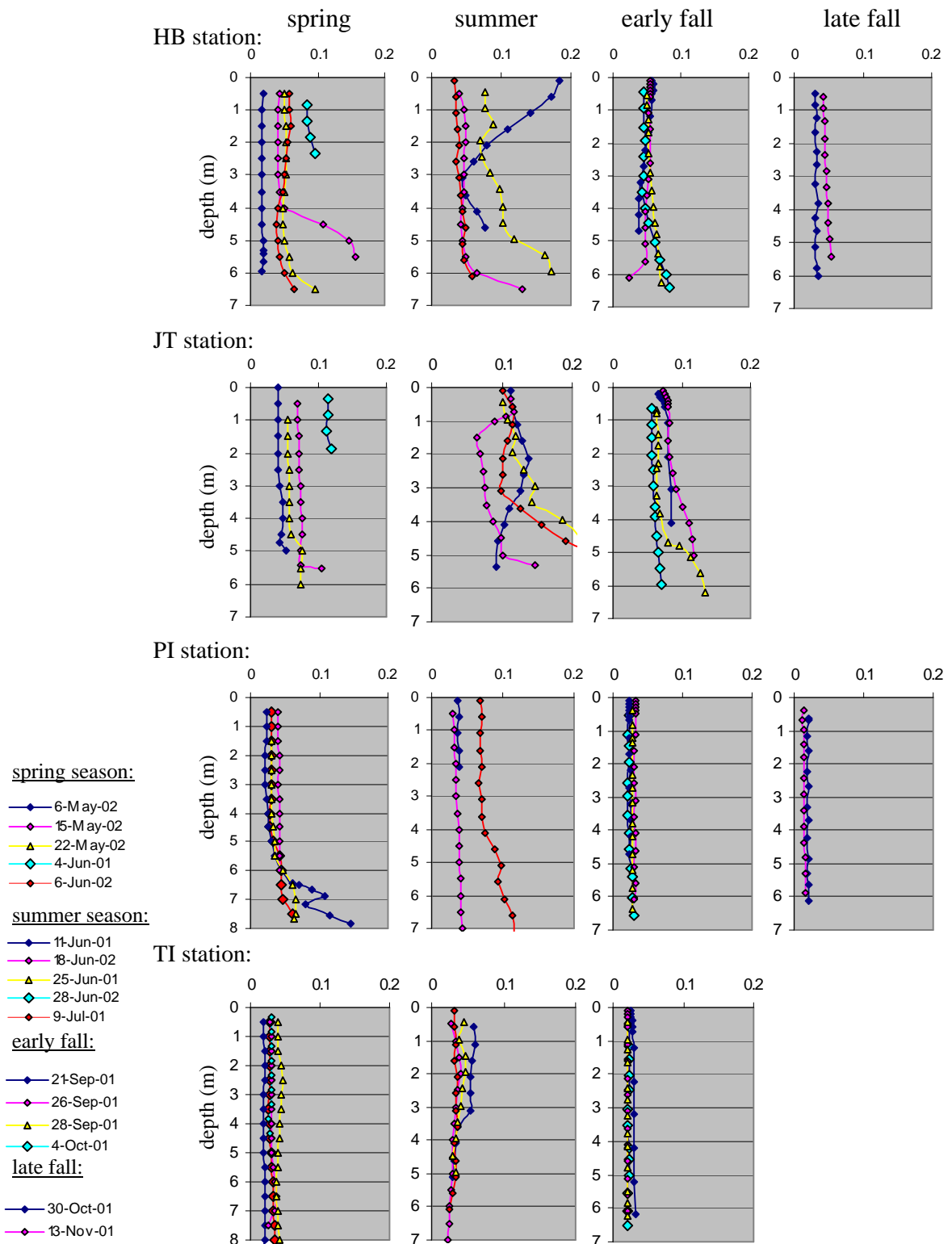


Figure 2.3-6: Profiles of $b_b(530)$ (in m^{-1}) measured at the HB, JT, PI and TI stations, during the spring, summer, early and late fall cruises of 2001 and 2002.

constant temperature and salinity profiles and low vertical variation in measured total absorption and attenuation) observed during the fall months. The temporal variation in surface $b_b(530)$ values (0-1m), at HB, JT, PI and TI stations, is shown in figure 2.3-7. During almost all of the cruises significantly higher backscattering values at all three wavelengths (450, 530 and 650 nm) were measured at the HB station and especially at the JT station. Both of these stations are located closer to western shore of the Bay. As is shown in figure 2.3-7, the less turbid PI and TI stations were both characterized by much lower values of backscattering coefficients.

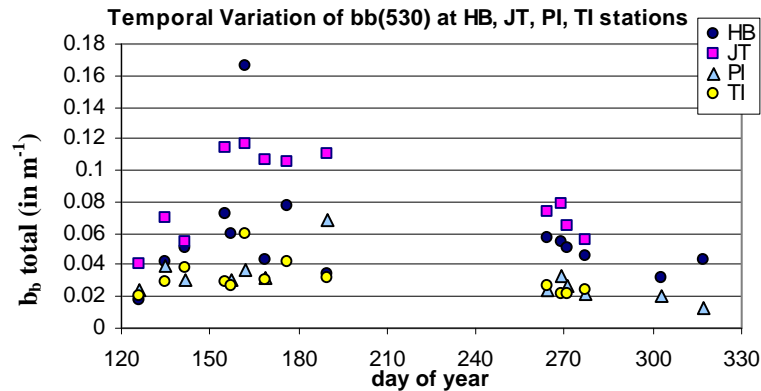


Figure 2.3-7: Temporal variation in surface (0-1m) total backscattering values at 530 nm, $b_b(530)$, measured at HB, JT, PI and TI stations.

Values of the backscattering fraction b_b/b were estimated using the AC9 measurements of b_{t-w} ($b_{t-w}=c_{t-w}-a_{t-w}$) and the ECOVSF measurements of b_b . Measurements of b_{t-w} (at the nine AC9 wavelengths 412-715 nm) were interpolated to obtain scattering coefficients at the three ECOVSF wavelengths 450, 530 and 650 nm. Since b_b is the total backscattering in the water, backscattering due to pure water ($b_{bw}=0.5 \cdot b_w$, with b_w the Smith and Baker coefficients) had to be subtracted from b_b to obtain the particulate backscattering coefficient b_{bp} . The b_b and b profiles measurements had to be corrected for depth offsets

between the AC9 and ECOVSF instruments during the measurements. Inaccuracies associated with these corrections would affect the accuracy of the estimated b_b/b_p values.

The backscattering fraction measured in the Chesapeake Bay waters during our cruises had an average value of 0.0128 with a standard deviation of ± 0.0033 , at 530 nm. The average value of b_{bp}/b_p at 450 nm was 0.0133 with a standard deviation of ± 0.0032 , while average b_{bp}/b_p at 650 nm was 0.0106 with a standard deviation of ± 0.0029 . The minimum, maximum and average values of b_{bp}/b_p at 450, 530 and 650 nm, along with the estimated standard deviations are shown in table 2.3-5.

Table 2.3-5: Minimum, maximum and average b_b/b_p values (for particulate matter) measured at 450, 530 and 650 nm during the 2001-2002 cruises in the northern Chesapeake Bay.

Wavelength	$b_b/b(450)$	$b_b/b(530)$	$b_b/b(650)$
minimum	0.00641	0.00577	0.00447
maximum	0.03387	0.03692	0.03296
average	0.01323	0.01288	0.01062
stdev	0.00327	0.00327	0.00294

The b_{bp}/b_p values measured at various depths and at each station during the cruises, are shown in figure 2.3-8(a) (HB station: blue diamonds, JT station: red squares, PI station: yellow triangles, JT station: white circles). The largest values of b_{bp}/b_p , with $b_{bp}/b_p=0.026$ and $b_{bp}/b_p=0.036$, were measured at JT station on 9 July 2001 at depths 4.9 and 5.4 m respectively (close to the bottom of the water column at JT station during that cruise). Resuspended, high index of refraction sediments close to the bottom, could be responsible for the jump in b_{bp}/b_p values. Figure 2.3-8(b) shows the b_{bp}/b_p values measured

at the four stations only within the first three meters below the water surface. According to the measurements shown in fig. 2.3-8(b) lower values of b_b/b were measured in the spring cruises (May 2002), while cases with high b_b/b were observed during the summer cruises on 11 June , 25 June and 9 July 2001. Similarly to the spatial pattern observed in the b_b measurements, higher b_b/b values (at all three wavelengths 450, 530 and 650 nm, only 530 nm shown in figure 2.3-8(b)) were measured at the JT station during most of the cruises, while lower b_b/b values were observed at the less turbid TI station.

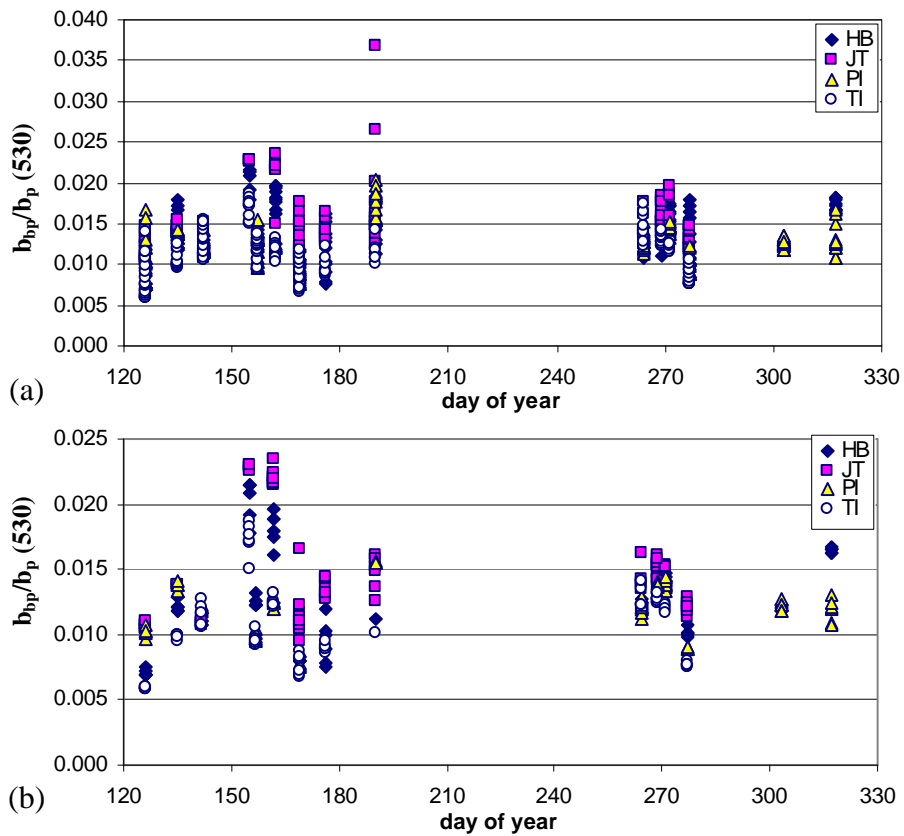


Figure 2.3-8: Backscattering fraction, b_b/b , measured (a) at various depths in the water column (0-9m) and (b) only within the 3 meters below the water surface, at the stations HB, JT, PI and TI, during the 2001-2002 cruises in the Chesapeake Bay. (HB station: blue diamonds, JT station: red squares, PI station: yellow triangles, JT station: white circles). The two largest b_b/b values, $b_b/b = 0.026$ and $b_b/b = 0.036$ (shown in (a)) were measured at JT station on 9 July 2001, at depths 4.9 and 5.4 m respectively, close to the bottom of the water column at JT station during that cruise.

2.3.4 Absorption spectra by non-pigmented particulates, phytoplankton, CDOM

2.3.4.1 Particulate non-pigmented absorption

Laboratory measurements of absorption by particulate, non-pigmented matter were performed, using the CARY spectrophotometer, on water samples collected from the stations HB, PI, TI and JT (methodology described in paragraph 2.2.2.2). The term “ a_{npp} ” will be used in the following and for the rest of this document, to describe absorption by all non-pigmented particles (including detrital material, inorganic minerals and all particulate substances remained on the filters after methanol extraction of pigments).

Particulate non-pigmented absorption spectra, normalized to particulate non-pigmented absorption at 440 nm, are shown in figure 2.3-9(A)(a, b, c, d) for the four stations: HB (39 spectra), JT (37 spectra), PI (40 spectra) and TI (41 spectra). Measurements are shown at wavelengths 412-715 nm (wavelengths of $a_{\text{t-w}}$ and $c_{\text{t-w}}$ AC9 measurements, and also wavelength region used in ocean color satellite measurements). Measurements of a_{npp} in the spectral region 300-750 nm are shown in figure 2.3-9(B). The “average” normalized spectra, $a_{\text{npp}}(\lambda)/a_{\text{npp}}(440)$, along with the estimated standard deviations (stdev) at each wavelength, are also shown in figures 2.3-9 (e, f, g, h), (and in table 2.3-6).

The normalized spectra measured in the visible wavelength region, 412-715 nm, at each of the four stations, show very similar wavelength dependence, especially for the stations HB and JT. The estimated standard deviations from the average normalized spectra are small especially at HB (maximum stdev of 0.027 at 555 nm) and JT (maximum stdev of

0.019 at 510 nm). For TI and PI stations slightly larger variation among the normalized spectra was observed (maximum stdev of 0.043 at 510 nm at TI and 0.052 at 555 nm at PI station). Some of the variation observed close to 676 nm was due to imperfect extraction of the pigmented material (fig.2.3-9).

Table 2.3-6: Average normalized spectra, $a_{\text{npp}}(\lambda)/a_{\text{npp}}(440)$, measured at HB, JT, PI and TI stations, (412-715 nm) along with the standard deviations (stdev)

station		715	676	650	555	532	510	488	440	412
HB	average	0.029	0.097	0.128	0.290	0.382	0.474	0.587	1.000	1.269
	stdev	0.007	0.016	0.014	0.027	0.026	0.026	0.023	0.000	0.031
JT	average	0.029	0.098	0.125	0.287	0.380	0.476	0.592	1.000	1.271
	stdev	0.005	0.015	0.011	0.018	0.018	0.019	0.017	0.000	0.027
PI	average	0.026	0.089	0.116	0.264	0.357	0.449	0.565	1.000	1.287
	stdev	0.009	0.026	0.024	0.052	0.052	0.051	0.045	0.000	0.030
TI	average	0.027	0.095	0.127	0.283	0.375	0.464	0.573	1.000	1.284
	stdev	0.008	0.023	0.020	0.036	0.037	0.043	0.043	0.000	0.039

Non-linear exponential fits were applied to the average normalized absorption spectra, (wavelength region 412-715 nm) according to:

$$a_{\text{npp}}(\lambda) / a_{\text{npp}}(440) = A * \exp [-S_{\text{npp}} (\lambda - 440)] \quad (2.3-1)$$

that is often used to model absorption by non-pigmented particulate matter. In eq. 2.3-1, $a_{\text{npp}}(\lambda)$ and $a_{\text{npp}}(440)$ are non-pigmented particulate absorption at wavelength λ and at 440 nm respectively, A accounts for measurements' uncertainty in $a_{\text{npp}}(440)$, and S_{npp} is the exponential slope. The estimated exponential slopes were very similar for the four stations and equal to $S_{\text{npp}}=0.0102 \text{ nm}^{-1}$ at HB, $S_{\text{npp}}=0.0102 \text{ nm}^{-1}$ at JT, $S_{\text{npp}}= 0.0109 \text{ nm}^{-1}$ at PI and $S_{\text{npp}}=0.0104 \text{ nm}^{-1}$ at TI station. The values of the intercept A were very close to 1 at all stations. R^2 values were larger than 0.99. The estimated values of S_{npp} , A and R^2 are shown in table 2.3-7 for each one of the stations.

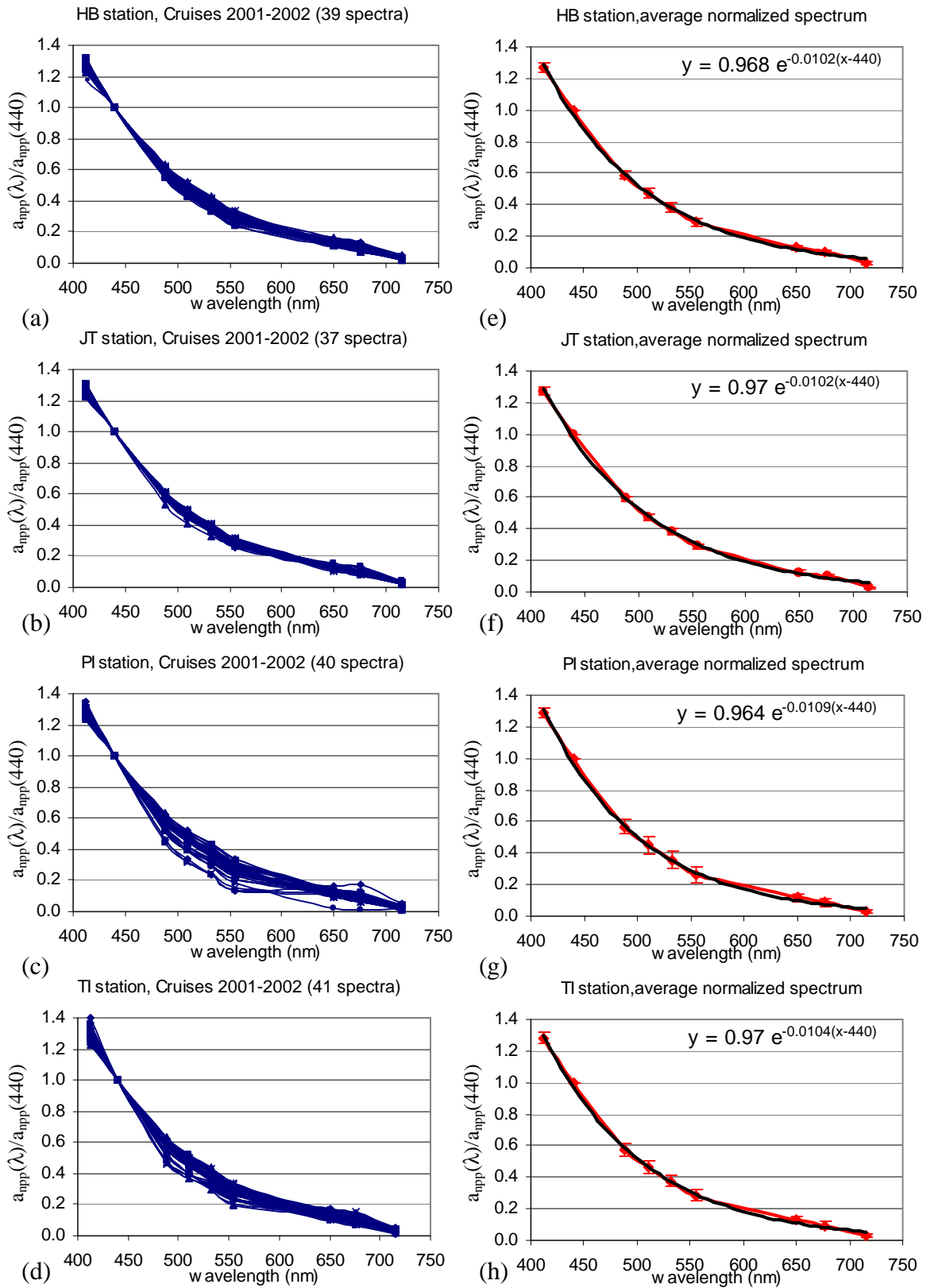


Figure 2.3-9(A): Normalized spectra, $a_{npp}(\lambda)/a_{npp}(440)$, measured at (a) HB (b) JT (c) PI and (d) TI stations (400-715nm). The average normalized spectra along with the standard deviations and the non-linear exponential fit, are shown in figures (e), (f) (g) (h).

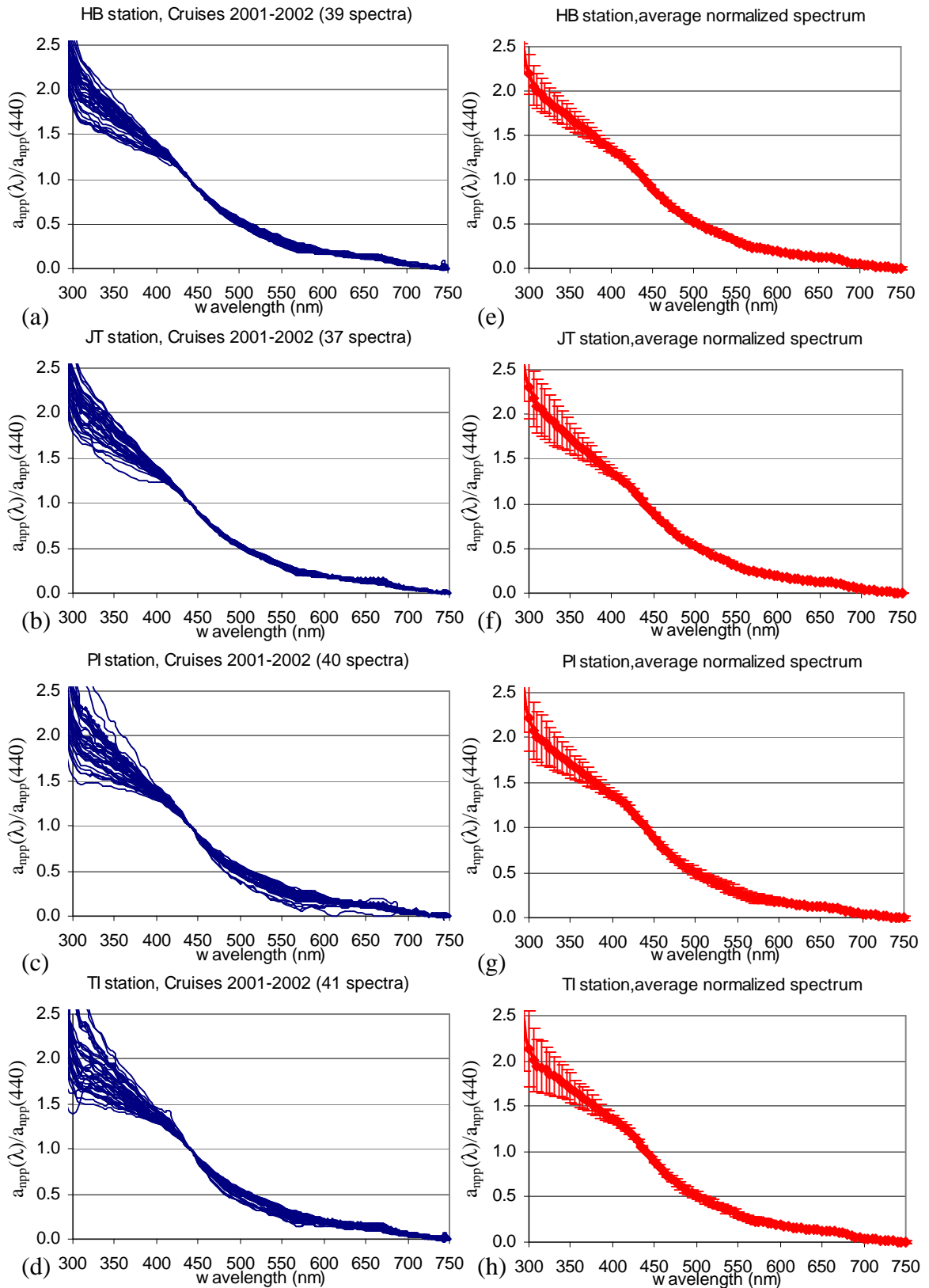


Figure 2.3-9(B): Normalized spectra, $a_{npp}(\lambda)/a_{npp}(440)$, measured at (a) HB (b) JT (c) PI and (d) TI stations (300-750nm). The average normalized spectra along with the standard deviations, are shown in figures (e), (f) (g) (h) for each station.

Table 2.3-7: Values of S_{npp} , A and R^2 corresponding to eq.(2.3-1) for absorption by non-pigmented particulate matter at HB, JT, PI and TI stations (exponential fits shown in fig. 2.3-9(A)).

station	HB	JT	PI	TI
S_{npp} (nm^{-1})	0.0102	0.0102	0.0109	0.0104
A	0.968	0.97	0.964	0.97
R^2	0.998	0.998	0.998	0.998

Figure 2.3-10 shows the temporal variation in $a_{npp}(440)$ measured at various depths (0-5 m) and at the four stations HB, JT, PI, TI, during the 2001 and 2002 cruises.

Measurements of absorption were corrected for pathlength amplification using $\beta=1.5$ (methodology described in paragraph 2.2.2.3). Higher absorption by non-pigmented particulate matter was measured at 440 nm during the summer months, in agreement with the temporal patterns of total absorption at 412 nm in these waters. Absorption by non-pigmented particles decreased during the fall months when more clear water conditions were observed in the Bay. Higher values of $a_{npp}(440)$ were observed, during almost all of the cruises, at the most turbid station, JT, and also at HB station, compared to measurements at TI and PI.

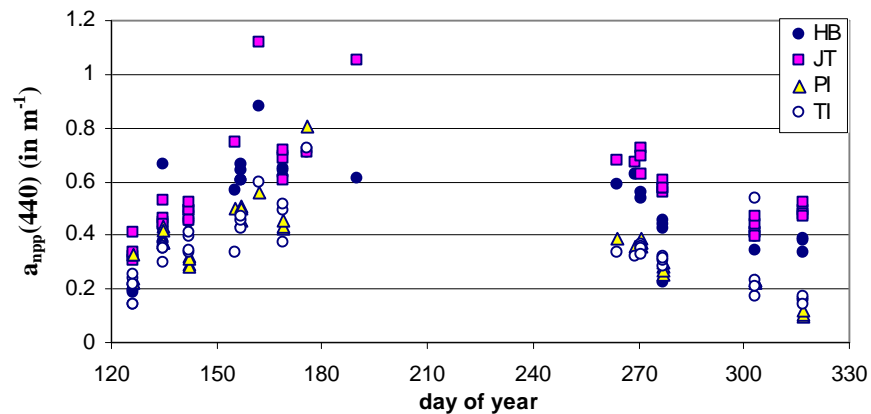


Figure 2.3-10: Temporal variation in $a_{npp}(440)$ measured at the four stations HB (blue circles), JT (red squares), PI (yellow triangles), TI (white circles), during the 2001 and 2002 cruises in the Bay.

2.3.4.2 Particulate pigmented (phytoplankton) absorption

Water samples collected from various depths (0-5m) at the four stations HB, JT, PI and TI, during the cruises in the Bay, were analyzed for absorption by phytoplankton pigments. The phytoplankton absorption spectra were normalized to phytoplankton absorption at 676 nm, which is one of the chl-a absorption maxima. The normalized spectra (visible wavelength region) are shown in figure 2.3-11(A) (a, b, c, d) for the four stations HB (39 spectra), JT (37 spectra), PI (41 spectra) and TI (41 spectra). The “average” normalized spectra, $a_{\text{phyt}}(\lambda)/a_{\text{phyt}}(676)$, along with the estimated standard deviations (stdev) at each wavelength, are also shown in figure 2.3-11(A)(e, f, g, h) (also in table 2.3-8). Large variation was observed among the normalized spectra measured at the four stations, which resulted in the large standard deviations shown in figure 2.3-11(A). Strong absorption in the UV wavelength region (~325-330 nm) was observed in certain cases during the spring and summer cruises (fig 2.3-11(B)) most probably due to the presence of mycosporine-like amino acids (MAAs).

Table 2.3-8: Average normalized spectra, $a_{\text{phyt}}(\lambda)/a_{\text{phyt}}(676)$, measured at HB, JT, PI and TI stations, (412-715 nm) along with the standard deviations (stdev)

station		715	676	650	555	532	510	488	440	412
HB	average	0.050	1.000	0.384	0.380	0.526	0.750	1.004	1.572	1.354
	stdev	0.025	0.000	0.040	0.106	0.132	0.171	0.245	0.321	0.389
JT	average	0.051	1.000	0.388	0.379	0.522	0.725	0.976	1.533	1.327
	stdev	0.024	0.000	0.039	0.083	0.094	0.095	0.119	0.116	0.144
PI	average	0.056	1.000	0.382	0.405	0.540	0.760	1.004	1.591	1.381
	stdev	0.015	0.000	0.032	0.107	0.112	0.122	0.152	0.199	0.235
TI	average	0.048	1.000	0.380	0.378	0.518	0.742	0.997	1.574	1.344
	stdev	0.016	0.000	0.025	0.073	0.086	0.126	0.184	0.180	0.184

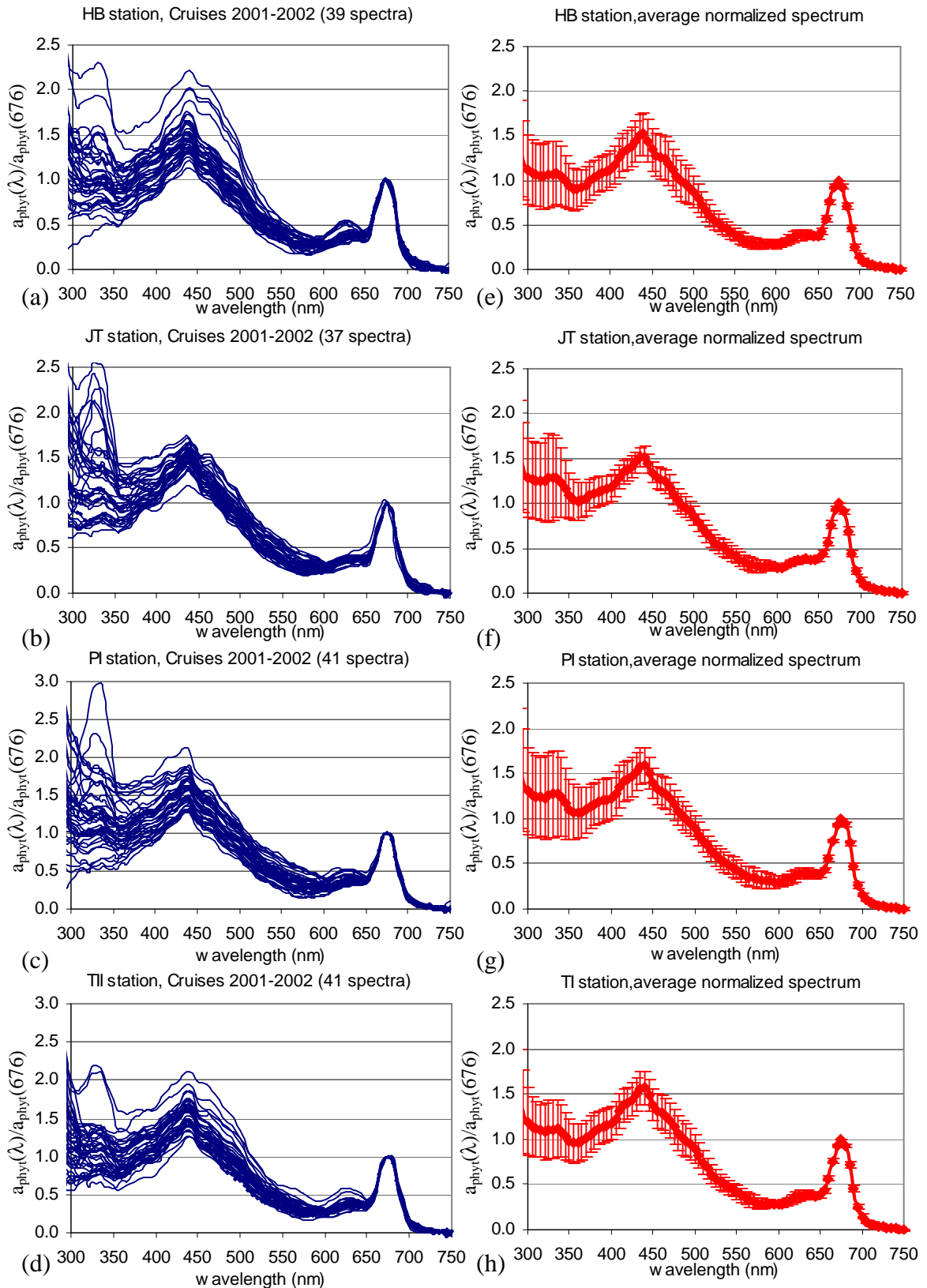


Figure 2.3-11(A): Normalized spectra, $a_{\text{phyt}}(\lambda)/a_{\text{phyt}}(676)$, measured at (a) HB (b) JT (c) PI and (d) TI stations (300-750 nm). The average normalized spectra along with the standard deviations are shown in figures (e), (f) (g) (h) for each station

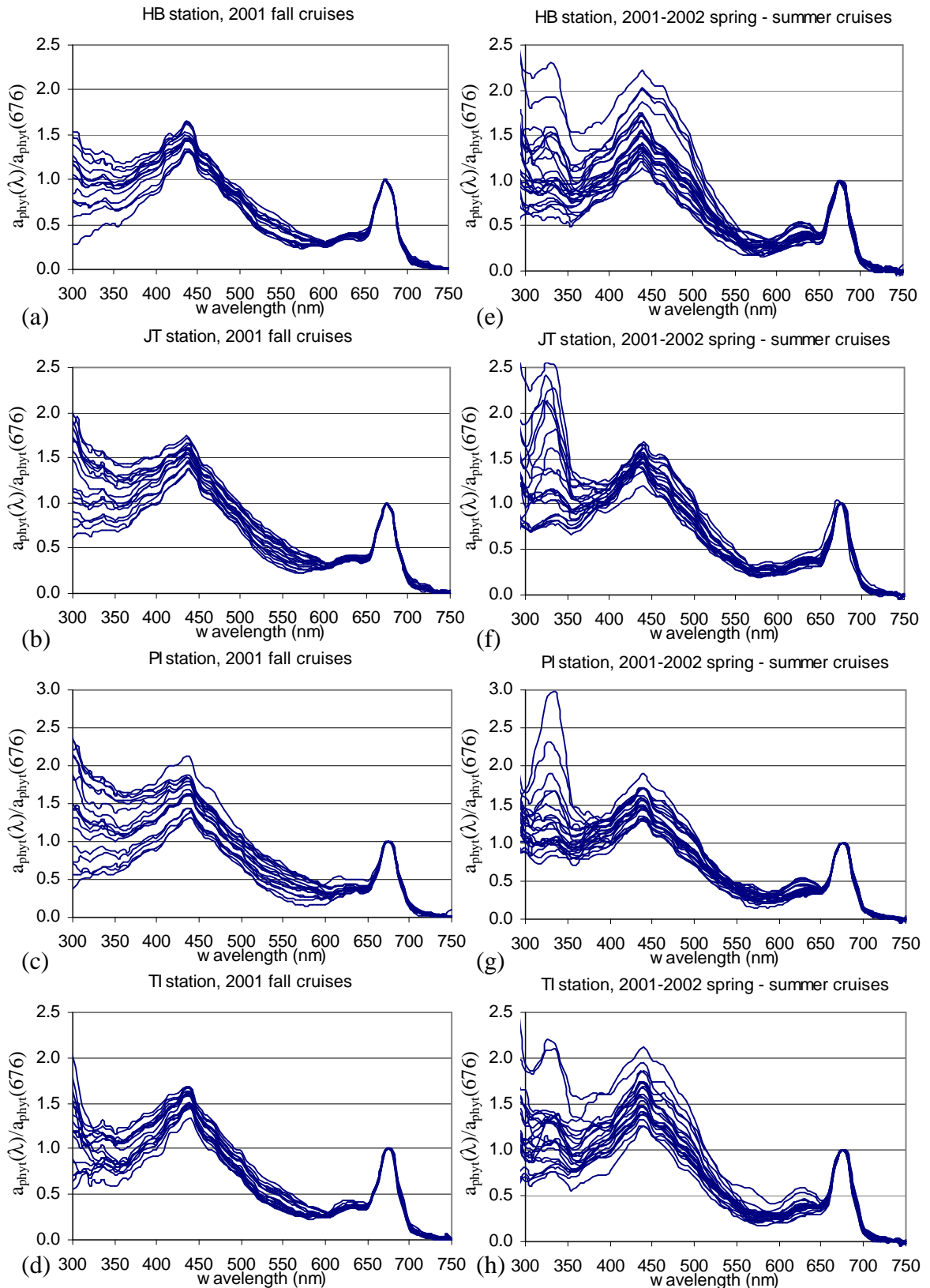


Figure 2.3-11(B): Normalized spectra, $a_{\text{phyt}}(\lambda)/a_{\text{phyt}}(676)$, measured at HB, JT, PI and TI stations during the fall 2001 (a,b,c,d) and also during the spring and summer 2001-2002 (e,f,g,h) cruises when strong absorption by MAAs was evident in the UV wavelengths.

The temporal variation in $a_{\text{phyt}}(676)$ values measured at the four stations HB, JT, PI, TI, during the 2001 and 2002 cruises, is shown in figure 2.3-12. Measurements of absorption were corrected for pathlength amplification using $\beta=1.5$. Higher absorption by phytoplankton at 676 nm was measured during the summer months, in agreement with the temporal patterns of total absorption at 676 nm, $a_{t-w}(676)$, measured in-situ using the AC9 instrument (paragraph 2.3.2). Particularly high phytoplankton absorption values were measured at HB (blue circles in fig. 2.3-12) and JT stations (red squares in fig. 2.3-12) during the phytoplankton bloom events observed on 11 June 2001, 25 June 2001 and 18 June 2002. Absorption by phytoplankton decreased during the fall months.

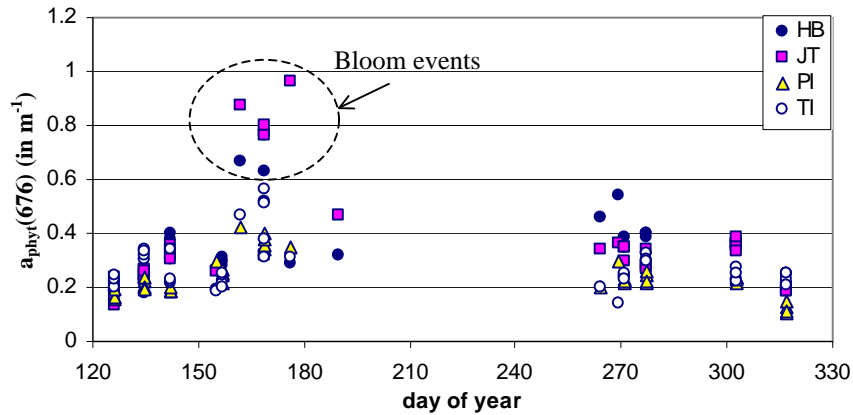


Figure 2.3-12: Temporal variation in $a_{\text{phyt}}(676)$ measured at the four stations HB (blue circles), JT (red squares), PI (yellow triangles), TI (white circles), during the 2001 and 2002 cruises in the Bay.

2.3.4.3 Chromophoric Dissolved Organic Matter absorption spectra

Measurements of absorption by CDOM have been performed on the water samples collected from the northern part of the mainstream of the Chesapeake Bay (methodology described in paragraph 2.2.2.2). The measured CDOM absorption spectra, normalized to CDOM absorption at 440 nm, are shown in figure 2.3-13(A) (a, b, c, d) (measurements in the visible wavelength region 412-715nm), for the four stations: HB (38 spectra), JT (32 spectra), PI (41 spectra) and TI (41 spectra). The “average” normalized spectra, $a_{\text{CDOM}}(\lambda)/a_{\text{CDOM}}(440)$, along with the estimated standard deviations (stdev) at each wavelength, are also shown in figure 2.3-13(A) (e, f, g, h). The spectrophotometric scans showed the typical exponential decrease of CDOM absorption with increasing wavelength (Bricaud et al, 1981). However, large variation was observed among the exponential slopes of the normalized spectra measured at the four stations during the cruises, which resulted in the large standard deviations shown in figure 2.3-13(A)(e, f, g, h). The CDOM absorption spectra in the wavelength region 300-750 nm are shown in figure 2.3-13(B). Due to the large variation in the exponential slope, standard deviations from the average normalized spectra were even more pronounced at the shorter wavelengths.

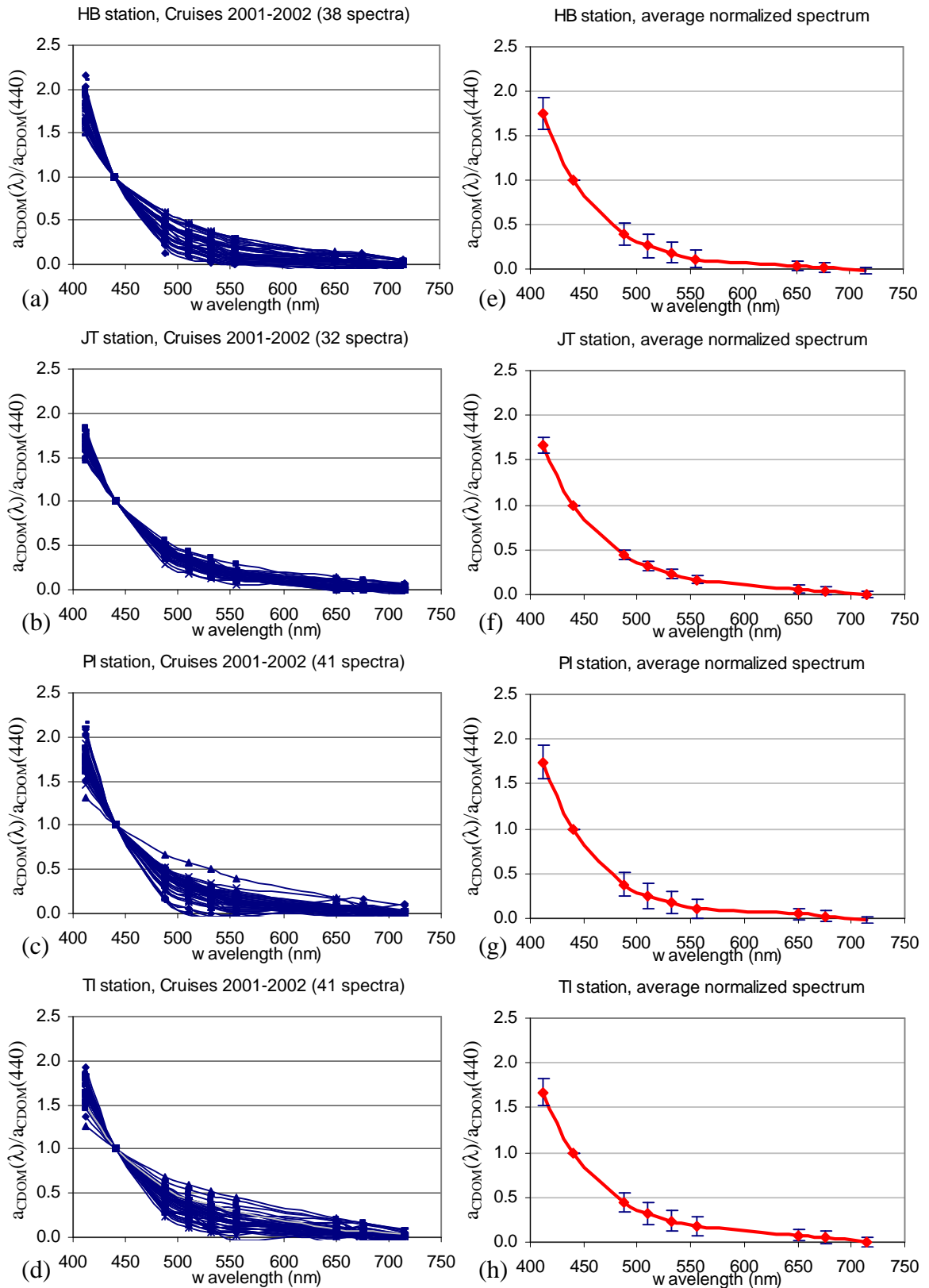


Figure 2.3-13(A): Normalized spectra, $a_{CDOM}(\lambda)/a_{CDOM}(440)$, measured at (a) HB (b) JT (c) PI and (d) TI stations (400-715 nm). The average normalized spectra along with the standard deviations are shown in figures (e), (f) (g) (h) for each station

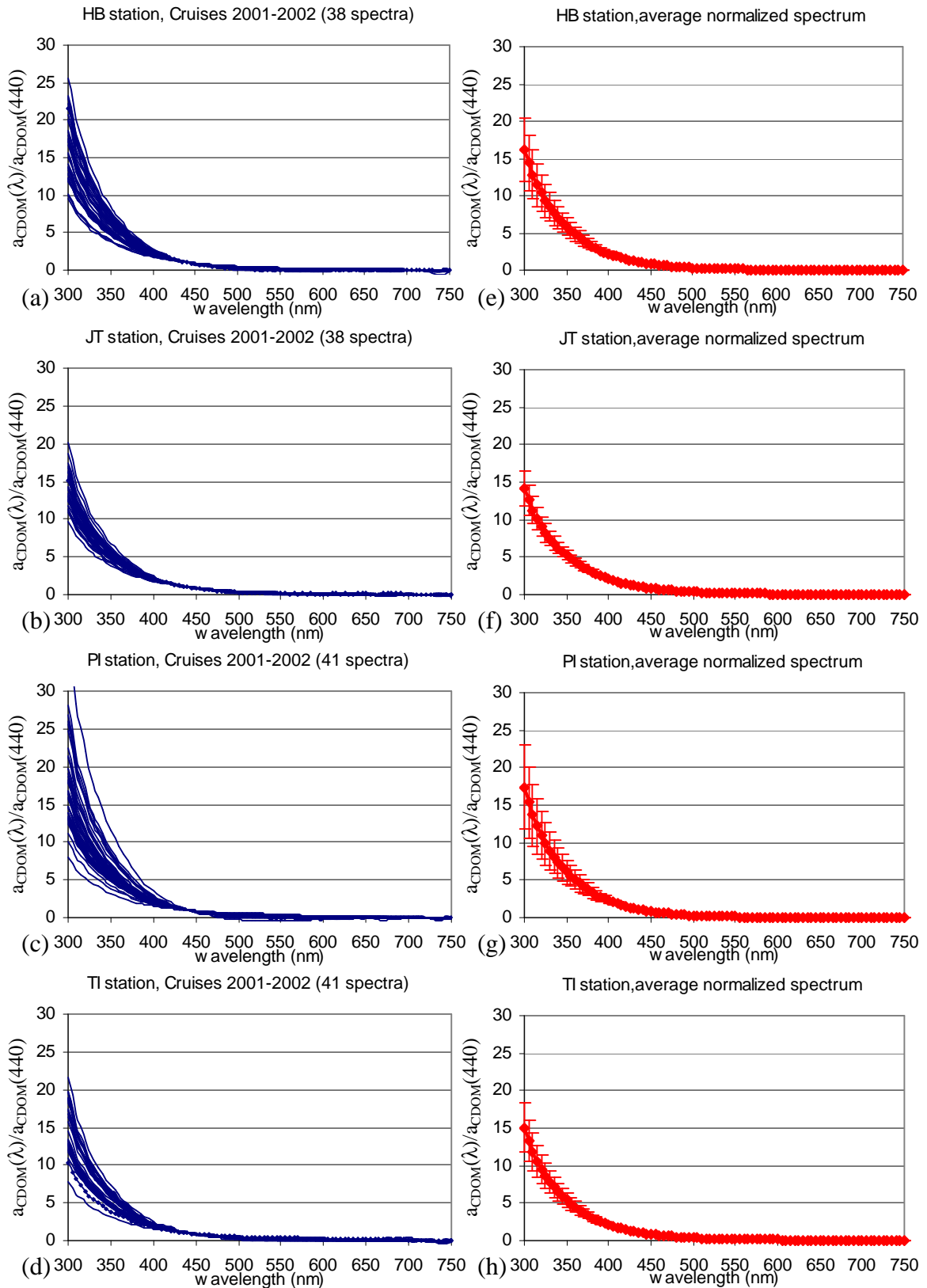


Figure 2.3-13(B): Normalized spectra, $a_{CDOM}(\lambda)/a_{CDOM}(440)$, measured at (a) HB (b) JT (c) PI and (d) TI stations (300-750 nm). The average normalized spectra along with the standard deviations are shown in figures (e), (f) (g) (h) for each station

The values of $a_{\text{CDOM}}(440)$ measured at the four stations, during the specific cruises in 2001 and 2002, are shown in figure 2.3-14. Measured $a_{\text{CDOM}}(440)$ ranged from 0.09 to 0.55m^{-1} . Relatively higher values of $a_{\text{CDOM}}(440)$ were observed at all stations during the early spring cruise on 15 May 2001, and especially at HB and JT stations on 22 May 2002. With the exception of HB station (located very close to the western shore of Chesapeake Bay), where absorption by CDOM at 440 nm was relatively large, $a_{\text{CDOM}}(440)$ values showed some decrease during the fall cruises. However, no clear spatial or seasonal pattern was observed at $a_{\text{CDOM}}(440)$. The minimum, maximum and average $a_{\text{CDOM}}(440)$ values observed at each station, are shown in table 2.3-9.

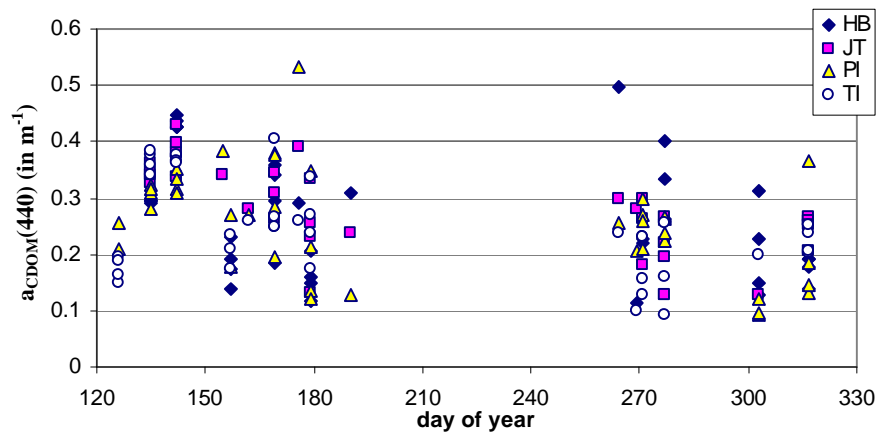


Figure 2.3-14: Measurements of $a_{\text{CDOM}}(440)$ performed at the four stations, HB (blue pixels), JT (red squares), PI (yellow triangles) and TI (white circles).

Table 2.3-9: Minimum, maximum and average $a_{\text{CDOM}}(440)$ values measured at the four stations HB, JT, PI and TI during the 2001-2002 cruises in the northern Chesapeake Bay.

station	Meas. $a_{\text{CDOM}}(440)$			
	min	max	avg	stdev
HB	0.1123	0.4956	0.2713	0.1023
JT	0.1268	0.4293	0.2825	0.0768
PI	0.0970	0.5339	0.2751	0.0848
TI	0.0937	0.4042	0.2472	0.0839

Since absorption by CDOM decreases with increasing wavelength in an exponential fashion, non-linear exponential fits were applied to the CDOM absorption spectra, according to expression:

$$a_{\text{CDOM}}(\lambda) = a_{\text{CDOM}}(440) * \exp [-S_{\text{CDOM}} (\lambda-440)] \quad (2.3-2)$$

that is typically used to model absorption by CDOM (discussion in paragraph 1.5.6). In eq. 2.3-2, $a_{\text{CDOM}}(\lambda)$ are the measured CDOM absorption coefficients at wavelengths λ , $a_{\text{CDOM}}(440)$ is the CDOM absorption at 440 nm, and S_{CDOM} is the exponential slope that defines how rapidly the absorption decreases with wavelength. The non-linear exponential fits were performed in the visible wavelength region 400-700 nm (since the main focus of this study was on the water's optical properties in the visible) and also in the complete spectral range of the measurements 290-700 nm (for comparison with other studies on CDOM optical characteristics, e.g Blough and DelVecchio, 2002). The R^2 values of the non-linear exponential fits were in almost all of the cases larger than 0.99.

Figure 2.3-15 shows the comparison between S_{CDOM} values estimated after applying a non-linear exponential fit to the $a_{\text{CDOM}}(\lambda)$ measurements in the wavelength regions i) 290-700 and ii) 400-700 nm. The comparison between the measured and fitted a_{CDOM} values at the visible wavelengths 443, 488 and 555 nm are shown in figure 2.3-16. The average values of the residuals $a_{\text{CDOM}}(\lambda)_{\text{measured}} - a_{\text{CDOM}}(\lambda)_{\text{fitted}}$, at several wavelengths in the visible wavelength region, along with the estimated standard deviations are shown in figure 2.3-17. The $a_{\text{CDOM}}(\lambda)$ values estimated when fitting the data in the wavelength region 290-700 nm were underestimated compared to the measured $a_{\text{CDOM}}(\lambda)$ values, while the $a_{\text{CDOM}}(\lambda)$ measurements were in better agreement with the $a_{\text{CDOM}}(\lambda)$ values

estimated when fitting the data in the visible wavelength region. The minimum, maximum and average S_{CDOM} and $a_{\text{CDOM}}(440)$ values estimated using the two methods described above to fit the measurements performed at HB, JT, PI and TI stations, are shown in tables 2.3-10(a) and (b).

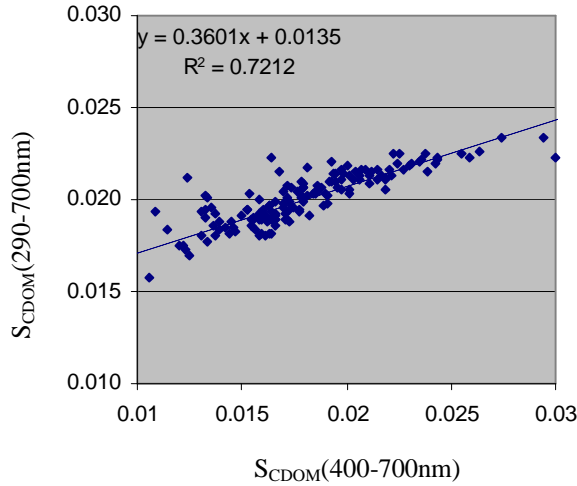


Figure 2.3-15: Comparison between S_{CDOM} values obtained when applying a non-linear exponential fit to measured $a_{\text{CDOM}}(\lambda)$ values in the wavelength regions 290-700 and 400-700 nm.

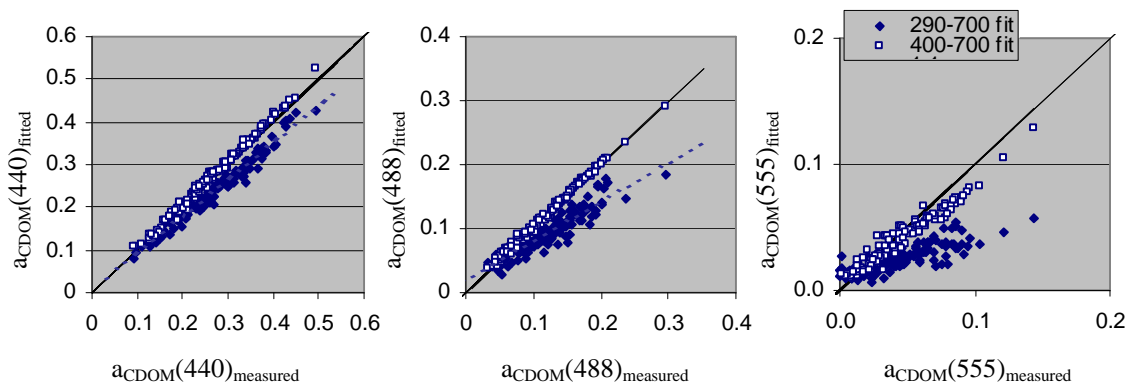


Figure 2.3-16: Comparison between the measured and fitted a_{CDOM} values at the visible wavelengths 443, 488 and 555 nm, for the two cases when the non-linear exponential fit was applied to a_{CDOM} measurements i) in the 290-700 nm wavelength region (blue pixels) and ii) in the visible wavelengths 400-700nm (white pixels).

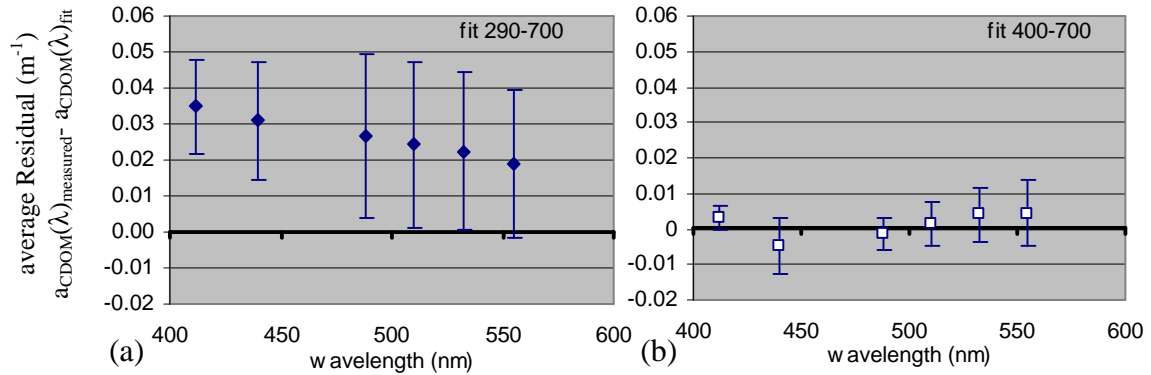


Figure 2.3-17: Average values of the residuals $a_{CDOM}(\lambda)_{measured} - a_{CDOM}(\lambda)_{fitted}$, at several visible wavelengths, along with the estimated standard deviations, for the two cases when the non-linear exponential fit was applied to measurements (a) in the 290-700 nm wavelength region and (b) in the visible wavelengths 400-700nm.

Table 2.3-10(a): Minimum, maximum and average $a_{CDOM}(440)$ and S_{CDOM} values (estimated after applying an exponential fit to a_{CDOM} measurements in the wavelength region 400-700 nm), at the four stations HB, JT, PI and TI

station	$a_{CDOM} (440)$				S_{CDOM}			
	min	max	avg	stdev	min	max	avg	stdev
HB	0.1129	0.5247	0.2766	0.1079	0.0120	0.0263	0.0185	0.0040
JT	0.1285	0.4360	0.2871	0.0779	0.0125	0.0211	0.0171	0.0021
PI	0.0904	0.5426	0.2773	0.0893	0.0085	0.0301	0.0186	0.0041
TI	0.1055	0.4165	0.2518	0.0869	0.0114	0.0243	0.0176	0.0033

Table 2.3-10(b): Minimum, maximum and average $a_{CDOM}(440)$ and S_{CDOM} values (estimated after applying an exponential fit to a_{CDOM} measurements in the wavelength region 290-700 nm), at the four stations HB, JT, PI and TI

station	$a_{CDOM} (440)$				S_{CDOM}			
	min	max	avg	stdev	min	max	avg	stdev
HB	0.1082	0.4248	0.2444	0.0904	0.0173	0.0226	0.0200	0.0016
JT	0.1122	0.3882	0.2476	0.0675	0.0170	0.0216	0.0197	0.0011
PI	0.1041	0.4132	0.2379	0.0661	0.0165	0.0234	0.0204	0.0015
TI	0.0813	0.3475	0.2156	0.0740	0.0177	0.0225	0.0202	0.0013

A general decrease in the estimated absolute S_{CDOM} values, with increase in the absorption by CDOM at 440 was observed during the measurements in the Bay. The relationship between $a_{CDOM}(440)$ and S_{CDOM} is shown in figures 2.3-18(a),(b). Figure 2.3-19 shows the relationship between a_{CDOM} and salinity and between S_{CDOM} and salinity measured at HB, JT, PI and TI stations. No strong correlation was found overall between salinity and a_{CDOM} or salinity and S_{CDOM} during the cruises in the Bay.

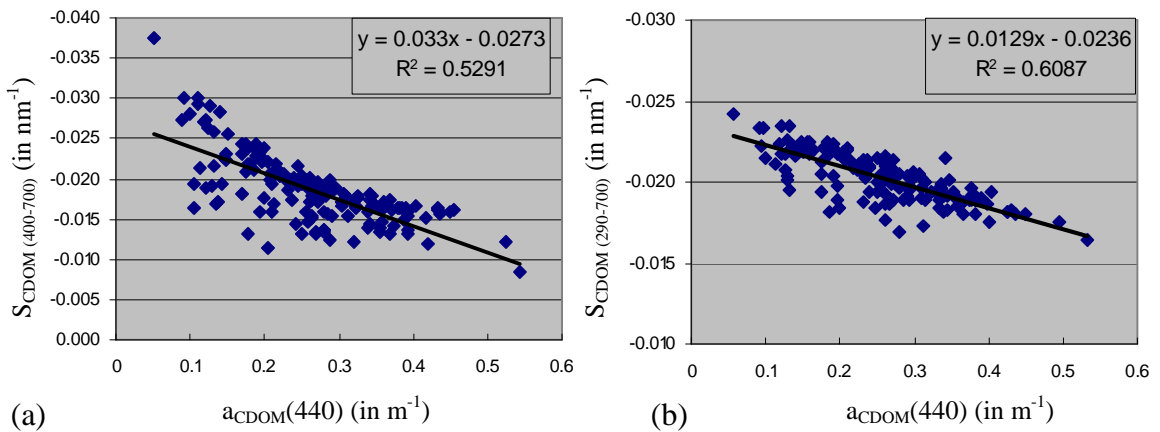


Figure 2.3-18: Relationship between (a) $a_{CDOM}(440)$ (m^{-1}) and $S_{CDOM(400-700nm)}$ (nm^{-1}), (b) $a_{CDOM}(440)$ (m^{-1}) and $S_{CDOM(290-700nm)}$ (nm^{-1}), for measurements performed at HB, JT, PI and TI stations.

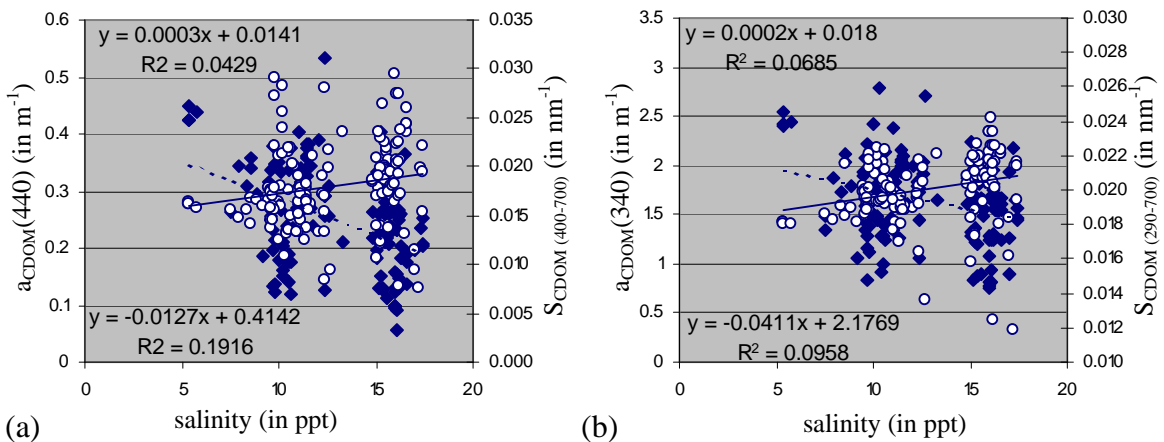


Figure 2.3-19: Relationship (a) between $a_{CDOM}(440)$ (m^{-1}) and salinity (in ppt) (blue circles) and $S_{CDOM(400-700nm)}$ (nm^{-1}) and salinity (white circles), (b) between $a_{CDOM}(340)$ (m^{-1}) and salinity (in ppt) (blue circles) and $S_{CDOM(290-700nm)}$ (nm^{-1}) and salinity (white circles), for measurements performed at HB, JT, PI and TI stations

2.3.4.4 Contribution to total a_{t-w} absorption

The contribution of CDOM, phytoplankton and non-pigmented particulate matter to the total absorption in the water was estimated based on the spectrophotometric measurements of absorption by dissolved and particulate matter discussed in paragraphs 2.3.4.1-2.3.4.3. The comparisons were performed at nine wavelengths in the visible wavelength region 412-715 nm (412, 443, 488, 510, 532, 555, 650, 676 and 715 nm, similarly to the AC9 wavelength bands). Measurements from all depths were included. The total absorption was estimated as:

$$a_{t-w}(\lambda) = a_{CDOM}(\lambda) + a_{phyt}(\lambda) + a_{npp}(\lambda) \quad (2.3-3)$$

where absorption by particulate matter (phytoplankton and non-pigmented matter) was corrected for optical pathlength amplification using $\beta=1.5$. The average percent contribution (n=136) of each one of the three components, CDOM, phytoplankton and non-pigmented particles to a_{t-w} , at each wavelength, is shown in figure 2.3-20, along with the ± 1 standard deviations.

The results on the percent contribution by phytoplankton, non-pigmented particles and CDOM to a_{t-w} , were very similar to those shown in figure 2.3-20 when water samples collected from the surface waters (0-1 m) and water samples collected from ~ 5m depth were examined separately. The results are shown in tables 2.3-11(a)-(b). No water samples were collected during the measurements from larger depths closer to the bottom of the water column.

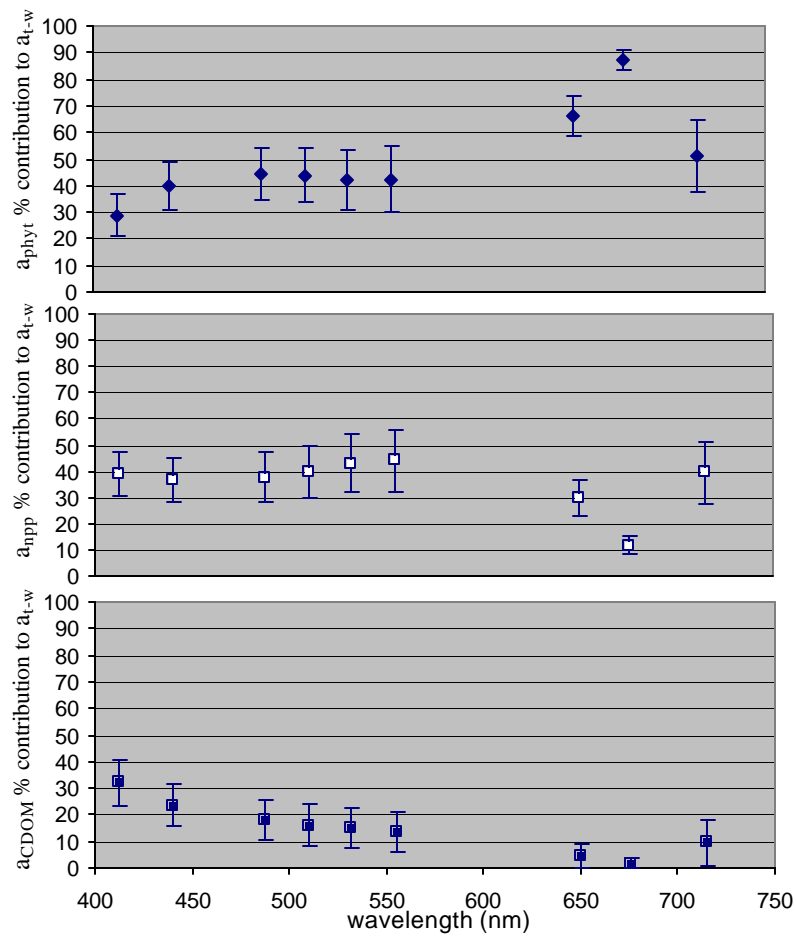


Figure 2.3-20: Average percent contribution of phytoplankton (graph at the top), non-pigmented particulate matter (at the middle) and CDOM (at the bottom) to total (minus pure water) absorption, a_{t-w} , along with the ± 1 standard deviation ($n=136$). Results are shown at the nine wavelengths 412, 443, 488, 510, 532, 555, 650, 676 and 715 nm.

Table 2.3-11(a): Average percent contribution of a_{phyt} , a_{npp} , a_{CDOM} to $a_{\text{t-w}}$, along with the (stdev) standard deviation values. Only water samples from 0-1m depths were examined.

% contribution		715	676	650	555	532	510	488	440	412
a_{phyt}	average	48.86	86.64	64.86	38.61	38.82	41.10	41.79	38.13	27.27
	stdev	12.72	4.25	8.88	12.24	11.04	10.21	9.81	8.44	7.28
a_{npp}	average	40.47	11.56	30.28	47.40	46.15	42.78	40.44	39.03	41.68
	stdev	10.78	3.28	7.53	11.56	10.64	9.74	9.36	8.37	8.68
a_{CDOM}	average	10.67	1.80	4.86	13.98	15.03	16.12	17.77	22.84	31.04
	stdev	10.23	2.23	4.49	6.85	6.63	6.51	6.53	6.98	8.35

Table 2.3-11(b): Average percent contribution of a_{phyt} , a_{npp} , a_{CDOM} to $a_{\text{t-w}}$, along with the (stdev) standard deviation values. Only water samples from 5m depth were examined.

% contribution		715	676	650	555	532	510	488	440	412
a_{phyt}	average	48.38	85.77	64.07	40.02	39.99	41.58	41.83	38.05	27.73
	stdev	13.68	4.52	9.19	11.87	11.15	10.28	9.87	8.67	7.91
a_{npp}	average	40.55	12.22	30.65	46.14	45.18	42.46	40.55	39.36	41.78
	stdev	11.97	3.62	8.20	12.32	11.54	10.55	9.93	8.55	8.93
a_{CDOM}	average	11.07	2.00	5.28	13.84	14.83	15.96	17.62	22.59	30.49
	stdev	11.73	2.70	5.99	9.38	9.17	8.96	8.82	8.48	9.22

The average percent contribution by phytoplankton, non-pigmented particulates and dissolved organic matter to the total absorption, $a_{\text{t-w}}$, was also examined separately for the four stations HB, JT, PI and TI. The results are shown in figure 2.3-21. The estimated standard deviations are not shown in the figure, since they were of the same order as those shown in figure 2.3-20. Percent contribution by a_{npp} to $a_{\text{t-w}}$ was larger (at all wavelengths) at JT station, compared to HB, PI and TI stations.

The relationships between absorption by phytoplankton, non-pigmented particulate matter, and CDOM, were examined for the measurements performed at the four stations. Positive correlation was observed between $a_{\text{phyt}}(676)$ and $a_{\text{npp}}(440)$, but the relationships were not very precise and would not be useful for predictive purposes (fig. 2.3-22). No

strong covariation was found between $a_{\text{phyt}}(676)$ and $a_{\text{CDOM}}(440)$ for the measurements performed in the northern Chesapeake Bay waters (fig. 2.3-23).

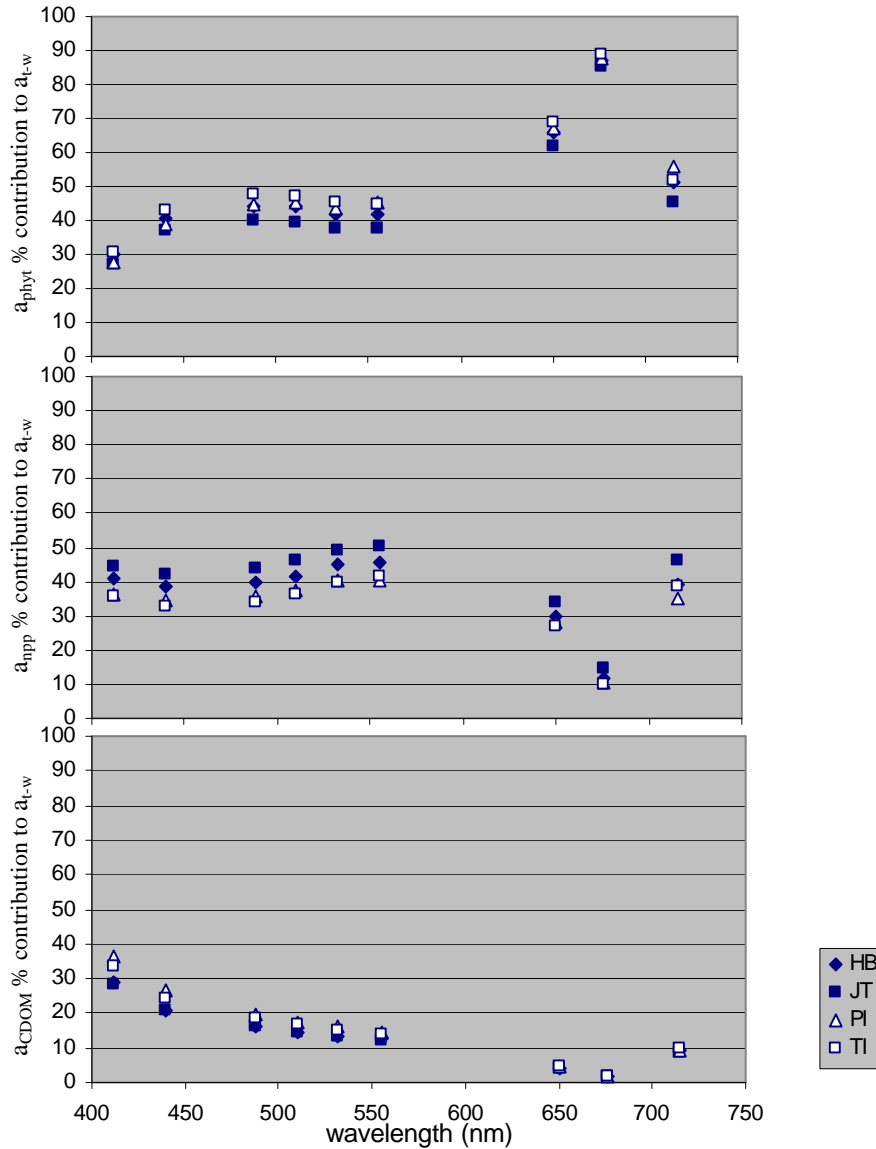


Figure 2.3-21: Average percent contribution of phytoplankton (graph at the top), non-pigmented particulate matter (graph at the middle) and CDOM (graph at the bottom) to total (minus pure water) absorption, a_{t-w} , at the four stations HB (blue pixels), JT (blue squares), PI (white triangles) and TI (white squares). Results are shown at the nine wavelengths 412, 443, 488, 510, 532, 555, 650, 676 and 715 nm. Standard deviations are not shown (in order to be easier to separate the various symbols), but are similar to those shown in figure 2.3-20.

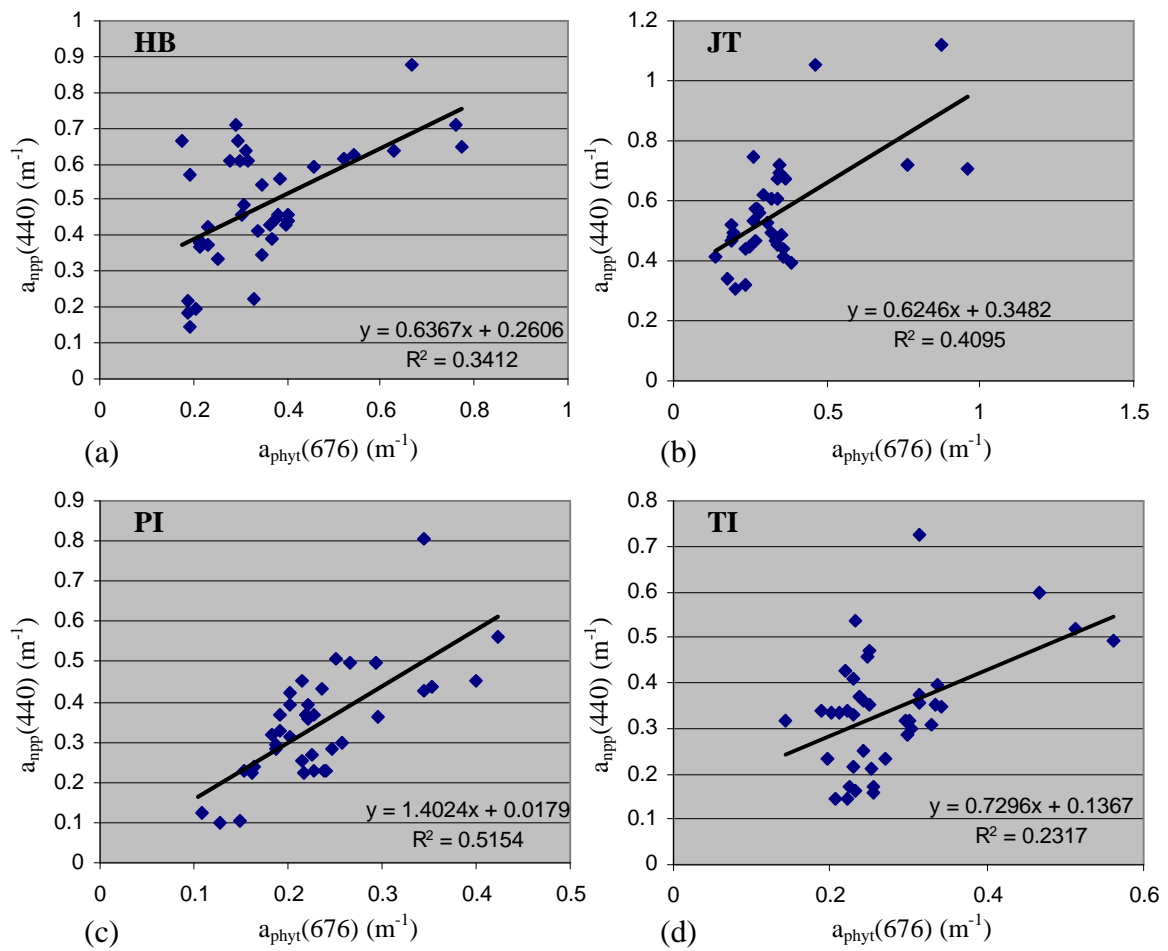


Figure 2.3-22: Relationship between $a_{npp}(440)$ and $a_{phyt}(676)$ measured at (a) HB (b) JT (c) PI and (d) TI station.

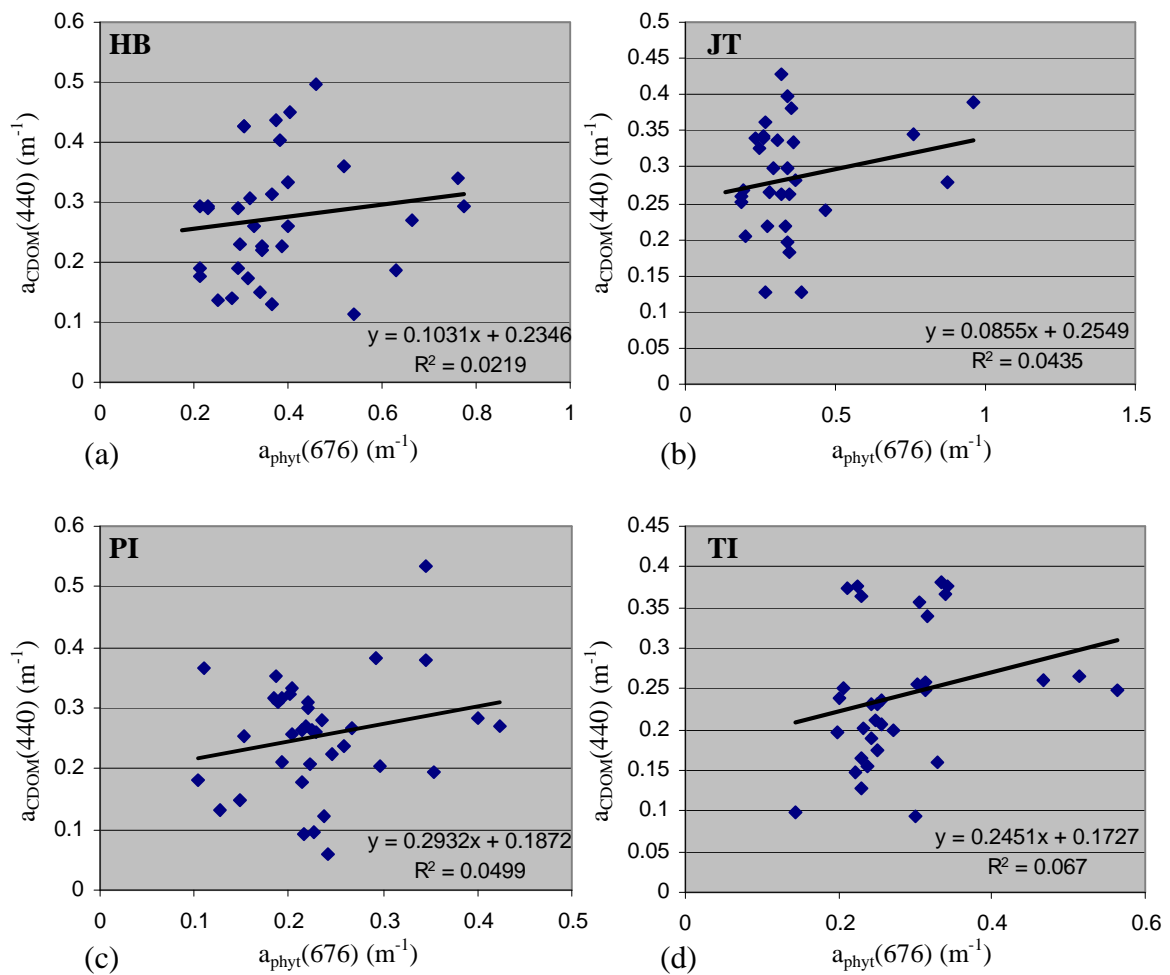


Figure 2.3-23: Relationship between $a_{\text{CDOM}}(440)$ and $a_{\text{phyt}}(676)$ measured at (a) HB (b) JT (c) PI and (d) TI station.

2.4 Discussion

The northern part of the mainstream of the Chesapeake Bay estuary is an area of considerable seasonal variability, where semidiurnal tidal patterns, saltwater influx from the ocean, and river and sub-estuarine outflows during rainfall and storm events, drive the estuarine circulation. Seasonal and spatial variability in the water characteristics, caused by physical processes in this estuarine environment, affect the chemical and biological processes such as growth, mortality and behavior of the aquatic organisms, and result to changes in the biological, chemical and optical properties of the organic and inorganic, dissolved and particulate material present in these waters.

Spatial and temporal variation in water's inherent optical properties, temperature and salinity patterns

According to measurements of total absorption and attenuation performed at the northern part of the Chesapeake Bay during our cruises, relatively clear waters were observed during the late fall months, with absorption at 412 nm, $a_{t-w}(412)$, between 0.75 and 1.35 m^{-1} , attenuation at 412 nm, $c_{t-w}(412)$, between 1.72 and 5.39 m^{-1} and total backscattering at 530 nm, $b_b(530)$, between 0.012 and 0.054 m^{-1} . Optically thicker waters, with much higher total attenuation and absorption were observed during the summer months, with $a_{t-w}(412)$ between 1.19 and 4.4 m^{-1} , $c_{t-w}(412)$ between 3.85 and 19.41 m^{-1} and $b_b(530)$ between 0.033 and 0.25 m^{-1} (tables 2.3-1 - 2.3-4, and figures 2.3-4, 2.3-6). Changes in the water's inherent optical properties were associated with vertical stratification patterns, mixing processes and phytoplankton bloom events, observed in the Chesapeake Bay waters, during the specific cruises.

Density stratification, brought about by vertical variation in temperature and salinity, affects significantly mixing processes, and hence also, vertical variations in optical properties, within the water column. According to measurements of water temperature performed in the Bay from June through November 2001 and from beginning of May through end of June 2002, T_w ranged between 12°C and 27.5°C, and showed a seasonal variation with low values measured during the late fall and spring months, and higher values measured during the warmer summer months (fig. 2.3-1(A)). Salinity values ranged between 6 ppt and 17.5 ppt, during the measurements performed in the Bay (fig. 2.3-2(A)). Less saline waters were observed during the late-spring and early-summer months, while salinity increased during the late fall months (fig. 2.3-2(B)).

Evapotranspiration and freshwater input to the Bay during rainfall events, are among the main drivers of annual salinity patterns in the Chesapeake Bay. According to rainfall measurements performed at SERC since 1967, relatively higher amounts of rainfall are typically observed during the spring and early summer months, while fall and winter are usually the driest seasons of the year. During the wet, spring months, rainfall and melting snow result in large quantities of freshwater input to the estuary and salinity may decrease significantly. In the beginning of June 2001, after the relatively higher amounts of rainfall in the spring (fig. 2.3-3), salinity values close to the water surface at HB, PI, TI and JT stations, were around 11 ppt. By September, after the lower rainfall during the end of summer, salinity increased to 15 - 16 ppt at all four stations, and reached 16-17.5 ppt during the last fall cruise, on 13 November 2001. After the high rainfall again during the wet spring months of 2002, salinity values dropped to 10 ppt in the beginning of June 2002 (fig. 2.3-2(A)).

The Bay waters were characterized by greater vertical homogeneity during the cruises performed in the fall season. Stronger winds and stronger vertical mixing during the fall months, September through November, resulted in almost homogeneous waters with depth. Measured temperature and salinity profiles were almost constant with depth (fig. 2.3-1(B) and fig. 2.3-2(B)). The water's inherent optical properties, total absorption, attenuation, and backscattering, were also almost constant with depth during the early and late fall months (fig. 2.3-4, 2.3-5, 2.3-6). During the fall months, relatively higher values of attenuation were observed at a few stations only close to the bottom of the water column, most probably associated with the presence of resuspended sediments. High values of b_b were also measured in these cases, due to high backscattering from the small size, high index of refraction particles of re-suspended minerals (Stramski and Kiefer, 1991) (fig. 2.3-6).

During the cruises in the spring and summer months of 2002 higher thermal stratification, due to increased heating of the water close to the surface, was observed. During the cruises performed on 6 and 22 May and 6 and 18 June 2002, T_w showed some variation with depth, with higher T_w values measured in the upper 2-3 meters and lower T_w values closer to the bottom of the water column. Salinity also showed some vertical variation during the same cruises, with lower values measured in the upper water layers and higher values (by 2-3 ppt during the June 2002 cruises) at depths larger than 4-5 meters. However, windy conditions, rough water surface and mixing of the water during some of the spring-summer cruises (e.g. 15 May 2002), disturbed the stratification patterns and resulted in some cases with well-mixed, homogeneous waters, with constant

temperature and salinity profiles. Almost constant values of absorption, attenuation and backscattering were measured during that cruise in the upper 4-5 meters, while higher values of $a_{t-w}(412)$, $c_{t-w}(412)$ and $b_b(530)$ were measured deeper in the water column, due to the presence of re-suspended minerals close to the bottom of the water column.

Stronger stratification during the late spring - early summer months results in a decrease of the mixed layer depth through which the phytoplankton circulates. This, in combination with higher levels of incident radiation and increased availability of nutrients during this time of the year, typically results in intense biological activity and favorable conditions for phytoplankton growth and bloom events. Three intense and localized phytoplankton bloom events were observed during the summer 2001 and 2002 cruises, along the western shore of the Bay. A phytoplankton bloom event was observed at HB and JT stations on 11 June 2001, and also at HB station during the following cruise on 25 June 2001. Another bloom was observed at JT station during the cruise on 18 June 2002. Total absorption values at 676 nm, during these bloom events, ranged between $1.2 - 2 \text{ m}^{-1}$, while the average $a_{t-w}(676)$ estimated from all the measurements performed during the cruises in the Bay was 0.29 m^{-1} . The water at the location of the bloom events was also characterized by high total attenuation, with $c_{t-w}(676)=11 \text{ m}^{-1}$ at HB on 11 June, and $c_{t-w}(676)=9 \text{ m}^{-1}$ at HB on 25 June 2001 (mean $c_{t-w}(676)$ from all cruises was 3.4 m^{-1}). Water samples collected from the location of the blooms and analyzed at the laboratory, showed large absorption by both phytoplankton and non-pigmented particulate matter during the specific cruises (fig. 2.3-10, 2.3-12). The phytoplankton absorption spectra measured on water samples collected from the four stations during the late spring –

summer months, showed also high absorption in the UV wavelengths (~ 325-330 nm), characteristic of the presence of MAAs (fig. 2.3-11). The MAAs occur in diverse phytoplankton taxonomic groups (e.g. diatoms, dinoflagellates, red algae) and may offer a photoprotective mechanism against UV exposure by serving as a sunscreen (Lesser et al, 1996, Neale et al, 1998), especially during the spring and summer months when both PAR and UV radiation are significantly increased (Moisan and Mitchell, 2001).

Spectral shapes of absorption by phytoplankton, non-pigmented particles and CDOM

Several inversion algorithms (e.g. semianalytic MODIS chl-algorithm) and methods of partitioning total absorption coefficients into absorption by various components are based on previous knowledge, models, parameterizations and assumptions about the spectral shape of absorption by different materials. Laboratory spectrophotometric absorption measurements were used in this project, to study the absorption characteristics of phytoplankton pigments, $a_{\text{phyt}}(\lambda)$, non-pigmented particulate matter, $a_{\text{npp}}(\lambda)$ and CDOM, $a_{\text{CDOM}}(\lambda)$, and the variations observed on the absorption spectral shapes of these substances, during our cruises in the Bay. The contribution of phytoplankton, non-pigmented particles and CDOM to the total absorption of light at various wavelengths in the visible was also examined, in these optically complex estuarine waters.

Non-pigmented particles absorption spectra:

The particulate non-pigmented absorption spectra showed the typical negative exponential decline within the visible wavelength region (Kishino et al, 1985, Roesler et al, 1989), $a_{\text{npp}}(\lambda) = a_{\text{npp}}(440) \exp[-S_{\text{npp}} \cdot (\lambda - 440)]$ (eq. 2.3-1). The normalized

$a_{\text{npp}}(\lambda)/a_{\text{npp}}(440)$ absorption spectra, didn't show large temporal or spatial variability (fig. 2.3-9(a)-(d)). Mean normalized absorption spectra were estimated at each station (fig. 2.3-9(e)-(h)) and the standard deviations were small in the visible wavelength region (table 2.3-6) (estimated percent standard deviations less than 10% for $400 < \lambda < 650$ nm at HB, TI and JT stations). The exponential slope, S_{npp} , estimated after applying non-linear exponential regression to the measurements, was 0.0102 nm^{-1} at HB, 0.0102 nm^{-1} at JT, 0.0109 nm^{-1} at PI and 0.0104 nm^{-1} at TI station. These values are very close to the mean spectral slope of 0.0104 nm^{-1} estimated by Gallegos et al (1990), for measurements performed in the Rhode River and the Chesapeake Bay waters, and also in good agreement with other studies, such as those by Roesler et al (1989), Iturriaga and Siegel (1988), Morrow et al (1989), where measurements were performed at various sites and types of water. From the measurements in the Bay, it seems that an exponential model with an exponential slope of $S_{\text{npp}} = 0.0105 \text{ nm}^{-1}$, provides a very good fit to the non-pigmented particulate matter absorption spectra measured in the visible wavelengths (400-750 nm). Larger variation and a change in the exponential slope were observed for $a_{\text{npp}}(\lambda)$ values measured in the UV region. It should be noted, that errors in the measurements, such as imperfect extraction of pigments using the methanol extraction method, are expected to affect the accuracy of measurements of absorption by non-pigmented particles, as well as the accuracy of measurements of absorption by phytoplankton pigments.

Phytoplankton absorption spectra:

Large variability was observed in the phytoplankton normalized absorption spectra, $a_{\text{phyt}}(\lambda)/a_{\text{phyt}}(676)$ measured in the Bay during our cruises (fig. 2.3-11). Although the

average normalized spectra estimated from measurements performed at each station were similar at the four stations, the estimated standard deviations of the average spectra were large (estimated percent standard deviations between 10-30% for $400 < \lambda < 650$ nm).

Variations in the shape of the $a_{\text{phyt}}(\lambda)$ spectrum are associated with seasonal variations in light and nutrient availability in the Bay waters, changes in phytoplankton species and size distributions and changes in the concentration and composition of photosynthetic pigments (such as chl-b and chl-c, carotenoids that absorb strongly in 450-500 nm or phycoerythrins that absorb in ~630 nm). Pigment packaging is another source of spectral variance in $a_{\text{phyt}}(\lambda)$, due to self shading effects and flattening of the absorption peaks (Morel and Bricaud, 1981). Even larger variability was observed in the normalized phytoplankton absorption spectra in the UV wavelength region. Strong absorption in the UV, most probably due to the presence of MAA compounds, was observed during most of the spring and summer cruises, affecting significantly the shape of the measured phytoplankton absorption spectra. The ratio $a_{\text{phyt}}(330)/a_{\text{phyt}}(676)$ ranged between 0.7 to 3, during the spring and summer cruises (fig. 2.3-11(B)).

The large variations observed in the normalized phytoplankton absorption spectra measured in the Chesapeake Bay waters and the uncertainties associated with modeling the phytoplankton absorption wavelength dependence in the visible and UV region, would affect significantly the accuracy of inversion algorithms and absorption-partitioning methods. In the MODIS semianalytic algorithm (Carder et al, 2002, MODIS ATBD 19) variations in $a_{\text{phyt}}(\lambda_i)/a_{\text{phyt}}(676)$ (for $\lambda_i = 412, 443, 488, 551$ nm) are expressed as a function of $a_{\text{phyt}}(676)$. However, no relation was found between normalized

phytoplankton absorption coefficients and $a_{\text{phyt}}(676)$ for the measurements from the Chesapeake Bay waters. More studies are needed for better parameterizations of phytoplankton absorption spectra in estuarine waters.

CDOM absorption spectra:

Absorption by CDOM showed the typical exponential increase with decreasing wavelength (Bricaud et al, 1981) through the visible region of the spectrum and also in the UV wavelengths (fig. 2.3-13). The exponential slope, S_{CDOM} , was estimated after applying non-linear exponential regression to $a_{\text{CDOM}}(\lambda)$ values measured i) in the visible wavelength region, 400-700 nm, since the main focus of this study was on the water's optical properties in the visible and their effect on the amount of water-leaving radiance that can be measured remotely by satellites (visible wavelengths) (chapters 4, 5) and ii) in the complete spectral range of the measurements 290-700 nm, for comparison with other studies on CDOM optical characteristics, (e.g. Blough and DeVecchio, 2002). The non-linear exponential regression method was used, instead of calculating S_{CDOM} through least-squares regression of the log-transformed data, since with the non-linear regression larger weighting is given to the higher and better measured absorption values at the shorter wavelengths. The R^2 values of the non-linear exponential fits were in almost all of the cases larger than 0.99.

Fitted $a_{\text{CDOM}}(\lambda)$ values were compared to measured $a_{\text{CDOM}}(\lambda)$ values at various visible wavelengths (443, 488 and 555 nm shown in figure 2.3-16). The $a_{\text{CDOM}}(\lambda)$ values estimated when fitting the data in the wavelength region 290-700 nm were underestimated compared to the measured $a_{\text{CDOM}}(\lambda)$ values, while better agreement was

found between the measured $a_{\text{CDOM}}(\lambda)$ and the $a_{\text{CDOM}}(\lambda)$ values estimated when fitting the data in the visible wavelength region. The residuals $a_{\text{CDOM}}(\lambda)_{\text{measured}} - a_{\text{CDOM}}(\lambda)_{\text{fitted}}$, were estimated at several wavelengths in the visible wavelength region (fig. 2.3-17). The average values of the residuals $a_{\text{CDOM}}(\lambda)_{\text{measured}} - a_{\text{CDOM}}(\lambda)_{\text{fitted}(290-700)}$ were larger than the photometric accuracy of the CARY instrument (photometric accuracy of 10^{-4} OD units as reported by manufacturer, corresponding to 0.005 m^{-1} for a 5 cm cuvette) or the standard error of the a_{CDOM} measurements. The standard error of the a_{CDOM} measurements ($a_{\text{CDOM}} = a_{\text{CDOM}}' - a_{\text{blank}}$), as estimated based on replicate measurements of the blank (distilled water at both reference and sample cuvette) and the sample absorption, was in the order of $\sim 0.022 \text{ m}^{-1}$. The residuals $a_{\text{CDOM}}(\lambda)_{\text{measured}} - a_{\text{CDOM}}(\lambda)_{\text{fitted}(400-700)}$ were smaller and close to the standard error of the CDOM absorption measurements. Therefore, the non-linear exponential fit in the 400-700 nm wavelength region seemed to provide a better fit to the measured $a_{\text{CDOM}}(\lambda)$ values in the visible wavelengths. However, it should be noted that CDOM absorption in the visible is much lower and less well measured than in the shorter UV wavelengths. For studies that include the UV wavelengths non-linear fits applied to the full spectrum 290-700 nm should be used, or a combination of two exponentials in the UV and visible wavelengths (Blough and DelVecchio, 2002).

The mean S_{CDOM} values estimated from measurements performed at each one of the four stations (non-linear fits in the visible wavelength region), were not largely different among the four stations (tables 2.3-10, 2.3-11), with $S_{\text{CDOM}(400-700)} = 0.0185$ at HB, $S_{\text{CDOM}(400-700)} = 0.0171$ at JT, $S_{\text{CDOM}(400-700)} = 0.0186$ at PI and $S_{\text{CDOM}(400-700)} = 0.0176$ at TI station. These values are in agreement with values of S_{CDOM} reported in previous studies

(e.g. Bricaud et al, 1981, Roesler et al, 1989). However, the estimated S_{CDOM} values showed large variation around the average S_{CDOM} estimated at each station. The standard deviation of the exponential slope, S_{CDOM} , as estimated based on replicate measurements of CDOM absorption (e.g. surface sample, TI station, 15 May 2002) was in the order of $3.3 \cdot 10^{-4} \text{ nm}^{-1}$ for $S_{\text{CDOM}(290-700)}$ and $6 \cdot 10^{-4} \text{ nm}^{-1}$ for $S_{\text{CDOM}(400-700)}$. According to studies on CDOM optical characteristics (e.g. Carder et al, 1989; Green and Blough, 1994; Blough and DelVecchio, 2002), values of S_{CDOM} for CDOM from a wide variety of sources, range from as low as 0.01 to as high as 0.030 nm^{-1} . S_{CDOM} and a_{CDOM} vary with the source and composition of the dissolved material, with terrestrial humic substances showing lower S_{CDOM} and higher absorption at 440 nm, than CDOM in oligotrophic seawaters (Carder et al, 1989). Previous studies in coastal regions (Blough et al., 1993; Green and Blough, 1994; Nelson and Guarda, 1995; Vodacek et al., 1997) have shown that S_{CDOM} usually increases with decreasing absorption and increasing salinity during transit of the terrestrial CDOM to offshore waters. The increase in S from coastal to offshore waters is thought to arise from the transformation of terrestrially derived CDOM and (or) its replacement by CDOM generated in-situ (Blough et al, 1993; Blough and Green, 1995; Vodacek et al, 1997). Mixing processes, photochemical or biological processes, or most probably a combination of the above, can result in changes in the CDOM optical characteristics.

Although a negative relationship was observed between a_{CDOM} and S_{CDOM} during the measurements in the Bay, with S_{CDOM} decreasing with increasing $a_{\text{CDOM}(440)}$ (fig. 2.3-18), no strong correlation was found overall between salinity and a_{CDOM} or salinity and

S_{CDOM} during the cruises in the Bay (fig. 2.3-19). During almost all of the cruises the highest salinity values were observed at the TI station (figure 2.3-2(B), green solid line). This station is located towards the middle of the mainstream of the Chesapeake Bay (fig. 2.2-1) and, among the four stations, is the one located at the largest distance from the Bay's shores. The lowest salinity values were observed, during almost all of the cruises, at the most turbid JT station (figure 2.3-2(B), red solid line), which is located along the western Bay shore and closest to the mouth of the Rhode-River sub-estuary (fig. 2.2-1). However, the four stations HB, PI, TI and JT encompass only a small portion of the entire mouth-to-head salinity gradient of the Bay, and salinity differences among the four stations were less than 2-3 ppt during individual cruises. An exception to this was the cruise performed on 22 May 2002, when low salinity values of 6 ppt, along with relatively high a_{CDOM} values were measured at HB ($a_{\text{CDOM}}(440)=0.44 \text{ m}^{-1}$, $S_{\text{CDOM}}=0.016 \text{ nm}^{-1}$) and JT stations ($a_{\text{CDOM}}(440)=0.43 \text{ m}^{-1}$, $S_{\text{CDOM}}=0.0156 \text{ nm}^{-1}$), close to the western shore of the Bay. This was most probably associated with a spike in flow from the Susquehanna River about 2 weeks earlier (fig. 2.4-1) (Gallegos, personal communication). Salinity values at PI station (eastern shore of Chesapeake Bay) during that day were ~ 10 ppt, while measurements of CDOM absorption were relatively lower ($a_{\text{CDOM}}=0.3 \text{ m}^{-1}$, $S_{\text{CDOM}}=0.0178 \text{ nm}^{-1}$). Measurements of the CDOM absorption properties performed in the Rhode River sub-estuary (data not shown in this study) showed a stronger relationship between salinity and S_{CDOM} . The salinity gradient among the stations sampled in the Rhode River was relatively large, with salinity values, during individual cruises, ranging from 0 ppt (at the tidal creek) to 18 ppt (at the mouth of the sub-estuary). According to the measurements, a strong increase in S_{CDOM} and decrease in

$a_{\text{CDOM}}(440)$ was observed with increase in salinity, during individual transects from the tidal creek towards the mouth of the sub-estuary.

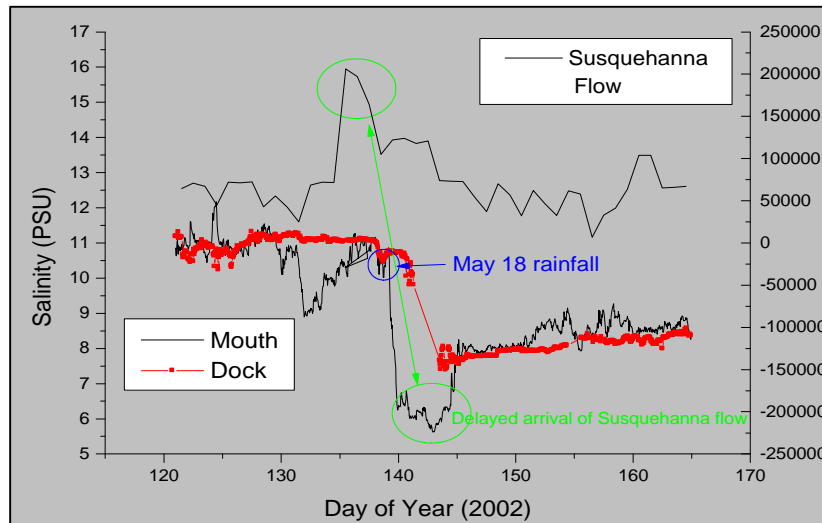


Figure 2.4-1: Decrease in salinity (in psu) measured at the SERC dock (black line) and at the mouth of the Rhode River sub-estuary (red line), probably associated with a spike in flow from the Susquehanna River about 2 weeks earlier (Gallegos, personal communication).

Due to the large variability in S_{CDOM} values observed during the measurements in the Bay, an exponential model of the form $a_{\text{CDOM}}(\lambda) = a_{\text{CDOM}}(440) \exp[-0.018 \cdot (\lambda - 440)]$, should be used with caution in inversion algorithms (e.g. MODIS semianalytic algorithm for estimation of [Chl-a], discussion in Chapter 5), since S_{CDOM} values estimated for individual CDOM absorption spectra could diverge substantially from the average S_{CDOM} value of 0.018 nm^{-1} . More work, related to studies on temporal and seasonal variations in CDOM optical characteristics and their relation to physical, chemical and biological processes in the Bay, is definitely needed.

Absorption by particulate matter, backscattering, b_b , and backscattering fraction, b_b/b

Absolute values of absorption by phytoplankton ($a_{\text{phyt}}(676)$) shown in fig. 2.3-12) showed some seasonal variation in the Bay waters, with lower values during the early spring and late fall months and larger values during the phytoplankton bloom events observed in the Bay during the summer cruises. The bloom events that were observed during the cruises on 11 June 2001, 25 June 2001, 18 June 2002, were localized events observed at HB and JT stations, along the western shore of the Bay. According to Harding et al (2002), phytoplankton blooms observed in the bay during the late spring and summer months, are typically dominated by dinoflagellates populations. These “red tide” events can be very patchy and are often more prevalent on the western side of the mainstream of the Bay and in the mouths of certain tributaries (Harding et al, 2001). Since no studies on the characterization of the phytoplankton species were performed in the framework of this project, there is not sufficient information to identify the phytoplankton species during the bloom events observed in the Bay. With the exception of the large spatial variation in phytoplankton absorption observed during the specific, localized phytoplankton bloom events mentioned above, no particular spatial pattern was observed in $a_{\text{phyt}}(676)$ or $a_{\text{t-w}}(676)$ measured at the four stations HB, PI, TI and JT during our cruises (fig 2.3-12).

Measurements of absorption by non-pigmented particulate matter at 440 nm, $a_{\text{npp}}(440)$, showed large seasonal variation with higher values observed during the late spring and summer months, and relatively lower values measured during the fall (fig. 2.3-10). Riverine discharges during the spring and summer months, when rainfall amounts in the

Bay are typically higher, are expected to result in optically thick waters and higher concentrations of inorganic particles of terrestrial origin. At the same time, higher biological activity during the summer months and large phytoplankton bloom events, could be associated with higher amounts of detrital, non-living organic particulate material. According to Gallegos and Jordan (2002), high absorption by non-pigmented particulate matter was measured after a large phytoplankton bloom event observed in the Rhode River sub-estuary in April-May 2000, extending the period of high attenuation coefficients into the first week of May. According to Gallegos and Jordan, dying cells from the bloom were, initially, the source of elevated detrital absorption. Such labile organic matter could have stimulated microbial decomposition and associated heterotrophic protists, resulting in high $a_{npp}(440)$ values, after the peak of the bloom. High values of $a_{npp}(440)$, $b_b(530)$ and $b_b/b(530)$ were measured at the HB and JT stations during the bloom event on 11 June 2001 (fig. 2.3-7, 2.3-8, 2.3-10). Higher values of $a_{npp}(440)$, as well as $b_b(530)$, were observed during almost all of the cruises at the HB and JT stations, compared to measurements at PI and TI stations. At the turbid JT station, during some of the cruises, measured $a_{npp}(440)$ and $b_b(530)$ values were larger by more than a factor of 2 compared to measurements at PI and TI stations. The higher abundance of non-pigmented particulate matter at the JT station, is mainly due to the proximity of the station to land, the stronger influence of inflow of terrigenous organic and inorganic particulate matter, and also the shallower depths measured at this region of the Bay.

Estimated values of the backscattering fraction, b_b/b , ranged, during our cruises, between 0.006 and 0.036 at 530 nm, with an average value of 0.013 (± 0.0033 standard

deviation) (fig. 2.3-8, table 2.3-5). The largest b_b/b values ($b_b/b=0.026$ and $b_b/b = 0.036$) were measured at depths 4.9 m and 5.4 m respectively (close to the bottom of the water column) at the JT station, on 9 July 2001. Resuspended, small size and high index of refraction sediments close to the bottom, could be responsible for the jump in b_b/b values at such depths in the water column. Similarly to the spatial patterns observed at $a_{pp}(440)$, higher $b_b(530)$ and $b_b/b(530)$ were measured during most of the cruises at the JT station, and lower b_b/b values were measured at the less turbid TI station. The measured b_b/b values suggest that the backscattering fraction can show considerable variation, depending on water type, mixing processes, biological activity. According to the measurements, the backscattering fraction in the Bay waters can be much different than the Petzold “average particle” backscattering fraction, $b_b/b=0.018$, that has been widely used as a default value for modeling backscattering in moderately turbid waters. Measured $b_b/b(530)$ values, by Mobley et al (2002), for the case 2 waters at the LDEO15 site off the coast of New Jersey were also lower than the Petzold value and ranged between 0.005 (surface waters) and 0.0015 (closer to the bottom of the water column). As discussed in chapter 3, using scattering phase functions with the correct backscatter fraction and overall shape is very important for accurate model simulations and prediction of the underwater light fields. Therefore, accurate measurements of backscattering and backscattering fraction are crucial to achieving model-data closure (chapter 3).

Percent contribution by various substances to total water absorption

From the measurements of absorption by phytoplankton, CDOM and non-pigmented particulate matter performed during the cruises, it is evident that pigmented and non-pigmented, particulate and dissolved substances affect significantly the bulk optical characteristics in the Bay waters throughout the year. The percent contribution of phytoplankton, CDOM and non-pigmented particles to the total (minus water) absorption, $a_{t-w} = a_{\text{phyt}} + a_{\text{CDOM}} + a_{\text{npp}}$, measured in the Bay waters, was shown in fig 2.3-20, 2.3-21, for certain wavelengths in the visible. According to the results, 80-90% of the total (minus water) absorption at 676 nm was due to phytoplankton, with only a small 10-20 % contribution by non-pigmented particulate matter and CDOM. This is due to the fact that 676 nm is a maximum in the chl-a absorption spectrum, and also due to the exponential decrease of both absorption by CDOM and non-pigmented particulate matter, with increasing wavelength. However, in the blue and green wavelengths, contribution by CDOM and non-pigmented particles becomes significantly larger. At 555 nm contribution by phytoplankton to a_{t-w} was only 40% (average percent value), while $a_{\text{npp}}(555)$ accounted, in average, for 45% and $a_{\text{CDOM}}(555)$ for 15% of the total a_{t-w} . Contribution by CDOM to total in-water absorption increased at shorter wavelengths due to the large exponential increase of a_{CDOM} with decreasing wavelength (average $S_{\text{CDOM}}=0.018$). At 412 nm contribution by CDOM to a_{t-w} was in average 31% (stdev=8.35), contribution by non-pigmented particles was almost 40% (stdev=8.68), while contribution by phytoplankton was less than 30% (stdev=7.28). Although high absorption by both phytoplankton and non-pigmented particles was observed during the bloom events in the summer months, no strong covariation was observed overall between

$a_{\text{phyt}}(676)$ and $a_{\text{npp}}(440)$, or between $a_{\text{phyt}}(676)$ and $a_{\text{CDOM}}(440)$ during the cruises (fig. 2.3-22, 2.3-23). Therefore, in the Chesapeake Bay estuarine waters, CDOM and non-pigmented particles, substances that do not necessarily covary with phytoplankton absorption or chl-a concentration, significantly affect the underwater light fields and the amount of radiance leaving the water surface in the blue and green regions of the wavelength spectrum. This has significant implications on the accuracy of MODIS chlorophyll algorithms that are based on measurements of remote sensing reflectances in the blue-green wavelength region (discussion in chapter 5).

2.5 Summary and Conclusions

In-situ measurements of water optical characteristics were performed in the northern part of the Chesapeake Bay as part of this project. Specific cases of stratified and vertically homogeneous waters, relatively clear or optically thicker waters, phytoplankton bloom events, rainfall events, and riverine outflows were examined in order to study the total absorption and attenuation of light under various conditions. Water samples were analyzed at the laboratory, to estimate the optical properties of individual components (phytoplankton, non-pigmented particles and CDOM) and study the temporal and seasonal variation in their optical characteristics, in this specific region of the Bay. The contribution of phytoplankton, non-pigmented particles and CDOM to the total absorption of light at various wavelengths in the visible was also examined. The most significant points and conclusions from the in-situ measurements performed in the northern Chesapeake Bay region (2001-2002) are summarized in table 2.5-1.

Table 2.5-1: Chapter 2 - Significant points

- Measurements using the integrating sphere method showed small, but not-zero particulate absorption in the wavelength region 700-730 nm. Several methods that are used to correct spectrophotometric absorption measurements for scattering errors, are based on the assumption that total (minus pure water) absorption in the NIR wavelengths (e.g. 715 nm) is zero. Accounting for the small NIR absorption, a_{t-w} , can be important in model simulations of underwater light fields, especially in the green wavelengths, where a_{t-w} is relatively small.
- Instrument self shading correction (Gordon and Ding, 1992), applied to radiometric measurements of $Lu(z)$ performed in the Bay, was found to be important, especially in the blue (large absorption by CDOM and non-pigmented particles) and red (large absorption by water) regions of the visible spectrum (~10% increase on the estimated Lu). However, the presence of highly scattering material in the turbid Chesapeake Bay waters could reduce the instrument self-shading error below that theoretically predicted by the Gordon-Ding model. More work is needed for more accurate application of the self-shading correction in turbid waters, where scattering is large relative to absorption.
- Water temperature, T_w , and salinity, S_w , showed the typical patterns expected for Chesapeake Bay waters, with high temperature (and low salinity) values during the summer cruises and a decrease in temperature (and increase in salinity) during the colder (and drier) fall months. Thermal and density stratification patterns observed during some of the summer cruises affected the vertical structure in water's optical properties.
- Larger vertical stratification (as shown by vertical profiles of T_w and S_w) and higher nutrient and light availability during the late spring- early summer months, resulted in more intense biological activity and favorable conditions for phytoplankton growth. Surface phytoplankton bloom events were observed during some of the spring and summer cruises in the Bay. With the exception of the localized phytoplankton bloom events, when high spatial variability was observed in phytoplankton absorption, $a_{\text{phyt}}(676)$ did not show large spatial variation among the four stations.
- Large spatial variation was observed in absorption by non-pigmented particulate matter, $a_{\text{npp}}(\lambda)$, with higher values observed, consistently, at the turbid JT station. The higher abundance of non-pigmented particulate matter at the JT station, could be due to the proximity of the station to land, the stronger influence of inflow of terrigenous particulate matter, and also the shallower depths measured at this region of the Bay.
- The backscattering fraction $b_b/b(530)$ had an average value of 0.013 (smaller than the widely used b_b/b value for the Petzold "average particle", $b_b/b=0.018$). Considerable variation was observed in the measured b_b/b in the Bay, with values as low as 0.006 and higher than 0.036 (larger values close to the bottom, probably due to re-suspension of inorganic sediments with high index of refraction). Seasonal and temporal variation in backscattering, b_b , was related more strongly to $a_{\text{npp}}(\lambda)$ seasonal and temporal patterns, than to seasonal and temporal variation of $a_{\text{phyt}}(\lambda)$.
- Absorption by non-pigmented particles, $a_{\text{npp}}(\lambda)$, showed an exponential decrease with wavelength. Small variability was observed in the spectral shape of $a_{\text{npp}}(\lambda)$, with average exponential spectral slope $S_{\text{npp}}=0.010-0.011 \text{ nm}^{-1}$ and small standard deviation. Therefore, an exponential model (eq. 2.3-1) with $S_{\text{npp}}=0.0105 \text{ nm}^{-1}$, provides a very good fit to the non-pigmented particulate matter normalized absorption spectra, measured in the Chesapeake Bay waters.
- Large variation was observed in the normalized, $a_{\text{phyt}}(\lambda_i)/a_{\text{phyt}}(676)$, phytoplankton absorption spectra, mainly due to natural variations in light and nutrient conditions, variations in phytoplankton species and composition of photosynthetic pigments. Higher variability was observed in the UV region, during the summer cruises, when optical characteristics of MAAs (or/and presence of other photoprotective pigments) affect the spectral shape of phytoplankton absorption curves.

Table 2.5-1: Chapter 2 - Significant points (continued)

- Absorption by CDOM showed the typical exponential decrease with wavelength. However, large variability was observed in the CDOM exponential slope. An inverse relationship was observed between S_{CDOM} and $a_{\text{CDOM}}(440)$. However, no strong relationship was observed between salinity and S_{CDOM} or salinity and $a_{\text{CDOM}}(440)$. It should be noted that the salinity gradient sampled during most of the cruises was small, with salinity differences among the four stations less than 2-3 ppt. Several factors such as biological and chemical processes, as well as mixing processes of dissolved material of different origins, or most probably a combination of the above, influence the CDOM optical characteristics in the main stem of the Bay. The high variability observed in the CDOM exponential slope and the uncertainties associated with modeling the phytoplankton absorption wavelength dependence, would affect the accuracy of inversion algorithms and absorption partitioning methods, such as those used currently in satellite algorithms.

- Contribution by phytoplankton to total (minus water) absorption was found to be large (more than 80%) in the 676 nm wavelength region (chl-a absorption maximum). However, contribution by CDOM and non-pigmented particles was found to be large in the blue-green wavelength region (average 60% combined contribution to $a_{\text{t-w}}(488)$ by CDOM and non-pigmented particles, and even larger at the shorter wavelengths 443 and 412 nm). No strong covariation was found between absorption by phytoplankton and absorption by non-pigmented particulate matter or CDOM during our cruises. Therefore, total absorption and attenuation of light at wavelengths 412, 443 and 488 nm in the Chesapeake Bay waters, is largely affected by substances other than phytoplankton, that do not necessarily covary with [Chl-a]. This has significant implications on the accuracy of satellite algorithms that estimate [Chl-a] based on measurements of remote sensing reflectances in the blue-green wavelength region (chapter 5).

CHAPTER 3

Model estimations of underwater radiation fields and water-leaving radiances in the Chesapeake Bay – Closure Experiment

3.1 Introduction – Background

Two basic methods for studying water's physical, chemical, biological properties through hydrologic optics, are, first, laboratory or in-situ analysis of inherent optical properties, and, second, inference of marine optical properties based on measured properties of light within and leaving the water. Because of the marine environment's complex composition, interpretation of emerging and underwater radiation fields requires the use of an accurate and detailed radiative transfer model. The model must account for absorption and scattering of light penetrating into the water for various different wavelengths, under varying conditions of water optical properties, and atmospheric composition. When detailed in-situ radiance/irradiance measurements are not available (for example in remote environments where such measurements are difficult to make), theoretical estimations can provide the needed information on underwater radiation fields. By changing the water-model assumptions (e.g., inclusion or not of processes such as bioluminescence, fluorescence by chlorophyll and CDOM), and matching calculated and measured radiances, it is possible to study the significance of particular natural processes (such as chlorophyll fluorescence) on the underwater light field. By varying the water's inherent optical properties (e.g. concentration of chlorophyll or inorganic particulate matter or amount of dissolved organic compounds of terrigenous origin) the

model simulations can be used to predict how changes in water quality, caused by human activities, could affect the underwater light field and the related growth of phytoplankton or submerged grasses in the aquatic environment.

Radiances detected by a downward-looking imaging spectrometer onboard a satellite contain both the water-leaving radiance (the signal, which carries the information about the water body itself), the sky radiance reflected by the sea surface, and the solar radiance backscattered towards the satellite by atmospheric gases and aerosols. Numerical models separately compute each of these contributions and provide the information necessary to convert the signal detected by remote sensors into ocean optical properties. When detailed in-situ or remotely sensed measurements are available for both the atmosphere and water, the combination of measurements and model estimations forms a “closure experiment”, in the sense that measured inherent optical properties can be used as input information to the model, while the radiance and irradiance profile measurements can be compared with the models’ output. Such closure experiments can reveal errors related to the methodology of the measurements and the accuracy of the instruments, as well as errors in radiative transfer methods and uncertainties in assumptions of underwater optical properties or parameterizations used in satellite algorithms.

Various numerical models are in use today for computing underwater light fields that use different numerical techniques (both analytical or probabilistic) for solving the radiative transfer equation, and are based on different assumptions. The main distinction is the varying degree of sophistication regarding the mathematical representation of

physical processes, with increased sophistication usually coming at the price of increased computational expense. One of the more sophisticated methods is the extensively validated Hydrolight underwater radiative transfer program (Mobley, 1988). Hydrolight was used in the framework of this project to perform model estimations of water-leaving radiance and underwater radiation fields within the Chesapeake Bay estuarine waters. The results demonstrate the conditions under which theoretical calculations of radiation fields can produce close agreement with experimental results, and help reveal the causes of any disagreement between measured and modeled quantities.

3.2 Hydrolight Model

3.2.1 Description of the model – Input data needed and assumptions

“Hydrolight” is a commercially available one-dimensional radiative transfer model that uses the invariant imbedding method to generate an approximate solution to the time-independent, monochromatic radiative transfer equation:

$$\mathbf{m} \frac{\partial L(\mathbf{t}, \mathbf{m}, \mathbf{j})}{\partial \mathbf{t}} = -L(\mathbf{t}, \mathbf{m}, \mathbf{j}) + \omega_o(\mathbf{t}) \iint_{\mu', \mathbf{j}' \in \Xi} L(\mathbf{t}, \mathbf{m}', \mathbf{j}') \times \tilde{\mathbf{b}}(\mathbf{t}, \mathbf{m}', \mathbf{j}') d\mathbf{m}' d\mathbf{j}' + S(\mathbf{t}, \mathbf{m}, \mathbf{j}) \quad (3.2-1)$$

where $L(\tau, \mu, \phi)$ is the unpolarized spectral radiance (at wavelength λ) at optical depth τ , and in direction (μ, ϕ) , $\mu = \cos\theta$ (θ is the polar angle), ϕ is the azimuth angle, ω_o is the single scattering albedo ($\omega_o = \text{total scattering} / \text{total attenuation}$), $\tilde{\mathbf{b}}(\tau, \mu, \phi)$ is the scattering phase function and S represents any internal source of radiance (Mobley et al,


1993). The depth τ is measured as positive downward from the mean sea surface and the polar angle θ is measured from the nadir direction. The model solves eq. 3.2-1 by partitioning the set of all directions Ξ into regions bounded by constant μ and ϕ , plus two polar caps. These quadrilateral regions and polar caps are collectively called quads. The individual quads Q_{uv} are labeled by discrete indexes u,v . The fundamental quantities computed by Hydrolight are the quad-averaged radiances

$$L(\mathbf{t}, u, v) = \frac{1}{\Omega_{uv}} \iint_{\mathbf{m}\mathbf{j} \in Q_{uv}} L(\mathbf{t}, \mathbf{m}\mathbf{j}) d\mathbf{m}\mathbf{j} \quad (3.2-2)$$

where $L(\tau, u, v)$ is the average radiance over the set of directions contained in the uv quad, Q_{uv} , which subtends a solid angle of size Ω_{uv} . According to Mobley (1989) and Mobley et al (1993), by standard techniques of Fourier analysis and invariant imbedding theory, the equations for $L(\tau, u, v)$ are transformed into a set of Riccati differential equations governing the depth dependence of certain reflectance and transmittance functions within the water body. The $L(\tau, u, v)$ at all depths are estimated after depth integration of the Riccati equations and incorporation of the air-water surface and bottom boundary conditions (Mobley and Preisendorfer, 1988). Water absorption and scattering properties, sky conditions, and bottom boundary conditions are needed as input information to run the numerical model. The model solves the radiative transfer equation and computes the in-water light field and other quantities of interest, such as the water-leaving radiance and remote-sensing reflectance, in the wavelength region 350-800 nm (Mobley, 1989). A modified version of Hydrolight, that can be used from 400 nm down to 290 nm, has been developed recently by Vassilkov et al (2003), for studies of UV penetration in the water.

The basic assumptions and characteristics of Hydrolight are summarized in table 3.2-1 (Mobley and Sundman, 2000). The model solves eq (3.2-1) for a plane-parallel water body that is horizontally homogeneous, but may be inhomogeneous with depth (depending on the inherent optical properties used as input information). The upper boundary of the water body is the air-water interface. The model uses a Monte Carlo simulation of the wind-blown surface and the Cox-Munk (1995) wave slope statistics to compute the reflectance and transmittance functions that describe the optical effects of the sea surface. The lower boundary can be either a reflecting bottom (such as clean sea-grass, coral sand, brown algae) at a finite depth, or an infinitely thick layer of water below the greatest depth of interest. The model neglects polarization. It includes all orders of multiple scattering. It also includes inelastic scattering, such as Raman scattering by water and fluorescence by chlorophyll and CDOM, as well as internal sources such as bioluminescence.

Table 3.2-1: Hydrolight Model characteristics and assumptions

<ul style="list-style-type: none"> - time-independent - horizontally homogeneous IOPs and boundary conditions - arbitrary depth dependence of IOPs - wavelength region: 350 - 800 nm (in the UV extended version: 290 - 800 nm) - Cox-Munk (1995) wave slope statistics - infinitely deep (non-Lambertian) or finite bottom - includes all orders of multiple scattering - includes Raman scattering by water - includes fluorescence by chlorophyll and CDOM - includes internal sources such as bioluminescence - does not include polarization 	
--	---

- Input Information:

Information needed as input to the model consists of:

- i) Inherent optical properties (IOPs) of the water body (i.e. absorption and scattering coefficients and scattering phase function).

These properties must be specified as functions of depth and wavelength and can be obtained from measurements or from analytical models. To compare model calculations with in-situ data, it is very important to have detailed information about absorption, attenuation and scattering (forward and backward directions) in the water.

- ii) Roughness of the ocean surface.

Hydrolight uses the Cox and Munk (1995) wave slope statistics, which include both capillary and gravity wave slope effects (Mobley, 2002) to model the rough ocean surface. In the Cox-Munk distribution, the variance of the slopes of the waves on the ocean surface is linearly related to the wind speed over the ocean surface. Therefore, only the wind speed needs to be specified before running the code.

- iii) The nature of the bottom of the water column (finite or infinitely deep water).

The bottom boundary is described in terms of a bi-directional reflectance distribution function. Hydrolight provides data files containing irradiance reflectances for several different bottom types. These values include measured reflectance values for coral sand, brown, red and green algae (Maritorena et al 1994) and for clean sea grass leaves (provided by Zimmerman). The user's own data files can be added to the list of available bottom reflectance spectra.

iv) The sun and sky radiance incident on the sea surface.

The sky spectral radiance distribution can be obtained from semi-empirical models that are built into the model (RADTRAN model, Gregg and Carder, 1990, to estimate irradiance for a given atmosphere and sky conditions and the Harrison and Coombes (1988) normalized sky radiance model to specify the distribution of sky irradiance), from observations, or from a separate user-supplied atmospheric radiative transfer model. The UV region requires a more sophisticated atmospheric model that better accounts for aerosol scattering and for polarization effects from Rayleigh scattering than the above models (Vasilkov et al., 2002).

The user can run Hydrolight selecting models for case 1 waters, which are based on user supplied chlorophyll distributions. One of the case 1 models available in Hydrolight is based on a recent reformulation (Morel and Maritorena, 2000) of the historical “Gordon-Morel” case 1 water, empirical model (Mobley 1994). The absorption coefficient is modeled as the sum of three components:

$$a_{\text{total}}(z, \lambda) = a_w(z, \lambda) + a_p(z, \lambda) + a_{\text{CDOM}}(z, \lambda) \quad (3.2-3)$$

where a_w is absorption by pure water, a_p is absorption by chlorophyll-bearing particles, and a_{CDOM} is absorption by co-varying CDOM. The particle absorption is given by

$$a_p(z, \lambda) = 0.06 a_{\text{Chl}}^*(\lambda) [\text{Chl}(z)]^{0.65} \quad (3.2-4)$$

where $[\text{Chl}(z)]$ is the user-supplied chlorophyll profile in $(\text{mg Chl})\text{m}^{-3}$, and $a_{\text{Chl}}^*(\lambda)$ is the non-dimensional chlorophyll-specific absorption coefficient given in Prieur and Sathyentranath (1981). Absorption by “yellow” matter co-varies with particle absorption according to:

$$a_{\text{CDOM}}(z, \lambda) = 0.2 a_p(z, 440 \text{ nm}) \exp [-0.014(\lambda-440)] \quad (3.2-5)$$

The scattering coefficient for the particles is given by (Gordon and Morel, 1983):

$$b(z, \lambda) = 0.3 [\text{Chl}(z, \lambda)]^{0.62} (550 / \lambda) \quad (3.2-6)$$

which assumes explicit co-variance with chlorophyll, while CDOM is assumed to be non-scattering.

The pure-water absorption in Hydrolight calculations, can be Pope and Fry's (1997) 'pure water', or Smith and Baker's (1981) 'clearest natural water' absorption values, or can be supplied by the user. The pure water scattering is from Smith and Baker (1981). In the Hydrolight runs performed in the framework of this project, the 'Pope and Fry' (1997) water absorption values and the 'Smith and Baker' (1981) water scattering coefficients were used.

There is a second chlorophyll-based IOP model, recently published by Haltrin (1999). This model is a four-component model for case 1 waters that partitions the total absorption and scattering into pure water, large chlorophyll-bearing particles, CDOM (with contributions by fulvic and humic acids), and small terrigenous particles. The humic and fulvic acids are assumed to be purely absorbing while the small terrigenous particles are assumed to be non-absorbing. Kopelevich's "large particle" and "small particle" scattering models are used to model large chlorophyll-bearing particles and small terrigenous matter, respectively. Each of these components (other than pure water) is parameterized by the chlorophyll concentration. For this "simple" case, the chlorophyll profile is the only input that needs to be specified by the user.

For case 2 waters, the user can specify concentration profiles and IOP models for each of four components: water, CDOM, pigmented and non-pigmented particulate matter. For case 2 waters, information on water's optical properties can also be provided by using actual measurements of total absorption and scattering, a , b and b_b/b (for example using an AC9 instrument to determine the absorption, a , and scattering, b , and an ECO-VSF instrument to determine b_b , the backscattering coefficient). This last approach was followed in this study, since the necessary detailed measurements were available from our field-observations in Chesapeake Bay.

- Output of the model:

Output from Hydrolight includes information on various irradiances (upward, downward, scalar and plane irradiances), radiances in various directions, reflectances and diffuse attenuation coefficients and other quantities of interest in remote sensing, such as incident and reflected sky radiance and water-leaving radiance.

3.2.2 Hydrolight Sensitivity Studies

Model simulations of underwater light fields have been performed in this study using as input information measurements of water's inherent optical properties (e.g. total in-water absorption, scattering, backscattering) and boundary conditions (e.g. downwelling surface irradiance) performed during our cruises in the Bay. Therefore, specific Hydrolight runs were performed to study the sensitivity of the model to input information and assumptions needed to perform the model simulations and to test the importance of some natural processes (such as chlorophyll or CDOM fluorescence) for estimations of underwater and water-leaving radiances. These Hydrolight runs are discussed in the following paragraphs (paragraphs 3.2.2.1-3.2.2-8).

3.2.2.1 Changes in downwelling irradiance E_s

As discussed in the next section (paragraph 3.3, "Closure experiment in the Chesapeake Bay waters"), measurements of total downwelling surface irradiance, $E_s(\lambda)$, were used as input information to perform the model estimations of underwater light fields in the Chesapeake Bay waters. What is the accuracy of the $E_s(\lambda)$ measurements performed, and what would be the effect of inaccuracies in the $E_s(\lambda)$ measurements to the model estimations of underwater light fields and remote sensing reflectances? To address the above, the Hydrolight model was run using measurements performed at PI station on 28 September 2001 as input information. During the model simulations, all parameters (a , c , b_b , sza , cloudiness, wind speed, etc.) were kept constant, except for the downwelling

surface irradiance, $E_s(\lambda)$, which was varied by $\pm 3\%$ (the MicroPro irradiance sensors' accuracy, personal communication Scott McLean, Satlantic). The standard deviation estimated from 3 independent measurement casts for E_s performed at PI during the specific cruise (28 September 2001, when no change in cloudiness conditions was observed during the measurements) was less than $\pm 1\%$. Since all other parameters, such as solar zenith angle, cloud fraction and atmospheric conditions, were kept constant, the ratio of direct to diffuse irradiance components and the angular pattern of the sky radiance distribution remained constant during the Hydrolight runs.

Figure 3.2.2.1 shows the spectrum of mean $E_s(\lambda)$ measured at PI station on 28 September 2001 (estimated as the average of the 3 casts), bracketed by the lines of $\pm 3\%$. This variation in downwelling irradiance just above the water surface is carried over to the underwater $L_u(z)$ and $E_d(z)$ profiles, and results in a $\pm 3\%$ change in the estimated $L_u(z)$ and $E_d(z)$ values at all depths (fig. 3.2.2.2), as well as in the estimated L_w (fig. 3.2.2.3(a)), since L_w is just the upwelling radiance below the water surface ($L_u(z=0^-)$) transmitted through the water interface. Therefore, errors in measured $E_s(\lambda)$ would affect the comparisons between model estimated and measured underwater $E_d(z)$ and $L_u(z)$ profiles, as well as the comparison between model estimated and measured water-leaving radiances. As expected, the model estimated remote sensing reflectance, $R_{rs}=L_w/E_s$, remains almost unaffected by any changes in (or uncertainties based on measurements of) the surface downwelling irradiance E_s (fig. 3.2.2.3(b)).

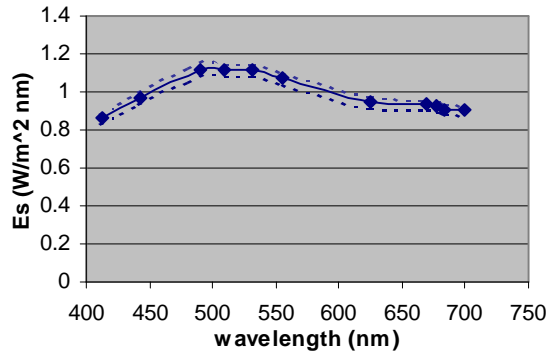


Figure 3.2.2.1: Average downwelling surface irradiance, $E_{s,avg}(\lambda)$, measured at PI station on 28 September 2001, bracketed by the lines of $\pm 3\%$, MicroPro irradiance sensors' accuracy.

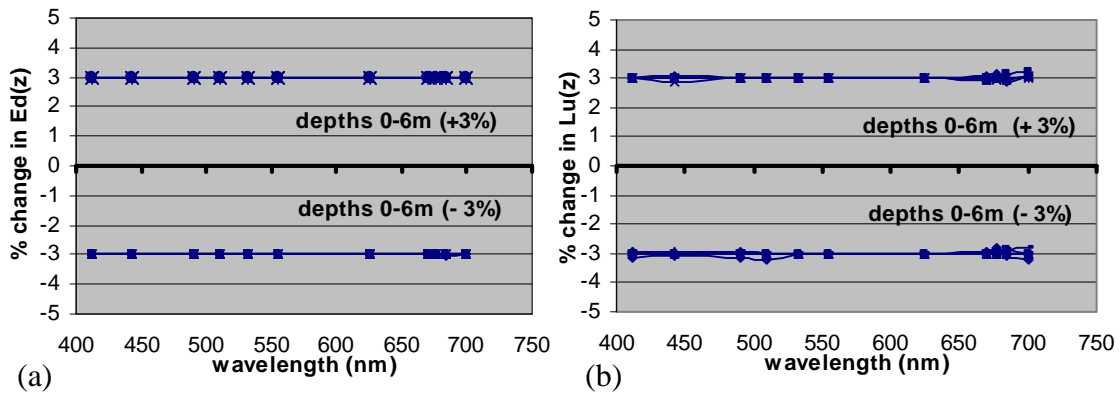


Figure 3.2.2.2: Percent change in (a) $Ed(z)$ and (b) $Lu(z)$, estimated at depths $z = 0, 1, 2, 3, 4, 5, 6m$, according to: $\frac{Ed_{(Es=E_{s,avg} \pm 3\%)} - Ed_{(Es=E_{s,avg})}}{Ed_{(Es=E_{s,avg})}}$ (similarly for Lu).

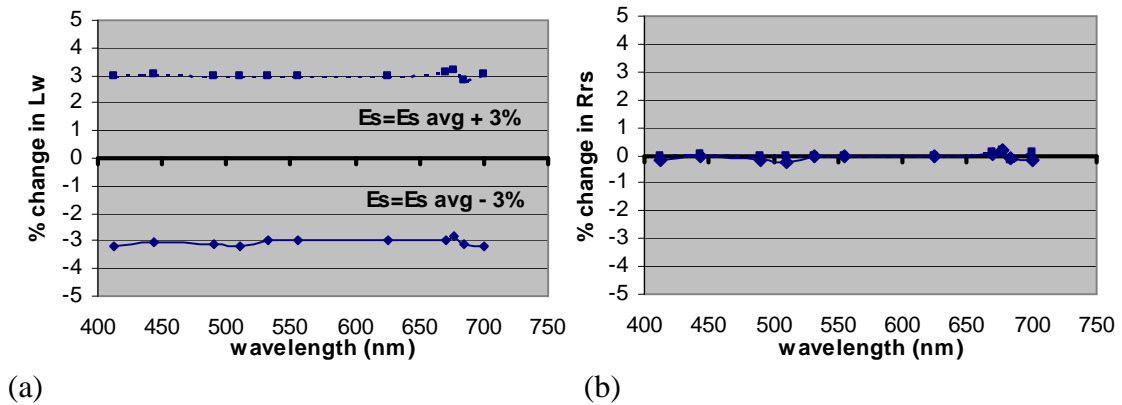


Figure 3.2.2.3: Percent change in (a) Lw and (b) Rrs estimated according to: $\frac{Lw_{(Es=E_{s,avg} \pm 3\%)} - Lw_{(Es=E_{s,avg})}}{Lw_{(Es=E_{s,avg})}}$ (similarly for Rrs).

3.2.2.2 Absorption at 715 nm

This section discusses how various assumptions for total-minus-water absorption, a_{t-w} , at near-infrared and infrared wavelengths affect the model estimations of normalized water leaving radiances, remote sensing reflectances, and underwater radiation fields (upwelling radiance and downwelling irradiance profiles). For example, setting a_{t-w} at longer wavelengths (e.g. $\lambda = 715$ nm) to zero is one of the key assumptions usually used to correct spectrophotometric absorption measurements for scattering errors (Zaneveld et al., 1994) (chapter 2, Methodology AC9 instrument). As shown in later sections, the use of small but non-zero absorption a_{t-w} at $\lambda = 715$ nm improves the agreement between measured and modeled values.

To perform the model estimations, Hydrolight was run using input information from measurements performed at PI station on 28 September 2001 for three cases:

i) AC9 absorption values corrected assuming that total-minus-water at $\lambda = 715$ nm is zero, according to the Zaneveld correction for scattering in AC9 (Zaneveld et al., 1994):

$a_{t-w}(\lambda) = a_{t-w,m}(\lambda) - [b_{t-w,m}(\lambda)/b_{t-w,m}(715)] \cdot a_{t-w,m}(715)$, where $a_{t-w}(\lambda)$ is the corrected absorption (minus absorption by pure water) at a wavelength λ , $a_{t-w,m}$ is the measured absorption and $b_{t-w,m}$ is the measured scattering.

ii) AC9 absorption values corrected assuming that total-minus-water absorption at 715 nm equals the total absorption ($a_{CARY} = a_{detr} + a_{phyt} + a_{CDOM}$) measured spectrophotometrically using the CARY spectrophotometer. To correct the CARY measurements of particulate absorption ($a_{pA} = a_{detr} + a_{phyt}$) for scattering, the absorption value measured at 750 nm was subtracted from all wavelengths. The particulate

absorption measurements were also corrected for the effect of multiple scattering inside the glass-fiber filters that results in pathlength amplification. To estimate the value of the amplification factor, measurements of absorption by particulate matter retained on filter pads were compared to absorption values measured in particle suspension. According to these comparisons, β values were only slightly wavelength dependent and were within the range 1.5 – 2 (paragraph 2.2.2.3). During the second Hydrolight run an amplification factor $\beta=2$ (Roesler, 1998), was used to correct for amplification of the optical pathlength in the filter pad. The AC9 absorption measurements were then corrected according to:

$$a_{t-w}(\lambda) = a_{t-w,m}(\lambda) - [b_{t-w,m}(\lambda)/b_{t-w,m}(715)] \cdot [a_{t-w,m}(715) - a_{CARY}(715)], \text{ where } a_{CARY}(715) = [a_{PA}(715)/2] + a_{CDOM}(715)$$

iii) In the third case, the AC9 absorption values were corrected assuming that absorption at 715 nm equals the total absorption measured using the CARY spectrophotometer. Particulate absorption spectra were corrected for Mie scattering by subtracting the absorption at 750 nm from the entire spectrum. In this case, no correction for the amplification factor was applied (or $\beta=1$), and thus the estimate of absorption at 715 nm using the spectrophotometric technique was the maximum value of what would be expected.

Figure 3.2.2.4 (a) shows the percent difference of the total-minus-water absorption, a_{t-w} , (which is also the absorption measured by the AC9 instrument), between case 1 (assumption that $a_{t-w}(715) = 0$) and case 2 (assumption that $a_{t-w}(715)$ equals the absorption measured at 715nm using the CARY spectrophotometer, according to:

$$a_{t-w}(715) = [(a_{PA}(715) / \beta) + a_{CDOM}(715)] = 0.0146 \text{ m}^{-1}, \text{ for } \beta=2 \text{). The maximum percent}$$

difference in a_{t-w} is, as expected, at 715 nm (100%) while percent differences larger than 5% were observed at the green to red wavelengths (532-676 nm). Figure 3.2.2.4(b) shows the percent difference of the total absorption, $a_t = a_w + a_{PA} + a_{CDOM}$, between the two cases.

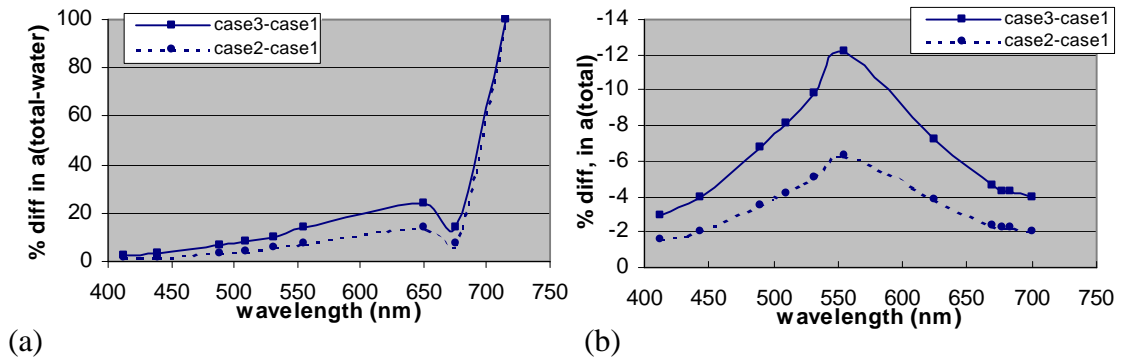


Figure 3.2.2.4: Percent differences of (a) the total minus the water absorption, a_{t-w} and (b) the total absorption, $a_t = a_w + a_{PA} + a_{CDOM}$, between case-1 (assumption that $a_{t-w}(715) = 0$) and case-2 ($a_{t-w}(715) = [(a_{PA}(715) / \beta) + a_{CDOM}(715)]$ for $\beta=2$), and between case-1 and case-3 ($a_{t-w}(715) = [(a_{PA}(715) / \beta) + a_{CDOM}(715)]$ for $\beta=1$).

When the water absorption is also taken into account, the effect of the residual absorption at 715 nm is larger in the green wavelengths, with maximum percent difference occurring at 550 nm. In the blue region of the spectrum, absorption by CDOM and non-pigmented particulate matter is large ($a_t = 1.12 \text{ m}^{-1}$ at 412 nm) and the effect of the residual absorption at 715 nm ($a_{CARY}(715) = 0.0146 \text{ m}^{-1}$, for $\beta=2$) is too small to significantly change the total absorption (less than 2% change in a_t). In the red region of the spectrum, strong absorption by water itself results in relatively high total absorption ($a_t = 0.7 \text{ m}^{-1}$) and, again, the effect of the residual absorption at 715 nm is too small to change the total absorption significantly ($\Delta a/a = 0.0146 / 0.7 = 2\%$ change in a_t). However, in the green region of the spectrum ($\lambda=550 \text{ nm}$) total absorption is relatively smaller ($a_t = 0.25 \text{ m}^{-1}$), and a change in the absorption by 0.0145 m^{-1} translates to a 6% change in total absorption (fig. 3.2.2.4 (b)).

The percent differences in total-minus-water absorption and in total absorption, between case 1 (assumption that $a_{t-w}(715) = 0$) and case 3 (assumption that $a_{t-w}(715)$ equals the absorption measured at 715 nm using the CARY instrument, according to: $a_{t-w}(715) = [a_{PA}(715)/\beta + a_{CDOM}(715)] = 0.028 \text{ m}^{-1}$, for $\beta=1$), are also shown in figures 3.2.2.4 (a),(b) (dotted lines). In this case, a change in the absorption by 0.028 m^{-1} translates to a 12% change in total absorption at 550 nm (fig. 3.2.2.4 (b)).

The effect of the above changes on the model estimations of $Ed(z)$ and $Lu(z)$ underwater profiles (model calculations at 0, 1, 2, 3, 4, 5 and 6 m depths) are shown in figures 3.2.2.5-3.2.2.6. As was expected, the larger percent differences were observed at the green wavelengths where the percent changes of the total absorption values were relatively larger. Even in the case where the spectrophotometric values of particulate absorption have been corrected for $\beta=2$ ($a_{CARY}(715)=0.0146\text{m}^{-1}$), the percent differences in $Lu_{(550)}$ (estimated as $\frac{Lu_{(a715=aCARY)} - Lu_{(a715=0)}}{Lu_{(a715=0)}}$) are larger than 5% just below the water surface and reach more than 15% at a depth of 6 meters. Ed values in the first couple of meters below the water surface were only slightly affected by the change in the absorption values. However, $Ed(z)$ values at a depth of 5-6 m below the water surface were affected by almost 10%. The effect of the change in the absorption values on the $Ed(z)$ and $Lu(z)$ is almost double for case 3, where a value of $\beta=1$ (instead of $\beta=2$) was assumed. $Ed(z)$ changed by almost 20% at a depth of 6 meters, while $Lu(550)$ changed by 10% just below the water surface and by more than 25% deeper than 5 m in the water column.

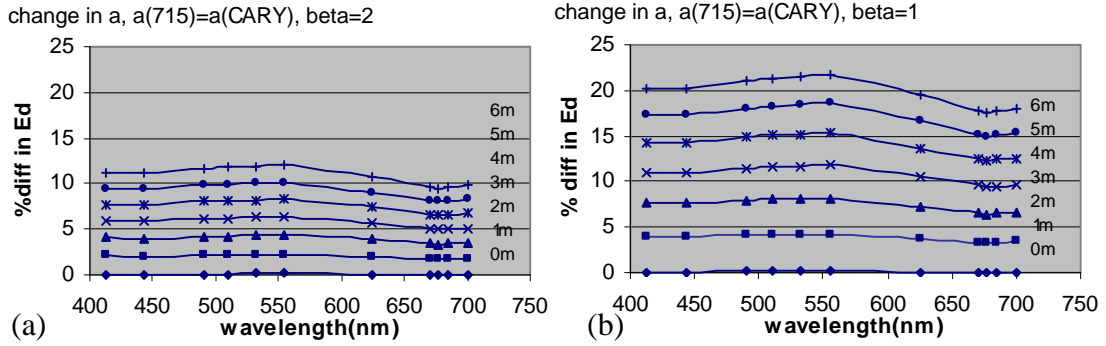


Figure 3.2.2.5: Percent differences in $Ed(\lambda)$, between (a) case-1 and case-2 and (b) case-1 and case-3, estimated as $\frac{Ed_{(case2_or_case3)} - Ed_{(case1)}}{Ed_{(case1)}}$, for various depths (0-6m).

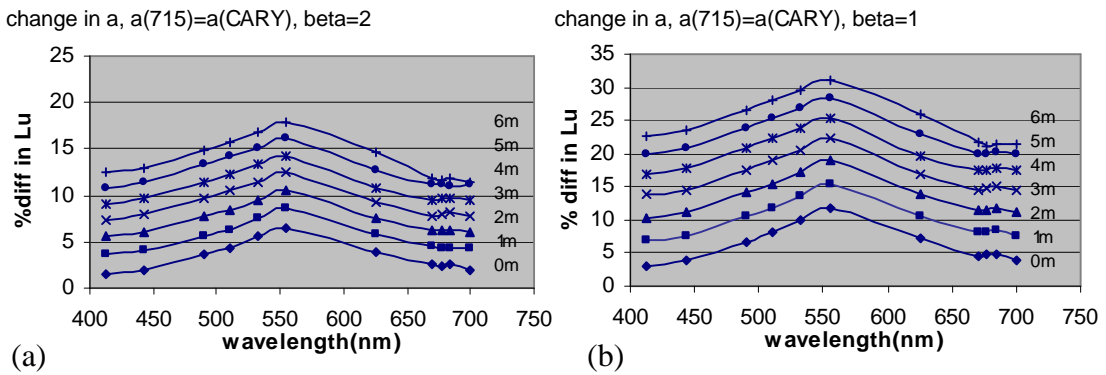


Figure 3.2.2.6: Percent differences in $Lu(\lambda)$, between (a) case-1 and case-2 and (b) case-1 and case-3, estimated as $\frac{Lu_{(case2_or_case3)} - Lu_{(case1)}}{Lu_{(case1)}}$, for various depths (0-6m).

The effect of assuming non-zero absorption $a_{t-w}(715)$ on the estimated water leaving radiances, L_w , and remote sensing reflectances, R_{rs} , (which are quantities that can be measured remotely by sensors onboard satellites or aircrafts) is shown in figures 3.2.2.7, 3.2.2.8. Since for the remote sensing reflectance $R_{rs} \sim b_b / (b_b + a_t)$ and b_b had the same (and relatively small compared to absorption) values for all cases 1, 2 and 3, the effect of a residual absorption at 715 nm on R_{rs} (and similarly on the water-leaving radiance, L_w , since $R_{rs} = L_w / E_s$, and E_s was the same in all Hydrolight runs) should be almost the

same as the percent change on the total absorption. Therefore, Rrs and Lw are mostly affected within the green region of the spectrum and especially at 550 nm. The estimated Rrs(550) and Lw(550) values for non-zero $a_{t-w}(715)$, with $\beta=2$, are 6% lower than those estimated for $a_{t-w}(715)=0$, while Rrs and Lw at the blue (412-443nm) and red (670-700nm) wavelengths change only by ~2%. The estimated Rrs(550) and Lw(550) values for non-zero $a_{t-w}(715)$, with $\beta=1$, are 12% lower than those estimated for $a_{t-w}(715)=0$.

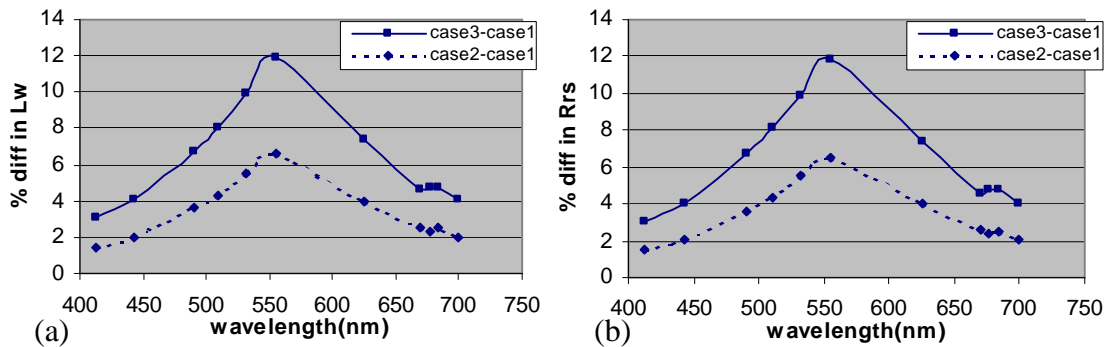


Figure 3.2.2.7: Percent differences in (a) Lw and (b) Rrs estimated according to:

$$\frac{Lw_{(case2_or_case3)} - Lw_{(case1)}}{Lw_{(case1)}} \quad (\text{similarly for Rrs}).$$

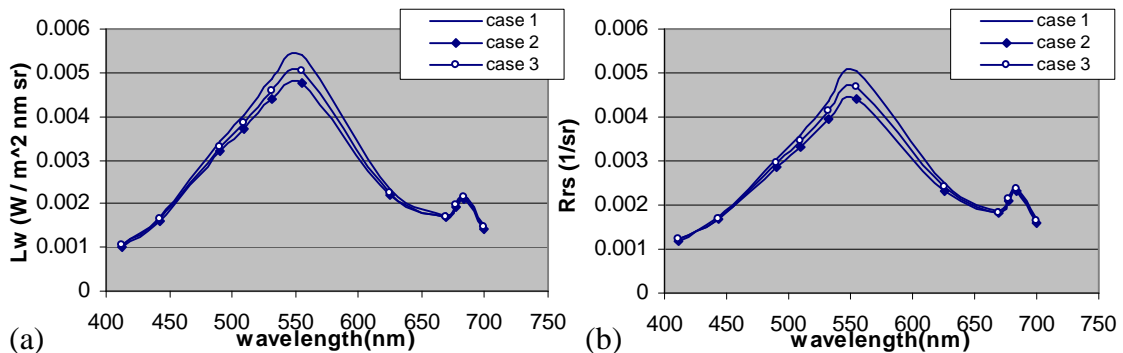


Figure 3.2.2.8: (a) Lw and (b) Rrs spectra estimated for cases 1, 2, 3. Low Ed and Lu values in the blue and red wavelengths are due to the high absorption by CDOM and non-pigmented particulate matter (blue wavelength region) and by pure sea-water (red region). The maximum in Lu at ~ 685 nm is due to the chlorophyll fluorescence.

3.2.2.3 Scattering phase function

The backscattering coefficient, b_b , is one of the most significant inherent optical properties of a water body, and one of the most critical parameters in estimations of the amount of radiance leaving the water surface and eventually measured by a remote sensing instrument. The backscattering properties of a natural water body can be specified in Hydrolight runs by: 1) using measured values of the backscattering coefficient by an instrument such as ECOVSF (WETLabs) or Hydrosat (HOBILabs). 2) By selecting one of the discretized phase functions supplied with Hydrolight (such as the Petzold “average particle” phase function, the ‘pure water’ phase function, the Kopelevich’s “small particle” or the Kopelevich’s “large particle” phase function). The Petzold ‘average particle’ scattering phase function has been widely used as representative of most natural, moderately turbid waters, especially in cases when measured values of b_b/b are not available. 3) By defining a wavelength- and depth-dependent value for the backscattering to scattering ratio, b_b/b , and using a Fournier-Forand scattering phase function with the same b_b/b ratio (Mobley and Sundman, 2000).

In our case, the total backscattering coefficient, b_b , was measured at PI station, on 28 September 2001, using an ECOVSF instrument, while measurements of particulate scattering, b_{t-w} , were performed using an AC9 instrument (b_{t-w} was estimated as the difference between measured attenuation and absorption values, $b=c-a$). Therefore, measurements of b_b/b for particulate matter at 450-650 nm were available to use in the model estimations (fig. 3.2.2.9). To study the effect of the choice of scattering phase function on the model estimated $E_d(z)$, $L_u(z)$, R_{rs} , L_w , Hydrolight was run for three cases:

- i) using as input information the measured b_b/b and a Fournier Forand phase function
- ii) selecting the ‘average particle’ Petzold phase function ($b_b/b=0.0183$) for estimation of the backscattering component and
- iii) selecting a Fournier-Forand phase function with $b_b/b=0.015$ for particulate matter (constant with depth and wavelength), since the average measured b_b/b at 500-550 nm was close to 1.5%. The percent differences in the estimated $Lu(z)$, $Ed(z)$, Rrs and Lw are shown in figures 3.2.2-10 - 3.2.2-13.

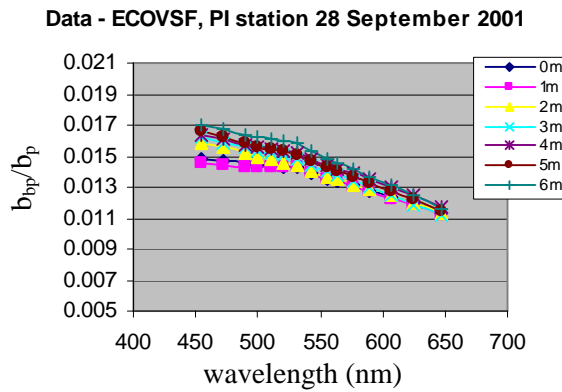


Figure 3.2.2.9: Measurements of b_b/b , performed at depths 0-6 m, at PI station, on 28 September 2001, using an ECOVSF instrument (to measure backscattering, b_b , at 450, 530 and 650 nm) and an AC9 instrument (to measure scattering, b_{t-w} , at seven wavelengths in the region 412-715 nm)

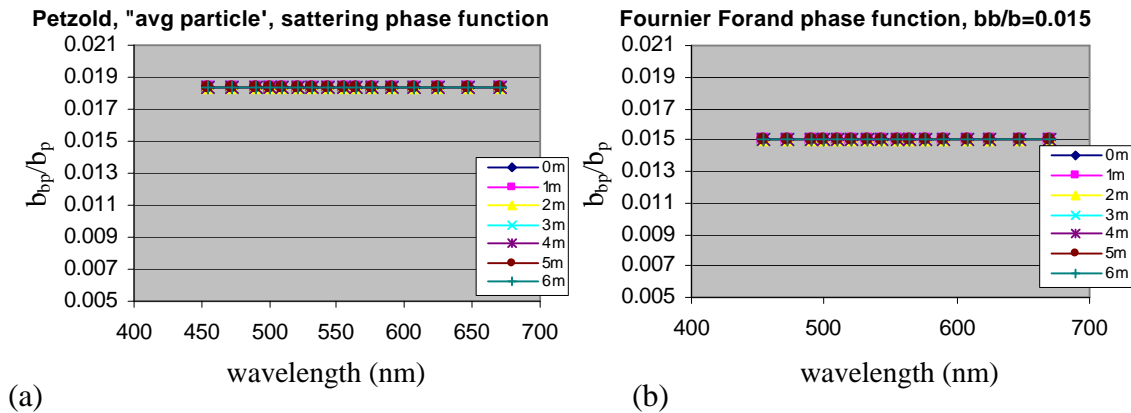


Figure 3.2.2.10: Estimated b_b/b using (a) the ‘average particle’ Petzold phase function ($b_b/b=1.83\%$) and (b) a Fournier-Forand phase function with $b_b/b=1.5\%$

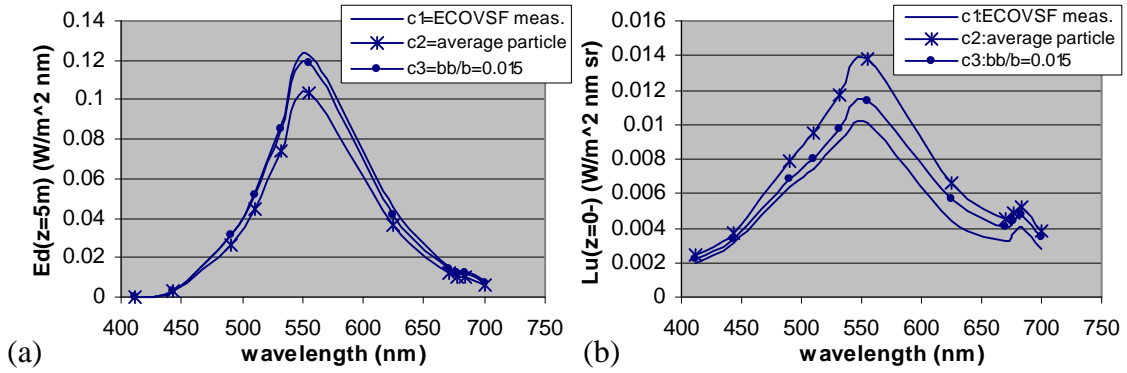


Figure 3.2.2.11: (a) $E_d(z=5m)$ and (b) $L_u(z=0)$ spectra estimated using the three different b_b/b ratios

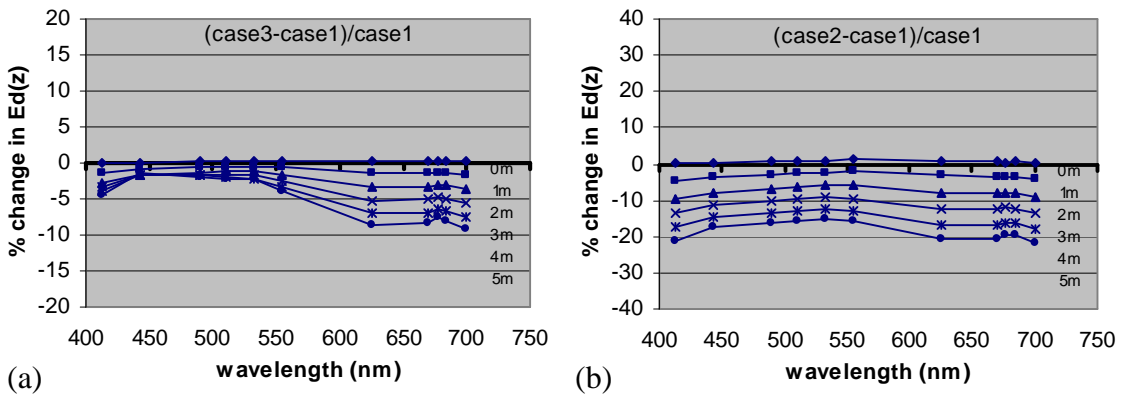


Figure 3.2.2.12: Percent differences in $E_d(z)$ (depths 0-5m) estimated between (a) case 3 ($b_b/b=0.015$) and case 1 (b_b/b measured using ECOVSF) and (b) case 2 (b_b/b Petzold “average particle”) and case 1 (b_b/b measured using ECOVSF) . The percent differences

were estimated according to:
$$\frac{E_d(\text{case3_or_case2}) - E_d(\text{case1})}{E_d(\text{case1})}$$

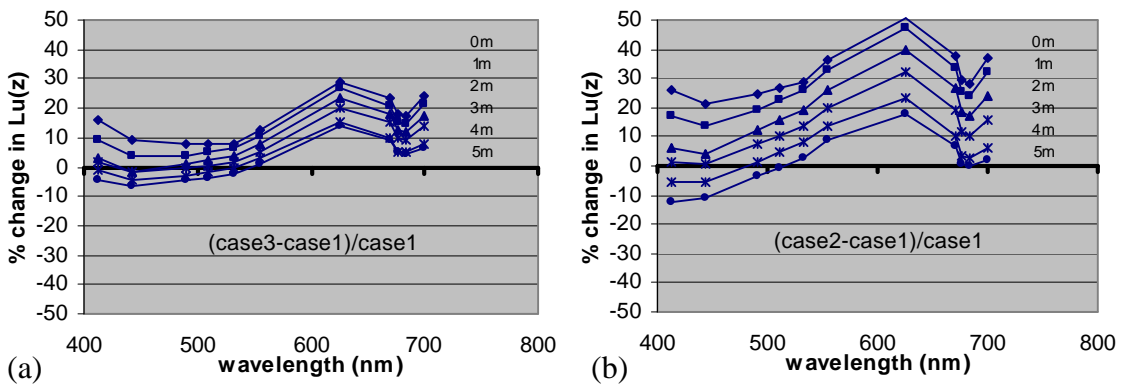


Figure 3.2.2.13: Percent differences in $L_u(z)$ (depths 0-5m) estimated between (a) case 3 ($b_b/b=0.015$) and case 1 (b_b/b measured using ECOVSF) and (b) case 2 (b_b/b Petzold “average particle”) and case 1 (b_b/b measured using ECOVSF) . The percent differences

were estimated according to:
$$\frac{L_u(\text{case3_or_case2}) - L_u(\text{case1})}{L_u(\text{case1})}$$

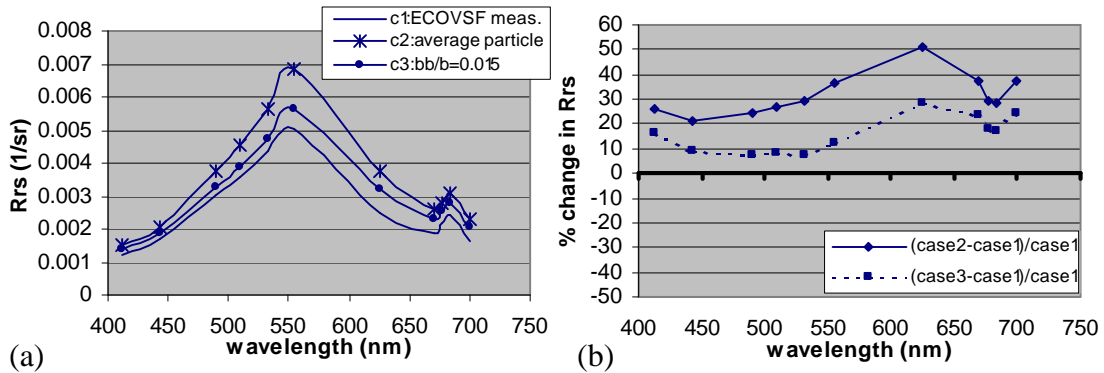


Figure 3.2.2.14: (a) Rrs spectra estimated using the three different b_b/b ratios and (b) percent differences in Rrs between cases 2 and case 1 (solid line) and case 3 and case 1 (dotted line)

According to the model simulations, the assumptions made about the backscattering properties of the water body significantly affect the model-estimated downwelling irradiance and, especially, the upwelling radiance just below the water surface and the water-leaving radiance. Use of the ‘average particle’ Petzold phase function in the model estimations, for the specific case (PI station, 28 September 2001), results in an underestimation of E_d by 10-20% at 3-5m depths compared to model results using the measured b_b/b values for particulate scattering (combination of AC9 and ECOVSF measurements). L_u at $z=0^-$ (as well as L_w and R_{rs}) is overestimated by 20% in the blue wavelengths, and by as much as 35-50% within the 550-650 nm wavelength region, compared to L_u values estimated using the measured b_b/b values. Use of a constant b_b/b ratio for all wavelengths, $b_b/b=1.5\%$ (a value close to the average b_b/b measured at 500-550nm at all depths during the specific cruise), results in an overestimation of R_{rs} by less than 10% in the blue-green wavelengths and by 20-30% within the red wavelength region. Therefore, accurate knowledge of the actual backscattering properties of the water is very important in model simulations of radiation fields, especially in estuarine waters where b_b , as well as b_b/b , can show large temporal and spatial variation.

3.2.2.4 Variations in measured backscattering coefficient, b_b

Measurements of total backscattering coefficient, b_b , were performed during the cruises in Chesapeake Bay, using an ECOVSF instrument. Several factors, such as instrument noise and natural variability in the water properties during the duration of the measurements, can cause some variation in the total backscattering value measured at a specific depth. To study how these variations in measured b_b at a specific depth would affect model estimations of underwater and water-leaving radiances, the Hydrolight code was run using as input information (a, b, sza , clouds, surface-wind, [Chl-a], Es) measurements performed at PI station on 28 September 2001,

i) with backscattering coefficient, b_b , equal to the average b_b measured at each depth, at PI station on 28 September and

ii) with $b_b(z) = b_{b\text{ avg}}(z) \pm \text{standard-error}$, where the standard-error was in the order of 1.5-2.5% (depending on wavelength and depth). The standard error was estimated as the ratio $\frac{stdev}{\sqrt{n}}$, where *stdev* is the standard deviation of the n measurements of backward scattering performed at each depth used to estimate the average $b_b(z)$ at that depth.

Figures 3.2.2-15 - 3.2.2-16 show the percent difference in the model estimated $E_d(z)$, $L_u(z)$, L_w and R_{rs} . Increasing b_b by the standard error, results (for the specific case studied) in less than 1% decrease in E_d at all depths (due to larger backward redirection of the light), and less than 2% increase in L_u . Similarly, decreasing b_b by the standard error, results in less than 1% increase in E_d at all depths (due to lower backward scattering), and less than 2% decrease in L_u . The water-leaving radiance, and as a result the remote sensing reflectance, are affected by almost 2%.

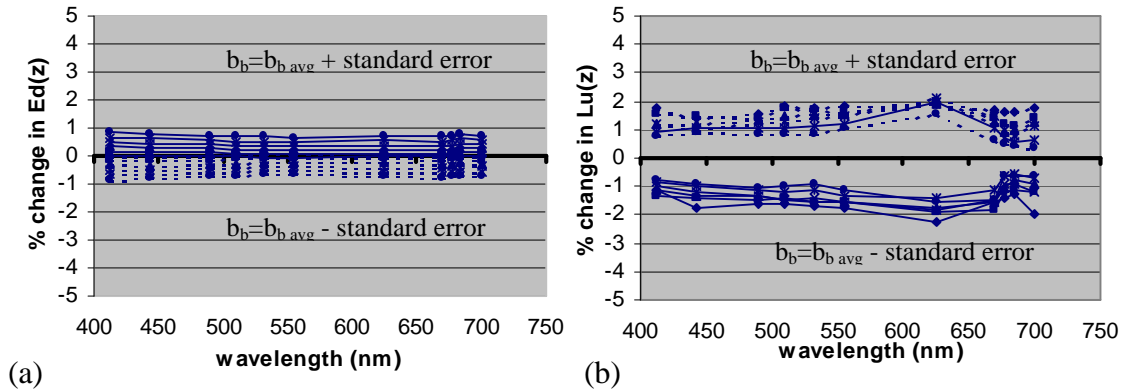


Figure 3.2.2-15: Percent differences in (a) $Ed(z)$ (depths 0-5m) and (b) $Lu(z)$ (depths 0-5m), estimated between running Hydrolight with $b_b = b_{b,avg}$ and $b_b = b_{b,avg} + \text{standard-error}$ (dotted lines) and between running Hydrolight with $b_b = b_{b,avg}$ and $b_b = b_{b,avg} - \text{standard-error}$ (solid lines). The percent differences were estimated for Ed (and similarly for Lu)

according to:
$$\frac{Ed_{(bbavg \pm sterror)} - Ed_{(bbavg)}}{Ed_{(bbavg)}}$$

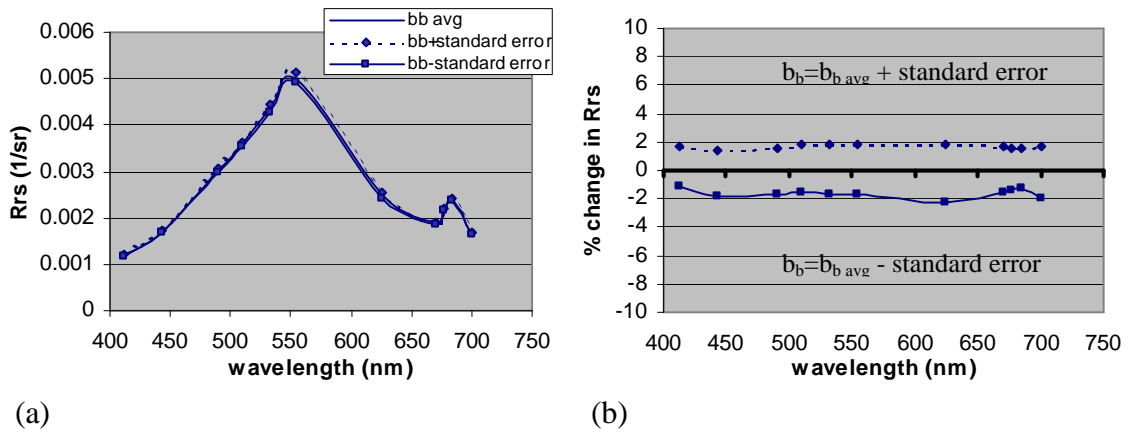


Figure 3.2.2-16: (a) Rrs spectra and (b) percent differences in Rrs , estimated between running Hydrolight with $b_b = b_{b,avg}$ and $b_b = b_{b,avg} + \text{standard-error}$ (dotted lines) and between running Hydrolight with $b_b = b_{b,avg}$ and $b_b = b_{b,avg} - \text{standard-error}$ (solid lines).

The percent differences were estimated according to:
$$\frac{Rrs_{(bbavg \pm sterror)} - Rrs_{(bbavg)}}{Rrs_{(bbavg)}}$$

3.2.2.5 Variation in measured underwater absorption and attenuation

Measurements of total absorption (minus pure water absorption), $a_{t-w}(\lambda)$, and attenuation, $c_{t-w}(\lambda)$, in the Chesapeake Bay waters were performed using an AC9 instrument. The scattering coefficient, $b_{t-w}(\lambda)$, was estimated as the difference between the measured values of $a_{t-w}(\lambda)$ and $c_{t-w}(\lambda)$. To study how variations in measured absorption and attenuation (due to instrument noise and natural variability in the water properties during the measurements at a specific depth) affect the model estimations of water-leaving radiance, L_w , and underwater $Ed(z)$ and $Lu(z)$, several Hydrolight runs were performed keeping all parameters constant, but varying input information on absorption or attenuation. Input information was obtained from measurements of b_b , sza , Es , and observations of cloudiness and wind-speed made at PI station on 28 September 2001. The absorption, $a_{t-w}(z)$, at each depth (and similarly for the attenuation, $c_{t-w}(z)$) was estimated as the mean value of n ($n \sim 15$) AC9 absorption measurements performed at the specific depth. Absorption was corrected for scattering using the Zaneveld correction and varied by \pm percent standard error. The standard error of the mean absorption was estimated as the ratio $stdev/\sqrt{n}$, where $stdev$ is the standard deviation of the n measurements of absorption performed at each depth, that were used to estimate the mean $a_{t-w}(z)$ at that depth. The estimated standard errors in the AC9 absorption and attenuation measurements were less than 2.5 %, with largest values close to the surface (for the specific case studied here).

Changes in the measured absorption, a_{t-w} , by \pm percent standard error, affected the model estimated Ed and Lu by less than 4% at all wavelengths and all depths from 0 to

5m, with larger percent differences estimated deeper in the water column and at short wavelengths (fig. 3.2.2-17). The water leaving radiance (fig. 3.2.2-19(a)) is affected only by less than 2% at all wavelengths.

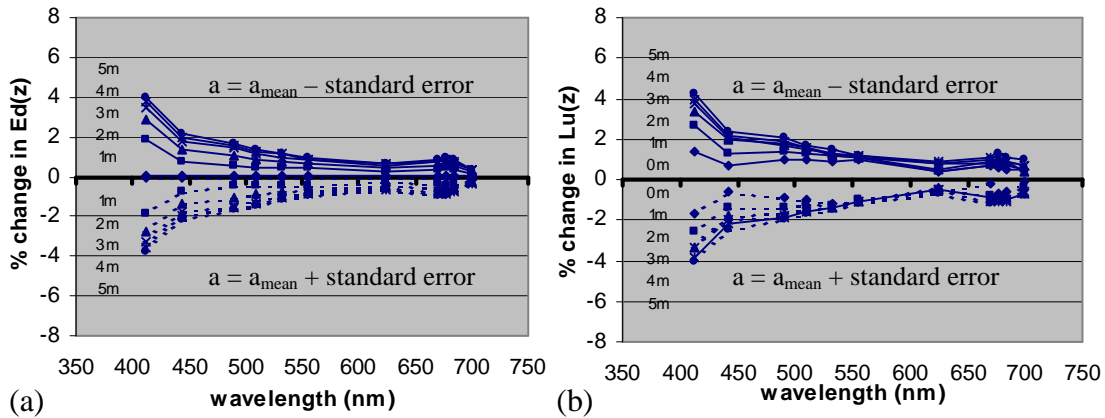


Figure 3.2.2-17: Percent change in (a) $E_d(z)$ and (b) $L_u(z)$, estimated at depths $z = 0, 1, 2, 3, 4, 5$ m, according to: $\frac{E_d(a=a_{mean} \pm st.error) - E_d(a=a_{mean})}{E_d(a=a_{mean})}$ and similarly for L_u . As was

expected increased absorption by the water medium results in lower E_d and L_u values in the water column.

The effect of changes in the attenuation values by \pm standard error, on the model estimated downwelling irradiance, E_d , and upwelling radiance, L_u , is less than 1% at all wavelengths and all depths from 0 to 5m below the water surface (fig. 3.2.2-18). The water leaving radiance (fig. 3.2.2-19(b)) is also affected by less than 1% at all wavelengths.

According to the model simulations, the small variability of the AC9 measurements, estimated for the specific case (water surface relatively calm and IOPs not highly variable with depth) has only a small influence in the model estimations of underwater radiation

fields. Under conditions of rougher water-surface (larger uncertainties in instrument's depth) or less homogeneous waters (larger variation in a_{t-w} with depth), larger errors in a_{t-w} (or c_{t-w}) measurements could occur, that would have a larger effect in R_{rs} , $Ed(z)$ and $Lu(z)$ (see results in 3.2.2.2).

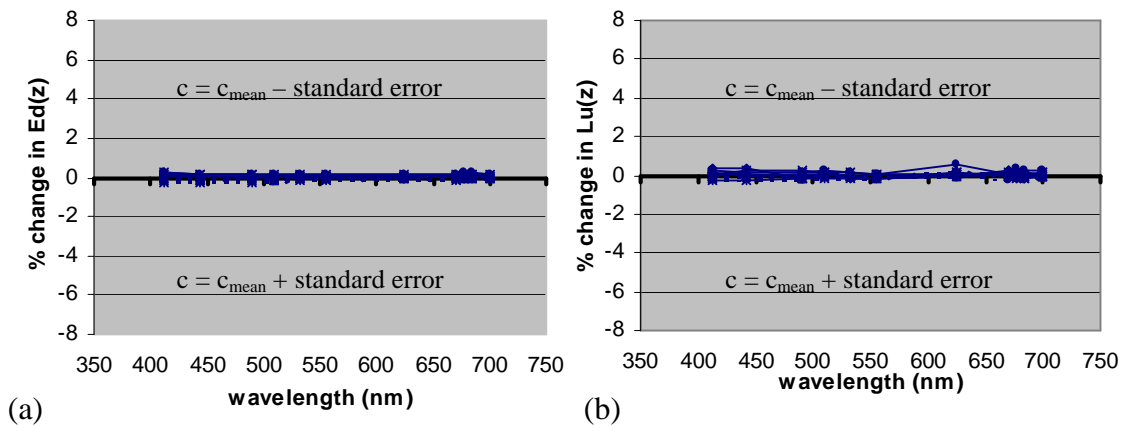


Figure 3.2.2-18: Percent change in (a) $Ed(z)$ and (b) $Lu(z)$, estimated at depths $z = 0, 1, 2, 3, 4$ and $5m$, according to:

$$\frac{Ed_{(c=c_{mean} \pm \text{error})} - Ed_{(c=c_{mean})}}{Ed_{(c=c_{mean})}} \quad (\text{similarly for } Lu).$$

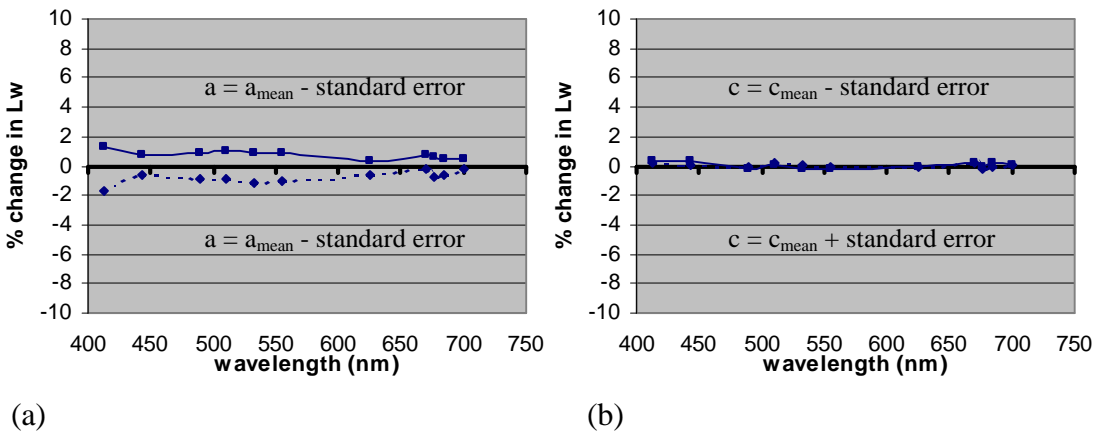


Figure 3.2.2-19: Percent changes in water leaving radiance, L_w , estimated for (a) changes in mean measured absorption, a , by \pm standard error and (b) changes in mean measured attenuation, c , by \pm standard error.

3.2.2.6 Inelastic Scattering processes

Inelastic scattering processes, such as Raman scattering by water molecules and fluorescence by phytoplankton pigments and dissolved organic material, can be of considerable significance in natural waters. To study the effect of including the contribution of inelastic scattering processes to the model estimations of water-leaving radiances and underwater light fields, several Hydrolight runs were performed using as input information measurements performed on 28 September 2001, at PI station. The model estimations were performed for clear sky conditions (cloud fraction 0%) and 5m/s average wind speed.

Chlorophyll fluorescence

To estimate the amount of light fluoresced by chlorophyll, Hydrolight uses information on chlorophyll absorption (or chlorophyll concentration, from which chlorophyll absorption can be estimated) and assumptions about chlorophyll fluorescence efficiency and the wavelength redistribution function (the default chlorophyll fluorescence efficiency value of 0.02 was used in the following simulations) (Mobley, 1994; Mobley Technical Documentation, 2000).

To study the contribution of chlorophyll fluorescence to the model estimations of underwater light field, the following cases were considered:

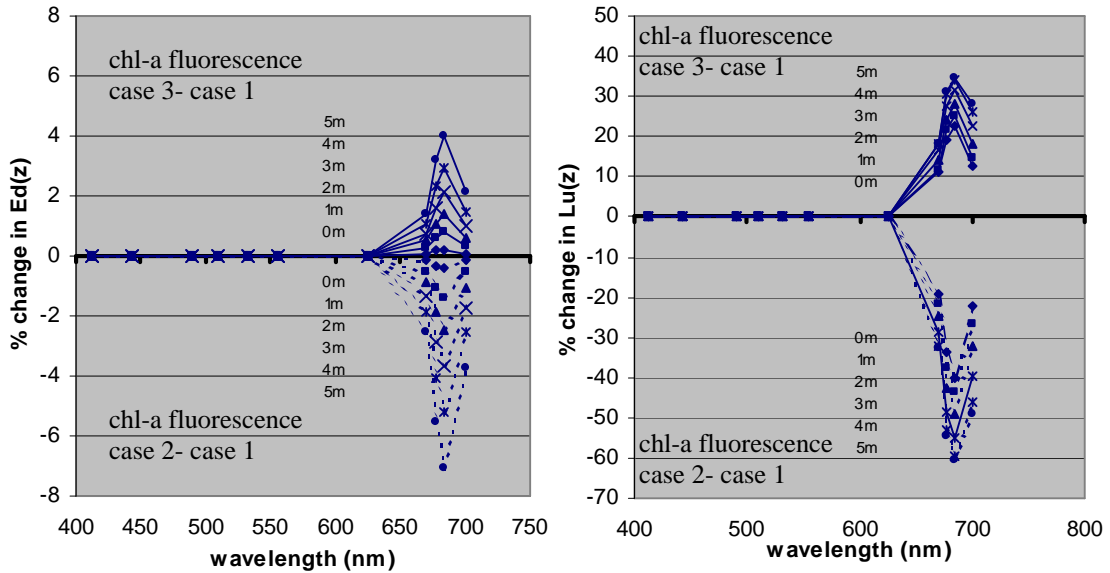
i) including the process of chlorophyll fluorescence, for a chlorophyll concentration of $[\text{Chl-a}] = 7.25 \text{ mg m}^{-3}$, which was the average chlorophyll concentration within the water

column (1-5m depth) measured at PI station, on 28 September 2001. This amount is also consistent with the average chlorophyll concentration, $[\text{Chl-a}]_{\text{avg}}=7.3 \pm 1.5 \text{ mg m}^{-3}$, measured at PI station (1-5m) during the 5 fall cruises in September-October 2001.

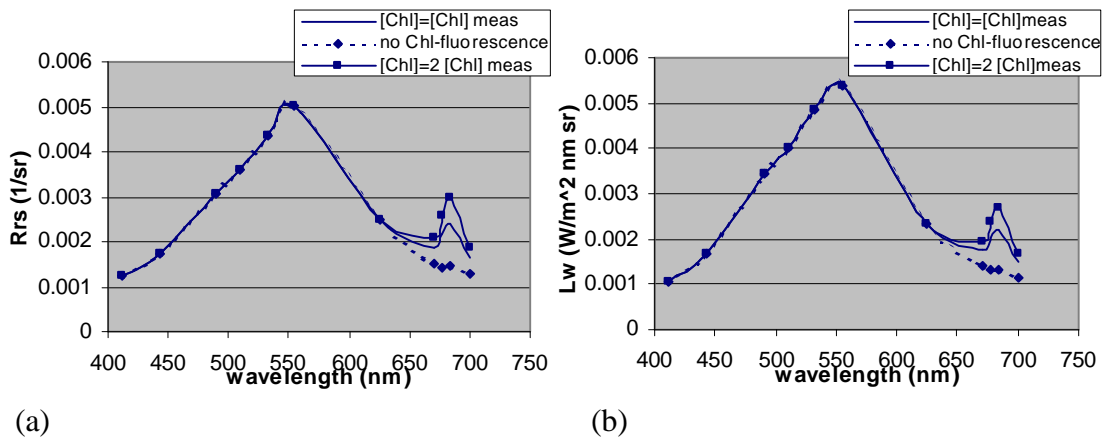
ii) without including the effect of chlorophyll fluorescence

iii) including the effect of chlorophyll fluorescence, but for the extreme case of double the measured chlorophyll concentration: $2[\text{Chl-a}]=14.5 \text{ mg m}^{-3}$ (which corresponds to 100% error in the $[\text{Chl-a}]$ measurement). Raman scattering by water molecules and CDOM fluorescence (for $a_{\text{CDOM}}(440)=0.3 \text{ m}^{-1}$) were included in all runs. The contribution of the chlorophyll fluorescence to the estimation of $\text{Lu}(z)$, $\text{Ed}(z)$, Lw and Rrs , in the wavelength region 400 – 700 nm, is shown in figures 3.2.2-20 – 3.2.2-22.

According to the model simulations, the inelastic process of chlorophyll fluorescence can significantly affect the estimated upwelling and downwelling radiance profiles within the wavelength range 650-700 nm, and especially at 685 nm, since this is the wavelength region where chl-a fluoresces regardless of whether it is excited by light in the UV or visible wavelengths. When chlorophyll fluorescence is not included in the model estimations (case 2), $\text{Ed}(z)$ can be underestimated by 7% at a depth of 5 meters, while the percent difference is less than 3% in the first 3 meters for the specific case of measurements performed at the PI station (fig. 3.2.2-20(a)). However, the effect is more pronounced for the upwelling radiance, $\text{Lu}(z)$, which may be underestimated by as much as 40% just below the water surface. This change in Lu , translates to a 40% change in the estimated water-leaving radiance and remote sensing reflectance (fig. 3.2.2-21-3.2.2-22), that can significantly affect comparisons with remotely sensed water-leaving radiances.



(a) (b)
 Figure 3.2.2-20: Percent differences in the estimated by the model (a) $Ed(z)$ and (b) $Lu(z)$ values, between case 1 (chl-fluorescence included, for the measured chl-a concentration, $[Chl-a] = 7.25 \text{ mg m}^{-3}$) and case 2 (chl-fluorescence not included), and between case 1 and case 3 (chl- fluorescence included, for $[Chl-a] = 14.5 \text{ mg m}^{-3}$). The % differences were estimated as: $\frac{Ed_{(no-Chl-fluor)} - Ed_{([Chl]=7.25)}}{Ed_{([Chl]=7.25)}}$, $\frac{Ed_{([Chl]=14.5)} - Ed_{([Chl]=7.25)}}{Ed_{([Chl]=7.25)}}$ (similarly for Lu).



(a) (b)
 Figure 3.2.2-21: Model estimations of (a) Rrs and (b) Lw , for case 1 (chl-fluorescence included, $[Chl-a]=7.25 \text{ mg m}^{-3}$) (solid line), for case 2 (chlorophyll fluorescence not included) (squares, dotted line), and case 3 (chlorophyll fluorescence included, $[Chl-a]=14.5 \text{ mg m}^{-3}$) (squares, solid line).

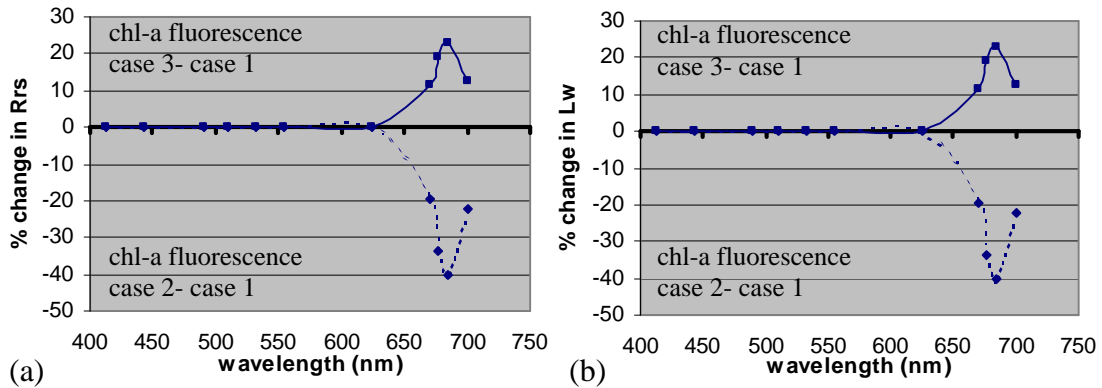


Figure 3.2.2-22: Percent differences in the model estimated (a) Rrs and (b) Lw values, between case 1 (chl-fluorescence included, for the measured [Chl-a], [Chl-a]=7.25mgm⁻³) and case 2 (chl-fluorescence not included), and between case 1 and case 3 (chlorophyll fluorescence included, for [Chl-a] = 14.5 mg m⁻³). Percent differences were estimated as:

$$\frac{Rrs_{(no-Chl-fluor)} - Rrs_{([Chl]=7.25)}}{Rrs_{([Chl]=7.25)}} \quad \text{and} \quad \frac{Rrs_{([Chl]=14.5)} - Rrs_{([Chl]=7.25)}}{Rrs_{([Chl]=7.25)}} \quad (\text{similarly for } Lw).$$

Fluorescence by chromophoric dissolved organic matter

In Hydrolight simulations the default CDOM fluorescence quantum efficiency function is taken from Hawes (1992) and is based on measurements of spectral fluorescence quantum efficiency functions performed on water samples collected from a variety of waters. Hawes found values of CDOM fluorescence quantum efficiency between 0.005 and 0.015. According to Blough and Del Vecchio (2002) the CDOM excitation and emission fluorescence spectra are very broad and unstructured, with the maxima in the excitation and emission spectra usually falling between 300-400 nm and 400-500 nm, respectively.

When inelastic scattering effects are included in Hydrolight runs, some consideration arises in the choice of the wavelength domain over which the model should be run. This is because, if one is interested on including the contributions of fluorescence or Raman

scattering to the light field in the visible wavelengths, then Hydrolight must be run also for all shorter wavelengths that might contribute to inelastic scattering within the wavelength region of interest. To include the effects of Raman scattering the model should be run starting at 390-400 nm, since excitation at wavelengths around 400 nm results in Raman scattering near 450 nm. To include the effect of CDOM fluorescence, the model should be run starting at 350 nm, since CDOM shows strong fluorescence throughout the visible wavelengths, when excited by ultraviolet light (Mobley, 2000).

One of the measured parameters used as an input in Hydrolight, is the downwelling irradiance just above the water surface, $E_s(\lambda)$. This quantity was measured on 28 September 2001, using a MicroPro instrument, over the wavelength region 400-700nm. Therefore, when running Hydrolight starting at 350 nm (to include the effect of CDOM fluorescence) care should be taken on the extrapolation from the measured E_s value at the shortest wavelength (400 nm) to 350 nm. Figures 3.2.2-23 – 3.2.2-24 show how the choice of the wavelength region over which the model is run affects the model estimations of $E_d(z)$, $L_u(z)$, R_{rs} , L_w when the inelastic process of CDOM fluorescence is included (for $a_{CDOM}(440)=0.3 \text{ m}^{-1}$, and $S_{CDOM}=0.019$ according to spectrophotometric measurements performed using water samples collected from PI station on 28 September 2001). The model was run:

i) starting at 350 nm and using the measured E_s spectrum (400-700nm) with no extrapolation to 350 nm (in which case $E_{s(\lambda < 400 \text{ nm})} = E_{s(400 \text{ nm})}$, which results in an overestimation of $E_{s(\lambda < 400 \text{ nm})}$, and thus, in an overestimation of the contribution of CDOM fluorescence in the visible),

ii) starting at 400 nm and using the measured E_s spectrum (400-700 nm), in which case excitation by wavelengths shorter than 400 nm is not included in the model estimations,

iii) starting at 350 nm and using the measured E_s spectrum (400-700 nm) extrapolated to 350 nm based on the wavelength dependence estimated using RADTRAN model (Gregg and Carder, 1990).

The percent change in the estimated Lu , Ed , Rrs and Lw values between case 1 and case 3 and between case 2 and case 3, are shown in figures 3.2.2-23 – 3.2.2-24. The choice of the wavelength region over which the model is run when CDOM fluorescence is included in model estimations, affects the model output at the shorter wavelengths 400 - 532 nm, while longer wavelengths remain unaffected. The changes in $Ed(z)$ between case 1 (running Hydrolight starting at 350 nm with $E_{s(\lambda < 400 \text{ nm})} = E_{s(400 \text{ nm})}$) and case 3 (running Hydrolight starting at 350 nm and extrapolating $E_{s(400 \text{ nm})}$ to 350 nm using RADTRAN model), and between case 2 (running Hydrolight starting at 400 nm, thus not including CDOM excitation by wavelengths shorter than 400 nm) and case 3, are shown in figure 3.2.2-23(a) and are not large, less than 0.5 % at all depths (0-5m). The change in $Lu(z)$ is less than 2% between case 1 and case 3, with higher Lu values estimated in case 1, since the effect of CDOM fluorescence is somewhat overestimated due to the larger (than estimated by the atmospheric model) assumed E_s values below 400nm. The percent change in $Lu(z)$ between cases 2 and 3 reaches 3.4% at 443 nm (fig. 3.2.2-23(b)) with smaller Lu values at the blue wavelengths when CDOM excitation by ultraviolet wavelengths is not taken into account (case 2). These changes result in less than 2% changes in Rrs and Lw when running the model starting at 350 nm but not extrapolating

the E_s values measured using MicroPro to shorter wavelengths, and in 2-4% changes in R_{rs} and L_w when running the model starting at 400 nm instead of starting at 350 nm.

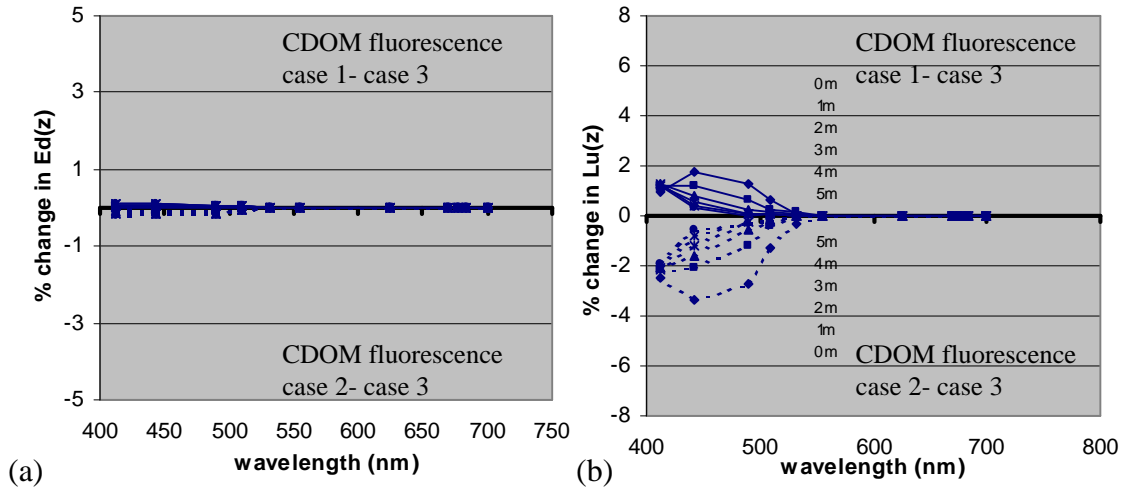


Figure 3.2.2-23: Percent differences in the estimated by the model (a) $Ed(z)$ and (b) $Lu(z)$ values, between case 1 and case 3 (positive % changes) and between case 2 and case 3 (negative % changes). The percent differences were estimated according to:

$$\frac{Ed_{(case1_or_case2)} - Ed_{(case3)}}{Ed_{(case3)}} \quad (\text{similarly for } Lu).$$

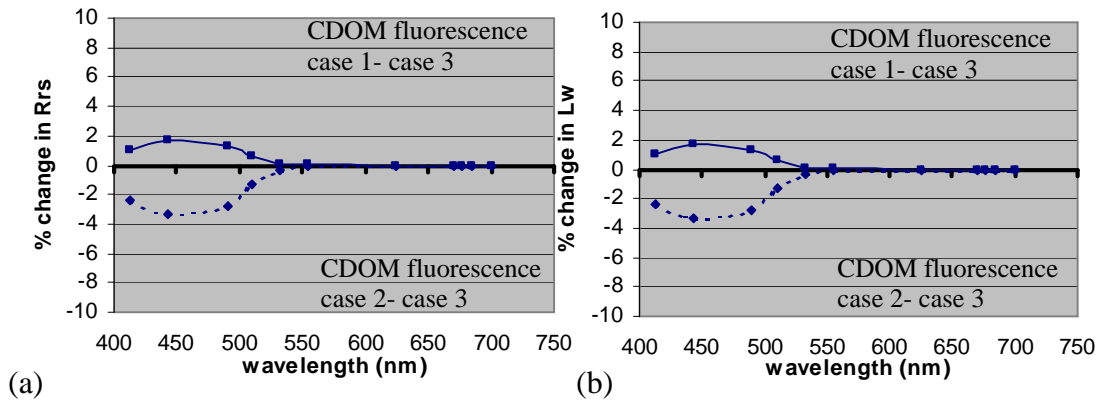


Figure 3.2.2-24: Percent differences in the model estimated R_{rs} and L_w values, between case 1 and case 3 (solid line) and between case 2 and case 3 (dotted line). The percent

differences were estimated as: $\frac{Rrs_{(case1_or_case2)} - Rrs_{(case3)}}{Rrs_{(case3)}}$ (similarly for L_w).

To study the effect of including CDOM fluorescence in the model estimations of water-leaving radiance and underwater radiance and irradiance profiles, the model was run:

i) including CDOM fluorescence for $a_{\text{CDOM}}(440)=0.3 \text{ m}^{-1}$, $S_{\text{CDOM}} = 0.019\text{nm}^{-1}$, which are the CDOM absorption at 440 nm and exponential slope measured spectrophotometrically using water samples collected from PI station on 28 September 2001,

ii) without including the effect of CDOM fluorescence

iii) including the effect of CDOM fluorescence but for 100% higher absorption by dissolved material at 440 nm than the one actually measured, $a'_{\text{CDOM}}(440)=0.6 \text{ m}^{-1}$.

CDOM fluorescence was the only inelastic scattering process included in the runs. In all cases, Hydrolight was run starting at 350 nm, and using as input information E_s values measured by the MicroPro instrument (400 –700 nm) and extrapolated to 350 nm using RADTRAN code. The contribution of CDOM fluorescence to the estimation of $L_u(z)$, $E_d(z)$, L_w and R_{rs} is shown in figures 3.2.2-25 - 3.2.2-26.

From the comparisons it is evident that CDOM fluorescence affects the underwater light field at wavelengths smaller than 530 nm. The effect in the model estimations of $E_d(z)$ is less than 0.5%, for all depths (0-5m). The effect of excluding CDOM fluorescence in the model estimations of $L_u(z)$ (percent changes between case 1 and case 2) is less than 4-5% , with maximum values at 443-490 nm. The effect of including CDOM fluorescence, with $a_{\text{CDOM}}(440)=0.6 \text{ m}^{-1}$, instead of $a_{\text{CDOM}}(440)= 0.3 \text{ m}^{-1}$ (which was the CDOM absorption actually measured at PI on 28 September 2001), results in 4-5 % irradiance increases (since CDOM fluorescence gets larger as CDOM absorption increases), with maximum percent changes at 443-490 nm, close to the surface. The

effect of including CDOM fluorescence in the model estimations of remote sensing reflectance, R_{rs} , and water leaving radiance, L_w , is also in the order of 4-5 % maximum within the blue wavelength region 443-490 nm.

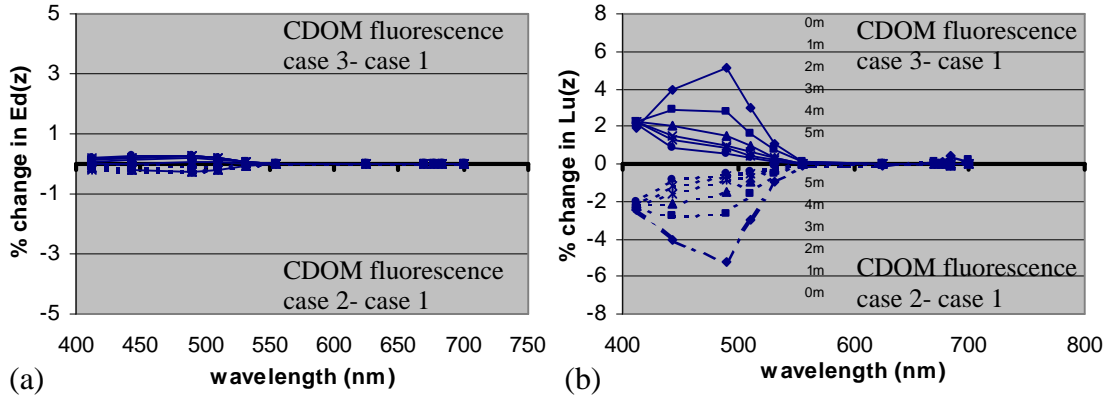


Figure 3.2.2-25: Percent differences in the model estimated (a) $Ed(z)$ and (b) $Lu(z)$, between case 1 (CDOM fluorescence included, for the measured CDOM absorption spectrum, $a_{CDOM}(440)=0.3m^{-1}$ and $S_{CDOM} = 0.019nm^{-1}$) and case 2 (CDOM fluorescence not included), and between case 1 and case 3 (CDOM fluorescence included, for $a_{CDOM}(440)=0.6m^{-1}$). The percent differences were estimated according to:

$$\frac{Ed_{(no-CDOM-fluor)} - Ed_{(a_{CDOM}=0.3)}}{Ed_{(a_{CDOM}=0.3)}} \text{ and } \frac{Ed_{(a_{CDOM}=0.6)} - Ed_{(a_{CDOM}=0.3)}}{Ed_{(a_{CDOM}=0.3)}} \text{ (similarly for Lu).}$$

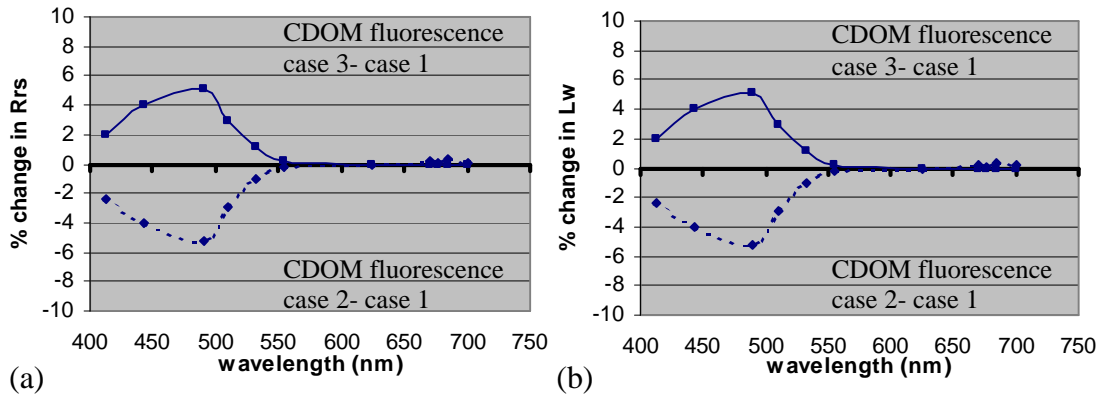


Figure 3.2.2-26: Percent differences in the estimated by the model R_{rs} and L_w values, between case 1 (CDOM fluorescence included, for the measured CDOM absorption spectrum, $a_{CDOM}(440)=0.3m^{-1}$ and $S_{CDOM} = 0.019nm^{-1}$) and case 2 (CDOM fluorescence not included), and between case 1 and case 3 (CDOM fluorescence included, for $a_{CDOM}(440)=0.6m^{-1}$). The percent differences were estimated as:

$$\frac{Rrs_{(no-CDOM-fluor)} - Rrs_{(a_{CDOM}=0.3)}}{Rrs_{(a_{CDOM}=0.3)}} \text{ and } \frac{Rrs_{(a_{CDOM}=0.6)} - Rrs_{(a_{CDOM}=0.3)}}{Rrs_{(a_{CDOM}=0.3)}} \text{ (similarly for } L_w).$$

Raman Scattering

To study how the process of Raman scattering affects the results of model estimations of underwater radiation fields, Hydrolight was run for two cases, including and excluding Raman scattering. CDOM and chlorophyll fluorescence were not included in these runs. In both cases, Hydrolight was run starting at 350 nm, and E_s values, measured using the MicroPro instrument (400–700 nm) and extrapolated to 350 nm using RADTRAN, were used as input information. The contribution of Raman scattering to the estimation of $L_u(z)$, $E_d(z)$, L_w and R_{rs} is shown in figures 3.2.2-27 – 3.2.2-28. The Raman scattering process operates at all wavelengths and depths, but the inelastically scattered light is usually negligible compared to the ambient solar light at shallow depths and blue-green wavelengths (fig. 3.3.3-27) (Mobley, 1994). K_u is also more sensitive than K_d to the effects of Raman-scattered light, since elastic backscattering is much weaker than elastic forward scattering and therefore, the Raman contribution will be relatively greater to upwelling than to downwelling directions (scattering phase function for Raman is symmetric about ψ).

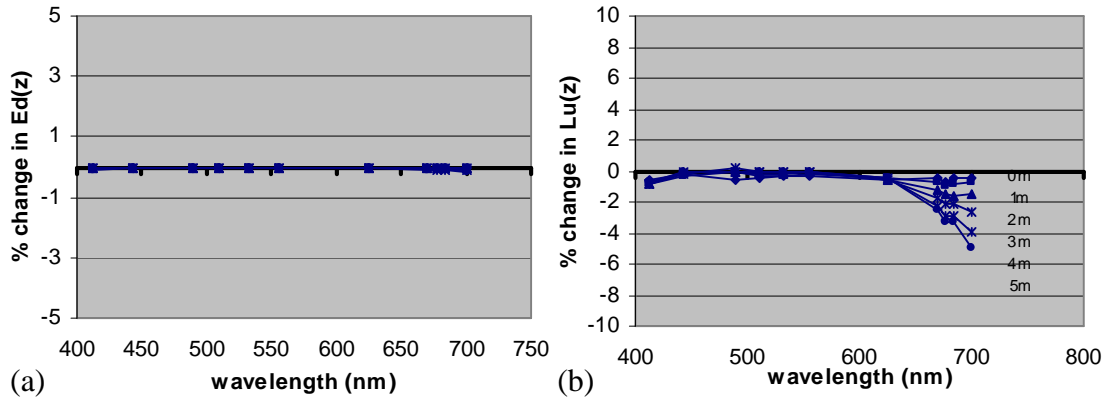


Figure 3.2.2-27: Percent differences in the estimated by the model (a) $Ed(z)$ and (b) $Lu(z)$ values, between case 1 (Raman scattering included) and case 2 (Raman scattering not included), estimated as: $\frac{Ed_{(no_Raman)} - Ed_{(Raman)}}{Ed_{(Raman)}}$ (similarly for Lu) at depths 0-5m.

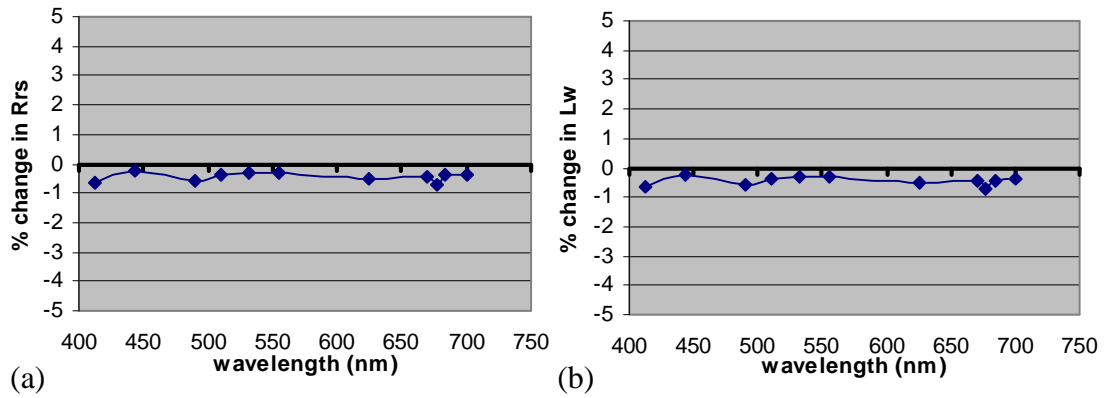


Figure 3.2.2-28: Percent differences in the model calculated (a) Rrs and (b) Lw values, estimated according to: $\frac{Rrs_{(no_Raman)} - Rrs_{(Raman)}}{Rrs_{(Raman)}}$ (similarly for Lw).

3.2.2.7 Changes in percent cloud cover

One of the parameters that can be specified in Hydrolight to perform the model simulations is information on the sky conditions and the percent cloud fraction. When measurements of the total incident sky irradiance, $E_s(\lambda)$, are provided as input information for the model estimations, then information on the percent cloud cover is used in the estimation of the diffuse and direct components of the sky downwelling irradiance (RADTRAN Gregg and Carder (1990) model) and the estimation of the angular distribution of radiances (Harrison and Coombes, 1988, model). Cloud conditions also affect the reflectance and transmittance of light through the water interface. Information on the cloudiness is based on sky observations performed during the measurements at each site, and frequently is associated with some uncertainty. Therefore, several Hydrolight runs were performed using as input information IOPs measured at PI station on 28 September 2001, to study what is the effect of varying the cloud fraction between 0-100% on the model estimations.

During the measurements performed at PI station on 28 September 2001, the sky was clear, with 0-5% cloud cover. Hydrolight was run assuming cloud cover of 0%, 10%, 30%, 50%, 80% and 100% to study the effect of cloudiness on the model estimations of $L_u(z)$, $E_d(z)$, R_{rs} and L_w . All other parameters were kept constant during the runs (wind speed=5m/s, $sza=20^\circ$, absorption, scattering and backscattering). Measurements of $E_s(\lambda)$, performed using the MicroPro instrument were provided as input information and kept constant during the runs. Inelastic scattering processes (Raman scattering and CDOM and chlorophyll fluorescence) were included in all runs. The results are shown in figures

3.2.2-29 – 3.2.2-31. Similar Hydrolight runs were also performed for $\text{sza}=50^\circ$ (fig. 3.2.2-31 (a)-(d)).

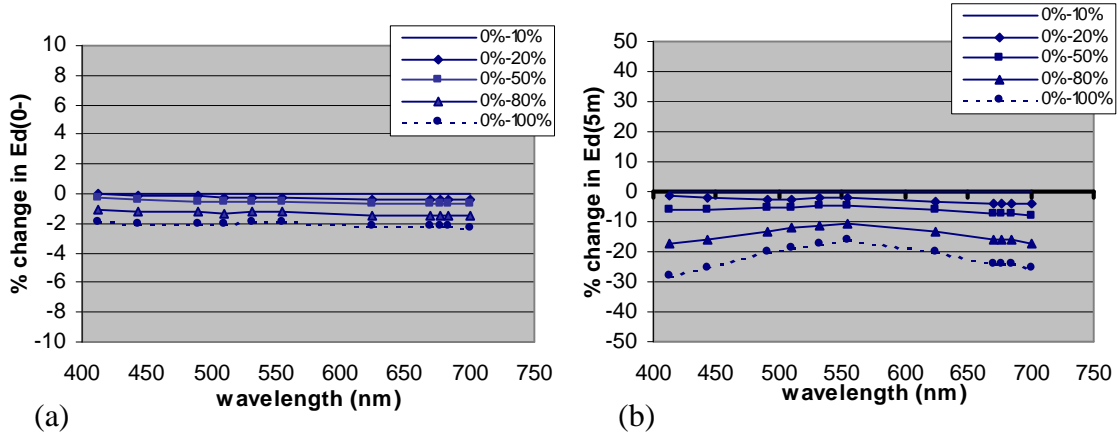


Figure 3.2.2-29: Percent differences in estimated Ed values (a) just below the water surface and (b) at 5 meters below the water surface, for clear skies (0% cloudiness) and cloud cover of 10, 30, 50, 80 and 100%. The percent differences were estimated

according to: $\frac{Ed_{(clouds)} - Ed_{(clear)}}{Ed_{(clear)}} \text{ (sza}=20^\circ\text{)}$.

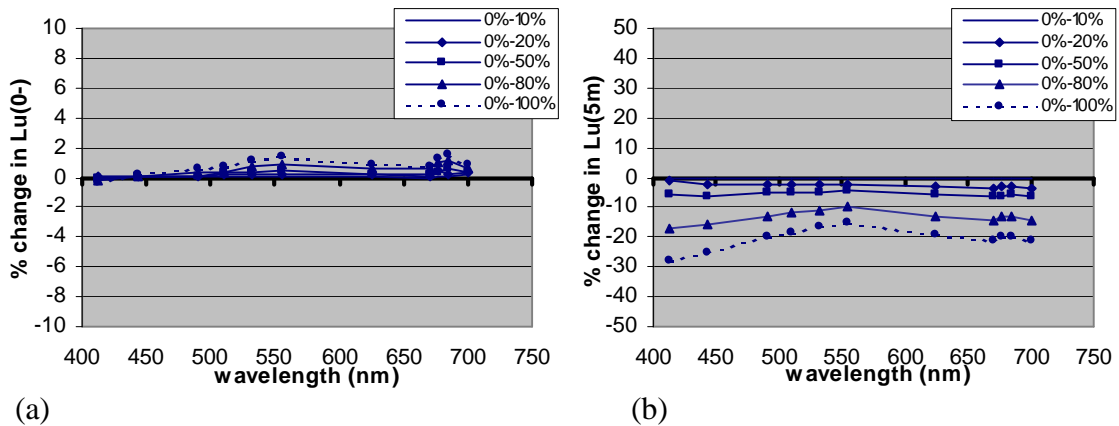


Figure 3.2.2-30: Percent differences in estimated Lu values (a) just below the water surface and (b) at 5 meters below the water surface, for clear skies (0% cloudiness) and cloud cover of 10, 30, 50, 80 and 100%. The percent differences were estimated

according to: $\frac{Lu_{(clouds)} - Lu_{(clear)}}{Lu_{(clear)}} \text{ (sza}=20^\circ\text{)}$.

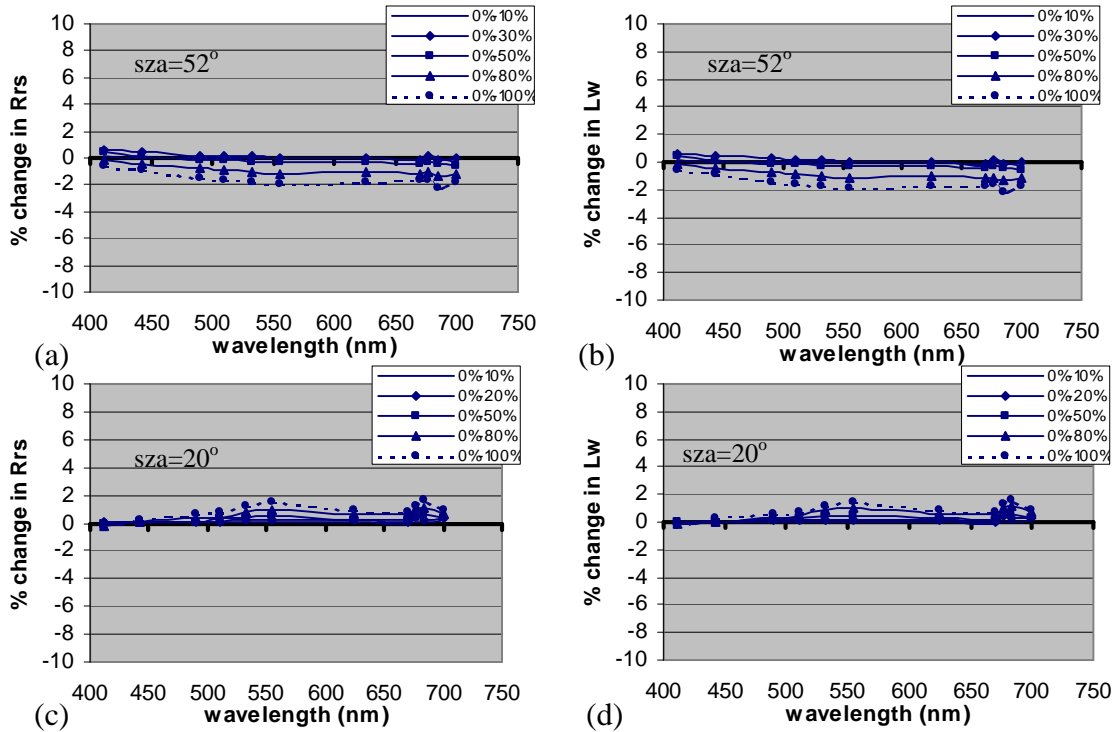


Figure 3.2.2-31: Percent differences in estimated (a) Rrs ($sza=52^\circ$), (b) Lw ($sza=52^\circ$), (c) Rrs ($sza=20^\circ$), and (d) Lw ($sza=20^\circ$) for clear skies (0% cloudiness) and cloud cover of 10, 30, 50, 80 and 100%. The percent differences were estimated according to:

$$\frac{Rrs_{(clouds)} - Rrs_{(clear)}}{Rrs_{(clear)}} \quad (\text{similarly for Lw}).$$

When measured Es values are used as input information to run the model, uncertainties in the observed cloud coverage do not have a large effect on the model estimated Lw and Rrs values. For the specific case studied, changes in the cloud coverage between 0% (clear skies) and 100% (overcast) resulted in changes of less than 2% in Lw, for both sets of Hydrolight runs ($sza=52^\circ$, $sza=20^\circ$). The percent change in the estimated Ed(z) and Lu(z) between running the model for 0% and 100% cloud fraction (in cases when information on cloud cover is not available) can be significant deeper in the water column (10-30 % depending on the wavelength). However, changing the cloud cover from 0% to 10 % or 30 %, results in less than 5% change in the estimated Lu(z) and Ed(z) at all depths.

3.2.2.8 Changes in surface wind speed, u (m/s)

To study the effect of surface wind speed on the model estimations of $Ed(z)$, $Lu(z)$, Rrs and Lw , several Hydrolight runs were performed using as input information measurements of incident irradiance, Es , and water optical properties performed at PI station on 28 September 2001 (for $sza=52^\circ$), and varying the surface wind speed from 0 to 10 m/s. Figure 3.2.2-32 shows the percent changes in $Ed(z)$ just below the water surface and at 5m depth, estimated as: $\frac{Ed(u_i) - Ed(u_0)}{Ed(u_0)}$, where $u_0=0$ m/s and $u_i = 1, 3, 5, 7, 10$ m/s. The percent changes in $Ed(z)$ are in the order of 2%. The percent changes in estimated $Lu(z)$ just below the water surface and at 5m depth, are shown in fig. 3.2.2-33. As in the case of downward irradiances, the percent changes in the upwelling radiances were found to be in the order of 2%. The effect of varying the surface wind speed on the estimated remote sensing reflectances, Rrs , and the water leaving radiances, Lw , is shown in fig. 3.2.2-34. The percent change in Lw and Rrs is less than 2%.

The model simulations suggest that changing the surface wind-speed in the range 0 – 10 m/s affects the underwater upwelling radiances and downwelling irradiances by less than 2% for the specific set of measured boundary conditions and water inherent optical properties. However, changes in the wind speed may significantly affect estimations of total $Lu(0^+)$ just above the water surface, since the total upwelling irradiance just above the water surface is the sum of the underwater upwelling radiance transmitted through the water interface, Lw , plus the downwelling sun and sky irradiance just above the water surface that is reflected upward by the sea surface itself.

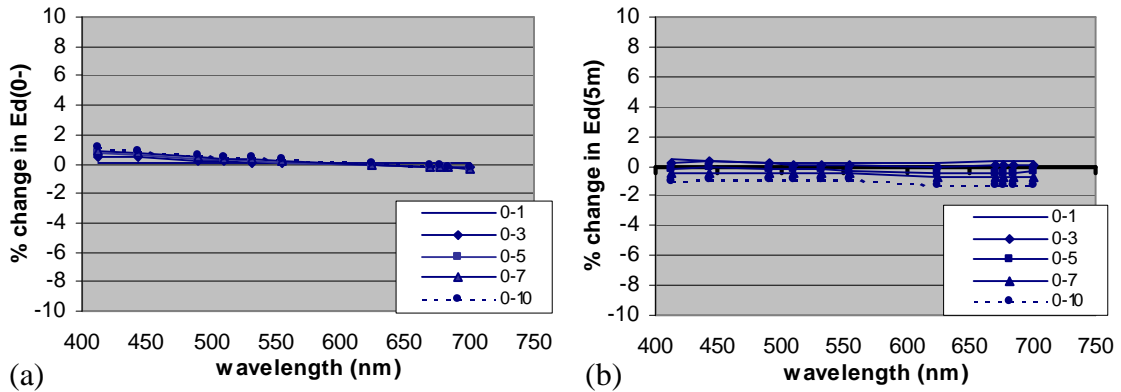


Figure 3.2.2-32: Percent difference in estimated Ed values (a) just below the water surface and (b) at 5 meters below the water surface, for wind speed, u_i , 1, 3, 5, 7, 10 m/s

(compared to 0m/s). The % differences were estimated according to: $\frac{Ed_{(u_i)} - Ed_{(u=0)}}{Ed_{(u=0)}}$

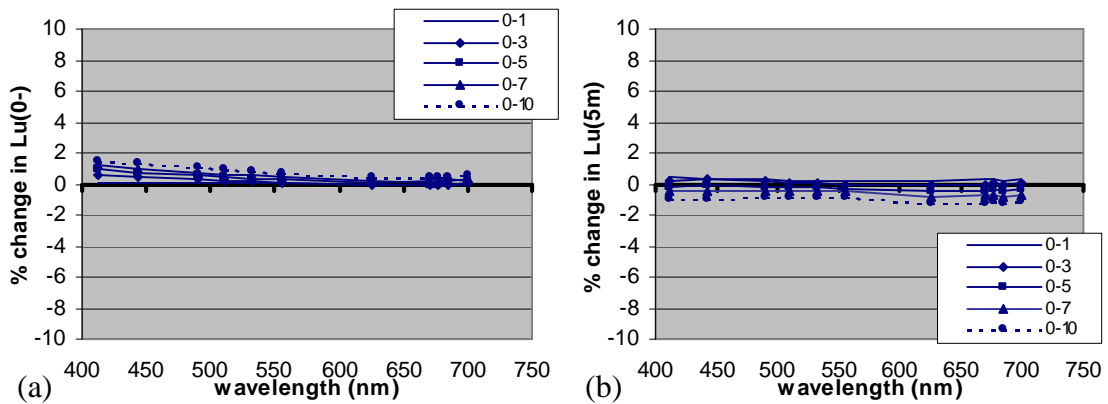


Figure 3.2.2-33: Percent difference in estimated Lu (a) just below the water surface and (b) 5 meters below the water surface, for wind speed, u_i , 1, 3, 5, 7, 10 m/s (compared to

$u=0$ m/s). The percent differences were estimated according to: $\frac{Lu_{(u_i)} - Lu_{(u=0)}}{Lu_{(u=0)}}$

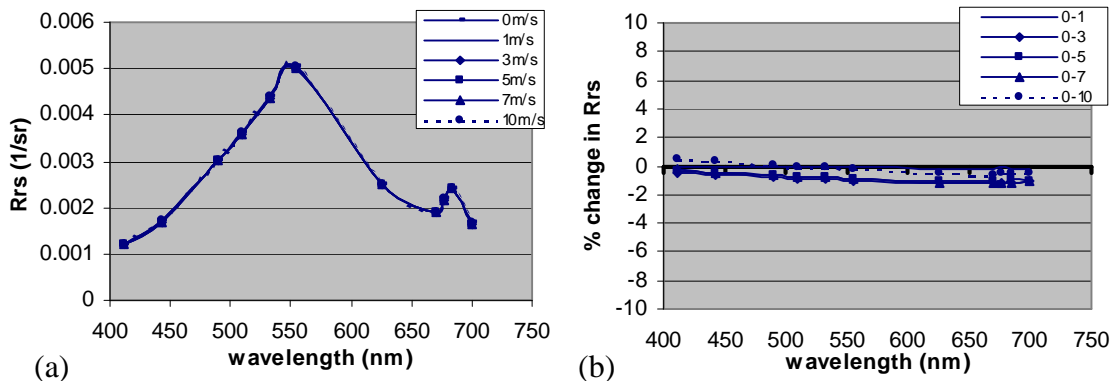


Figure 3.2.2-34:(a) Estimated Rrs for various wind speeds (0, 1, 3, 5, 7, 10m/s) (b) percent differences in estimated Rrs values for 1, 3,5, 7, 10 m/s (compared to 0 m/s).

Percent differences were estimated according to: $\frac{Rrs_{(u_i)} - Rrs_{(u=0)}}{Rrs_{(u=0)}}$ ($sza=52^\circ$).

Similar Hydrolight runs were also performed for $\text{sza} = 20^\circ$ to study the effect of changing the surface wind speed on L_w and R_{rs} , at a lower solar zenith angle (fig. 3.2.2-35). A solar zenith angle of 20° is closer to the average solar zenith angle for the measurements performed during the Chesapeake Bay late-spring. In this case too, changing the surface wind-speed, within the range 0 – 10 m/s, affects by less than 2% the estimated upwelling radiance, L_u , just below the water surface, the water leaving radiance, L_w , and the remote sensing reflectance, R_{rs} .

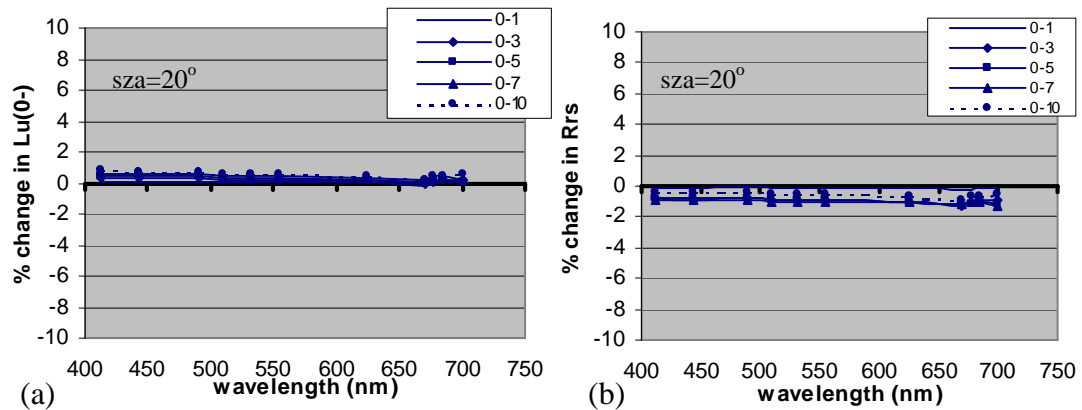


Figure 3.2.2-35: Percent difference in estimated (a) L_u values just below the water surface and (b) R_{rs} , for $\text{sza}=20^\circ$, and for wind speed of 1, 3, 5, 7, 10 m/s (compared to 0 m/s). The percent differences were estimated according to: $\frac{Lu_{(ui)} - Lu_{(u=0)}}{Lu_{(u=0)}}$ and

$$\frac{Rrs_{(ui)} - Rrs_{(u=0)}}{Rrs_{(u=0)}}$$

3.3 “Closure” Experiment in the Chesapeake Bay waters - Methodology

One of the main objectives of this project has been to study the underwater radiation fields, water-leaving radiances, $L_w(\lambda)$, and remote sensing reflectances, $R_{rs}(\lambda)$ within the estuarine Chesapeake Bay environment, estimated, under various atmospheric conditions and in-water properties, using both measurements and theoretical radiative-transfer model calculations. One of the issues was to study the degree of agreement or disagreement between the model simulations and in-situ observations of underwater radiation fields, and to obtain a better understanding of the sources and magnitude of errors associated with these two different methods of estimating $L_w(\lambda)$ and $R_{rs}(\lambda)$. Measured boundary conditions and in-water inherent optical properties can be used as input information to perform the model estimations of underwater and water-leaving radiances. To what extent can we obtain “closure” between the measured and the theoretically estimated radiation fields, in the optically complex estuarine waters of Chesapeake Bay?

3.3.1 Radiative Transfer Model Calculations using Hydrolight

The Hydrolight radiative transfer code was used to estimate underwater, upwelling and downwelling radiance and irradiance profiles, and water-leaving radiances during some of the cruises performed in the framework of our detailed measurements program in the Chesapeake Bay. Model simulations were performed for those days when upwelling radiance (L_u) and downwelling irradiance (E_d) profile measurements of high vertical resolution were performed, using a MicroPro multi-spectral profiler.

The quantities that were used as input information to perform the model estimations, included: i) Total downwelling surface irradiance, $E_s(\lambda)$, measured using the OCI-507 Satlantic surface sensors (the Greg and Carder GCIRRAD model is used in Hydrolight to estimate the diffuse to direct irradiance ratio). ii) Total absorption, $a(\lambda)$, and attenuation, $c(\lambda)$, coefficients (by all substances within the water body, other than pure water), measured using an AC9 instrument (scattering $b(\lambda)$, can be estimated as the difference $b=c-a$). The absorption measurements were corrected for scattering assuming that absorption at 715 nm equals the absorption a_{t-w} measured using the CARY spectrophotometer (particulate absorption was corrected for pathlength amplification using $\beta=1.5$, according to the discussion in paragraph 2.2.2.3). iii) Total backscattering coefficients, $b_b(\lambda)$, measured using an ECO-VSF instrument iv) observations of surface wind-speed and cloudiness, performed during the in-situ measurements v) solar zenith angle (sza) estimations, performed using information on the exact time of the measurements and the site location (latitude and longitude). The model was run using the Pope and Fry (1997) absorption values for pure water and the Smith and Baker (1981) scattering coefficients for pure sea-water, with the Rayleigh-like pure-water scattering phase function. The water column was assumed to be infinitely deep below the greatest depth of interest. Inelastic processes, such as Raman scattering, CDOM fluorescence and chlorophyll fluorescence were included in all model runs. Measurements of chlorophyll-a concentration were used as input information to estimate the chlorophyll fluorescence. Measurements of CDOM absorption, $a_{CDOM}(440)$, and exponential slope, S_{CDOM} , obtained by using the CARY spectrophotometer, were used as input information in the model

estimations of CDOM fluorescence. The model runs were performed within the 350-700 nm wavelength range, to include the relevant excitation and emission wavelengths.

3.3.2 In-situ measurements of underwater and water-leaving radiances

A Satlantic MicroPro free-falling radiometer was used in 7 of our cruises (table 3.3-1) in Chesapeake Bay to measure profiles of upwelling radiance, L_u , and downwelling irradiance, E_d , in the water column. The MicroPro measures in-water profiles of L_u and E_d at 14 bands (400, 412, 443, 455, 490, 510, 532, 554, 564, 590, 625, 670, 684, 700 nm). It has a smaller diameter (6.4 cm) compared to other radiometric instruments and as a result is less subject to instrument self-shading (Harding and Magnuson, 2001).

Table 3.3-1: Dates of cruises in the Bay, and instrumentation for measurements of radiation fields

Date of cruise	<i>Instrument used for radiation fields</i>
2001, June 4	Satlantic OCI-200
2001, June 11	Satlantic OCI-200
2001, June 25	Satlantic OCI-200
2001, July 9	Satlantic OCI-200
2001, September 21	Satlantic SMSR
2001, September 26	Satlantic MicroPro
2001, September 28	Satlantic MicroPro
2001, October 4	Satlantic OCI-200
2001, October 30	Satlantic MicroPro
2001, November 13	Satlantic OCI-200
2002, May 6	Satlantic MicroPro
2002, May 15	Satlantic MicroPro
2002, May 22	Satlantic MicroPro
2002, June 6	Satlantic OCI-200
2002, June 18	Satlantic OCI-200
2002, June 28	-
2002, November 8	Satlantic MicroPro

Three MicroPro casts were made at each one of the stations, during each cruise, and all casts were completed within 5-8 minutes. Figure 3.3-1 shows an example of upwelling

radiance, $Lu(z)$, and downwelling irradiance, $Ed(z)$, profile measurements (3 casts) performed at PI station on 28 September 2001 (similarly for all stations during the rest of the cruises). Simultaneous measurements of surface irradiance (E_s) were obtained using the Surface Reference Satlantic OCR-507 Irradiance sensors. Figure 3.3-2 shows the measurements of downwelling surface irradiance, E_s , (3 casts) performed at PI station on 28 September 2001 (similarly for all stations during the rest of the cruises).

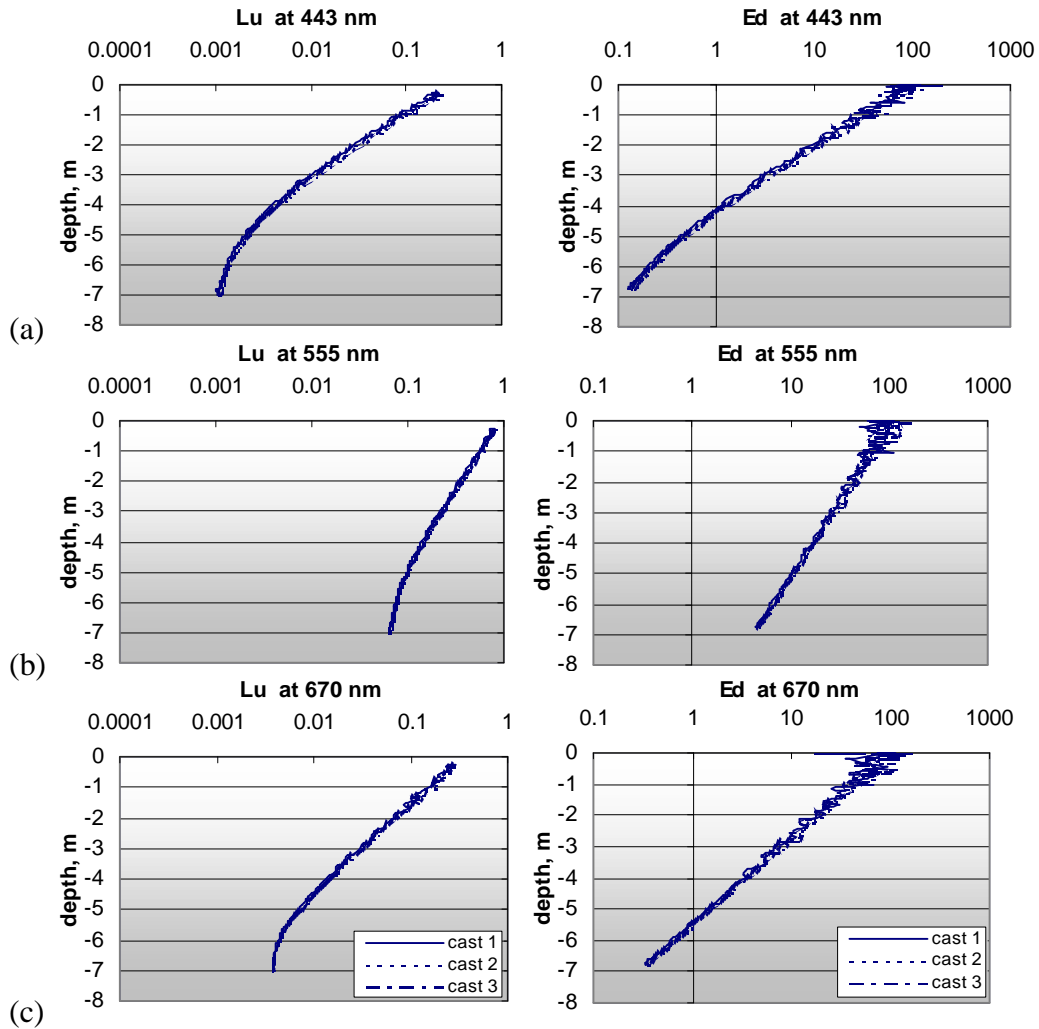


Figure 3.3-1: Measurements of $Lu(z)$ (in $\mu Wnm^{-1}cm^{-2}sr^{-1}$) and $Ed(z)$ (in $\mu Wnm^{-1}cm^{-2}$) (logarithmic scale) at (a) 443, (b) 555 and (c) 670 nm, performed at PI station on 28 September 2001, using the MicroPro Satlantic multi-spectral profiler.

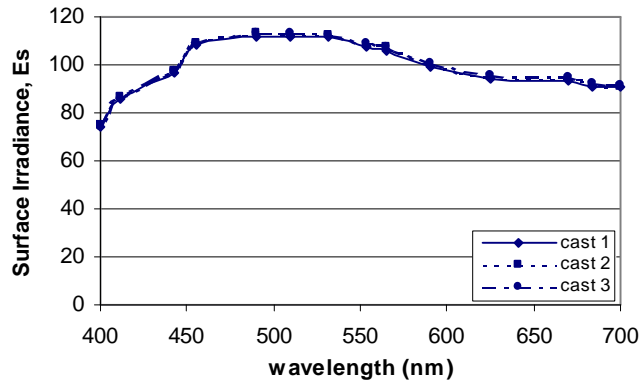


Figure 3.3-2: Measurements of downwelling surface irradiance, E_s , (in $\mu\text{Wnm}^{-1}\text{cm}^{-2}$) performed at PI station on 28 September 2001

Casts characterized by large tilt-angles and changing cloudiness conditions were not included in the following comparisons. Therefore, in some cases only one cast was used to estimate L_w , while in cases when all casts were of good quality L_w was estimated as the average of all 3 casts. Measurements of $L_u(z)$ were corrected for the self-shading effect according to Gordon and Ding (1992), Zibordi and Ferrari (1995) (the correction methodology is discussed in paragraph 2.2.2.6). The radiance measurements were also corrected for the depth offset between the E_d and L_u sensors.

To estimate the water-leaving radiance, L_w , the in-water measurements of upwelling radiance, $L_u(z)$, must be extrapolated to $z = 0^-$ and, then, transmitted through the water-air interface. According to the measurements performed during the specific days when the MicroPro was used, the upwelling radiances decreased approximately exponentially with depth, at least down to a depth of 3-4 m (figure 3.3-1 for PI station, 28 Sept 2001, and similarly for other cases). Therefore, $L_u(z)$ can be expressed as :

$$L_u(z, I) = L_u(0, I) \cdot \exp(-K \cdot z) \quad (3.3-1)$$

where $Lu(0, \lambda)$ is the upwelling radiance just beneath the water's surface and K is the diffuse attenuation coefficient for the radiance. For the measurements performed during the specific days in Chesapeake Bay, K can be considered to be, to a good approximation, constant down to a depth of 3-4 m. Simultaneous measurements performed using the AC-9 instrument show that the total absorption in these waters was also constant down to a depth of 3-4 m (fig. 2.3-4, chapter 2). The upwelling radiance just below the water's surface, $Lu(0^-, \lambda)$ was estimated through non-linear least squares fits of the measured upwelling radiances, $Lu(z, \lambda)$, according to $y = a \cdot \exp(b \cdot x)$, where $y = Lu(z, \lambda)$, $\alpha = Lu(0^-, \lambda)$, $b = K$ (constant) and $x = \text{depth}$. Nonlinear regression was performed using the Marquardt-Levenberg algorithm (SigmaStat software) to find the coefficients (parameters) of the independent variables giving the 'best fit' between the equation and the data. To compare with the nonlinear fits, linear least squares regression fits of the natural logarithm of the measured upwelling radiances, $\ln[Lu(z, \lambda)]$, were also estimated, according to $y = a + b \cdot x$, where $y = \ln[Lu(z, \lambda)]$, $\alpha = \ln[Lu(0^-, \lambda)]$, $b = K$ (constant) and $x = \text{depth}$. The advantage of using nonlinear exponential fits, is that relatively greater weighting is given to the larger and more accurate values of upwelling radiances, $Lu(z, \lambda)$, measured closer to the water's surface. As a result, estimations of $Lu(0^-, \lambda)$, from non-linear fits are more accurate. The R^2 (square of correlation coefficient) values of the non-linear exponential fits were in most of the cases larger than 0.99.

To estimate the water-leaving radiance, L_w , the upwelling radiance just-beneath the water surface, $Lu(0^-, \lambda)$, was propagated through the interface according to the relationship:

$$L_w(\mathbf{l}, \mathbf{q}, \mathbf{j}) = Lu(0^-, \mathbf{l}, \mathbf{q}', \mathbf{j}) \frac{(1 - r(\mathbf{q}', \mathbf{q}))}{n_w^2} \quad (3.3-2)$$

where θ' is the direction of the upward traveling photons incident from the water body onto the water surface, θ is the direction of the transmitted photons, $r(\theta', \theta)$ is the Fresnel reflectance for the associated directions θ' and θ , and n_w is the index of refraction of water ($n_w \sim 1.34$). According to Austin and Halikas (1976) the index of refraction of seawater changes with temperature and wavelength. At a given temperature T , $n_w(\lambda, T)$ decreases by about 1% throughout the visible spectrum, while at a given wavelength, $n_w(\lambda, T)$ decreases by about 0.1% for an increase in temperature from 0 to 30°C. However, these changes are very small and the index of refraction of seawater can be considered constant to a good approximation. The behavior of the Fresnel reflectance, $r(\theta', \theta)$, as a function of the incident angle θ' , and for the minimum and maximum values of the real index of refraction n_w encountered in natural waters (Mobley, 1994) is shown in figure 3.3-3. According to Mobley (1994), for rays with incident angles of less than 30° the reflectance is practically constant (2 to 3%) and the transmittance is $(1 - r(\theta', \theta)) = 0.98$. For angles greater than 30° the reflectance increases rapidly with total internal reflection, $r(\theta', \theta) = 1$, occurring when θ' for 'water-incident' rays (upward traveling photons incident from the water body to the water surface) exceeds the critical angle ($\theta'_c = 48^\circ$ for $n_w = 1.34$).

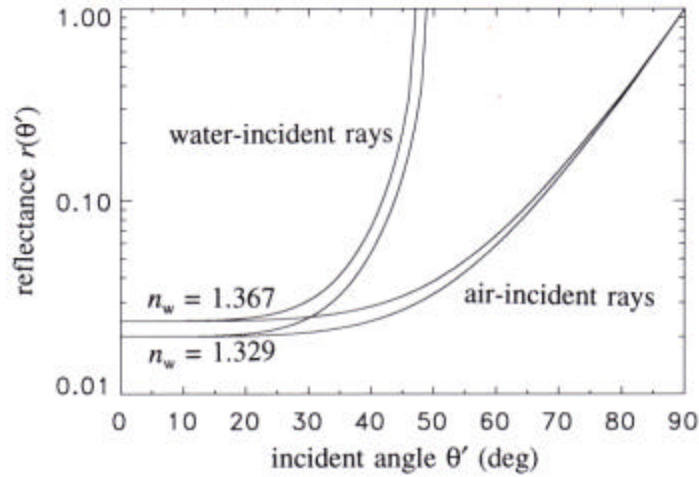


Figure 3.3-3: Fresnel reflectance, r , as a function of incident angle θ' , for index of refraction of seawater $n_w=1.367$ and $n_w=1.329$. After Mobley (1994)

For our in-water $L_u(z)$ measurements, the zenith angle of water leaving radiance and the nadir angle of in-water upward radiance, are zero ($\theta' = \theta = 0$) and the transmittance is $(1 - \rho(\theta', \theta)) \approx 0.98$. Therefore, the water leaving radiance $L_w(\lambda)$ can be estimated from the upwelling radiance just beneath the water, $L_u(0^-, \lambda)$, as :

$$L_w(\mathbf{l}, \mathbf{q}, \mathbf{j}) = L_u(0^-, \mathbf{l}, \mathbf{q}', \mathbf{j}) \frac{(1 - r(\mathbf{q}', \mathbf{q}))}{n_w^2} \quad (3.3-3)$$

$$L_w(\mathbf{l}) = L_u(0^-, \mathbf{l}) \frac{0.98}{(1.34)^2} \quad (3.3-4)$$

or:

$$L_w(\lambda) = 0.544 L_u(0^-, \lambda) \quad (3.3-5)$$

3.4 “Closure” Experiment in the Chesapeake Bay waters - Results

Figures 3.4-1 – 3.4-6 show the measured and the model estimated downwelling irradiances (E_d) and upwelling radiances (L_u), at wavelengths 412, 555 and 670 nm, for measurements performed during the three 2001 fall cruises (26 and 28 September, 30 October) and the three 2002 spring cruises (6, 15 and 22 May). During those cruises L_u and E_d profile measurements of high vertical resolution were performed using a MicroPro multi-spectral profiler. Comparisons were not made for certain sites during those cruises (changing cloudiness conditions resulted in highly variable E_s measurements during all casts at JT on 28 September 2001, no backscattering measurements were available for TI and JT stations on 30 October 2001).

The model estimated E_d and L_u values were in good agreement with the measurements, especially within the first three meters in the water column. The percent differences at 1m below the water surface are shown in table 3.4-1 for L_u and table 3.4-2 for the downwelling irradiance, E_d . Percent differences for $E_d(z)$ were estimated from:

$$\text{Percent difference} = \frac{E_{d(\text{InSitu})} - E_{d(\text{model})}}{\frac{1}{2}(E_{d(\text{InSitu})} + E_{d(\text{model})})} \cdot 100 \quad (3.4-1)$$

and similarly for $L_u(z)$. At 15 out of 17 cases, the percent differences between measured and model-estimated E_d values were less than 9% at 443 nm (absolute average of 6.5%), less than 10% at 555 nm (absolute average of 5.2%) and less than 11% at 670 nm (absolute average of 5.9%). For the upwelling radiance, L_u , the percent differences between model-estimated and the measured values at 1m depth below the water surface, were, in almost all of the cases, less than 15.5% at 443 nm (with an absolute average of

7.8%), less than 19% at 555 nm (absolute average of 12.8%), and less than 22% at 670 nm (absolute average of 8.7%).

Figures 3.4-7 – 3.4-12 show the comparison between water-leaving radiances estimated using the in-situ measurements of upwelling radiances, $LW_{(InSitu)}$, (methodology described previously) and those estimated by Hydrolight, $LW_{(model)}$, (using as input information measured boundary conditions and IOPs). The percent differences, shown in table 3.4-3, were estimated according to:

$$\text{Percent difference} = \frac{LW_{(InSitu)} - LW_{(model)}}{\frac{1}{2}(LW_{(InSitu)} + LW_{(model)})} \cdot 100 \quad (3.4-2)$$

The model estimated water-leaving radiances were in very good agreement with those based on measurements of upwelling radiances, in most of the cases studied. In almost all of the cases, the percent differences between ‘measured’ and ‘model-estimated’ water-leaving radiances, were less than $\pm 11.6\%$ at 443 nm (with an absolute average of 6.25%), less than $\pm 15.2\%$ at 555nm (with an absolute average of 8.3%) and less than $\pm 11.5\%$ at 670nm (with an absolute average of 6.85%).

Table 3.4-1: Percent differences in estimated upwelling radiances, Lu, at depth = 1 m, and various wavelengths (412-685 nm) using in-situ measurements and model simulations (negative values correspond to $Lu_{(InSitu)}$ estimates smaller than the Hydrolight estimated $Lu_{(model)}$).

Station/Date	412	443	490	510	532	554	670	685
PI, 26 Sept '01	-9.40	-6.14	-13.72	-8.42	-7.18	-11.39	6.69	-12.29
HB, 26 Sept '01	-7.20	-0.81	-14.62	-13.23	-17.72	-14.83	0.59	-11.64
TI, 26 Sept '01	-14.33	-7.02	-11.82	-11.51	-14.32	-10.74	8.24	-7.90
PI, 28 Sept '01	-3.95	-3.37	-9.05	-1.94	-0.81	-5.76	8.84	-3.94
HB, 28 Sept '01	-21.14	-17.21	-26.40	-19.53	-19.45	-18.84	-3.45	-17.97
TI, 28 Sept '01	-14.27	-12.99	-25.79	-21.39	-19.32	-19.24	-22.02	-38.17
PI, 30 Oct '01	7.93	-10.06	-16.49	-7.18	-2.87	-10.96	-7.28	-23.06
HB, 30 Oct '01	-1.20	-1.06	-13.06	-6.70	-6.05	-16.05	-3.20	-16.83
HB, 6 May '02	1.63	-3.69	-20.50	-13.63	-17.42	-14.00	-24.65	-36.96
TI, 6 May '02	16.16	6.29	-17.80	-14.93	-13.61	-12.17	-4.72	-13.98
PI, 15 May '02	2.81	-1.18	-23.25	-19.08	-17.92	-21.17	-14.95	-30.95
TI, 15 May '02	-7.52	-5.83	-21.20	-11.70	-8.09	7.31	21.62	5.80
JT, 15 May '02	14.82	11.81	0.39	-1.30	-6.28	-8.15	-0.36	-10.68
PI, 22 May '02	-10.09	-17.42	-28.95	-25.13	-20.31	-7.41	-0.56	-17.22
HB, 22 May '01	5.55	4.07	-14.33	-21.13	-21.90	-11.63	-5.60	-17.09
JT, 22 May '02	16.97	15.51	-19.50	-16.92	-16.47	-16.36	-6.76	-16.13

Table 3.4-2: Percent differences in estimated downwelling irradiances, Ed, at depth =1 m, and various wavelengths (412-685 nm) using in-situ measurements and model simulations (negative values correspond to $Ed_{(InSitu)}$ estimates smaller than the Hydrolight estimated $Ed_{(model)}$).

Station/Date	412	443	490	510	532	554	670	685
PI, 26 Sept '01	20.77	14.84	9.45	6.76	6.19	-0.36	11.98	7.87
HB, 26 Sept '01	11.13	4.48	-2.62	-7.65	-9.13	-10.71	-3.14	-5.12
TI, 26 Sept '01	8.83	5.03	1.68	-1.69	-0.69	-4.20	6.54	3.58
PI, 28 Sept '01	24.93	18.30	9.56	8.95	12.12	0.94	9.58	6.43
HB, 28 Sept '01	3.69	1.60	-0.26	0.46	1.06	-7.93	-4.26	-5.63
TI, 28 Sept '01	-5.11	-7.06	-7.97	-9.01	-8.62	-12.43	-5.08	-7.58
PI, 30 Oct '01	26.36	5.84	-0.92	-1.25	0.91	-1.28	12.21	5.97
HB, 30 Oct '01	10.74	4.01	1.47	2.91	4.03	-2.20	2.73	-0.17
HB, 6 May '02	8.71	-5.67	-5.40	-2.62	3.85	-7.18	-1.67	-1.42
TI, 6 May '02	22.02	7.51	1.79	3.44	10.01	-0.76	9.00	6.59
PI, 15 May '02	4.02	-4.43	-1.86	2.95	13.67	-2.13	-1.71	-5.75
TI, 15 May '02	16.85	8.43	-0.56	1.06	11.05	-6.56	-2.97	-3.04
JT, 15 May '02	16.52	2.11	-0.20	-1.90	4.12	-10.06	-11.01	-11.28
PI, 22 May '02	7.73	-3.49	-1.96	0.87	8.92	-6.48	-5.52	-5.07
HB, 22 May '01	2.07	-8.90	-6.39	-3.62	3.82	-0.38	-0.83	1.24
JT, 22 May '02	16.11	2.97	-8.46	-8.26	0.56	-9.01	-5.84	-6.78

Table 3.4-3: Percent differences in estimated water leaving radiances, L_w , at various wavelengths (412-685 nm) using in-situ measurements and model simulations (negative values correspond to $L_{w(\text{InSitu})}$ estimates smaller than the Hydrolight estimated $L_{w(\text{model})}$).

Station/Date	412	443	490	510	532	554	670	685
PI, 26 Sept '01	21.67	19.44	22.27	16.59	13.08	14.34	0.29	15.79
HB, 26 Sept '01	2.59	5.52	0.11	0.58	-2.10	2.75	7.41	-4.96
TI, 26 Sept '01	-12.96	-8.53	-6.62	-4.67	-5.11	-5.10	0.64	-14.98
JT, 26 Sept '01	-1.81	0.57	-7.27	-8.89	-12.00	-15.18	-2.07	-11.26
PI, 28 Sept '01	-0.84	-1.89	-6.37	0.23	2.04	-0.56	7.67	-4.34
HB, 28 Sept '01	-0.64	-2.94	-10.35	-5.03	-5.53	-6.96	2.95	-11.65
TI, 28 Sept '01	4.75	-1.07	-16.58	-14.83	-14.04	-12.75	-8.01	-20.30
PI, 30 Oct '01	19.72	2.15	-7.20	1.07	4.63	-1.24	3.85	-14.35
HB, 30 Oct '01	-0.55	-1.52	-10.21	-3.88	-2.83	-9.54	-1.40	-17.02
HB, 6 May '02	10.02	1.69	-14.14	-10.30	-15.32	-9.99	-18.22	-21.56
TI, 6 May '02	14.00	7.49	-9.52	-5.70	-4.76	-2.26	-3.07	-16.26
PI, 15 May '02	1.44	-4.29	-18.80	-13.87	-12.10	-17.41	-6.93	-22.84
TI, 15 May '02	1.97	-15.87	-22.69	-10.53	-3.78	18.63	22.42	4.20
JT, 15 May '02	2.83	-1.92	0.05	4.89	5.09	6.13	7.02	-5.94
PI, 22 May '02	2.30	-11.63	-18.75	-13.46	-10.09	2.73	6.54	-15.52
HB, 22 May '01	11.52	11.04	-3.67	-5.10	-12.09	1.77	6.55	-9.07
JT, 22 May '02	13.57	8.52	-12.09	-11.50	-11.78	-13.73	-11.48	-19.94

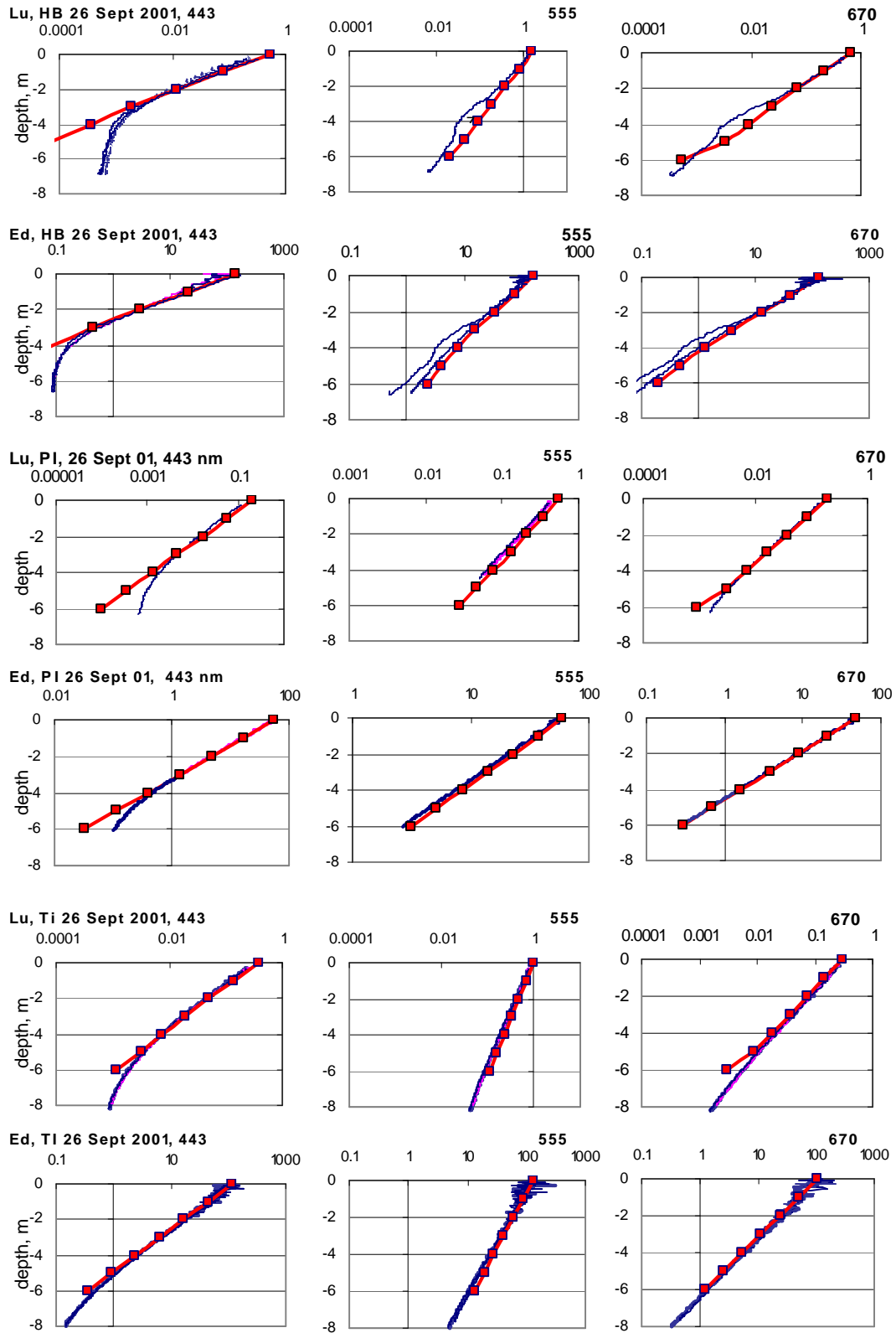


Figure 3.4-1: In-situ measurements (blue lines) and model estimations (red lines) of upwelling radiances (Lu) and downwelling irradiances (Ed), at 443, 555 and 670 nm, for 26 September 2001.

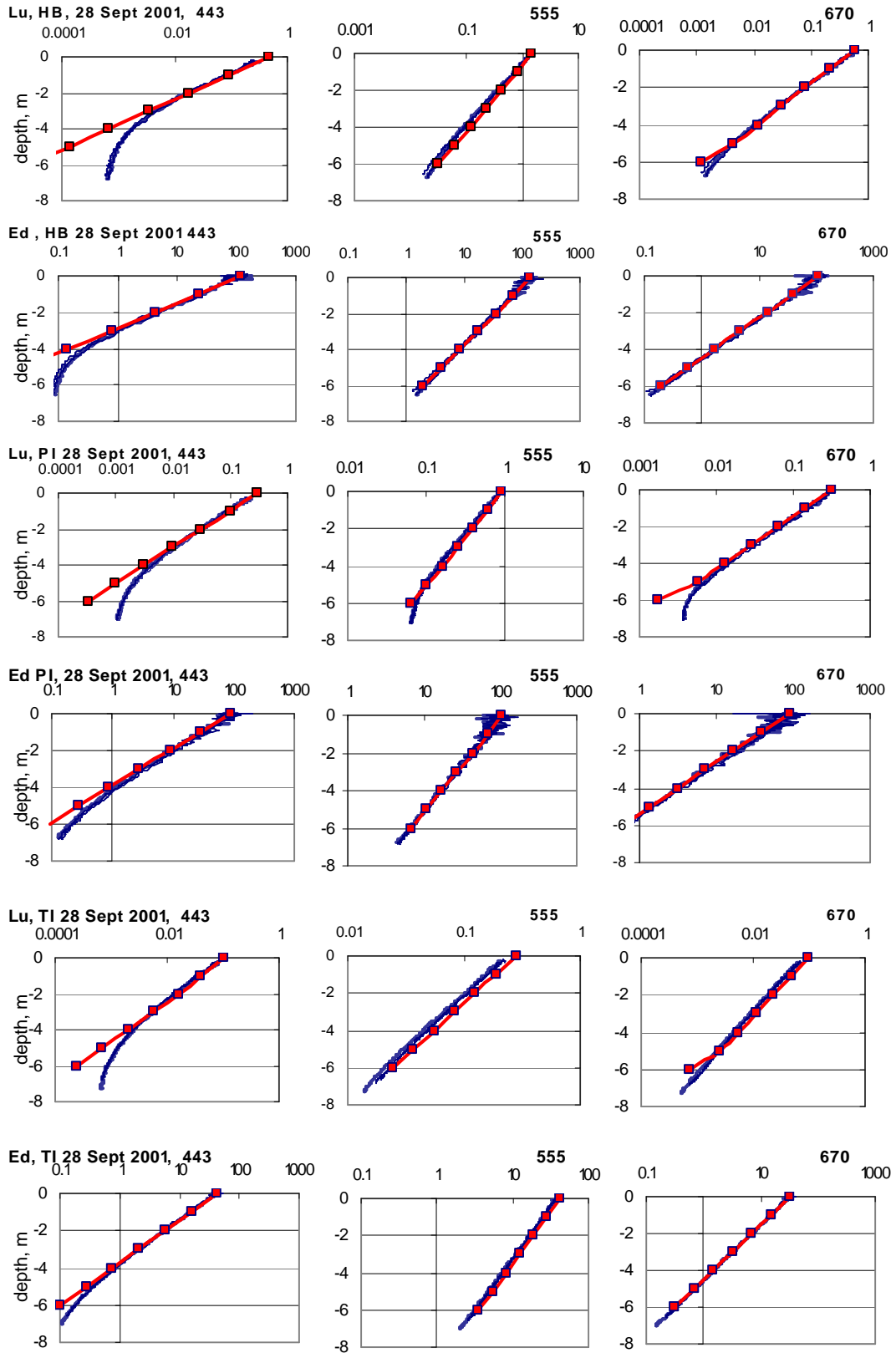


Figure 3.4-2: Same as figure 3.4-1, for 28 September 2001.

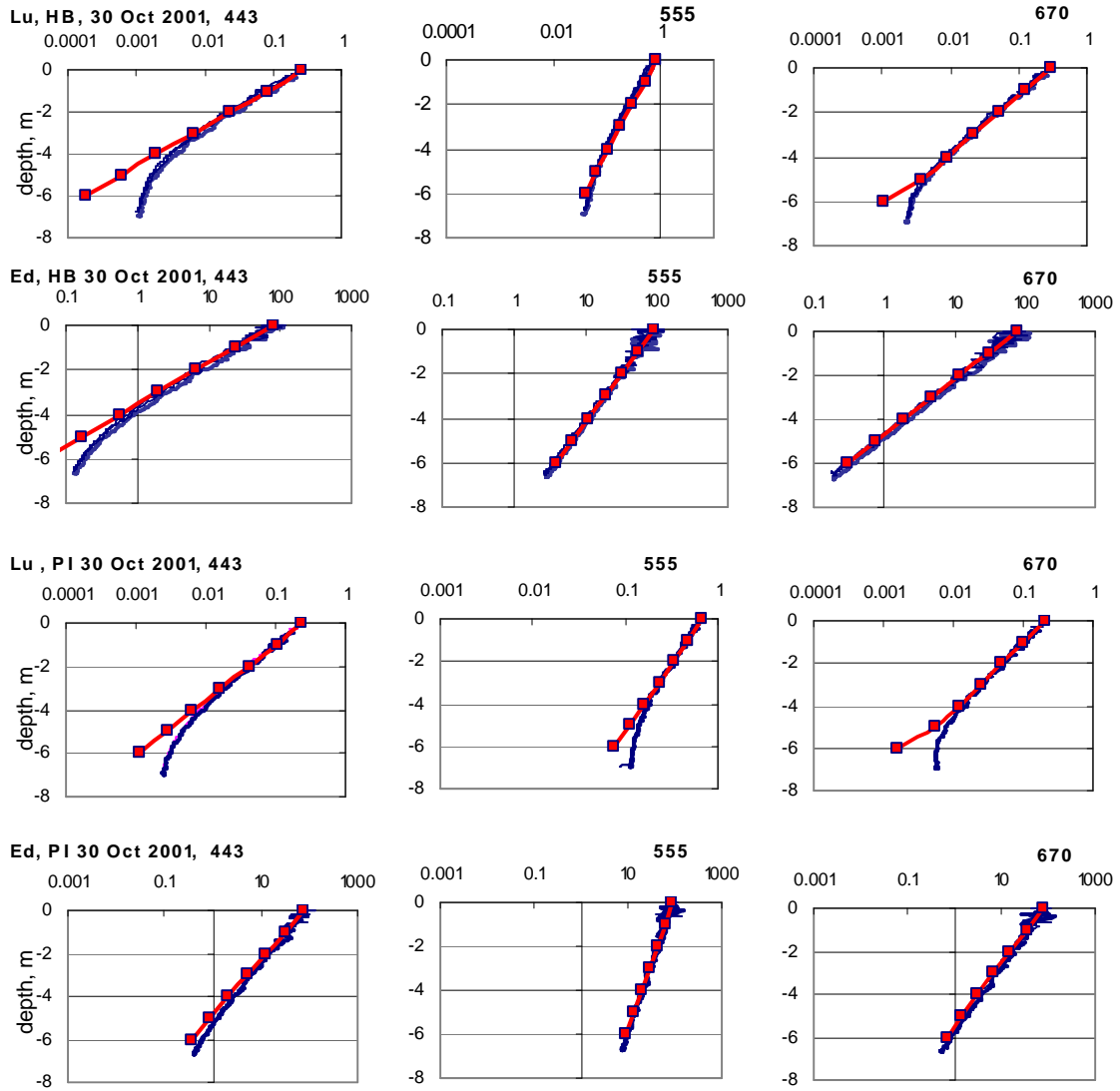


Figure 3.4-3: Same as figure 3.4-1, for 30 October 2001.

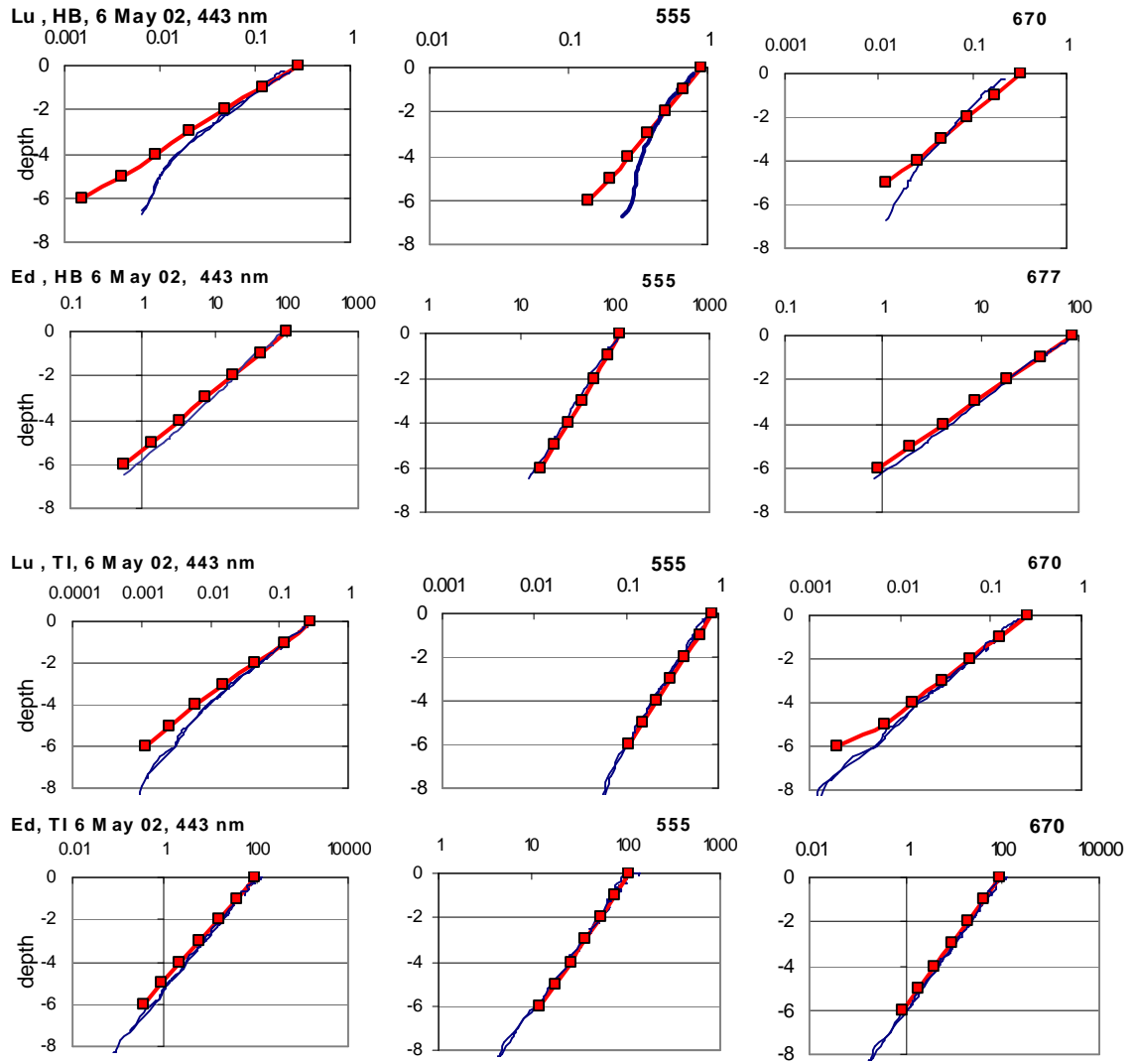


Figure 3.4-4: Same as figure 3.4-1, for 6 May 2002.

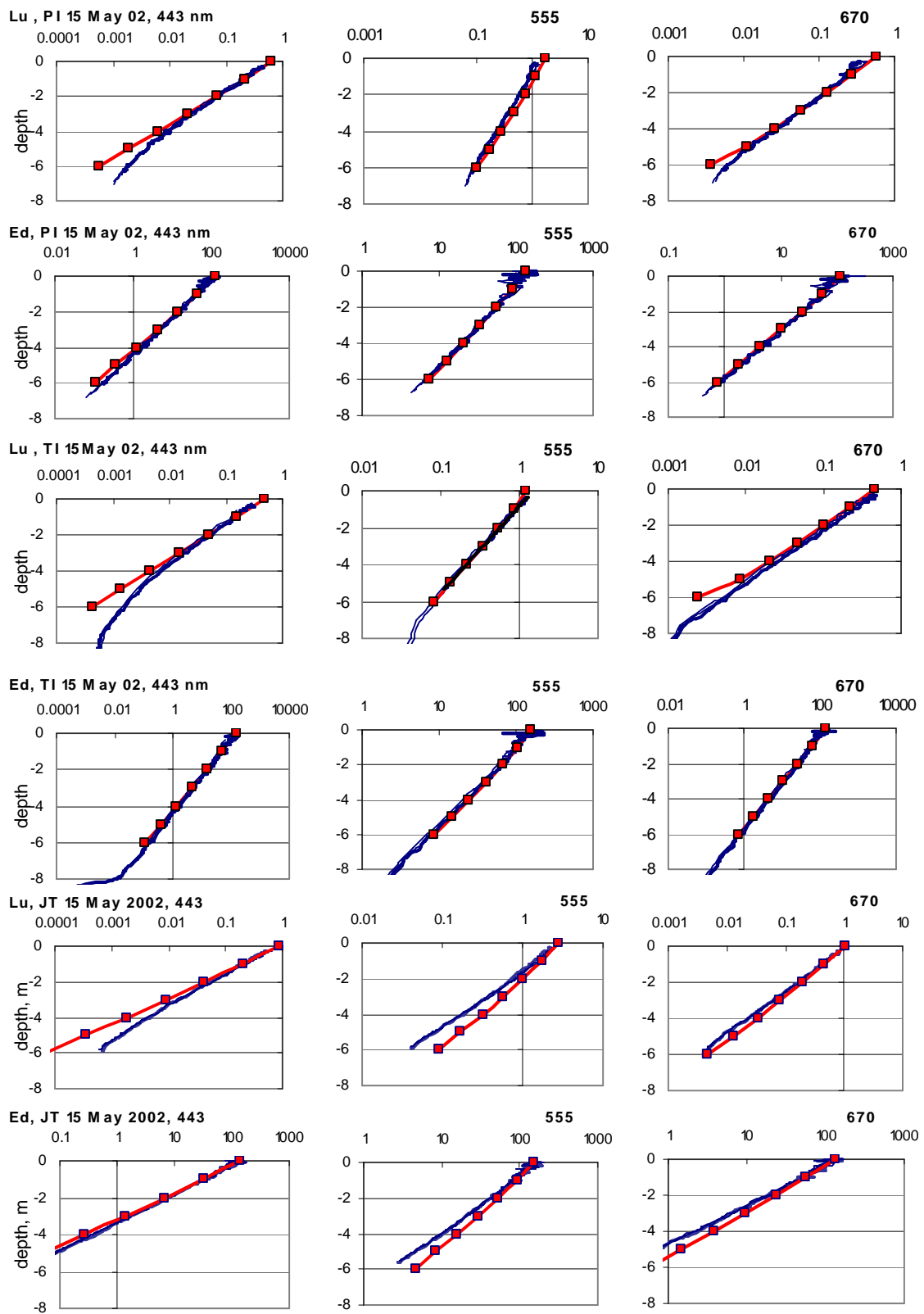


Figure 3.4-5: Same as figure 3.4-1, for 15 May 2002.

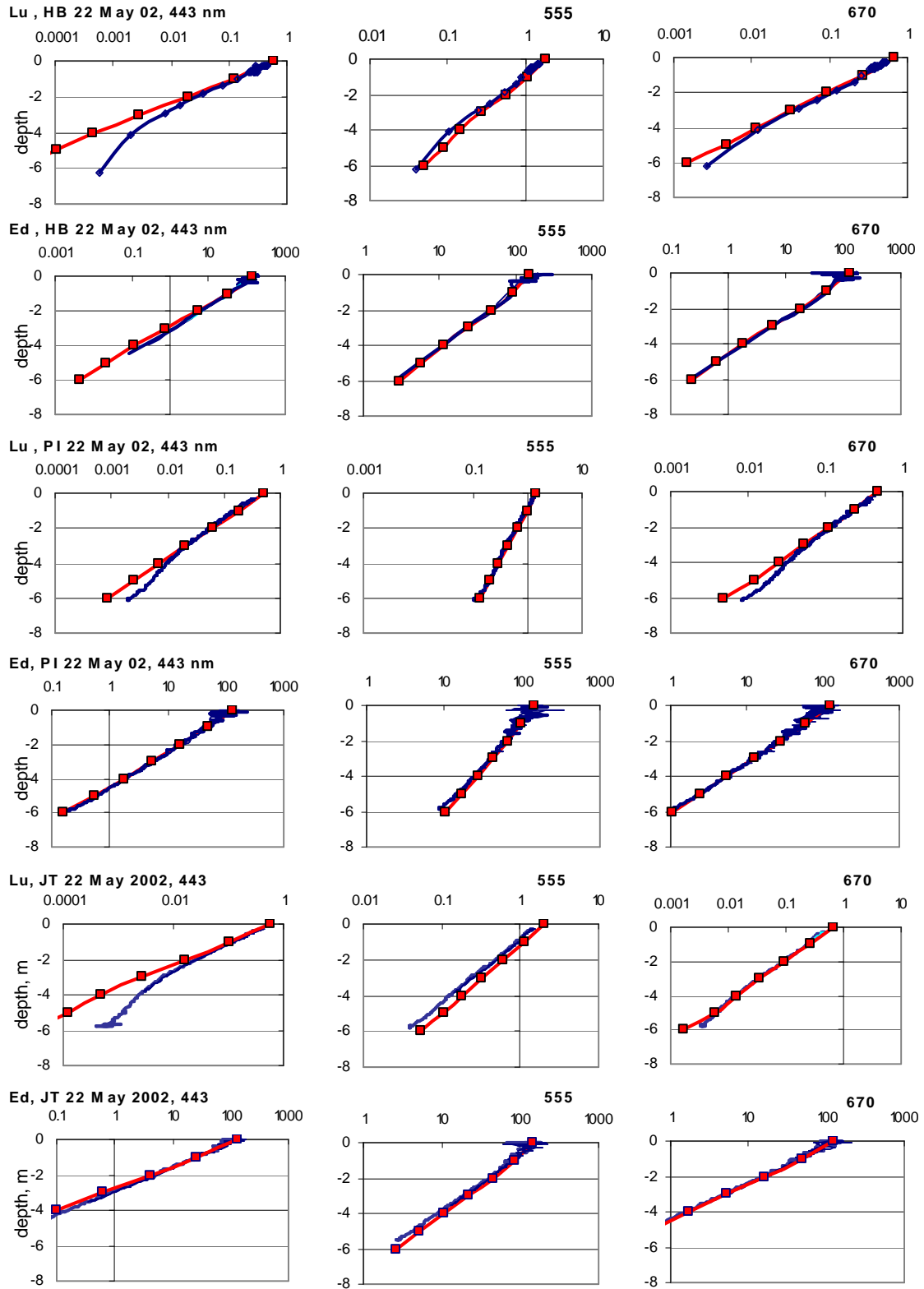


Figure 3.4-6: Same as figure 3.4-1, for 22 May 2002.

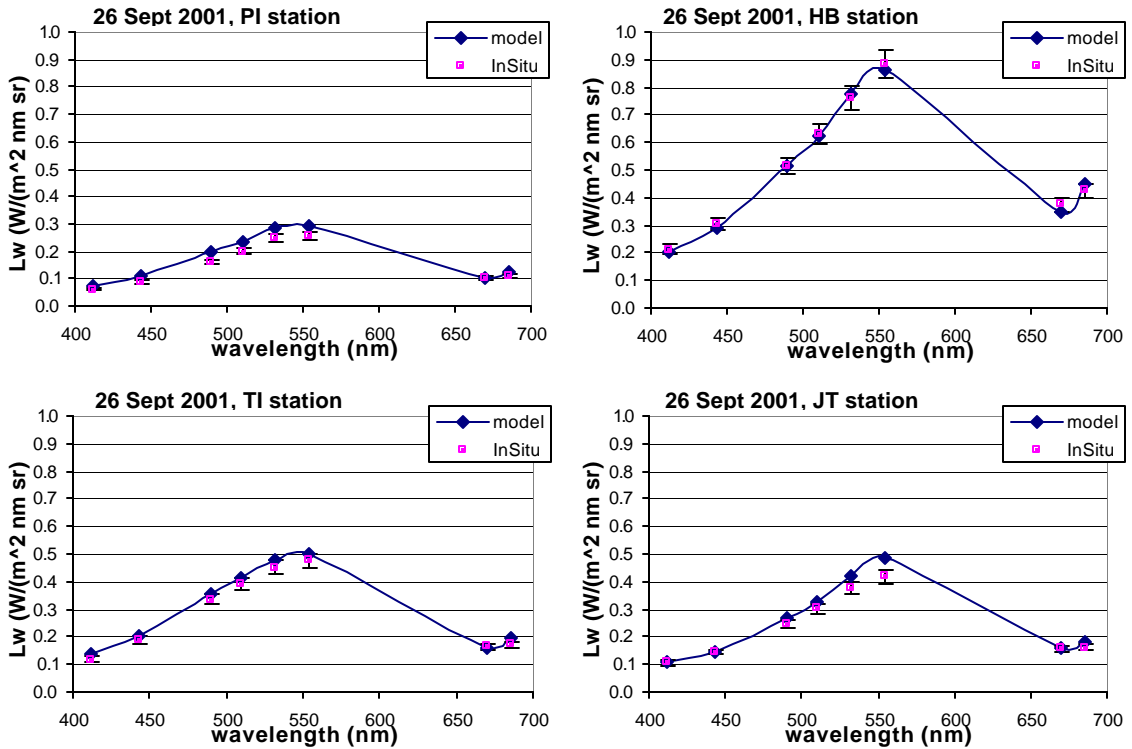


Figure 3.4-7: Water-leaving radiances, L_w , measured in-situ (red pixels) and estimated by the model (blue line), for measurements performed on 26 September 2001

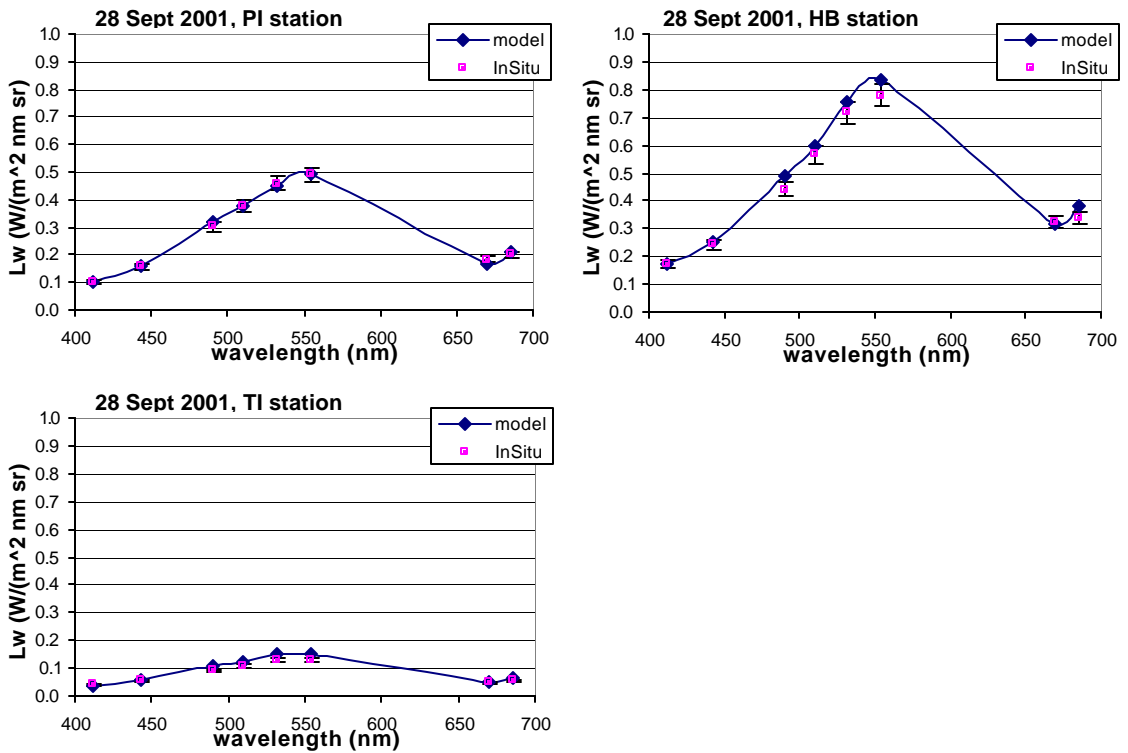


Figure 3.4-8: Same as figure 3.4-7 for measurements performed on 28 September 2001

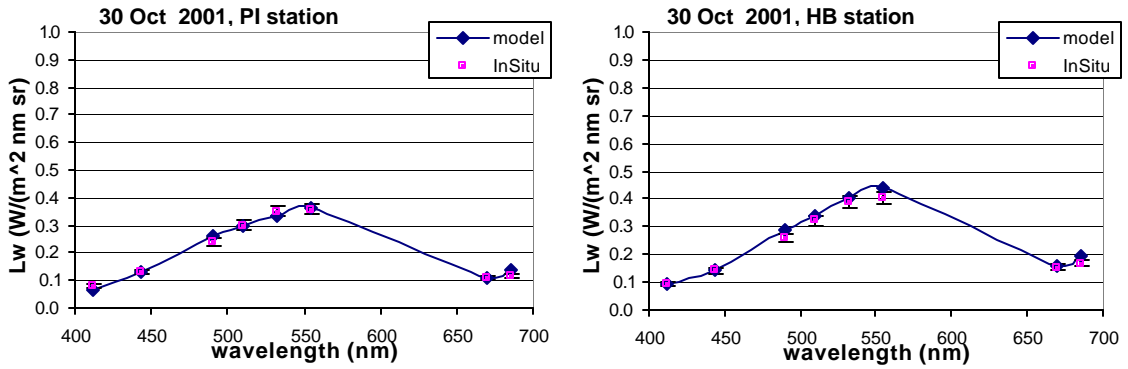


Figure 3.4-9: Same as figure 3.4-7 for measurements performed on 30 October 2001

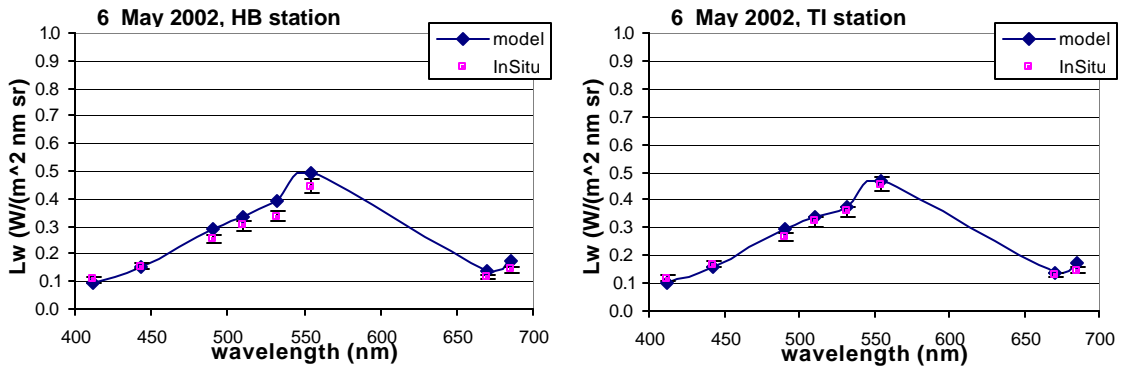


Figure 3.4-10: Same as figure 3.4-7 for measurements performed on 6 May 2002

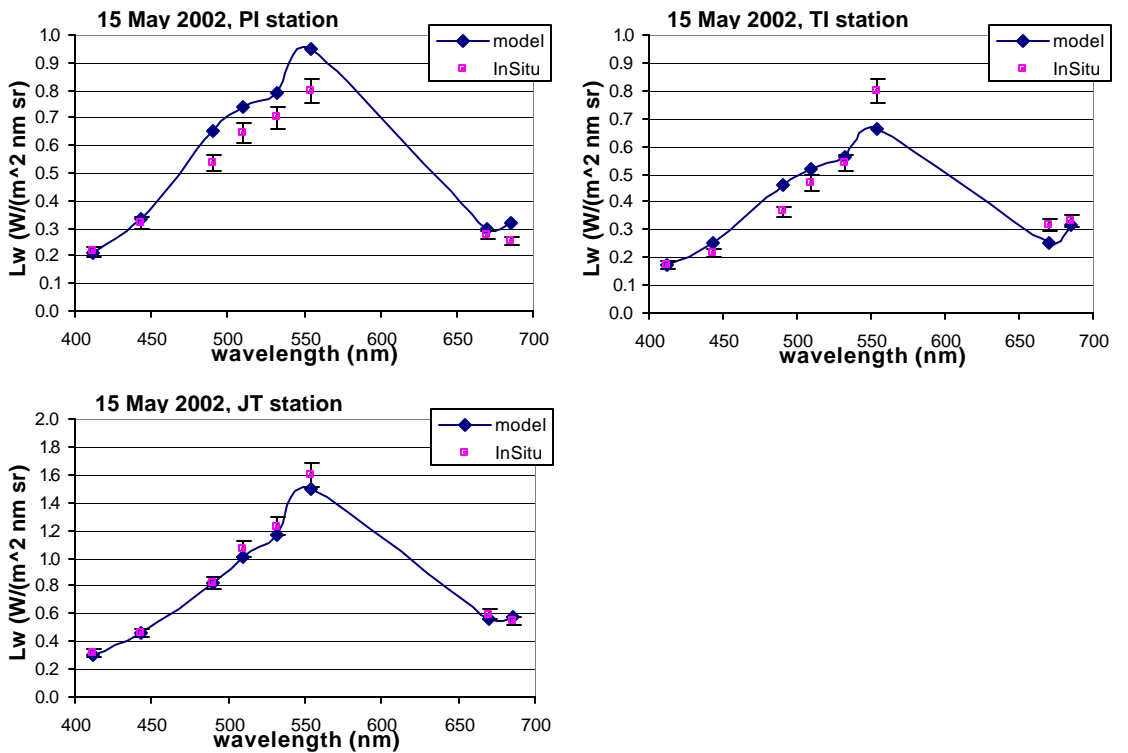


Figure 3.4-11: Same as figure 3.4-7 for measurements performed on 15 May 2002

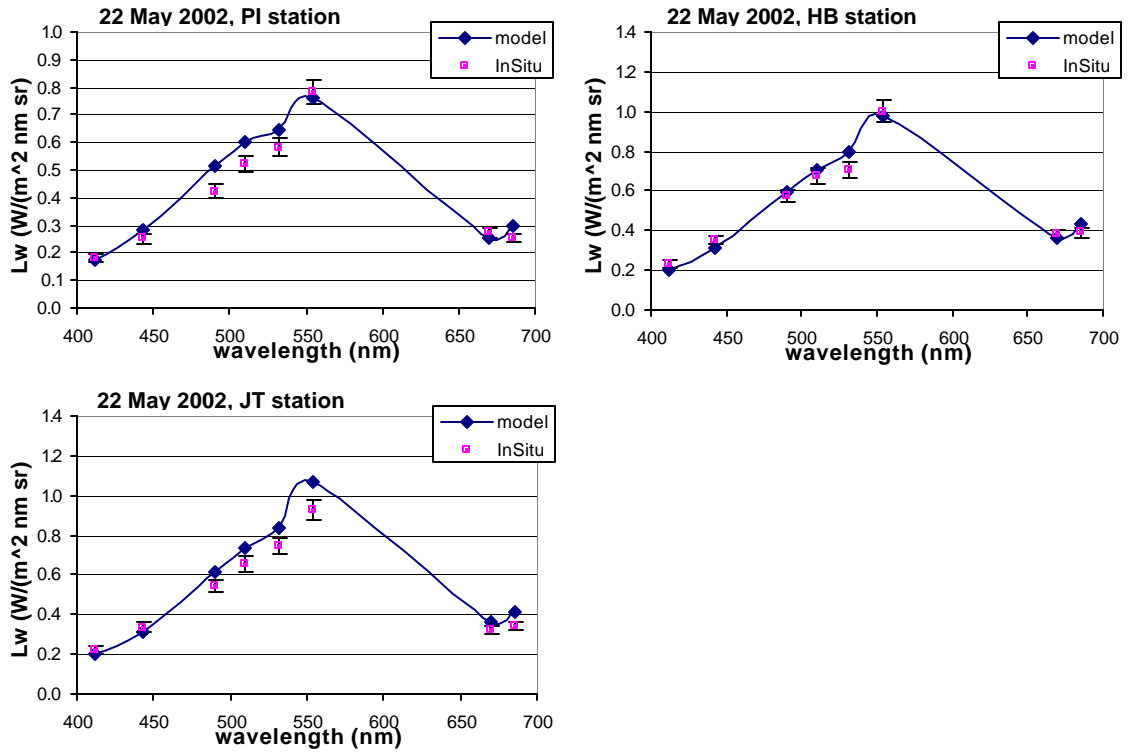


Figure 3.4-12: Same as figure 3.4-7 for measurements performed on 22 May 2002

3.5 Discussion

The underwater radiation fields and water-leaving radiances within the estuarine Chesapeake Bay environment were measured under various atmospheric conditions and in-water optical characteristics in the northern part of the Bay (cruises during 2001-2002). Measured boundary conditions and in-water inherent optical properties were used as input information to perform radiative transfer model estimations of underwater radiation fields using the Hydrolight code. The main objectives were: i) to obtain a better understanding of the sources and magnitude of errors associated with these two different methods of estimating $L_w(\lambda)$ and $R_{rs}(\lambda)$ and ii) to study to what extent we can demonstrate ‘closure’ with measured data and comparisons with theoretically estimated radiation fields in this optically complex estuarine environment.

Good agreement was obtained between measured and model estimated E_d and L_u values (figures 3.4-1 - 3.4-6, tables 3.4-1 - 3.4-2), especially within the first three meters below the water surface. For average values of attenuation $c(412)=5.5 \text{ m}^{-1}$ and $c(532)=4.2 \text{ m}^{-1}$ measured in the Bay during our cruises, these depths correspond to optical depths ($\zeta = c z$) of 16.5m and 12.5m, respectively. According to the results shown in figures 3.4-1 - 3.4-6, good agreement of 3 orders of magnitude dynamic range was obtained between model results and measurements. In 15 out of 17 cases, the percent differences between measured and model-estimated E_d values, at 1 m below the water surface, were less than 9% at 443 nm (average of absolute percent differences was 6.5%), less than 10% at 555 nm (average of absolute percent differences was 5.2%) and less than 11% at 670 nm (average of absolute percent differences was 5.9%). For the upwelling

radiance, L_u , the percent differences between model-estimated and measured values, at 1m depth below the water surface, were in almost all of the cases, less than 15.5% at 443 nm (average of absolute percent differences was 7.8%), less than 19% at 555 nm (average of absolute percent differences was 12.8%), and less than 22% at 670 nm (average of absolute percent differences was 8.7%). As light penetrates deeper into the water column, small errors associated with measurements of the absorption and scattering, used as input information to run the model, propagate in the radiative transfer model calculations and result in larger differences between measured and estimated radiances at larger depths. At the same time, other factors such as very low light levels down to 5-6 m depths in the blue wavelengths (low values were measured especially for the upwelling radiances, L_u), as well as bottom reflectance, affect both the accuracy of the measurements close to the bottom and the accuracy of the assumptions used to perform the model estimations. Information on bottom reflectance was not available from the measurements performed in the Bay. The assumption of an infinitely deep water-column used in the model simulations might be a source of error in the model estimations.

The model-estimated water-leaving radiances were in very good agreement with the water-leaving radiances estimated based on the measurements of upwelling radiances. For almost all of the cases, the percent differences between measured and model-estimated water-leaving radiances were less than $\pm 11.6\%$ at 443nm (average of absolute percent differences was 6.25%), less than $\pm 15.2\%$ at 555nm (average of absolute percent differences was 8.3%) and less than $\pm 11.5\%$ at 670nm (average of absolute percent differences was 6.85%). Studies by Chang et al (2003), at the relatively turbid, New

Jersey near-shore waters, showed that the average absolute percent differences between measured (using an Ocean Profiler OCI-100 free falling radiometer) and theoretical estimated (using the Hydrolight code) $L_w(\lambda)$ values were in the order of 20% at 443 nm, 22% at 555 nm and 17 % at 682 nm, larger than those estimated in this study. In their study, Chang et al assumed that the shape of the volume scattering phase functions, VSFs, (measured at one wavelength, 532 nm, and single depths) were independent of wavelength and depth.

The agreement between measured and model-estimated water-leaving radiances in the Chesapeake Bay waters is very good, especially when one takes into account the errors associated with measured quantities used as input information to run the model, the assumptions made in the model simulations, and the errors associated with the radiometric measurements. Two main assumptions made in the model simulations of the underwater light fields, improved the agreement with the measurements in the Bay:

i) The use of a Fournier Forand scattering phase function, as determined by measured wavelength- and depth-dependent backscattering fractions, in place of the widely used “Petzold” average particle scattering phase function (that has a backscattering to scattering ratio of 0.018) (paragraph 3.2.2.3). ii) The assumption of small, but not-zero, total-minus-water absorption at near-infrared (e.g. 715 nm) wavelengths, supported by spectrophotometric measurements of absorption spectra in the 290-750 nm wavelength region (paragraphs 2.2.2.3 and 3.2.2.2). The assumptions made in the model simulations, as well as the inaccuracies and errors associated with the in-situ measurements performed in the Bay, are discussed in the following paragraphs.

According to Mobley et al (2002), use of a scattering phase function with the correct backscattering ratio, b_b/b , and correct overall shape at intermediate and backward-scattering angles, is necessary for accurate prediction of underwater light fields and crucial to achieving model-data agreement. The backscattering properties of a natural water body can be specified in Hydrolight runs in several ways. i) By using a measured volume scattering phase function. ii) By selecting one of the discretized phase functions supplied with Hydrolight (such as the widely used Petzold “average particle” phase function, the ‘pure water’ phase function, the Kopelevich’s “small particle” or the Kopelevich’s “large particle” phase function). 3) By defining a wavelength- and depth-dependent value for the backscattering to scattering ratio, b_b/b , and using a Fournier-Forand scattering phase function with the same b_b/b ratio (Mobley and Sundman, 2000). According to Mobley et al (2002), in an example analysis of case-2 waters (LDEO-15 site, off the coast of New Jersey), the use of a depth- and wavelength- dependent Fournier-Forand scattering phase function for the particle component, gave much better agreement with measured downwelling irradiances and upwelling radiances than did the commonly used Petzold phase function, which had too large a backscatter fraction.

The effect of the choice of scattering phase function on the Hydrolight estimations of $E_d(z)$, $L_u(z)$, R_{rs} and L_w , was discussed in paragraph 3.2.2.3. For measurements performed at PI station on 28 September 2001, use of a Petzold phase function ($b_b/b_{\text{Petzold}}=0.018$), instead of a Fournier-Forand phase function as determined by the measured (fig. 3.2.2-9) wavelength- and depth-dependent b_b/b values (with $b_b/b_{\text{meas}}=0.015$ at 530 nm), resulted, due to the larger Petzold backscatter fraction, in an

underestimation of E_d by 10-20% at 3-5 m depths, and an overestimation of $Lu(z=0^-)$, L_w and R_{rs} by 20% in the blue wavelengths and by 30-50% in the 550-650 nm wavelength region (fig. 3.2.2-13(b)). Use of Fournier Forand scattering phase function and a constant b_b/b ratio, $b_b/b=0.015$ (close to the measured b_b/b , but no wavelength or depth dependence), resulted in an overestimation of R_{rs} by less than 10% in the blue green wavelengths (since $b_b/b_{meas}=0.015$ at 530 nm), and by 20-30% within the red wavelength region (since $b_b/b_{meas}<0.015$ at 650 nm). These model simulations suggest that accurate information on the backscattering fraction, as well as its spectral shape and vertical structure is very important for accurate model estimations.

The volume scattering phase function is rarely measured in the ocean because of instrumental difficulties. Since the phase function was not measured during our cruises in the Bay, a depth- and wavelength-dependent Fournier Forand phase function, as determined by measured b_b/b profiles, was used in order to obtain the most accurate model estimations of underwater radiation fields (Mobley et al, 2002). The ECOVSF instrument was used to measure total backscattering, b_b , (at 3 wavelengths 450-650 nm and at various depths in the water column), while the AC9 instrument was used to determine scattering b_{t-w} as the difference between measured attenuation and absorption (at 9 wavelengths 412-715 nm, and at various depths in the water column). The backscattering fraction was then estimated by Hydrolight using the AC9 profile measurements of $b_{t-w}(z)$ and the ECOVSF measured profiles of $b_b(z)$. This approach improved the agreement of radiative transfer calculations with the measurements (paragraph 3.2.2.3).

Another change in the model input parameters that improved the agreement between modeled and measured radiances, was the assumption of non-zero absorption, a_{t-w} , at the near-infrared wavelengths (e.g. 715 nm), based on spectrophotometric measurements of absorption spectra in the 290-750 nm wavelength region. Laboratory measurements of particulate absorption were performed using a CARY spectrophotometer and by placing a sample of the particle suspension inside an integrating sphere, to minimize scattering errors (methodology and discussion in chapter 2, paragraph 2.2.2.3). According to the measurements, particulate absorption was small, but non-zero, in the wavelength region 700-730 nm (fig. 2.2-7, chapter 2). These results are in agreement with recent studies by Tassan and Ferrari (2003). Therefore, the AC9 absorption measurements used as input information to perform the model simulations, were corrected for scattering similarly to the Zaneveld correction (chapter 2, paragraph 2.2.2.1), but assuming that total-minus-water absorption at 715 nm (the longest AC9 wavelength band), is non-zero and equal to the absorption measured using the CARY spectrophotometer, according to:

$a_{t-w}(\lambda) = a_{t-w, m}(\lambda) - [b_{t-w, m}(\lambda) / b_{t-w, m}(715)] \cdot [a_{t-w, m}(715) - a_{CARY}(715)]$, where a_{CARY} is the sum of the absorption by particulate (pigmented and non-pigmented) and dissolved material.

The particulate absorption values measured using CARY were corrected for an amplification factor $\beta = 1.5$ (discussion in chapter 2).

Figures 3.5-1(a)-(b) show the comparison between measured and model-estimated Lu and Ed profiles for measurements performed at TI station on 26 September 2001

i) assuming that $a_{t-w}(715) = 0$ (fig. 3.5-1(a)) and ii) assuming that $a_{t-w}(715) = a_{CARY}(715)$ (fig. 3.5-1(b)).

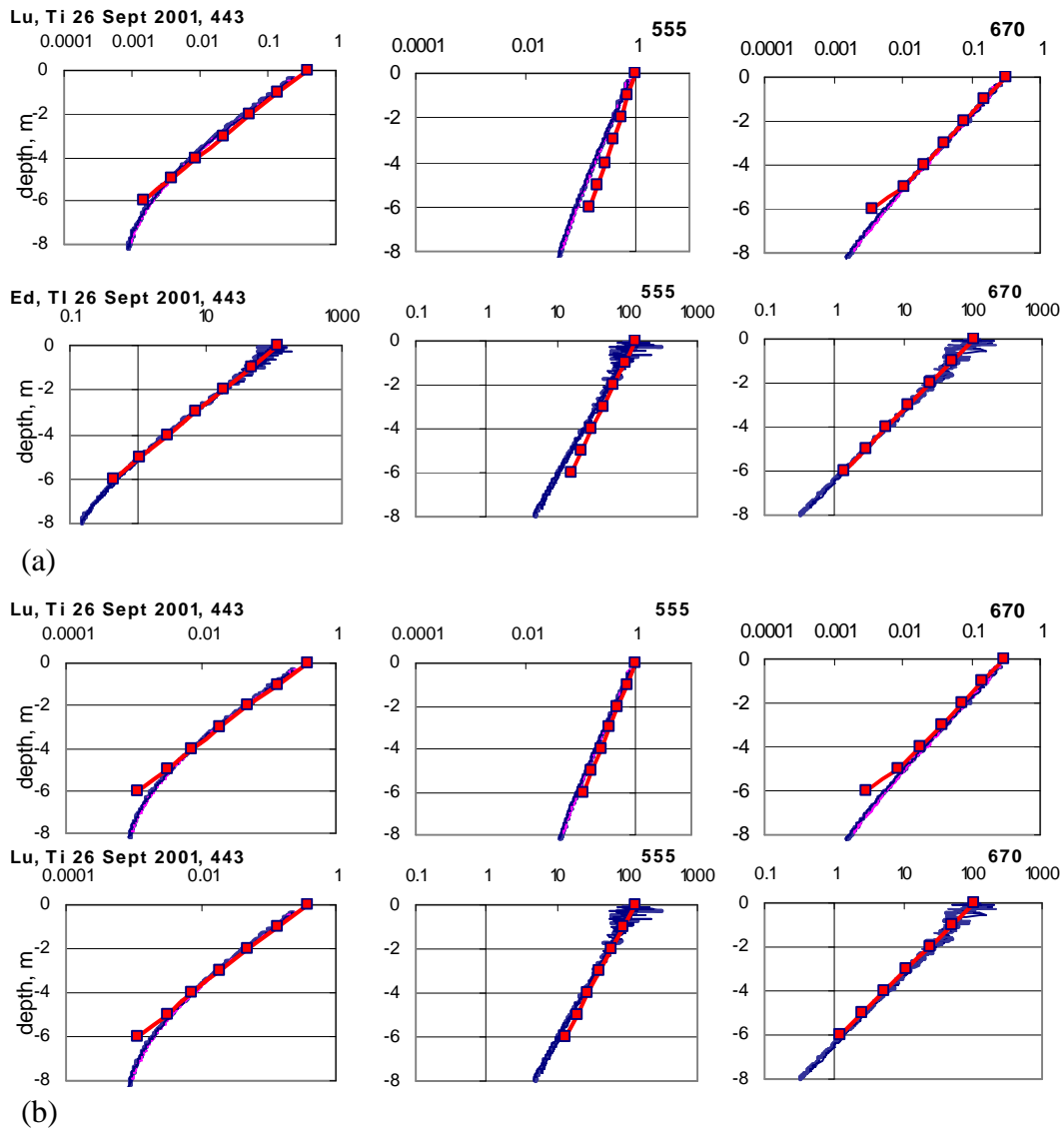


Figure 3.5-1: Comparison between measured (blue lines) and model-estimated (thick red lines) $Lu(z)$ and $Ed(z)$ profiles at 443, 555 and 670 nm, for measurements performed at TI station, on 26 September 2001, (a) assuming that $a_{t-w}(715)=0$ and (b) assuming that $a_{t-w}(715)=a_{CARY}(715)$. When the assumption $a_{t-w}(715)=0$ was used, the model overestimated both $Ed(z)$ and $Lu(z)$ at 555 nm (and similarly for other wavelengths close to 555nm, such as 510 and 532 nm, not shown here). Similar results were obtained when comparing Hydrolight simulations to in-situ measurements performed during the rest of the cruises at PI, HB, TI and JT stations.

When model simulations were performed assuming zero $a_{t-w}(715)$, larger differences between measured and model-estimated quantities were observed at the green wavelengths. Percent differences (calculated according to eq. 3.4-1) between model-estimated and measured Lu values at 1m depth were -21.3% at 490 nm and -24.3% at 555 nm. The model overestimated both $Ed(z)$ and $Lu(z)$, and the disagreement between measurements and model estimations increased with increasing depth (fig 3.5-1). When the model was run assuming non-zero total-minus-water absorption at 715 nm, $a_{t-w}(715)=a_{CARY}(715)$, the agreement between measurements and model results was improved. Percent differences between model-estimated and measured Lu values at 1m depth were -11.8% at 490 nm and -10.7% at 555 nm. Similar results were obtained when comparing Hydrolight simulations to in-situ measurements performed during most of the cruises at PI, HB, TI and JT stations.

As was discussed in the Hydrolight sensitivity studies section (paragraph 3.2.2.2), correction of the AC9 measurements using non-zero $a_{t-w}(715)$, would be expected to have a larger effect on the model estimations in the green wavelengths. In the blue region of the spectrum, absorption by CDOM and non-pigmented particulate matter is typically large and the effect of a residual absorption at 715 nm is too small to significantly change the total absorption and affect the model estimations of $Lu(z)$, $Ed(z)$, L_w or R_{rs} . In the red region of the spectrum, strong absorption by pure sea-water itself results in relatively high total absorption and, again, the effect of the residual absorption at 715 nm is too small to change the total absorption significantly. However, in the green region of the spectrum ($\lambda=550$ nm) total absorption is relatively smaller, and a small change in the

absorption (equal to the residual absorption at 715 nm) can affect the model estimations of remote sensing reflectances (fig.3.3.2-7(b)).

Inelastic processes such as CDOM and chlorophyll fluorescence affect the amount of water-leaving radiance in natural waters. According to the sensitivity studies discussed in paragraph 3.2.2.6, $Lu(0^-)$ values at 677-685 nm, estimated by the model using as input information measurements performed at PI station on 28 September 2001, were underestimated by as much as 30-40% when chlorophyll fluorescence was not included in the model simulations, compared to model results when chl-a fluorescence was included in the simulations. This underestimation of $Lu(0^-)$ at wavelengths close to 685 nm (which is the chl-a fluorescence emission maximum) would result in an underestimation of L_w and R_{rs} at these wavelengths, significantly affecting comparisons with in-situ and remote sensing measurements of water-leaving radiance. Hydrolight estimations of the amount of light fluoresced by chlorophyll are affected by the model assumptions about the chlorophyll-specific phytoplankton absorption spectrum, $a^*_{\text{phyt}}(\lambda)$, chlorophyll fluorescence efficiency and wavelength redistribution function. Measured chlorophyll concentrations can be used as input information for the model estimations of phytoplankton absorption. Therefore, errors in measurements of [Chl-a] can also affect the accuracy of the model calculations. The default chlorophyll fluorescence efficiency value of 0.02 was used in the framework of this study, to perform the model simulations. According to Mobley (1994) chl-a fluorescence efficiency in oceanic phytoplankton is, to a good approximation, wavelength-independent. However, it depends on phytoplankton species and physiological state, and is influenced by the availability of light and nutrients

and the presence of toxic pollutants in the water. With these uncertainties, chlorophyll fluorescence efficiency may actually range from 0.01 to 0.1, with 0.01-0.05 being typical values (Mobley, 1994).

Hydrolight models CDOM fluorescence using a spectral fluorescence quantum efficiency function proposed by Hawes (1992). This function is based on measurements of CDOM spectral fluorescence quantum efficiency functions performed on water samples collected from a variety of waters (e.g. Gulf of Mexico). According to Hawes, values of CDOM fluorescence quantum efficiency fall in the range 0.005-0.015, for the water samples he studied. According to the model simulations discussed in paragraph 3.2.2.6, the model-estimated CDOM fluorescence signal affected the underwater light fields only at wavelengths smaller than 550 nm (figure 3.2.2-26). For the specific case studied, the effect of CDOM fluorescence was a 2-5% change in the model estimated R_{rs} and L_w values at the blue wavelengths. The effect was negligible at wavelengths longer than 530 nm. Measurements of chlorophyll or CDOM fluorescence quantum efficiencies were not performed in the framework of this study. Therefore, the Hydrolight assumptions about the CDOM and chlorophyll fluorescence quantum efficiency and spectral quantum efficiency functions might be another source of error in the model estimations of underwater radiance fields.

Uncertainties and errors in the measurements of surface irradiance, E_s (Satlantic instrument), absorption and scattering coefficients (AC9 instrument), backscattering (ECOVSF instrument) and [Chl-a] (measured spectrophotometrically), are additional

possible sources of error in the model estimations of underwater and water-leaving radiances, since these parameters are used as input information to perform the model simulations. According to Hydrolight sensitivity studies (section 3.2.2) variation in E_s by $\pm 3\%$ (MicroPro irradiance sensors' accuracy, personal communication Scott McLean, Satlantic) affects the L_u , E_d , L_w values by $\pm 3\%$, without affecting the model-estimated R_{rs} , since R_{rs} is defined as the ratio $R_{rs} = L_w/E_d$. Variations in the measured backscattering, b_b , absorption, a_{t-w} , and attenuation, c_{t-w} , by \pm standard error resulted in less than 2-3% changes in the model-estimated L_w and R_{rs} values for the specific measurements in the Chesapeake Bay waters. However, measurements of b_b were available only at wavelengths 450, 530 and 650 nm. Since there is not enough in the literature on the wavelength dependence of b_b expected for the Chesapeake Bay waters, no extrapolation of the b_b measurements was performed for wavelengths shorter than 450 nm (e.g., 412 nm) or longer than 650 nm (e.g., 685 nm). These uncertainties in the accuracy of the b_b values at $\lambda < 450$ nm and $\lambda > 650$ nm could be additional possible sources of error for the model estimations of water-leaving radiances at the blue and infrared wavelengths.

Imperfect instrument calibration, errors and uncertainties associated with the in-situ measurements of underwater E_d and L_u profiles as well as with the estimation of L_w based on the underwater measurements of L_u , may also contribute to discrepancies when comparing the measurements to the model estimations. The MicroPro irradiance and radiance sensors' accuracy is reported to be $\pm 3\%$ and $\pm 4\%$ respectively (personal communication Scott McLean, Satlantic). However, additional uncertainties occur when

further processing the data and correcting for self-shading effects (methodology and discussion in chapter 2). According to Gordon and Ding (1992) and Zibordi and Ferrari (1995), the magnitude of an instrument's self-shading error depends mainly on the size of the radiometer, the solar zenith angle and the total in-water absorption, and can be very significant in highly absorbing, coastal waters. Correction for the instrument's self-shading (Gordon and Ding, 1992; Zibordi and Ferrari, 1995) was applied to the radiometric measurements obtained using the MicroPro instrument during our cruises. However, the Gordon and Ding model is based on the assumption that scattering in the water is smaller than total absorption. Field observations by Zibordi and Ferrari (1995) suggest that the presence of highly scattering material, as in the case of the highly turbid Chesapeake Bay waters, could reduce the self-shading error below that theoretically predicted. Further studies are needed for improvement of the theoretical estimations of self-shading errors in highly scattering waters. Other sources of error, associated with the in-situ radiance measurements include instrument tilt and noise in the measurements, as well as uncertainties in the extrapolation of underwater $L_u(z)$ measurements to $L_u(0)$ just below the water surface and the estimation of the water-leaving radiances, L_w (methodology described in 3.3.2, equations 3.3-1 and 3.3-2).

Very good agreement was obtained between measurements and model-estimated $E_d(z)$, $L_u(z)$ and L_w values in the optically complex, estuarine environment of Chesapeake Bay, especially when one takes into account all of the assumptions made in the model simulations, the errors associated with the measured quantities used as input information

to run the model, and the errors associated with the radiometric measurements, mentioned in the previous paragraphs.

Table 3.5-1 shows the range of values of IOPs (absorption, a_{t-w} , attenuation, c_{t-w} , backscattering fraction, b_b/b , and chlorophyll-a concentration, [Chl-a]) measured in the Bay waters during cruises where theoretical estimations of underwater light fields were compared to in-situ radiance measurements (using the MicroPro instrument). Almost 80-85% of the IOP values measured in the Chesapeake Bay waters during our 17 cruises (table 3.3-1) were within the range of values shown in table 3.5-1. The range of atmospheric and air-water surface boundary conditions observed during the cruises for which Hydrolight runs were performed are shown in table 3.5-2.

Table 3.5-1: Range of values (min-max) of IOPs for which Hydrolight simulations were performed in the Chesapeake Bay waters.

	$a_{t-w}(440)$ (m^{-1})	$a_{t-w}(676)$ (m^{-1})	$c_{t-w}(440)$ (m^{-1})	$c_{t-w}(676)$ (m^{-1})	$b_b/b(530)$	[Chl-a] ($mg\ m^{-3}$)
minimum	0.6	0.12	2.5	1.6	0.006	4.8
maximum	1.44	0.44	8.5	6.3	0.020	23

Table 3.5-2: Range of atmospheric and air-water surface boundary conditions for which Hydrolight simulations were performed in the Chesapeake Bay waters.

	sza ($^{\circ}$)	Wind speed (m/s)	Cloud fraction (%)
Minimum	19	2	0 (clear)
Maximum	54	5	100 (overcast)

Obtaining such good agreement between measurements and theoretical estimations, over a wide range of inherent optical properties values and air-water surface boundary conditions, increases confidence in the accuracy of the in-situ measurements performed in the Bay, and demonstrates “closure” between the independently measured water’s inherent and apparent optical properties (optical closure).

The good agreement between measured and theoretically estimated water-leaving radiances suggests that, when in-situ radiance measurements are not available, the radiative transfer model can be used to estimate the radiation fields in the Chesapeake Bay waters or other coastal waters, provided that accurate and detailed measurements of the inherent optical properties of the water body, needed as input to perform the model simulations, are available.

3.6 Summary - Conclusions

In-situ measurements of in-water optical properties, together with theoretical models and laboratory experiments, are essential to our efforts to understand the penetration and distribution of solar radiation in the marine environment. Measurements of underwater radiation fields and water's inherent optical properties, have been performed under various atmospheric conditions and in-water optical characteristics in the northern part of the Chesapeake Bay (cruises 2001- 2002). The combination of measurements forms a "closure experiment", since measured inherent optical properties and boundary conditions can be used as input information to perform theoretical estimations of the underwater light field using a radiative transfer model, while measured radiometric quantities can be compared to the model's output. The Hydrolight underwater radiative transfer code (Mobley, 1988) was used in this project to perform the model simulations. The main objectives were: i) to obtain a better understanding of the sources and magnitude of errors associated with measurements and theoretical estimations of underwater light fields and water-leaving radiances and ii) to study to what extent we can obtain 'closure' between water's apparent and inherent optical properties, in this optically complex, estuarine environment. The most significant points and conclusions related to the "closure experiment" and the theoretical estimations of underwater light fields and water-leaving radiances in the Chesapeake Bay waters, are shown in table 3.6-1.

Table 3.6-1: Chapter 3 – Conclusion and Significant Points

- Good agreement was obtained between measured and model estimated underwater E_d and L_u values, especially within the first 3 meters below the water surface. At larger depths, factors such as very low light levels (low L_u values at 5-6 m depths in the blue wavelengths), as well as bottom reflectance, affect both the accuracy of the measurements and the accuracy of the assumptions used in the model simulations.
- The model-estimated L_w values were in very good agreement with those based on measurements of upwelling radiances. For almost all of the cases, the percent differences between measured and model-estimated L_w , were less than $\pm 11.6\%$ at 443 nm (absolute average of 6.25%), less than $\pm 15.2\%$ at 555nm (absolute average of 8.3%) and less than $\pm 11.5\%$ at 670nm (absolute average of 6.85%).
- Two main assumptions made in the model simulations of the underwater light fields, improved the agreement with the measurements:
 - i) Use of a Fournier Forand scattering phase function, as determined by measured wavelength- and depth-dependent backscattering fractions, in place of the widely used “Petzold” average particle scattering phase function.
 - ii) The assumption of non-zero particulate absorption at the near-infrared wavelengths (e.g. 715 nm), based on laboratory spectrophotometric measurements of absorption spectra in the 290-750 nm wavelength region.
- Hydrolight simulations showed that underwater radiances and irradiances, as well as water-leaving radiances and reflectances, are sensitive to the value of b_b/b ratio, and the b_b/b vertical structure and wavelength dependence. Mobley et al (2002), have shown that underwater light fields are also sensitive to the shape of the scattering phase function at intermediate and large scattering angles, and they concluded that when the particle phase function is not measured, a Fournier Forand phase function with the correct backscatter fraction could provide a satisfactory substitute to perform the model simulations. As discussed in Chapter 2, considerable variation was observed in the measured b_b/b values in the Chesapeake Bay during our cruises, with values as low as 0.006 and higher than 0.025. The backscattering fraction $b_b/b(530)$ had an average value of 0.013, much smaller than the widely used b_b/b value for the Petzold “average particle”, $b_b/b=0.018$. Performing the model simulations using the Petzold phase function would result in significantly overestimated water-leaving radiances for most of the cases studied in the Chesapeake Bay waters. Therefore, accurate measurements of b_b/b are crucial for accurate predictions of underwater light fields and for achieving good agreement between data and model.
- Use of non-zero absorption, a_{t-w} , at the near-infrared wavelengths (e.g. 715 nm), supported by spectrophotometric measurements of absorption spectra in the 290-750 nm wavelength region, improved the agreement between modeled and measured radiances and irradiances. The assumption of non-zero absorption at 715 nm is in agreement with recent studies by Tassan and Ferrari (2003). Correction of the AC9 absorption measurements (used as input information to run the model) assuming non-zero absorption at 715 nm, $a_{t-w}(715)=a_{CARY}(715)$, had a larger effect on the model estimations of water-leaving radiances in the green wavelengths, than blue or red wavelengths, since total absorption in the green region of the spectrum ($\lambda=550$ nm) is relatively small.
- Hydrolight simulations showed that inclusion of the inelastic process of chlorophyll fluorescence, can significantly affect (e.g., by 30-40%) the model estimated water-leaving radiances around 685 nm (chl-a fluorescence emission maximum). According to the model simulations, the model-estimated CDOM fluorescence signal affected the underwater light fields only at wavelengths smaller than 550 nm, and by less than 5% for the specific case studied. The Hydrolight assumptions about the CDOM and chlorophyll fluorescence quantum efficiency and spectral quantum efficiency functions might be a significant source of error in the model estimations of underwater radiation fields.

Table 3.6-1: (continued)

- Uncertainties and errors in the measurements of surface irradiance, absorption and scattering coefficients, backscattering and chlorophyll concentrations are additional possible sources of error in the model estimations of underwater and water-leaving radiances, since these parameters are used as input information to perform the model simulations. However, the standard errors estimated for measurements of total absorption, attenuation and backscattering were smaller than 2-3 % for the specific case studied (calm water surface and IOPs not highly variable with depth) and varying these quantities by \pm standard error did not have a large effect on the model estimated L_w or R_{rs} values.

- A larger source of error could be associated with the uncertainties concerning the wavelength dependence of b_b and the extrapolation of the b_b values measured at 450, 530 and 650 nm to wavelengths shorter than 450 nm or longer than 650 nm.

- Imperfect calibration and errors associated with the in-situ measurements of underwater E_d and L_u profiles, instrument tilt and noise in the radiometric measurements close to the surface, as well as uncertainties in the estimation of L_w based on the underwater measurements of $L_u(z)$, may also contribute to discrepancies when comparing the measurements to the model estimations.

- Given all the assumptions made in the model simulations and the errors associated with the measured quantities, the agreement obtained between measurements in the Bay and model-estimations is very good. Obtaining such a good agreement between measurements and theoretical estimations:

i) suggests that, when in-situ radiance measurements are not available, the radiative transfer model can be used to accurately estimate the radiation fields in the Chesapeake Bay or other coastal waters, provided that accurate and detailed measurements of the inherent optical properties of the water body are available.

ii) increases confidence in the accuracy of the in-situ measurements performed in the Chesapeake Bay and demonstrates “closure” between the independently measured inherent and apparent water optical properties. This is extremely important when in-situ measurements and radiative transfer modeling are used in the interpretation and validation of satellite, remote sensing observations.

CHAPTER 4

Observations of Remote Sensing Reflectance in the Chesapeake Bay, using the MODIS/Terra satellite instrument and in-situ measurements

4.1 Remote Sensing in Ocean studies

Studies on the effects of natural and human induced processes on aquatic environments at a global scale, require repeated monitoring of the oceans and synoptic observations over large areas that can be monitored only remotely, by instruments mounted on aircrafts or on board satellites. These locations are normally inaccessible to ground instruments. Within the last decades great progress has been made on remote sensing applied to oceanographic research. Spatially detailed measurements of sea-surface temperature, ocean color, surface roughness or slope, can be made today over wide areas, providing a global view and a novel perspective of the ocean.

Satellite observations of the ocean rely on detecting the light signal that leaves the water surface and reaches sensors onboard a satellite. The water itself and its constituents (phytoplankton, non-algal particulate matter, chromophoric dissolved organic material) absorb and scatter light at near-IR, visible, and UV wavelengths of the spectrum. Changes in the concentration and composition of the water constituents, due to biological, chemical or physical processes, affect light penetration in the water and the spectral signature of light that leaves the water surface. Therefore, a satellite sensor that makes measurements in the visible wavelengths can be used to measure changes in the

“color” of the ocean that provides information on the “optically active” components of the water.

In open-ocean, case-1 waters, phytoplankton and their by-products are the major constituents affecting changes in the spectral signature of light leaving the water’s surface. Satellite observations of ocean color have contributed significantly in gaining a better understanding of the temporal and spatial variations of phytoplankton biomass and biological activity in the world’s oceans (McClain et al, 1993; Yoder et al, 1993). Obtaining a better understanding of the oceanic primary production on a global scale is important for studies on the ocean’s role in the global carbon cycle and climate change. Moreover, satellite observations have contributed to the development and improvement of global, coupled biophysical models, able to describe and predict earth system change accurately enough to contribute to the environmental decision-making process.

There have been many efforts recently, to develop techniques for measuring water-leaving radiances and algal biomass by using satellite observations. The Coastal Zone Color Scanner (CZCS) flown onboard NASA's Nimbus-7 satellite was the first instrument designed to provide frequent global measurements of water-leaving radiances (Nov. 1978 – June 1986). The Ocean Color and Temperature Sensor (OCTS) was launched by NASDA (National Space Development Agency of Japan) in August 1996, and was operational till June 1997. Since September 1997, the NASA SeaWiFS (Sea-viewing Wide Field-of-view Sensor) instrument, a follow-on sensor to CZCS, has been providing very high quality ocean color data. On December of 1999 MODIS (Moderate

Resolution Imaging Spectroradiometer) was launched by NASA. MODIS is not just designed for ocean-color measurements, but also for measurements on atmospheric characteristics and terrestrial vegetation. Other ocean color sensors include MERIS (MEdium Resolution Imaging Spectrometer) GLI (Global Imager), MOS (Modular Optoelectronic Scanner), OCI (Ocean Color Imager), OCM (Ocean Color Monitor), OSMI (Ocean Scanning Multispectral Imager), POLDER (Polarization and Directionality of the Earth's Reflectances).

One major obstacle for remote monitoring is the fact that remote sensing observations are restricted to the upper layers of the ocean. Especially in optically thick coastal waters, light does not penetrate very far into the water column, so that only information on the surface water optical properties can be obtained remotely. Therefore, complementary, in-situ observations from ships or moored systems, that provide detailed information on the vertical distribution of phytoplankton, are necessary for further studies such as quantitative analysis of biomass productivity (Piazena and Häder, 1997).

While having broad spatial coverage, remote sensing measurements are of much lower spatial resolution compared to field observations (e.g. 1.1 km spatial resolution at nadir for SeaWiFS instrument) and are restricted by orbit orientation and altitude. Another limitation in remote sensing measurements is that they are significantly affected by atmospheric conditions (e.g., clouds and aerosols). Almost 90% of the signal detected by a satellite sensor at the top of the atmosphere originates from the atmosphere itself (molecular and aerosol scattering), and only the remaining few percent originate from the

ocean, even under clear atmospheric conditions (under overcast cloudy conditions no satellite measurements of ocean color can be performed). Careful correction for the effects of the intervening atmosphere is critical for obtaining accurate satellite measurements of water-leaving radiances and ocean color.

In order to be able to use ocean-color measurements to extract information on the concentration and composition of optically active substances in the water, it is necessary to develop bio-optical algorithms that relate the water-leaving radiance to the optical properties of the substances present in the water. The determination of geophysical parameters, such as chlorophyll concentration, based on water-leaving radiances, is relatively less complex for case 1 (mostly open ocean) waters where the spectral signature of the emerging light is mostly affected by phytoplankton and their by-products. The situation is very different in case 2 coastal and estuarine waters that are characterized by higher optical and biological complexity, since other substances such as detritus, mineral particles, dissolved organic and inorganic material, also affect the light signal measured by the satellite sensor.

4.1.1 Brief description of the MODIS instrument

The MODIS (Moderate Resolution Imaging Spectroradiometer) instrument is a satellite sensor designed to provide remote-sensing observations of processes occurring on the land, in the oceans and in the lower atmosphere. According to the MODIS Ocean User's Guide, the primary objective of MODIS is to provide satellite data that will be used to

study the interactions between ocean, atmosphere, land, and biosphere and that will allow scientists to interrelate the processes driving global climate.

Two MODIS instruments are currently in orbit, one aboard the TERRA (EOS AM) satellite that passes from north to south across the equator in the morning (~ 10:30 AM local daytime equator crossing, descending mode) and one aboard the Aqua (EOS PM) satellite that passes from south to north across the equator in the afternoon (~ 1:30 PM local daytime equator crossing, ascending mode). The two instruments are viewing the entire Earth's surface every 1 to 2 days, acquiring data in 36 spectral bands (400 nm to 14.4 μm) (table 4.1-2) with spatial resolutions of 250m (bands 1-2), 500m (bands 3-7) and 1000m (bands 8-36) at nadir (MODIS website: <http://modis.gsfc.nasa.gov>). However, at 55° satellite scan angle, spatial resolution decreases to approximately 4.8 km (along satellite scan) by 2 km (along satellite track).

The three basic categories of MODIS ocean products are ocean color, sea-surface temperature (SST), and ocean primary production (MODIS Ocean User's Guide). The primary MODIS products are the normalized water-leaving radiances, estimated from the light signal detected by the sensor at the top of the atmosphere. From these primary products and by using the appropriate algorithms, other geophysical parameters, such as chlorophyll or calcite concentration and water's absorption coefficients, are derived. Ocean color and SST measurements are available as Level 2 and Level 3 gridded and binned data (table 4.1-1). Ocean primary production data are available only as gridded or

binned Level 4 data. A description of the MODIS Level 2, 3, and 4 data is given in table 4.1-1.

Table 4.1-1: MODIS Data Levels

Level	Description
Level 2	All Level 2 pixels have 1 km spatial resolution at nadir. Each Level 2 MODIS "granule" represents 5 minutes of MODIS viewing. Level 2 MODIS products include ocean color products (only collected during the day) and SST products (collected both day and night).
Level 3	Temporal and spatial aggregates of Level 2 SST (4 parameters) and Ocean Color data (36 parameters). The Level-3 products are global binned data (at 4.63 km spatial resolution) or global gridded maps (4.89 km, 39 km, or 1 degree grids). Temporal resolution is one day, 8 days, a month, or a year.
Level 4	Weekly or yearly averaged global products. Level 4 data are organized spatially as either 4.63 km bins or as gridded maps (4.89 km, 39 km, or 1 degree grids). The MODIS Level 4 binned products are global ocean primary productivity products.

The MODIS Level 2 ocean products (daily, 1-km spatial resolution at nadir) include 36 ocean color parameters (MODOCL2, MODOCL2A and MODOCL2B data products) and 4 SST parameters (MODO28L2 data product) (table 4.1-3). Along with these ocean products, there are 16 ocean-color and 20 SST quality control (QC) parameters (table 4.1-4). The QC parameters are used as inputs to the ocean and atmospheric correction algorithms. The MODIS Level-2 products do not include information on the latitude and longitude for each pixel. This information is given separately in the MODIS "Geolocation" data product (MOD03 files for MODIS/Terra). The MODIS Level 4 ocean primary productivity products are given in table 4.1-5.

Table 4.1-2: MODIS 36 spectral bands and their primary use
(information from MODIS website, MODIS Technical specifications)

Primary Use	Band	Bandwidth (nm)
Land/Cloud/Aerosols Boundaries	1	620 - 670
	2	841 - 876
Land/Cloud/Aerosols Properties	3	459 - 479
	4	545 - 565
	5	1230 - 1250
	6	1628 - 1652
	7	2105 - 2155
Ocean Color/Phytoplankton/ Biogeochemistry	8	405 - 420
	9	438 - 448
	10	483 - 493
	11	526 - 536
	12	546 - 556
	13	662 - 672
	14	673 - 683
	15	743 - 753
	16	862 - 877
Atmospheric Water Vapor	17	890 - 920
	18	931 - 941
	19	915 - 965
Surface/Cloud Temperature	20	3.660 - 3.840
	21	3.929 - 3.989
	22	3.929 - 3.989
	23	4.020 - 4.080
Atmospheric Temperature	24	4.433 - 4.498
	25	4.482 - 4.549
Cirrus Clouds Water Vapor	26	1.360 - 1.390
	27	6.535 - 6.895
	28	7.175 - 7.475
Cloud Properties	29	8.400 - 8.700
Ozone	30	9.580 - 9.880
Surface/Cloud Temperature	31	10.780 - 11.280
	32	11.770 - 12.270
Cloud Top Altitude	33	13.185 - 13.485
	34	13.485 - 13.785
	35	13.785 - 14.085
	36	14.085 - 14.385

Table 4.1-3: MODIS Ocean product parameters (numbers 1-40)
(MODIS Ocean User's Guide)

Parameter No	Parameter Description	Units
MODIS/Terra Ocean Color Radiance Products (1 km) , MODOCL2 files		
1 - 7	Normalized water-leaving radiances : at 412, 443, 488, 531, 551, 667 and 678 nm	W/m ² /μm/sr
8	Aerosol optical thickness at 865 nm	non-dimensional
9	Epsilon of aerosol correction at 765, 865nm	non-dimensional
10, 11	Aerosol model identification numbers 1 and 2	non-dimensional
12	Epsilon of clear water aerosol correction at 531 and 667 nm	non-dimensional
MODIS/Terra Ocean Color Derived Products Group 1 (1 km), MODOCL2A files		
13	Chl-a + pheopigment (fluorometric, empirical)	mg/m ³
14	Chl-a concentration, "chlor_MODIS" (HPLC, empirical)	mg/m ³
15	Total pigment concentration (HPLC, empirical)	mg/m ³
16	Chlorophyll fluorescence line height	W/m ² /μm/sr
17	Chlorophyll fluorescence baseline	W/m ² /μm/sr
18	Chlorophyll fluorescence efficiency	non-dimensional
19	Total suspended matter concentration in ocean	g/m ³
20	Pigment concentration in coccolithophore blooms	mg/m ³
21	Detached coccolithophore concentration	1/m ³
22	Calcite concentration	mgC/m ³
23	Diffuse attenuation coefficient at 490 nm	1/m
24	Phycoerythrobilin concentration	1/m
25	Phycourobilin concentration	1/m
MODIS/Terra Ocean Color Derived Products Group 2 (1 km), MODOCL2B files		
26	Chl-a concentration, "chlor_a_2" (SeaWiFS analog)	mg/m ³
27	Chl-a concentration, "chlor_a_3" (semianalytic)	mg/m ³
28	Instantaneous photosynthetically available radiation	Ein/m ² /sec
29	Instantaneous absorbed radiation by phytoplankton for fluorescence	Ein/m ² /sec
30	Gelbstoff absorption coefficient at 400 nm	1/m
31	Phytoplankton absorption coefficient at 675 nm	1/m
32	Total absorption coefficient at 412 nm	1/m
33	Total absorption coefficient at 443 nm	1/m
34	Total absorption coefficient at 488 nm	1/m
35	Total absorption coefficient at 531 nm	1/m
36	Total absorption coefficient at 551 nm	1/m
MODIS/Terra Sea Surface Temperature Products (1km), MODO28L2 files		
37 (D1)-38 (D2)	Sea surface temperature (daytime), 11 μm and 4 μm	°C
39 (N1)-40 (N2)	Sea surface temperature (nighttime), 11 μm and 4 μm	°C

Table 4.1-4: MODIS Ocean Quality Control (QC) parameters (1 km)
(parameter numbers 41-78) (information obtained from MODIS Ocean User's Guide)

Parameter No	Parameter Description	Units
MODIS/Terra Sea Surface Temperature QC Products (1km), MODO28QC files		
41-45	Channel 20, 22, 23, 31, 32 brightness temperature (daytime)	° C
46-50	Channel 20, 22, 23, 31, 32 radiance (daytime)	W/m ² /μm/sr
69-73	Channel 20, 22, 23, 31, 32 brightness temperature (nighttime)	° C
74-78	Channel 20, 22, 23, 31, 32 radiance (nighttime)	W/m ² /μm/sr
MODIS/Terra Ocean Color QC Products (1km), MODOCQC files		
51	U_Wind	m/s
52	V_Wind	m/s
53	Pressure	mBar
54	Humidity	kg/m ²
55	Ozone	DU
56	Latitude	degree
57	Longitude	degree
58	Solar Zenith Angle	angle
59	Solar Azimuth Angle	angle
60	Satellite Zenith Angle	angle
61	Satellite Azimuth Angle	angle
62	(Product unavailable)	-
63	Aerosol radiance 765	W/m ² /μm/sr
64	Rayleigh radiance 443	W/m ² /μm/sr
65	Glint radiance	W/m ² /μm/sr
66	Whitecap radiance	W/m ² /μm/sr

Table 4.1-5: MODIS Level 4 Ocean Primary Productivity products
(information obtained from MODIS Ocean User's Guide)

Parameter Number	Parameter Description
1	Behrenfeld-Falkowski primary production index (semi-analytical model)
2	Howard-Yoder-Ryan primary production index (semi-analytical model)
P	Ocean carbon primary production (statistical model)
N	New nitrogen production (statistical model)
X	Export carbon production (statistical model)
C	Annual chlorophyll-a concentration (semianalytic, chlor_a_3)
E	Photosynthetically available radiation
D	Mixed-layer depth

4.1.2 MODIS measurements of water-leaving radiance and atmospheric correction algorithm

Accurately accounting for the optical properties of the atmosphere (primarily Rayleigh scattering plus aerosol scattering and absorption) presents a major difficulty in obtaining accurate water-leaving radiance data from satellites. Due to the presence of the atmosphere, the radiance detected by a satellite sensor is composed of water leaving radiance, atmospherically backscattered radiance, direct reflected solar radiance from the sea surface, and downward scattered radiance reflected from the sea surface. The water leaving radiance, L_w , which carries information about the water composition, represents less than 10% (Mobley, 1994) of the total radiance reaching a satellite instrument (figure 4.1-1). The maximal return from water leaving radiance occurs in the blue wavelengths at clear waters, while for large chlorophyll concentrations or high absorption by CDOM and non-pigmented particles, the water leaving radiance can be much lower in the blue wavelength region. A small error in estimating the atmosphere's optical properties can result in a large error in water leaving radiance and in the derived underwater composition.

An accurate radiative transfer calculation must be performed to remove the atmospheric effect from satellite imagery over the ocean and recover the water leaving radiance. This calculation depends on the relative position of the sun and the sensor, as well as on the nature and vertical distribution of atmospheric gases and aerosols.

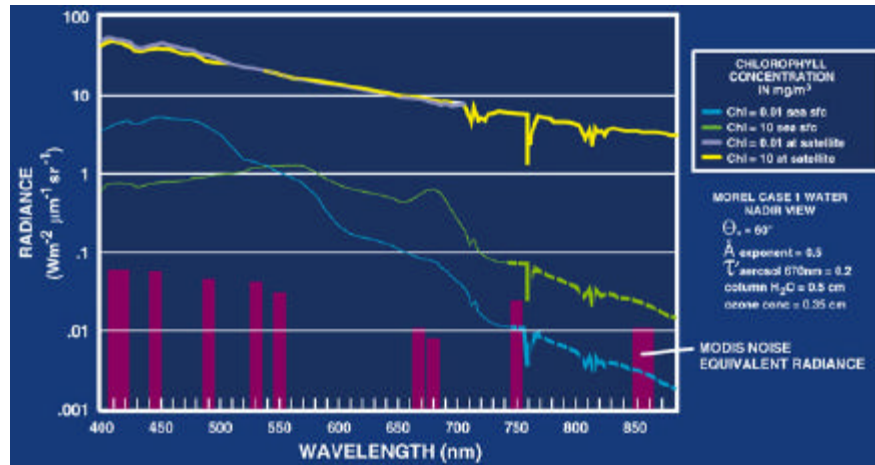


Figure 4.1-1: Water leaving radiances (blue and green lines) and radiances measured by a satellite at the top of the atmosphere (purple and yellow lines) in high ([Chl-a]=10mgm⁻³) and low ([Chl-a]=1 mgm⁻³) chlorophyll waters. The MODIS wavelength bands are also shown (Esaias et al, 1997).

Atmospheric correction algorithms were developed for the CZCS in the past, by Gordon (1978), Gordon and Clark (1980, 1981), Gordon et al (1983). The radiometric sensitivity of the CZCS was sufficiently low that it was not necessary to deal with the full complexities of multiple scattering. However, with the increased sensitivity of SeaWiFS and MODIS, multiple scattering in the atmosphere is an important issue in atmospheric correction algorithms. A comprehensive review of the present state of atmospheric correction is provided by Gordon and Voss (1999) (MODIS ATBD 18).

The normalized water leaving radiance, nL_w, was defined by Gordon and Clark (1981):

$$L_w(\lambda) = nL_w(\lambda) \cos \theta_o \exp [- (\tau_r(\lambda) / 2 + \tau_{Oz}(\lambda)) (1 / \cos \theta_o)] \quad (4.1.1)$$

where L_w(λ) is the water-leaving radiance at wavelength λ, τ_r(λ) and τ_{Oz}(λ) are the optical thickness of the atmosphere associated with molecular (Rayleigh) scattering and ozone absorption respectively and θ_o is the solar zenith angle. Ignoring bidirectional

effects (Morel and Gentili, 1991) the normalized water leaving radiance is approximately the radiance that would exit the ocean in the absence of the atmosphere, with the sun at the zenith. The normalized water leaving radiance is the ‘first order’ satellite product that is used in satellite algorithms to derive geophysical parameters in the oceans, such as chlorophyll concentration.

The total radiance received by a sensor at the top of the atmosphere, in a spectral band centered at wavelength λ_i , $L_t(\lambda_i)$, is the sum of: i) the water leaving radiance, ii) the radiance generated along the optical path by scattering (Rayleigh and aerosols) in the atmosphere and by specular reflection of atmospherically scattered light from the sea surface, $L_{\text{path}}(\lambda_i)$, iii) the radiance arising from specular reflection of direct sunlight from the sea surface (sun glint), $L_g(\lambda_i)$, and iv) the contribution arising from reflection of skylight and direct sunlight from individual whitecaps on the sea surface, $L_{\text{wc}}(\lambda_i)$.

Therefore:

$$L_t(\lambda_i) = t(\lambda_i) \cdot L_w(\lambda_i) + L_{\text{path}}(\lambda_i) + T(\lambda_i) \cdot L_g(\lambda_i) + t(\lambda_i) \cdot L_{\text{wc}}(\lambda_i) \quad (4.1.2)$$

or in terms of reflectance, $\rho(\lambda_i)$, ($\rho = \pi L / F_o \cos \theta_o$, where F_o is the solar irradiance at the top of the atmosphere):

$$\rho_t(\lambda_i) = t(\lambda_i) \cdot \rho_w(\lambda_i) + \rho_{\text{path}}(\lambda_i) + T(\lambda_i) \cdot \rho_g(\lambda_i) + t(\lambda_i) \cdot \rho_{\text{wc}}(\lambda_i) \quad (4.1.3)$$

where $t(\lambda_i)$ is the diffuse transmittance of the atmosphere and $T(\lambda_i)$ is the direct transmittance (expressions for $t(\lambda_i)$ and $T(\lambda_i)$ are given in MODIS ATBD18, 1999). The term $\rho_{\text{path}}(\lambda_i)$ can be decomposed to $\rho_{\text{path}}(\lambda_i) = \rho_r(\lambda_i) + \rho_a(\lambda_i) + \rho_{\text{ra}}(\lambda_i)$, where ρ_r is the reflectance resulting from multiple scattering by air molecules (Rayleigh scattering) in the absence of aerosols, ρ_a is the reflectance resulting from multiple scattering by

aerosols in the absence of the air, ρ_{ra} is the interaction term between molecular and aerosol scattering. According to Gordon and Voss (1999), in equations (4.1.2) and (4.1.3) the diffuse transmittance is appropriate for the water-leaving radiance and the whitecap radiance, since they have near-uniform angular distribution, while the direct transmittance is used for the highly directional (except at very high wind speeds) sun glint. The contribution of the sun glint can be very large near the specular image of the sun, but rapidly decreases away from this point. Since the water-leaving signal near the sun's specular image cannot be retrieved accurately, the contribution of sun glint is generally ignored, by disregarding the imagery where ρ_g is significant. The small whitecap contribution can be calculated from an estimate of the wind speed from numerical weather models (Frouin et al, 1996; Gordon and Wang, 1994). The Rayleigh scattering contribution can be precisely computed, even accounting for polarization effects, given estimates of the wind speed (numerical weather models) and the surface atmospheric pressure (Gordon et al, 1988). In order to estimate the water leaving reflectance ρ_w from the reflectance ρ_t measured by the sensor at the top of the atmosphere, the aerosol contribution, $\rho_A = \rho_a + \rho_{ra}$, needs to be estimated. This is the most difficult part of the atmospheric correction problem because of the high spatial and temporal variability of the physical, chemical and optical properties of aerosols. At the level of accuracy required for modern sensors, multiple scattering effects cannot be neglected (Esaias et al., 1997).

The original MODIS atmospheric algorithm was based on the assumption that the water leaving radiance at NIR wavelengths (bands 749 and 869 nm) is negligible, so that for the

NIR bands the only unknown in eq (4.1.3) is the contribution from the atmosphere. However, this assumption can be applied only to case 1 waters, while in the most turbid, case 2 waters high backscattering may result in non-zero water leaving radiances. As mentioned in the MODIS Data Quality Summary for Terra nLw Collection-4 (last updated: August 6, 2002), in collection 4, v4.2 (MODIS data used in this project) improvements were made in the NIR atmospheric correction to allow some water leaving radiance to be present at 749 and 869 nm (Siegel et al, 2000). Therefore, for the two NIR MODIS bands it is possible to have an estimate of ρ_A at each satellite pixel. The spectral variation of ρ_A between the two MODIS wavelengths can be used to select two aerosol models from a list of candidates (aerosol models developed by Shettle and Fenn, 1979) and then use the two aerosol models to extrapolate ρ_A into the shorter visible wavelengths. For the extrapolation, a set of look-up tables is used that provides ρ_A as a function of the aerosol concentration for various sun-viewing geometries. The look-up tables were computed assuming hypothetical atmospheres with a two-layer structure, with the aerosols occupying the lower layer and all of the Rayleigh scattering confined to the upper layer. This extrapolation method could result in errors in the atmospheric correction at the shorter visible wavelengths.

According to Gordon and Voss (1999), the MODIS multiple scattering algorithm can provide very good results as long as the aerosol is weakly absorbing and follows the relationship between size distribution and refractive index that is implicit in the choice of the candidate aerosol models. The algorithm fails when the aerosol is strongly absorbing, unless the candidate aerosol models are restricted to those with values of single scattering

albedo similar to the true aerosol. Therefore, for regions where there are significant amounts of strongly absorbing aerosols (e.g. urban aerosols or desert dust transported over large distance over the ocean by winds), the atmospheric correction algorithm may not work accurately. Furthermore, according to Gordon and Voss (1999), for strongly absorbing aerosols, even if the appropriate candidate aerosol models are used, knowledge of the vertical distribution of the aerosols (accuracy of $\pm 1\text{km}$) is required for an adequate correction, since the vertical distribution of strongly absorbing aerosols influences the top-of-the-atmosphere reflectance in the visible (especially in the blue) but not in the NIR. New algorithms have been developed, that are based on simultaneous determination of oceanic and atmospheric properties and show promise in dealing with strongly absorbing aerosols (Chomko and Gordon, 1998; Gordon et al, 1997). Use of these algorithms should enhance the MODIS atmospheric correction.

Another improvement of the MODIS algorithm is associated with removing bi-directional effects (dependence of satellite measured water-leaving radiance on solar and satellite zenith and azimuth angles) and incorporating a ρ_w BRDF (bi-directional reflectance distribution function) model into the processing stream, to determine the satellite nadir-viewing normalized water-leaving radiance. The same BRDF model is planned to be used for better estimations of the diffuse transmittance $t(\lambda_i)$ in equations 4.1.2, 4.1.3.

4.2 In-situ measurements and Satellite (MODIS) estimates of Remote Sensing Reflectance - Methodology

4.2.1 In-situ measurements and theoretical estimations of Remote Sensing Reflectance

Measurements of underwater upwelling radiance, L_u , and downwelling irradiance, E_d , profiles at 14 visible wavelengths (400-700nm) were obtained using the multi-spectral MicroPro free-falling radiometer, during seven of our cruises in the Chesapeake Bay waters (table 4.2-1). For these specific cruises, the in-water measurements of upwelling radiance, $L_u(z)$, were used to estimate the water leaving radiance, L_w , just above the water surface, according to the methodology described in chapter 3, (section 3.3). Using simultaneous measurements of the incident surface irradiance, E_s , performed with the surface-reference Satlantic OCR-507 irradiance sensors, the remote sensing reflectance, defined as the ratio of the water-leaving radiance to the total incident irradiance, was estimated according to:

$$R_{rs}(\lambda) = \frac{L_w(\mathbf{I})}{E_s(\mathbf{I})} \quad (4.2-1)$$

The normalized water leaving radiance, $nL_w(\lambda)$, was estimated from the remote sensing reflectance, $R_{rs}(\lambda)$, by multiplying with the solar irradiance at the top of the atmosphere, $F_o(\lambda)$, (Neckel and Labs, 1984) according to:

$$nL_w(\mathbf{I}) = R_{rs}(\mathbf{I}) \cdot F_o(\mathbf{I}) \quad (4.2-2)$$

Table 4.2-1: Cruise Summary and Instrumentation

No	Date of cruise	Instrument used for radiation fields
1	2001, June 4	Satlantic OCI-200
2	2001, June 11	Satlantic OCI-200
3	2001, June 25	Satlantic OCI-200
4	2001, July 9	Satlantic OCI-200
5	2001, September 21	Satlantic SMSR
6	2001, September 26	Satlantic MicroPro
7	2001, September 28	Satlantic MicroPro
8	2001, October 4	Satlantic OCI-200
9	2001, October 30	Satlantic MicroPro
10	2001, November 13	Satlantic OCI-200
11	2002, May 6	Satlantic MicroPro
12	2002, May 15	Satlantic MicroPro
13	2002, May 22	Satlantic MicroPro
14	2002, June 6	Satlantic OCI-200
15	2002, June 18	Satlantic OCI-200
16	2002, June 28	No Lu or Ed measurements
17	2002, November 8	Satlantic MicroPro

As was already mentioned in chapter 3, theoretical estimations of water-leaving radiances have been performed using the Hydrolight radiative transfer code for those cases when MicroPro measurements of underwater radiation fields and simultaneous detailed measurements of the water's inherent optical properties were available. As discussed in chapter 3, the estimated by the model water-leaving radiances, $L_{W(model)}$, and the estimated water-leaving radiances based on the in-situ measurements of L_u , $L_{W(InSitu)}$, were in very good agreement in almost all of the cases studied, which gives us confidence in the accuracy of the in-situ measurements (both inherent and apparent optical properties). At the same time, the good agreement between 'measured' and theoretically estimated water-leaving radiances suggests that when in-situ measurements of underwater radiances are not available, the radiative transfer model can be used to estimate the radiation fields, provided that accurate information on the inherent optical properties of the water is available.

Therefore, the Hydrolight code was used to estimate the remote sensing reflectance, $R_{rs}(\lambda)$, for those cruises when the MicroPro instrument was not used, but measurements of total incident irradiance, E_s , and water inherent optical properties were performed. During those cruises the downwelling surface irradiance was measured using the Satlantic, OCI-200 irradiance sensors (table 2.2-2, chapter 2). The normalized water leaving, nLw , was estimated in this case from the theoretically estimated remote sensing reflectance, by multiplying again with the solar irradiance at the top of the atmosphere, $F_o(\lambda)$, according to:

$$nLw(\mathbf{I}) = R_{rs_model}(\mathbf{I}) \cdot F_o(\mathbf{I}) \quad (4.2-3)$$

4.2.2 Satellite pixels around the location of each station

The in-situ measurements in Chesapeake Bay were usually performed within a time window of $\pm 2-3$ hours around the time of MODIS/Terra overpass. Due to the presence of currents in the Bay, the water mass sampled at each station during the cruises does not always correspond to the satellite pixel that was “geographically closest” to the station, at the time of the satellite overpass. Because of this, a number of satellite pixels around the location of each site were examined when comparing the satellite observations to the in-situ measurements.

Measurements of current speed (in cm/s) and current direction (in degrees from polar north) have been performed, over the last two years, at the Chesapeake Bay Mid-Bay station (station located closest to the location of HB, JT, PI and TI stations), by the

Chesapeake Bay Observing System - CBOS (W. Boicourt, C. Derry, T. Wazniak, R. Cone, W. Boynton). According to the measurements (data and plots available at the CBOS website: <http://www.cbos.org/>), maximum current speeds of 50 cm/s or 1.8 km/h have been observed at the Mid Bay station during specific dates coincident with the dates of some of our in-situ measurements (e.g. 21 and 26 September 2001, 4 October 2001). Therefore, when comparing the in-situ measurements to the satellite estimations of remote sensing reflectances (1 km resolution at nadir), all 5x5 pixels around the location of each station have been studied, since the time-difference between in-situ measurements and satellite overpass, during our cruises, was $\pm 2-3$ h.

4.2.3 Satellite observations of Remote Sensing Reflectance

Satellite measurements of remote sensing reflectances, R_{rs} , in the Chesapeake Bay waters, were studied using data from the MODIS instrument aboard the EOS Terra satellite. Among the derived MODIS / Terra ocean Level-2 products are values of normalized water leaving radiance, nLw , (measured in $W/m^2/\mu m/sr$) estimated at seven of the MODIS wavelength bands, centered at 412, 443, 488, 531, 551, 667 and 678 nm (products 1-7 in table 4.1-3). In-situ measurements of radiation fields were used to interpret the water-leaving radiance spectra measured by the satellite during the days of the cruises in the northern Chesapeake Bay (table 4.2-2).

Table 4.2-2: MODIS overpasses during the dates of the cruises

Date of cruise	MODIS overpass	Time (GMT) of MODIS overpass	Satellite zenith angle (°)	Atmospheric conditions
2001, June 4	✓	16:30	35°	~ clear sky
2001, June 11	✓	16:35	42°	clouds/haze
2001, June 25	-	-	-	
2001, July 9	✓	15:20	-61°	
2001, September 21	✓	15:55	-18°	clouds
2001, September 26	✓	16:15	15°	~ clear sky
2001, September 28	✓	16:00	-7°	clouds
2001, October 4	✓	15:25	-57°	~ clear sky
2001, October 30	✓	16:00	-8°	~ clear sky
2001, November 13	✓	16:10	16°	~ clear sky
2002, May 6	✓	16:20	35°	clouds/haze
2002, May 15	✓	16:15	26°	
2002, May 22	✓	16:20	36°	~ clear sky
2002, June 6	✓	15:40	-38°	
2002, June 18	✓	16:05	5°	
2002, June 28	✓	16:40	55°	clouds
2002, November 8	✓	15:25	-57	~ clear sky

All MODIS ocean Level 2 products are available in the Hierarchical Data Format (HDF) (MODIS Ocean Data Guide, MODIS website). The MODIS HDF files can be read in SeaDAS (SeaWiFS Data Analysis System, a widely used software package developed and supported by NASA, that is intended to be used with ocean color satellite data), IDL and Matlab, and available subroutines in FORTRAN, C, and other languages. However, when the SeaDAS program was used to read the MODIS data, small changes on the latitude and longitude information occurred, compared to the actual information stored in the MODIS geolocation file (e.g. differences in the order of 0.01° or ~ 1km for the Chesapeake Bay latitude). The reason for this is that SeaDAS uses interpolation to reshape the MODIS geolocation field in order to allow the user to easily choose Pixel/Line Sample Rate in SeaDAS image display (personal communication L.Wang). Such an interpolation also smoothes the “bow-tie” effect (satellite-pixels’ size growth and

overlap towards the edge of the satellite's scan) in MODIS measurements (MODIS Level 1A Earth Location, ATBD, 1997). To obtain higher accuracy on the pixels' location, the MODIS measurements of $nLw(\lambda)$ used in this study have been read directly from the MODIS/Terra "MODOCL2" HDF files (version 4, ".004"), using the IDL function "HDF_SD_GETDATA". Information on the location (latitude and longitude) of each pixel was obtained (again using IDL commands) from the corresponding "MODO3" geolocation files (version 4 ".004" for all files except days 6 June 2002 and 28 June 2002 for which only version ".003" geolocation files were available). The accuracy of the geolocation data is better than (less than) 50 m Root Mean Square Error (RMSE) in the scan and track directions in nadir equivalent units (personal communication R. Wolfe). This is 0.00045° in latitude and longitude at the equator, and $\sim 0.00057^\circ$ at the latitude at HB, PI, TI and JT stations.

The MODIS normalized water-leaving radiances are characterized by a certain "quality level", depending on which ones of the "common" flags and the "product specific" flags are clear. The "quality levels" range from 0 to 3, with 0: good, 1: questionable, 2: cloud/sunglint contaminated and 3: bad. Information on the quality level of the MODOCL2 parameters (MODIS parameters 1-12 in table 4.1-1) is stored in the MODIS MODOCL2 files as an array of type Byte (8 bits). Information on the quality level of the nLw values is stored in the first two bits of the Byte array. The MODIS "common" and "nLw-product specific" flags are shown in table 4.2-3, while a description of the MODIS quality levels for all nLw parameters is given in table 4.2-4. A certain pixel is of the best quality (quality = 0), concerning the nLw products, if common flags 1-3, 6, 8 are clear

and product specific L2 flags 1 and 9-16 are clear (“L2QLflags.V4.html” document, K. Kilpatrick, 2003). In the case of large satellite or solar zenith angle, the pixel is of questionable quality (quality=1). The solar zenith angle threshold is 70° . The satellite zenith angle threshold for ocean color products is 65° (personal communication K. Kilpatrick and “productflags.V4.html” document, K. Kilpatrick, 2003) (documents “L2QLflags.V4.html” and “productflags.V4.html” are given in the APPENDIX). In previous versions of MODIS data (Terra Collection 1, “L2QLflags.V1.html” document, K. Kilpatrick) pixels flagged as “shallow” waters (definition in table 4.2-4) would also be characterized as of quality 1. Almost the whole Chesapeake Bay is flagged as a shallow waters region. The nLw products are of quality 2 when the pixel is cloud or sun-glint contaminated. The quality level is 3 (bad, other than cloud) if any input radiances are negative or saturated, or the atmospheric correction has failed, or aerosol model=16, or land (table 4.2-4).

Among the pixels examined in this study (5x5 pixels around each site) there were few cases (e.g. MODIS overpass, date: 9 July 2001) where pixels with flagged nLw values (nLw negative or zero) at all wavelengths were characterized as of quality 0. For the measurements performed on 9 July 2001, those pixels were close to the edge of the satellite scan (satellite zenith angle over Chesapeake Bay was -61° on 9 July 2001, very close to the satellite zenith angle threshold of 65°). After examining (September 2003) the accuracy and performance of the IDL code (“mocean_l2_map.pro”, K. Kilpatrick, 1999) that was used, in the framework of this project, to extract the nLw and quality values from the MODIS MODOCL2 HDF files, it turned out that the MODIS “Bit function” that

is used in the IDL code to decode the quality Byte (and return a value of 0, 1, 2 or 3 as a quality level for nLw) is correct and so, the problem mentioned above (pixels with $nLw < 0$ at all wavelengths, characterized as pixels of 'best quality level') is related to the actual information stored in the quality Bytes in the MODIS HDF files. Pixels of quality level 2 were found only during two of the cruises in the Chesapeake Bay (on 15 May 2002 and 18 June 2002). The majority of the pixels were of quality level 3.

Pixels of all quality levels have been examined in this study. This was mainly because:

- i) The number of pixels with quality level 0 was too small and the number of pixels with quality-level=1 was zero (since there were no cases with satellite and solar zenith angle larger than the threshold values).
- ii) In some cases (e.g. 9 July 2001, 4 October 2001, 22 May 2002, 8 November 2002 in figures 4.3-3(c), 4.3-6 (c), 4.3-10(c) and 4.3-13(c)) pixels of quality-level=0 gave flagged radiances at most or all of the MODIS wavelengths
- iii) in some cases pixels of quality-level=3 had water-leaving radiances that were in good agreement (at least at some of the wavelengths) with the in-situ measurements. However, pixels with flagged normalized water-leaving radiances ($nLw = 0$ or -1) at all seven wavelengths have been discarded (independent of the value of quality level). Pixels with $nLw(\lambda) = -5$ have also been discarded, since -5 is the fill value that is given to the MODIS nLw product when a pixel is not processed or when the pixel is on land (K. Kilpatrick , personal communication).

Table 4.2-3:MODIS ‘common’ and “product specific’ flags
(from “productflags.V4.html”, K. Kilpatrick, 2003, MODIS website)

Common flags	Product-specific L2 MODIS flags
1. Pixel not processed	1. Atm Correction; Invalid Rayleigh scattering data
2. Atmospheric Correction Failed	2. Calculated nLw551 too low
3. Satellite Zenith Angle > 65°	3. Coccolithophorid Radiance exceeds threshold
4. Solar Zenith Angle > 70°	4. Turbid case 2
5. Shallow water (i.e. < 5km from coast or < 50 m deep, or inland lake)	5. High_La865
6. Sun Glint greater than threshold	6. Input Lw’s for clear water epsilon bad
7. Ancillary data missing or invalid	7. Epsilon < 0.67
8. Land	8. -
	9. Cloudy, Albedo at 865 threshold
	10. Missing Lw
	11. Lw(xxx) <=0
	12. Any Lw counts < 0
	13. Questionable polarization
	14. Gordon Aerosol Failure
	15. Epsilon out of range
	16. Any La(xxx) <=0

Table 4.2-4:Level 2 Quality-Level Flags (Terra Collection 4) for nLw parameters
(from “L2QLflags.V4.html” K. Kilpatrick, 2003, MODIS website)

Bits in the quality array of type BYTE	Description
1-2	0 = good (if common flags 1-3, 6, 8 are clear and product specific L2 flags 1 and 9-16 are clear)
	1 = questionable (if large satellite or solar zenith angles)
	2 = cloud or sun-glint contaminated (if there are clouds or sun-glint contamination)
	3 = bad (if any input radiances are negative or saturated or if the atmospheric correction has failed, or if aerosol model = 16, or if land)

4.3 MODIS and in-situ measurements of Remote Sensing Reflectance - Results

The four sites, HB, PI, TI and JT, where in-situ measurements were performed in the framework of this project, are located in the northern Chesapeake Bay, within an area sufficiently wide to have several satellite pixels sampling the water (Level 2 MODIS data with 1 km resolution at nadir). This area extends from 76.34° W to 76.54° W longitude and from 38.71° N to 38.89° N latitude (fig. 2.2-1, chapter 2). The MODIS view of this region is shown in figures 4.3-1(a)-4.3-13 (a), for the days of the cruises in the bay.

The exact location of the four sites, their proximity to land (red color represents land area in the figures) and the route followed by the boat (yellow line) from PI station (at the northeast) to HB station (at the southwest), to TI station (at the southeast), to JT station (at the northwest), are shown in figures 4.3.1(b)-4.3.13(b) for each cruise. The MODIS 551 nm normalized water-leaving radiances, $nLw(551)$, measured at each satellite pixel, are also shown in these figures. Satellite pixels not processed or with negative $nLw(551)$ are shown as black pixels. During the cruise performed on 25 June 2001 no MODIS data (no MODIS granules) were available. During three of the cruises (28 September 2001, 6 May 2002 and 28 June 2002), all of the MODIS pixels within the region of interest were characterized by flagged water-leaving radiances at all wavelengths and, thus, no comparisons between in-situ and satellite measurements were performed during these days (for this reason only 13 out of the 17 days of the cruises are shown in figures 4.3-1 - 4.3-13). A summary of all the days and sites when both in-situ and satellite data were available, is given in table 4.3-1, along with some comments on the atmospheric conditions observed over the region of interest at around the time of the MODIS

overpass. Measurements of aerosol optical thickness (AOT) were performed during the field observations both onboard the vessel (using a handheld Microtops sunphotometer) and on shore, at the SERC campus (measurements performed by a CIMEL sunphotometer located on top of a 120 ft tower, at 38.89° N, 76.56° W).

Figures 4.3-1(c) - 4.3-13(c) show the MODIS/Terra $nLw(\lambda)$ measured within the 5x5-pixels-region around each one of the four sites (PI, HB, TI, JT), during each cruise when MicroPro measurements or Hydrolight estimates of nLw were available. Measurements at pixels of quality level 0 (concerning the nLw products) are shown as red lines, while pixels of quality level 2 or 3 are shown as blue lines. The in-situ $nLw(\lambda)$ values measured (or theoretically estimated based on measured IOPs and boundary conditions) at each site, are also shown for comparison (thick yellow line).

According to the measurements shown in figures 4.3-1(c) - 4.3-13(c), there are many cases where the MODIS nLw at 412 and 443 nm is flagged as -1 or 0. A summary of the number of pixels with negative $nLw(\lambda)$ values at the MODIS ocean wavelengths, is shown in table 4.3-2. Almost 70 % of the MODIS pixels (that did not have flagged nLw values at all seven wavelengths) had flagged nLw values at the two shortest wavelength bands centered at 412 nm and 443 nm (423 out of 623 pixels had $nLw(412) = 0$ and 414 out of 623 pixels had $nLw(443) = 0$). Figure 4.3-14 shows the location of the MODIS pixels with negative normalized water-leaving radiances at some of the MODIS wavelengths. The location of the pixel with the best agreement with the in-situ measurements at 488, 551, 667 nm wavelength bands, is also shown in the same figure.

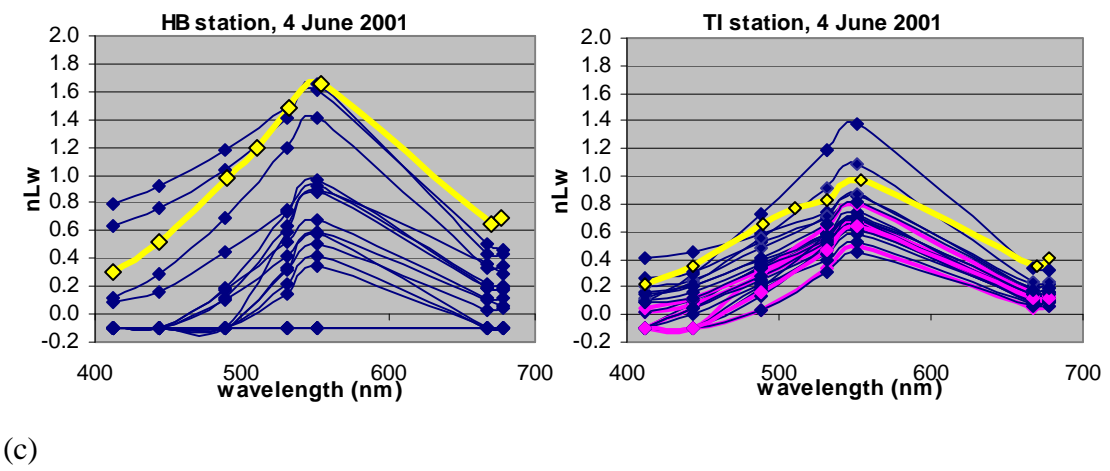
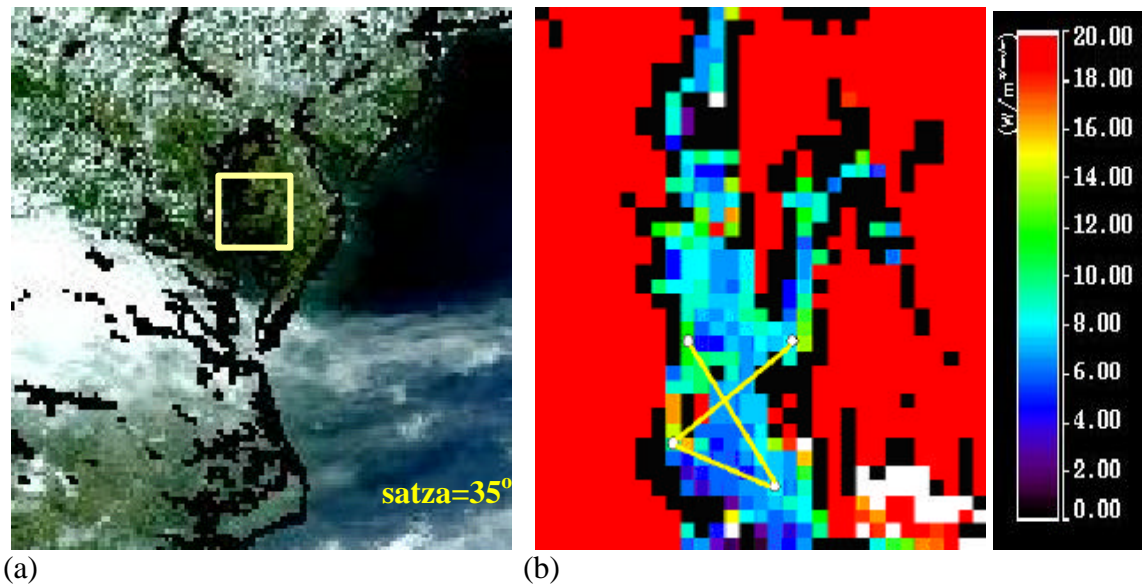
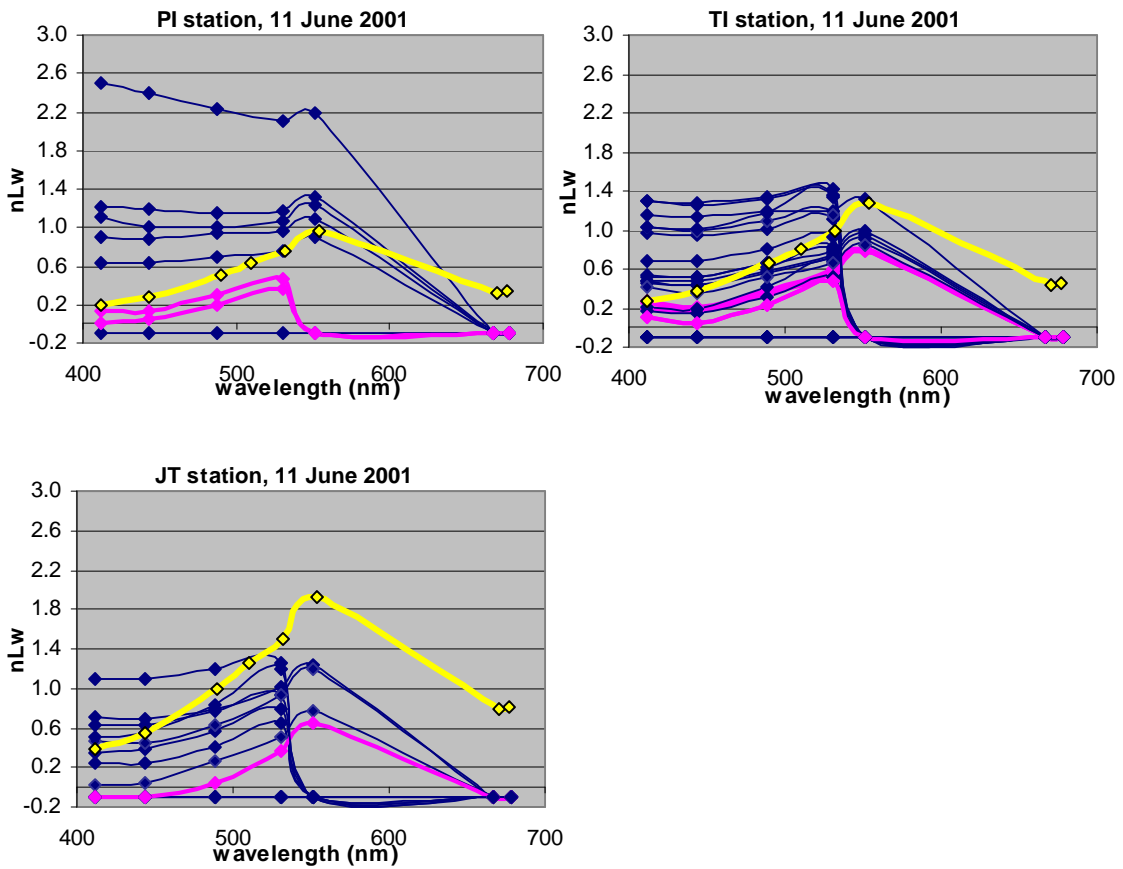
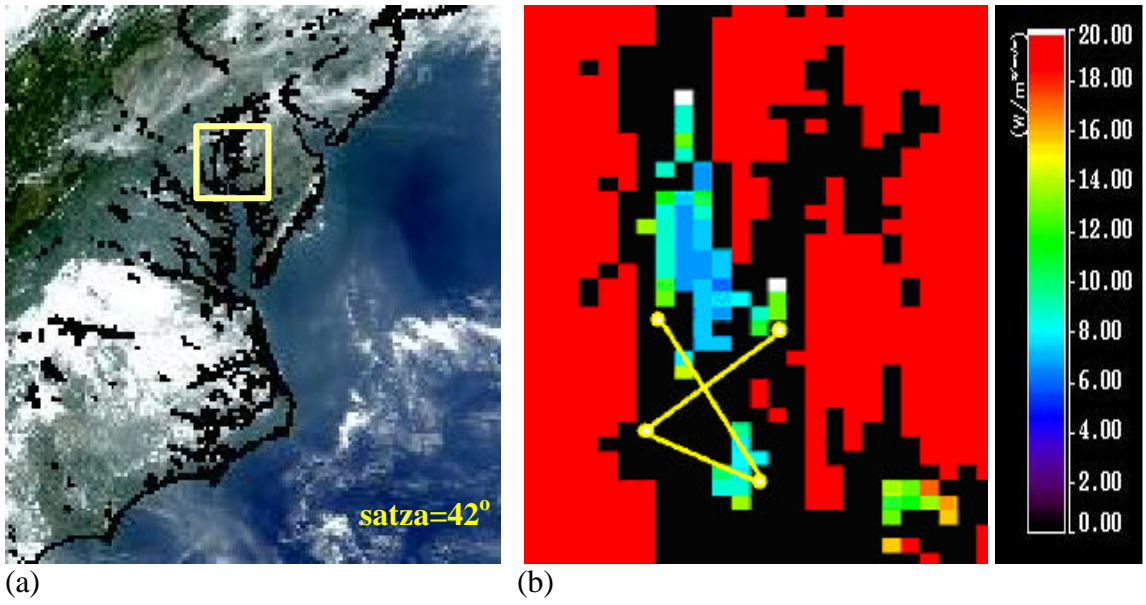


Figure 4.3-1: Satellite and in-situ (or model estimated) nLw spectra, 4 June 2001. Satellite zenith angle over the Chesapeake Bay region was 35°. (a) MODIS view of Chesapeake Bay (b) MODIS nLw(551) values (color bar in $Wm^{-2}\mu m^{-1}sr^{-1}$ units). The location of the four stations and the route of the boat are also shown. (c) In-situ and MODIS nLw spectra (in $\mu Wcm^{-2}nm^{-1}sr^{-1}$ units) at the stations where measurements were performed during this cruise. In-situ nLw spectra are shown as a thick yellow line. MODIS measurements (5x5 pixels around each station) are shown as red lines for pixels of quality level 0, and blue lines for pixels of quality level 2 or 3.



(c)
 Figure 4.3-2: Same a figure 4.3-1, for measurements on 11 June 2001. Satellite zenith angle over the Chesapeake Bay region was 42° .

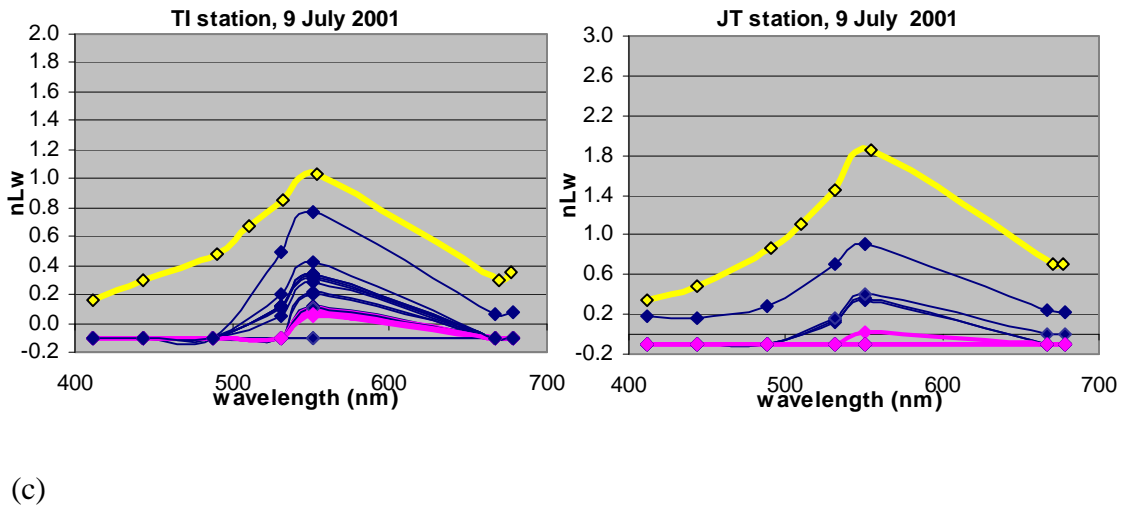
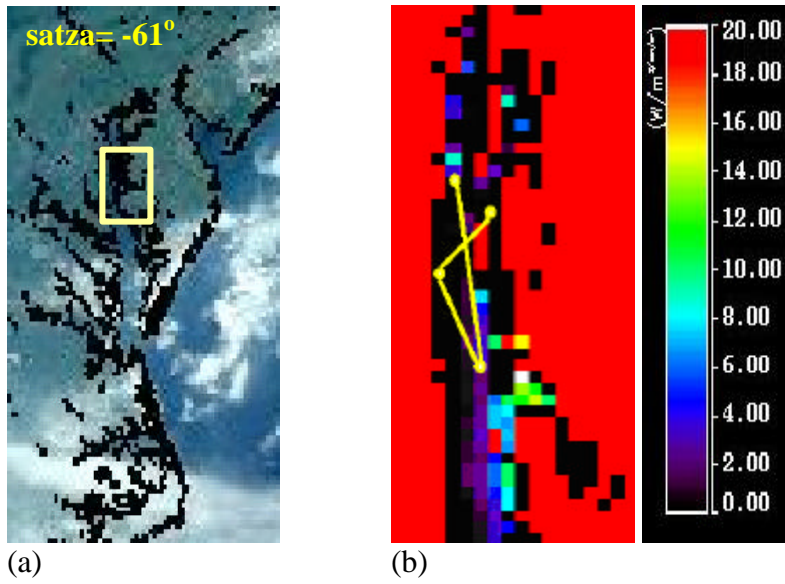


Figure 4.3-3: Same a figure 4.3-1, for measurements on 9 July 2001. Satellite zenith angle over the Chesapeake Bay region was -61° .

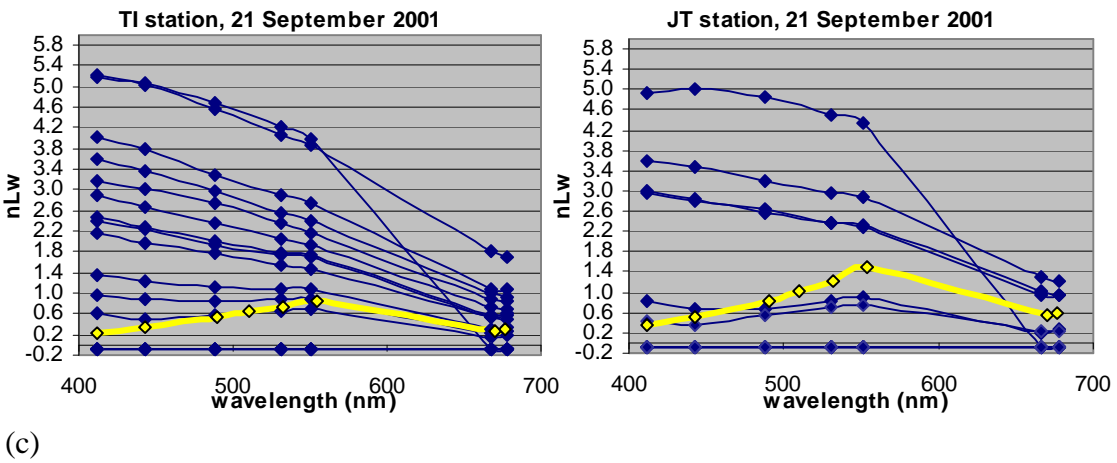
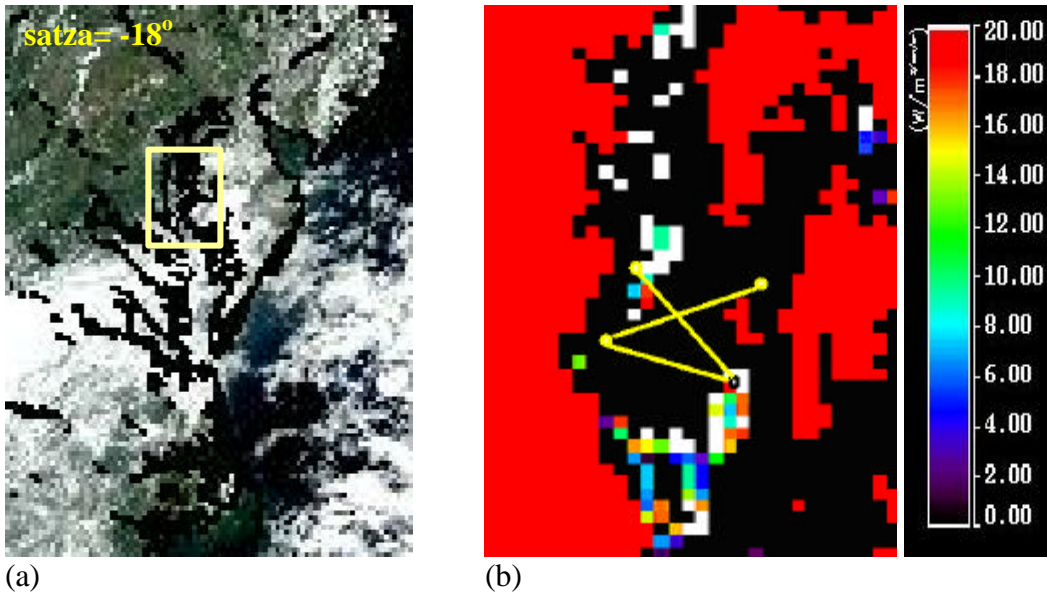
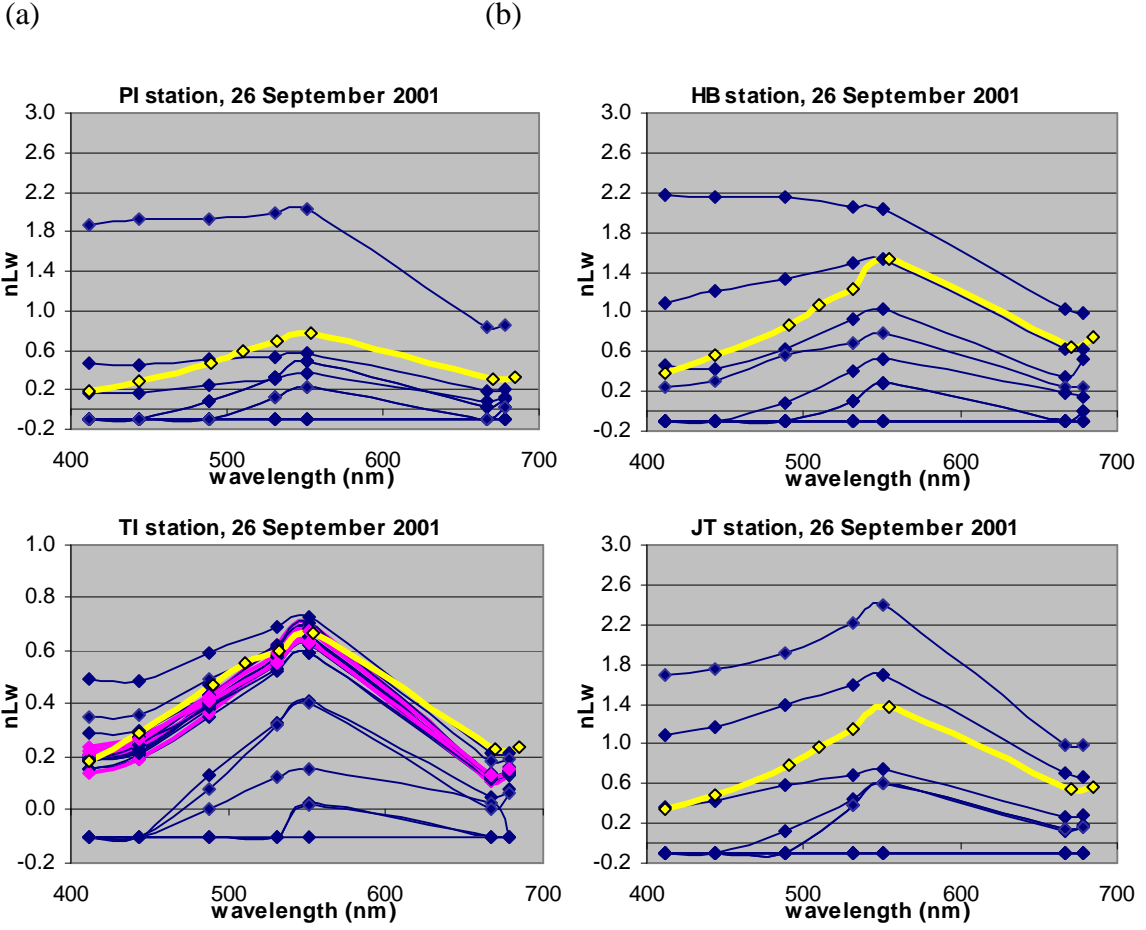
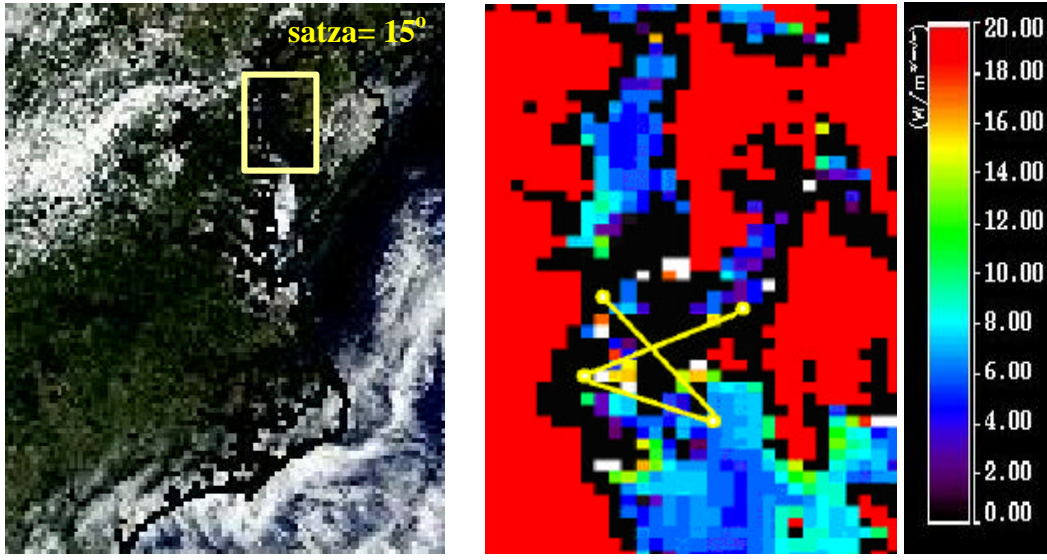


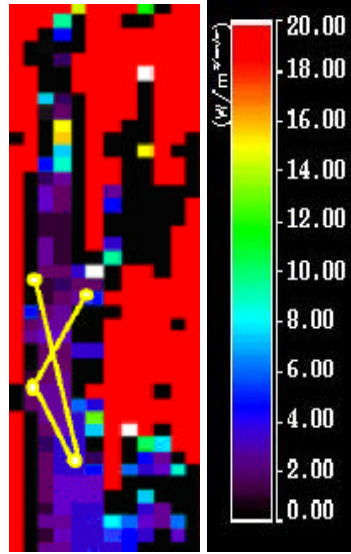
Figure 4.3-4: Same a figure 4.3-1, for measurements on 21 September 2001. Satellite zenith angle over the Chesapeake Bay region was -18° . No satellite pixels of quality level 0 (concerning nLw products) were found at TI and JT stations during this day.



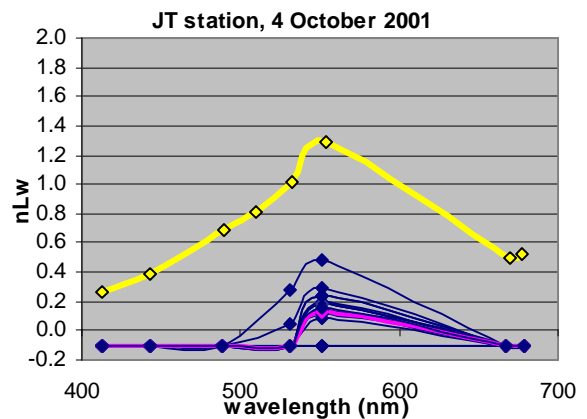
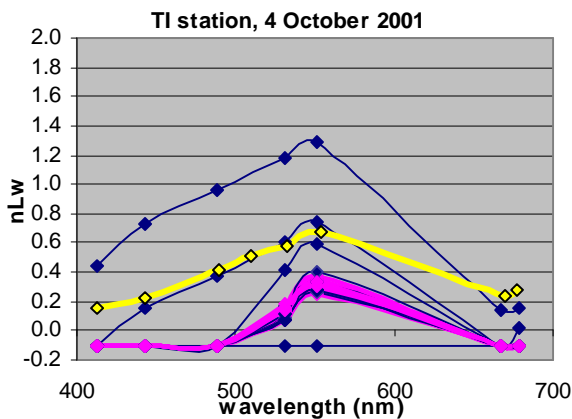
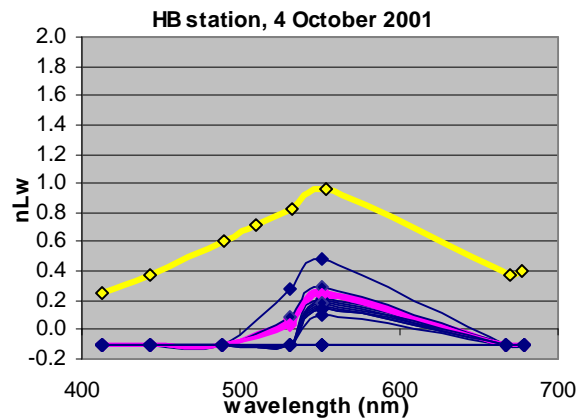
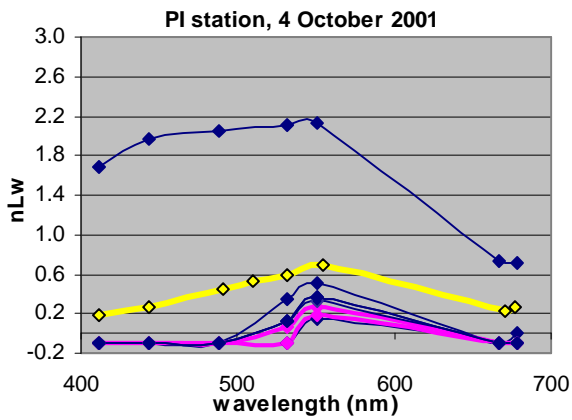
(c) Figure 4.3-5: Same a figure 4.3-1, for measurements on 26 September 2001. Satellite zenith angle over the Chesapeake Bay region was 15° .



(a)



(b)



(c)

Figure 4.3-6: Same a figure 4.3-1, for measurements on 4 October 2001. Satellite zenith angle over the Chesapeake Bay region was -57° .

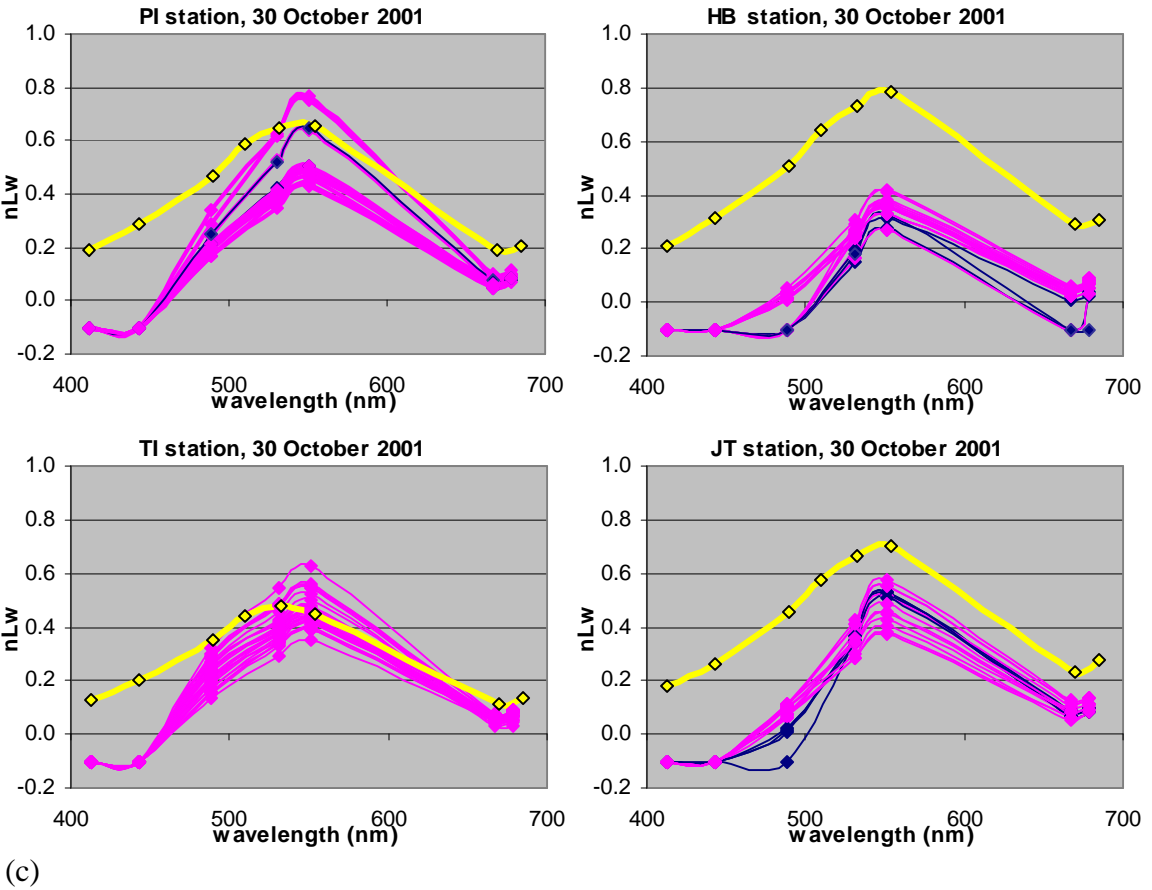
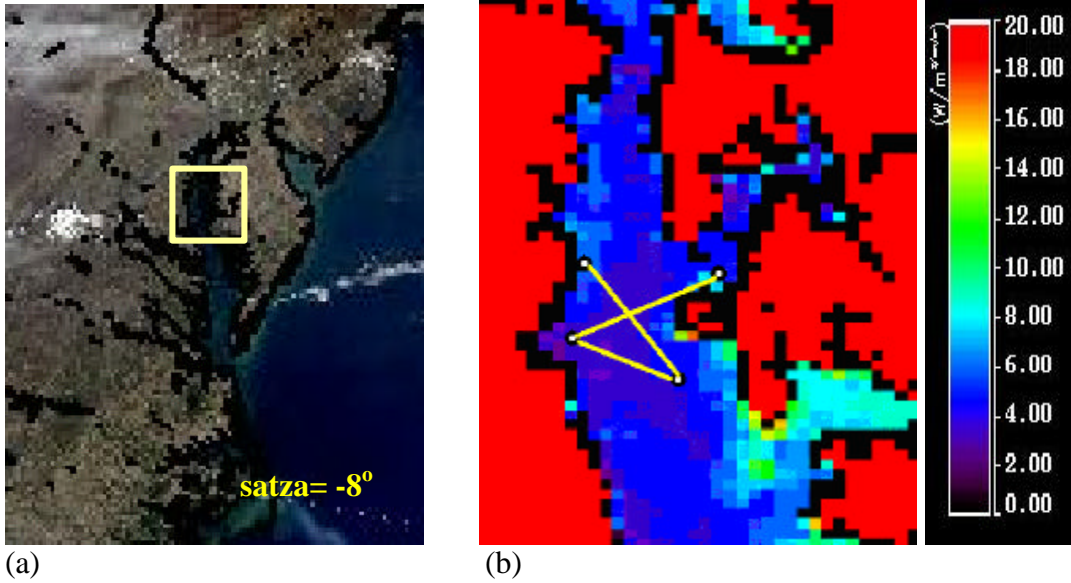


Figure 4.3-7: Same a figure 4.3-1, for measurements on 30 October 2001. Satellite zenith angle over the Chesapeake Bay region was -8° .

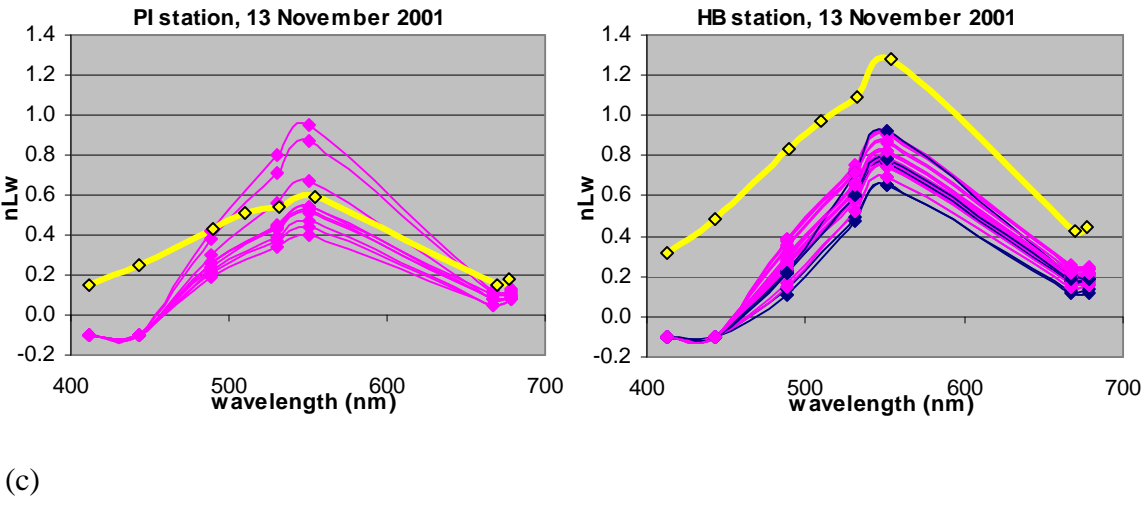
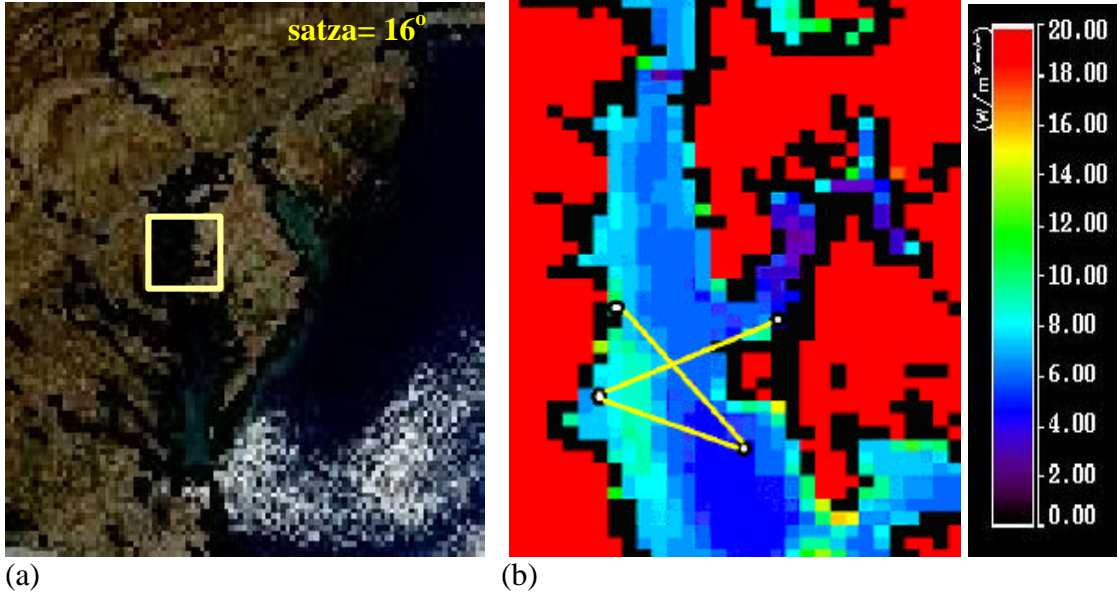
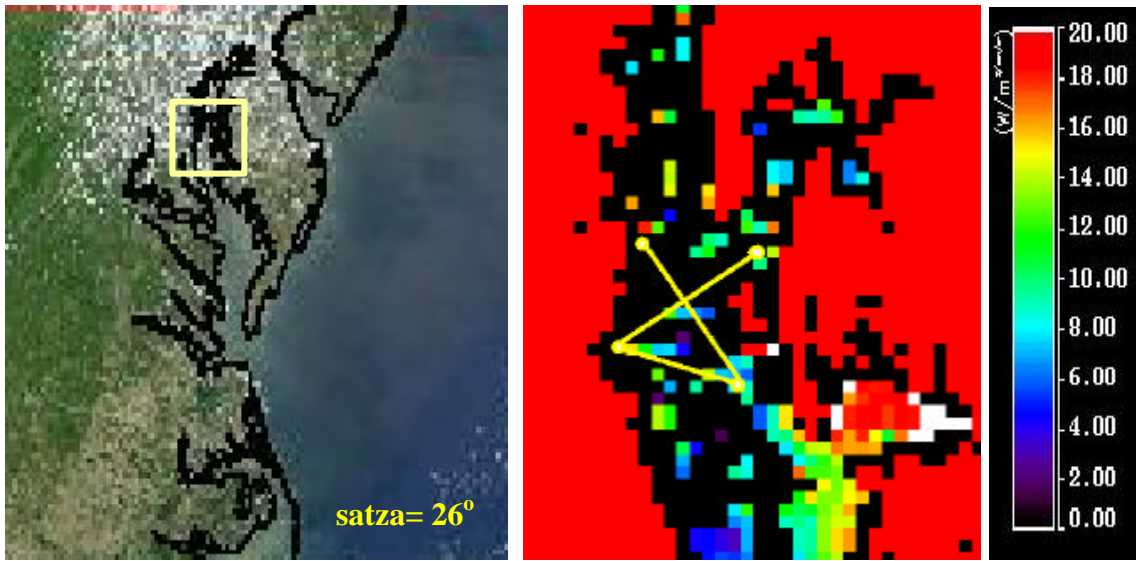
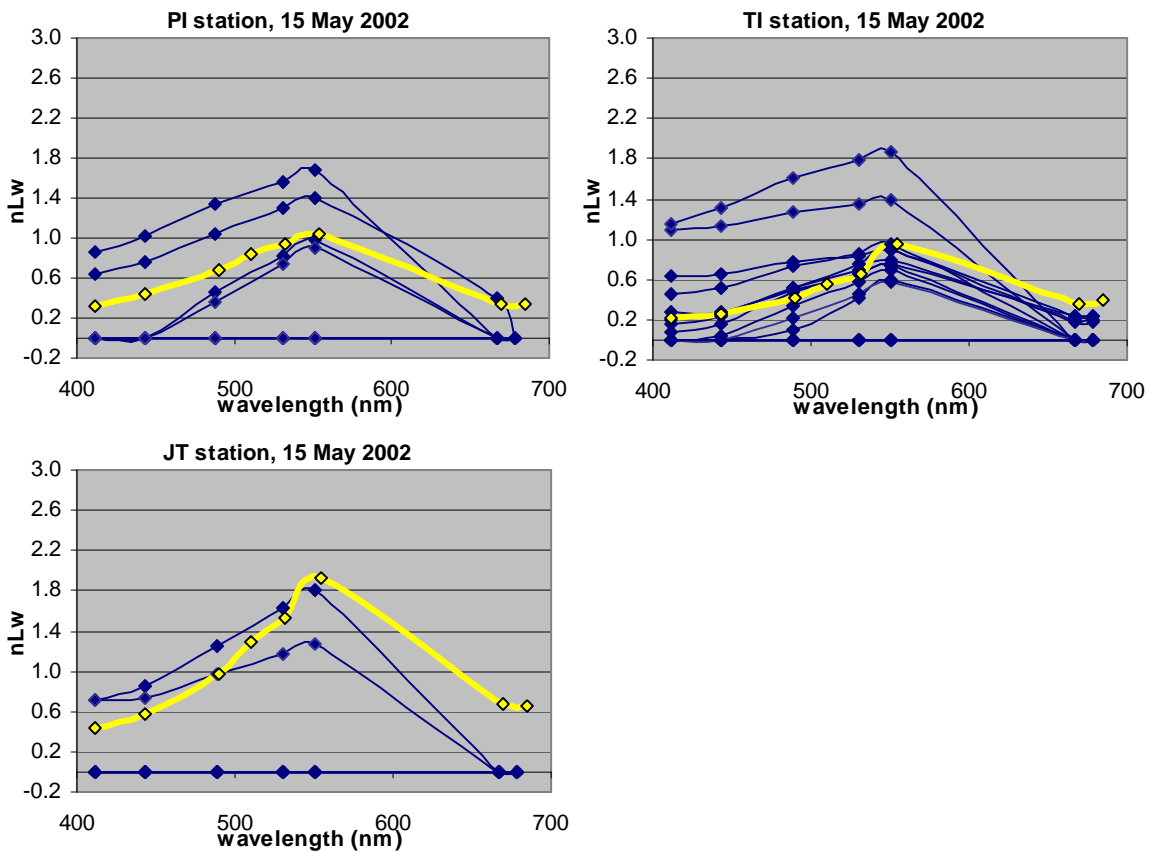


Figure 4.3-8: Same a figure 4.3-1, for measurements on 13 November 2001. Satellite zenith angle over the Chesapeake Bay region was 16° .



(a)

(b)



(c)

Figure 4.3-9: Same a figure 4.3-1, for measurements on 15 May 2002. Satellite zenith angle over the Chesapeake Bay region was 26° .

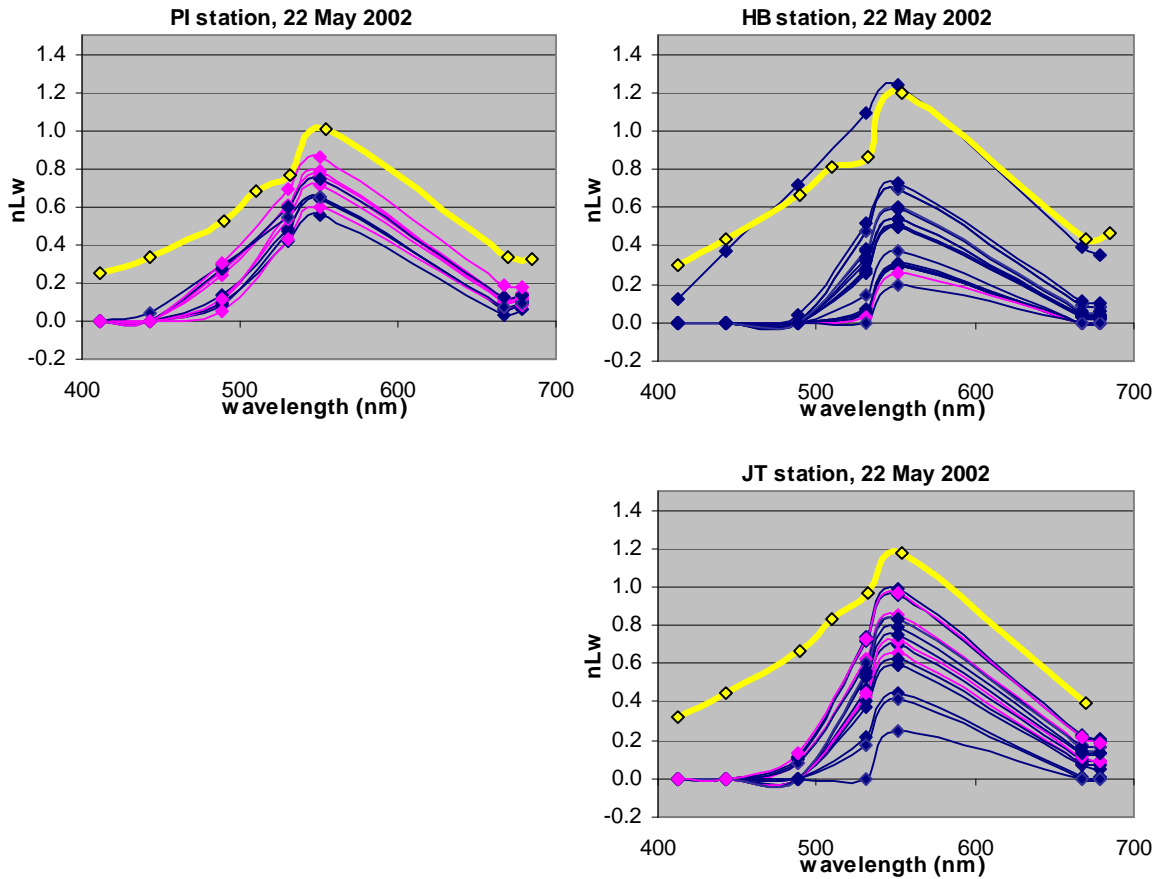
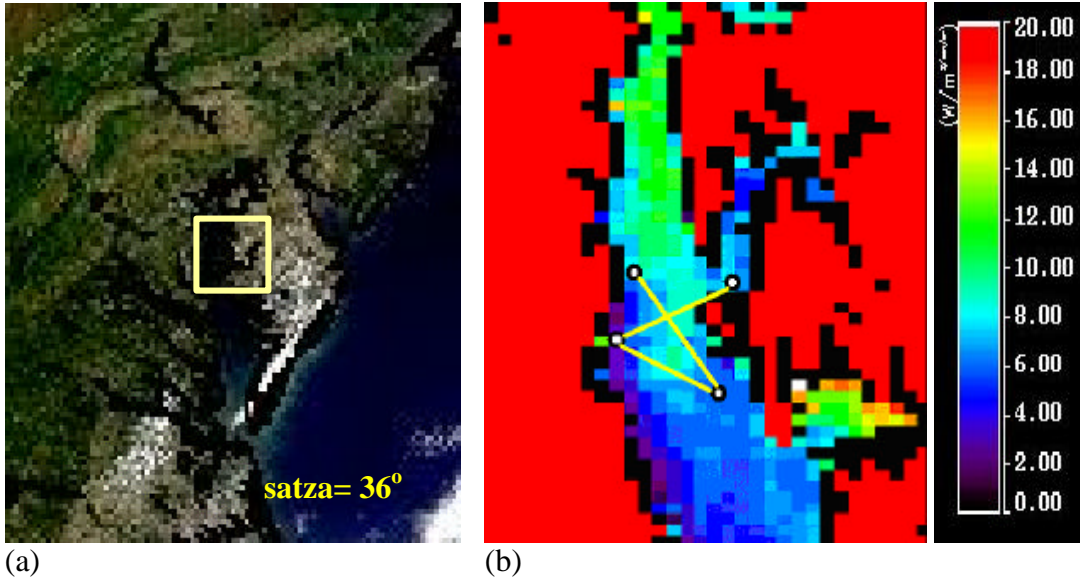
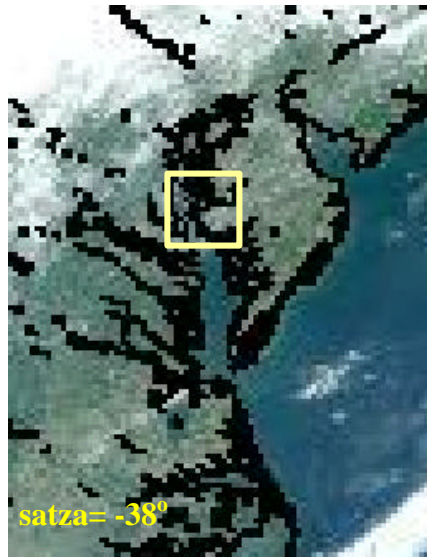
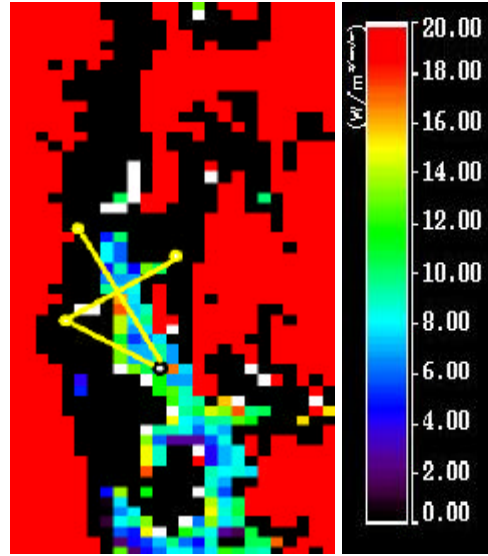


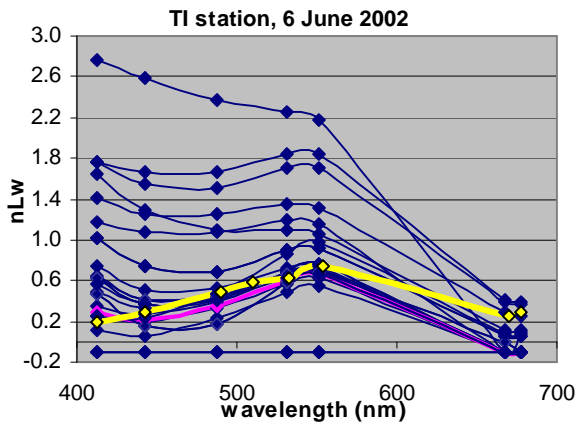
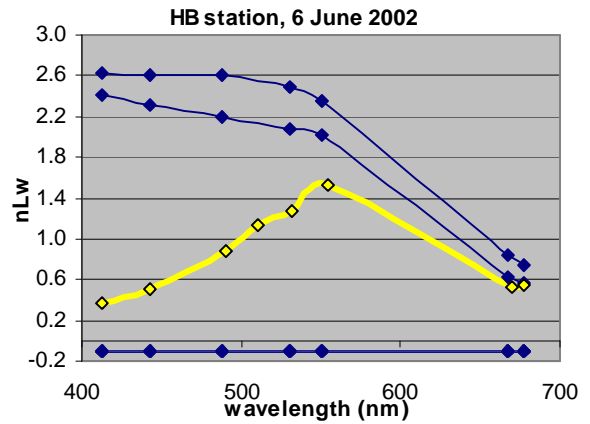
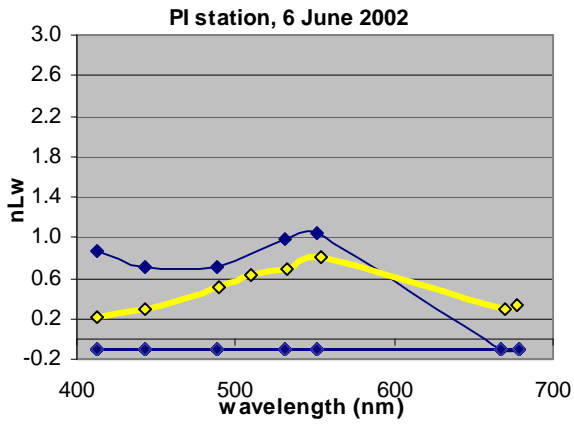
Figure 4.3-10: Same a figure 4.3-1, for measurements on 22 May 2002. Satellite zenith angle over the Chesapeake Bay region was 36° .



(a)



(b)



(c)

Figure 4.3-11: Same a figure 4.3-1, for measurements on 6 June 2002. Satellite zenith angle over the Chesapeake Bay region was -38° .

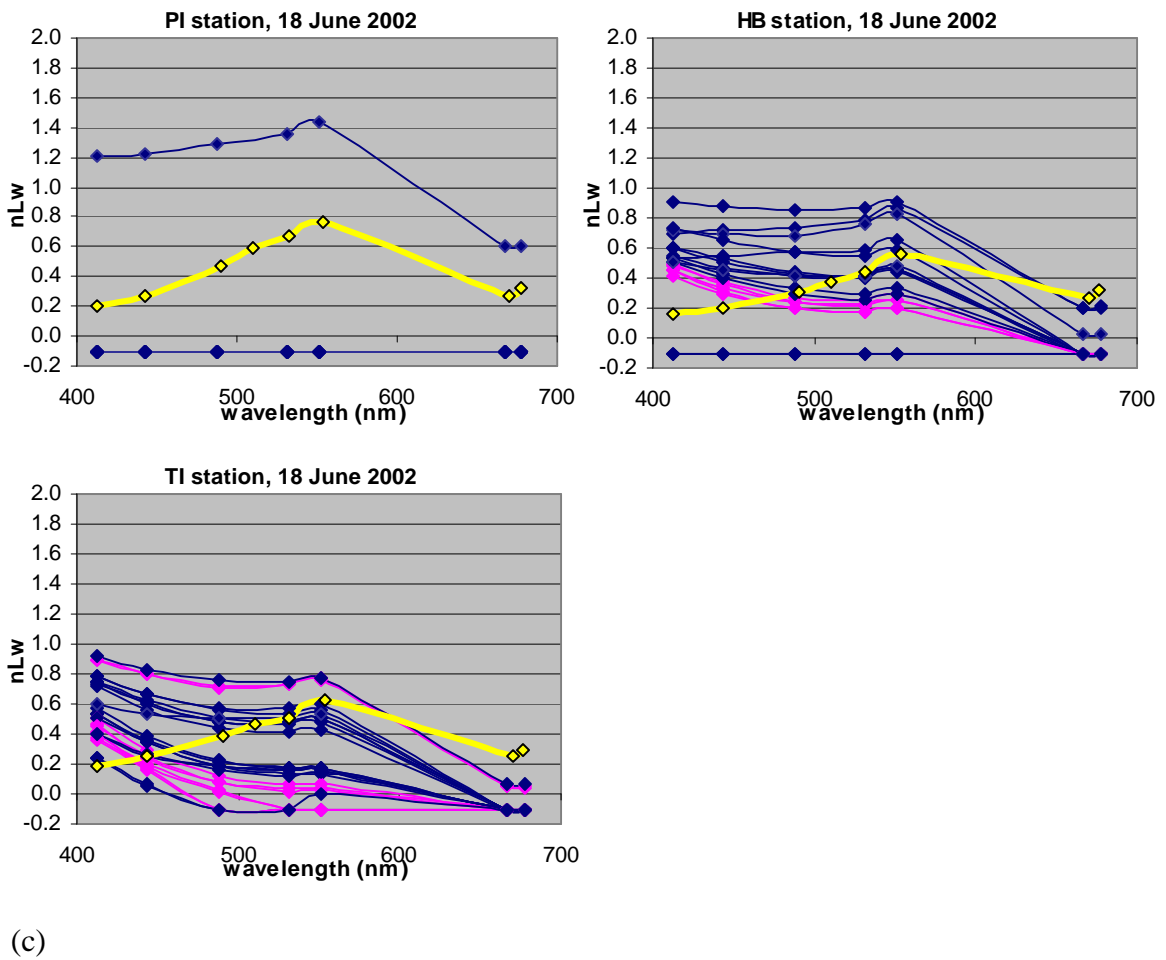
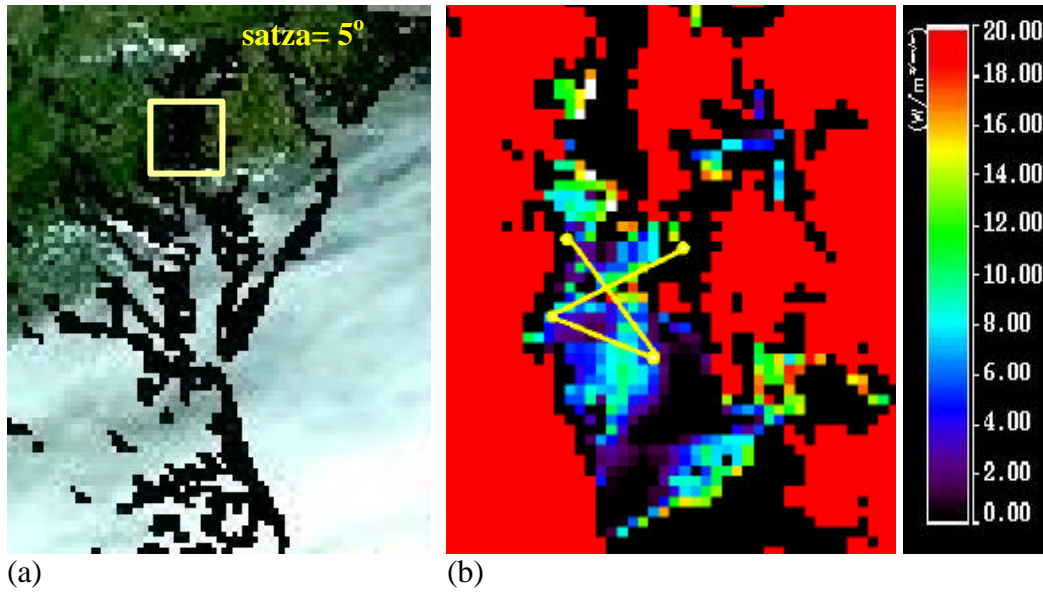


Figure 4.3-12: Same a figure 4.3-1, for measurements on 18 June 2002. Satellite zenith angle over the Chesapeake Bay region was 5°.

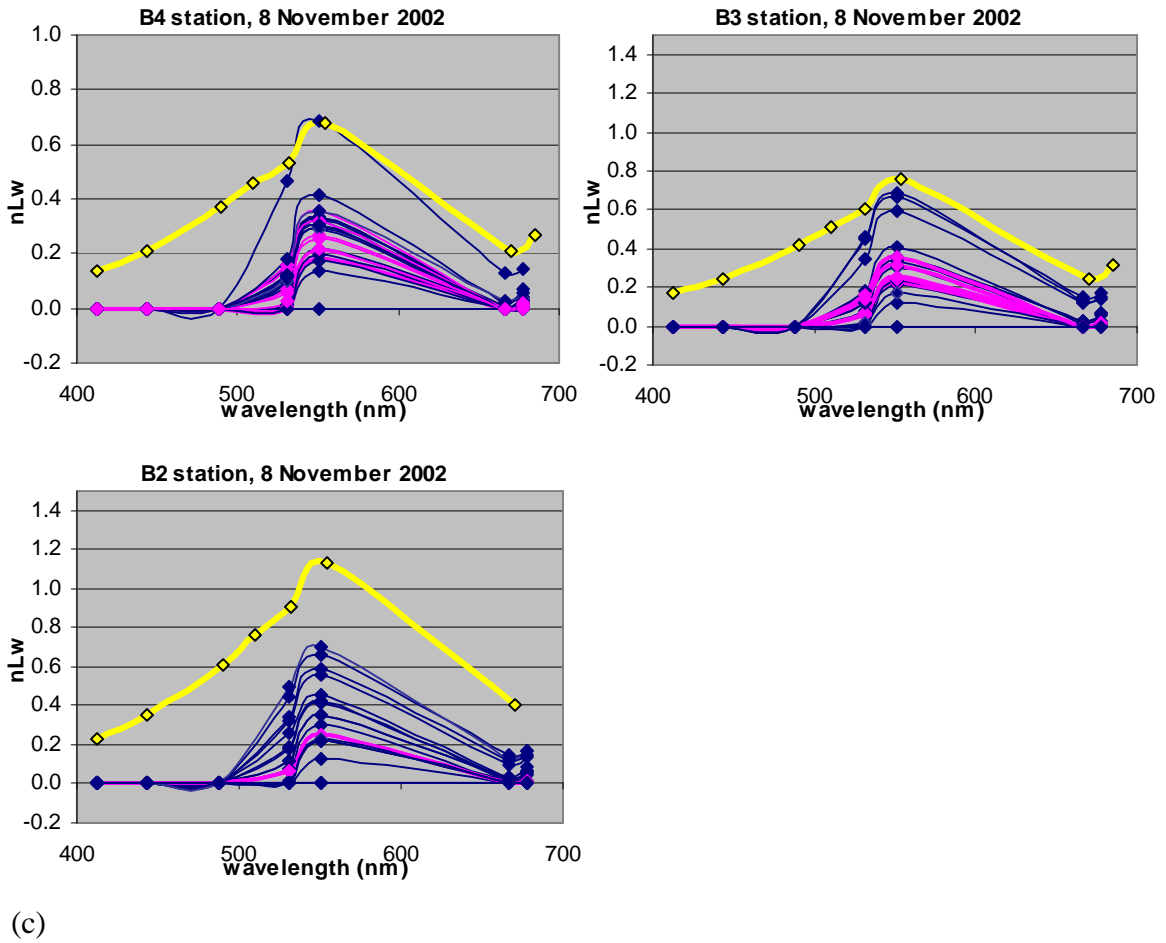
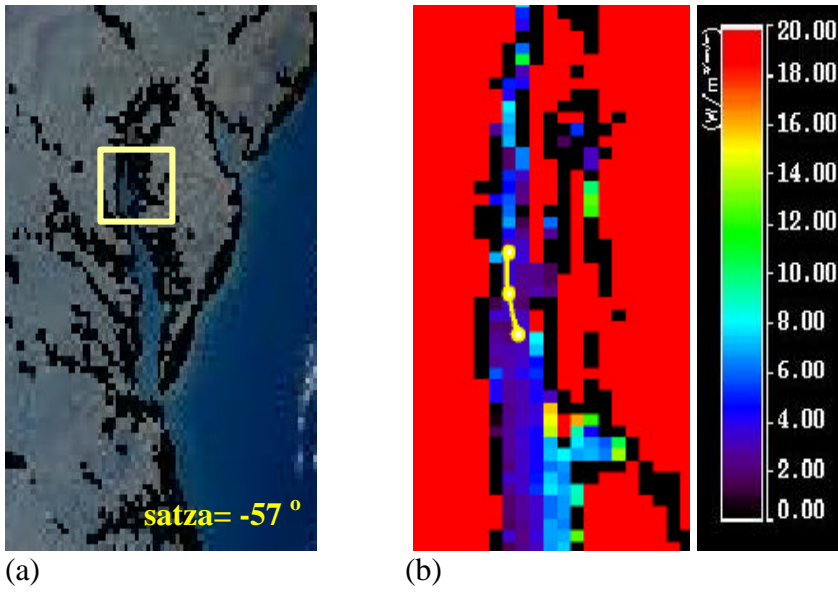


Figure 4.3-13: Same a figure 4.3-1, for measurements on 8 November 2002. Satellite zenith angle over the Chesapeake Bay region was -57° .

Table 4.3-1: Quality of in-situ measurements and satellite pixels
 Measurements performed in the Chesapeake Bay during June-November 2001
 (yellow background for those days when MicroPro instrument was used)

Date	Site	Quality of InSitu/MODIS observations	Pixels' Quality-level (Q=0-3)	Best Pixel Qual	Comments Atmospheric Conditions
01/06/04	PI	No InSitu IOPs			~ clear day : AOT ₍₅₅₀₎ = 0.15 (MTOPS) AOT ₍₅₅₀₎ =0.1 (CIMEL)
	HB		25/25:Q=3	Q=3	
	TI		6/25:Q=0, 19/25:Q=3	Q=3	
	JT	No InSitu IOPs			
01/06/11	PI		2/25:Q=0, 23/25:Q=3	Q=3	Haze/clouds: AOT ₍₅₅₀₎ =0.8 (CIMEL) AOT ₍₅₅₀₎ = 1.2 (MTOPS) "Gordon Aer. Failure"
	HB	MODIS all nLw <0			
	TI		5/25:Q=0, 20/25:Q=3	Q=3	
	JT		1/25:Q=0, 24/25:Q=3	Q=3	
01/06/25	All	No MODIS			
01/07/09	PI	MODIS all nLw <0			Satellite zenith angle=- 61 AOT ₍₅₅₀₎ = 0.25 (MTOPS)
	HB	MODIS all nLw <0			
	TI		7/25:Q=0, 18/25:Q=3	Q=3	
	JT		4/25:Q=0, 21/25:Q=3	Q=3	
01/09/21	PI	MODIS all nLw <0			AOT ₍₅₅₀₎ = 2.3 (MTOPS) "Atm Corr. Failed" or "Gordon Aerosol Failure" for most of the pixels
	HB	MODIS all nLw <0			
	TI		25/25:Q=3	Q=3	
	JT		25/25:Q=3	Q=3	
01/09/26	PI		25/25:Q=3	Q=3	clear day: AOT ₍₅₅₀₎ = 0.1 (CIMEL) AOT ₍₅₅₀₎ = 0.11 (MTOPS)
	HB		25/25:Q=3	Q=3	
	TI		6/25:Q=0, 19/25:Q=3	Q=3	
	JT		25/25:Q=3	Q=3	
01/09/28	All	MODIS all nLw < 0			
01/10/04	PI		2/25:Q=0, 23/25:Q=3	Q=3	AOT ₍₅₅₀₎ = 0.2 (CIMEL) AOT ₍₅₅₀₎ = 0.2 (MTOPS) Satellite zenith angle=-57
	HB		3/25:Q=0, 22/25:Q=3	Q=3	
	TI		12/25:Q=0, 13/25:Q=3	Q=3	
	JT		1/25:Q=0, 24/25:Q=3	Q=3	
01/10/30	PI		10/25:Q=0, 15/25:Q=3	Q=0	AOT ₍₅₅₀₎ = 0.2 (MTOPS)
	HB		16/25:Q=0, 9/25:Q=3	Q=0	
	TI		25/25:Q=0	Q=0	
	JT		11/25:Q=0, 14/25:Q=3	Q=0	
01/11/13	PI		10/25:Q=0, 15/25:Q=3	Q=0	AOT ₍₅₅₀₎ =0.07 (MTOPS) Very few pixels flagged as "Atm Corr Failed" "Gordon Aer. Failure"
	HB		17/25:Q=0, 8/25:Q=3	Q=0	
	TI	No InSitu bb			
	JT	No InSitu bb			

Table 4.3-1 (continued):

Measurements performed in the Chesapeake Bay during May-November 2002

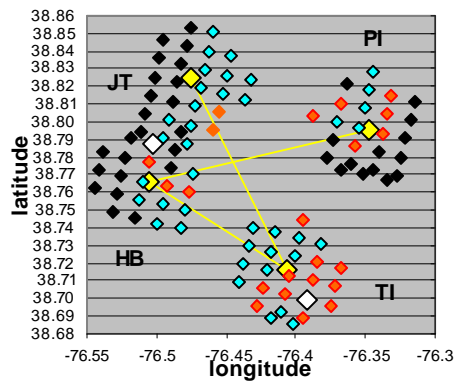
Date	Site	Quality of InSitu/MODIS observations	Pixels' Quality	Best Pixel Qual	Comments Atmospheric Conditions
02/05/06	All	MODIS all nLw <0			AOT ₍₅₅₀₎ =1.0 (MTOPS)
02/05/15	PI		25/25:Q=3	Q=3	AOT ₍₅₅₀₎ =0.25 (MTOPS) All pixels flagged as: "Atm Corr. Failed" or "Gordon Aer. Failure"
	HB	No InSitu Es			
	TI		25/25:Q=3	Q=3	
	JT		25/25:Q=3	Q=3	
02/05/22	PI		6/25:Q=0, 19/25:Q=3	Q=0	~ clear: AOT ₍₅₅₀₎ =0.08 (CIMEL) AOT ₍₅₅₀₎ =0.1 (MTOPS)
	HB		1/25:Q=0, 24/25:Q=3	Q=3	
	TI	No InSitu Lu			
	JT		4/25:Q=0, 21/25:Q=3	Q=0	
02/06/06	PI		25/25:Q=3	Q=3	AOT ₍₅₅₀₎ =0.7 (MTOPS) Pixels flagged as : "Atm Corr. Failed" or "Gordon Aer. Failure"
	HB		25/25:Q=3	Q=3	
	TI		1/25:Q=0, 24/25:Q=3	Q=3	
	JT	No InSitu IOPs			
02/06/18	PI		25/25:Q=3	Q=3	AOT ₍₅₅₀₎ =0.25 (CIMEL) AOT ₍₅₅₀₎ =0.26 (MTOPS)
	HB		5/25:Q=0, 20/25:Q=3	Q=3	
	TI		9/25:Q=0, 14/25:Q=3	Q=3	
	JT		25/25:Q=3	Q=3	
02/06/28	All	MODIS all nLw <0			
02/11/08	B4		7/25:Q=0, 18/25:Q=3	Q=3	~ clear: AOT ₍₅₅₀₎ =0.07 (CIMEL) Satellite zenith angle=-57
	B3		5/25:Q=0, 20/25:Q=3	Q=3	
	B2		2/25:Q=0, 23/25:Q=3	Q=3	

Table 4.3-2: Number of MODIS pixels with nLw = 0 at some of the wavelength bands (“total pixels” in the third column is the total number of pixels with positive nLw values at more than one wavelength bands. Only the pixels with positive nLw values at more than one wavelength have been examined)

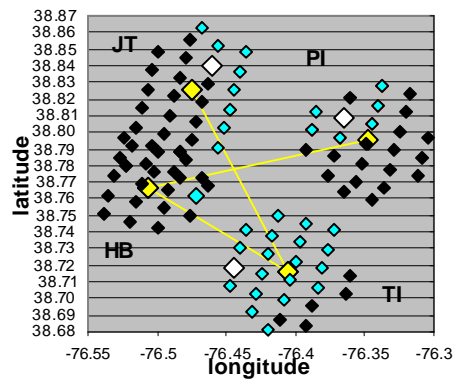
day	station	total pixels	number of pixels with nLw <0 or nLw =0 at each wavelength band						
			nLw412	nLw443	nLw488	nLw531	nLw551	nLw667	nLw678
155	PI	11	5	5	1	0	0	0	0
	HB	13	9	9	5	0	0	3	3
	TI	25	13	8	0	0	0	0	0
	JT	14	12	12	6	0	0	1	1
162	PI	7	0	0	0	0	2	7	7
	HB	1	0	0	0	0	1	1	1
	TI	20	0	0	0	0	11	20	20
	JT	9	1	1	0	0	5	9	9
190	PI	5	5	5	5	3	0	5	5
	HB	1	1	1	1	1	0	1	1
	TI	18	18	18	18	11	0	17	17
	JT	5	4	4	4	1	0	3	3
264	PI	0	0	0	0	0	0	0	0
	HB	0	0	0	0	0	0	0	0
	TI	12	0	0	0	0	0	1	1
	JT	6	0	0	0	0	0	1	1
269	PI	7	4	4	2	0	0	2	0
	HB	7	3	3	2	0	0	2	0
	TI	24	5	5	2	2	0	2	3
	JT	6	3	3	2	0	0	0	0
277	PI	8	7	7	7	2	0	7	6
	HB	13	13	13	13	8	0	13	13
	TI	22	21	20	20	0	0	21	20
	JT	13	13	13	13	11	0	13	13
303	PI	12	12	12	0	0	0	0	0
	HB	20	20	20	11	0	0	4	1
	TI	25	25	25	0	0	0	0	0
	JT	15	15	15	1	0	0	0	0
317	PI	10	10	10	0	0	0	0	0
	HB	22	22	22	0	0	0	0	0
	TI	25	25	25	0	0	0	0	0
	JT	16	16	15	0	0	0	0	0
135	PI	4	2	2	0	0	0	3	4
	HB	3	0	0	0	0	0	3	3
	TI	11	3	2	0	0	0	7	7
	JT	2	0	0	0	0	0	2	2
142	PI	11	11	10	0	0	0	0	0
	HB	19	18	18	17	1	0	8	8
	TI	25	25	25	5	0	0	0	0

	JT	16	16	16	10	1	0	2	2
157	PI	1	0	0	0	0	0	1	1
	HB	2	0	0	0	0	0	0	0
	TI	22	0	0	0	0	0	13	14
	JT	3	0	0	0	0	0	1	1
169	PI	1	0	0	0	0	0	0	0
	HB	16	0	0	0	0	0	13	13
	TI	25	0	0	4	6	5	22	22
	JT	13	9	9	9	1	0	8	3
312	B4	23	23	23	23	3	0	19	5
	B3	18	18	18	18	1	0	12	4
	B2	16	16	16	16	2	0	7	3
SUM pixels		623	423	414	215	54	24	254	217

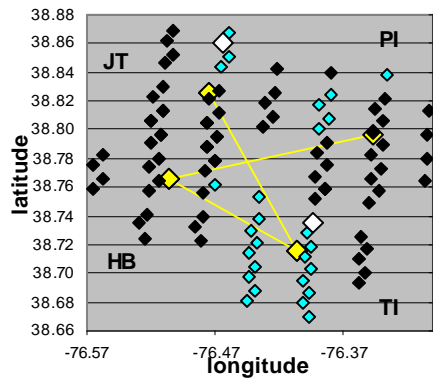
percent negative values:	67.90	66.45	34.51	8.67	3.85	40.77	34.83
---------------------------------	-------	-------	-------	------	------	-------	-------



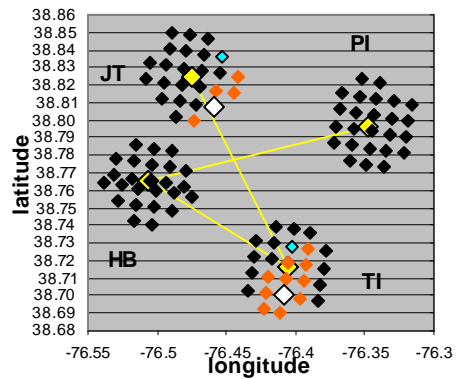
(a) 4 June 2001 (satza=35°)



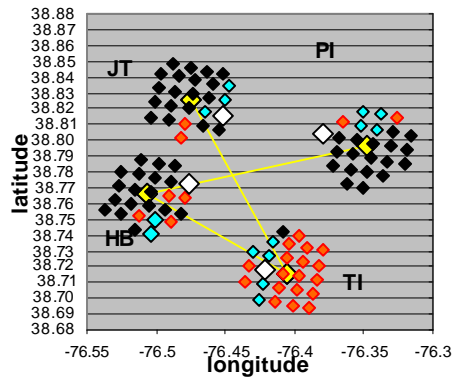
(b) 11 June 2001 (satza=42°)



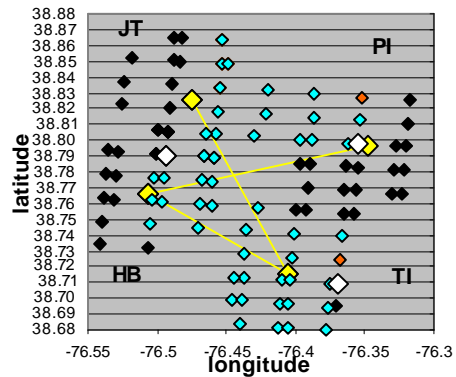
(c) 9 July 2001 (satza=-61°)



(d) 21 September 2001 (satza=-18°)

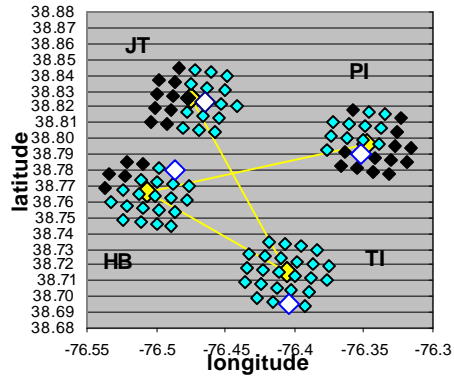


(e) 26 September 2001 (satza=15°)

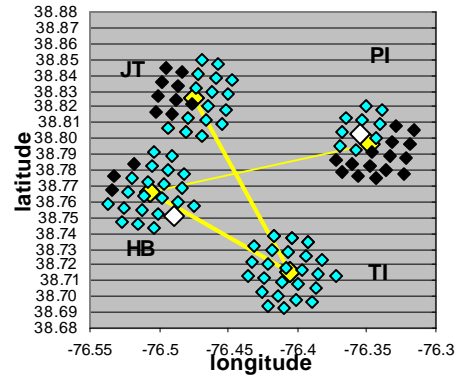


(f) 4 October 2001 (satza=-57°)

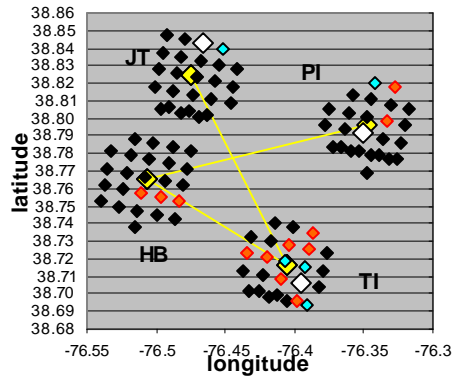
Figure 4.3-14: Location of the 5x5 MODIS pixels around each station (PI, HB, TI and JT) during the cruises in the Chesapeake Bay. i) MODIS pixels with negative ($nLw=-1$ or $nLw=-5$) or zero normalized water-leaving radiances at all of the MODIS wavelength bands are shown as black pixels. ii) MODIS pixels with negative ($nLw=-1$) or zero normalized water-leaving radiances at some of the MODIS wavelengths are shown as blue pixels. iii) MODIS pixels with $nLw > 0$ at all wavelengths are shown as red pixels. The MODIS pixel with water leaving radiances that showed the best agreement with the in-situ measurements, is shown as white pixel.



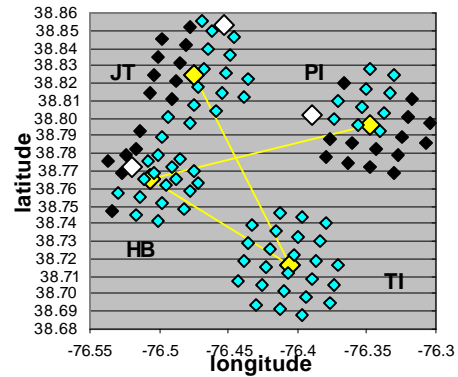
(g) 30 October 2001 (satza= -8°)



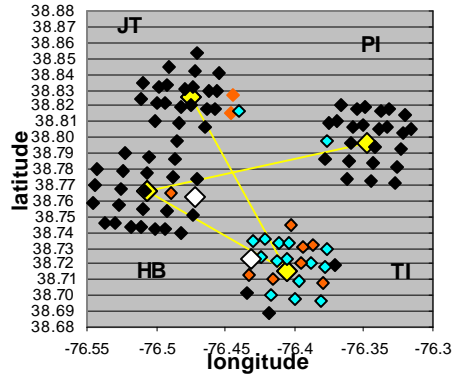
(h) 13 November 2001 (satza= 16°)



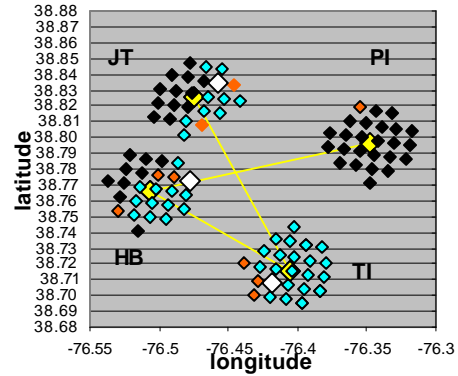
(i) 15 May 2002 (satza= 26°)



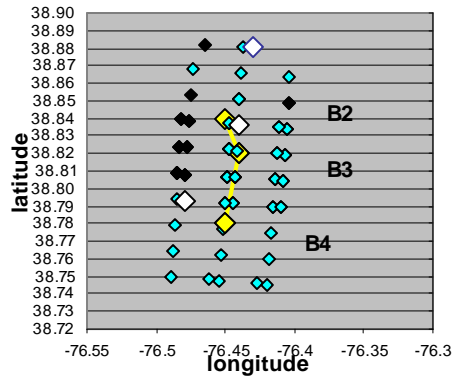
(j) 22 May 2002 (satza= 36°)



(k) 6 June 2002 (satza= -38°)



(l) 18 June 2002 (satza= 5°)



(m) 8 November 2002 (satza= -57°)

Figure 4.3-14: (continued)

From the measurements shown in figures 4.3-1(c) - 4.3-13(c) it is evident that the comparison between satellite and in-situ measurements is problematic during those days (9 July 2001, 4 October 2001, 8 November 2002) when satellite observations were performed at a large satellite zenith angle (shown as narrow satellite images of the bay in figures 4.3.1-4.3.13), although the satellite zenith angles (-61° , -57° and -57° , respectively) were smaller than the threshold value of the satellite zenith angle ($\pm 65^{\circ}$) set for the ocean color products. During those days, MODIS nLw values were flagged as 0 or -1 at most of the wavelength bands and at most of the satellite pixels, even at pixels characterized as of the best quality, quality level=0 (e.g. at both TI and JT stations on 9 July 2001).

Cloudy and hazy atmospheric conditions also affected the satellite observations, resulting in bad quality satellite measurements (e.g. measurements on 11 June 2001, 21 September 2001 and 6 June 2002), with flagged or very large MODIS nLw values at 412 and 443 nm (fig. 4.3-2, 4.3-11, 4.3-12). In cases when relatively clear sky conditions were observed, the agreement between MODIS and in-situ measurements of nLw was better, especially at the less turbid TI station (e.g. 26 September 2001, 30 October 2001) which is located at a larger distance from the bay shores. However, in some of the cases (4 June 2001), although the in-situ measurements of nLw agree pretty well to the MODIS measurements at some of the pixels close to the four stations, large variation was observed among the MODIS nLw measurements at the 5x5 pixels around each station.

The normalized water leaving radiances, $nLw(\lambda)$, that were measured in-situ at each station, or were estimated theoretically using Hydrolight and measured water IOPs, were compared to the MODIS $nLw(\lambda)$ values measured at the pixel that was geographically “closest” to the location of each station, at the time of the MODIS overpass. However, due to the presence of currents in the bay, the geographically closest pixel does not necessarily describe the water mass at the location of the station during the in-situ measurements. Since detailed information on currents’ speed and direction at the exact location of the HB, PI, TI, JT stations was not available, the water mass sampled at each station during the in-situ measurements could be anywhere within a distance of ~5 km from the station, at the time of the MODIS overpass (discussion in Methodology, paragraph 4.2.2). Therefore, the in-situ or modeled nLw values were also compared to the MODIS $nLw(\lambda)$ values measured at the pixel, for which the satellite nLw values showed the best agreement (among all the 5x5 pixels around each site) with the in-situ measured nLw spectra. This “best” pixel was selected based on:

$$\sum_{i=1}^3 |nLw(Ii)_{(MODIS)} - nLw(Ii)_{(InSitu)}| = \text{minimum, for } \lambda_1=488, \lambda_2=551, \lambda_3=667 \text{ nm.}$$

For the “best” pixel the nLw values were of quality level 0 (best quality) during the measurements performed on 30 October 2001 (at all stations), 13 November 2001 (at all stations) and 22 May 2002 (at PI and JT stations) (table 4.3-1). For the HB, JT and PI stations, in most of the cases the ‘best’ pixel was located towards the middle of the bay (fig. 4.3-14), since most of the pixels close to the bay shores are affected by land (proximity to bright source, stray light effects, more shallow and turbid waters) and are often flagged as pixels where the atmospheric correction algorithm has failed.

The results of the comparisons between in-situ $nLw(\lambda)$ measurements and MODIS $nLw(\lambda)$ values measured at the “closest” and “best” pixels, are shown in the scatter-plots in figure 4.3-15. The comparison between in-situ and MODIS nLw values at the “closest” pixel shows a lot of scattering around the 1:1 line, with R^2 values of less than 0.4 at all wavelengths (fig. 4.3-15(a)). Larger nLw values were measured by MODIS at 412 and 443 nm compared to the in-situ measurements. The highest $nLw(412)$ and $nLw(443)$ values were measured at the MODIS closest pixels on 21 September 2001 and 6 June 2002, which were both days when high aerosol optical thickness was measured ($AOT(550)=2.3$ on 21 September 2001, and $AOT(550)=0.7$ on 6 June 2001).

The normalized water-leaving radiances measured at the MODIS “best” pixels showed a better overall agreement with the measured nLw values (figure 4.3-15(b)). The comparison was fairly good, especially at the green (551 nm) and red (667 and 678 nm) wavelengths, with R^2 values of ~ 0.7 , slope close to 0.8-0.85 and small intercept values (~ 0.07 -0.08). In this case, too, large nLw values were measured at all wavelengths (especially at 412 and 443 nm) on 6 June 2002 (day with high aerosol optical thickness, $AOT(550)=0.7$). The comparison between the in-situ data and the MODIS nLw values measured at the ‘best’ pixels is shown in figure 4.3-16(a) for only those cases when almost clear atmospheric conditions ($AOT(550)$ values of less than 0.2) and not very large satellite zenith angles were observed (days: 4 June 2001, 26 September 2001, 30 October 2001, 13 November 2001, 22 May 2002). During these relatively clear days, MODIS data were characterized by the largest number of pixels with quality level=0 (best quality) (table 4.3-1). The MODIS ‘best’ pixels were of quality level 0 only during

these relatively clear days (although MODIS nLw(412) and nLw(443) were flagged as negative values in some of these cases). The R^2 values at 551, 667 and 678 were between 0.7-0.8 in this case, the slope between measured and satellite values was again ~ 0.8 and the intercept values were small ($\sim 0.03 - 0.06$). The comparison between the in-situ data and the MODIS nLw values measured at the ‘best’ pixels for these days when large AOT values were measured (11 June 2001, 21 September 2001, 6 June 2002, 18 June 2002) is shown in figure 4.3-16(b). For these days, even at the “best” satellite pixels, MODIS estimates of nLw(412) and nLw(443) were largely overestimated (by more than a factor of 2 in most of the cases) compared to in-situ nLw measurements.

Figures 4.3-17(a) - 4.3-17(d) show the comparison between the satellite (best pixel) and in-situ measurements of nLw, for measurements performed at the four stations PI, HB, TI, JT, during all of the cruises in the Bay. Better agreement between MODIS and in-situ measurements was observed at the less turbid, and located further away from the land, TI station (fig. 4.3-17(a)), especially at the 551 nm wavelength band. With the exception of one measurement (nLw(551) measured on 11 June 2001, which was a cloudy/hazy day with $AOT(550)=0.8$ measured by CIMEL and $AOT(550)=1.2$ measured using Microtops) the nLw(551) values measured by MODIS at the ‘best’ satellite pixel were in good agreement with the in-situ observations ($R^2 = 0.94$, slope 0.8, and intercept 0.1). Larger differences between satellite and in-situ nLw values were found for the measurements performed at PI, HB and JT stations which are located close to the bay shores. The MODIS measurements of nLw at the two shortest wavelengths 412 nm and 443 nm were overestimated at all four stations, compared to the in-situ measurements.

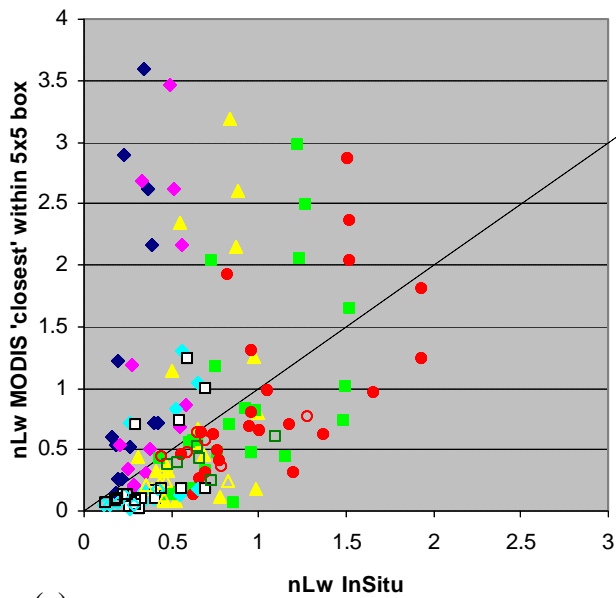


Table 4.3-3(a): “closest” pixel

	slope	intercept	Rsqr	n
412	4.90	-0.09	0.17	13
443	4.26	-0.50	0.25	14
488	1.81	-0.36	0.19	26
531	1.32	-0.34	0.34	33
551	1.05	-0.18	0.41	32
667	1.37	-0.20	0.34	21
678	1.27	-0.21	0.37	23

(a)

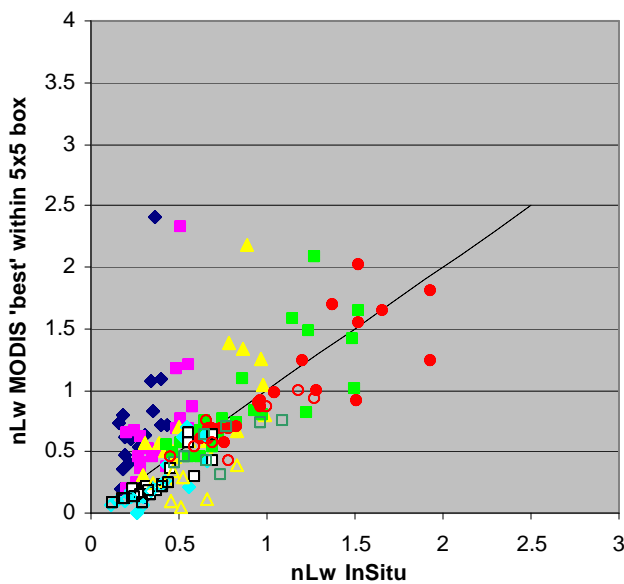


Table 4.3-3 (b): “best” pixel

	slope	intercept	Rsqr	n
412	2.72	-0.04	0.23	19
443	2.12	-0.12	0.33	19
488	1.39	-0.22	0.41	28
531	1.05	-0.08	0.63	31
551	0.88	0.03	0.73	31
667	1.02	-0.12	0.67	24
678	0.90	-0.09	0.71	23

(b)

Figure 4.3-15: In-situ measurements of normalized water-leaving radiances, $nLw(\lambda)$ and MODIS $nLw(\lambda)$ values measured at the 7 wavelengths 412, 443, 488, 531, 551, 667 and 678 nm. The In-Situ $nLw(\lambda)$ are compared to the MODIS $nLw(\lambda)$ measured (a) at the geographically “closest” pixel (b) at the “best” MODIS pixel. The R^2 , slope and intercept between the in-situ and satellite data are shown in tables 4.3-3 (a) and 4.3-3 (b). Pixels of all quality levels have been included in the comparisons (pixels of quality 0 shown as empty symbols, while pixels of quality 1-3 are shown as full symbols). The 1:1 line is also shown for comparison.

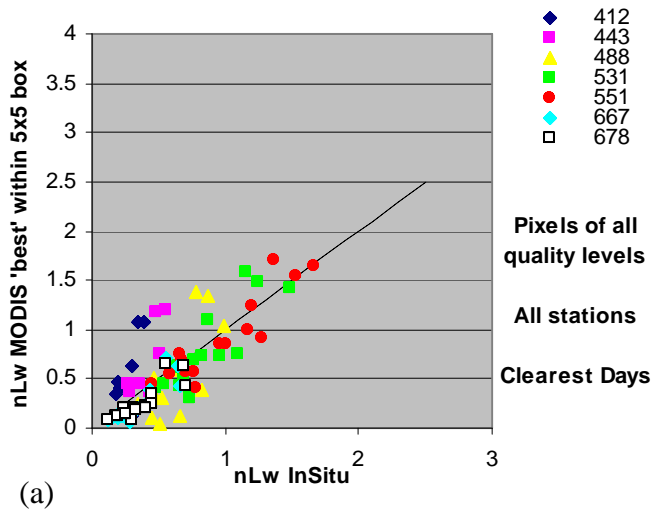


Table 4.3-4 (a): clearest days

	slope	intercept	Rsqr	n
412	3.14	-0.27	0.47	7
443	2.64	-0.42	0.63	7
488	1.61	-0.45	0.50	15
531	1.23	-0.26	0.72	15
551	1.07	-0.14	0.83	15
667	1.03	-0.11	0.76	15
678	0.90	-0.08	0.75	15

(a)

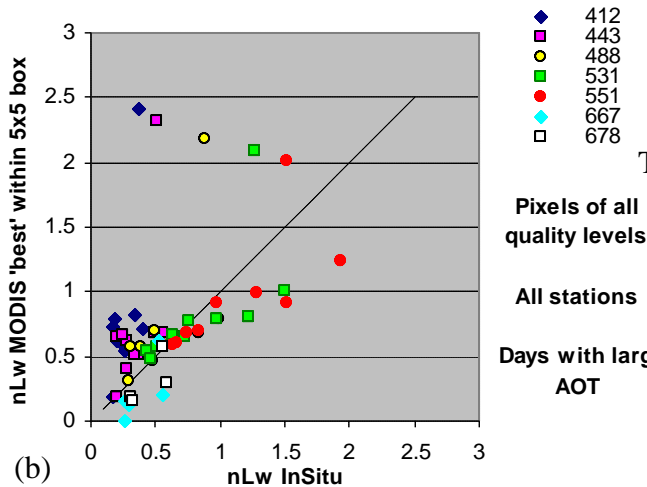


Table 4.3-4 (b): days with large AOT

	slope	intercept	Rsqr	n
412	3.65	-0.12	0.29	10
443	2.42	-0.12	0.29	10
488	1.25	0.01	0.34	10
531	0.82	0.14	0.44	10
551	0.68	0.19	0.54	10
667	1.08	-0.19	0.47	5
678	0.87	-0.08	0.51	4

(b)

Figure 4.3-16: Comparison between in-situ nLw measurements and MODIS nLw values measured at the 'best' pixels (a) for those cases when almost clear atmospheric conditions (AOT values of less than 0.2) and not very large satellite zenith angles were observed (days: 4 June 2001, 26 September 2001, 30 October 2001, 13 November 2001, 22 May 2002) (b) for those cases when large aerosol optical thickness was measured in the atmosphere above the location of the four stations (days: 11 June 2001, 21 September 2001, 6 June 2001, 18 June 2002). Pixels of all quality levels have been included in the comparisons. The R^2 , slope and intercept between the in-situ and satellite data are shown in tables 4.3-4(a), (b).

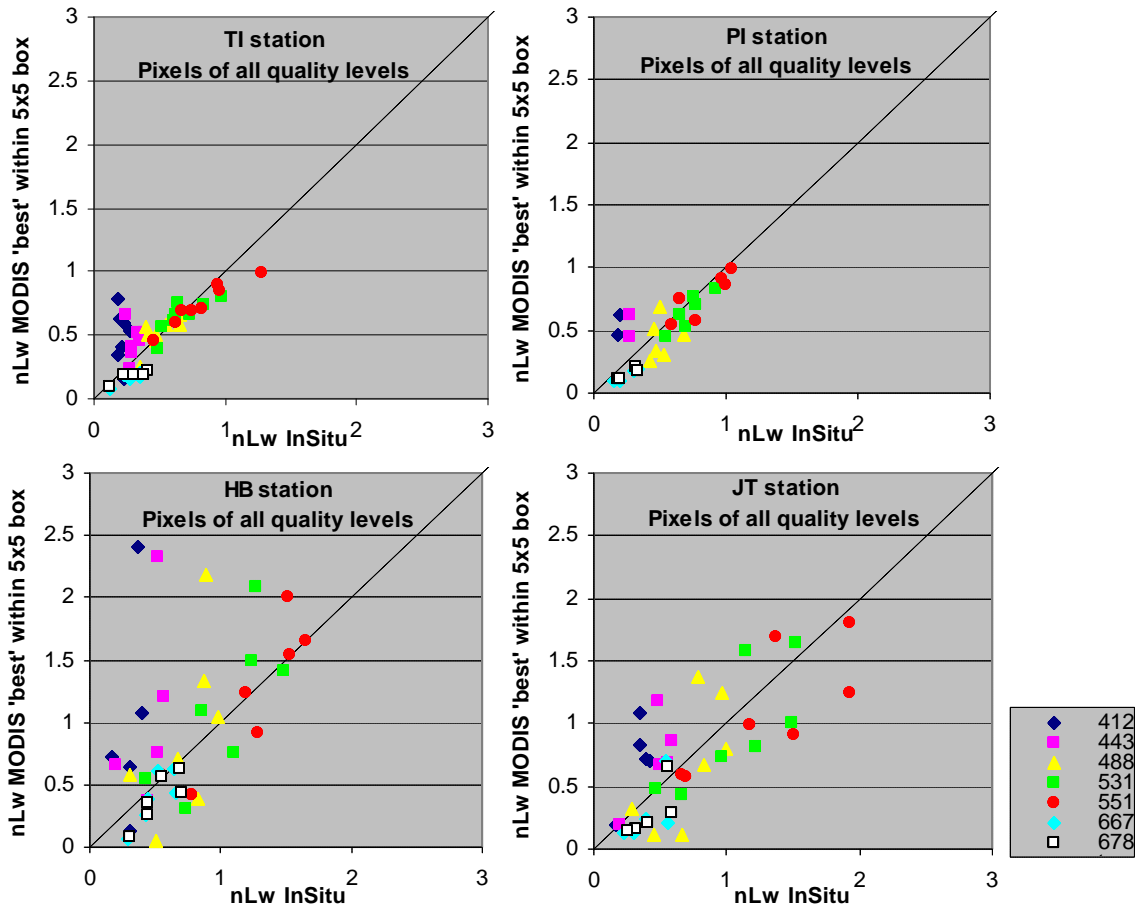


Table 4.3-5(a): TI station

	slope	Int.	R ²	n
412	-1.43	0.80	0.04	7
443	0.28	0.36	0.01	7
488	0.78	0.13	0.51	8
531	0.62	0.23	0.67	8
551	0.65	0.21	0.93	8
667	0.46	0.04	0.75	5
678	0.39	0.06	0.73	5

Table 4.3-5(b): PI station

	slope	Int.	R ²	n
412	-	-	-	2
443	-	-	-	2
488	0.32	0.26	0.03	6
531	0.97	-0.05	0.81	6
551	0.81	0.09	0.74	6
667	0.50	0.02	0.96	4
678	0.58	0.01	0.89	4

Table 4.3-5(c): HB station

	slope	Int.	R ²	n
412	4.35	-0.34	0.20	5
443	2.32	0.03	0.18	5
488	1.68	-0.32	0.32	7
531	1.33	-0.27	0.65	7
551	1.21	-0.27	0.82	7
667	1.15	-0.17	0.77	6
678	1.05	-0.16	0.80	6

Table 4.3-5(d): JT station

	slope	Int.	R ²	n
412	2.25	-0.05	0.47	5
443	1.74	-0.09	0.55	5
488	1.36	-0.31	0.47	7
531	0.92	-0.03	0.57	7
551	0.73	0.15	0.60	7
667	1.06	-0.15	0.41	5
678	1.03	-0.15	0.51	5

Figure 4.3-17: Comparison between the satellite and in-situ measurements of nLw, for measurements performed at the four stations (a) TI, (b) PI, (c) HB and (d) JT, during all of our cruises in Chesapeake Bay. Pixels of all quality levels have been included in these comparisons. The R², slope and intercept values are shown in tables 4.3-5(a)-(d)

4.4 MODIS and in-situ measurements of Remote Sensing Reflectance – Discussion and Conclusions

Measurements of remote sensing reflectance in the Chesapeake Bay waters have been studied using both in-situ observations and satellite data from the MODIS instrument aboard the EOS/Terra satellite. The in-situ measurements during each cruise had been performed within a time-period of 2-3 hours around the satellite overpass. Therefore, and due to the presence of currents in the Bay, a region encompassing the 5x5 satellite pixels around the location of each station was studied when comparing the satellite estimations to the in-situ measurements (discussion in “Methodology” section).

Although satellite measurements of the best quality are those characterized by a quality level of 0 or at most 1 (table 4.2-5), satellite pixels with nLw values of all quality levels have been examined in this study, mainly for two reasons:

i) The number of pixels with nLw values of quality-level = 0 (best quality level) was small for the Chesapeake Bay waters. Only 18% of the total number of pixels studied (25 pixels around the location of each station) and 22% of the MODIS ‘best’ pixels around each site, were of quality-level zero concerning the nLw products (more details on the quality levels of the satellite pixels are given in table 4.3-1). No pixels with nLw values of quality-level=1 were found for the cases studied. A pixel is of quality-level 1 (concerning the nLw values) if the solar or satellite zenith angle is large (table 4.2-4), and satellite and solar zenith angles, during our cruises, were always smaller than the threshold values (65° for satellite zenith angle and 70° for solar zenith angle).

ii) In certain cases (e.g. 9 July 2001, 4 October 2001, 22 May 2002, 8 November 2002) pixels of quality level 0 (concerning the nLw products) had nLw values negative at most or all of the satellite wavelength bands, while pixels of quality level 3 had nLw values in closer agreement with the nLw values measured in-situ. As mentioned in the Methodology section, the problem of having satellite pixels characterized as of quality-level=0 (concerning the nLw products) while nLw values were flagged at all MODIS wavelength bands, was examined thoroughly and was found to be related to the actual information concerning the value of the nLw quality-level that is stored in the quality Bytes in the MODIS HDF files. Satellite pixels with negative or zero nLw values at all wavelength bands (nLw = 0, nLw = -1 or nLw = -5), have been discarded. A large number of pixels with nLw = -5 (negative value that is used to flag MODIS pixels not processed or pixels on land) was found at a short distance from the HB, JT and PI stations, since these stations are located close to land, with HB and JT stations close to the western shore of the Chesapeake Bay and PI close to the Poplar and Tilghman Islands along the eastern shore of the bay.

Negative nLw values measured by MODIS:

Almost 70% of the MODIS pixels (that did not have negative nLw values at all seven wavelengths) had negative (flagged) nLw values at the two shortest satellite wavelength bands, centered at 412 and 443 nm (table 4.3-2). Due to high absorption by phytoplankton, non-pigmented particulate matter and CDOM, within the blue wavelength region, the remote sensing reflectances at 412 and 443 nm are typically small in the Chesapeake Bay waters (in-situ nLw(λ) measurements are shown in fig. 4.3-1 - 4.3-13).

Therefore, small errors in the atmospheric correction applied to the satellite measurements could result in erroneous satellite nLw values at 412 and 443 nm. These errors in the estimation of nLw at the two short wavelength bands, have significant implications on the estimation of chlorophyll concentration, using the HPLC empirical chlorophyll algorithm (“chlor_MODIS” product, updated version 19 Feb 2002, D. Clark), since this algorithm is based on an empirical relationship between [Chl-a] and the nLw ratio $[(nLw(443)+nLw(488))/nLw(551)]$, and therefore, uses as input information the MODIS nLw(443) measurements (description of the algorithm in chapter 5). The accuracy of the case-2, semianalytic MODIS chl-a algorithm (semianalytic version of “chlor_a_3” product, Carder et al, 2002) is also affected by the quality and accuracy of the MODIS measurements at the shorter wavelengths, since the algorithm uses the remote sensing reflectance ratios $Rrs(412):Rrs(551)$ and $Rrs(443):Rrs(551)$ to estimate water’s absorption coefficients and chlorophyll concentrations. According to Carder et al (2002) the semianalytic algorithm cannot perform properly for waters with high CDOM and chlorophyll concentrations, because nLw(412) and nLw(443) are expected to be small. The other two MODIS [Chl-a] products (empirical version of “chlor_a_3” product and SeaWiFS analog “chlor_a_2” product) are based (for [Chl-a] larger than 2 mg m^{-3}) on empirical relationships between [Chl-a] and the ratio $Rrs(488)/Rrs(551)$. The percentage of pixels with negative (flagged) nLw values at 488 nm was ~35% for the cases studied, similar to the percentage of pixels with negative nLw values at 667 and 678 nm. Most of the pixels with zero or negative nLw values (excluding pixels flagged as “land”), were found around the three stations, HB, JT and PI, that are located closer to the bay shores (fig.2.2-1, chapter 2). This is because many parameters, such as proximity to

the bright land surface, stray-light effects, presence of shallow and highly turbid waters and failure of the atmospheric correction algorithm, affect in a negative way the quality of nLw measurements at satellite pixels located at a short distance from the shore.

Large Satellite Zenith Angles:

According to the results shown in figures 4.3-1 – 4.3-13, the quality of the satellite data was reduced for those days (9 July 2001, 4 October 2001, 8 November 2002) when satellite observations were performed at a large satellite scan angle. Errors in the atmospheric correction of the satellite observations become larger when satellite measurements are performed at high solar or scan angles. At the same time, satellite spatial resolution decreases closer to the edge of the satellite scan (4.83 km along satellite scan and 2 km along satellite track at 55° satellite scan angle). The satellite zenith angle over the Chesapeake Bay region was -61° on 9 July 2001, -57° on 4 October 2001 and -57° on 8 November 2002. These satellite zenith angles are smaller than, but close to, the satellite zenith angle threshold value of $\pm 65^\circ$ set for the MODIS ocean color products. During the days mentioned above, the MODIS normalized water-leaving radiances were flagged as zero or negative values at most of the wavelengths (e.g. at 412, 443, 488, 667 and 678 nm) and at almost all of the 5x5 satellite pixels around the location of each site, even at pixels characterized as of the best quality level (quality level=0) concerning the nLw products.

Atmospheric conditions:

Atmospheric conditions significantly affected the quality of satellite observations and estimations of MODIS normalized water-leaving radiance spectra during our cruises. During the measurements performed on 11 June 2001, 21 September 2001 and 6 June 2002, high aerosol optical thickness (AOT) was measured due to the presence of aerosols or thin clouds in the atmosphere. Aerosol optical thickness values at 550 nm, AOT(550), measured at the time of the MODIS overpass using either the Microtops instrument or the CIMEL sunphotometer, were 0.8-1.2 on 11 June 2001, 2.3 on 21 September 2001 and 0.7 on 6 June 2002 (table 4.3-1). During those days large disagreement was observed between satellite and in-situ nLw spectra or between satellite and model estimated (using Hydrolight and measured inherent water optical properties) nLw values. Satellite measurements showed large remote sensing reflectances in the blue region of the visible spectrum (412, 443, 488 nm) although significant absorption by CDOM, phytoplankton and non-pigmented particulate matter was measured at the blue wavelengths during the summer cruises in the Chesapeake Bay waters (results in chapter 2). During the cruise on 11 June 2001, a large phytoplankton bloom was observed with measured chl-a concentrations of 50 –75 mg/m³ at HB and JT stations. Such high chl-a concentrations, combined with the effect of high absorption in the blue wavelengths by CDOM and detrital material, would be expected to result in remote sensing reflectance spectra with maximum values in the green region of the spectrum and not in the blue wavelengths. The satellite measured nLw values at 412, 443 and 488 nm were overestimated compared to the in-situ nLw values measured during the days mentioned above (fig. 4.3-2, 4.3-4, 4.3-11, 4.3-12). Such overestimations of the nLw values in the blue wavelengths by

MODIS, due to errors in the atmospheric correction under conditions of high aerosol optical thickness, are expected to result in large underestimations of the chlorophyll concentrations in the Chesapeake Bay waters using the MODIS [Chl-a] empirical algorithms (discussion in chapter 5).

Better agreement between satellite and in-situ (or modeled) nLw values was observed under relatively clear atmospheric conditions, especially at the less turbid TI station, which is located in the mid of the Bay, at a larger distance from the Bay shores compared to the other three stations. However, in some of the cases, such as the measurements performed on 4 June 2001, although there was good agreement between in-situ and MODIS nLw measurements (especially at 531 and 551 nm) at some of the pixels close to HB and TI stations, large variation was observed among the MODIS nLw measurements at the 5x5 pixels around each station. Large spatial variability would be expected during the spring-summer months in the Bay, due to patchy and ephemeral phytoplankton blooms events (e.g. phytoplankton bloom event observed on 11 June 2001) and more intense biological activity (chapter 2). Especially good agreement between satellite and in-situ nLw values was observed at TI station on 26 September 2001 (fig. 4.3-5). During that day, the satellite zenith angle over the Chesapeake Bay was small ($\sim 15^\circ$), and atmospheric conditions were relatively clear, with aerosol optical thickness measured at the time of the MODIS overpass $AOT(550)=0.1$. Moreover, during that day the time of the MODIS overpass (16:15 GMT) was very close to the time of the in-situ measurements at the TI station (16:30 GMT). The satellite nLw values measured at all the 'quality-level=0' pixels around the TI station were in good agreement with each other

(fig. 4.3.5 (c)) and were also in good agreement with the in-situ nLw values measured at the TI site, especially in the 490-550 wavelength region. Percent differences between MODIS (at 'best' pixel) and in-situ nLw values at 488, 531 and 551 nm (estimated as: $(nLw_{InStu} - nLw_{MODIS}) / nLw_{InStu}$) were -6%, -2% and -3% respectively (with MODIS slightly overestimating nLw). Good agreement between satellite and in-situ nLw measurements were also observed at TI station on 30 October 2001. Measured aerosol optical thickness during that day was $AOT(550)=0.2$ and satellite zenith angle was small, $\sim 8^\circ$. All of the pixels around TI station during that day were of quality level=0. Percent differences between MODIS (best pixel) and in-situ nLw values at 531 and 551 nm, were 17% and -1% respectively.

For match-up comparisons, the in-situ measurements of $nLw(\lambda)$ (or the model estimated $nLw(\lambda)$ values for those days when in-situ measurements were not available) were compared to the $nLw(\lambda)$ values measured by MODIS at the pixel that was geographically "closest" to the location of each station at the time of the MODIS overpass (fig. 4.3-15(a)). The results of the linear least-squares regression between measured and satellite measurements at each wavelength are shown in table 4.3-3(a). Large differences between satellite and in-situ measurements were observed in most of the cases (large scattering around the 1:1 line in the scatterplot in fig. 4.3-15 (a)), with R^2 values less than 0.4. Larger nLw values, compared to in-situ measurements, were measured by MODIS at 412 nm and 443 nm, with the largest differences measured at those days when high aerosol optical thickness was measured in the atmosphere above the location of the four stations in the Bay. However, as was mentioned in the

“Methodology” section, due to the presence of currents and the time difference between the MODIS overpass and the in-situ measurements at the Bay, the geographically “closest” satellite pixel does not necessarily correspond to the water mass that was at the location of the station during the in-situ measurements.

Therefore, the in-situ (or modeled estimated) nLw values were also compared to the MODIS nLw(λ) values measured at the “best” satellite pixel, for which the nLw values showed the best agreement (among all the 5x5 pixels around the location of each station) with the in-situ measured nLw spectra. The nLw values measured at the “best” pixel were of quality level 0 during the measurements performed on 30 October 2001, 13 November 2001 and 22 May 2002 (table 4.3-1). In most of the cases where the in-situ measurements at a station were performed close to the time of the MODIS overpass, the satellite “best” pixel was located at a distance of less than 1-1.5 km from the station. On 21 and 26 September 2001 the time of the MODIS overpass (15:55 GMT and 16:15 GMT respectively) was closest to the time of the in-situ measurements at the TI station and the “best” pixel at TI was at a distance of less than 1.5 km from the station. On 30 October and 13 November 2001, the time of the MODIS overpass (16:00 GMT and 16:10 GMT respectively) was closest to the time of the in-situ measurements at the PI station and the “best” pixel around PI was at a distance of less than 1 km from the PI location.

The satellite and in-situ nLw measurements were in better overall agreement, as was expected, when the in-situ measurements were compared to nLw values measured at the “best” satellite pixel (scatterplot in fig. 4.3-15 (b)). Fairly good agreement was obtained

between in-situ and satellite (“best” pixel) nLw measurements at 551, 667 and 678 nm, (R^2 values of ~ 0.7 , slope close to 0.9, small intercept values ~ -0.09) with MODIS, however, underestimating to some extent the normalized water leaving radiances, especially at 678 nm. Significantly larger nLw(412) and nLw(443) values, compared to the in-situ measurements, were measured at the satellite “best” pixels on 6 June 2002, when with high aerosol optical thickness (AOT(550)=0.7) was measured in the atmosphere. During that day, percent differences between MODIS and in-situ nLw values at 412 and 443 nm were -555% and -351% respectively at HB station (close to the Bay shore), and -218% and -44% at TI station.

When the in-situ nLw measurements were compared to the MODIS measurements at the “best” pixel for only those cases with relatively clear atmospheric conditions (AOT(550) less than 0.2) and not large satellite zenith angles (days: 4 June 2001, 26 September 2001, 30 October 2001, 13 November 2001, 22 May 2002), the scattering around the 1:1 line was reduced (fig. 4.3-16(a)). Fairly good agreement was observed again at the green and red wavelengths, with MODIS still underestimating nLw at 678 nm. R^2 values at 551, 667 and 678 were between 0.75-0.83 in this case, the slope between measured and satellite values was between 0.9-1.07 and the intercept values were between -0.14 and -0.08 . However, the comparison between in-situ and satellite measurements was not good at the short wavelengths 412-490 nm, even for the relatively clear days (R^2 , slope and intercept values given in table 4.3-4). In most of the cases, satellite nLw measurements were considerably overestimated or flagged as negative values. On 30 October 2001 and 13 November 2001 relative clear atmospheric

conditions were observed and most of the pixels around the location of each station were of best quality level (quality level =0). However, MODIS nLw(412) and nLw(443) values were negative at all 25 pixels around each station (fig. 4.3-7, 4.3-8).

As was discussed in chapter 2, the water optical characteristics vary among the four stations in the Bay, where the field observations have been performed, with higher backscattering of light usually observed at the more turbid HB and JT stations, located close to the western shore of the Chesapeake Bay. According to the results shown in figure 4.3-17, higher values of normalized water leaving radiances were measured both in-situ and by MODIS at HB and JT stations compared to TI and PI. This is in agreement with the higher abundance of non-pigmented particles and the higher backscattering coefficients measured in-situ at the turbid HB and JT stations, compared to PI and TI (discussion in chapter 2). The higher backscattering at HB and JT results in larger portion of radiation scattered in the backward direction, and eventually leaving the water surface.

The comparison between satellite and in-situ nLw measurements was examined separately for the four stations HB, PI, TI and JT (fig. 4.3-17(a) – 4.3-17(d)). Although the number of match-ups is small when looking at the four sites separately, MODIS and in-situ data showed better overall agreement for measurements performed at the less turbid PI and TI stations (fig. 4.3-17 (a)). TI station is also located further away from the bay shores and, therefore, satellite pixels around this station are less affected by land (bright source, stray light effects, shallow and more turbid waters). The agreement at TI

station was good, especially at 551 nm where the remote sensing reflectance signal for the Chesapeake Bay waters is usually higher compared to other wavelengths. With the exception of the measurements performed on 11 June 2001 (which was a cloudy/hazy day with $AOT(550)_{CIMEL}=0.8$ and $AOT(550)_{MicroTOPS}=1.2$) the in-situ and satellite $nLw(551)$ measurements were in very good agreement ($R^2 = 0.94$, slope 0.8, and intercept 0.1). However, nLw measurements at 678 nm were significantly underestimated by MODIS compared to the in-situ observations ($R^2= 0.73$, slope 0.4 and intercept 0.06). The comparison was worse for measurements performed at HB and JT stations (fig. 4.3-17(b) and 4.3-17(d)), which are located close to the western Chesapeake Bay shore and are also characterized by more turbid waters. Satellite nLw measurements at JT were underestimated at 551, 667 and 678 nm, compared to the in-situ observations. MODIS measurements of nLw at the shorter wavelengths (412 and 443 nm) were either flagged (as negative values) or significantly overestimated compared to in-situ measurements, for most cases studied, and at all four stations.

Errors in the in-situ measurements and model-estimations of remote sensing reflectances may have contributed to discrepancies when comparing these values to satellite observations. The good agreement obtained between our in-situ measurements in the Bay and theoretical estimations of underwater radiation fields and water-leaving radiances (results and discussion in chapter 3) increases confidence in the accuracy of the in-situ measurements by demonstrating “closure” between the independently measured inherent and apparent water optical properties.

The implementation of atmospheric correction in the version of MODIS data used in this study, was based on the assumption that ρ_w (water-leaving reflectance) is totally diffuse. BRDF effects could be another source of error in the comparisons between satellite and in-situ observations. Future improvement of the MODIS algorithm is associated with removing bi-directional effects from satellite observations and incorporating a ρ_w BRDF model into the processing stream, to determine the satellite nadir-viewing normalized water-leaving radiance.

Due to high absorption by CDOM, non-pigmented particulate matter and phytoplankton, R_{rs} values at the blue wavelengths are small in the Chesapeake Bay waters. High absorption by pure sea-water at the longer, NIR wavelengths, results in low R_{rs} values in the red region of the spectrum. Small errors in atmospheric correction in the blue and red portions of the spectrum, associated with the NIR correction applied (Siegel et al, 2000), the assumptions on the aerosol models in the atmosphere, and the extrapolation of ρ_A from NIR to the shorter, blue wavelengths, could result in large relative errors in the satellite estimations. Spectral optimization atmospheric correction algorithms have been recently developed (e.g. Gordon et al, 1997). Application of such algorithms in coastal regions, such as Chesapeake Bay, could improve the quality and accuracy of MODIS estimations of remote sensing reflectances.

Table 4.4-1:Chapter 4 – Significant points and Conclusions

- All MODIS ocean Level 2 products are available in the Hierarchical Data Format (HDF) and can be read in SeaDAS, IDL, Matlab, and available subroutines in FORTRAN, C, and other languages. To obtain higher accuracy on the pixels' location, the MODIS measurements of nLw(λ) used in this study and information on geolocation have been read directly from the HDF files using IDL routines. When the SeaDAS program is used to read the MODIS data, small changes on the latitude and longitude information may occur, compared to the actual information stored in the MODIS geolocation file (e.g. differences in the order of 1 km), since SeaDAS uses interpolation to reshape the MODIS geolocation field and allow the user to easily choose Pixel/Line Sample Rate in SeaDAS image display.
- Although satellite measurements of the best quality are those characterized by a quality-level 0 or at most 1, satellite pixels with nLw values of all quality-levels have been examined in this study, mainly for two reasons: i) Only 18% of the total number of pixels studied were of quality-level zero, concerning the nLw products, for the Chesapeake Bay waters. ii) In certain cases, pixels of quality level 0 (concerning the nLw products) had flagged nLw values at most or all of the satellite wavelength bands, while pixels of quality-level 3 had nLw values in closer agreement with the nLw values measured in-situ. The problem of having satellite pixels of quality-level=0 while MODIS nLw values are flagged at all wavelength bands was found to be related to the actual information concerning the value of the nLw quality-level, that is stored in the quality Bytes in the MODIS HDF files
- Almost 70% of the MODIS pixels in the Chesapeake Bay waters had flagged nLw values at 412 and 443 nm (table 4.3-2). This has significant implications on the estimation of chlorophyll concentration, using the MODIS HPLC empirical chlorophyll algorithm ("chlor_MODIS" product, D. Clark, 2002), since this algorithm is based on an empirical relationship between [Chl-a] and nLw values measured at the blue-green wavelengths (discussion in chapter 5).
- The quality of MODIS nLw values was reduced (nLw flagged at most of the wavelengths and at almost all of the 5x5 satellite pixels around the location of each station, even at pixels of quality-level 0) for satellite measurements performed at satellite zenith angles between 55° and 65°, although these satellite zenith angles are smaller than the MODIS threshold of 65°, set for ocean color products.
- The quality of MODIS nLw spectra was reduced under conditions of high aerosol optical thickness (e.g. cases with AOT(550)=0.7 or AOT(550)=2.3). Under such conditions, errors in the atmospheric correction may result in negative (flagged) or highly overestimated nLw MODIS values in the blue wavelength region. Such overestimations of the nLw values at the blue wavelengths are expected to result in large underestimations of [Chl-a] by MODIS in the Chesapeake Bay waters (chapter 5).
- Higher nLw values were measured both in-situ and by MODIS at the HB and JT stations compared to TI and PI. This is in agreement with the higher abundance of non-pigmented particles and the higher backscattering coefficients measured in-situ at the turbid HB and JT stations, compared to PI and TI (chapter 2).
- The quality of nLw values is affected at pixels close to land (more shallow / turbid waters, proximity to bright source, atmospheric correction algorithm failure). Better agreement between MODIS and in-situ measurements was found at the TI station, which is located at a larger distance from the bay shores, especially for days with relatively clear atmospheric conditions (AOT(550)<0.7).
- The agreement between MODIS and in-situ measurements was found to be better, for satellite zenith angles smaller than 55° and under relatively clear atmospheric conditions, at 551, 667, 678 nm ($R^2 \sim 0.75-0.83$, slope 0.9-1.07, intercept values (-0.14) - (-0.08)). However, MODIS nLw values were underestimated compared to in-situ measurements, especially at 678 nm. MODIS measurements of nLw at 412 nm and 443 nm were in most of the cases either negative (flagged) or significantly overestimated compared to in-situ measurements.

Table 4.4-1 (continued):

- Due to high absorption by CDOM, non-pigmented particulate matter and phytoplankton, R_{rs} values at the blue wavelengths are small in the northern Chesapeake Bay waters. High absorption by pure sea-water at the longer, NIR wavelengths, results in low R_{rs} values in the red region of the spectrum. Small errors in atmospheric correction in the blue and red portions of the spectrum, could result in large relative errors in the satellite estimations. Errors and uncertainties associated with the in-situ measurements and model-estimations of R_{rs} may have contributed to discrepancies when comparing these values to satellite observations. BRDF effects could be another source of error in the comparisons between satellite and in-situ observations. Future improvements of the MODIS algorithm are associated with incorporating a ρ_w BRDF model into the processing stream, to remove bi-directional effects from satellite measurements and determine the satellite nadir-viewing normalized water-leaving radiance.

CHAPTER 5

In-situ and Satellite Measurements of Remote Sensing Reflectance and their relation to chl-a concentration and in-water optical properties

5.1 Introduction

One of the most commonly measured biological properties of the oceans, and one of the most widely used products derived remotely from ocean color measurements, is the concentration of chlorophyll-a, (chl-a). Chl-a is the major photosynthetic pigment found in all phytoplankton species. Although pigment composition (chlorophylls a, b, c, carotenoids and phycobilisomes) and concentration depend on phytoplankton species, cell's physiology, light intensity, light spectral quality and nutrient availability, chl-a concentration has been widely used as a measure of phytoplankton biomass in aquatic environments. One reason for this may be the fact that measurements of chl-a concentration are relatively simple and direct. The most widely used laboratory methods for measuring chlorophyll-a concentration, [Chl-a], are i) spectrophotometric method, ii) fluorometric method and iii) High Pressure Liquid Chromatography (HPLC). The above methods are based on the absorption and fluorescence spectral characteristics of the chlorophyll-a pigment.

Satellite estimations of surface concentration of chlorophyll-a and associated pigments have contributed significantly in gaining a better understanding on the temporal and spatial variations of phytoplankton biomass and biological activity in the world's oceans and the role of phytoplankton in the climate system (e.g. McClain et al, 1993, Yoder et al, 1993,

Sullivan et al, 1993). As mentioned previously, remote sensing observations of ocean color rely on detecting the light signal that leaves the water surface and reaches a sensor onboard a satellite, carrying with it information on the optical properties of the water.

The magnitude of the remote sensing reflectance, R_{rs} , is related to the processes of backscattering, b_b , which allows downwelling photons to travel backward and eventually leave the water surface, and absorption, a , within the water. Morel and Prieur (1977) and Gordon et al (1988) showed that irradiance reflectance, $R=Eu/Ed$, is related to the water inherent optical properties, $R \sim b_b/(a+b_b)$. According to Lee et al (1994), the remote sensing reflectance, $R_{rs}(\lambda)$ can be related to $b_b(\lambda)$ and $a(\lambda)$ according to:

$$R_{rs}(I) = \frac{f}{Q(I)} \cdot \frac{t_{(w,a)}t_{(a,w)}}{n_w^2} \cdot \frac{b_b(I)}{a(I) + b_b(I)} \quad (5.1-1)$$

where, $t_{(w,a)}$ is the transmittance from air to water, $t_{(a,w)}$ is the water-air transmittance, n_w is the real part of the water refractive index that can be assumed to be almost constant, $n=1.34$, f is an empirical factor which is a function of the solar zenith angle and is influenced by the relative importance of the molecular and particle scattering in the total scattering process (Morel and Gentili, 1991), and Q is the ratio of upwelling irradiance to upwelling radiance, $Q= Eu(\lambda)/Lu(\lambda)$. Typically, for the transmittances through the air-water and water-air surface, $t_{(w,a)} = 0.98$ and $t_{(a,w)}=0.96$ (Mobley, 1994), and the quantity

$\frac{t_{(w,a)}t_{(a,w)}}{n_w^2}$ can be assumed to be relatively independent of wavelength and approximately

equal to 0.54. Early studies have shown that f has an average value of about 0.32–0.33 (Gordon et al., 1975; Morel and Prieur, 1977) when the sun is near zenith. However, the global range of variation in f is from about 0.3 to 0.6. According to Morel and Mueller

(2002), since both the f and Q functions experience concomitant increases when the sun zenith angle increases, their ratio is less dependent on solar zenith angle. As is mentioned in Carder et al (2002), according to Morel and Gentili (1993) and Gordon et al., (1988) the ratio f/Q is relatively independent of solar zenith angle for sun and viewing angles expected for the MODIS orbit, with values of $f/Q = 0.0936, 0.0944, 0.0929,$ and $0.0881,$ (standard deviation ± 0.005), for $\lambda = 440, 500, 565,$ and 665 nm, respectively, according to Morel and Gentili (1993) and $f/Q = 0.0949,$ for $\text{sza} < 20^\circ$ according to Gordon et al., (1988). In the MODIS semianalytic chlorophyll algorithm (described in paragraph 5.2.2.3), the f/Q ratio is assumed to be independent of wavelength and solar zenith angle. According to Morel and Mueller (2002) variations in the ratio f/Q remain within the range $0.08 < f/Q < 0.15.$

Satellite remote sensing measurements of [Chl-a] rely on the absorption and scattering characteristics of phytoplankton and the way these optical properties affect the underwater light field and the R_{rs} (or nL_w) values measured by the satellite sensor. Information on chlorophyll concentration is obtained by using appropriate algorithms that relate measurements of remote sensing reflectance spectra either directly to chlorophyll concentration (empirical algorithms), or to optical properties of phytoplankton and other optically active materials in the water (semi-analytical algorithms, based on radiative transfer and theoretical relationships such as eq (5.1-1)).

The MODIS ocean color products include three products of chl-a concentration and two pigment concentration products (table 4.1-3, chapter 4). The “CZCS_pigment”

(parameter 13), analog to CZCS chlorophyll, provides an estimate of chlorophyll-a and pheophytin-a and is based on an empirical algorithm derived from fluorometric measurements. The “pigment_c1_total” (parameter 15) product provides an estimate of all pigments that absorb in the blue MODIS bands and is based on an empirical algorithm derived from HPLC (High Pressure Liquid Chromatography) measurements. The “chlor_MODIS” (parameter 14) is a chlorophyll product based on an empirical algorithm derived from HPLC measurements of chl-a. The “chlor_a_2” (parameter 26) is a chlorophyll product analog to the SeaWiFS case 1 and case 2 waters chlorophyll concentration. The “chlor_a_3” product (parameter 27) is based on a semianalytic algorithm that relates the remote sensing reflectance measurements to absorption by various substances (phytoplankton, CDOM and non-pigmented particulate matter) present in the water, whose concentration may or may not covary with chlorophyll concentration. Therefore, this algorithm is the most appropriate for use in case 2 waters. However, for optically thick waters with chlorophyll concentrations larger than 1.5-2.0 mg m⁻³ this algorithm also becomes an empirical algorithm based on the relationship between remote sensing reflectance ratios and chlorophyll concentration. The three MODIS chlorophyll algorithms are discussed in more details in the “Methodology” section (paragraph 5.2.2).

In coastal and estuarine environments, such as Chesapeake Bay, the concentration and distribution of phytoplankton is of major water quality and ecologic concern. Human activities can increase phytoplankton concentration to significantly high levels in coastal regions, by increasing nutrient loadings to the water. According to Harding et al (1992)

large production of particulate organic carbon during dense phytoplankton blooms in the Bay, is linked to important processes in the estuary, such as nutrient utilization, fisheries productivity, light availability in the water column and the seasonal development of hypoxic/anoxic conditions (Kemp and Boynton, 1992; Harding et al, 1986; Malone et al, 1988; Malone, 1992). Therefore, [Chl-a] is one of the biological properties measured regularly in the framework of coastal water-quality monitoring programs (such as the CISNet program at SERC, 1980-present). Measurements of [Chl-a] were performed as part of our detailed measurements program in the northern part of the Chesapeake Bay.

One of the questions addressed in this chapter is how accurate are the MODIS [Chl-a] estimations in the case of the optically complex, estuarine waters of the northern Chesapeake Bay region. In paragraph 5.3-2 of the 'Results' section, in-situ [Chl-a] measurements are compared to various MODIS chlorophyll products, to examine the performance of the MODIS chlorophyll algorithms. What was the range of [Chl-a] values measured in-situ in the Chesapeake Bay waters during our cruises? How do overestimations or underestimations of MODIS Rrs values (due to errors, for example, on the atmospheric correction) affect the accuracy of satellite estimated chlorophyll concentrations? What is the performance of the satellite chlorophyll algorithms when in-situ measurements of Rrs are used as input information to estimate [Chl-a] in the Chesapeake Bay waters? As mentioned in chapter 2, in the Chesapeake Bay waters, substances such as CDOM and non-pigmented particulate matter, that do not necessarily covary with [Chl-a], significantly affect the spectral signature of radiance leaving the water surface. Are the bio-optical models or empirical relationships used currently in

satellite chlorophyll algorithms applicable to the Chesapeake Bay region? Based on information on the optical properties of Chesapeake Bay waters obtained during our in-situ measurements in the Bay, what are the relationships between Rrs spectra, that can be measured remotely, and surface chlorophyll concentrations, or absorption and backscattering by phytoplankton and other optically active substances in these waters? These issues are addressed in the following paragraphs.

5.2 Methodology

5.2.1 In-situ measurements of chl-a concentration

Measurements of chl-a concentration were performed regularly during the 2001-2002 cruises in the northern part of the Chesapeake Bay. The Chl-a pigment concentrations were determined spectrophotometrically, filtering whole water samples, collected from the four stations, through glass-fiber, Whatman GF/F filters. The water samples were collected from discrete depths (0, 1, 3, 5m) during the fall 2001 and spring-summer 2002 cruises, while only integrated water samples were collected during the summer 2001 cruises. Filters were extracted in 10 ml of 90% acetone overnight at 4°C, either immediately after the cruise or after freezing for less than 2 weeks. Absorbances of extracts were, then, measured at selected wavelengths and concentrations of the chl-a pigment were determined by using the Jeffrey and Humphrey (1975) equation:

$$[\text{Chl-a}] \text{ (in mg m}^{-3}\text{)} = [11.85 \cdot \text{OD}(664) - 1.54 \cdot \text{OD}(647) - 0.08 \cdot \text{OD}(630)] \cdot l^{-1} \cdot V^{-1} \quad (5.2-1)$$

where OD is the absorbance measured spectrophotometrically, v is the volume of acetone (in ml), l is the length of the cuvette (in cm) and V is the volume of filtered water (in l).

5.2.2. MODIS chl-a algorithms, bio-optical models and empirical relationships

The MODIS chlorophyll algorithms used in the estimations of the three available MODIS chlorophyll products (“chlor_MODIS”, “chlor_a_2” and “chlor_a_3”), are discussed in more details in the following paragraphs.

5.2.2.1 Chlorophyll-a concentration, HPLC – Empirical MODIS algorithm

The MODIS empirical-HPLC chlorophyll algorithm (parameter 14, “chlor_MODIS”) is an empirical algorithm derived for case 1 and 2 waters, which follows the CZCS analog, in which the sea-surface spectral radiance ratios are related empirically to in-situ data sets of chl-a concentration (sum of compounds: chl-a monovinyl and divinyl, chl-a allomer, chl-a epimer and chlorophyllide-a) measured using the HPLC method (MODIS ATBD 18, D. Clark, 1997).

The initially proposed algorithm for the chlor_MODIS product (D.Clark, 1997), was based on the original CZCS experimental database (case 1 waters), and was a linear relationship between the log of [Chl-a] and the log of MODIS $\frac{nLw(443)}{nLw(551)}$, according to:

$$\log_{10}[\text{Chl} - a] = A \cdot \left[\log_{10} \left(\frac{nLw(443)}{nLw(551)} \right) \right] + B \quad (5.2-2)$$

where A and B are least squares regression coefficients, A=-1.4, B=0.07.

The revised algorithm (D. Clark, updated 19 Feb. 2002), used in the Collection 4 MODIS data, that is used in the framework of this study, was a 3rd - order polynomial,

relating [Chl-a] to the sum of the MODIS nLw ratios, $\frac{nLw(443)}{nLw(551)}$ and $\frac{nLw(488)}{nLw(551)}$ (D.

Clark, personal communication, 2003). The chlor_MODIS parameter was computed according to:

$$\log_{10}[\text{Chl} - a] = (A(\log(X))^3 + B(\log(X))^2 + C(\log(X))^1 + D)/E \quad (5.2-3)$$

where: $X = \frac{nLw(443) + nLw(488)}{nLw(551)}$ and A, B, C, D, E are least squares regression

coefficients, with values: A=-2.8237, B=4.7122, C=-3.9110, D=0.8904, E=1.0 for the case of high total chl-a pigment, and A=-8.1067, B=12.0707, C=-6.0171, D=0.8791, E=1.0 for the case of low total chl-a pigment. The switch between the low and high total chl-a pigment cases, was done based on the value of the switching point, sp (defined as

$sp = \log_{10} \frac{nLw(443)}{nLw(551)}$), with $sp > 0.98$ indicating low total chl-a pigment, and $sp < 0.98$

indicating high total chl-a pigment.

The last revision of the algorithm (D. Clark, updated 19 March 2003), used in the MODIS reprocessing that started on 2 October 2003, is a 5th- order polynomial, that is expected to perform better in very high and very low chlorophyll environments.

According to the last updated algorithm:

$$\log_{10}[\text{Chl}-a] = [A(\log(X))^5 + B(\log(X))^4 + C(\log(X))^3 + D(\log(X))^2 + E(\log(X)) + F]/G \quad (5.2-4)$$

where:

$X = \frac{nLw(443) + nLw(488)}{nLw(551)}$, and A, B, C, D, E, F and G are least squares regression

coefficients: A=-10.399, B=27.937, C=-27.158, D=11.638, E=-3.926, F=0.789, G=1.0.

5.2.2.2 MODIS OC3M - SeaWiFS analog chl-a algorithm

The MODIS SeaWiFS compatible (OC3M) chlorophyll-a algorithm (parameter 26, “chlor_a_2” product) is an empirical algorithm, proposed by the developers of the SeaWiFS chl-a OC4-v4 algorithm and based on the same in-situ data set (case 1 and case 2 waters) of remote sensing reflectances, R_{rs} , and [Chl-a], that was used to parameterize the SeaWiFS OC4-v4 algorithm (O’Reilly J. et al, 2000). In this sense, the OC3M algorithm (“3” for the bands used, and “M” for MODIS) is a “SeaWiFS compatible” algorithm and has been used in many cases to compare estimations of [Chl-a] derived by SeaWiFS to [Chl-a] values derived by MODIS.

The OC3M is an empirical algorithm that uses the $\frac{R_{rs}(443)}{R_{rs}(551)}$ and $\frac{R_{rs}(488)}{R_{rs}(551)}$ ratios

(whichever is greater), and is expressed by the formula:

$$[\text{Chl-a}] = 10.0^{0.2830 - 2.753 \cdot R3M + 1.457 \cdot R3M^2 + 0.659 R3M^3 - 1.403 R3M^4} \quad (5.2-5)$$

where $R3M = \log_{10} \left(\max \left[\frac{R_{rs}(443)}{R_{rs}(551)}, \frac{R_{rs}(488)}{R_{rs}(551)} \right] \right)$

The 443:551 R_{rs} ratio is greater in low-chlorophyll (blue) waters, but as the chl-a concentration increases, absorption at 443 nm (Soret band) becomes larger, reflectance in the 443 band becomes lower, and the 488:551 R_{rs} ratio becomes larger. According to the MODIS “chlor_a_2” Data Quality Summary (July 2001), use of this algorithm in case 2 waters is likely to produce an overestimate of the chlorophyll concentration (since the algorithm does not account for absorption by other substances, such as CDOM and detritus, at the blue wavelengths).

5.2.2.3 MODIS Semianalytic chl-a algorithm, Case 2 waters

The case 2 MODIS semianalytic chlorophyll-a algorithm (parameter 27, “chlor_a_3”) is based on a semi-analytical, bio-optical model that relates the remote sensing reflectance measured by the satellite, to the water inherent optical properties absorption and backscattering.

The algorithm uses an “analytic” approach in the sense that the relationship between water reflectance and water IOPs is based on radiative transfer theory and the approximation $R_{rs}(\lambda) = \text{const} \cdot (b_b(\lambda)/a(\lambda))$. Using spectral ratios of remote sensing reflectances, the “const” term is eliminated. The spectral reflectance model is inverted to solve for chlorophyll-a concentration in the presence of other optically active substances (like CDOM and non-pigmented particulate matter) that do not covary with chlorophyll. Therefore, the algorithm is suitable for use in complex, case 2 waters. However, the bio-optical pieces of the radiative model, such as spectral shape of absorption by dissolved and particulate matter, or backscattering wavelength dependence, are expressed by empirical relationships and parameterizations (such as those discussed in Chapter 2 for the specific case of Chesapeake Bay waters) that should be determined on time and site specific basis. In this sense, the algorithm is “semi-analytic”.

In the semianalytical MODIS chl-algorithm, chl-a concentration is determined via a direct relationship to the algorithm-estimated phytoplankton absorption at 675nm, $a_{\text{phyt}}(675)$, according to: $[\text{Chl-a}] = P_0 [a_{\text{phyt}}(675)]^{P_1}$, where P_0 and P_1 are empirical

coefficients (Carder et al, 2002). According to Carder et al (2002), this step of relating [Chl-a] to $a_{\text{phyt}}(675)$, requires knowledge of the chlorophyll-a specific phytoplankton absorption coefficients. The chlorophyll specific phytoplankton absorption coefficients, $a_{\text{phyt}}^*(\lambda)$, can vary widely depending on phytoplankton species, light and nutrient history, pigment composition, cell size and pigment packaging. According to Carder et al (2002) $a_{\text{phyt}}^*(440)$ can vary by more than a factor of 10 between nutrient poor, photon rich subtropical gyres (increased photoprotective pigments, low packaging) and nutrient rich, photon poor upwelling or high latitude waters (less photoprotective pigments, high packaging). In the MODIS “chlor_a_3” algorithm, parameters P_0 and P_1 are adjusted dynamically in order to account for pigment packaging effects in nutrient-replete and nutrient-deplete conditions. The algorithm has been parameterized for three different bio-optical domains: (1) high ratios of photoprotective pigments to chlorophyll and low self-shading, designated as ‘unpacked’ (2) low ratios and high self-shading, designated as ‘packaged’ and (3) a transitional or global-average type. According to Kamykowski (1987) and Carder et al. (2002), these domains can be identified from space by comparing sea-surface temperature (SST), a derived MODIS product, to nitrogen-depletion temperatures (NDT) for each domain. According to Carder et al (2002) within a given bio-optical domain, there is only a very weak change in $a_{\text{phyt}}^*(675)$ with [Chl-a].

The accuracy of the chl-a concentration estimated using the “semi-analytic” MODIS algorithm depends on the accuracy of the remote sensing reflectance measured at 551 nm,

$R_{rs}(551)$, and the reflectance ratios $\frac{R_{rs}(412)}{R_{rs}(443)}$ and $\frac{R_{rs}(443)}{R_{rs}(551)}$. However, for waters with

high chlorophyll and CDOM concentrations (such as those in Chesapeake Bay), the

remote sensing reflectances in the blue wavelengths (412, 443 nm) can be very small (due to large absorption by CDOM and chlorophyll) (chapter 4), which could prevent the algorithm from performing properly (Carder et al, 2002). For this reason, the semianalytic algorithm is designed to return values only when modeled $a_{\text{phyt}}(675)$ is less than 0.03 m^{-1} , or chlorophyll concentration is less than $1.5\text{-}2.0 \text{ mg m}^{-3}$. During our cruises in the Chesapeake Bay waters, measured chlorophyll concentrations were always larger than 2 mg m^{-3} . Therefore, the performance of the semianalytic algorithm could not be tested using these measurements of [Chl-a]. More information on the algorithm is given in the MODIS ATBD 19 (Carder et al, 2002).

When the semi-analytical algorithm does not return a value for $a_{\text{phyt}}(675)$, an empirical, two-wavelength algorithm for [Chl-a] is used by default (Aiken et al., 1995) which is based on the $Lw(488)/Lw(551)$ ratio:

$$\log_{10}[\text{Chl} - a]_{\text{emp}} = c_0 + c_1 \log_{10}(X) + c_2 [\log_{10}(X)]^2 + c_3 [\log_{10}(X)]^3 \quad (5.2-6)$$

where $X = \frac{Rrs(488)}{Rrs(551)}$. The coefficients c_0, c_1, c_2, c_3 were derived applying a cubic

regression of $\log_{10}[\text{Chl-a}]$ vs $\log_{10}(X)$ measurements, performed in both open ocean and riverine influenced waters. As in the case of P_0 and P_1 parameters used in the relationship between [Chl-a] and $a_{\text{phyt}}(675)$ in the semianalytical version of the algorithm, coefficients c_0, c_1, c_2, c_3 in the empirical version of the algorithm are also adjusted dynamically in order to account for pigment packaging effects in nutrient-replete and nutrient-deplete conditions (table 5.2-2).

In order to have a smooth transition in [Chl-a] values when the algorithm switches from the semi-analytical to the empirical method, a weighted average of the [Chl-a] values is used when near the transition border ($0.015 < a_{\text{phyt}}(675) < 0.03$) :

$$[\text{Chl-a}] = w [\text{Chl-a}]_{\text{sa}} + (1-w) [\text{Chl-a}]_{\text{emp}} \quad (5.2-7)$$

The weighting factor, w , is defined as $w = [0.03 - a_{\text{phyt}}(675)]/0.015$. A weighted algorithm is also used to transition between a “highly packaged” and a “low packaged” region, according to:

$$[\text{Chl-a}] = w [\text{Chl-a}]_{\text{UP}} + (1-w) [\text{Chl-a}]_{\text{FP}} \quad (5.2-8)$$

where $[\text{Chl-a}]_{\text{UP}}$ is the unpackaged value, $[\text{Chl-a}]_{\text{FP}}$ is the fully packaged value and the weighting factor is $w = [1.0 + (\text{SST} - \text{NDT})]/5.0$.

When the semi-analytical algorithm does not return a value for $a_{\text{phyt}}(675)$, the values for $a_{\text{phyt}}(675)$ and $a_g(400)$ (“ a_g ” is absorption for “gelbstoff”, combined CDOM and non-pigmented particulate matter) are estimated through empirical, multi-wavelength algorithms based on $a_{\text{phyt}}(440)$ and $a_g(440)$ (Lee et al., 1998). Using these results, the empirical, default algorithms for high $a_{\text{phyt}}(675)$ values are determined by adjusting Lee’s results to 675 nm for phytoplankton and to 400 nm for gelbstoff,

$$a_{\text{phyt}}(675)_{\text{emp}} = 0.328 \cdot [10^{-0.919 + 1.037 r_{25} - 0.407 r_{25}^2 - 3.531 r_{35} + 1.702 r_{35}^2} - 0.008] \quad (5.2-9)$$

$$a_g(400)_{\text{emp}} = 1.5 \cdot [10^{-1.147 + 1.963 r_{15} - 1.01 r_{15}^2 + 0.856 r_{25} + 1.702 r_{25}^2}] \quad (5.2-10)$$

where ρ_{ij} are log of the ratio of the remote sensing reflectance of MODIS channel i to channel j . A weighted absorption algorithm is used for each of these components to transition from the semi-analytical expression to the default expression.

Table 5.2-1: MODIS chlorophyll algorithms. Significant points.

<ul style="list-style-type: none"> - The quality and accuracy of the MODIS chl-a concentration products depend on the quality of the MODIS remote sensing reflectances used as input information to the chl-algorithms. - The MODIS algorithms used in the estimation of chlorophyll concentration larger than $\sim 2 \text{ mg/m}^3$, are based on empirical relationships between [Chl-a] and Rrs or nLw ratios at the blue-green wavelengths: <ul style="list-style-type: none"> i) use of $\frac{nLw(443) + nLw(488)}{nLw(551)}$, for “chlor_MODIS” ii) use of $\frac{RRS(443)}{RRS(551)}$ or $\frac{RRS(488)}{RRS(551)}$ (whichever is greater), , for “chlor_a_2” iii) use of $\frac{RRS(488)}{RRS(551)}$, for “chlor_a_3” <p>A summary of the three MODIS algorithms used in the estimation of [Chl-a] for cases with [Chl-a] larger than 2 mg m^{-3} is given in Table 5.2-2.</p>
--

Table 5.2-2: Summary of MODIS empirical chl-a algorithms

MODIS empirical chl-a algorithms	Parameters												
<p>Product: “chlor_MODIS”:</p> $\log_{10}[\text{Chl-a}] = [A(\log_{10}(X))^3 + B(\log_{10}(X))^2 + C(\log_{10}(X)) + D]/E$	$X = \frac{nLw(443) + nLw(488)}{nLw(551)}$ <table style="width: 100%; border-collapse: collapse;"> <tr> <td style="text-align: center; border-bottom: 1px solid black;"><u>High Chl-a pigm</u></td> <td style="text-align: center; border-bottom: 1px solid black;"><u>Low Chl-a pigm.</u></td> </tr> <tr> <td style="text-align: center;">A=-2.8237</td> <td style="text-align: center;">A=-8.1067</td> </tr> <tr> <td style="text-align: center;">B=4.7122</td> <td style="text-align: center;">B=12.0707</td> </tr> <tr> <td style="text-align: center;">C=-3.9110</td> <td style="text-align: center;">C=-6.0171</td> </tr> <tr> <td style="text-align: center;">D=0.8904</td> <td style="text-align: center;">D=0.8791</td> </tr> <tr> <td style="text-align: center;">E=1.0</td> <td style="text-align: center;">E=1.0</td> </tr> </table>	<u>High Chl-a pigm</u>	<u>Low Chl-a pigm.</u>	A=-2.8237	A=-8.1067	B=4.7122	B=12.0707	C=-3.9110	C=-6.0171	D=0.8904	D=0.8791	E=1.0	E=1.0
<u>High Chl-a pigm</u>	<u>Low Chl-a pigm.</u>												
A=-2.8237	A=-8.1067												
B=4.7122	B=12.0707												
C=-3.9110	C=-6.0171												
D=0.8904	D=0.8791												
E=1.0	E=1.0												
<p>Product: “chlor_a_2”:</p> $\log_{10}[\text{Chl-a}] = A + B \cdot R_{3M} + C \cdot R_{3M}^2 + D \cdot R_{3M}^3 + E \cdot R_{3M}^4$	$R_{3M} = \log_{10}(\max[\frac{Rrs(443)}{Rrs(551)}, \frac{Rrs(488)}{Rrs(551)}])$ <p>A=0.283 B=-2.753 C=1.457 D=0.659 E=-1.403</p>												
<p>Product: “chlor_a_3”:</p> $\log_{10}[\text{Chl-a}] = c_0 + c_1 \log_{10}(X) + c_2 (\log_{10}(X))^2 + c_3 (\log_{10}(X))^3$	$X = \frac{Rrs(488)}{Rrs(551)}$ <table style="width: 100%; border-collapse: collapse;"> <tr> <td style="text-align: center; border-bottom: 1px solid black;"><u>Unpackaged</u></td> <td style="text-align: center; border-bottom: 1px solid black;"><u>Fully Packaged</u></td> </tr> <tr> <td style="text-align: center;">c₀ = 0.2818</td> <td style="text-align: center;">c₀ = 0.51</td> </tr> <tr> <td style="text-align: center;">c₁ = -2.783</td> <td style="text-align: center;">c₁ = -2.34</td> </tr> <tr> <td style="text-align: center;">c₂ = 1.863</td> <td style="text-align: center;">c₂ = 0.4</td> </tr> <tr> <td style="text-align: center;">c₃ = -2.387</td> <td style="text-align: center;">c₃ = 0.0</td> </tr> </table>	<u>Unpackaged</u>	<u>Fully Packaged</u>	c ₀ = 0.2818	c ₀ = 0.51	c ₁ = -2.783	c ₁ = -2.34	c ₂ = 1.863	c ₂ = 0.4	c ₃ = -2.387	c ₃ = 0.0		
<u>Unpackaged</u>	<u>Fully Packaged</u>												
c ₀ = 0.2818	c ₀ = 0.51												
c ₁ = -2.783	c ₁ = -2.34												
c ₂ = 1.863	c ₂ = 0.4												
c ₃ = -2.387	c ₃ = 0.0												

5.3 Results

5.3.1 In-situ measurements of chlorophyll concentration in the Chesapeake Bay waters

Large temporal variability in chl-a concentration was observed during our measurements at the four stations in the northern part of the Chesapeake Bay, with [Chl-a] values ranging from 3.5 mg/m³ (PI station, 13 November 2001) to 74 mg/m³ (HB station, 11 June 2001). A frequency histogram of the surface [Chl-a] values (estimated as average concentrations from measurements performed within the first meter below the water surface) is shown in figure 5.3-1.

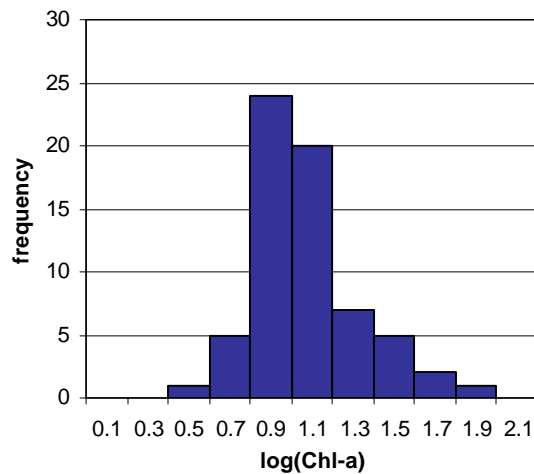


Figure 5.3-1: Frequency histogram of the surface [Chl-a] log-transformed values measured at the four stations, in the northern part of the Chesapeake Bay.

The temporal and spatial variation of chl-a concentration measured at the sites PI, HB, TI and JT during the 17 cruises in the northern part of the bay, are shown in figure 5.3-2 (measurements performed at the four different stations are shown as different symbols). Relatively clear waters, with low biological activity and low [Chl-a] values at all four stations were observed during the 2002 early spring season and the late 2001 and 2002 fall seasons. High biological activity, associated with high light and nutrient availability,

occurred during the early summer months of both 2001 and 2002 years. Patchy phytoplankton bloom events with large chl-a concentration values, $[Chl-a] > 20 \text{ mg/m}^3$, were observed in the Chesapeake Bay waters during those months, resulting in high spatial and temporal variability in the water's optical properties. A large phytoplankton bloom was observed during the cruise on 11 June 2001, with $[Chl-a]$ values of 60 mg/m^3 at JT station and 74 mg/m^3 at HB station. Figure 5.3-3(a) shows the phytoplankton absorption spectra (300-750 nm) measured spectrophotometrically on water samples collected from HB, PI, TI and JT stations during that day (the methodology for the spectrophotometric measurements of phytoplankton absorption is described in section 2.2.2.2, chapter 2). The phytoplankton absorption spectra measured at the same stations on 28 September 2001, when waters in the Bay were relatively clear and $[Chl-a]$ was much lower (ranging from 7.5 mg/m^3 at PI station to 14.5 mg/m^3 at HB station), are shown in figure 5.3-3(b) for comparison. The absorption spectra measured on 11 June 2001 were characterized by high absorption values in the UV range ($\sim 325 \text{ nm}$), probably caused by the presence of mycosporine-like amino acids (MAAs).

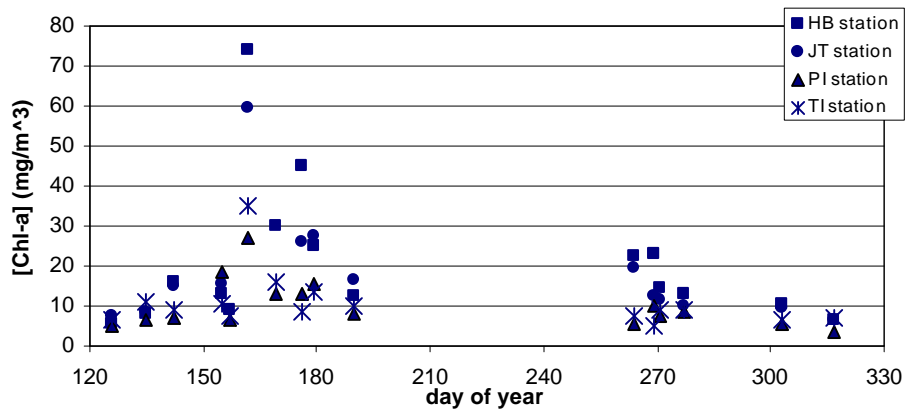
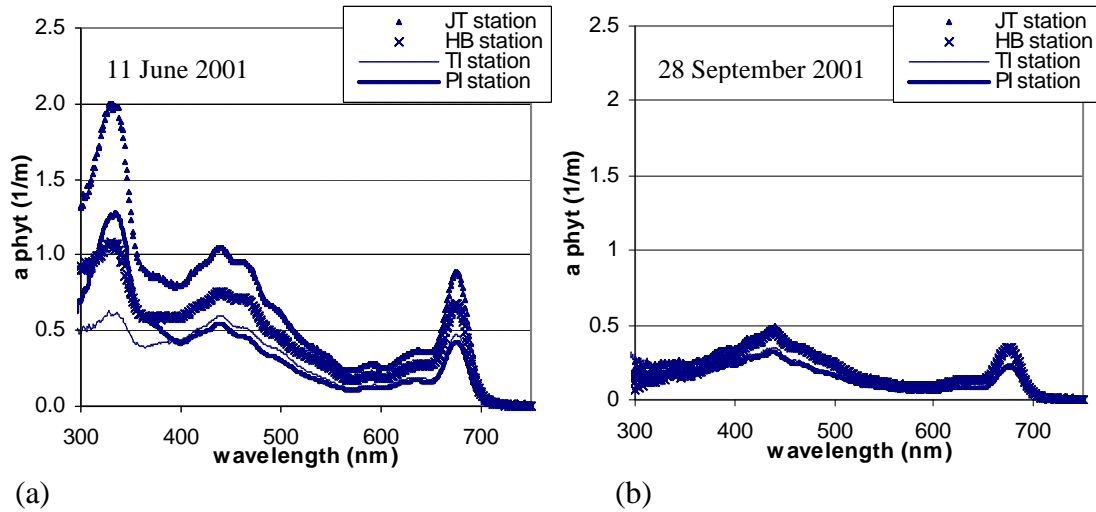


Figure 5.3-2: Temporal variation of $[Chl-a]$ measured within the first meter below the water surface. Measurements are from cruises performed during 2001 and 2002 at HB, JT, PI and TI stations.



(a) (b)
 Figure 5.3-3: (a) Phytoplankton absorption spectra (300-750nm), measured at HB, PI, TI and JT stations, during the phytoplankton bloom observed on 11 June 2001. High absorption in the UV range (~ 325 nm) was probably caused by the presence of MAAs. (b) Phytoplankton absorption spectra measured at HB, PI, TI and JT stations, during 28 September 2001, when waters in the Bay were relatively clear. (Particulate absorption values were calculated using $\beta=1.5$)

The [Chl-a] profiles for the cruises 28 September 2001 - 8 November 2002 are shown in figure 5.3-4. During those days [Chl-a] measurements were performed on water samples collected from discrete depths at 0, 1, 3, 5 m. As discussed in chapter 2, during the cruises performed in the fall and early spring seasons the water was fairly well mixed and [Chl-a] profiles were almost constant with depth (discussion in chapter 2). Vertical thermal and density stratification, observed during some of the summer cruises, resulted in some variation of [Chl-a] with depth (e.g. cruises on 22 May 2002, 18 June 2002). The vertical distribution of [Chl-a] could not be studied for the 2001 summer cruises, since only integrated water samples were available for those cruises. However, vertical profiles of $a_{t-w}(676)$ measured on 11 and 25 June 2001 at HB station showed much higher values within the first 2 meters below the water's surface (fig. 2.3-4(b)), suggesting that the

phytoplankton blooms observed at HB during those days were close to the water's surface.

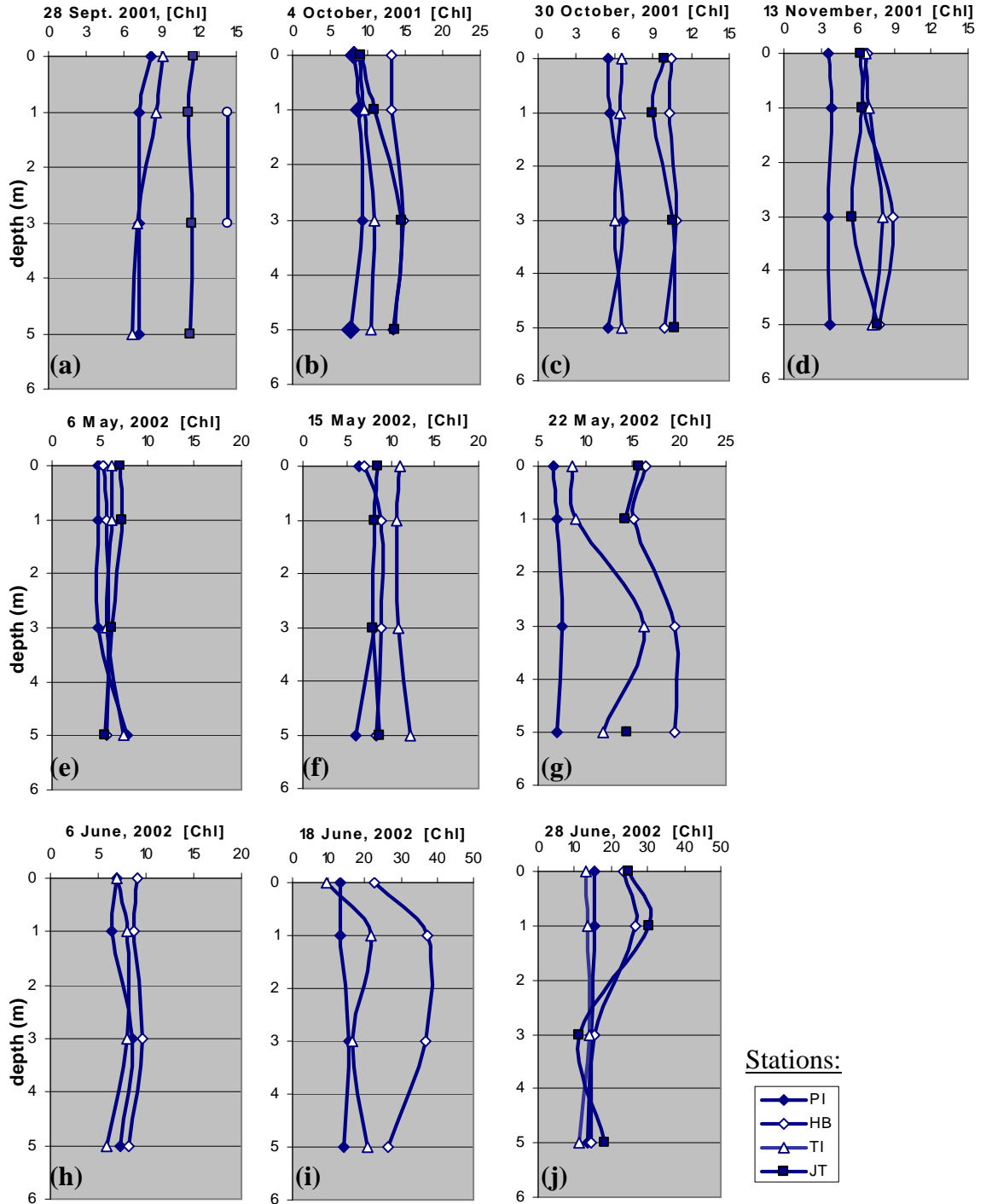


Figure 5.3-4: Vertical profiles of chl-a concentration measured at Chesapeake Bay during the cruises 28 September 2001(a) - 8 November 2002(j)

Since satellite measurements are restricted to the upper layers of the water, surface chl-a concentration values were estimated from the in-situ measurements performed in the Bay. The comparison between the surface [Chl-a] values estimated i) as the average within the first meter (measurements performed at 0 m and 1 m depths) and ii) as the average within the first three meters below the water surface (measurements performed at 0 m, 1 m and 3 m depths), is shown in figure 5.3-5, along with the 1:1 line for comparison. The values fall close to the 1:1 line, since in most of the cases (especially during the fall cruises) chl-a concentration did not show very large variation with depth. An exception to this, with $[\text{Chl-a}]_{\text{avg}(0-1\text{m})}$ larger than $[\text{Chl-a}]_{\text{avg}(0-3\text{m})}$, is measurements performed at HB and JT station on 28 June 2002, but these [Chl-a] values were not used for comparisons to satellite measurements since MODIS measurements were not available for 28 June 2002. MODIS measurements were not available, either, on 25 June 2001 (surface phytoplankton bloom event observed at HB station). Therefore, in most of the cases, estimations of surface [Chl-a] as the average within the first meter below the water surface were not largely different than surface [Chl-a] values estimated as the average within the first three meters below the water surface.

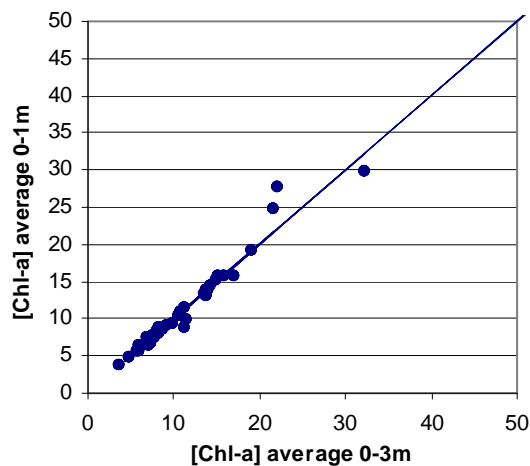


Figure 5.3-5: Comparison between surface [Chl-a] values estimated as the average i) within the first meter and ii) within the first three meters below the water surface. The comparison is close to 1:1 line for almost all of the cases.

The relation between chl-a concentration and phytoplankton absorption at 676 nm, $a_{\text{phyt}}(676)$, for measurements performed on water samples collected from the four stations during the cruises (depths 0, 1, 3, 5m) is shown in figure 5.3-6. The phytoplankton absorption values were corrected for optical pathlength amplification using $\beta=1.5$. Measurements of [Chl-a] and absorption performed during the large phytoplankton bloom on 11 June 2001 are shown as white circles in figure 5.3-6.

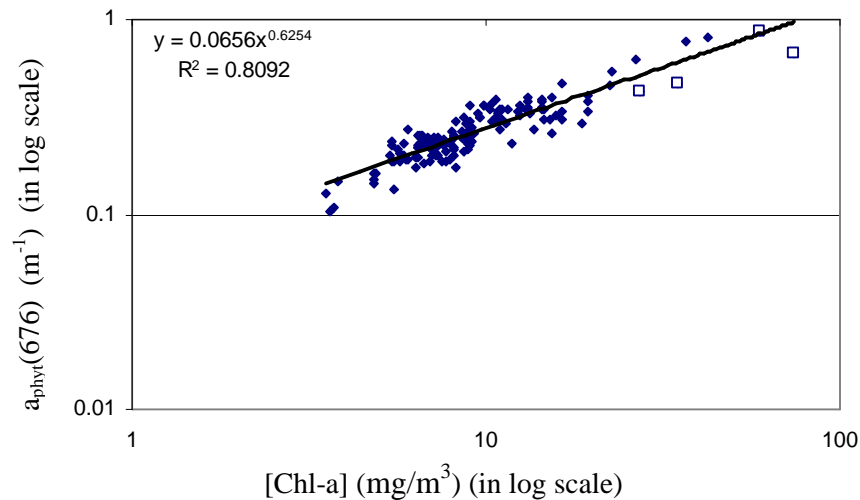


Figure 5.3-6: Relation between [Chl-a] and phytoplankton absorption at 676 nm, $a_{\text{phyt}}(676)$, measured using the CARY spectrophotometer (methodology in paragraph 2.2.2.2, chapter 2). Measurements performed on 11 June 2001 (large phytoplankton bloom) are shown as white squares.

5.3.2 Comparisons between in-situ and MODIS chlorophyll concentration measurements

The three MODIS products of chlorophyll concentration were studied for the northern region of the Chesapeake Bay and for the dates of the cruises performed during 2001-2002 in the Bay. The satellite observations were compared to the in-situ surface [Chl-a] measurements in order to study the performance of the satellite algorithms in these optically complex, case-2 waters (fig. 5.3-7). Since in-situ [Chl-a] measurements were always larger than 2 mg/m^3 during the measurements in the Chesapeake Bay, the in-situ measurements were compared to the MODIS [Chl-a] products estimated based on the empirical MODIS algorithms described in the Methodology section (table 5.2-2). The in-situ [Chl-a] measurements were compared to the MODIS [Chl-a] values measured at the 'best' MODIS pixels, since the 'best' pixel was selected as the pixel for which the satellite nLw values showed the best agreement with the in-situ nLw measurements at 488, 551 and 667 nm.

When a MODIS chlorophyll algorithm fails, the MODIS [Chl-a] values are flagged as negative values. One reason for the algorithm's failure is input of incorrect (or flagged) nLw values at the specific wavelengths used in each chl-algorithm. All MODIS [Chl-a] values were flagged, as expected based on the description of the algorithms, for these pixels characterized by negative nLw (or Rrs) values at 443 or 488 nm. These cases (almost 38% of the total) are shown as red pixels in figures 5.3-7 (a), (c), (e).

As was discussed in chapter 4, some of the cruise days were characterized by high aerosol optical thickness in the atmosphere (e.g. 11 June 2001, 21 September 2001, 6

June 2002). During those days, a large disagreement between in-situ and MODIS nLw (or Rrs) measurements was observed, especially at the short wavelengths, probably due to errors in the satellite atmospheric correction under conditions of high aerosol optical thickness. The [Chl-a] values estimated by MODIS during those days were also in large disagreement with the in-situ measured chlorophyll concentrations (31% of the cases, shown as white pixels in figure 5.3-7). Percent differences between in-situ [Chl-a] and MODIS chlorophyll products, estimated as $100 \cdot ([\text{Chl-a}]_{\text{InSitu}} - [\text{Chl-a}]_{\text{MODIS}}) / [\text{Chl-a}]_{\text{InSitu}}$, were between 50 and 95%.

The comparison between MODIS and in-situ [Chl-a] values, for cases with almost clear atmospheric conditions and no negative MODIS nLw values at 443 or 488 nm (almost 31% of the cases studied), is also shown in figure 5.3-7 (blue pixels, also shown at log-log scale at figures 5.3-7 (b), (d), (f)). A lot of scattering around the 1:1 line was observed in the comparisons between the in-situ [Chl-a] values and the “chlor_MODIS” product. Less scattering around the 1:1 line was observed for the “chlor_a_2” SeaWiFS analog, and especially the “chlor_a_3” product. Percent differences between in-situ [Chl-a] and MODIS ‘chlor_a_3’ were between -20% and 2%, for $[\text{Chl-a}] < 10 \text{ mg m}^{-3}$. However, large disagreement was observed at larger chlorophyll concentrations (percent differences -500% to 30%, for $[\text{Chl-a}] > 10 \text{ mg m}^{-3}$).

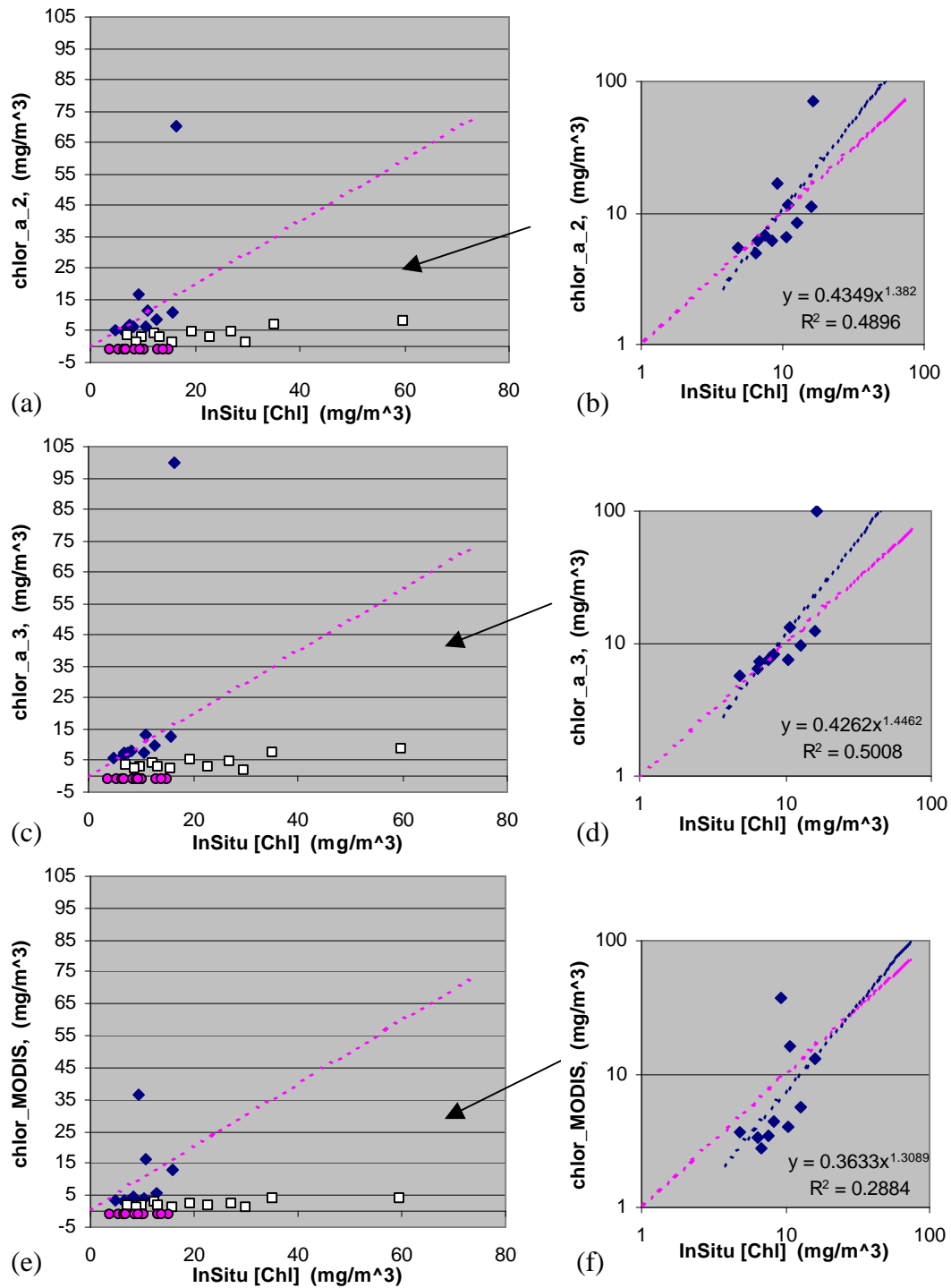


Figure 5.3-7: Comparison between in-situ [Chl-a] measurements and the MODIS [Chl-a] products (a) “chlor_a_2” (c) “chlor_a_3” (e) “chlor_MODIS”. MODIS measurements were obtained for the “best” pixel around the location of each site. MODIS [Chl-a] were flagged (-1) for those cases when the chl-algorithms failed (e.g due to negative or flagged nLw(443), nLw(488) values) (red circles). The satellite [Chl-a] values were underestimated for pixels with overestimated nLw(443), nLw(488) (white squares) (days with high AOT). The rest of the pixels are shown as blue pixels (also in log-log scale at figures (b), (d), (f)).

To examine the performance of the satellite chl-algorithms in the Bay waters, the three MODIS chl-algorithms (“chlor_MODIS” 3rd and 5th order polynomials, SeaWiFS analog “chlor_a_2”, and empirical version of “chlor_a_3” for fully packaged and unpackaged pigments) were used to estimate [Chl-a] using as input the Rrs spectra measured in-situ in the Chesapeake Bay waters or estimated by Hydrolight (based on detailed measurements of boundary conditions and water optical properties). Equations 5.2-3 – 5.2-6 (also shown in table 5.2-2) were used to estimate [Chl-a] from the in-situ measured Rrs or nLw ratios. The results were compared to the in-situ measurements of surface [Chl-a] (figure 5.3-8).

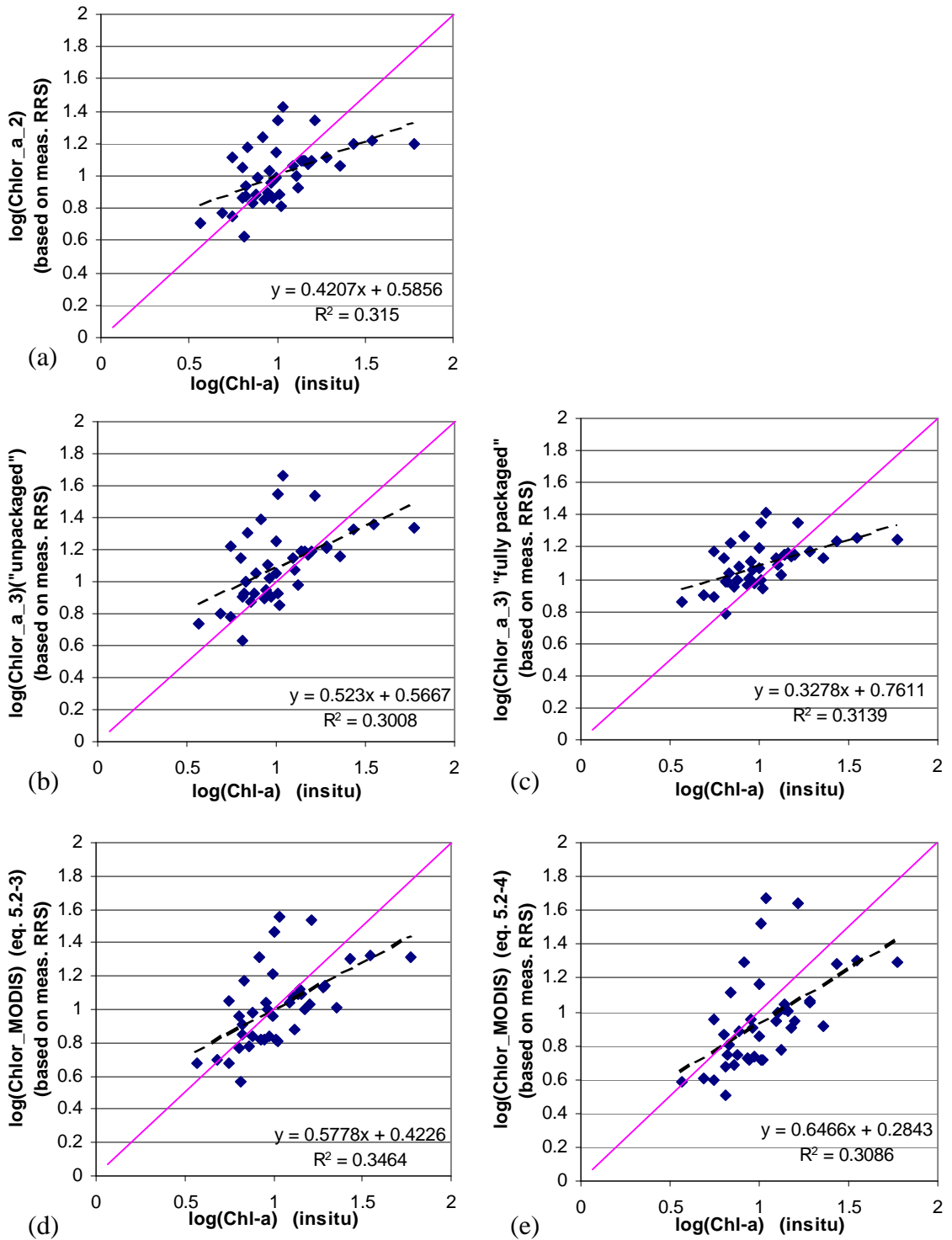


Figure 5.3-8: Comparisons between in-situ $\log_{10}(\text{Chl-a})$ and chlorophyll concentrations estimated using the MODIS empirical algorithms and measurements of Rrs (or nLw) as input information (in logarithmic values). The MODIS chl-algorithms used were: (a) “chlor_a_2” (eq. 5.2-5), (b)-(c) “chlor_a_3” (eq. 5.2-6) for the “unpacked” and the “fully packaged” cases, (d)-(e) “chlor_MODIS” (eq. 5.2-3, 3rd order polynomial for the case of high Chl-a pigment and eq.5.2-4, 5th order polynomial).

5.3.3 Relationships between chlorophyll concentration and Remote Sensing Reflectance in the Bay waters

Since most satellite [Chl-a] algorithms for case 1 and case 2 waters are based on empirical relationships between [Chl-a] and ratios of remote sensing reflectance measured at certain wavelength bands, the relationships between Rrs at various wavelengths and [Chl-a] were examined for the Chesapeake Bay waters, using in-situ measurements performed during the 2001-2002 cruises in the Bay. Laboratory measurements of surface chl-a concentration were compared to in-situ measurements of Rrs for those cruises when accurate MicroPro measurements were available, and to model-estimated (using Hydrolight code) Rrs values for those cruises when MicroPro measurements were not performed but detailed information on the boundary conditions and the inherent optical properties of the water was available.

The relationship between [Chl-a] and $Rrs(\lambda_i) / Rrs(\lambda_j)$ (in log-log scaling) for $\lambda_j = 554$ nm and $\lambda_i = 412, 443, 488, 531, 670$ and 677 nm, is shown in figure 5.3-9. Significant relationships were found between $\log_{10}[\text{Chl-a}]$ and $\log_{10}(Rrs(\lambda_i) / Rrs(554))$ values for $\lambda_i = 443, 488, 670$ and 677 nm (P-value in linear regression was small, $P < 0.05$). However, as is shown in figure 5.3-9, small R^2 values (coefficient of determination) were found in the linear regression $\log_{10}[\text{Chl-a}]$ vs $\log_{10}(Rrs(\lambda_i) / Rrs(554))$, for 443 and 488 nm. Stronger relationship (with $R^2 = 0.54$) was observed between $\log_{10}[\text{Chl-a}]$ and $\log_{10}(Rrs(677) / Rrs(554))$.

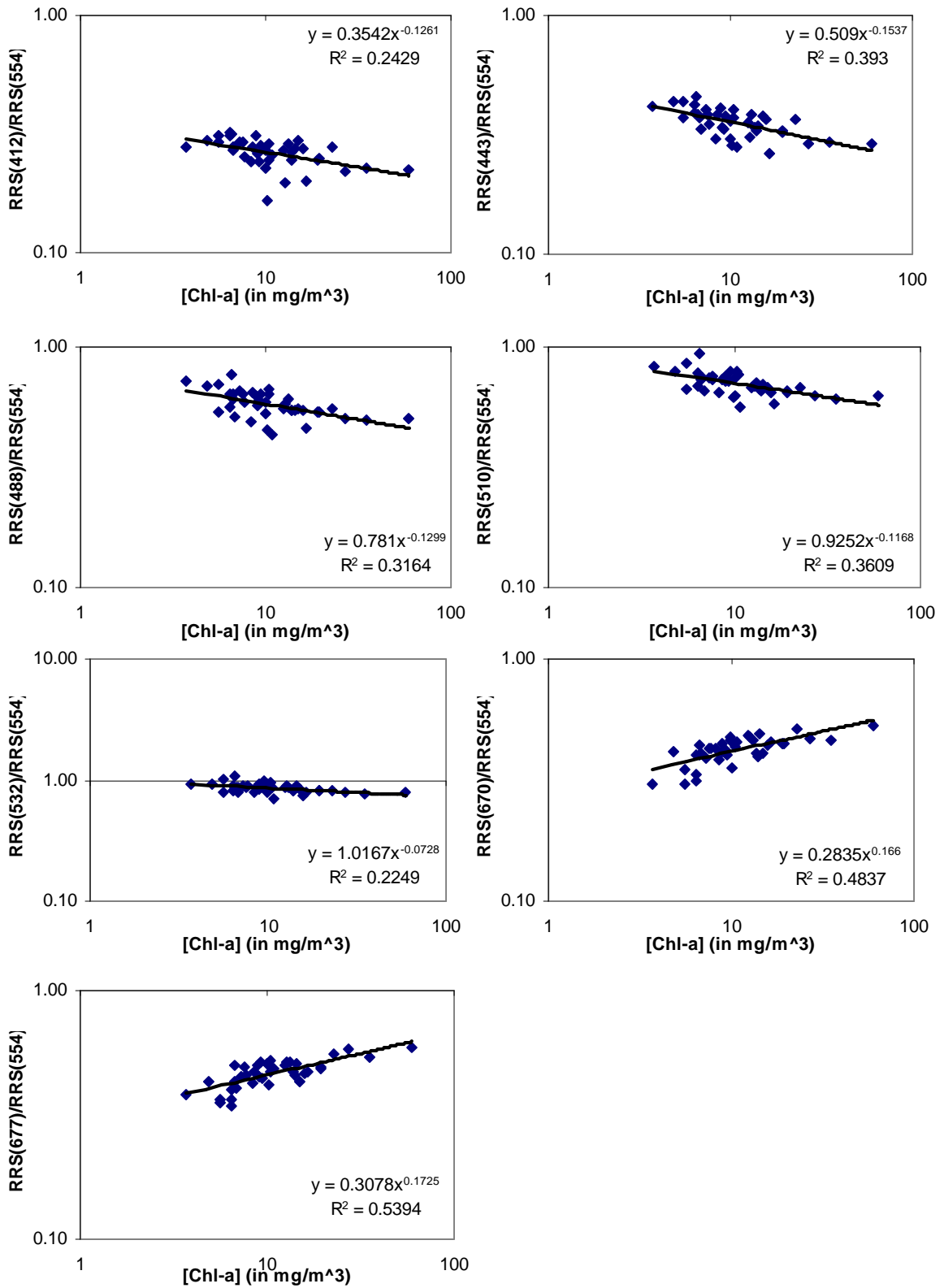


Figure 5.3-9: Relationship between laboratory measurements of [Chl-a] and in-situ measured or Hydrolight estimated $Rrs(\lambda_i)/Rrs(554)$ for $\lambda_i = 412, 443, 488, 510, 532, 670$ and 677 nm

A polynomial fit was applied to the $\log_{10}[\text{Chl-a}]$ vs $\log_{10}(\text{Rrs}(488)/\text{Rrs}(554))$ measurements (fig.5.3.10), similarly to the polynomial equations used to estimate [Chl-a] in the MODIS empirical algorithms “chlor_a_2” and “chlor_a_3” (table 5.2-2). The coefficient of determination was not significantly improved, compared to the results of the linear regression (in fig. 5.3-9). The 3rd order polynomial used in the “chlor_a_3” MODIS algorithm to estimate [Chl-a] from the MODIS Rrs(488)/ Rrs(554) values, is also shown in figure 5.3-9 (red line) for comparison.

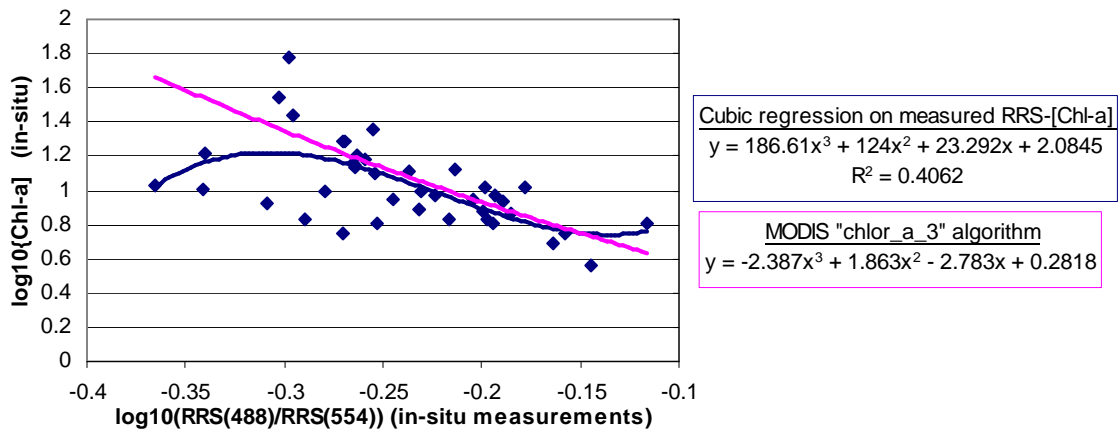


Figure 5.3-10: Cubic regression on the log transformed laboratory measurements of [Chl-a] and in-situ measurements of Rrs(488)/ Rrs(554). A 3-rd order polynomial between $\log_{10}[\text{Chl-a}]$ and $\log_{10}(\text{Rrs}(488)/\text{Rrs}(554))$ is used in the MODIS empirical algorithms “chlor_a_2” and “chlor_a_3” (table 5.2-2). The 3rd order polynomial used in the “chlor_a_3” MODIS algorithm to estimate [Chl-a] from the MODIS Rrs(488)/Rrs(554) values, is also shown (red line) for comparison.

5.3.4 Relationships between Remote Sensing Reflectance, total absorption and backscattering

As mentioned in the introduction, the remote sensing reflectance, R_{rs} , measured by a satellite sensor, is related to the processes of backscattering, b_b , and absorption, a , within the water. According to Lee (1994) the remote sensing reflectance, $R_{rs}(\lambda)$ can be related to $b_b(\lambda)$ and $a(\lambda)$ according to:

$$R_{rs}(I) = \frac{f}{Q(I)} \cdot \frac{t_{(w,a)}t_{(a,w)}}{n_w^2} \cdot \frac{b_b(I)}{a(I) + b_b(I)} \quad (5.3-1)$$

where $\frac{t_{(w,a)}t_{(a,w)}}{n_w^2} \cong 0.54$ (Mobley, 1994) and the ratio $\frac{f}{Q(I)} \cdot \frac{t_{(w,a)}t_{(a,w)}}{n_w^2}$ is expected to be within the range of 0.043 – 0.08 (Morel and Mueller, 2002).

The relation between the $R_{rs}(\lambda)$ values and the ratio $\frac{b_b(I)}{a(I) + b_b(I)}$, and the variability in the quantity $\frac{f}{Q(I)} \cdot \frac{t_{(w,a)}t_{(a,w)}}{n_w^2}$, were examined for the case 2 Chesapeake Bay waters, using in-situ measurements of $R_{rs}(\lambda)$, and surface measurements of total in-water $b_b(\lambda)$ and $a(\lambda)$, performed at PI, HB, TI and JT stations. The ratio $b_b/(a+b_b)$ was estimated using the ECO-VSF measurements of total backscattering (see also methodology section in chapter 2) and the AC9 measurements of total-minus-water absorption (corrected for scattering errors assuming non-zero absorption at 715nm). The total absorption was estimated adding the Pope and Fry (1997) coefficients to the AC9 values. Therefore,

$\frac{b_b(\mathbf{I})}{a(\mathbf{I})+b_b(\mathbf{I})} = \frac{b_b(\mathbf{I})}{a_w(\mathbf{I})+a_{AC9}(\mathbf{I})+b_b(\mathbf{I})}$. The relationship between measured $Rrs(\lambda)$ and

measured $\frac{b_b(\mathbf{I})}{a(\mathbf{I})+b_b(\mathbf{I})}$ is shown in figures 5.3-11, for the three wavelengths 440, 530 and

670 nm (yellow pixels). In the same figure, the relationship between measured

$\frac{b_b(\mathbf{I})}{a(\mathbf{I})+b_b(\mathbf{I})}$ and model-estimated $Rrs(\lambda)$ values is also shown (blue pixels) since for some

of the cruises in-situ MicroPro measurements of Rrs were not available. According to the

results the measured Rrs values are highly correlated to the ratio $\frac{b_b(\mathbf{I})}{a(\mathbf{I})+b_b(\mathbf{I})}$ at all three

wavelengths. Moreover, the least-square regression fits for Rrs_{measured} versus $b_b/(a+b_b)$

were very similar to the least-square regression fits for Rrs_{model} versus $b_b/(a+b_b)$.

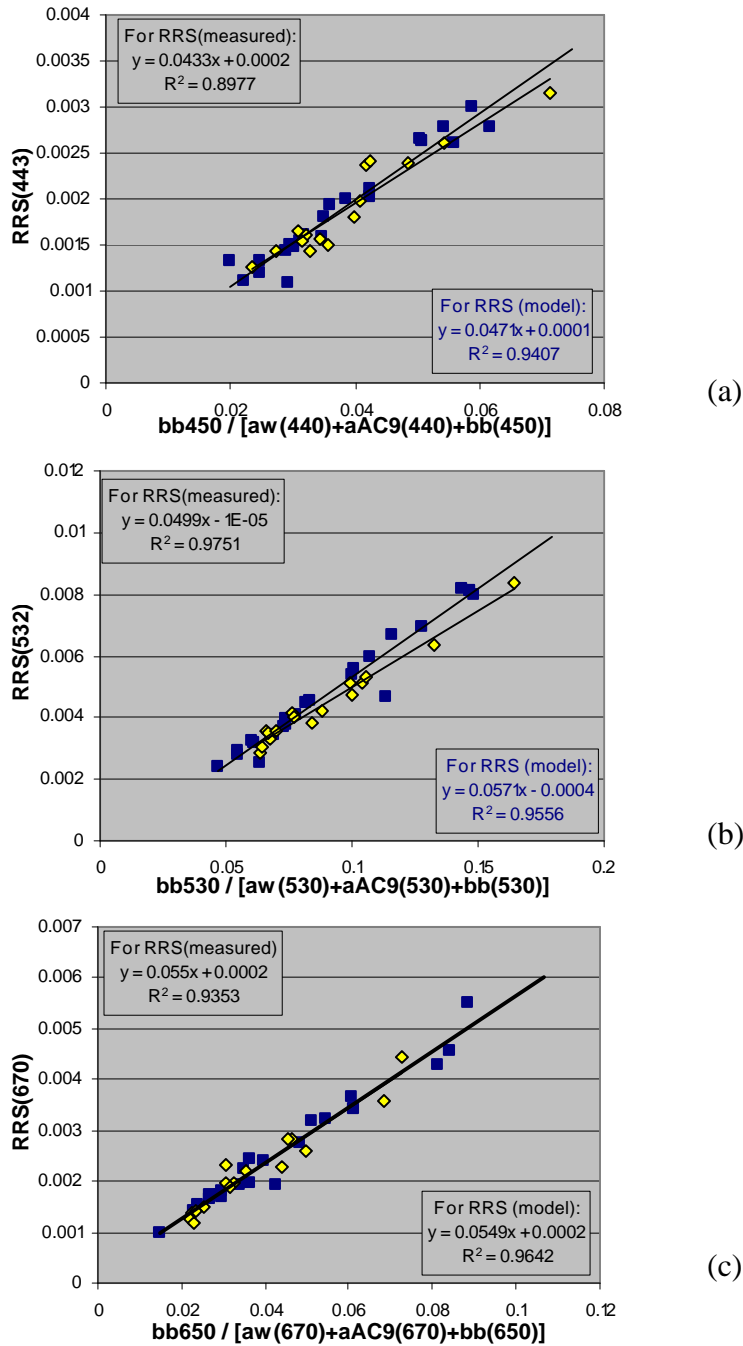


Figure 5.3-11: Relation between measured $Rrs(\lambda)$ values and measured $\frac{b_b(\mathbf{I})}{a(\mathbf{I})+b_b(\mathbf{I})}$ (yellow pixels) and between model-estimated $Rrs(\lambda)$ values and measured $\frac{b_b(\mathbf{I})}{a(\mathbf{I})+b_b(\mathbf{I})}$ (blue pixels) at (a) 440 nm, (b) 530 nm and (c) 670 nm. The linear least-squares regression fits are also shown, for each case.

5.3.5 Relationships between Remote Sensing Reflectance, total backscattering and absorption by non-pigmented particulate matter

The relationship between $R_{rs}(\lambda)$ and $b_b(\lambda)$ was also examined, to study if the measured remote sensing reflectances can be directly related to total backscattering in the highly turbid Chesapeake Bay waters. Figure 5.3-12 shows the relation between measured $b_b(\lambda)$ and measured (yellow pixels), as well as model-estimated (blue pixels) $R_{rs}(\lambda)$ at the wavelengths 443 nm (b_b measured at 450 nm), 532 nm (b_b measured at 530 nm) and 670 nm (b_b measured at 650 nm). Linear least-squares regression fits were performed for all measurements and the results are shown in figures 5.3-12 (a)-(c). A strong relationship ($R^2=0.88$) was found between the total backscattering at 650 nm and the remote sensing reflectance measured at 670 nm.

The relationship between $b_b(650)$ and satellite measurements of $R_{rs}(670)$ was also examined, and the results are shown in figure 5.3-13(b). An increase of the MODIS $R_{rs}(670)$ values was observed for increase at the surface $b_b(650)$. The coefficient of determination was $R^2=0.5$ (only 15 points were used in this case, since in some of the cases MODIS $R_{rs}(670)$ values were negative or $b_b(650)$ measurements were not available). Comparisons between MODIS and in-situ measurements of R_{rs} (chapter 4) showed that the correlation coefficient between satellite and in-situ $R_{rs}(670)$ measurements was relatively large (with $R^2 \cong 0.7$), with MODIS systematically underestimating $R_{rs}(670)$ compared to the in-situ observations (fig. 5.3-13(a)).

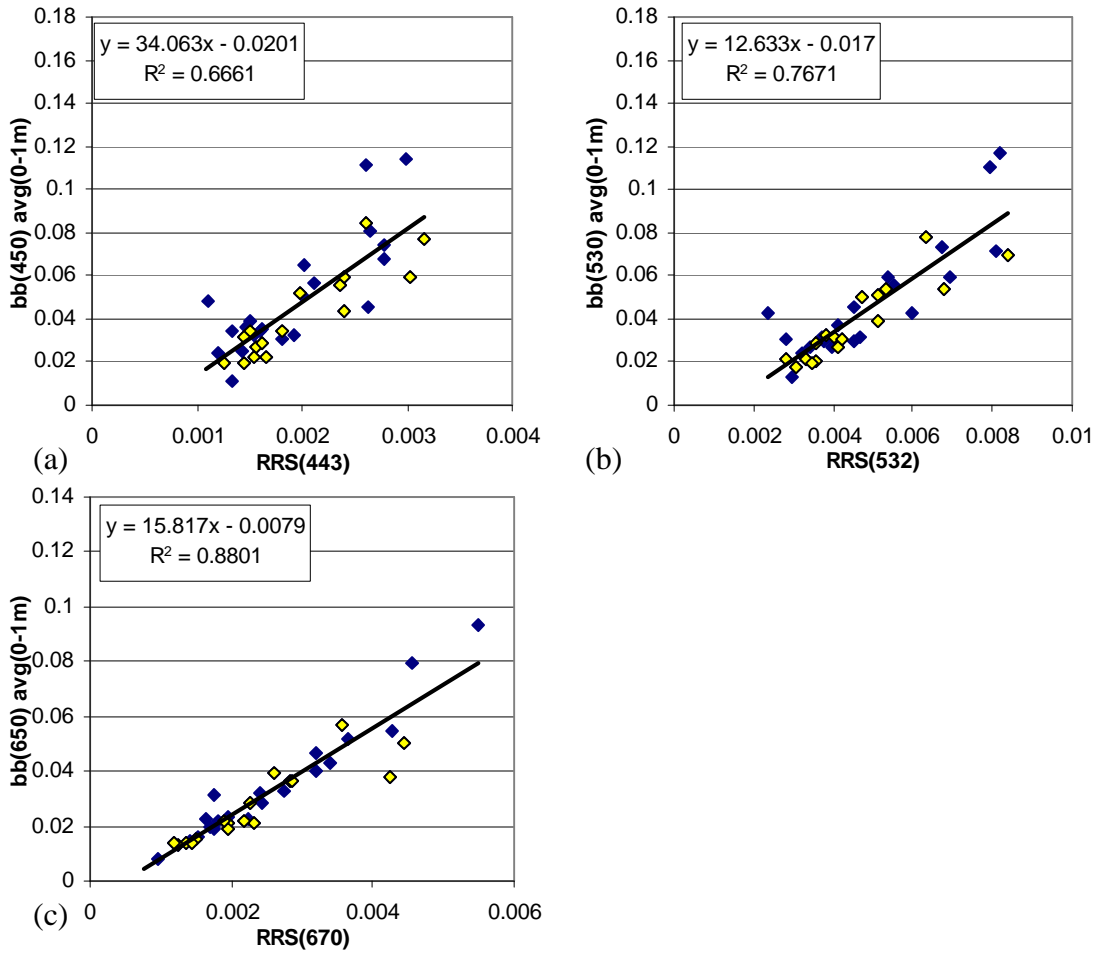


Figure 5.3-12: Relation between measured b_b and measured (yellow pixels), as well as model-estimated (blue pixels) Rrs at the wavelengths (a) 443 nm (b_b measured at 450 nm), (b) 532 nm (b_b measured at 530 nm) and (c) 670 nm (b_b measured at 650 nm).

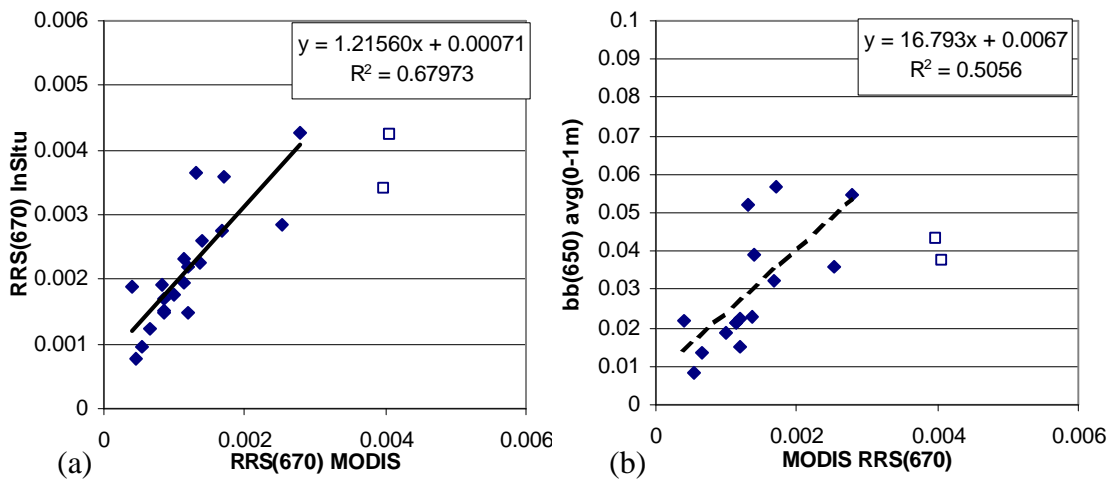


Figure 5.3-13: (a) Relation between in-situ and MODIS $Rrs(670)$. For almost all of the cases MODIS underestimated $Rrs(670)$ compared to the in-situ and modeled estimated $Rrs(670)$ values. (b) Relation between measured $b_b(650)$ and MODIS Rrs at 670 nm.

Since the backscattering $b_b(650)$ was found to be strongly related to the remote sensing reflectance at 670 nm (a quantity that can be measured remotely from instruments onboard an aircraft or a satellite), it was of interest to examine the relationship between $b_b(650)$ and chl-a concentration, as well as the relationship between surface total b_b and absorption by non-pigmented particulate matter, for the measurements performed in the Chesapeake Bay. The relationship between surface total b_b and surface [Chl-a] (figure 5.3-14) showed a lot of scattering, especially at large [Chl-a] values. However, the surface total b_b was found to be strongly related to surface values of absorption by non-pigmented particulate matter. Figures 5.3-15, 5.3-16 show the relation between measured surface b_b at 530 and 650 nm, and surface measurements of a_{npp} at 412 and 380 nm. The square correlation coefficients, R^2 , improved when two of the measurements (out of 45 total) were excluded in the estimation of the linear least-squares regression fits (figures 5.3-16 (c), (d)).

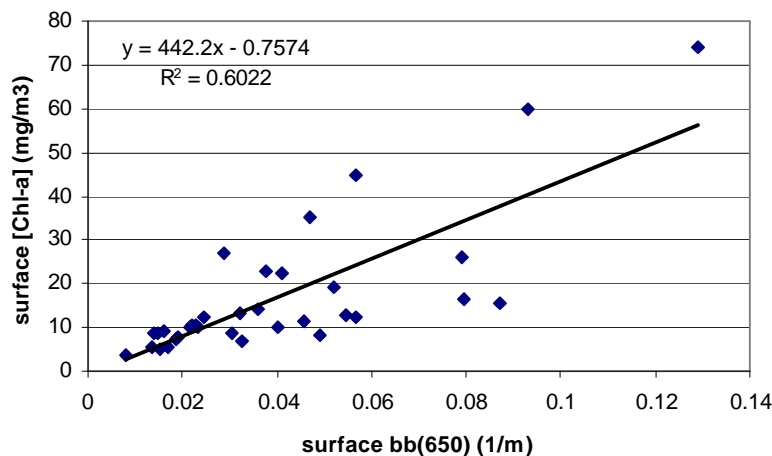


Figure 5.3-14: Relation between surface [Chl-a] and surface $b_b(650)$ measurements in the Chesapeake Bay waters.

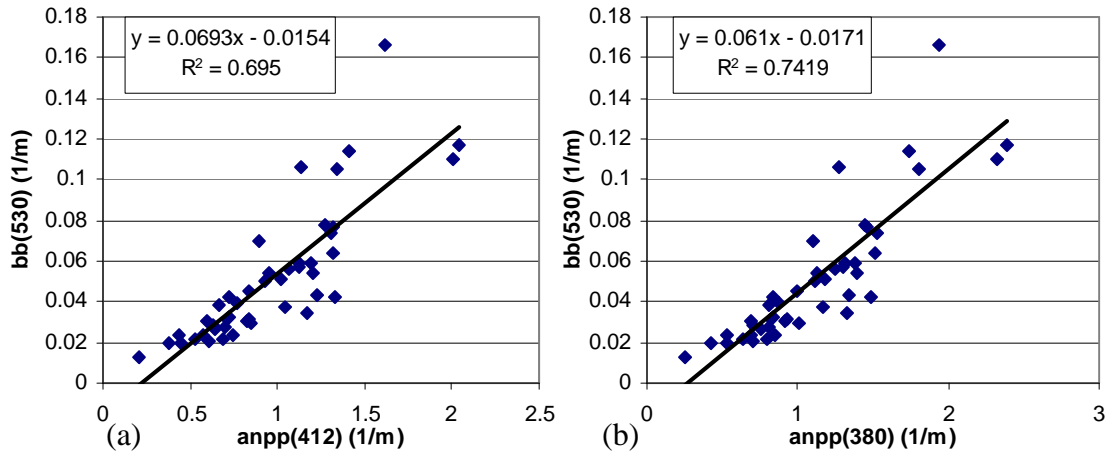


Figure 5.3-15: Relation between measured surface b_b at 530 nm and surface measurements of absorption by non-pigmented material at (a) 412 nm and (b) 380 nm.

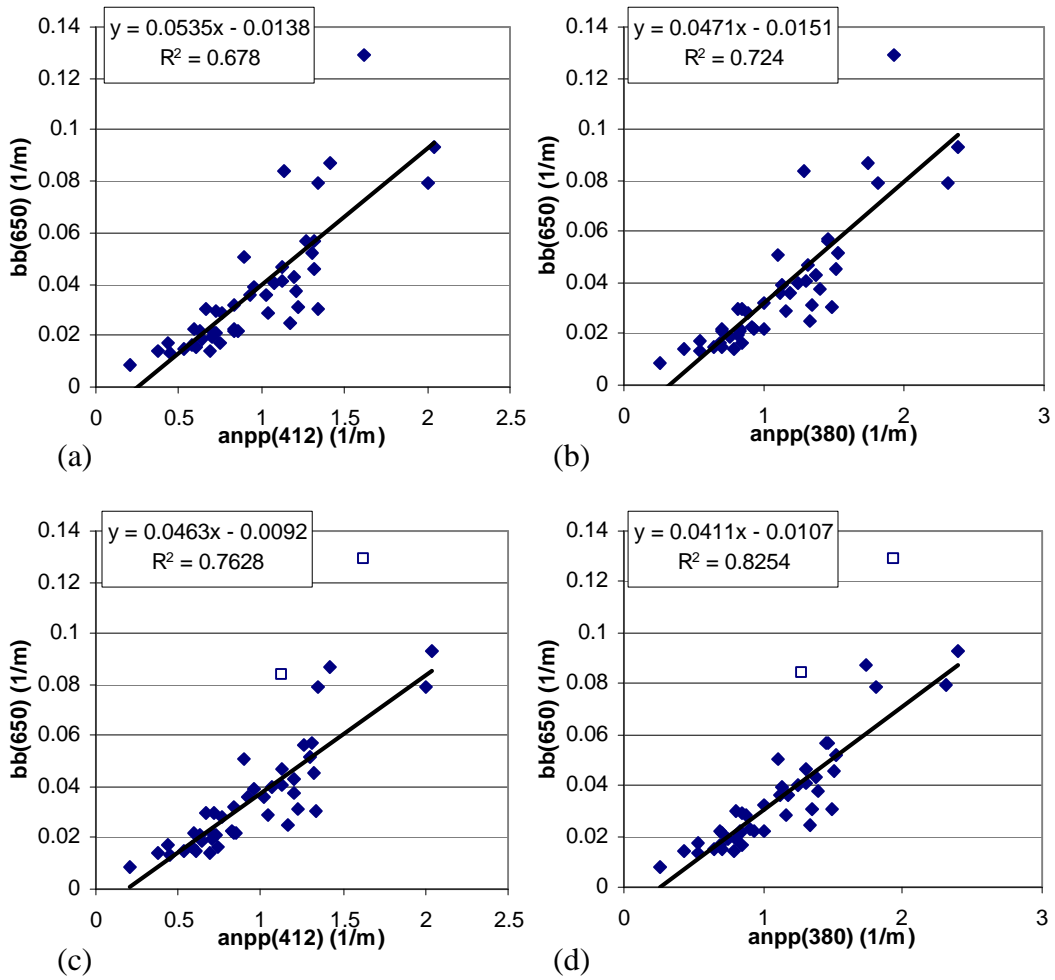


Figure 5.3-16: Relation between surface measurements of b_b at 650 nm and surface measurements of absorption by non-pigmented material at (a) 412 nm and (b) 380 nm. (c), (d): same as (a), (b) but two cases where not included in the linear least-squares fits.

The above relationships between $b_b(650)$ and $a_{npp}(412)$, $a_{npp}(380)$, could be used to relate $a_{npp}(\lambda)$ to the remote sensing reflectance at 670 nm, since strong correlation was found between $R_{rs}(670)$ and surface $b_b(650)$ ($R^2=0.88$). The relationships between in-situ $R_{rs}(670)$, $a_{npp}(412)$ and $a_{npp}(380)$, for the measurements performed in the Bay, are shown in figures 5.3-17(a), (b).

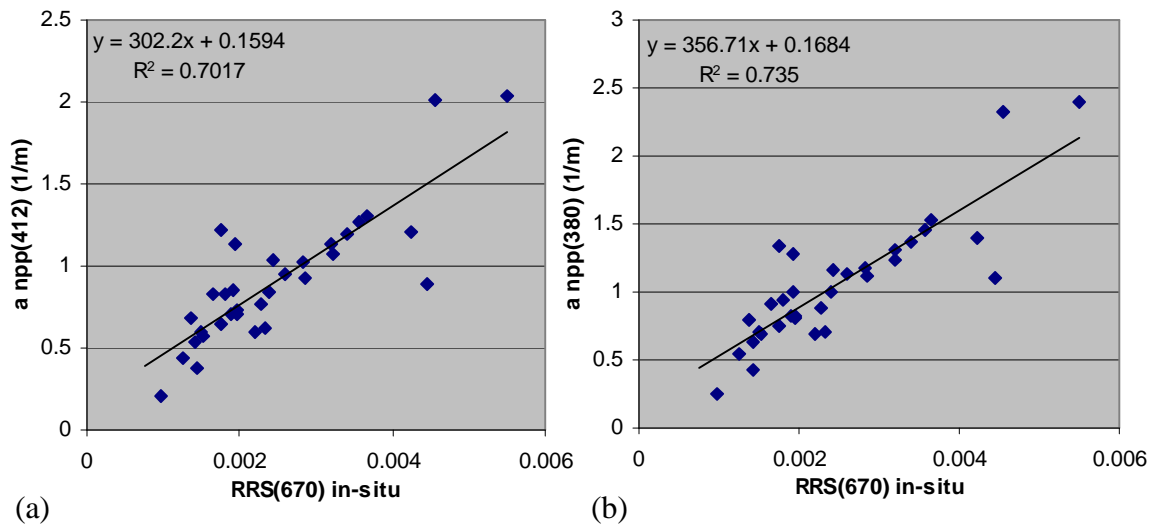


Figure 5.3-17: Relation between measured or model-estimated (based on measured IOPs) R_{rs} values at 670 nm and surface measurements of absorption by non-pigmented material at (a) 412 nm and (b) 380 nm

5.4 Discussion and Conclusions

5.4.1 In-situ Measurements of [Chl-a] in the Chesapeake Bay waters

The distribution of phytoplankton in coastal and estuarine waters, such as those of Chesapeake Bay, is characterized by high spatial and temporal variation. According to studies in the Chesapeake Bay (e.g. D'Elia et al., 1983, 1986; Harding et al., 1985, 1986; Malone et al., 1986, 1988, 1991, 1996; Marshall & Lacouture, 1986; Sellner & Kachur, 1987; Conley & Malone, 1992; Malone 1992; Harding et al., 1992, 1994, 1999; Harding, 1994; Glibert et al., 1995; Harding & Perry, 1997), the annual cycle of phytoplankton in the Bay typically includes a peak in the spring (April to mid May) that is dominated by diatom phytoplankton populations. The characteristics of the spring chlorophyll maximum (timing, position, magnitude of the peak) are highly variable and depend mainly on the amount of river flow, nutrient and light conditions in these waters. By late spring, concentrations of chlorophyll generally decline, due to grazing and nutrient limitation. A switch to summer flora rapidly ensues and flagellated forms replace the diatoms of the spring. Large concentrations of dinoflagellates ($50-100 \text{ mg m}^{-3}$) may occur during the early summer months. The high concentrations observed during these blooms can be very patchy and are often more prevalent on the western side of the Bay and in the mouths of certain tributaries. By the late summer and fall months, chlorophyll concentrations usually show a significant decrease, throughout the Bay (Harding, 1994).

Large seasonal variation was observed in chlorophyll concentrations measured in the northern Chesapeake Bay region during our 2001-2002 cruises (fig. 5.3-2). [Chl-a] values

ranged between 3.5 mg/m^3 (PI station, 13 November 2001) and 74 mg/m^3 (HB station, 11 June 2001). The frequency distribution of chlorophyll concentrations measured in-situ was shown to be lognormal (fig 5.3-1). Relatively clear waters, with low biological activity and low [Chl-a] values were observed at all four stations during the 2001 fall months and the 2002 spring (early May) cruises. Low rainfall amounts and low nutrient loadings, especially during the late fall months, may have contributed to the low chl-a concentrations measured. Fairly well mixed waters were observed during most of the cruises in the fall season, and [Chl-a] profiles were almost constant with depth (figure 5.3-4). Temperature and salinity profiles, as well as profiles of total absorption and attenuation in the water, also showed little variation with depth during these cruises (discussion in chapter 2). Estimations of average surface [Chl-a] within the first meter below the water's surface were not very different compared to surface [Chl-a] values estimated as the average within the first three meters.

Larger vertical stratification (as shown by vertical profiles of temperature and salinity) and higher nutrient and light availability during the late spring and summer months, resulted in more intense biological activity and favorable conditions for phytoplankton growth. Surface phytoplankton bloom events were observed during some of our spring and summer cruises in the Bay. Chl-a concentrations reached 60 mg/m^3 at JT station and 74 mg/m^3 at HB station, during the cruise on 11 June 2001. Chlorophyll concentrations higher than 20 mg m^{-3} were also observed at HB and JT stations during the following cruise on 25 June 2001. The phytoplankton absorption spectra measured on water samples collected during those cruises (fig. 5.3-3) showed high absorption in the UV

wavelengths (~325 nm) that could be attributed to the presence of MAAs, which provide a photoprotective mechanism against UV exposure in marine organisms. Large [Chl-a] values, $[Chl-a] > 25 \text{ mg/m}^3$, associated with surface phytoplankton bloom events, were again observed during the summer cruises in 2002 (18 and 28 June 2002). Studies on the characterization of phytoplankton species were not performed in the framework of this project, so there is not sufficient information to identify the specific species of phytoplankton during the observed bloom events in the Chesapeake Bay. The stronger vertical stratification observed during some of the cruises in summer, resulted in some variation of [Chl-a] with depth (e.g. cruises on 22 May 2002, 18 and 28 June 2002). One of the limitations of satellite observations (especially in optically thick, coastal regions) is that they are restricted to the upper layers of the water and cannot provide information on vertical distributions of [Chl-a], such as those measured in-situ during some of the summer cruises in the Bay.

Chlorophyll-a concentrations measured in the Bay during our cruises, were always larger than 3.5 mg m^{-3} . These [Chl-a] values were too large for validation of the semianalytical MODIS chlorophyll algorithm (Carder et al, 2002). This algorithm is considered to be the most suitable for use in case 2 waters, since it allows for estimation of phytoplankton absorption and chlorophyll concentration in the presence of other optically active substances in the water that may or may not covary with [Chl-a]. However, according to Carder et al (2002), for waters with high concentration of detritus, CDOM and chlorophyll, remote sensing reflectance values at 412 and 443 nm are small and the semianalytic algorithm cannot perform properly. As a result, the algorithm is

designed to return values only when modeled $a_{\text{phyt}}(675)$ is less than 0.03 m^{-1} , which is equivalent to [Chl-a] of about $1.5\text{-}2 \text{ mg m}^{-3}$. Therefore, the chlorophyll values measured in the Chesapeake Bay waters were used to study the performance of the empirical MODIS chlorophyll algorithms that directly relate Rrs values to chlorophyll concentrations, based on empirical relationships.

5.4.2 MODIS measurements of [Chl-a] and quality of MODIS nLw, Rrs values

As mentioned in the MODIS Data Quality Summary for the SeaWiFS compatible “chlor_a_2” chlorophyll product (Data Quality Summary, MOD21, Parameter 26, July 2001), the quality of all MODIS chlorophyll concentration products depends: i) on the quality of the input variables (MODIS measurements of nLw or Rrs) and ii) on the accuracy of the bio-optical algorithms used. The dependence of the MODIS [Chl-a] products on the quality of the MODIS nLw (or Rrs) values was shown in figure 5.3-7, where in-situ [Chl-a] measurements were compared to MODIS [Chl-a] estimations.

For all those cases with nLw(443) or nLw(488) flagged as negative values (almost 38% of the total 39 comparisons), no [Chl-a] values were estimated by MODIS. As was mentioned in chapter 4, the percentage of pixels with negative nLw values at 443 and 488 nm was 66% and 35% respectively, when all the 25 pixels around the location of each station were studied.

There were several cases, among those studied (almost 31 %), when large disagreement was observed between satellite and in-situ [Chl-a] values, with all three MODIS

algorithms significantly underestimating [Chl-a] (white squares in figure 5.3-7). As mentioned in the 'Results', percent differences between in-situ [Chl-a] and MODIS chlorophyll products, estimated as $100 \cdot ([\text{Chl-a}]_{\text{InSitu}} - [\text{Chl-a}]_{\text{MODIS}}) / [\text{Chl-a}]_{\text{InSitu}}$, were between 50 and 95%. Most of those days (e.g 11 June 2001, 21 September 2001, 6 June 2002) were characterized by high aerosol optical thickness in the atmosphere (table 4.3-1, chapter 4). Comparison between MODIS and in-situ nLw measurements for those days (e.g figures 4.3-2, 4.3-4, 4.3-11, 4.3-12), showed large disagreement, especially at the short wavelengths, probably due to failure of the satellite atmospheric correction algorithm under conditions of high aerosol optical thickness. The Rrs values measured by MODIS at the short 412, 443 nm wavelength bands were much larger compared to in-situ Rrs measurements or model estimations. The large satellite Rrs values measured at the blue wavelengths during those days were not consistent with the high absorption measured at the blue wavelengths, especially during the summer cruises in the Bay.

During the cruise on 11 June 2001, a large phytoplankton bloom was observed in the northern part of the Bay, with [Chl-a] values reaching 60 mg/m^3 at HB station and 74 mg/m^3 at JT (discussion in paragraph 5.4-1). Such high chlorophyll concentrations, combined with high absorption by CDOM and non-pigmented particulate matter in the blue wavelength region, would be expected to result in Rrs spectra with a maximum in the green wavelength region and not in the blue. The MODIS nLw values measured at PI station on 11 June 2001 (AOT(550)=1.2) are shown in fig. 5.4-1 along with the in-situ nLw measurements. The shape of Rrs spectra measured by MODIS at the satellite pixels around PI, with high Rrs values at 412 nm, low Rrs at 530 nm, increase of Rrs at 550 nm

and again decrease at 670 nm, is not physically expected for the optical properties measured in the Bay waters. The large $R_{rs}(443)$ and $R_{rs}(488)$ values measured by MODIS, due to errors in atmospheric correction under conditions of high aerosol optical thickness ($AOT(550)_{MTOPS}=1.2$), result in significantly overestimated remote sensing reflectance ratios, $R_{rs}(443)/R_{rs}(554)$ and $R_{rs}(488)/R_{rs}(554)$ by MODIS. According to equations (5.2-3), (5.2-5) and (5.2-6), such an overestimation of the ratios $R_{rs}(443)/R_{rs}(554)$ and $R_{rs}(488)/R_{rs}(554)$ by MODIS results in significantly underestimated satellite chlorophyll concentrations. Although chlorophyll concentration measured in-situ at PI station on 11 June 2001 was 27 mg m^{-3} , MODIS [Chl-a] values around PI station were less than 5 mg m^{-3} .

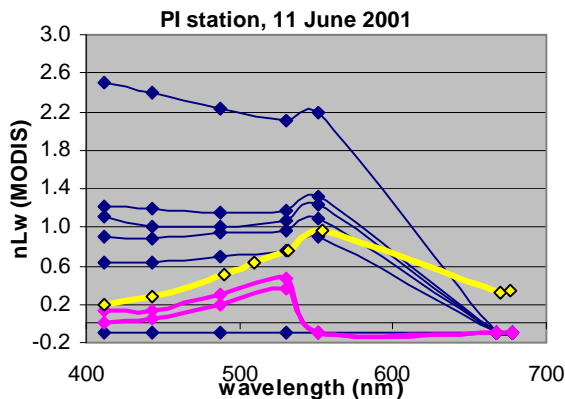


Figure 5.4-1: Satellite and in-situ nLw spectra for 11 June 2001 ($AOT(550) = 1.2$ at the time of the MODIS overpass). The in-situ nLw spectrum is shown as a thick yellow line. MODIS nLw spectra (5x5 pixels around each station) are shown as red lines for pixels of quality level 0, and blue lines for pixels of quality level 2 or 3. The quality of the MODIS nLw values is reduced ($nLw < 0$ at $\lambda > 550 \text{ nm}$) even at pixels of the best quality level (quality level=0) concerning the nLw values.

The comparison between MODIS and in-situ [Chl-a] measurements, for cases with almost clear atmospheric conditions and no negative MODIS nLw values at 443 and 488 nm (almost 31% of the cases studied here), was shown in figure 5.3-7 (blue pixels, also

shown in log-log scale in figures 5.3-7 (b), (d), (f)). According to the results, disagreement was observed between the in-situ [Chl-a] values and the “chlor_MODIS” product, with underestimated satellite [Chl-a] at the lower values and overestimated [Chl-a] at the larger values. Less scattering around the 1:1 line was observed for the “chlor_a_2” SeaWiFS analog, and especially the “chlor_a_3” product. However, there is still some disagreement between MODIS and in-situ [Chl-a] values, especially at larger chlorophyll concentrations (percent differences between in-situ [Chl-a] and MODIS ‘chlor_a_3’ were -500% to 30%, for [Chl-a]>10mg m⁻³). The main reason for this disagreement in the case of Chesapeake Bay waters, is that the remote sensing reflectances at 443 and 488 nm (wavelength bands used in the MODIS empirical chlorophyll algorithms) are affected not only by the phytoplankton optical properties, but also by the optical characteristics of other substances (such as CDOM and non-pigmented particulate matter), that do not necessarily covary with chlorophyll-a concentration. As was discussed in chapter 2, contribution by phytoplankton to total in-water absorption at 488 nm, ranges from 20 to 70 %, while contribution by non-pigmented particulate matter ranges from 15 to 60 % and contribution by CDOM ranges from 2 to 30%. The percent contribution by CDOM and non-pigmented particles increases at 412 nm, mainly due to the exponential increase of their absorption with decreasing wavelength.

5.4.3 Relationships between [Chl-a] and Rrs in the Chesapeake Bay waters

When the MODIS chl-a algorithms (HLPC-empirical, SeaWiFS-analog and semianalytic) are applied to the Chesapeake Bay waters, chl-a concentration is determined through empirical relationships that use the MODIS derived remote sensing

reflectance ratio $R_{rs}(488)/R_{rs}(554)$, for “chlor_a_3” and “chlor_a_2” products, and both ratios $R_{rs}(443)/R_{rs}(554)$ and $R_{rs}(488)/R_{rs}(554)$, for “chlor_MODIS” product. Although significant relationships were found between in-situ measured $\log_{10}[\text{Chl-a}]$ and $\log_{10}(R_{rs}(\lambda_i)/R_{rs}(554))$ for $\lambda_i = 443, 488, 670$ and 677 nm (P-value in linear regression was small, $P < 0.05$), the coefficients of determination (R^2 values) in the linear regression $\log_{10}(R_{rs}(\lambda_i)/R_{rs}(554))$ versus $\log_{10}[\text{Chl-a}]$ were small for $\lambda_i = 443, 488$ nm ($R^2 = 0.4$ and $R^2 = 0.31$ respectively). When a cubic regression was applied to the log transformed $[\text{Chl-a}]$ and R_{rs} values (similarly to the methodology used to derive the MODIS empirical algorithms “chlor_a_2” and “chlor_a_3”) a coefficient of determination $R^2=0.4$ was obtained (fig. 5.3-10). When interpreting the results of the comparisons, one should keep in mind the errors associated with the measurements (both laboratory measurements of $[\text{Chl-a}]$ and in-situ measurements of radiometric quantities) as well as the uncertainties in the model estimated R_{rs} values (due to errors in the measured input parameters and the assumptions in the model estimations). However, based on the optical properties measured in the Bay, it could be expected that $[\text{Chl-a}]$ and R_{rs} at the blue-green wavelengths are not strongly correlated for these specific case-2 waters. This is mainly due to the fact that although one of the chl-a absorption maxima is in the 443 nm wavelength region (“Soret” band), the optical characteristics of CDOM and non-pigmented particulate matter strongly interfere with the chl-a optical properties at the short wavelengths, significantly affecting the amount of light leaving the water surface.

Concentrations of CDOM and non-algal particulates (detrital material and minerals) do not necessarily covary with phytoplankton amount or concentration of chl-a pigment in estuarine and coastal waters. Measurements of $a_{\text{pp}}(440)$ and $a_{\text{CDOM}}(440)$ showed large

variation in the Bay waters during our cruises. However, no strong covariation was found between absorption by phytoplankton and absorption by non-pigmented material or CDOM (discussion in chapter 2). Since absorption by CDOM and non-pigmented particles increases exponentially with decreasing wavelength, the role of these substances in the attenuation of light becomes increasingly significant at the shorter wavelengths of the visible spectrum. According to measurements performed at PI station on 6 June 2002, contribution by phytoplankton to $a_{t-w}(488)$ was 42%, contribution by non-pigmented particles was 46%, while CDOM contribution was 12%. At 443 nm, the contribution by phytoplankton to $a_{t-w}(443)$ was 36%, contribution by non-pigmented particles was 45%, while CDOM contribution was 19%.

A stronger relationship (based on the values of the correlation coefficient, R^2) was observed between the ratio $R_{rs}(677)/R_{rs}(554)$ and [Chl-a], with $R^2=0.57$ (figure 5.3-9). Chl-a absorption spectra are characterized by a second absorption maximum in the 676 nm wavelength region. At these wavelengths absorption by CDOM is usually very small and absorption by non-pigmented particles, although not negligible, is significantly lower than absorption by phytoplankton (less than 15% contribution to total-minus-water absorption). Therefore, most of the total in-water absorption (minus the absorption by pure water) in the 676 nm wavelength region is due to the presence of phytoplankton (larger than 80% contribution by phytoplankton in most of the cases). However, significant absorption at 676 nm is due to the pure-water itself, with $a_w(676)=0.45 \text{ m}^{-1}$ (Pope and Fry, 1997).

The relationship between $Rrs(677)/Rrs(554)$ and [Chl-a] is examined in the following paragraphs, using some relationships between the backscattering and absorption coefficients observed in the Chesapeake Bay waters. An approximate form of the relationship (5.1-1) for the remote sensing reflectance ratio at 554 and 677 nm, is:

$$\frac{RRS(677)}{RRS(554)} = \frac{b_b(677)}{b_b(554)} \cdot \frac{a(554)}{a(677)} = \frac{b_b(677)}{b_b(554)} \cdot \frac{a_w(554) + a_{t-w}(554)}{a_w(677) + a_{t-w}(677)} \quad (5.4-1)$$

which is based on the assumptions that i) $t_{(a,w)}t_{(w,a)}/n^2$ is almost equal to 0.54, ii) f/Q is independent of wavelength and iii) $b_b \ll a$. The semianalytic MODIS chl-algorithm is based on the above simplified version of relationship (5.1-1). However, eq(5.4-1) should be used only as an approximation, since i) total backscattering in Chesapeake Bay waters is typically smaller than total absorption, but not negligible compared to absorption (especially at 550 nm, where absorption is relatively small $a_{t-w}(550)_{avg} = 0.29 \text{ m}^{-1}$

(stdev=0.2 m^{-1}) and $b_b(550) = 0.05 \text{ m}^{-1}$ (stdev=0.03 m^{-1})) and ii) the ratio $\frac{f}{Q(I)} \cdot \frac{t_{(w,a)}t_{(a,w)}}{n_w^2}$

is not constant, but varies with wavelength, solar zenith angle, [Chl-a] (Morel and Mueller, 2002).

Figure 5.4-2 shows the relationship between [Chl-a] measurements and total-minus-water absorption at 676 nm, $a_{t-w}(676)$ (measured using the AC9 instrument).

Measurements of absorption and [Chl-a] were performed on the same water samples collected from the four stations in the northern part of Chesapeake Bay. The chlorophyll-specific phytoplankton absorption, $a^*_{\text{phyt}}(676) = a_{\text{phyt}}(676) / [\text{Chl-a}]$, depends on various parameters such as phytoplankton species composition, phytoplankton cells' physiology and size (effect of packaging and self-shading on light absorption) and is influenced by

light conditions (related to season and cloudiness) as well as nutrient availability (influenced by riverine discharges, proximity to land, mixing processes). Therefore, some variation in estimations of $a_{\text{phyt}}^*(676)$ is expected, among the measurements performed during the 2001- 2002 cruises. Nevertheless, $a_{\text{t-w}}(676)$ showed a good correlation with [Chl-a] and least squares regression gave:

$$a_{\text{t-w}}(676) = 0.0166 \cdot [\text{Chl-a}] + 0.0603, R^2 = 0.9147 \quad (5.4-2)$$

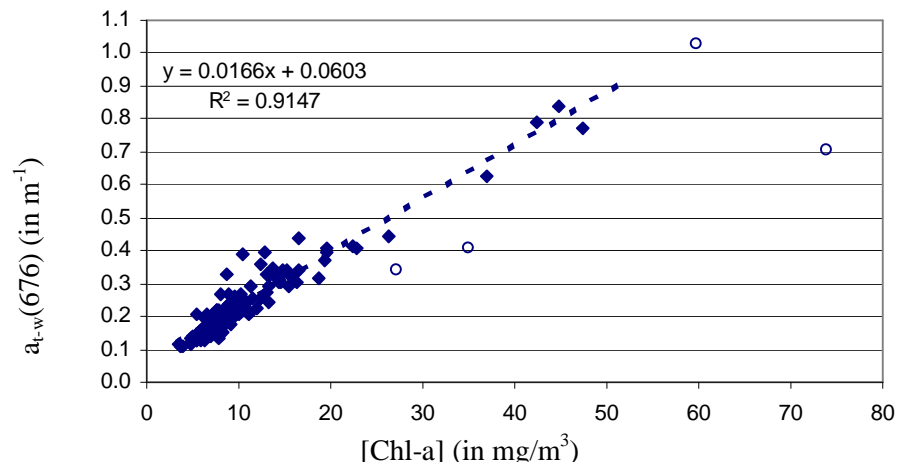


Figure 5.4-2: Relationship between [Chl-a] and $a_{\text{t-w}}(676)$. Measurements were performed on water samples collected from PI, HB, TI and JT. Measurements performed on 11 June 2001 (large phytoplankton bloom) are shown as open circles.

The constant 0.06 in eq. (5.4-2) could be due to the small, but non-zero absorption by CDOM and non-pigmented particulate matter at 676 nm. Measurements performed on 11 June 2001 (shown as open circles in figure 5.4-2) were not included in the least-square regression, since specific absorption coefficients were found to be much lower at HB, PI and TI stations during this cruise, when a large phytoplankton bloom was observed (measurements of $a_{\text{t-w}}(676)$ and [Chl-a] performed on 11 June 2001 at HB, PI and TI stations fall below the regression line obtained from measurements performed during the rest of the cruises in the Bay).

The relationship between $b_b(530)$ and $b_b(650)$ measured during the cruises in Chesapeake Bay, using the ECOVSF instrument, is shown in figure 5.4-3(a). Linear least

square regression gave: $\frac{b_b(650)}{b_b(530)} = 0.7431$, with $R^2 = 0.9929$. Expressing the b_b

wavelength dependence between 650 and 530 nm as $b_b \sim \lambda^{-n}$, results in $n=1.45$ for our measurements in the Bay. Since measurements of backscattering at 677 nm are not available and since there is not enough literature on the wavelength dependence of b_b in this type of waters, the same wavelength dependence was assumed for $b_b(677)/b_b(554)$. However, the remote sensing reflectance at 677 nm is additionally affected by the chl-a fluorescence signal, which is related to chl-a absorption and, consequently chl-a concentration. When chl-a is excited by light in the visible wavelengths, it fluoresces in the wavelength region around 685 nm. Therefore, the amount of radiance that leaves the water surface, within the wavelength region around 685 nm (and thus at 677 nm), is significantly increased due to the chl-a fluorescence.

The relationship between $a_{t-w}(554)$ and $a_{t-w}(677)$ is shown in figure 5.4-3(b) for measurements performed using the AC9 instrument (for the specific days when laboratory measurements of [Chl-a] and in-situ or model-estimated R_{rs} values were available). Although contribution by CDOM and non-pigmented particulate matter to the total absorption at 550 nm is larger than at 677 nm, an approximate relationship can be derived between $a_{t-w}(554)$ and $a_{t-w}(677)$ based on the AC9 measurements (fig. 5.4-3(b)). A similar relationship between $a_{t-w}(677)$ and $a_{t-w}(554)$ (with $R^2 = 0.85$) was also observed when looking at the laboratory spectrophotometric absorption measurements ($a_{t-w}(\lambda) = a_{CDOM}(\lambda) + a_{phyt}(\lambda) + a_{npp}(\lambda)$).

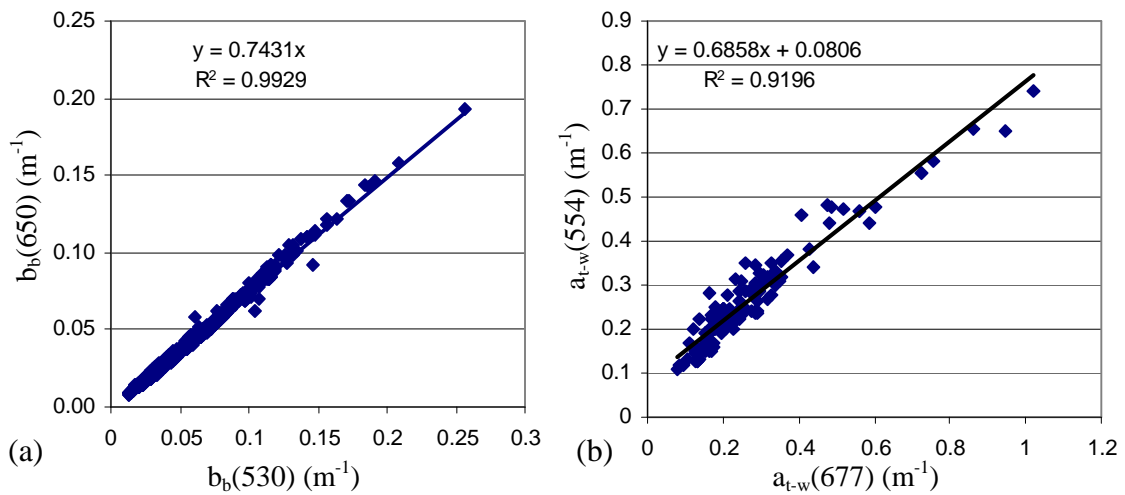


Figure 5.4-3: (a) Relationship between $b_b(530)$ and $b_b(650)$ from measurements performed in Chesapeake Bay, using the ECOVSF instrument (measurements performed at all depths and during all cruises are included here) (b) Relationship between $a_{t-w}(554)$ and $a_{t-w}(677)$ from measurements performed using the AC9 instrument.

Figure 5.4-4 shows the relationship expected between [Chl-a] and the remote sensing reflectance ratio $R_{rs}(677)/R_{rs}(554)$, based on the approximate relationship (5.4-3) and the relationships found between i) $b_b(650)$ and $b_b(530)$, ii) $a_{t-w}(554)$ and $a_{t-w}(676)$, iii) $a_{t-w}(676)$ and [Chl-a], for the Chesapeake Bay waters, without accounting, however, for the effect of chl-a fluorescence (figure 5.4-4, solid line). The measured [Chl-a] and $R_{rs}(677)/R_{rs}(554)$ are also shown (blue pixels, with the logarithmic best fit shown as thick solid line). According to the Hydrolight sensitivity studies discussed in chapter 2, not-including the effect of chl-a fluorescence in the model estimations of the remote sensing reflectance at 676 nm, resulted in an underestimation of $R_{rs}(677)$ by as much as 40%, for the specific case studied (28 September 2001). Although this percentage is not expected to be the same for all the cases studied here, increase of $R_{rs}(677)$ by 30-50% (two dotted lines in figure 5.4-4) results to a relationship between $R_{rs}(677)/R_{rs}(554)$ and

[Chl-a] that is in much better agreement with the relationship between measured $Rrs(677)/Rrs(554)$ and [Chl-a].

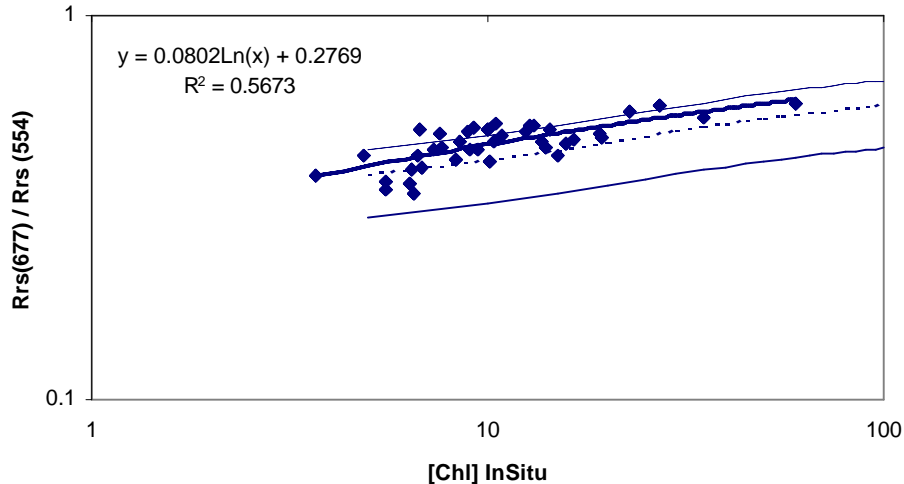


Figure 5.4-4: Approximate relationship between $Rrs(677)/Rrs(554)$ and [Chl-a], estimated based on eq (5.4-4) and in-situ measurements of backscattering and absorption, without accounting for the effect of chl-a fluorescence (blue solid line) and assuming an increase of $Rrs(677)$ by 30 and 50% (dotted lines) (the effect of chl-a fluorescence for measurements performed at PI station on 28 September 2001 was ~40% increase in $Rrs(677)$). The measured [Chl-a] and $Rrs(677)/Rrs(554)$ are also shown (blue pixels, with the logarithmic best fit shown as thick line).

The accuracy of an algorithm that is using $Rrs(677)/Rrs(554)$ to estimate [Chl-a] depends, as was discussed earlier, on the accuracy of the input nLw or Rrs ratio values. When the empirical relationship that was found between the in-situ measurements of [Chl-a] and $Rrs(677)/Rrs(554)$, was used to estimate [Chl-a] using as input the MODIS $Rrs(677)$ and $Rrs(554)$ values (measured at the ‘best’ satellite pixel), the estimated [Chl-a] values were not in good agreement with the measured [Chl-a] values. This was mainly due to the large disagreement observed in almost all of the cases between the remote sensing reflectance ratios $Rrs(677)/Rrs(554)_{MODIS}$ and $Rrs(677)/Rrs(554)_{InSitu}$. As was discussed in chapter 4, the MODIS $Rrs(677)$ and $Rrs(554)$ values showed good correlation to the in-situ Rrs values at the same wavelengths for the ‘best’ MODIS pixel

(correlation coefficients, R, larger than 0.83). The ratio $Rrs(677)/Rrs(554)_{MODIS}$, however, was not in good agreement with the ratio $Rrs(677)/Rrs(554)_{InSitu}$ (fig 5.4-5). This is, mainly, because: i) $nLw(677)_{MODIS}$ values were underestimated compared to $nLw(677)_{InSitu}$ more than $nLw(554)_{MODIS}$ values were underestimated compared to $nLw(554)_{InSitu}$ (fig. 5.4-5 (a), (b)) and ii) percent differences between MODIS and in-situ nLw measurements did not show strong covariation at 677 and 554 nm wavelengths. Therefore, the percent differences between MODIS and in-situ Rrs ratios, at these wavelengths, are large, and they would result in large differences between measured and estimated [Chl-a] values.

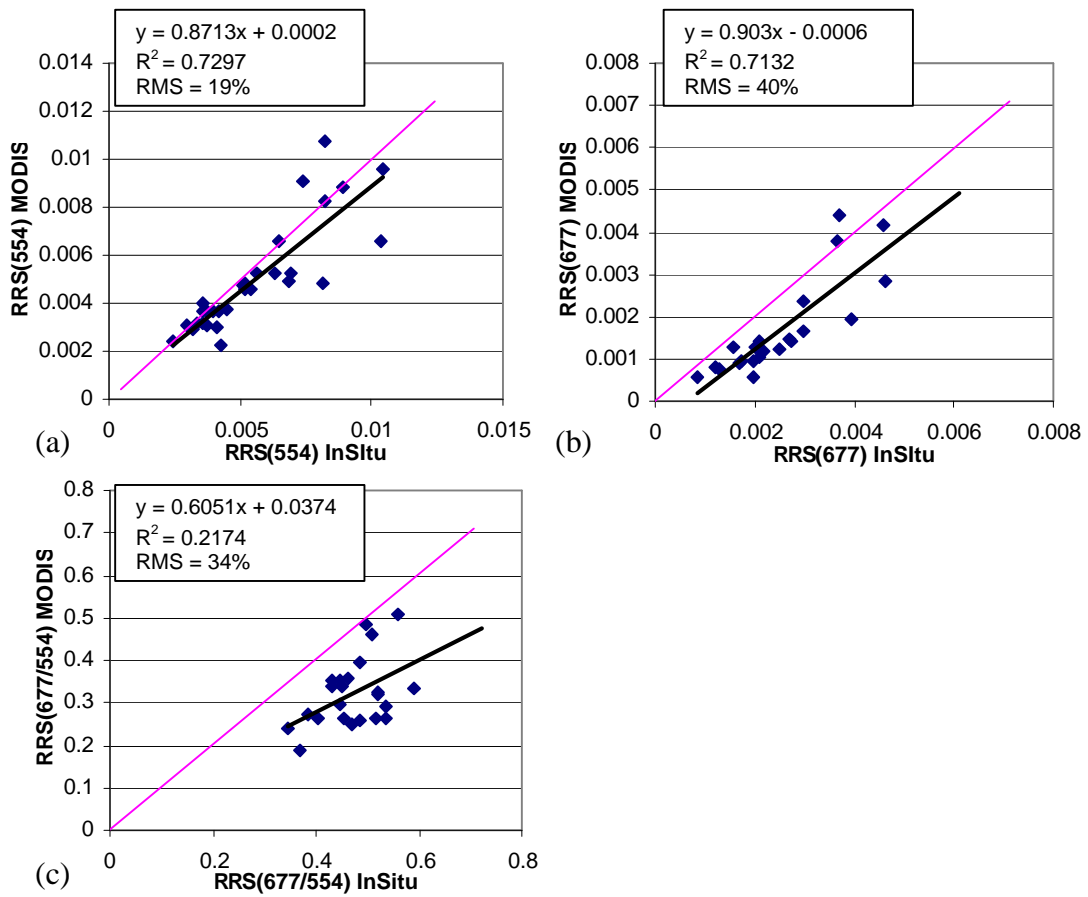


Figure 5.4-5: Comparison between MODIS and in-situ measurements of Rrs (a) at 554 nm and (b) 677 nm. (c) Comparison between the MODIS and in-situ Rrs ratios at 677 and 554 nm, $Rrs(677)/Rrs(554)$.

5.4.4 Rrs and total absorption and backscattering in the Chesapeake Bay waters

Since backscattering for the Chesapeake Bay waters is not negligible compared to absorption, the relationship between $Rrs(\lambda)$ and $\frac{b_b(I)}{a(I)+b_b(I)}$ was examined at (a) 443 nm (b_b measured at 450 nm), (b) 532 nm (b_b measured at 530 nm) and (c) 670 nm (b_b measured at 650 nm) (fig. 5.3-11).

Very good relationship was found between $\frac{b_b(I)}{a(I)+b_b(I)}$ and both in-situ measurements of Rrs and Hydrolight-estimated Rrs values (fig. 5.3-11, yellow pixels for measured Rrs and blue pixels for model-estimated Rrs) with R^2 values larger than 0.9 for all cases (all wavelengths and both in-situ and model estimated Rrs). The intercept coefficients of the linear least squares regression fits were small (< 0.0004) and the slope coefficients were in all cases within the range 0.043 – 0.057. The slope coefficient in the linear least-

squares regression lines, corresponds to the ratio $\frac{f}{Q(I)} \cdot \frac{t_{(w,a)}t_{(a,w)}}{n_w^2}$ in the relation

$$Rrs(I) = \frac{f}{Q(I)} \cdot \frac{t_{(w,a)}t_{(a,w)}}{n_w^2} \cdot \frac{b_b(I)}{a(I)+b_b(I)} \text{ (eq.5.1-1).}$$

Taking into account that f/Q (in eq. 5.1-1) varies within 0.08-0.15 (Morel and Mueller, 2002) and that $t_{(a,w)}t_{(w,a)}/n^2$ is approximately equal to 0.54 (Mobley, 1994), the slope of a linear least-squares fit on

Rrs vs $\frac{b_b(I)}{a(I)+b_b(I)}$ would be expected to be within the range 0.042 and 0.081. It should be

noted that in Morel and Mueller (2002) only vertically homogeneous, case 1 waters have been considered. According to Morel and Mueller (2002), for nadir-viewing measurements of Rrs (as was the case for our in-situ measurements) f/Q varies between

0.08 and 0.11 (their figure 13.10) and depends on [Chl-a], wavelength and solar zenith angle. Therefore, for nadir-viewing geometry, the ratio $\frac{f}{Q(I)} \cdot \frac{t_{(w,a)} t_{(a,w)}}{n_w^2}$ would be expected to vary between 0.042 and 0.059. These values are close to the slope coefficients in the linear least-squares regression lines shown in figure 5.3-11.

The good agreement between measurements and quantities theoretically estimated based on equation (5.1-1) and Hydrolight simulations, demonstrates closure between the apparent and inherent optical properties measured in the Bay (chapter 3).

5.4.5 Backscattering and Remote Sensing Reflectance in Chesapeake Bay

Both measured and Hydrolight estimated $R_{rs}(670)$ values were found to be strongly related to backscattering values at 650 nm, with coefficient of determination of the linear least-squares regression, $R^2=0.88$ (fig 5.3-12(c)). This could be explained if one takes into account that, in the relation $R_{rs}(670) \sim \frac{b_b(670)}{a(670)+b_b(670)}$, total absorption at 670 nm is largely due to pure water itself. Absorption by pure water at 670 nm is constant and equal to 0.44 m^{-1} (Pope and Fry pure water absorption coefficients). Therefore, changes in $a_{t-w}(670)$ by an order of magnitude ($0.1-1 \text{ m}^{-1}$) are masked by the large, constant absorption by pure water and correspond to changes in the total absorption $a_t(670)$ by a factor of 3. The surface backscattering values, $b_b(650)$, measured in Chesapeake Bay during the specific cruises, were between 0.008 and 0.12 m^{-1} (some b_b values are not shown in figure 5.3-12, because for some cases R_{rs} values were not available) and

therefore changes in b_b by an order of magnitude could result in significant changes in $R_{rs}(670)$. Absorption by pure water, however, is considerably smaller at lower wavelengths. Therefore R_{rs} at 443 and 530 nm will be affected equally by changes in both absorption and backscattering. Although MODIS generally underestimated R_{rs} at 670 nm (fig. 5.3-13 (a)), a good correlation was found between the MODIS measured $R_{rs}(670)$ and backscattering at 650 nm (fig. 5.3-13 (b)), with MODIS $R_{rs}(670)$ increasing with increasing $b_b(650)$. The R^2 of the linear least squares regression was 0.5. However, fewer measurements were available when comparing b_b to the satellite data, mainly because of bad quality satellite data during some of the cruises (e.g. 40% of the pixels had negative $nLw(670)$ values, for the cases studied).

The strong relationship between $R_{rs}(670)$, a quantity that can be measured remotely by an aircraft or a satellite, and $b_b(650)$ in the Chesapeake Bay waters, is important, since b_b is an optical property characteristic of the particulate matter present in these waters. According to previous studies (Stramski and Kiefer, 1991) the major source of particulate backscattering in the water is small, non-living particles, which may include decaying biogenous products of organic and inorganic nature, extract of organisms, as well as terrigenous material such as minerals and organic debris. The relationship between surface total b_b and absorption by non-pigmented particulate matter was examined for the measurements performed in the Chesapeake Bay (fig. 5.3-15, 5.3-16). The surface total b_b measurements at all three wavelengths (only 530 and 650 nm shown in fig. 5.3-15, 5.3-16) were found to be strongly correlated to the surface values of absorption by non-pigmented particulate matter, a_{npp} , especially at the short wavelengths 412 nm or 380 nm,

where absorption by non-pigmented particles is stronger. The R^2 values were $R^2 = 0.76$ and $R^2 = 0.83$ (for 412 and 380 nm respectively), when 2 points (out of the total 45) were not included in the regression. The relationship between b_b and [Chl-a] showed more scattering, especially at large chlorophyll concentrations (fig. 5.3-14), and smaller correlation coefficient, $R^2=0.6$. These results indicate that re-suspended sediments and detrital material of organic and inorganic nature seem to be responsible for most of the backscattering in the Chesapeake Bay waters.

The relationships between $Rrs(670)$, $b_b(650)$ and $a_{npp}(412)$ could potentially be used in remote estimations of the abundance of non-pigmented particulate matter in the water. Strong correlation was found between in-situ $Rrs(670)$ and absorption by non-pigmented particulate matter for the measurements performed in the Bay during our 2001-2002 cruises (R^2 values of 0.7 and 0.74 for the linear least-squares regression between $Rrs(670)$ and $a_{npp}(412)$ and between $Rrs(670)$ and $a_{npp}(380)$ respectively) (figure 5.3-17). In the MODIS semianalytic algorithm (Carder et al, 2002) non-pigmented particles and CDOM are combined to one term (gelbstoff) owing to the similarity in the absorption spectral shapes of these substances and the difficulties associated with separating their contribution to total light absorption. Relationships such as those between $Rrs(670)$, $b_b(650)$ and $a_{npp}(412)$ which are based on the backscattering properties of the non-pigmented particles could be used to separately estimate contribution by non-pigmented particles to total light attenuation.

Table 5.4-1:Chapter 5 – Conclusions and Significant points

-Chlorophyll-a concentrations measured in the Bay during our cruises, ranged between 3.5-74 mgm⁻³. These [Chl-a] values were too large for validation of the semianalytical MODIS chlorophyll algorithm (Carder et al, 2002). This algorithm is considered to be the most suitable for use in case 2 waters. However, according to Carder et al (2002), for waters with high concentration of detritus, CDOM and chlorophyll (such as the waters in Chesapeake Bay), Rrs values at 412 and 443 nm are small, the semianalytic algorithm cannot perform properly and it switches to an empirical algorithm that relates Rrs directly to [Chl-a]. For [Chl-a]>2 mg m⁻³ (always the case during our cruises in the Bay) estimations of [Chl-a] by MODIS ('chlor_a_3', 'chlor_a_2' and 'chlor_MODIS' products) are based on empirical relationships between [Chl-a] and Rrs(443)/ Rrs(551) or/and Rrs(488)/ Rrs(551).

- The quality of all MODIS chlorophyll concentration products depends on the accuracy of the satellite bio-optical algorithms and on the quality of the input variables (MODIS measurements of nLw or Rrs). i) For all cases with nLw(443) or nLw(488) flagged as negative values (38% of the total 39 comparisons), no [Chl-a] values were estimated by MODIS. ii) Under conditions of high aerosol optical thickness all three MODIS chl-algorithms significantly underestimated [Chl-a], due to overestimations of the MODIS nLw values in the blue wavelengths. Percent differences were between 50% and 95%. iii) For cases with almost clear atmospheric conditions and no negative MODIS nLw values at 443 and 488 nm, MODIS chlorophyll products (especially chlor_a_3), showed better agreement with in-situ [Chl-a] values, especially for low [Chl-a] (percent differences: -20% to 2%, for [Chl-a]<10mg m⁻³). However, large disagreement was observed at larger chlorophyll concentrations. The main reason for this disagreement in the Chesapeake Bay waters, is that the remote sensing reflectances at 443 and 488 nm (wavelength bands used in the MODIS empirical chlorophyll algorithms) are affected not only by the phytoplankton optical properties, but also by the optical characteristics of other substances (such as CDOM and non-pigmented particulate mater), that do not necessarily covary with chlorophyll-a concentration.

- When the relationships between in-situ [Chl-a] and Rrs(λ_i)/ Rrs(554) values were examined for $\lambda_i = 443, 488$, estimated correlation coefficients were small. A stronger relationship was observed between the ratio Rrs(677)/ Rrs(554) and [Chl-a] for the Bay waters. In the 676 nm wavelength region, absorption by CDOM is usually very small, absorption by non-pigmented particles is significantly lower than absorption by phytoplankton and most of the total in-water absorption (minus the absorption by pure water) is due to the presence of phytoplankton (contribution by phytoplankton to $a_{t-w}(676)$ larger than 80%). Therefore, an algorithm that is based on the relationship between Rrs(677)/ Rrs(554) and [Chl-a] could be used for [Chl-a] estimations in the Chesapeake Bay waters.

- The accuracy of a chl-algorithm that is based on the relationship between Rrs(677)/ Rrs(554) and [Chl-a], depends on the accuracy of the input Rrs ratio values. When MODIS Rrs values were used as input information to estimate [Chl-a] in the Bay using the relationship found between in-situ measurements of [Chl-a] and Rrs(677)/ Rrs(554), large disagreement between measured and estimated [Chl-a] values was observed. This was, mainly, because percent differences between MODIS and in-situ Rrs measurements did not show strong covariation at 677 and 554 nm wavelengths. Therefore, large disagreement was observed, in almost all of the cases, between the ratios Rrs(677)/ Rrs (554)_{MODIS} and Rrs (677)/ Rrs (554)_{InSitu}, which, as expected, resulted in large errors in the estimated [Chl-a] values.

- Strong relationship was found between $\frac{b_b(I)}{a(I)+b_b(I)}$ and Rrs values (both measured and Hydrolight-estimated) in the Bay waters (R^2 values larger than 0.9 for all cases). The slope coefficients in the

linear least-squares regression lines (that correspond to the ratio $\frac{f}{Q(I)} \cdot \frac{t_{(w,a)}t_{(a,w)}}{n_w^2}$ in eq. 5.1-1) were

Table 5.4-1 (continued):

in all cases within the range 0.043 – 0.057. Since $t_{(w,a)}t_{(a,w)}/n_w^2$ is approximately 0.54 (Mobley, 1994), these results show that the ratio f/Q during our measurements was within the range 0.08-0.105, which is in good agreement with the f/Q values theoretically expected (~ 0.08-0.11) for measurements performed at nadir-viewing geometry. In agreement to the discussion in chapter 3, these results demonstrate closure between the apparent and inherent optical properties measured in the Bay.

- Both measured and Hydrolight estimated $R_{rs}(670)$ values were found to be strongly related to backscattering values at 650 nm ($R^2=0.88$). Although MODIS generally underestimated R_{rs} at 670 nm a good correlation was also found between backscattering at 650 nm and MODIS measurements of $R_{rs}(670)$.

- The strong relationship between $R_{rs}(670)$, a quantity that can be measured remotely by an aircraft or a satellite, and $b_b(650)$ in the Chesapeake Bay waters, is very important, since b_b is an optical property characteristic of the particulate matter present in these waters. Surface values of b_b were strongly related to surface values of a_{npp} especially at 412 and 380 nm, where absorption by non-pigmented particles is strong ($R^2 = 0.76$ and $R^2 = 0.83$, for 412 and 380 nm respectively). The relationship between b_b and [Chl-a] showed more scattering, especially at large chlorophyll concentrations, and smaller correlation coefficient ($R^2=0.6$). These results indicate that re-suspended sediments and detrital material of organic and inorganic nature seem to be responsible for most of the backscattering in the Chesapeake Bay waters.

- The relationships between $R_{rs}(670)$, $b_b(650)$ and $a_{npp}(412)$ could potentially be used in remote estimations of the abundance of non-pigmented particulate matter in the water. Strong relationships were found between $R_{rs}(670)$ and $a_{npp}(412)$ and between $R_{rs}(670)$ and $a_{npp}(380)$ measured in the northern Chesapeake Bay. In the MODIS semianalytic algorithm (Carder et al, 2002) non-pigmented particles and CDOM are combined in one term (gelbstoff) owing to the similarity in the absorption spectral shapes of these substances and the difficulties associated with separating their contribution to total light absorption. Relationships such as those between $R_{rs}(670)$, $b_b(650)$ and $a_{npp}(412)$, which are based on the backscattering properties of the non-pigmented particles, could be used to separately estimate contribution by non-pigmented particles to total light attenuation in turbid waters.

CHAPTER 6

Summary and Conclusions

Coastal and estuarine regions, such as the Chesapeake Bay, are complex and dynamic environments, where terrestrial, oceanic, atmospheric and human inputs of energy and matter converge. Since the water optical characteristics are strongly related to biological, chemical and physical processes in the water, in-situ measurements of water optical properties and theoretical estimations of underwater light fields play a critical role in our efforts to determine changes in the composition and concentration of optically active substances in coastal regions, monitor the water quality and identify the underlying causes (human activities or natural processes) of any changes in the water characteristics. At the same time, by using appropriate bio-optical models, remote sensing observations of ocean color can uniquely provide a synoptic, spatially and temporally cohesive picture of the distribution and abundance of dissolved and particulate material in the surface coastal waters. This information can be used to investigate biological productivity in the oceans, and study the interaction between physical processes (e.g. currents) and ocean biology as well as the effects of human activities on the oceanic environment.

However, the large variety of physical, chemical and biological phenomena along the coastal regions poses great difficulties for systematic scientific studies. The presence of quite shallow areas, high turbidity and re-suspended sediments in the water, the proximity to landmass, and the large concentrations of highly absorbing aerosols in the atmosphere, greatly complicate satellite estimations of underwater properties. A major obstacle to the remote observations of coastal chlorophyll concentrations or distribution of other

optically active substances has been the lack of precise information concerning the optical properties of inland, estuarine and coastal waters. While bio-optical models currently used in satellite algorithms adequately describe the optical properties of open-ocean waters, where phytoplankton and covarying material are the major optical component, they are not necessarily applicable in the coastal zones, where bio-optical characteristics depend on the composition, distribution and concentration of various living and non-living, dissolved and particulate material of marine or terrestrial origin. The core subject of this thesis was the development of coordinated atmospheric, in-water, and laboratory measurements leading to characterization of in-water optical properties in the northern Chesapeake Bay case-2 waters. One of the main objectives was obtaining a sufficiently complete suite of measurements, combined with detailed radiative transfer calculations, so as to produce a closure experiment for the underwater inherent and apparent optical properties. The in-situ results were applied to the interpretation of satellite (MODIS) water leaving radiance data and their validation.

Specific questions addressed in the framework of this thesis were:

- i) What are the optical characteristics of phytoplankton, CDOM and non-pigmented particulate matter in the Chesapeake Bay waters? How do these optical characteristics affect the penetration of light and especially the water-leaving radiance, since this is the quantity measured remotely by a satellite sensor or an airborne instrument?
- ii) What is the contribution of phytoplankton, CDOM and non-pigmented particulate matter to the total light attenuation in the Chesapeake Bay waters?
- iii) To what extent can we obtain “closure” between measured inherent and apparent

optical properties based on theoretical estimations of radiation fields in this optically complex, estuarine environment? How accurately can we predict the underwater radiation fields and can we use the model estimations when underwater radiances are not measured, but detailed information on the water's optical characteristics is available? What are the measured input parameters to the model, that most significantly affect the model estimations of radiation fields, and what changes in the model assumptions can improve the agreement with measurements?

iv) What is the interpretation of satellite (MODIS) remote sensing reflectance data in the case-2 Chesapeake Bay waters? How do atmospheric conditions, satellite zenith angle, proximity to land, affect the quality and accuracy of satellite observations?

v) How do errors and inaccuracies in satellite R_{rs} measurements (due, for example, to errors in atmospheric correction) affect the derived satellite products of chlorophyll concentration?

vi) Are the bio-optical models or empirical relationships currently used in MODIS satellite chlorophyll algorithms applicable to the Chesapeake Bay waters?

vii) What are the relationships between remote sensing reflectances and water's inherent optical properties (such as chlorophyll concentration and total backscattering) that could be used in the Chesapeake Bay waters, where various substances, which do not necessarily covary with each other, affect the light that eventually leaves the water surface?

To address the above issues, I performed detailed in-situ measurements of in-water inherent optical properties (vertical profiles of $a(\lambda)$, $b(\lambda)$, $c(\lambda)$, $b_b(\lambda)$, and [Chl-a]) and

radiation fields (surface measurements of $E_s(\lambda)$, and vertical profiles of $E_d(\lambda)$, $L_u(\lambda)$), analyzed laboratory measurements of phytoplankton, non-pigmented particulate matter and CDOM absorption properties, and made measurements of atmospheric transmission characteristics within the northern part of the main stem of the Chesapeake Bay estuary. Seventeen cruises were performed between 4 June 2001 and 8 November 2002. Specific cases of stratified and vertically homogeneous waters, relatively clear or optically thicker waters, phytoplankton bloom events, rainfall events, and riverine outflows were examined in order to study the total absorption and attenuation of light under various conditions (chapter 2).

Water temperature, T_w , and salinity, S_w , showed the typical patterns expected for Chesapeake Bay waters, with high temperature (and low salinity) values during the summer cruises and a decrease in temperature (and increase in salinity) during the colder (and drier) fall months. Density stratification, brought about by vertical variation in temperature and salinity during the summer cruises, affected mixing processes, and hence also, vertical variations in optical properties, within the water column. The larger vertical stratification, in combination with higher levels of incident radiation and increased availability of nutrients during the late spring - early summer months, resulted in more intense biological activity and favorable conditions for phytoplankton growth. Surface phytoplankton bloom events were observed during some of the spring and summer cruises in the Bay. With the exception of the localized phytoplankton bloom events, when high spatial variability was observed in phytoplankton absorption, $a_{\text{phyt}}(676)$ did not show large spatial variation among the four stations. Large spatial variation was observed in

absorption by non-pigmented particulate matter, $a_{\text{npp}}(\lambda)$, with higher values observed, consistently, at the turbid JT station, most probably due to the proximity of the station to land, the stronger influence of inflow of terrigenous particulate matter, and also the shallower depths measured at this region of the Bay.

Large spatial variation was observed in the total backscattering, b_b , measured in the northern Bay waters, with higher values, during most of the stations, at the turbid JT station. The backscattering fraction $b_b/b(530)$ had an average value of 0.013 (smaller than the widely used b_b/b value for the Petzold “average particle”, $b_b/b=0.018$). Considerable variation was observed in the measured b_b/b in the Bay, with values as low as 0.006 and higher than 0.036, with larger values close to the bottom, probably due to re-suspension of inorganic sediments with high index of refraction. Seasonal and temporal variation in backscattering, b_b , were related strongly to seasonal and temporal patterns of absorption by non-pigmented particulate matter, a_{npp} . Surface values of b_b were strongly correlated to surface values of a_{npp} especially at 412 nm and 380 nm, where absorption by non-pigmented particles is strong. Smaller correlation was found between b_b and [Chl-a], especially at large chlorophyll concentrations. These results are in agreement with previous studies (Stramski and Kiefer, 1991) according to which the major source of particulate backscattering in the water is small, non-living particles, which may include decaying biogenous products of organic and inorganic nature, extract of organisms, as well as terrigenous material such as minerals and organic debris. The strong relationship between a_{npp} and b_b and their effect on the remote sensing reflectances measured in-situ and by MODIS in these waters, was further investigated in chapter 5.

Small variability was observed in the spectral shape of $a_{\text{npp}}(\lambda)$ measured during the cruises, with average value for the exponential slope $S_{\text{npp}}=0.010\text{-}0.011 \text{ nm}^{-1}$ and small standard deviation. Therefore, an exponential model with an exponential slope of $S_{\text{npp}} = 0.0105 \text{ nm}^{-1}$, would provide a very good fit to the non-pigmented particulate matter absorption spectra measured in the Bay waters. Larger variation was observed in the normalized, $a_{\text{phyt}}(\lambda_i)/a_{\text{phyt}}(676)$, phytoplankton absorption spectra, as well as in the CDOM exponential slope, S_{CDOM} . Although an inverse relationship was observed between a_{CDOM} and S_{CDOM} during the measurements in the Bay, with S_{CDOM} decreasing with increasing $a_{\text{CDOM}}(440)$, no strong correlation was found overall between salinity and a_{CDOM} or salinity and S_{CDOM} during the cruises in the Bay. However, the four stations sampled, encompass only a small portion of the entire mouth-to-head salinity gradient of the Bay, and salinity differences among the four stations were less than 2-3 ppt during individual cruises. The high variability observed in the CDOM exponential slope and the uncertainties associated with modeling the phytoplankton absorption wavelength dependence in the Bay waters, would affect the accuracy of inversion algorithms and absorption partitioning methods, such as those used currently in satellite algorithms (e.g MODIS semianalytical chl-algorithm). More research related to studies on the temporal and seasonal variation in CDOM optical characteristics and their relation to physical, chemical and photobiological processes in the Bay, is needed.

Contribution by phytoplankton to total (minus water) absorption was found to be large (larger than 80%) in the 676 nm wavelength region. However, contribution by CDOM and non-pigmented particles to total absorption in the Chesapeake Bay waters was found to be large in the blue-green wavelength region (average contribution by CDOM and

non-pigmented particulate matter to a_{t-w} was 60% at 488 nm, and even larger at the shorter wavelengths 412 and 443 nm, due to the exponential increase of a_{CDOM} and a_{npp} with decreasing wavelength). No strong covariation was found between absorption by phytoplankton and absorption by non-pigmented particulate matter or CDOM during our cruises. Therefore, total absorption and attenuation of light at wavelengths 412, 443 and 488 nm in the Chesapeake Bay waters, is largely affected by substances other than phytoplankton, that do not covary with [Chl-a]. As shown in chapter 5, this has significant implications on the accuracy of the chlorophyll algorithms currently used by MODIS.

The combination of measurements in the Chesapeake Bay formed a “closure experiment”, since measured inherent optical properties and boundary conditions can be used as input information to perform theoretical estimations of the underwater light field using a radiative transfer model, while measured radiometric quantities can be compared to the model’s output. The detailed suite of measurements performed in the Bay, made it possible to perform the model simulations with minimum assumptions on the water’s optical characteristics, using the detailed in-situ measurements of inherent optical properties and boundary conditions as input information to the model (chapter 3).

Good agreement was obtained between measured and model estimated underwater radiation fields and water-leaving radiances. For almost all of the cases, the percent differences between measured and model-estimated water-leaving radiances, L_w , were less than $\pm 11.6\%$ at 443 nm (absolute average of 6.25%), less than $\pm 15.2\%$ at 555nm

(absolute average of 8.3%) and less than $\pm 11.5\%$ at 670nm (absolute average of 6.85%).

Two main assumptions made in the model simulations of the underwater light fields (based on the measurements of optical properties in the Chesapeake Bay waters), improved the agreement between model-estimated and measured radiation fields:

i) Use of a Fournier Forand scattering phase function, as determined by measured wavelength- and depth-dependent backscattering fractions, in place of the widely used “Petzold” average particle scattering phase function (Mobley et al, 2002). ii) The assumption of non-zero total-minus-water absorption at the near-infrared wavelengths (e.g. 715 nm), supported by laboratory spectrophotometric measurements of absorption spectra in the 290-750 nm wavelength region (chapter 2). Accounting for the small NIR absorption (total minus water), was important in model simulations of underwater light fields, especially in the green wavelengths where a_{t-w} is relatively small.

As discussed in chapter 2, the in-situ measurements of backscattering fraction in the Bay showed that b_b/b can be much different than the Petzold “average particle” backscattering fraction, $b_b/b=0.018$, that has been widely used as a default value for modeling backscattering in moderately turbid waters. Hydrolight simulations showed that underwater radiances and irradiances, as well as water-leaving radiances and reflectances, are sensitive to the value of b_b/b , and the b_b/b vertical structure and wavelength dependence. Therefore, accurate depth- and wavelength-dependent measurements of b_b/b are crucial for accurate predictions of underwater light fields and for achieving good agreement between data and model. According to the Hydrolight simulations, inclusion of the inelastic process of chlorophyll fluorescence, can also significantly affect (e.g., by

30-40%) the model estimated water-leaving radiances around 685 nm (chl-a fluorescence emission maximum). However, since measurements of chlorophyll and CDOM fluorescence efficiencies were not performed in this study, Hydrolight assumptions about the CDOM and chlorophyll fluorescence quantum efficiency and spectral quantum efficiency functions might be a source of error in the model estimations.

Given all the errors associated with the measured quantities used as input information to run the model, the errors associated with the radiometric measurements, and the assumptions made in the model simulations, the agreement obtained between measurements in the Bay and model-estimations is remarkably good. Obtaining such a good agreement between measurements and theoretical estimations:

i) Suggests that, when in-situ radiance measurements are not available, the Hydrolight radiative transfer model can be used to accurately estimate the radiation fields in the Chesapeake Bay and other open ocean or coastal waters, provided that accurate and detailed measurements of the inherent optical properties of the water body are available.

ii) Increases confidence on the accuracy of the in-situ measurements performed in the Chesapeake Bay and demonstrates “closure” between the independently measured inherent and apparent water optical properties. This was extremely important for moving to my next goal: using the in-situ measurements and radiative transfer modelling in the interpretation and validation of remote-sensing, satellite observations (chapter 4).

The accuracy of all satellite derived ocean color products (such as chlorophyll concentration, calcite concentration or ocean primary productivity products) depends on the quality and accuracy of the ‘primary’ parameters (normalized water leaving radiances

or remote sensing reflectances) measured by the satellite sensor. The in-situ measurements and theoretical estimations of water leaving radiances in the Bay waters were applied to the interpretation and validation of satellite (MODIS/Terra) observations of normalized water-leaving radiances, under various atmospheric conditions and in-water optical properties. The main questions addressed were: i) How good is the agreement between satellite and in-situ measurements of remote sensing reflectance in the case 2 Chesapeake Bay waters? ii) How do atmospheric conditions and large concentrations of highly absorbing aerosols, large satellite scan angle, proximity to land, affect the quality of satellite observations of ocean color in this coastal region?

Although satellite measurements of the best quality are those characterized by a quality-level 0 or at most 1, satellite pixels with nLw values of all quality-levels have been examined in this study, mainly because the number of pixels of quality-level 0 (concerning the nLw products) was small for the Bay waters (only 18% of the total number of pixels studied), and also because in certain cases, pixels of quality-level 0 had flagged nLw values (negative or zero) at most or all of the satellite wavelength bands, while MODIS nLw values measured at pixels of quality-level 3 were in closer agreement with the nLw values measured in-situ.

The quality of MODIS nLw values was reduced for satellite measurements performed at satellite zenith angles between 55° and 65° , although these satellite zenith angles are smaller than the MODIS threshold set for ocean color products. Atmospheric conditions with high aerosol optical thickness significantly affected the quality of MODIS nLw spectra. Under such conditions, errors in the atmospheric correction resulted in erroneous

(flagged as negative or zero values) or highly overestimated (compared to in-situ measurements and model estimations) nLw MODIS values in the blue wavelength region. The quality of nLw values was affected at pixels close to land, due to the presence of more shallow turbid waters, proximity to bright source and atmospheric correction algorithm failure.

The agreement between MODIS and in-situ measurements was found to be better, for satellite zenith angles smaller than 55° and under relatively clear atmospheric conditions, at 551, 667, 677 nm, especially at the TI station that is located farther away from the bay shores. However, MODIS nLw values were underestimated compared to in-situ measurements, especially at 677 nm. MODIS measurements of nLw at the shorter, blue wavelengths 412 nm and 443 nm were in most of the cases either flagged as negative values or significantly overestimated compared to in-situ measurements. Higher nLw values at 551 nm were measured both in-situ and by MODIS at HB and JT stations compared to TI and PI. This is in agreement with the higher abundance of non-pigmented particles and the higher backscattering coefficients measured in-situ at the turbid HB and JT stations, compared to PI and TI (chapter 2).

The dependence of the MODIS chlorophyll products on the MODIS nLw (or Rrs) measurements was clear for the cases studied: i) For all cases with nLw(443) or nLw(488) flagged as negative values, no [Chl-a] values were estimated by MODIS, since for high-chlorophyll waters, with $[\text{Chl-a}] > 2 \text{ mg m}^{-3}$ (always the case during our cruises in the Bay) MODIS estimations of [Chl-a] are based on empirical relationships between

Rrs(443)/Rrs(551) or Rrs(488)/Rrs(551) and [Chl-a]. ii) Under conditions of high aerosol optical thickness all three MODIS chl-algorithms significantly underestimated [Chl-a], due to overestimations of the MODIS nLw values in the blue wavelengths (discussion in chapter 5).

For cases with almost clear atmospheric conditions and no negative MODIS nLw values at 443 and 488 nm, MODIS chlorophyll products (especially chlor_a_3), showed better agreement with in-situ [Chl-a] values, especially for [Chl-a] less than 10 mg m^{-3} . However, large disagreement was observed at larger chlorophyll concentrations. The main reason for this disagreement in the Chesapeake Bay waters, is that CDOM and non-pigmented particulate mater, that do not necessarily covary with chlorophyll-a concentration, significantly affect the total absorption and backscattering of light, and therefore the remote sensing reflectances, at the blue-green wavelengths (443, 488 nm) used in the MODIS empirical chlorophyll algorithms.

When the relationships between in-situ $Rrs(\lambda_i)/Rrs(554)$ and [Chl-a] values were examined for $\lambda_i = 443, 488$, estimated correlation coefficients were small, while a stronger relationship was observed between the ratio $Rrs(677)/Rrs(554)$ and [Chl-a]. In the 676 nm wavelength region, absorption by CDOM and non-pigmented particles is relatively small and most of the total in-water absorption (minus the absorption by pure water) is due to the presence of phytoplankton (contribution by phytoplankton to $a_{t-w}(676)$ larger than 80%). Therefore, an algorithm that is based on the relationship between $Rrs(677)/Rrs(554)$ and [Chl-a] could be used for [Chl-a] estimations in the

Chesapeake Bay waters. However, large disagreement between the $R_{rs}(677)/R_{rs}(554)$ ratios measured by MODIS and in-situ, resulted in large errors in the estimated [Chl-a] values when the algorithm was applied to MODIS data. Improvements in the accuracy of MODIS R_{rs} measurements in future reprocessing could result in better application of such an algorithm to satellite observations.

Both measured and Hydrolight estimated $R_{rs}(670)$ values were found to be strongly related to backscattering values at 650 nm ($R^2=0.88$). Although MODIS generally underestimated R_{rs} at 670 nm a good correlation was observed between the MODIS measured $R_{rs}(670)$ and backscattering at 650 nm (figure 5.3-13). The strong relationship found between $R_{rs}(670)$, a quantity that can be measured remotely by an aircraft or a satellite, and $b_b(650)$ in the Chesapeake Bay waters is very important since b_b is an optical property characteristic of the particulate matter present in these waters. As mentioned previously, re-suspended sediments and detrital material of organic and inorganic nature seem to be responsible for most of backscattering in the Chesapeake Bay waters, with surface values of b_b being strongly correlated to surface values of a_{npp} especially at 412 nm and 380 nm where absorption by non-pigmented particles is strong (fig. 5.3-16, chapter 5).

The strong relationships found between $R_{rs}(670)$ and $b_b(650)$ and between $b_b(650)$ and $a_{npp}(412)$ could potentially be used in remote estimations of the amount of non-pigmented particulate matter in turbid waters (fig. 5.3-17, chapter 5). In the MODIS semianalytic algorithm (Carder et al, 2002) non-pigmented particles and CDOM are combined in one

term (gelbstoff) owing to the similarity in the absorption spectral shapes of these substances and the difficulties associated with separating their contribution to total light absorption. Relationships such as those between $R_{rs}(670)$, $b_b(650)$ and $a_{npp}(412)$, which are based on the backscattering properties of the non-pigmented particles, could be used to separately estimate contribution by non-pigmented particles to total light attenuation.

This research project is a contribution towards gaining a better understanding of the optical characteristics of various substances, such as phytoplankton, non-pigmented particles and CDOM, in the Chesapeake Bay waters, and the way they influence the amount of light leaving the water surface that can be measured in-situ or remotely from instruments on aircrafts or satellites. This knowledge is necessary when in-situ or satellite measurements of R_{rs} or nLw are used to extract information on the water's inherent optical properties (e.g. a_{npp} , a_{phyt} , b_b), or the abundance and distribution of chlorophyll or other optically active substances in these estuarine waters. The in-situ measurements performed in the Bay were applied to the interpretation of satellite (MODIS) water leaving radiance data and their validation. The applicability of bio-optical models and parameterizations currently used in satellite algorithms were examined for the case of the optically complex, Chesapeake Bay waters. Relationships between remotely sensed water leaving radiances and properties of optically active components in these waters were investigated. The resulting techniques and analysis should be broadly applicable to other coastal areas of the world. The results from this thesis, and other future work, will contribute to our ability to obtain more accurate information from remotely measured optical characteristics of estuarine and coastal regions. The combined use of in-situ

measurements and detailed radiative transfer modeling enables the improvement of both the theoretical models and satellite remote sensing algorithms needed to a better understanding of biotic responses to environmental forcing.

Future work involves: i) Testing the relationships found between Rrs ratios and [Chl-a] or Rrs(670) and $a_{\text{np}}(412)$, using future and improved reprocessing of MODIS data. Future improvements of MODIS data are associated with removing bi-directional effects from satellite observations, as well as using recently developed atmospheric correction algorithms (e.g Chomko and Gordon, 1998; Gordon et al, 1997) that are based on simultaneous determinations of oceanic and atmospheric properties and show promise in dealing with strongly absorbing aerosols. ii) More detailed studies on the CDOM optical characteristics. CDOM is the main absorber of light at the short, ultraviolet wavelengths that have the most harmful effects on aquatic organisms. Part of my research in the future will be focused on how variations in the optical and chemical characteristics of CDOM are related to mixing processes or photochemical and biological processes in estuarine and coastal environments. The information obtained will be used to help interpret satellite data for MODIS (visible) and in the future for OMI (UV+visible). iii) More research on water's optical properties in Chesapeake Bay and other coastal and estuarine environments, using a combination of radiative transfer modeling, in-situ measurements and remote sensing, in order to contribute towards gaining a better understanding on the interaction between natural and human-induced processes in these optically and biologically complex regions of the world's oceans.

APPENDIX

<!--[if !vml]--><!--[endif]-->

MODIS Ocean

[Home](#) [Data Products](#) [Quality Assurance](#) [Validation](#) [Data Processing](#) [References](#) [Links](#)

Level 2 Quality-Level Flags (Terra Collection 4) (Applies also to Aqua Collection 3)

MODOCL2 Quality Levels

NOTE: Values in the MODOCL2 'quality' SDS are of type BYTE. Bits 1-2 are the least significant bit pair; bits 7-8 are the most significant bit pair.

Bit	Description
1-2	Mandatory Quality for all of Gordon's nLw parameters 0 = good, if common flags 1-3,6,8 are clear, and product-specific L2_flags 1, 9-16 are clear. 1 = questionable, if large satellite or solar zenith angles 2 = cloud or sun glint contaminated 3 = bad other than cloud, if any input radiances are negative or saturated , or Atmospheric Correction failed, aerosol model==16,or Land
3-4	Mandatory Quality Carder's eps_clr_water parameter 0 = good, if common flags, input Lw flags and product specific L2_flag 15 is clear. 1 = questionable, if any of: shallow, large zenith angles, bad ancillary data, or product-specific L2_flag 15 is set. 2 = cloud or sun glint contaminated 3 = bad, if any input radiances are negative or saturated, or Atmospheric Correction failed, or Land
5-8	Spare

MODOCL2A Quality Levels

NOTE: The MODOCL2A 'quality' SDS is written as an unsigned long integer (ULONG). The byte containing bits 1-8 is the least significant byte and is unused. The byte containing bits 25-32 is the most significant byte.

Bit	Description
1-8	Spare
9-10	Mandatory Quality for Hoge's phycoeryth_conc and phycou_conc parameters 0 = good, if common flags are clear, input Lw flags are clear, and product-specific L2_flags 19-23 are clear

	<p>1 = questionable, if any: shallow, large satellite or solar zenith angles, bad ancillary data, or product specific flags 19-23 2 = if cloudy or glint 3 = bad, if any PEB or PUB values < 0 , input radiances are negative or saturated, or Atmospheric Correction failed, or Land, or product-specific L2_flags 1 value1-15 are set</p>
11-12	<p>Mandatory Quality for Clark Chlor_MODIS 0 = good, if pigc between 0.01 and 100 mg/m**3 1 = questionable, if high satellite zenith angle , shallow water, bad ancillary data, data values <0.01 or >100 mg/m**3 2 = Sun glint contaminated 3 = input radiances are negative or saturated, cloudy, aerosol model==16, land or atmospheric correction problem, pig_c <0.0 mg/m**3</p>
13-18	<p>spare</p>
19-20	<p>Mandatory Quality for Abbott's chlor_fluor_ht parameter (quality level demoted by 1 if high sat or solar zenith angle) 0 = good, if common flags except shallow are clear, input Lw flags are clear, product specific flags clear 1 = questionable, flags 7 (FLH/CHL too large) or 9 (FLH too large) 2 = if FLH/Chl way too large, FLH way too large, or modis_chl=-1 3 = bad, if input radiances are negative or saturated , cloudy/albedo, atmospheric correction problem, glint, bad ancillary data, or land</p>
21-22	<p>Mandatory Quality for Abbott's chlor_fluor_effic parameter (quality level demoted by 1 if high sat or solar zenith angle) 0 = good, if common flags except shallow are ok, input Lw flags are clear, and product-specific L2_flags are clear 1 = questionable, FLH quality == 1 or ARP quality ==1 2 = if any CFE >0.1 or FLH quality ==2, or ARP ==2 3 = bad if input radiances are negative or saturated, cloudy/albedo, atmospheric correction problem, glint, ancillary data problem, land, CFE > 0.15, or FLH quality ==3</p>
23-24	<p>Mandatory Quality for Gordon's cocco_pigmnt_conc, cocco_conc_detach, calcite_conc 0 = good, if common flags are clear, input Lw flags are clear, and product-specific L2_flags clear. 1 = questionable, if any of: shallow, large zenith angles, bad ancillary or product flags 15-17 2 = cloud, if any input radiances are negative and saturated, cloud, or glint 3 = bad, if any input radiances are negative or saturated, or Atmospheric Correction failed, aerosol model==16, Land, or product-specific flags 22-24 are set</p>
25-26	<p>Mandatory Quality for Clark's CZCS_pigment parameter 0 = good, if pigc between 0.01 and 100 mg/m**3 1 = if any high satellite zenith angle , shallow water, bad ancillary data, or data vales <0.01 or >100 mg/m**3 2 = Sun glint contaminated 3 = bad, if input radiances are negative or saturated , glint, cloudy, aerosol model==16, land or atmospheric correction problem , pig_c <0.0 mg/m**</p>

27-28	<p>Mandatory Quality for Clark's pigment_c1_total</p> <p>0 = good, if pigc between 0.01 and 200 mg/m³</p> <p>1 = questionable if any high Sateillite zenith angle, shallow water, bad ancillary data, data vales <0.01 or >200 mg/m³</p> <p>2 = Sun glint contaminated</p> <p>3 = bad, if any input radiances are negative or saturated, glint, cloudy, aerosol model==16, land or atmospheric correction problem , pig_c <0.0 mg/m³</p>
29-30	<p>Mandatory Quality for Clark's susp_solids_conc parameter</p> <p>0 = good, if values between 0.03 and 100 g/m³</p> <p>1 = questionable, susp_solid <0.03 or > 100 g/m³, high satellite or solar zenith angle, shallow water, bad ancillary data</p> <p>2 = sun glint contaminated</p> <p>3 = bad, if any input radiances are negative or saturated, or AtmosphericCorrection failed, aerosol model==16, or susp_solid less than 0.03 or greater than 100 g/m³, Land, cloudy</p>
31-32	<p>Mandatory Quality for Clark's K_490 parameter</p> <p>0 = good, K490 between 0.016 and 20.0</p> <p>1 = questionable, if any values <0.016 or > 20.0 , high satellite or solar zenith angle, shallow water, or bad ancillary data</p> <p>2 = glint contaminated</p> <p>3 = bad, if any input radiances are negative and or saturated, or Atmospheric Correction failed, aerosol model==16, k490 <0.0 or k490 >, if < 0, Land, or cloudy</p>

MODOCL2B Quality Levels

NOTE: Values in the MODOCL2B 'quality' SDS are of type BYTE. Bits 1-2 are the least significant bit pair; bits 7-8 are the most significant bit pair.

Bit	Description
1-2	<p>Mandatory Quality for Carder's chlor_a_3, absorp_coeff_gelb, chlor_absorb, tot_absorb_*</p> <p>0 = good, if common flags are clear, input Lw flags are clear, and product-specific L2_flags 1,9-16 are clear</p> <p>1 = questionable, if any of: shallow, large satellite or solar zenith angles, bad ancillary, aph675 too small, low 412 or 555 flag set, or calculated chlorophyll exceeds chl_incon._thresh</p> <p>2 = glint contaminated</p> <p>3 = bad, if any input radiances are negative or saturated, or Atmospheric Correction failed, or Land, aerosol model==16, RRS <0</p>
3-4	<p>Mandatory Quality Carder's IPAR</p> <p>0 = good, if common flags are clear, input Lw flags are clear, and product-specific L2_flags clear</p> <p>1 = questionable, if any of: shallow, large zenith angles, bad ancillary</p> <p>2 = cloud or glint contaminated</p> <p>3 = bad, if any input radiances are negative or saturated, or Atmospheric Correction failed, or Land, or aerosol model==16</p>
5-6	<p>Mandatory Quality Carder's ARP parameter</p> <p>0 = good, if common flags are clear, input Lw flags are clear, and product-specific L2_flags is clear</p> <p>1 = questionable, if any of: shallow, large satellite or solar zenith angles, bad ancillary, or high</p>

	windspeed flag set 2 = cloud or glint contaminated 3 = bad, if any input radiances are negative or saturated, or Atmospheric Correction failed, or Land, or aerosol model==16, or RRS< 0
7-8	Mandatory Quality for SeaWiFs analog OC3M Chlorophyll chlor_a2 0 = good, if product value between 0.01 and 100 mg/m**3 1 = Sat Zenth angle >70, shallow water, bad ancillary data, data vales <0.01 or >100 mg/m**3 2 = Sun glint contaminated 3 = input radiances are negative or saturated, glint, cloudy, aerosol model==16, land or atmospheric correction problem, pig

MOD28L2 Quality Levels

NOTE: Values in the MOD28L2 'quality' SDS are of type BYTE. Bits 1-2 are the least significant bit pair; bits 7-8 are the most significant bit pair.

Bit	Description
1-2	Mandatory Quality for SST products 0 = good, if common flags are clear, input radiance flags are clear, and product-specific L2_flags 9,11-16 are clear 1 = questionable, large zenith angle, bad ancillary or flags 3,10-11 2 = sun glint or channel uniformity bad contaminated 3 = if any input radiances are negative and not saturated, or Atmospheric Correction failed, or Land
3-4	Mandatory Quality for SST4 products 0 = good, if common flags are ok, inputs, both sat zenith tests, both sst4-sst, BT22-BT23-ref, both uniformity, brights, and reynolds(optional) 1 = questionable, if any of: if sst4-sst test2 , sat zenith test 2, or unif test2 2 = if sst4-sst test 1, sat zenith angle test 1, or uniformity test1 3 = if any input radiances are negative and not saturated, BT22-BT23-ref out of range, brights outside (-4..33)
5-8	Spare

Developed by: Kay Kilpatrick, RSMAS/U.Miami (kkilpatrick@rsmas.miami.edu)
Authorized by: Wayne E. Esaias, Code 971, NASA Goddard Space Flight Center

MODIS Ocean

[Home](#) [Data Products](#) [Quality Assurance](#) [Validation](#) [Data Processing](#) [References](#) [Links](#)

Common and Product Specific Flags (Level 2 and Level 3) for Terra Collection 4 (also applies to Aqua Collection 3)

For each parameter at Level 3 maps there are a maximum of 5 bytes of flags (common, maximum of three product specific, and one quality). Each byte is mapped to a separate file.

Common Flags

L3 maps MO*F*.hdf - 1 byte integer. Tests are the same for all 40 products.

MO*.F.{1:40}*.hdf

Common tests	L3 map bit	L3 binned bit	L2 bit
Pixel not processed	1	1	1
Atmospheric correction failed	2	2	2
Satellite zenith angle > 55 (SST), > 65 (Ocean Color)	3	3	3
Solar zenith angle >70	4	4	4
Shallow water (i.e. < 5km from coast or < 50 m deep, or inland lake)	5	5	5
Sun glint greater than threshold	6	6	6

Invalid or missing ancillary data	7	7	7
Land (includes ephemeral water)	8	8	8

Product-Specific Flags

Maximum of 3 bytes of flags per parameter, each byte mapped in a separate file in the level 3 maps.

Parameters 1-12 (Gordon products from MODOCL2 - 2 bytes of product specific flags.

(nLw_412, nLw_443, nLw_488, nLw_531, nLw_551, nLw_667, nLw_678, Tau_865, Eps_78, aer_model1, aer_model2)

Please note that in the MODOCL2 file the 2 bytes are contained in a single SDS in contrast to the maps where the information is stored into two separate files. In the L2 file the information is stored such that the least significant byte contains the MO*.2* bits with bit 1 being in the least significant bit. The most significant bit contains MO*.1* bit 8. For the L3 binned files the bytes are in the same order as that of the L2 file except the bytes are stored as a 4 byte field. MO*1*.hdf is always in the most significant byte of the 4 byte field, the two least significant bytes are not used in the Level 3 binned files.

Map MO*.1{1:12}*.hdf

Product specific test	L3 map bit	L3 binned bit	L2 MODOCL2 bit
Cloudy; Albedo @ 865 threshold	1	25	9
Bad_Lw; One or more bands missing	2	26	10
Bad_Lw; Any LwXXX <= 0	3	27	11
Bad_Lw; Any band counts < 0	4	28	12
Atmos_Corr; Questionable polarization correction/mirror reflectance (not currently used)	5	29	13
Atmos_Corr; Gordon aerosol failure	6	30	14
Atmos_Corr; epsilon out of range	7	31	15
Atmos_Corr - Any LaXXX <= 0	8	32	16

Map MO*.2{1-12}*.hdf

Product specific test	L3 map bit	L3 binned bit	L2 MODOCL2 bit
Atmos_Corr ; Invalid Raleigh scattering data	1	17	1
nLw550_low; Calculated nLw550 is too small	2	18	2
Cocco; Coccolithophorid radiance exceeds threshold	3	19	3
TurbidCase2; Actual_rrs555 Turbid_rs555	4	20	4
Hi_la865; Calculated La865 is too large	5	21	5
Input Lw's for Carder's clear water epsilon band (11,13) bad.	6	22	6
lo_eps; epsilon < 0.67	7	23	7
spare	8	24	8

Parameters 13-25 (derived products from MODOCL2A) 3 bytes of product specific flags.

(eps_clr_water, CZCS_pigment, chlor_MODIS, pigment_c1_total, chlor_fluor_ht, chlor_fluor_base, chlor_fluor_effic, susp_solids_conc, cocco_pigmnt_conc, cocco_conc_detach, clacite_conc, K_490, phycoeryth_conc, phycou_conc)

Please note that in the MODOCL2A file the 3 bytes are contained in a single 4-byte SDS in contrast to the maps where the information is stored into three separate files. In the L2 file the information is stored such that the most significant byte contains the MO*1.* bits with bit 8 of MO*1.*.hdf being in the most significant bit. The least significant byte of the 4 byte field is unused. For the L3 binned files the bytes are in the same order as that of the L2 file except the bytes are stored as a 4 byte field. MO*1.*.hdf is always in the most significant byte of the 4 byte field

Map MO*.1{13:25}*.hdf

Product specific test	L3 map bit	L3 binned bit	L2 MODOCL2A bit
pig_C input Lwís (bands 9 and 12) bad	1	25	25
chl_a input Lwís (bands 9,10,11,12) bad	2	26	26

pig_total input Lwís (bands 9,10,11,12) bad	3	27	27
susp_solid inout Lwís (bands 9,10,11,12) bad	4	28	28
K490 input Lwís (bands 9 and 12) bad	5	29	29
FLH/chl_modis way too high, not reasonable	6	30	30
FLH/chl_modis too high, approaching limit higher uncertainty	7	31	31
FLH way too high, not a reasonable value	8	32	32

Map MO*.2{13-25}.hdf

Product specific test	L3 map bit	L3 binned bit	L2 MODOCL2A bit
FLH_Range; approaching limit higher uncertainty	1	17	17
chl_modis == -1, algorithm failed, fill value present	2	18	18
ARP qual >= 2, questionable	3	19	19
ARP qual == 1 , higher uncertainty	4	20	20
CFE too high, not reasonable value	5	21	21
coccolith algorithm input Lwís (bands 9 and 12) bad	6	22	22
LoRadiance; radiance value below lower bound of coccolith lookup table	7	23	23
HiRadiance; radiance value above upper bound of coccolith lookup table	8	24	24

Map MO*.3{13-25}*.hdf

Product specific test	L3 map bit	L3 binned bit	L2 MODOCL2A bit
InvalidEntry; invalid data coccolith lookup table	1	9	9
PEB and PUB input Lw's (8-12) bad	2	10	10

range_iop_flags[1]: PEB/PUB algorithm calculated IOP outside realistic range	3	11	11
range_iop_flags[2]: PEB/PUB algorithm calculated IOP outside realistic range	4	12	12
range_iop_flags[3]: PEB/PUB algorithm calculated IOP outside realistic range	5	13	13
range_iop_flags[4]: PEB/PUB algorithm calculated IOP outside realistic range	6	14	14
range_iop_flags[5]: PEB/PUB algorithm calculated IOP outside realistic range	7	15	15
Cloudy - albedo @ 865 >threshold	8	16	16

Parameters 26 - 36 (Products from MODOCL2B) two bytes of product specific flags

(chlor_a_2, chlor_a_3, ipar, arp, absopr_coef_gelb, chlor_absorb, tot_absorb_412, tot_absorb_443, tot_absorb_488, tot_absorb_531, tot_absorb_551)

Please note that in the MODOCL2B file the 2 bytes are contained in a single SDS in contrast to the maps where the information is stored into two separate files. In the L2 file the information is stored such that the least significant byte contains the MO*.2* bits with bit 1 being in the least significant bit. The most significant bit contains MO*.1* bit 8. For the L3 binned files the bytes are in the same order as that of the L2 file except the bytes are stored as a 4 byte field. MO*1*.hdf is always in the most significant byte of the 4 byte field.

Map MO*.1{26-36}*.hdf

Product specific test	L3 map bit	L3 binned bit	L2 MODOCL2B bit
Input Lwís to Carder Chlorophyll routine (bands 8-13) bad	1	25	9
neg_rrs_flag; One or more remote sensing reflectance values are equal or less than zero	2	26	10
low_412_flag; rrs[0](412) less than thresh_412	3	27	11
low_555_flag; rrs[4](555) less than thresh_555	4	28	12
default_flag ; using default chlorophyll model	5	29	13
chl inconsistent flag; calculated chlorophyll	6	30	14

exceeds chl_incon._thresh			
Reserved; chl_quality_flag - (currently unused)	7	31	15
Reserved;hi_scatter_flag - (currently unused)	8	32	16

MAP MO*.2{26-36}*.hdf

Product specific test	L3 map bit	L3 binned bit	L2 MODOCL2B bit
blend_flag; aph_model between .03 and .06 (chlorophyll blended)	1	17	1
package_flag ; chlorophyll packaged	2	18	2
input nLw _{is} (bands 8-13) for ipar and arp products bad	3	19	3
hi_windspeed; wind speed 12 m/s	4	20	4
Cloudy ; Albedo @ 865 > threshold	5	21	5
chl_a3, high packaging	6	22	6
if (reynodolsst-ndtsst)> 3.0 ; Carder NDT un-packaged	7	23	7
If (reynodolsst-ndtsst)< 1.8; Carder NDT packaged	8	24	8

Parameters 37-40 (Products from MOD28L2) two bytes only

(SST_D1, SST4_D2, SST_N1, SST4_N2)

Please note that in the MOD28L2 file the 2 bytes are contained in a single SDS in contrast to the maps where the information is stored into two separate files. In the L2 file the information is stored such that the least significant byte contains the MO*.2* bits with bit 1 being in the least significant bit. The most significant bit contains MO*.1* bit 8. For the L3 binned files the bytes are in the same order as that of the L2 file except the bytes are stored as a 4 byte field. MO*1*.hdf is always in the most significant byte of the 4 byte field.

Map MO*.1{37:40}*hdf

Product specific test	L3 map bit	L3 binned bit	L2 MOD28L2 bit
SST input radiance bad;negative radiance in any of bands (20,31,32),	1	25	9
SST4 input radiances bad; negative values (20,22,23)	2	26	10
Band 31 or band 32 failed uniformity test 1 (max-min of 3x3 pixel box >0.7)	3	27	11
Band 31 or band 32 failed uniformity test 2 (max-min of 3x3 pixel box >1.2)	4	28	12
SST algorithm zenith angle test 1, sat zenith angle>40	5	29	13
SST algorithm zenith angle test 2, sat zenith angle >55	6	30	14
Failed SST tree tests	7	31	15
SST more than 2 degrees different from reference	8	32	16

Map MO*.2{37-40}*hdf

Product specific test	L3 map bit	L3 binned bit	L2 MOD28L2 bit
ch20/31/32 brightness temps bad; unreasonable values in one or more bands less than -10 or greater than 35.	1	17	1
SST4 algorithm uniformity test 1 (max-min of 3x3 pixel box >0.7)	2	18	2
SST4 algorithm uniformity test 2 (max-min of 3x3 pixel box >0.1.2)	3	19	3
SST4 algorithm zenith angle test 1; sat zenith angle >40	4	20	4

SST4 algorithm zenith angle test 2; sat zenith angle >55	5	21	5
Failed SST4 tree tests	6	22	6
SST4 more than 2 degrees C different from reference	7	23	7
ch20/22/23 brightness temps bad, unreasonable values in one or more bands less than -10 or greater than 35.	8	24	8

Developed by: Kay Kilpatrick, University of Miami (kkilpatrick@rsmas.miami.edu)
 Authorized by: Wayne E. Esaias, Code 971, NASA Goddard Space Flight Center

NOTATION

$a(\lambda)$	total absorption coefficient
$a_{t-w}(\lambda)$	total absorption coefficient minus absorption by pure sea-water
$a_{CDOM}(\lambda)$	CDOM absorption coefficient
$a_{npp}(\lambda)$	non-pigmented particulate matter absorption coefficient
$a_{\text{phyt}}^*(\lambda)$	phytoplankton absorption per unit concentration of chl-a + pheopigments
$a_{\text{phyt}}(\lambda)$	phytoplankton absorption coefficient
$a_w(\lambda)$	absorption coefficient of pure water
A_c	clearance area of filter
AOPs	Apparent Optical Properties
AOT	Aerosol Optical Thickness
$b(\lambda)$	total scattering coefficient
$b_b(\lambda)$	total backscattering coefficient
$b_{sw}(\lambda)$	scattering coefficient of pure sea water
$c(\lambda)$	total attenuation coefficient
CDOM	Chromophoric Dissolved Organic Matter
[Chl-a]	Chlorophyll-a concentration
chl-a	chlorophyll-a
chl-b	chlorophyll-b
chl-c	chlorophyll-c
chl-d	chlorophyll-d
DOM	Dissolved Organic Matter
E_d	in-water downwelling irradiance
E_s	surface downwelling irradiance
E_u	in-water upwelling irradiance
F_o	solar irradiance at the top of the atmosphere
IOPs	Inherent Optical Properties
K_d	downwelling irradiance diffuse attenuation coefficient
l_g	geometric optical pathlength
l_a	amplified optical pathlength
L_d	in-water downwelling radiance
L_u	in-water upwelling radiance
L_t	total radiance received by a sensor at the top of the atmosphere
L_{path}	radiance generated along the optical path by scattering (Rayleigh and aerosols) in the atmosphere and by specular reflection of atmospherically scattered light from the sea surface
L_g	contribution by sun glint to total radiance received by a sensor at the top of the atmosphere
L_{wc}	contribution to L_t arising from reflection of skylight and direct sunlight from individual whitecaps on the sea surface
L_w	Water-leaving radiance
MAAs	Mycosporine-like Amino Acids
nL_w	normalized water leaving radiance

n_w	index of refraction by water
OD	optical density
Rrs	remote sensing reflectance (defined as the ratio L_w/E_s)
S_{CDOM}	CDOM absorption spectral slope coefficient
S_{npp}	non-pigmented particulate matter absorption spectral slope coefficient
S_w	water salinity
sza	solar zenith angle
satza	satellite zenith angle
T_w	water temperature
$t(\lambda_i)$	diffuse transmittance of the atmosphere
$T(\lambda_i)$	direct transmittance of the atmosphere
UV	UltraViolet radiation

$\beta(\psi, \lambda)$	volume scattering function,
β	pathlength amplification factor
ϵ_{ss}	instrument's self-shading error
θ_o	solar zenith angle
θ_{sw}	solar angle measured in the water
λ	wavelength
ρ_w	water-leaving reflectance
τ	optical depth
ϕ	azimuth angle
ψ	scattering angle
ω_o	single scattering albedo

REFERENCES

- Aiken, J., G. F. Moore, C. C. Trees, S. B. Hooker, and D. K. Clark, 1995, "The SeaWiFS CZCS-type pigment algorithm", in SeaWiFS Technical Report Series, vol. 29, edited by S. B. Hooker and E. R. Firestone, Goddard Space Flight Center, Greenbelt, MD.
- Austin R. W. and G. Halikas, 1976, "The index of refraction of seawater", SIO Ref. No 76-1, Scripps Inst. Oceanogr. La Jolla, 121.
- Austin R. W., and T. J. Petzold, 1986, "Spectral dependence of the diffuse attenuation coefficient of light in ocean water", *Opt. Eng.*, 25(3), 471.
- Baker K. S and R. C. Smith, 1979, "Quasi-inherent characteristics of the diffuse attenuation coefficient for irradiance", *Ocean Optics VI*, S.Q. Duntley, Editor, Proc. SPIE 208, 60.
- Balch W. M., J. Vaughn, J. Novotny, D. T. Drapeau, R. Vaillancourt, J. Lapierre, and A. Ashe, 2000, "Light Scattering by Viral Suspensions", *Limnol. Oceanog.*, 45(2), 492-498.
- Bergh O., K. Y. Boersheim, G. Bratbak and M. Heldal, 1989, "High abundance of viruses found in aquatic environments", *Nature*, 340:467-468.
- Blough, N. V. and O. C. Zafiriou, 1993, "Optical absorption spectra of water from the Orinoco River outflow: Terrestrial input of colored organic matter to the Caribbean", *J. Geophys. Res.*, 98, 2271-2278.
- Blough, N. V. and R. DelVecchio, 2002, "Chromophoric DOM in the Coastal Environment", in "Biogeochemistry of Marine Dissolved Organic Matter" ed. by D. A. Hansell and C. A. Carlson, Chapter 10.
- Blough, N. V. and S. A. Green, 1995, "Spectroscopic characterization and remote sensing of non-living organic matter", in "The Role of Non-living Organic Matter in the Earth's Carbon Cycle", 23-45.
- Boivin, L. P., W. F. Davidson, R. S. Storey, D. Sinclair, and E. D. Earle, 1986, "Determination of the attenuation coefficient of visible and ultraviolet radiation in heavy water", *Applied Optics*, 25(6), 877-882.
- Boyd, T. J. and C. L. Osburn, 2003, "Changes in allochthonous and autochthonous CDOM excitation and emission fluorescence matrices (EEMS) from bacterial degradation", *Biogeochemical Cycles*, ASLO Meeting.
- Boynton, W. R., Garber, J. H., Summers, R., and Kemp, W. M., 1995, "Inputs, transformations, and transport of nitrogen and phosphorus in Chesapeake Bay and selected tributaries." *Estuaries* 18, 285-314

- Bricaud A. and D. Stramski, 1990, "Spectral absorption coefficients of living and non-algal biogenous matter: A comparison between the Peru upwelling and the Sargasso Sea", *Limnol. Oceanogr.*, 35, 562-585.
- Bricaud A., A. Morel, and L. Prieur, 1981, "Absorption by dissolved organic matter in the sea (yellow substance) in the UV and visible domains", *Limnol. Oceanogr.* 26, 43-53.
- Bricaud A., Morel A., and L. Prieur, 1983, "Optical efficiency factors of some phytoplanktoners", *Limnol. Oceanogr.*, 28, 816-832.
- Buiteveld, H., J. H. M. Hakvoort, and M. Donze, 1994, "The optical properties of pure water", in *Ocean Optics XII*, J. S. Jaffe, Editor, *Proc. Soc. Photo-Opt. Instrum. Eng.*, 2258, 174-183.
- Bukata, R. P, J. H. Jerome, K. Ya. Kondratyev, and D. V. Pozdnyakov, 1991, "Estimation of organic and inorganic matter in island waters: optical cross sections of Lakes Ontario and Ladoga", *J. Great Lakes Res.*, 17, 461-469.
- Bukata, R. P, J. H. Jerome, K. Ya. Kondratyev, and D. V. Pozdnyakov, 1995, "Optical Properties and Remote Sensing of Inland and Coastal Waters", CRC Press, 362.
- Butler W. L., 1962, "Absorption of light by turbid materials", *J. Opt. Soc. Am.*, 52, 292-299
- Campbell J. W., 1981, "An Algorithm for Computing Chlorophyll-a Concentrations Using a Dual-frequency Fluorosensor", in *Chesapeake Bay Plume Study – Superflux 1980* (J. W. Campbell and J. P. Thomas, Eds.) NASA Conf. Publ. 2188, NOAA/NEMP III 81 ABCDFG 0042
- Carder K., Stewart R., Harvey G., and Ortner P., 1989, "Marine humic and fulvic acids: Their effects on remote sensing of ocean chlorophyll", *Limnol Oceanogr.*, 34(1), 68-81.
- Carder, K. L., R. F. Chen, and J.P. Cannizzaro, 2002, "Case 2 Chlorophyll a" MODIS Ocean Science Team Algorithm Theoretical Basis Document, ATBD 19, Version 6
- Chang C. H. and L. A. Young, 1972, "Seawater temperature measurement from Raman Spectra", Research Note 920, N62269-72-C-0204, Advanced Research Project Agency, ARPA Order No. 1911.
- Chang, G. C., T. D. Dickey, C. D. Mobley, E. Boss, and W. S. Pegau, 2003, "Toward closure of upwelling radiance in costal waters", *Appl. Optics*, 42(9), 1574-1582.
- Chomko, R. and H. R. Gordon, 1998, "Atmospheric correction of ocean color imagery: Use of the Junge power-law aerosol size distribution with variable refractive index to handle aerosol absorption", *Appl. Optics*, 37, 5560-5572.
- Clark D. K., 1997, "Bio-Optical Algorithms Case 1 Waters" MODIS Algorithm Theoretical Basis Document

- Clark D.K, 2001, "MODIS Terra -Phytoplankton Pigments Data Quality Summary"
Product number -MOD 19
- Coble, P., M. Brophy, 1994, "Investigation of the geochemistry of dissolved organic matter in coastal waters using optical properties", SPIE - Ocean Optics XII 2258, 377-389.
- Conley, D. J. and T. C. Malone, 1992, "The annual cycle of dissolved silicate in Chesapeake Bay: implications for the production and fate of phytoplankton biomass." Marine Ecology Progress Series 81, 121–128.
- Cooper, S. R. and G. S. Brush, 1993, "A 2,500-year history of anoxia and eutrophication in Chesapeake Bay", Estuaries, Vol. 16, 617-626.
- Cox, C. and W. Munk, 1995, "Statistics of the sea surface derived from sun glitter", J. Mar. Res., 14, 198-227.
- D'Elia, C. F., D. M Nelson, and W. R Boynton, 1983, "Chesapeake Bay nutrient and plankton dynamics: III. The annual cycle of dissolved silicon". *Geochimica Cosmochimica Acta* 47, 1945–1955.
- D'Elia, C. F., J. G. Sanders, and W. R. Boynton, 1986, "Nutrient enrichment studies in a coastal plain estuary: phytoplankton growth in large-scale, continuous cultures". *Canadian Journal of Fisheries and Aquatic Science* 43, 397–406.
- Darrell, L.C., B.F. Majadi, J.S. Lizarraga, and J.D. Blomquist, 1998, "Nutrient and suspended-sediment concentrations, trends, loads, and yields, from the nontidal part of the Susquehanna, Potomac, Patuxent, and Choptank Rivers, 1985-96", U.S. Geological Survey Water-Resources Investigations Report 98-4177, 38 p.
- Ellison, R. L., and M. M. Nichols, 1975, "Modern and Holocene foraminifera in the Chesapeake Bay region", in Thomas, Charles, and Pelletier, B.R., eds., *First International Symposium on Benthonic Foraminifera of Continental Margins; pt. A, Ecology and biology, Maritime sediments: Fredericton, Canada, Atlantic Geoscience Society*, 131-151.
- Esaias W. S., M. R. Abbott, I. Barton, O. B. Brown, J. W. Campbell, K. L. Carder, D. K. Clark, R. L. Evans, F. E. Hoge, H. R. Gordon, W. P. Balch, R. Letelier, and P. J. Minnett, 1997, "An Overview of MODIS Capabilities for Ocean Science Observations", *Transactions on Geoscience and Remote Sensing, EOS-AM Special Issue*
- Fisher T. R., L. W. Harding, D. W. Stanley, and L. G. Ward, 1988, "Phytoplankton, nutrients, and turbidity in the Chesapeake, Delaware and Hudson estuaries", *Est. Coast. Shelf Sci.*, 27: 61-93
- Fournier, G., 2002, "Unified model of the UV absorption of pure water", *Proceedings Ocean Optics Meeting, Santa Fe, NM.*

- French, C. S., 1960, "The chlorophyll in vivo and in vitro", in W. Ruhland (ed), *Encyclopedia of Plant Physiology* (pp. 252-297), Berlin: Springer-Verlag.
- Frouin, R., M. Schwindling and P. Y. Deschamps, 1996, "Spectral reflectance of sea foam in the visible and near-infrared: In-situ measurements and implications for remote sensing of ocean color and aerosols", *Jour. Geophys. Res.*, 101C, 14,361-14,371.
- Fry, E. S., 2000, "Visible and near-ultraviolet absorption spectrum of liquid water: comment", *Appl. Opt.*, Vol 39, 16, 2743-2744.
- Fry, E. S., G. W. Kattawar, and R. M. Pope, 1992, "Integrating cavity absorption meter", *Appl. Opt.* 31, 2055-2065.
- Gallegos, C. L. and T. E. Jordan, 2002, "Impact of the Spring 2000 Phytoplankton Bloom in the Chesapeake Bay on Optical Properties and Light Penetration in the Rhode River, Maryland", *Estuaries*, 25(4A), 508-518.
- Gallie, A. E. and P. A. Murtha, 1992, "Specific absorption and backscattering spectra for suspended minerals and chlorophyll-a in Chilko Lake, British Columbia". *Rem. Sens. Environ.* 39, 103-118.
- Gao, H., and R. G. Zepp, 1998, "Factors influencing photoreactions of dissolved organic matter in a coastal river of the southeastern United States" *Envir. Sci. Technol.* 32, 2940-2946.
- Gibson, J. A. E., W. F. Vincent, B. Nieke, and R. Pienitz, 2000, "Control of biological exposure to UV radiation in the Arctic ocean : Comparison of the roles of ozone and riverine dissolved organic matter" . *Arctic* 53, 372-382.
- Glibert, P.M., D.J. Conley, T.R. Fisher, L.W. Harding, and T.C. Malone, 1995, "Dynamics of the 1990 winter/spring bloom in Chesapeake Bay." *Mar. Ecol. Prog. Ser.* 122:22-43.
- Gordon, H. R., 1978, "Removal of Atmospheric Effects from Satellite Imagery of the Oceans", *Appl. Optics*, 17, 1631-1636.
- Gordon, H. R., 1989, "Dependence of the diffuse reflectance of natural waters on the sun angle" *Limnol. Oceanogr.*, 34(8), 1389.
- Gordon, H. R. and A. Morel, 1983, "Remote Assessment of Ocean Color for Implementation of Satellite Visible Imagery, a Review; Lecture Notes on Coastal and Estuarine Studies, Volume 4" Springer VERLAG, New York, 114.
- Gordon, H. R. and D. K. Clark, 1980, "Atmospheric effects in the remote sensing of phytoplankton pigments", *Bound.-Layer Meteor.*, 18, 299-313.
- Gordon, H. R. and D. K. Clark, 1981, "Clear water radiances for atmospheric correction of coastal zone color scanner imagery", *Appl. Optics*, 20, 4175-4180.

- Gordon, H. R. and K. Ding, 1992, "Self-shading of in-water optical instruments", *Limnol. Oceanogr.*, 37, 491-500.
- Gordon, H. R. and K. J. Voss, 1999, "MODIS Normalized Water-leaving Radiance, Algorithm Theoretical Basis Document, Version 4", ATBD, MOD 18.
- Gordon, H. R. and M. Wang, 1994, "Influence of Oceanic Whitecaps on Atmospheric Correction of Sea-WiFS", *Appl. Optics*, 33, 7754-7763.
- Gordon, H. R., D. K. Clark, J. W. Brown, O. B. Brown, R. H. Evans and W. W. Broenkow, 1983, "Phytoplankton pigment concentrations in the Middle Atlantic Bight: comparison between ship determinations and Coastal Zone Color Scanner estimates", *Appl. Optics*, 22, 20-36.
- Gordon, H. R., Du, T., and Zhang, T. M., 1997, "Remote sensing of ocean color and aerosol properties: Resolving the issue of aerosol absorption". *Applied Optics*, 36(33), 8670-8684.
- Gordon, H. R., J. W. Brown and R. H. Evans, 1988, "Exact Rayleigh Scattering Calculations for use with the Nimbus-7 Coastal Zone Color Scanner", *Appl. Optics*, 27, 862-871.
- Gordon, H. R., O. B. Brown, and M. M. Jacobs, 1975, "Computed relationships between the inherent and apparent optical properties of a flat homogeneous ocean", *Appl. Optics*, 14, 417-427.
- Gordon, H. R., O. B. Brown, R. H. Evans, J. W. Brown, R. C. Smith, K. S. Baker, and D. K. Clark, 1988, "A semi-analytic model of ocean color", *J. Geophys. Res.*, 93, 10,909-10,924.
- Green, S. A., and N. V. Blough, 1994, "Optical absorption and fluorescence properties of chromophoric dissolved organic matter in natural waters", *Limnol. Oceanogr.*, 39, 1903-1916 .
- Gregg, W. W. and K. L. Carder, 1990, "A simple spectral solar irradiance model for cloudless maritime atmospheres", *Limnol. Oceanogr.*, 35(8), 1657-1675.
- Grew G. W., 1981, "Real Time Test of MOCS Algorithm During Superflux 1980", in *Chesapeake Bay Plume Study – Superflux 1980* (J. W. Campbell and J. P. Thomas, Eds.) NASA Conf. Publ. 2188, NOAA/NEMP III 81 ABCDFG 0042
- Grundinkina, N.P., 1956, "Absorption of ultraviolet radiation by water", *Opt. Spektrosk.*, 1, 658-662.
- Hale G. M. and M. R. Querry, 1973, "Optical constants of water in the 200-nm to 200- μ m wavelength region", *Appl. Optics* 12, 555-563.

- Haltrin, V. I. and G. Kattawar, 1991, "Light fields with Raman Scattering and fluorescence in sea water", Tech. Rept., Dept. Of Physics, Texas A&M Univ., College Station, 74.
- Haltrin, V. I. and G. Kattawar, 1993, "Self consistent solutions to the equation of transfer with elastic and inelastic scattering in oceanic optics: I. Model", *Appl. Optics*, 32(27), 5356-5367.
- Haltrin, V. I., (1999), "Chlorophyll-based model for seawater optical properties", *Appl. Optics*, 38(33), 6826-6832.
- Harding L. W., 1994, "Long-term trends in the distribution of phytoplankton in Chesapeake Bay: roles of light, nutrients and streamflow". *Marine Ecology Progress Series* 104:267-291.
- Harding L. W., and A. Magnuson, 2001, "Bio-Optical and Remote Sensing Observations in Chesapeake Bay", SIMBIOS Project Annual Report, Chapter 8.
- Harding L. W., and E. C. Itsweire, 1991, "Synoptic measurements of the distribution of chlorophyll in the Chesapeake Bay using aircraft remote sensing", in *New Perspectives in the Chesapeake System: A Research and Management Partnership* (J. Mihurski and A. Chaney Eds.), Proc. 2nd Chesapeake Bay Research Conference, Baltimore, MD, 4-6 Dec. 1990, Chesapeake Research Consortium, Solomons, MD, pp. 147-160
- Harding L. W., and E. Perry, 1997, "Long-term increase of phytoplankton biomass in Chesapeake Bay, 1950-94." *Marine Ecology Progress Series* 157, 39-52.
- Harding L. W., B. W. Meeson, and T. R. Fisher, 1985, "Photosynthesis patterns in Chesapeake Bay phytoplankton: short- and long-term responses of P-I curve parameters to light". *Marine Ecology Progress Series* 26, 99-111.
- Harding L. W., B. W. Meeson, and T. R. Fisher, 1986, "Phytoplankton production in two East Coast estuaries: Photosynthesis-light functions and patterns of carbon assimilation in Chesapeake and Delaware bays". *Estuarine, Coastal and Shelf Science* 23:773-806.
- Harding L. W., D. Degobbis, and R. Precali, 1999, "Production and fate of phytoplankton: annual cycles and interannual variability." In *Ecosystems at the Land Sea Margin: Drainage Basin to Coastal Sea* (Malone, T. C. et al., eds). American Geophysics Union, Coastal and Estuarine Studies, vol. 55, pp. 131-172.
- Harding L. W., E. C. Itsweire, and W. E. Esaias, 1992, "Determination of Phytoplankton Chlorophyll Concentrations in the Chesapeake Bay with Aircraft Remote Sensing", *Remote Sens. Environ.*, 40, 79-100.
- Harding L. W., E. C. Itsweire, and W. E. Esaias, 1994, "Estimates of phytoplankton biomass in the Chesapeake Bay from aircraft remote sensing of chlorophyll concentrations." *Remote Sensing of Environment* 49, 41-56.

- Harding L. W., E. C. Itsweire, and W. E. Esaias, 1995, "Algorithm Development for Recovering Chlorophyll Concentrations in the Chesapeake Bay Using Aircraft Remote Sensing, 1989-91", *Photogrammetric Engineering and Remote Sensing*, Vol. 61, No 2 , 177-185
- Harding L. W., M. E. Mallonee, and E. S. Perry, 2002, "Toward a Predictive Understanding of Primary Productivity in a Temperate, Partially Stratified Estuary", *Estuarine, Coastal and Shelf Science*, 55, 437-463
- Harrison A. W. and C. A. Coombes, 1988, "An opaque cloud cover model of sky short wavelength radiance", *Solar Energy*, 41(4), 387-392.
- Hass M. and J. W. Davisson, 1977, "Absorption coefficient of pure water at 488 and 541.5 nm by adiabatic laser calorimetry", *J. Opt. Soc. Am.*, 67, 622-624.
- Hawes S. K. 1992, "Quantum fluorescence efficiencies of marine fulvic and humic acids", Master's Thesis, Dept. of Marine Sc. Univ. of South Florida, St. Petersburg, FL, 92 pp
- Hodgman, C. D., 1933, "Transmission of ultraviolet radiation by water", *J. Opt. Soc. Am.* 23 426-429.
- Hoge F. E. and R. N. Swift, 1981, "Application of the NASA Airborne Oceanographic Lidar to the mapping of chlorophyll and other organic pigments", in *Chesapeake Bay Plume Study – Superflux 1980* (J. W. Campbell and J. P. Thomas, Eds.) NASA Conf. Publ. 2188, NOAA/NEMP III 81 ABCDFG 0042
- Hojerslev, N. K. and I. Trabjerg, 1990, "A new perspective for remote sensing of plankton pigments and water quality" *Univ. Copenhagen, Inst. Phys. Oceanogr. Rep.*, 51, 10.
- Hopkinson, C.S., I. Buffan, J. Hobbie, J. Vallino, M. Perdue, B. Eversmeyer, F. Prah, J. Covert, R. Hodson, M.A. Moran, E. Smith, J. Baross, B. Crump, S. Findlay, and K. Foreman, 1998, "Terrestrial inputs of organic matter to coastal ecosystems: An intercomparison of chemical characteristics and bioavailability." *Biogeochem.* 43:211-234.
- Itturiaga, R. and D. Siegel, 1988, "Microphotometric characterization of phytoplankton and detrital absorption properties in the Sargasso Sea", *Limnol. Oceanogr.*, 34(8), 1706.
- Jeffrey, S. W. and G. F. Humphrey, 1975, "New spectrophotometric equations for determining chlorophyll a, b, c, and c2 in higher plants algae and natural phytoplankton", *Biochemie and Physiologie der Pflanzen*, 167, 191-194.
- Jerlov, N. G., 1976, "Marine Optics", Amsterdam: Elsevier

Johnson D. R., A. Weidemann, R. Arnone, C. O. Davis, 2001, "Chesapeake Bay outflow plume and coastal upwelling events: Physical and optical properties", *Journal Geophys. Res.*, Vol 106, No C6, pp 11,613–11,622

Johnson Z., M.L. Landry, R.R. Bidigare, S.L. Brown, L. Campbell, J. Gunderson, J. Marra, and C. Trees, 1999, 'Energetics and growth kinetics of a deep *Prochlorococcus* spp population in the Arabian Sea", *Deep Sea Research Part II: Topical Studies In Oceanography* Vol. 46 (8-9) pp. 1719-1743

Kamykowski, D., 1987, "A preliminary biophysical model of the relationship between temperature and plant nutrients in the upper ocean", *Deep Sea Res., Part A*, 34, 1067–1079.

Kemp W. M. and W. B. Boynton, 1992, "Benthic-pelagic interactions: Nutrient and oxygen dynamics", p. 149-221. In D. E. Smith, M. Leffler, and G. Mackiernan (eds.), *Oxygen Dynamics in the Chesapeake Bay: A Synthesis of Research*. Maryland Sea Grant College, College Park, Maryland.

Kennish, M., 2001, "Practical Handbook on Marine Science, 3rd Edition", Marine Science Series.

Kepner, R.L., R.A. Wharton, Jr, and C.A. Shuttle, 1998, "Viruses in Antarctic lakes" *Limnol. Oceanogr.*, 43, 1754-1761.

Kirk, J. T. O., 1980, "Spectral absorption properties of natural waters: contribution of the soluble and particulate fractions to light absorption in some inland waters of southeastern Australia", *Aust. J. Mar. Freshwater Res.*, 31, 287-296.

Kirk, J. T. O., 1992, "Monte Carlo modeling of the performance of the reflective tube absorption meter", *Applied Optics*, 31, 6463-6468

Kirk, J. T. O., 1994, "Light and Photosynthesis in aquatic ecosystems, 2nd Edition", Cambridge University Press, Cambridge.

Kishino, M., M. Takahashi, N. Okami, and S. Ichimura, 1985, "Estimation of the spectral absorption coefficients of phytoplankton in the sea", *Bull. Mar. Sci.* 37, 634-642.

Kishino, M., N. Okami, M. Takahashi, and S. Ichimura, 1986, "Light utilization and quantum yield of phytoplankton in a thermally stratified sea", *Limnol. Oceanogr.*, 31, 557-566.

Kopelevich, O. V., 1983, "Small parameter model of optical properties of sea water", Chapter 8 in *Ocean Optics, Vol. 1: Physical Ocean Optics*, edited by A.S. Monin, Nauka Pub., Moscow.

Kopelevich, O. V., and V. I. Burenkov, 1977, "Relation between the spectral values of the light absorption coefficients of sea water, phytoplanktonic pigments, and the yellow substance", *Oceanology*, 17, 278-282.

- Kopelevich, O. V. and E. M. Mezhencher, 1983, "Calculation of spectral characteristics of light scattering by sea water", *Izv, Akad. Nauk SSSR, Fiz. Atmos. Okeana*, 19(2), 144.
- Kullenberg, G., 1974, "Observed and computed scattering functions", Chapter 2 in *Optical Aspects of Oceanography*, edited by N.G. Jerlov and E. S. Nielsen, Academic Press, New York, 25-49.
- Langland, M. J., 1998, "Changes in sediment and nutrient storage in three reservoirs in the lower Susquehanna River Basin and implications for the Chesapeake Bay", *Fact Sheet*, 98-003, 4 p.
- Langland, M. J.; Edwards, R. E.; Sprague, L. A.; and Yochum, S. E., 2002, "Summary of trends and status analysis for flow, nutrients, and sediments at selected nontidal sites, Chesapeake Bay basin, 1985-99", U.S. Geological Survey Open File Report 2001-73, 49 p.
- Lee, Z. P., K. L. Carder, R. G. Steward, T. G. Peacock, C. O. Davis, and J. S. Patch, 1998, "An empirical ocean color Algorithm for light absorption coefficients of optically deep waters", *J. Geophys. Res.*, 103, 27,967-27,978.
- Lee, Z. P., K. L. Carder, S. H. Hawes, R. G. Steward, T. G. Peacock, and C.O. Davis, 1994, "A model for interpretation of hyperspectral remote-sensing reflectance", *Appl. Optics*, 33, 5721-5732.
- Lesser M. P., P. J. Neale, and J. J. Cullen, 1996, "Acclimation of Antarctic phytoplankton to ultraviolet radiation: Ultraviolet absorbing compounds and carbon fixation", *Mol. Mar. Biol. Biotechnol.* 5, 314-325
- Leyendekkers J., 1967, "Fluorophores and light absorbing substances in natural waters", *Koninklijk Nederlands, Meteorologisch Inst. In Debit.* 67-1(IV-4).
- Lobitz, B., L. Johnson, K. Mountford, and P. Stokely, 1998, "AVIRIS analysis of water quality in the Chesapeake Bay." *Proceedings Fifth Int'l Conference Remote Sensing for Marine and Coastal Environments*, vol. 1, pg. 450, 5-7 October, San Diego CA.
- Mackiernan (eds.), *Oxygen Dynamics in the Chesapeake Bay: A Synthesis of Research*, Maryland Sea Grant College, College Park, MD.
- Malcom R. L., 1990, "The uniqueness of humic substances in each of soil, stream and marine environments", *Anal. Chim. Acta*, 232, 19-30.
- Malone, T. C., 1992, "Effects of water column processes on dissolved oxygen: nutrients, phytoplankton and zooplankton." In *Oxygen Dynamics in Chesapeake Bay: A Synthesis of Research* (Smith, D., Leer, M. & Mackiernan, G., eds). University of Maryland Sea Grant, College Park, MD, pp. 61-112.
- Malone, T. C., D. J. Conley, T. R. Fisher, P. M. Glibert, L. W. Harding, and K. G. Sellner, 1996, "Scales of Nutrient-Limited Phytoplankton Productivity in Chesapeake Bay", *Estuaries*, Vol. 19(2B), 371-385.

- Malone, T. C., Ducklow, H. W., Peele, E. R., and Pike, S. E., 1991, "Picoplankton carbon flux in Chesapeake Bay". *Marine Ecology Progress Series* 78, 11–22.
- Malone, T. C., Kemp, W. M., Ducklow, H. W., Boynton, W. R., Tuttle, J. H., and Jonas, R. B., 1986, "Lateral variation in the production and fate of phytoplankton in a partially stratified estuary". *Marine Ecology Progress Series* 32, 149–160.
- Malone, T. C., L. H. Crocker, S. E. Pike, and B. W. Wendler, 1988, "Influences of the river flow on the dynamics of the phytoplankton production in a partially stratified estuary", *Marine Ecology Progress Series*, 48, 235-249.
- Maritorena, S., A. Morel, and B. Gentili, 1994, "Diffuse reflectance of oceanic shallow waters: influence of the water depth and bottom albedo", *Limnol. Oceanogr.*, 39(7), 1689-1703
- Marshall, B. R. and R. C. Smith, 1990, "Raman scattering and in-water ocean optical properties", *Appl. Optics* 29(1), 71-84.
- Marshall, H. G. and R. V. Lacouture, 1986, "Seasonal patterns of growth and composition of phytoplankton in the lower Chesapeake Bay and vicinity". *Estuarine Coastal and Shelf Science* 23, 115–130.
- Maske, H. and H. Haardt, 1987, "Quantitative in vivo absorption spectra of phytoplankton: Detrital absorption and comparison with fluorescence excitation spectra.", *Limnol. Oceanogr.* 32, 620-633.
- McClain C. R., G. Feldman, and W. Esaias, 1993, "Oceanic Biological Productivity", in *Atlas of Satellite Observations Related to Global Change*, eds. R. J. Gurney, J. L. Foster, C. L. Parkinson, Cambridge U. Press, Cambridge, 251-263.
- Mie, G., 1908, "Beitrage zur Optik truber Medien, speziell kolloidalen Metall-losungen", *Ann. Phys.*, 25, 377-445.
- Mitchell B. G., 1990, "Algorithms for determining the absorption coefficient for aquatic particulates using the quantitative filter technique", *Ocean Optics, Proc SPIE* 1302, 137-148
- Mitchell G., A. Bricaud, K. Carder, J. Cleveland, G. Ferrari, R. Gould, M. Kahru, M. Kishino, H. Maske, T. Moisan, L. Moore, N. Nelson, D. Phinney, R. Reynolds, H. Sossik, D. Stramski, S. Tassan, C. C. Trees, A. Weidemann, J. Wieland and A. Vodacek, "Determination of spectral absorption coefficients of particles, dissolved material and phytoplankton for discrete water samples", 2000, in *Ocean Optics Protocols For Satellite Ocean Color Sensor Validation, Revision 2*, G. S. Fargion and J. L. Mueller, NASA/TM-2000-209966, Chapter 12
- Mobley C. D., 1988, "A numerical model for the computation of radiance distribution in natural waters with wind-roughened surfaces, part II; user's guide and code listing",

NOAA Tech. Memo ERL PMEL-81 (NTIS PB88-246871) (Pacific Marine Environmental Laboratory, Seattle, Wash.).

Mobley C. D., 1989, "A numerical model for the computation of radiance distributions in natural waters with wind-roughened surfaces", *Limnol. Oceanogr.*, 34 (8), 1473-1483.

Mobley C. D., 1994, "Light and Water, Radiative Transfer in Natural Waters", Academic Press.

Mobley C. D., 2002, "Hydrolight Technical Note 1: How well does Hydrolight simulate wind-blown sea surfaces?", Sequoia Scientific, Inc.

Mobley C. D. and R. W. Preisendorfer, 1988, "A numerical model for the computation of radiance distribution in natural waters with wind-roughened surfaces", NOAA Tech. Memo ERL PMEL-75 (NTIS PB88-192703) (Pacific Marine Environmental Laboratory, Seattle, Wash.)

Mobley, C. D. and L. K. Sundman, 2000, "Hydrolight 4.1 – Technical Documentation", Sequoia Scientific, Inc.

Mobley, C. D. and L. K. Sundman, 2000, "Hydrolight 4.1 – Users Guide", Sequoia Scientific, Inc.

Mobley, C. D., L. K. Sundman, and E. Boss, 2002, "Phase function effects on oceanic light fields", *Appl. Optics*, 41, 1035-1050.

Mobley, C. D., B. Gentili, H. R. Gordon, Z. Jin, G. W. Kattawar, A. Morel, P. Reinersman, K. Stamnes, and R. H. Stavn, 1993, "Comparison of numerical models for computing underwater light fields", *Appl. Optics*, 32, 7,484-7,504.

Moisan T. A., and B. G. Mitchel, 2001, "UV absorption by mycosporine-like amino acids in *Phaeochystis antarctica* Karsten by photosynthetically available radiation", *Marine Biology*, 138, 217-227.

Morel A., 1973, "Diffusion de la lumiere par les eaux de mer. Resultats experimentaux et approach theorique" in NATO AGARD lecture series No 61, *Optics of the Sea*, Chap. 3.1., 76, Translation by G. Halikas, Scripps Inst. Oceanogr., La Jolla, 1975, 161.

Morel A., 1974, "Optical Properties of pure water and pure sea water", Chapter 1 in *Optical Aspects of Oceanography*, Edited by N. G. Jerlov and E. S. Nielsen, Academic Press, New York, 1-24.

Morel A., 1988, "Optical Modeling of the upper ocean in relation to its biogenous matter content (case I waters)" *J. Geophys. Res.*, 93(C9), 10749.

Morel A., 1991, "Light and marine photosynthesis: a spectral model with geochemical and climatological implications", *Prog. Oceanogr.*, 26, 263-306.

- Morel A. and A. Bricaud, 1981, "Theoretical results concerning light absorption in a discrete medium, and application to specific absorption of phytoplankton", *Deep-Sea Res.*, 28, 1375-1393.
- Morel A. and A. Bricaud, 1981, "Theoretical results concerning the optics of phytoplankton with special reference to remote sensing applications", in *Oceanography from space*, J.F.R. GOWER, ed., Plenum, 313-327.
- Morel A. and B. Gentili, 1991, "Diffuse reflectance of oceanic waters: its dependence on Sun angle as influenced by the molecular scattering contribution", *Appl. Optics*, 30, 4427-4438.
- Morel A. and B. Gentili, 1993, "Diffuse reflectance of oceanic waters. II. Bidirectional aspects", *Appl. Optics*, 32, 6864-6879.
- Morel A. and B. Gentili, 1996, "Diffuse reflectance of oceanic waters. III. Implication of bidirectionality for the remote sensing problem", *Appl. Optics*, 35, 4850-4862.
- Morel A. and J. L. Mueller, 2002, "Normalized water-leaving radiance and remote sensing reflectance: Bidirectional reflectance and other factors", *Ocean Optics Protocols for satellite ocean color sensor validation*, Chapter 13
- Morel A. and L. Prieur, 1977, "Analysis of variations in ocean color" *Limnol. Oceanogr.*, 22, 709-722.
- Morel A. and S. Maritorena, 2000, "Bio-optical properties of oceanic waters: a reappraisal", *J. Geophys. Res.*
- Morel A. and Y-H Ahn, 1990, "Optical efficiency factors of free-living marine bacteria: influence of bacterioplankton upon the optical properties and particulate organic carbon in oceanic waters", *J. Marine Res.*, 48, 145.
- Morrow, J. H., W. S. Chamberlin, and D. A. Kiefer, 1989, "A two- component description of spectral absorption by marine particles", *Limnol. Oceanogr.*, 34(8), 1500-1509
- Mueller, J. L., 2002, "In-water radiometric profile measurements and data analysis protocols", in *Ocean Optics Protocols For Satellite Ocean Color Sensor Validation*, Revision 3, Vol. 1, Mueller J. L. and G. S. Fargion, NASA/TM-2002-210004, Chapter 10
- Neale, P. J. and D. J. Kieber, 2000, "Assessing biological and chemical effects of UV in the marine environment: Spectral weighting functions", in R. E. Hester and R. M. Harrison (eds.) "Causes and Environmental Implications of Increased U.V.-B. Radiation", 61-83, Royal Society of Chemistry. *Issues in Environmental Science and Technology*, 14.

- Neale, P. J., 2000, " Effects of ultraviolet radiation on estuarine phytoplankton production: Impact of variations in exposure and sensitivity to inhibition", *J. Photochem. Photobiol. B*.
- Neale, P. J., J. J. Cullen, and R. F. Davis, 1998, "Inhibition of marine photosynthesis by ultraviolet radiation: Variable sensitivity of phytoplankton in the Weddell-Scotia Confluence during the austral spring.", *Limnol Oceanogr*, 43(3), 433-448.
- Neckel, H. and D. Labs, 1984, "The Solar Radiation Between 3300 and 12500 Å", *Solar Physics*, 90, 205-258
- Nelson, N. B. and B. B. Prezelin, 1993, "Calibration of an integrating sphere for determining the absorption coefficient of scattering suspensions", *Appl. Optics*, 32, 6710-6717.
- Nishihama M., R. Wolfe, D. Solomon, F. Patt, J. Blanchette, A. Fleig, and E. Masuoka, 1997, "MODIS Level 1A Earth Location: Algorithm Theoretical Basis Document Version 3.0"
- O'Reilly, J.E. S. Maritorena, D.A. Siegel, M.C. O'Brien, D. Toole, B.G. Mitchell, M. Kahru, F.P. Chavez, P. Strutton, G.F. Cota, S.B. Hooker, C.R. McClain, K.L. Carder, F. Müller-Karger, L. Harding, A. Magnuson, D. Phinney, G.F. Moore, J. Aiken, K.R. Arrigo, R. Letelier, and M. Culver, "Ocean color chlorophyll a algorithms for SeaWiFS, OC2 and OC4: Version 4." In: *SeaWiFS Postlaunch Calibration and Validation Analyses, Part 3*. NASA Tech. Memo. 2000-206892, Vol. 11, S.B. Hooker and E.R. Firestone, Eds., NASA Goddard Space Flight Center, Greenbelt, Maryland, 9-23.
- OEUVRE (Ocean Ecology: Understanding and Vision for REsearch) Workshop, Keystone, Colorado, 1-6 March, 1998.
- Officer, C. B., R. B. Biggs, J. L. Taft, L. E. Cronin, M. Tyler, and W. R. Boynton, 1984, "Chesapeake Bay anoxia: Origin, development and significance" *Science*, 223, 22-27.
- Pages, J. and F. Gadel, 1990, "Dissolved organic matter and UV absorption in a tropical hyperhaline estuary" *Sci. Total Environ.*, 99, 173-204.
- Palmer, K. F. and D. Williams, 1974, "Optical properties of water in the near infrared", *J. Opt. Soc. Am.* 64, 1107-1110.
- Pegau, W. S., and J. R. V. Zaneveld, 1993, "Temperature dependant absorption of water in the red and near-infrared portions of the spectrum", *Limnol. Oceanogr.*, 38(1), 188-192.
- Pelevin, V. N., and V. A. Rutkovskaya, 1977, "On the optical classification of ocean waters from the spectral attenuation of solar radiation", *Oceanology*, 17, 28-32.
- Petzold, T. J., 1972, "Volume scattering functions for selected ocean waters". No. Ref. 72-78, 79, *Scripps Inst. Oceanogr.*

- Piazena H., and D. P. Hader, 1997, "Penetration of solar UV and PAR into different waters of the Baltic Sea and remote sensing of phytoplankton", in: D.-P. Hader (Ed.), *The Effects of Ozone Depletion on Aquatic Ecosystems*, ch. 5, Environmental Intelligence Unit, Academic Press and R.G. Landes Company, Austin, TX, 1997, pp.45-96.
- Pienitz, R. and W. F. Vincent, 2000, "Effect of climate change relative to ozone depletion on UV exposure in subarctic lake". *Nature* 404, 484-487.
- Pope, R. M. and E. S. Fry, 1997, "Absorption spectrum (380-700 nm) of pure water. II. Integrating measurements", *Appl. Optics*, 36, 8710-8723.
- Preisendorfer, R. W., 1961, "Application of radiative transfer theory to light measurements in the sea", *Union Geod. Geophys. Inst. Monogr.*, 10, 11-30.
- Preisendorfer, R. W., 1976, "Hydrological Optics (6 volumes)", U.S. Dept. of Comm., NOAA, Honolulu, HA.
- Prieur, L. and S. Sathyendranath, 1981, "An optical classification of coastal and oceanic waters based on the specific spectral absorption curves of phytoplankton pigments, dissolved organic matter and other particulate materials", *Limnol. Oceanogr.*, 26(4), 671-689.
- Proctor, L. M., and J. A. Fuhrman, 1990, "Viral mortality of marine bacteria and cyanobacteria", *Nature*, 343, 60-62.
- Quickenden, T. I. and J. A. Irvin, 1980, "The ultraviolet absorption spectrum of liquid water", *J. Chem. Phys.* 72, 4416-4428.
- Ravisankar, M., A. T. Reghunath, K. Sathianandan, and V. P. N. Nampoore, 1988, "Effect of dissolved NaCl, MgCl₂ and Na₂SO₄ in seawater on the optical attenuation in the region from 430 to 630 nm", *Appl. Optics*, 27, 3887-3894.
- Roesler C. S., 1998, "Theoretical and experimental approaches to improve the accuracy of particulate absorption coefficients derived from the quantitative filter technique", *Limnol. Oceanogr.* 43(7), 1649-1660.
- Roesler, C. S., M. J. Perry, and K. L. Carder, 1989, "Modeling in situ phytoplankton absorption from total absorption spectra in productive inland marine waters", *Limnol. Oceanogr.*, 34(8), 1510.
- Sathyendranath, S., L. Lazzara, and L. Prieur, 1987, "Variations in the spectral values of specific absorption of phytoplankton", *Limnol. Oceanogr.*, 32(2), 403-415.
- Satlantic, 2000, "Operation Manual for the MicroPro", Revision D, June 2002
- Sawyer, W. R., 1931, "The spectral absorption of light by pure water and Bay of Fundy water", *Contrib. Can. Biol. Fisheries* 7, 75-89.

- Seliger, H. H., Boggs, J. A., and W. H. Biggley, 1985, "Catastrophic anoxia in the Chesapeake Bay in 1984", *Science*, 228: 70-73
- Sellner, K. G. and M. E. Kachur, 1987, "Phytoplankton: relationships between phytoplankton, nutrients, oxygen flux and secondary producers". *Ecological studies in the middle reach of Chesapeake Bay: Calvert Clis* (Heck, K. L., Jr., ed.). *Lecture Notes on Coastal and Estuarine Studies*, Springer-Verlag, New York, pp. 12-37.
- Seritti, A, L. Nannicini, R. Del Vecchio, P. Giordani, V. Balboni, and S. Miserocchi, 1997, "Optical properties of sediment pore waters of the Adriatic Sea", *Toxicol. Environ. Chem.* 61, 195-209.
- Siegel, D. A., M. Wang, S. Maritorena, and W. Robinson, 2000, "Atmospheric Correction for satellite ocean color imagery: the black pixel assumption", *Appl. Optics*, 39, 3582-3591.
- Smith R. C. and K. S. Baker, 1981, "Optical properties of the clearest natural waters (200- 800 nm)", *Appl. Optics*, 20, 177-184.
- Smith, R. C. and J. J. Cullen, 1995, "Effects of UV radiation on phytoplankton", *Reviews of Geophysics*, Supplement, 1211-1223.
- Smith, R. C. and K. S. Baker, 1978, "Optical classification of natural waters", *Limnol. Oceanogr.*, 23, 260-267.
- Sogandares F. M. and E. S. Fry, "Absorption spectrum (340-640 nm) of pure water. I. Photothermal measurements", *Appl. Opt.* 36, 8699-8709, 1997
- Sogandares F., Z. Qi, and E. S. Fry, 1991, "Spectral absorption of water", *Presentation at the Optical Society of America Annual Meeting*, San Jose, CA.
- Spinrad R. W., H. Glover, B. B. Ward, L. A. Codispoti, and G. Kullenberg, 1989, "Suspended particle and bacterial maxima in Peruvian coastal water during a cold water anomaly", *Deep-Sea Res.*, 36(5), 715.
- Stramski D. and A. Morel, 1990, "Optical properties of photosynthetic picoplankton in different physiological states as affected by growth irradiance", *Deep-Sea Res.*, 37, 245-266.
- Stramski, D. and D. A. Kiefer D.A., 1991, "Light scattering by microorganisms in the open ocean", *Prog. Oceanogr.*, 28, 343-383.
- Sugihara S., M. Kishino, and M. Okami, 1984, "Contribution of Raman scattering to upward irradiance in the sea", *Journal of the Oceanographic Society of Japan*, 40, 397-404.

- Sullivan, C. W., K. R. Arrigo, C. R. McLain, J. C. Cosimo, and J. Firestone, 1993, "Distributions of Phytoplankton Blooms in the Southern Ocean", *Science*, 262, 1832-1837.
- Sullivan, S. A., 1963, "Experimental study of the absorption in distilled water, artificial sea-water, and heavy water in the visible region of the spectrum", *J. Opt. Soc. Am.* 53, 962-968.
- Taft, J. L., W. R. Taylor, E.O. Hartwig, and R. Loftus, 1980, "Seasonal Oxygen Depletion in Chesapeake Bay", *Estuaries* 3(4): 242-247.
- Tam, A. C. and C. K. N. Patel, 1979, "Optical absorptions of light and heavy water by laser optoacoustic spectroscopy", *Appl. Optics* 18, 3348-3358.
- Tassan, S. and G. M. Ferrari, 1995, "An alternative approach to absorption measurements of aquatic particles retained on filters", *Limnol. Oceanogr.*, 40(8), 1358-1368.
- Tassan, S. and G. M. Ferrari, 2003, "Variability of light absorption by aquatic particles in the near-infrared spectral region", *Applied Optics*, Vol. 42, 24, 4802-4810
- Tuttle J. H., R. B. Jonas, and T. C. Malone, 1987, "Origin, development and significance of Chesapeake Bay anoxia", in *Contaminant Problems and Management of Living Chesapeake Bay Resources* (S. K. Majumdar, L. W. Hall and H. M. Austin, Eds.), Penn. Acad. Sci., Phillisburg, NJ, pp. 442-472
- Twardowski M. S., J. R. V. Zaneveld, and C. Moore, 2001, "In-water measurement of optical backscattering at three angles with the WET Labs ECOVSF", Department of Research, WET Labs, Inc.
- Vasilkov A. P., J. R. Herman, Z. Ahmad, B. G. Mitchell, and M. Kahru, 2003, "A model for the assessment of UV penetration into ocean waters from space-based measurements and full radiative transfer calculations", *SPIE Proceedings*, San Diego, CA, Aug 2003
- Vasilkov, A. P., J. R. Herman, N. A. Krotkov, G. Mitchell, and M. Kahru, 2002, "Problems of assessment of UV penetration into natural waters from space-based measurements", *Opt. Eng.*, 41 (12)
- Vodacek A., N. V. Blough, M. D. DeGrandepre, E. T. Peltzer, and R. K. Nelson, 1997, "Seasonal variation of CDOM and DOC in the Middle Atlantic Bight: Terrestrial inputs and photooxidation", *Limnol Oceanogr*, 42(4), 674-686.
- WETLabs, 2003 "AC-9 Plus User's Guide", Revision F 7 April 2003
- White, C., 1989, "Chesapeake Bay, Nature of the Estuary", Tidewater Publishers.
- Whitehead, R. F., S. de Mora, S. Demers, M. Gosselin, P. Monfort, and B. Mostajir, 2000, "Interactions of ultraviolet-B radiation, mixing, and biological activity on

photobleaching of natural chromophoric dissolved organic matter: A mesocosm study”, *Limnol Oceanogr*, 45(2), 278-291.

Whitlock C. H., L. R. Poole, J. W. Usry, W. M. Houghton, W. G. Witte, W. D Morris, and E. A. Gurganis, 1981, “Comparison of reflectance with backscatter and absorption parameters for turbid waters”, *App. Opt.* 20, 517-522

Yentch, C. S., 1962, “Measurement of visible light absorption by particulate matter in the ocean”, *Limnol. Oceanogr.*, 7, 207-217.

Yoder J. A., C. R. McLain, G. C. Feldman, and W. E. Esaias, 1993, “Annual Cycles of Phytoplankton Chlorophyll Concentrations in the Global Ocean: A Satellite View”, *Global Biogeochem. Cyc.*, 7, 181-193.

Zaneveld, J. R. V., J. C. Kitchen, and C. Moore, 1994, “The scattering error correction of reflecting-tube absorption meters”, *Ocean Optics XII. Proc. Soc. Photo-Opt. Instrum. Eng. (SPIE)*, 2258, 44-55.

Zhao, X. Z., Z. Lu, and E.S. Fry, 2002, “Absorption spectrum (300-700 nm) of pure water using an integrating cavity absorption meter”, *Proceedings Ocean Optics Meeting*, Santa Fe, NM.

Zibordi, G. and G. M. Ferrari, 1995, “Instrument self-shading in underwater optical measurements: experimental data”, *Appl. Optics*, 34(15), 2750-2754.